

**SEDIMENTOLOGY AND RESERVOIR
CHARACTERISTICS OF THE CARBONIFEROUS
JOGGINS FORMATION, NOVA SCOTIA, ATLANTIC
CANADA**

by

Trevor Brian Kelly

Submitted in partial fulfilment of the requirements
for the degree of Doctor of Philosophy

at

**Dalhousie University
Halifax, Nova Scotia
August 2022**

© Copyright by Trevor Brian Kelly, 2022

Dedication Page

I dedicate this work to my mother (Diane) and father (Brian). They provided me with the opportunities and freedoms to pursue my educational desires.

Table of Contents

List of Tables	ix
List of Figures.....	x
Abstract.....	xv
List of Abbreviations and Symbols Used	xvi
Acknowledgements	xix
Chapter 1: Introduction	1
1.1 Overview	1
1.2 Dissertation Structure.....	4
1.3 Research Objectives	5
1.3.1 Objective 1	5
1.3.2 Rationale for Objective 1	6
1.3.3 Objective 2	9
1.3.4 Rationale for Objective 2	10
1.3.5 Objective 3	11
1.3.6 Rationale for Objective 3	11
1.3.7 Objective 4	12
1.3.8 Rationale for Objective 4	13
1.4 Chapters and Author Contributions	14
1.4.1 Chapter 2 – Georeferencing Workflow	14
1.4.2 Chapter 3 – Outcrop Study near Coal Mine Point	15
1.4.3 Chapter 4 – GPR Geoforensic Study.....	16
1.4.4 Chapter 5 – Joggins GPR Study.....	17
1.4.5 Chapter 6 – Tidal Bundles Study	19
1.4.6 Chapter 7 – Cyclostratigraphy Study	19
1.5 Key Research Contributions and Innovations	20
1.5.1 Chapter 2 – Georeferencing Workflow	20
1.5.2 Chapter 3 – Outcrop Study near Coal Mine Point	21
1.5.3 Chapter 4 – GPR Geoforensic Study.....	22
1.5.4 Chapter 5 – Joggins GPR Study.....	23
1.5.5 Chapter 6 – Tidal Bundles Study	23
1.5.6 Chapter 7 – Cyclostratigraphy Study	24
1.6 Research Timeline.....	25
1.7 References Cited in Chapter 1	26

Chapter 2: Post-Scan Georeferencing of Lidar Data from a Geological Exposure Using ArcGIS™ for Adjustment.....	39
2.1 Abstract.....	39
2.2 Introduction.....	40
2.3 Previous Work.....	43
2.4 Study Area.....	45
2.5 Equipment and Methods.....	48
2.5.1 Terrestrial Laser Scanning.....	48
2.5.2 Global Positioning System.....	50
2.5.3 Georeferencing Targets.....	52
2.6 Data.....	53
2.6.1 Lidar/Target Setup Locations.....	53
2.6.2 Lidar Point Cloud.....	54
2.7 Processing Procedure.....	54
2.7.1 Data Preparation.....	54
2.7.2 Shapefile Creation.....	55
2.7.3 Point Decimation.....	61
2.7.4 Point Cloud Adjustment.....	63
2.8 Results.....	66
2.9 Discussion and Conclusions.....	68
2.10 Acknowledgments.....	69
2.11 References Cited in Chapter 2.....	70
Chapter 3: Analysis and Factors Influencing the Interpretation of a Digitally Examined Fluvial Meanderbelt System: Joggins Formation, Nova Scotia.....	75
3.1 Abstract.....	75
3.2 Introduction.....	76
3.3 Study Area.....	79
3.4 Geological Setting.....	80
3.5 Sedimentology and Stratigraphy.....	82
3.6 Methods.....	84
3.6.1 Terrestrial Laser Scanning.....	84
3.6.2 Global Positioning System.....	86
3.6.3 Portable Handheld Gamma Ray Spectrometer.....	88
3.6.4 Portable Handheld Air Permeameter.....	89
3.6.5 Digital Image Porosity Analysis.....	91

3.7	Errors and Uncertainty	92
3.7.1	Terrestrial Laser Scanning	92
3.7.2	Global Positioning System	93
3.7.3	Portable Handheld Gamma Ray Spectrometer.....	94
3.7.4	Portable Handheld Air Permeameter.....	94
3.7.5	Digital Image Porosity Analysis	95
3.8	Results and Discussion.....	96
3.8.1	Gamma Ray Logs.....	96
3.8.2	Net-To-Gross (NTG) – Scaling Gamma Ray Log	100
3.8.3	Permeability	101
3.8.4	Porosity – Digital Analysis	104
3.8.5	Architectural Element Variability and Reservoir Connectivity	106
3.8.6	Quantitative Data Summary and Discussion.....	109
3.8.7	Geobody Analysis	114
3.8.8	Outcrop to Core Correlation.....	116
3.8.9	Drill Core Analysis.....	119
3.9	Conclusions	123
3.10	Acknowledgments.....	125
3.11	References Cited in Chapter 3	125
Chapter 4:	A Novel Approach to 3D Modelling Ground-Penetrating Radar (GPR) Data – A Case Study of a Cemetery and Applications for Criminal Investigation.....	135
4.1	Abstract.....	135
4.2	Introduction	136
4.3	Study Area and Site Characterization	139
4.4	Burial Practices and Decomposition Rates	142
4.5	Geological Background.....	144
4.5.1	Surficial Geology	144
4.5.2	Bedrock Geology.....	147
4.6	Equipment and software.....	148
4.6.1	Ground-Penetrating Radar.....	148
4.6.2	EKKO_Project™ GPR Software	150
4.6.3	Petrel™ E & P Software	150
4.7	Fieldwork and Survey Area	151
4.8	Data Processing	152
4.9	Model Building and Results	153
4.10	Discussion.....	168

4.11	Conclusions	175
4.12	Acknowledgements.....	176
4.13	References Cited in Chapter 4	176
Chapter 5: The Technical Challenges of Ground-Penetrating Radar: A Case Study from the Joggins Formation, Joggins, Nova Scotia.....187		
5.1	Abstract.....	187
5.2	Introduction	188
5.3	Study Area	192
5.4	Geological Background.....	194
5.4.1	Overburden Geology.....	194
5.4.2	Bedrock Geology	195
5.5	Equipment and Methods	198
5.6	Survey Area	204
5.7	Results	209
5.7.1	Processed Radargrams	209
5.7.2	Radar Reflectors.....	209
5.8	Discussion.....	217
5.9	Conclusions	229
5.10	Acknowledgments.....	231
5.11	References Cited in Chapter 5	231
Chapter 6: Episodic Marine Incursions Support a Late Carboniferous Mid-Euramerican Seaway: An Example from the Joggins Formation238		
6.1	Abstract.....	238
6.2	Introduction	239
6.3	Geological Setting.....	245
6.4	Dataset.....	247
6.5	Methods.....	249
6.5.1	Data Collection.....	249
6.5.2	Fast Fourier Transform Analysis.....	250
6.5.3	Continuous Wavelet Transform (Morlet) Analysis.....	251
6.6	Results	252
6.6.1	Tidal Rhythmite Intervals.....	252
6.6.2	Visual Cyclicity Analysis.....	254
6.6.3	Fast Fourier Transform Cyclicity Analysis.....	260

6.6.4	Continuous Wavelet Transform Cyclicity Analysis.....	261
6.7	Discussion.....	265
6.7.1	Comparison with Carboniferous Examples.....	266
6.7.2	Visual Cyclicity Analysis.....	267
6.7.3	Fast Fourier Transform Cyclicity Analysis.....	269
6.7.4	Continuous Wavelet Transform (Morlet) Analysis.....	270
6.7.5	Comparison to Modern Analogues	271
6.8	Conclusions	272
6.9	Acknowledgements.....	273
6.10	References Cited in Chapter 6	274
Chapter 7:	Uncovering the Milankovitch Record from a Late Carboniferous Cyclothem Succession in Paleoequatorial Euramerica	284
7.1	Abstract.....	284
7.2	Introduction	285
7.3	Geological Setting.....	290
7.4	Dataset.....	291
7.5	Methods.....	294
7.5.1	Palynology.....	294
7.5.2	Data Preprocessing.....	296
7.5.3	Fast Fourier Transform Analysis.....	297
7.5.4	Continuous Wavelet Transform Analysis	297
7.6	Results	299
7.6.1	Data Preprocessing.....	299
7.6.2	Fast Fourier Transform Cyclicity Analysis.....	300
7.6.3	Continuous Wavelet Transform Cyclicity Analysis.....	302
7.7	Discussion.....	304
7.8	Conclusion.....	310
7.9	Acknowledgements.....	311
7.10	References Cited in Chapter 7	311
Chapter 8:	Conclusions	322
8.1	Manuscript 1: Chapter 2 – Georeferencing Workflow.....	325
8.2	Manuscript 2: Chapter 3 – Outcrop Study near Coal Mine Point	326
8.3	Manuscript 3: Chapter 4 – GPR Geoforensic Study	328
8.4	Manuscript 4: Chapter 5 – Joggins GPR Study	329

8.5 Manuscript 5: Chapter 6 – Tidal Bundles Study	332
8.6 Manuscript 6: Chapter 7 – Cyclostratigraphy Study	333
8.7 Summary	335
8.8 References cited in Chapter 8	337
References	340
Appendix A: Copyright Release Letters and Responses	386
Appendix B: Processed Radargrams Supporting Chapter 4 – GPR Geoforensic Study	396
Appendix C: Processed Radargrams Supporting Chapter 5 – Joggins GPR Study	411
Appendix D: Drill Core Images of Borehole REI-B2-1	433
Appendix E: Drill Core Description of Borehole REI-B2-1	448
Appendix F: Drill Core Photography Gantry/Apparatus.....	470
Appendix G: Tidal Rhythmite (Bundles) Thickness Measurements used in Chapter 6	475
Appendix H: Correlation between the REI-B2-1 Borehole and the Outcrop using Major Coal Seams	499
Appendix I: Maps Showing the Major Coal Mines in the Joggins Area	501
Appendix J: Hand Sample Descriptions	504
Appendix K: Thin Section Descriptions (Mineralogy)	513
Appendix L: Thin Section Descriptions (Porosity)	530
Appendix M: Measured Sections near Coal Mine Point.....	554

List of Tables

Table 3.1: Permeability ranking.....	91
Table 3.2: Porosity ranking.....	92
Table 3.3: Average gamma ray measurements within the area scanned by lidar	97
Table 3.4: Gamma ray measurements from eight hand samples	100
Table 3.5: Air permeameter values with their corresponding permeability value.....	102
Table 3.6: Calculated average porosity, cement, and grain area values based on image analysis.....	104
Table 3.7: Summary of the measurements and descriptions completed in the study area.....	112
Table 3.8: Summary of the geobody number, geobody type, width, and thickness as measured from Figure 3.19.....	116
Table 3.9: Summary of coal seam intervals and thicknesses from borehole and outcrop.	117
Table 4.1: Representative soil profile for the study area	145
Table 4.2: Summary of the soil profile at the study area	147
Table 5.1: Summary table of GPR system setup parameters.....	201
Table 5.2: A summary of the 42 GPR lines collected at Joggins.	207
Table 6.1: Summary of tidal rhythmite intervals.	254
Table 6.2: Statistical analysis from the three tidal rhythmite sequences.	256
Table 6.3: Summary of tidal rhythmite interval cyclicity analysis results.	265
Table 7.1: Summary of core samples sent for palynological analysis.....	296
Table 7.2: Summary of palynostratigraphic results	296
Table 7.3: Statistics for various frequencies, including the four major orbital periods.	302
Table 8.1: A summary of the equipment/methods, software, and resulting innovations/contributions for each chapter of this dissertation.	323

List of Figures

Figure 1.1: An illustration of the basin to grain scale of geologic visualization with the methods utilized for this research under each.....	4
Figure 1.2: The scale of measurement of a reservoir that can be measured and interpreted using various techniques.	7
Figure 1.3: An example of the outcrop to flow simulation workflow	9
Figure 1.4: An example of data integration for the outcrop and behind the outcrop characterization.....	11
Figure 1.5: Timeline of my research with an emphasis on major milestones achieved.	25
Figure 2.1: A NASA JPL library spectroscopy solid sample data.....	42
Figure 2.2: Using successive, georeferenced lidar point clouds over some time	43
Figure 2.3: Location maps of the Joggins Formation study area.	47
Figure 2.4: A photograph of the Optech ILRIS-3D lidar scanner setup.....	49
Figure 2.5: Simplified sketch of the global positioning system equipment.....	51
Figure 2.6: Images of the utilized georeferencing targets.....	53
Figure 2.7: Unaltered and altered raw lidar intensity data.....	55
Figure 2.8: The creation of a shapefile from a text document.	56
Figure 2.9: A screen capture from ArcCatalog™ showing the newly created shapefile.....	57
Figure 2.10: Point clouds based on a single colour and on intensity.....	58
Figure 2.11: Locating the false georeferencing target locations from the intensity-based point cloud.	59
Figure 2.12: A table displaying the correct locations of the three georeferencing targets.....	60
Figure 2.13: The three shapefiles created and displayed.	61
Figure 2.14: The selection of erroneous points from the point cloud.....	62
Figure 2.15: The preparation of the point cloud for adjustment.	63
Figure 2.16: The transformation of the point cloud data to its proper location.	64
Figure 2.17: An image showing the adjusted point cloud and false georeferencing target locations.....	65
Figure 2.18: The updated attribute table showing the four new columns.....	66
Figure 2.19: Petrel™ E & P Software screen capture showing the point-decimated, fully georeferenced point cloud.....	67

Figure 2.20: Petrel E & P Software screen capture showing a view looking along the cliff face from the north.....	68
Figure 2.21: Petrel™ E & P Software screen capture showing a view looking down the cliff face from the north to the south	68
Figure 3.1: Schematic illustration showing the stacked, aggrading channel systems of the Joggins Formation and associated elements.....	77
Figure 3.2: The Joggins Formation outcrop.....	79
Figure 3.3: Digital photograph of the section of Joggins Formation scanned by lidar.	80
Figure 3.4: The extent of the Maritimes Basin of Eastern Canada showing the onshore distribution of Carboniferous to Permian outcrops.....	81
Figure 3.5: Simplified plan view showing the Joggins Fossil Cliffs geology	82
Figure 3.6: An image of the Optech ILRIS-3D lidar scanner setup.	85
Figure 3.7: Simplified sketch of the global positioning equipment.....	87
Figure 3.8: The permeability calibration chart	91
Figure 3.9: The location of spectrometer measurements along the studied section.	98
Figure 3.10: Measured section with gamma ray (red) and NTG (blue) curves	99
Figure 3.11: Values as from Table 3.5 plotted with the rank	103
Figure 3.12: Schematic illustration representing a cross-laminated or cross-bedded sandstone	104
Figure 3.13: Photomicrographs of thin section GW102-2013TK-1.	105
Figure 3.14: Photomicrographs of thin section GW106-2013TK-6.	105
Figure 3.15: The variation in calculated porosity for each thin section.....	106
Figure 3.16: The generated point cloud cliff section viewed from the West.....	108
Figure 3.17: Close-up view of the generated digital point cloud looking from the West.	108
Figure 3.18: Close-up view of the generated digital point cloud looking from the West showing numerous interpreted features.....	109
Figure 3.19: The lidar generated point cloud of the Joggins Formation outcrop viewed from the West.....	114
Figure 3.20: The generated point cloud section viewed from the West showing fluid flow lines in white.	116
Figure 3.21: A correlation of major coal seams between the REI-B2-1 borehole and the outcrop	119
Figure 3.22: Representative core photographs of the Joggins Formation.	121
Figure 3.23: Representative core photographs of the Joggins Formation.	122

Figure 4.1: Overview of study location.	140
Figure 4.2: Plan view sketch of the study area	141
Figure 4.3: A graph showing the total precipitation and mean temperature.....	141
Figure 4.4: Soil profile and bedrock geology maps of the study area.	146
Figure 4.5: A typical GPR cart setup	149
Figure 4.6: Close-up view of the study location, indicating grave site locations	151
Figure 4.7: A series of 2D depth slices showing reflectivity amplitude.....	155
Figure 4.8: Various ways previous 3D models have been displayed	156
Figure 4.9: A 3D render of the model created from the GPR data.	157
Figure 4.10: Depth slices and cross sections from the 3D model.	158
Figure 4.11: An example showing results from the north to south oriented line 13.....	160
Figure 4.12: An example showing results from the north to south oriented line 19.....	162
Figure 4.13: An example showing results from the north to south oriented line 27.....	163
Figure 4.14: An example showing results from the east to west oriented line 32.	165
Figure 4.15: An example showing results from the west to east trending line 35.....	167
Figure 4.16: An example showing results from the east to west trending line 40.....	168
Figure 4.17: Theoretical geological model for a GPR imaged grave	172
Figure 4.18: A generalized workflow for this case study	174
Figure 5.1: Location map of Joggins, Nova Scotia.....	193
Figure 5.2: Uninterpreted and interpreted images of the Joggins Formation study area.....	195
Figure 5.3: Map of the onshore/offshore regional Maritimes Basin.....	197
Figure 5.4: Plan view showing the Carboniferous Joggins Fossil Cliffs geology	198
Figure 5.5: The overall GPR SmartCart setup.	200
Figure 5.6: Sketch of the global positioning system equipment.....	202
Figure 5.7: A satellite image of the study area showing GPR line locations.....	205
Figure 5.8: A plan view sketch of the study area showing the GPR lines in relation to surficial features	206
Figure 5.9: Representative images of the four GPR survey areas.	208
Figure 5.10: Radargrams for lines 09 to 18 inclusive.....	212
Figure 5.11: Radar reflectors identified in the 42 radargrams from Joggins.	216
Figure 5.12: Uninterpreted and interpreted radargrams of lines 31 and 37	218
Figure 5.13: Uninterpreted and interpreted radargrams of lines 31 and 43	219

Figure 5.14: Uninterpreted and interpreted radargrams of lines 09 and 13	220
Figure 5.15: Uninterpreted and interpreted radargrams of lines 18 and 23	221
Figure 5.16: Uninterpreted and interpreted radargrams of lines 10 and 32	222
Figure 5.17: Uninterpreted and interpreted radargrams of lines 27 and 39	223
Figure 5.18: Uninterpreted and interpreted radargrams of lines 29 and 31	223
Figure 5.19: Uninterpreted radargrams of lines 19 and 20	224
Figure 5.20: Uninterpreted and interpreted radargrams of lines 14 and 26	224
Figure 5.21: Uninterpreted and interpreted radargram of line 30	225
Figure 5.22: Uninterpreted and interpreted radargrams of lines 45 and 46	226
Figure 5.23: Uninterpreted and interpreted radargram of line 25	226
Figure 5.24: Uninterpreted and interpreted radargrams of lines 09 and 10	227
Figure 6.1: Late Carboniferous position, present-day location map, and stratigraphic position of the study area	244
Figure 6.2: Carboniferous sketch of equatorial Euramerica	246
Figure 6.3: Simplified lithology, stratigraphy, and geophysical borehole log curves for the Joggins Formation interval of the examined borehole	248
Figure 6.4: Representational flow diagram emphasizing the quantitative techniques used in this study.	250
Figure 6.5: Visual cyclicity analysis results of core interval TR1	257
Figure 6.6: Visual cyclicity analysis results of core interval TR2	258
Figure 6.7: Visual cyclicity analysis results of core interval TR3	259
Figure 6.8: Lamina thickness histograms and accompanying periodograms for intervals TR1, TR2, and TR3.	260
Figure 6.9: Scalograms of interval TR1	262
Figure 6.10: Scalograms of interval TR2	263
Figure 6.11: Scalograms of interval TR3	264
Figure 7.1: Present-day location map, stratigraphic position, and position of the study area	289
Figure 7.2: Carboniferous reconstruction of equatorial Euramerica	292
Figure 7.3: Stratigraphy, simplified lithology, and geophysical borehole log curves for the studied borehole.	293
Figure 7.4: Schematic diagram emphasizing the quantitative methods used	299
Figure 7.5: Plots relating to the preprocessing of REI-B2-1 borehole gamma ray geophysical log	300
Figure 7.6: The FFT analysis of the borehole gamma ray geophysical log	301

Figure 7.7: The scalogram of the gamma ray geophysical log	303
Figure 7.8: A plot of the maximum module values for the Morlet wavelet coefficients.....	303
Figure 7.9: Plots of Morlet wavelet coefficients at the scales of $\alpha = 25$ and $\alpha = 100$	304
Figure 8.1: A summary of the basin to grain scale concept of visualization.	324

Abstract

Reservoir characterization has experienced significant changes within the energy industry due to technological innovation and computerization, but challenges remain, particularly with understanding reservoir compartmentalization and fluid flow. These challenges impact energy diversification and security on the pathway to achieving carbon neutrality through secondary recovery, CCS, geothermal, and geostorage. The SPE Research & Development Committee has identified five challenges the energy industry must resolve for further advancement. This dissertation investigates three of the five challenges through integration of outcrop and subsurface data from the Late Carboniferous Joggins Formation: (1) higher resolution subsurface imaging, (2) increasing recovery factors, and (3) carbon capture, utilization, and storage. This research defines stratigraphy, geobodies, architectural elements, and baffles and barriers to fluid flow, using shallow subsurface geophysical techniques (GPR and lidar) for reservoir outcrops at the well to seismic scale. Methodology developed from analogous studies in geoforensics using GPR and subsequent 3D renderings allows the delineation of shallow subsurface objects and is transferrable to the high-resolution delineation of architectural elements within geobodies. This dissertation documents for the first time Late Carboniferous tidal rhythmite intervals in the Joggins Formation, providing support for a mid-Euramerican seaway connecting to the Paleo-Tethys Ocean and demonstrating deposition in a semi-diurnal tidal model with a lunar monthly tidal cycle. The identification of these tidal processes and depositional environments through high-resolution Fourier transform analysis is an example that delineates the fine-scale baffles and barriers to fluid flow for reservoir characterization studies. Well-log data identified spectral peaks in an interval of the Joggins Formation corresponding to the four main orbital periods (400 kyr, 100 kyr, 40 kyr, and 20 kyr) of Milankovitch cyclicity with a ratio of 18.99:5.15:2.02:1. The identification of cyclic occurrences influencing deposition can facilitate stratigraphic correlation and high-resolution reservoir characterization.

List of Abbreviations and Symbols Used

α	scale
f	frequency
k	permeability, md
$k_{(v)}$	permeability (vertical), md
$k_{(hpar)}$	horizontal permeability (parallel to strike), md
$k_{(hper)}$	horizontal permeability (perpendicular to strike), md
kyr	thousand years
Φ	porosity
2D	two-dimensional
3D	three-dimensional
API	American Petroleum Institute
CALI	caliper log
CMP	common mid-point
cps	counts per second
CWT	continuous wavelet transform
dB/m	decibels per metre
DGPS	differential global positioning system
DVL	digital video logger
ERT	electrical resistivity tomography
FFT	fast Fourier transform
f.g.	fine grained
GPR	ground-penetrating radar

GR _{sand cutoff}	sand cutoff gamma ray value, counts per second (cps)
GR _{shale cutoff}	shale cutoff gamma ray value, counts per second (cps)
GR _{value}	gamma ray value, counts per second (cps)
ILRIS	Intelligent Laser Ranging and Imaging System
kHZ	kilohertz
lidar	light detection and ranging
md	millidarcies
m.g.	medium grained
mHZ	megahertz
Myr	million years
NAD	North American Datum
nm	nanometres
NPHI_SAN	neutron porosity-sandstone
ns	nanoseconds
NTG	net-to-gross ratio
ps	picoseconds
REI	Resource Enterprises Incorporated
RHOB	bulk density log
RR	radar reflector
RTK	real-time kinematic
SEC	Spreading and Exponential Compensation
sst	sandstone
TR	tidal rhythmite

TWT	Two-way travel time
UNESCO	United Nations Educational, Scientific and Cultural Organization
UTM	Universal Transverse Mercator
v.f.g	very fine grained

Acknowledgements

I want to thank my supervisor and committee members, Professor Grant Wach, Adjunct Professor Tom Martel, and Professor Adam Donaldson. I want to thank them for the opportunity and encouragement to pursue this research. I would also like to thank my external examiner, Shane Tyrrell, from the National University of Ireland, Galway. He provided a thorough examination and provided excellent feedback and comments.

Finally, I must express my sincere appreciation to my family for encouraging me throughout these past years. Thank you!

Chapter 1: Introduction

1.1 Overview

Joggins is world-renowned for its Carboniferous-aged exposures and unique fossil assemblages, but it is also an exemplary location in the surface and subsurface for studying reservoir characterization in fluvial and non-marine settings. This location offers a continuous, macroscopic view of Carboniferous sedimentation. It is easily accessible, which makes it ideal for conducting numerous outcrop measurements. In addition, the outcrop allows for the visualization of lateral facies changes and large-scale sedimentary features. This outcrop can be correlated to subsurface well and core data.

Reservoir characterization has recently experienced considerable change involving the technological progression within the energy resources industry and the expanding presence of computerized devices and equipment. Upcoming challenges will influence energy diversification and energy security, which will steer towards the goals of attaining carbon neutrality through CCS, geothermal, and geostorage, and warrant an additional understanding of reservoirs and fluid movement within them.

The SPE Research & Development Committee has established five challenges the energy resources industry needs to address for increased improvement. These five challenges are: 1) higher resolution subsurface imaging, 2) challenges in reusing produced water, 3) in-situ molecular manipulation, 4) increasing recovery factors, and 5) carbon capture, utilization, and storage (SPE Research & Development Committee 2012). This dissertation helps resolve three of the five challenges through the innovative application of outcrop and subsurface data from the Late Carboniferous Joggins Formation, used as a case study (Figure 1.1). The three challenges addressed are: (1) higher resolution subsurface

imaging, (2) increasing recovery factors, and (3) carbon capture, utilization, and storage (SPE Research & Development Committee 2012). The research will also add to the volume of work already on the sedimentology (e.g., Davies et al. 2005; Rygel 2005) aspects of the Joggins Formation with new insights provided through the application of new techniques for the study of the well-known outcrop and the lesser-known drill core. The research objectives will be discussed later on in further detail.

The Joggins Formation sediments are gently dipping and exposed approximately 3 km along Chignecto Bay in the Bay of Fundy of northwestern Nova Scotia. The Joggins Formation is heralded as being one of the world's best, if not the best, example of a coal-bearing Pennsylvanian-aged (Late Carboniferous) succession with abundant fossils, 76 coal seams, and 63 forested horizons exhibiting upright lycopsid trees that reach 5-6 m in height (Davies et al. 2005). The formation has been studied for nearly two centuries and still garners the attention of inquisitive researchers to this day. The majority of the research can be arranged into one of three distinct categories: 1) geology (e.g., geomorphology, mineralogy, petrology, sedimentology, stratigraphy, and tectonics), 2) paleobiology (e.g., discovery, micropaleontology, paleobotany, paleoecology, paleoichnology, and taxonomy), and 3) paleoenvironmental studies, which considers the first two categories (Grey and Finkel 2011).

Geology-based studies have been plentiful over the years, with research spanning the basin scale to the grain scale (e.g., Bell 1912; Copeland 1959; Scott 1998; Hower et al. 2000; Davies and Gibling 2003; Rygel et al. 2004; Calder et al. 2005; Davies et al. 2005; Rygel 2005; Rygel and Shipley 2005; Waldron and Rygel 2005; Gibling 2006; Rygel and Gibling 2006; Rafuse and Wach 2011; Wong 2014; Ielpi et al. 2015; Kelly and Wach 2020, 2021; Kelly et al. 2021a).

The Joggins succession has produced in excess of 200 fossilized species ranging the entire food web of the terrestrial realm (Grey and Finkel 2011). The research completed on the Joggins Formation in terms of paleobiology has produced an abundance of publications coming from these discoveries (e.g., Carroll 1967; Godfrey et al. 1991; Archer et al. 1995b; Reisz and Modesto 1996; Holmes et al. 1998; Falcon-Lang et al. 2004; Hebert and Calder 2004; Falcon-Lang 2005; Tibert and Dewey 2006; Keighley et al. 2008; Holmes and Carroll 2010; Utting et al. 2010; Stimson et al. 2012; Tanner 2013; Tibert et al. 2013; Prescott et al. 2014; Zatoń et al. 2014; Carpenter et al. 2015; Buhler and Grey 2017; Faulkner et al. 2017; Prokop et al. 2017; Bingham-Koslowski et al. 2018; King and Stimson 2018; Pardo and Mann 2018; King et al. 2019; Chipman et al. 2020; Maddin et al. 2020; Mann et al. 2020).

Paleoenvironmental studies have made use of both geological and paleobiological data to discern the biological, chemical, and physical environment of the ecosystem at the time of deposition during the Carboniferous Period (e.g., Calder et al. 2006; Falcon-Lang et al. 2006; DiMichele and Falcon-Lang 2011; Grey et al. 2011). A synopsis of the investigations performed on the Joggins Formation and nearby conformable strata can be found within Falcon-Lang (2006) and Grey and Finkel (2011).

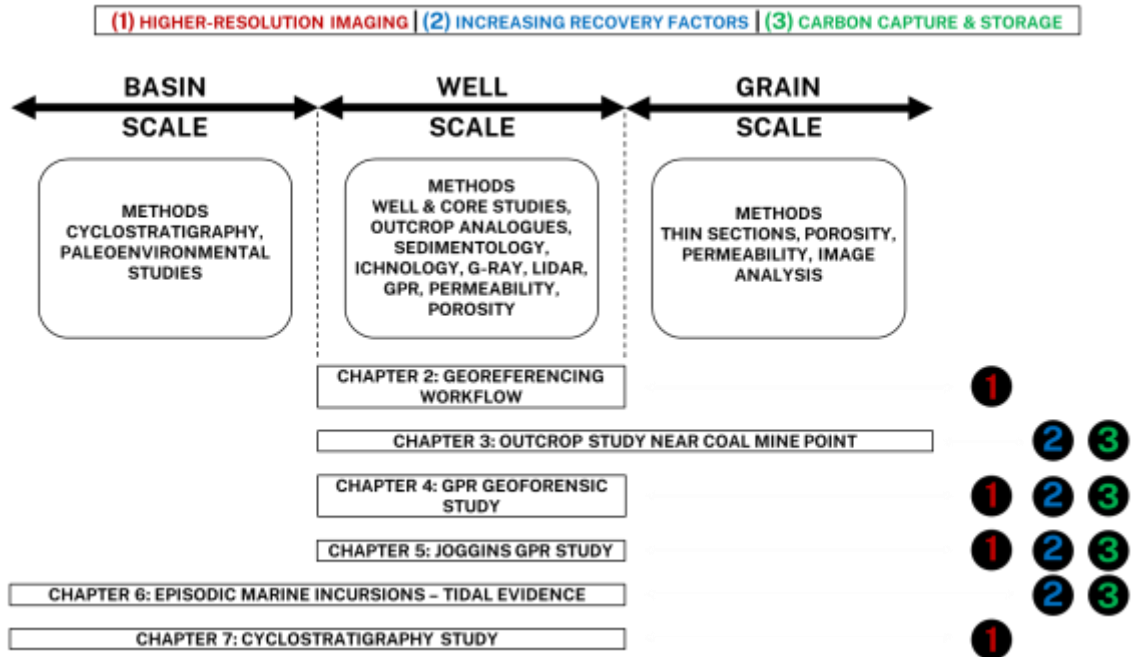


Figure 1.1: An illustration of the basin to grain scale of geologic visualization with the methods utilized for this research under each. The six chapters of this dissertation can be related to one or more of the visualization scales. The chapters can also be related to one or more of the research challenges highlighted by the SPE Research and Development Committee.

1.2 Dissertation Structure

This dissertation is presented as a collection of published manuscripts, bounded by an introductory chapter and a concluding chapter. This research takes advantage of numerous types of geological measuring equipment capabilities as well as diamond drill core, which has been primarily overlooked in past studies pertaining to the Joggins Formation in favour of the outcrop section.

The introductory chapter provides preliminary background information that puts this research in context, clarifies the focus of this study, points out the value, and specifies the specific research aims and objectives. Six research manuscripts comprise the dissertation work and are presented with the methodology papers first, which are grouped as the high-resolution outcrop characterization and geobody analysis papers. The composition of these individual manuscripts follows that typically applied in academia, with sections such as an

abstract, introduction, methods, results, discussions, and conclusions. The conclusions chapter summarizes the main findings of the work, places this work in the context of ongoing research concerning the Joggins Formation and suggests opportunities for further research building on this work. This section also provides the research objectives (a summary of your findings and the resulting conclusions), recommendations, and contributions to knowledge. As there is no set template for the references section, this dissertation follows a similar format to the more recent theses by Campbell (2011) and Allen (2016). Therefore, each chapter contains a list of references cited, with the master reference list for all chapters located after Chapter 8. The reference format for this dissertation follows a slightly modified version of the Canadian Journal of Earth Sciences reference format.

1.3 Research Objectives

The focus of this study is the Late Carboniferous strata of the Joggins Formation, with research that is applicable to three of the five challenges identified by the SPE Research & Development Committee (2012): (1) higher resolution subsurface imaging, (2) increasing recovery factors, and (3) carbon capture, utilization, and storage. This body of work will also add to the large volume of work concerning the sedimentology of the Joggins Formation with new insights provided through the study of the outcrop and drill core.

1.3.1 Objective 1

To integrate data from a ground-based localized lidar survey, a portable handheld spectrometer, an air permeameter, and porosity measurements from thin sections to develop the characteristics of key components impacting the reservoir. The scale of investigation

for the study is from the grain to the basin (Figure 1.2), particularly the digital analysis of geobodies within the fluvial meanderbelt system preserved in outcrop.

1.3.2 Rationale for Objective 1

Fluvial and non-marine reservoir systems form important producing and storage reservoirs, but often exhibit stratal complexities that compartmentalize the reservoir creating reservoir heterogeneity that impacts fluid flow and reservoir performance. In the energy resources industry, it is common to undertake comprehensive outcrop studies and apply the analogous outcrop data and results to a subsurface reservoir that is substantially more complicated and costly to obtain measurements directly. North and Prosser (1993) recognized the distribution and flow of reservoir fluids are regulated by the depositional system architecture and the internal structure and geometry of sedimentary features. The architectural variability and geological discontinuities need to be recognized to characterize the reservoir and understand and predict the distribution and flow of reservoir fluids. Only the larger-scale architectural elements are resolved from seismic imaging, while borehole data offers a higher resolution view but is typically too widely spaced within a reservoir (North and Prosser 1993; Figure 1.2). Hence, subsurface data is commonly incomplete regarding the spatial and architectural relationships of sandstone geobodies (e.g., van Lanen et al. 2009). This can produce highly interpretive geological models of subsurface reservoirs that may not be representative examples of the actual reservoir (van Lanen et al. 2009).

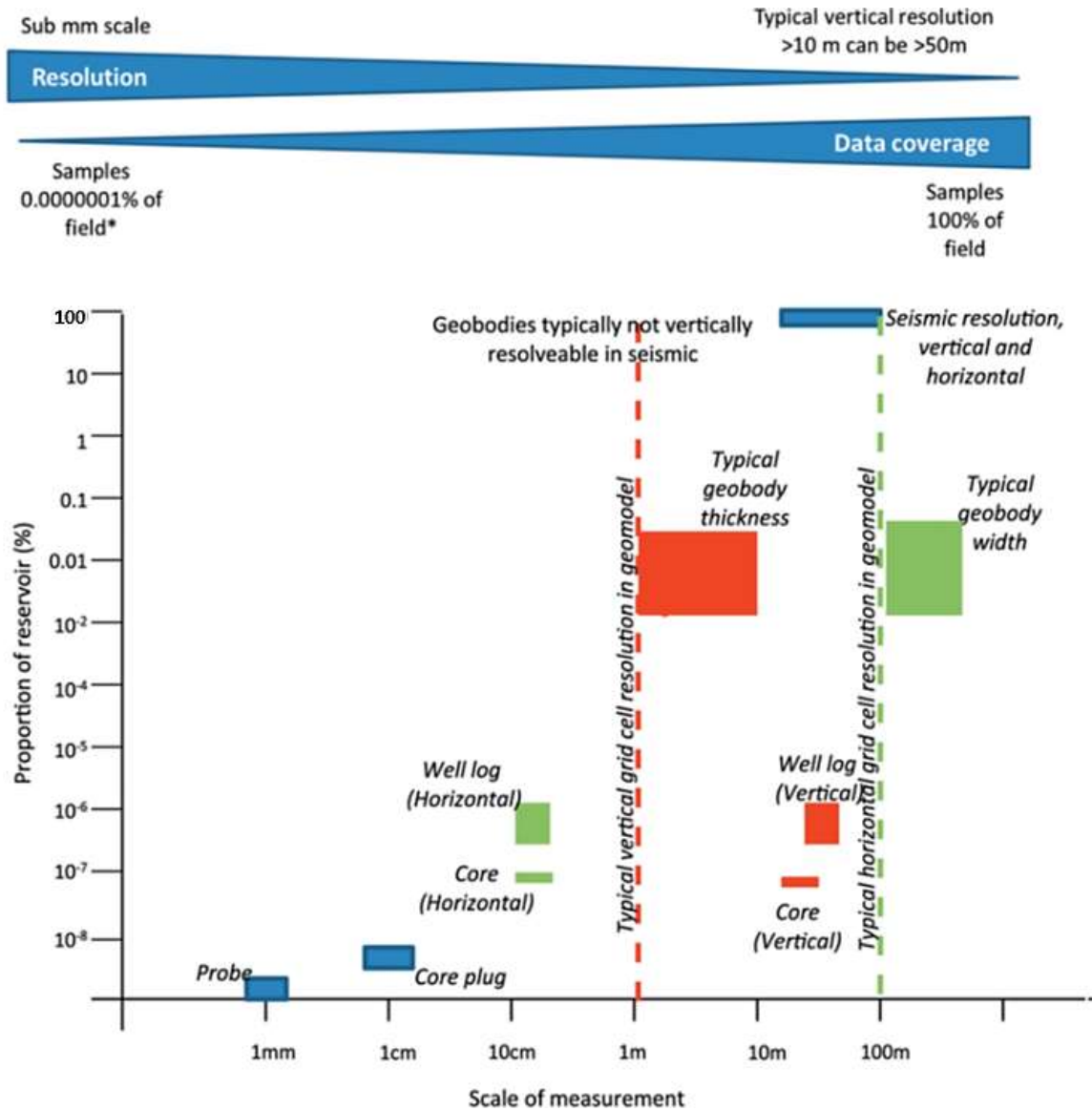


Figure 1.2: The scale of measurement of a reservoir that can be measured and interpreted using various techniques. While core and log data are high-resolution, they are only valid for a small percentage of the reservoir. Seismic has the capability of imaging the entire reservoir but lacks the resolution necessary to capture the geometry of geobodies (Howell et al. 2014).

To address the knowledge deficit in subsurface reservoir architecture, it becomes necessary to study modern analogues and ancient analogues from geological outcrops (e.g., Davies et al. 1992; Grammer et al. 2004). Depositional environments with similar traits to subsurface reservoirs over a wide range of scales (seismic to well) provide three-dimensionality and data continuity. Improvements in outcrop research have increased the cost-effectiveness and volume of data that can be compiled by means of portable digital

field equipment, such as a differential global positioning system with a stationary terrestrial (ground-based) laser scanner for the rapid acquisition of spatial data, for example (e.g., Bellian et al. 2005; Pringle et al. 2006; Buckley et al. 2010; Hodgetts 2013; Rarity et al. 2014; Figure 1.3).

Digital field methods used to study outcrops have been increasingly gaining traction as geoscientists recognize and acknowledge the benefits of these techniques, either as standalone techniques or incorporated with other digital field techniques (e.g., portable handheld spectrometer and air permeameter) and traditional field techniques (e.g. outcrop measurement logging and thin section analysis). Studies that have examined the most effective way to capture, visualize, and quantify the data from digital field techniques include Bellian et al. (2005); Enge et al. (2007); Buckley et al. (2008); Hodgetts (2013); Hartzell et al. (2014); Howell et al. (2014). Digital field techniques can also include those relating to structural and sedimentological analyses (e.g., Bellian et al. 2007; Labourdette and Jones 2007; Fabuel-Perez et al. 2009a; Rotevatn et al. 2009; van Lanen et al. 2009; Fabuel-Perez et al. 2010; Keogh et al. 2014; Minisini et al. 2014; Casini et al. 2016; Alhumimidi et al. 2017). Howell et al. (2014) provides an example whereby an outcrop is used to construct a reservoir model and subsequent fluid flow model using lidar (Figure 1.3).

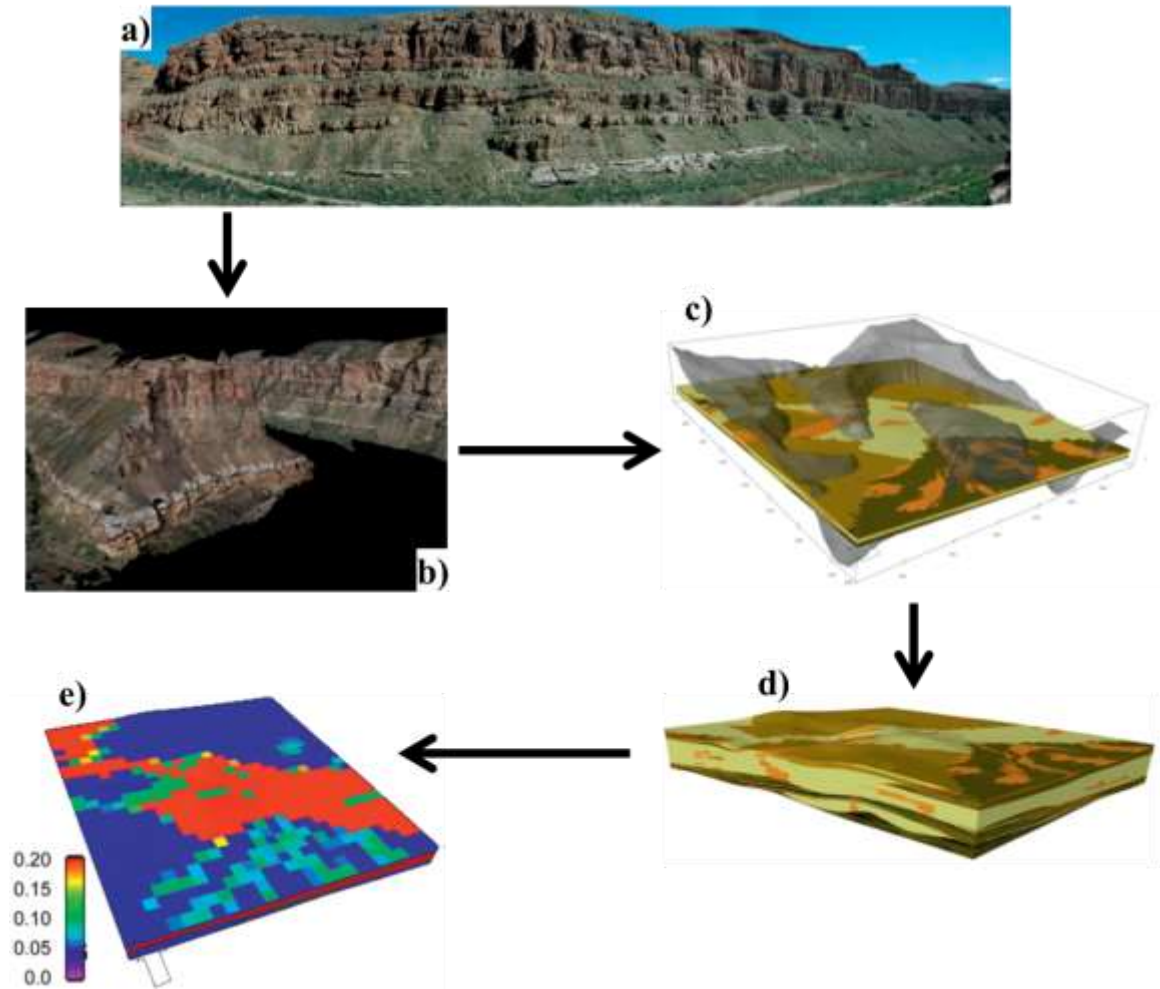


Figure 1.3: An example of the outcrop to flow simulation workflow (modified from Howell et al. 2014). (a) A photograph of the Cretaceous Blackhawk Formation outcrop as seen in Woodside Canyon, eastern Utah. (b) The lidar point cloud of the Blackhawk Formation outcrop. (c) A reservoir model of the outcrop depicting the non-marine section with the light grey representing the terrain surface. (d) The non-marine deposits modelled with yellow, green, black, and orange representing channel sandstone, overbank deposits, coal, and crevasse splay deposits, respectively. (e) The fluid simulation model with colours representing different scales of fluid saturation.

1.3.3 Objective 2

To provide subsurface imaging of the Joggins Formation using ground-penetrating radar (GPR) which would allow for the future construction of an empirical 3D sandstone reservoir model complete with geobodies and architectural elements suitable for fluid flow simulation.

1.3.4 Rationale for Objective 2

The recovery of hydrocarbons and sequestration and storage of carbon dioxide is improved through the use of geostatistically and geometrically accurate descriptions of siliciclastic reservoir flow units and permeability barriers within a reservoir partition (McMechan and Soegaard 1998). Realistic computer models, based exclusively on gathered outcrop data, have been used to enhance and define reservoir geometries and distributions of reservoir properties for use in simulation and locating extraction and injection wells for hydrocarbons and other fluids (e.g., Bryant and Flint 1993; Kerans et al. 1994; Pranter et al. 2007; Jones et al. 2008; Boro et al. 2014; Pranter et al. 2014; Siddiqui et al. 2018).

The issue with these models, according to McMechan and Soegaard (1998), is that they have always been 2D and thus lacked the third dimension. The use of GPR for characterizing reservoir heterogeneity allows for empirical 3D analogues of reservoir heterogeneity to be developed (e.g., Baker 1991; Gawthorpe et al. 1993; Bridge et al. 1995; McMechan et al. 1997; Tatum and Francke 2012; Del Sole et al. 2020; Figure 1.4). The data collected from a GPR survey can provide useful inputs to stochastic models of the Joggins Formation for the objective of understanding the inherent reservoir heterogeneity sensitivities of the analogous reservoir (Figure 1.4). The typical geometric measures that are employed for reservoir modelling using GPR include channel depth, channel width, sandstone thickness and channel-belt width (e.g., Table 3.8). From those measurements, four aspect ratios can be calculated, (1) channel depth versus sandstone thickness, (2) channel depth versus channel width, (3) channel-belt width versus channel depth, and (4) channel-belt width versus channel width.

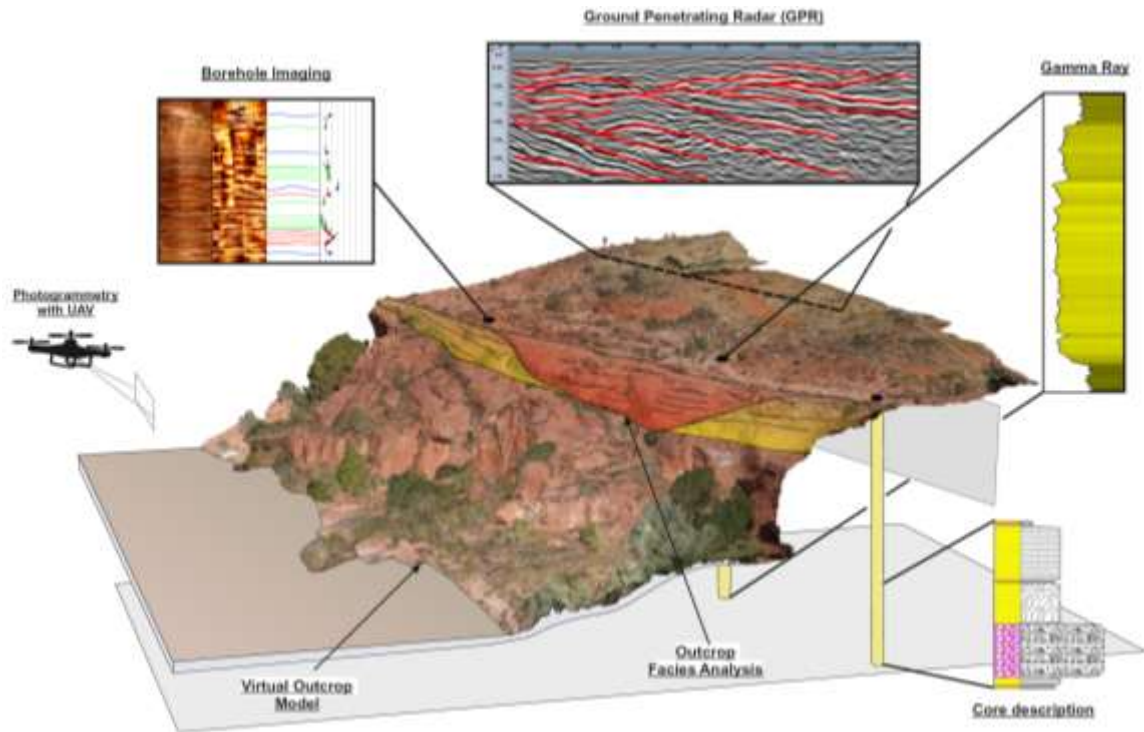


Figure 1.4: An example of data integration for the outcrop and behind the outcrop characterization (Yeste et al. 2019). In this example, various methods are utilized and integrated to allow for reservoir characterization. Many of the methods applied are like those used in this thesis but with the absence of borehole imaging and UAV imagery.

1.3.5 Objective 3

To test if orbital forcing signals are recognizable in the Late Carboniferous sediments of the Cumberland Basin. Identifying the controlling characteristics of Late Carboniferous climate change has implications for reconstructing the Late Carboniferous climate record but may also provide indications of future icehouse climate change.

1.3.6 Rationale for Objective 3

Cyclostratigraphy is defined by Strasser and Heckel (2007) as “the subdiscipline of stratigraphy that deals with the identification, characterization, correlation, and interpretation of cyclic variations in the stratigraphic record and, in particular, with their application in geochronology by improving the accuracy and resolution of time-

stratigraphic frameworks.” Consequently, it may be possible to interpret and relatively date the sedimentary record using astronomical cycles with known periodicities, of which Milankovitch cycles (precession, obliquity, and eccentricity) are the most important (Strasser and Heckel 2007). The Late Carboniferous was characterized by the deposition of repetitive sedimentary successions in the Pangean interior near the equatorial boundary known as cyclothems, which are climate-derived accumulations of cyclical and vertically accreted sandstone, thinly interbedded, heterolithic sandstone and mudrock, mudrock, limestone, and coal.

Several studies indicated that Milankovitch climate forcing was significant during the Carboniferous (e.g., van den Belt et al. 2015; Chesnel et al. 2016; Fang et al. 2018; Jirásek et al. 2018; del Strother et al. 2021). The examples illustrated various environments in which cycles have been observed (Schwarzacher 1993). Identifying the controlling characteristics of Late Carboniferous climate change not only has meaningful implications for reconstructing the Late Carboniferous climate record but may also provide indications of future icehouse climate change (Lear et al. 2021). This research relates to the central theme of reservoir characterization because of the implications for enhancing our understanding of paleoenvironments, which are vitally important for characterizing a reservoir.

1.3.7 Objective 4

Two centuries of research on the Joggins Formation has failed to conclusively define the paleoenvironment. Important questions remain concerning the paleoenvironment, including the extent of marine influence. Analysis of tidal rhythmite intervals may provide

evidence for the existence of shallow seas that transgressed westward from the Tethys Ocean along a mid-Euramerican seaway.

1.3.8 Rationale for Objective 4

Tidal rhythmite studies are common in the research literature, with abundant analyses conducted on sediments spanning the geologic timescale, including Carboniferous-aged sediments (e.g., Kvale et al. 1989; Archer 1991; Feldman et al. 1993; Archer et al. 1995a; Tessier et al. 1995; Miller and Eriksson 1997; Tape et al. 2003; Teedumae et al. 2004; Wells et al. 2005a; Bhattacharya et al. 2012; Coughenour et al. 2013).

Applying a comprehensive geomathematical analysis on tidal rhythmite intervals from a Joggins Formation borehole intersection may produce important evidence regarding the paleotidal regime of this area during the Late Carboniferous and advocate for the existence of shallow seas that transgressed westward from the Tethys Ocean along a theoretical mid-Euramerican seaway (e.g., Gibling et al. 1992; Calder 1998).

The prominent neap-spring-neap cyclicality recorded in the REI-B2-1 borehole of the upper (younger) portion of the Joggins Formation has significant connotations for reservoir characterization. Specifically, the vertical permeability and transmissibility pathways are directly impacted by tidal sedimentation (Dreyer 1992; Selim et al. 2021). The higher energy spring tides will deposit coarser-grained sediments with fewer mud-drapes and interbeds than neap tides. Sand beds are likely to undergo amalgamation because they are thicker and more erosive during the spring tidal cycles (e.g., Dreyer 1992; Musial et al. 2012). Consequently, spring tide deposits will have potentially higher net-to-gross ratio and fewer lateral baffles and barriers, thereby exhibiting a moderately good reservoir quality

(Dreyer 1992; Selim et al. 2021). Conversely, neap-tide deposits will demonstrate poor reservoir quality with low permeability and negligible transmissibility.

1.4 Chapters and Author Contributions

1.4.1 Chapter 2 – Georeferencing Workflow

Chapter 2 is based on the manuscript entitled “Post-Scan Georeferencing of LiDAR Data from a Geological Exposure using ArcGIS™ for Adjustment”, by Trevor B. Kelly, Grant D. Wach, and Darragh E. O’Connor. This manuscript was submitted to the peer-reviewed *Modern Environmental Science and Engineering* journal (of the Academic Star Publishing Company) and published on 22 January 2021. The initial manuscript was received on 14 March 2020 and was subsequently accepted for publication on 13 April 2020. The manuscript has not been modified substantially from the published version, though it has been reformatted to suit the dissertation. The copyright agreement form for this chapter can be found in Appendix A. The full reference is as follows:

Kelly, T.B., Wach, G.D., and O’Connor, D.E. 2020. Post-Scan Georeferencing of LiDAR Data from a Geological Exposure using ArcGIS™ for Adjustment. *Modern Environmental Science and Engineering* 6(6). doi: 10.15341/mese(2333-2581)/06.06.2020/001.

The idea for this manuscript was conceived by Trevor Kelly. The objective of the research investigation was the high-resolution definition of stratigraphic boundaries, geobodies, architectural elements, and baffles and barriers to reservoir fluid flow utilizing lidar. These underlying components must be recognized and understood, particularly with the continuing challenges of increasing recovery factors and the carbon capture, utilization, and storage of greenhouse gases. Trevor Kelly created the workflow, wrote the manuscript,

prepared the figures, edited the manuscript with input from the co-authors, and prepared the manuscript for publication. Grant Wach helped with the structure of the manuscript, revised all versions of the text, and provided valuable input on all sections of the manuscript. Darragh O'Connor helped with the creation of the workflow and provided advice and input on all aspects of the work.

1.4.2 Chapter 3 – Outcrop Study near Coal Mine Point

Chapter 3 is based on the manuscript entitled “Analysis of Factors Influencing the Interpretation of a Digitally Examined Fluvial Meanderbelt System: Joggins Formation, Nova Scotia”, by Trevor B. Kelly and Grant D. Wach. This manuscript was submitted to the peer-reviewed Canadian Journal of Earth Sciences (of the National Research Council (NRC) Research Press) and published on 13 August 2019. The initial manuscript was received on 11 October 2018 and was subsequently accepted for publication on 2 August 2019. This work is licensed under a Creative Commons Attribution 4.0 International License (CC BY 4.0), which permits unrestricted use, distribution, and reproduction in any medium, provided the original author(s) and source are credited. The manuscript has not been modified substantially from the published version, though it has been slightly upgraded and reformatted to suit the dissertation. The copyright agreement form for this chapter can be found in Appendix A. The full reference is as follows:

Kelly, T.B. and Wach, G.D. 2020. Analysis of Factors Influencing the Interpretation of a Digitally Examined Fluvial Meanderbelt System: Joggins Formation, Nova Scotia. Canadian Journal of Earth Sciences 57(4), 524-541. doi:10.1139/cjes-2018-0263.

The idea for this manuscript was conceived by Grant Wach and Trevor Kelly. The objective of the research investigation was to introduce an interpreted high-resolution

outcrop scan using lidar and integrate the data with a portable handheld gamma ray spectrometer, a portable handheld air permeameter, and hand samples that allow for porosity analysis. These combined data collection procedures emphasize the appreciation for reservoir heterogeneity, architectural elements, and baffles and barriers to reservoir fluid flow. The application of these techniques on the outcrop supports the understanding of lateral facies relationships for geobody analysis. Trevor Kelly conducted a large portion of the fieldwork and data collection, along with colleagues from the Dalhousie University Basin and Reservoir Laboratory. Trevor Kelly interpreted the results, wrote the manuscript, prepared the figures, edited the manuscript with input from the co-author, and prepared the manuscript for publication. Grant Wach helped with data collection, the structure of the manuscript, revised all versions of the text, and provided valuable input on all sections of the manuscript.

1.4.3 Chapter 4 – GPR Geoforensic Study

Chapter 4 is based on the manuscript entitled “A Novel Approach to 3D Modelling Ground-Penetrating Radar (GPR) Data – A Case Study of a Cemetery and Applications for Criminal Investigation”, by Trevor B. Kelly, Max N. Angel, Darragh E. O’Connor, Cambria C. Huff, Lauren E. Morris, and Grant D. Wach. This manuscript was submitted to the peer-reviewed Forensic Science International journal, which is published by Elsevier. The initial manuscript was submitted on 14 September 2020 and was subsequently accepted for publication on 17 June 2021. This work is licensed under a Creative Commons Attribution 4.0 International License (CC BY 4.0), which permits unrestricted use, distribution, and reproduction in any medium, provided the original author(s) and source are credited. The manuscript has not been modified substantially from the published

version, though it has been reformatted to suit the dissertation. The copyright agreement form for this chapter can be found in Appendix A. The full reference is as follows:

Kelly, T.B., Angel, M.N., O'Connor, D.E., Huff, C.C., Morris, L.E., Wach, G.D., 2021. A Novel Approach to 3D Modelling Ground-Penetrating Radar (GPR) data—A Case Study of a Cemetery and Applications for Criminal Investigation. *Forensic Science International* 325, 1-15. doi: 10.1016/j.forsciint.2021.110882.

The idea of this manuscript was developed by Trevor Kelly, Darragh O'Connor, and Grant Wach. The objective of the research investigation was to facilitate the elucidation of shallow subsurface objects which are is transferrable to the high-resolution definition of architectural components within geobodies. Data collection was performed by Trevor Kelly, Philip Sedore, Darragh O'Connor, Max Angel, Ryan Taylor, and Grant Wach. Max Angel assembled a partial rough draft of the manuscript. Darragh O'Connor and Trevor Kelly interpreted the results and prepared the figures and tables. Cambria Huff completed background research and wrote the sections on decomposition and leachate plumes. Trevor Kelly edited the manuscript with input from the co-authors and organized the manuscript for publication. Trevor Kelly completed and edited the final manuscript with Grant Wach, Darragh O'Connor, Cambria Huff, and Lauren Morris. Trevor Kelly and Grant Wach completed the revisions as per the anonymous reviewers and re-submitted the manuscript.

1.4.4 Chapter 5 – Joggins GPR Study

Chapter 5 is based on the manuscript entitled “The Technical Challenges and Outcomes of Ground-Penetrating Radar: A Site-Specific Example from Joggins, Nova Scotia”, by Trevor B. Kelly, Grant D. Wach, and Darragh E. O'Connor. This manuscript was submitted to the peer-reviewed American Institute of Mathematical Sciences (AIMS)

Geoscience's journal (of the AIMS Press) and published on 18 January 2021. The initial manuscript was received on 15 December 2020 and was subsequently accepted for publication on 7 January 2021. This work is licensed under a Creative Commons Attribution 4.0 International License (CC BY 4.0), which permits unrestricted use, distribution, and reproduction in any medium, provided the original author(s) and source are credited. The manuscript has not been modified substantially from the published version, though it has been reformatted to suit the dissertation. The copyright agreement form for this chapter can be found in Appendix A. The full reference is as follows:

Kelly, T.B., Wach, G.D., and O'Connor, D.E. 2021. The Technical Challenges and Outcomes of Ground-Penetrating Radar: A Site-Specific Example from Joggins, Nova Scotia. *AIMS Geosciences* 7(1), 22-55. doi: 10.3934/geosci.2021002.

The idea for this manuscript was conceived by Trevor Kelly. The objective of the research investigation was to facilitate the elucidation of shallow subsurface objects which are is transferrable to the high-resolution definition of architectural components within geobodies. Trevor Kelly conducted a large portion of the fieldwork and data collection, along with colleagues from the Dalhousie University Basin and Reservoir Laboratory. Trevor Kelly interpreted the results, wrote the manuscript, prepared the figures and tables, edited the manuscript with input from the co-authors, and organized the manuscript for publication. Grant Wach helped with data collection, the structure of the manuscript, revised all versions of the text, and provided valuable input on all sections of the manuscript. Darragh O'Connor helped with data collection, the interpretation of results and provided advice and input on all aspects of the work.

1.4.5 Chapter 6 – Tidal Bundles Study

Chapter 6 is based on the manuscript entitled “Episodic Marine Incursions Support a Late Carboniferous Mid-Euramerican Seaway”, by Trevor B. Kelly and Grant D. Wach. This manuscript was submitted to the peer-reviewed *Sedimentary Geology* journal, which is published by Elsevier. The initial manuscript was submitted on the 24th of February 2022. The manuscript has not been modified substantially from the submitted version, though it has been slightly updated and reformatted to suit the dissertation. Since this manuscript has not been accepted, there is no full reference yet. It is a possibility that this manuscript might be submitted to an alternate journal pending the outcome of the review.

The idea of this manuscript was conceived by Grant Wach and Trevor Kelly. The objective of the research investigation was the identification of tidal processes and related depositional environments using a high-resolution geomathematical approach consisting of Fourier transform and continuous wavelet transform analyses which is an example of the delineation of fine-scale baffles and barriers to fluid flow for reservoir characterization studies. Trevor Kelly visited the core library, collected the data, learned how MATLAB could be applied, interpreted the results, wrote the manuscript, prepared the figures and tables, edited the manuscript with input from the co-authors, and prepared the manuscript for publication. Grant Wach helped with the structure of the manuscript, revised all versions of the text, and provided valuable input on all sections of the manuscript.

1.4.6 Chapter 7 – Cyclostratigraphy Study

Chapter 7 is based on the manuscript entitled “Uncovering the Milankovitch Record from a Late Carboniferous Cyclothem Succession in Paleoequatorial Euramerica”, by

Trevor B. Kelly, Grant D. Wach, and Bill (F.W.) Richards. This manuscript will be submitted at a later date to the peer-reviewed Atlantic Geology journal, which is published by the Atlantic Geoscience Society (AGS). Since this manuscript is quite focussed on the sediments of the Cumberland Basin, a journal that covers geoscience aspects of Atlantic Canada made the most sense; hence, the choice of submitting to Atlantic Geology.

The idea for this manuscript was devised by Bill Richards and Trevor Kelly. The objective of the research investigation was the identification of spectral peaks corresponding to the four main orbital periods (400 kyr, 100 kyr, 40 kyr, and 20 kyr) of Milankovitch cyclicity. The detection of cyclic events affecting deposition can facilitate stratigraphic correlation and high-resolution reservoir characterization. Trevor Kelly reviewed previous regional and global cyclostratigraphy research, learned how MATLAB could be applied, performed the data analysis, interpreted the results, wrote the manuscript, prepared the figures and tables, edited the manuscript with input from the co-authors, and prepared the manuscript for publication. Grant Wach helped with data analysis, data interpretation, the structure of the manuscript, revised all versions of the text, and provided valuable input on all sections of the manuscript. Bill Richards helped with data analysis, the interpretation of results and provided advice and input on all aspects of the work.

1.5 Key Research Contributions and Innovations

1.5.1 Chapter 2 – Georeferencing Workflow

The contributions of Chapter 2, entitled “Post-Scan Georeferencing of LiDAR Data from a Geological Exposure using ArcGIS™ for Adjustment” are:

- (1) Directly applicable to defining stratigraphy, geobodies, architectural elements, and baffles and barriers to fluid flow.
- (2) A unique example emphasizing the integration of lidar software with ArcGIS™ and Schlumberger Petrel™ software.
- (3) A novel and unique workflow detailing the steps to achieve a fully georeferenced point cloud by knowing the ground locations of three targets incorporated into the lidar scan using conventional software, in this case, ArcGIS™.

1.5.2 Chapter 3 – Outcrop Study near Coal Mine Point

The contributions of Chapter 3, entitled “Analysis of Factors Influencing the Interpretation of a Digitally Examined Fluvial Meanderbelt System: Joggins Formation, Nova Scotia” are:

- (1) An increased understanding of subsurface reservoirs, particularly of the fluvial meanderbelt type, through the study of an outcrop, which provides the lateral facies relationships for geobody analysis.
- (2) Significance and limitations of a combined digital data collection approach for the analysis of a sedimentary outcrop.
- (3) Demonstrate methodology for the integration and modelling of data.
- (4) Demonstrate the architectural complexity of a fluvial meanderbelt system.
- (5) De-risk production from fluvial reservoirs by providing awareness of reservoir heterogeneity, architectural elements, and baffles and barriers to fluid flow.
- (6) Offer a range of architectural element data from a fluvial case study (Joggins Formation), which may be transferrable to other analogues.

- (7) Illustrate how traditional field data has been collected and is integrated with modern field data.

1.5.3 Chapter 4 – GPR Geoforensic Study

The contributions of Chapter 4, entitled “A Novel Approach to 3D Modelling Ground-Penetrating Radar (GPR) Data – A Case Study of a Cemetery and Applications for Criminal Investigation” are:

- (1) The methodology and 3D renderings for the delineation of shallow objects (burials) in the subsurface are directly transferrable to the high-resolution delineation of architectural elements within geobodies.
- (2) Created an overall more intuitive, easily manipulatable 3D model to optimize visualization.
- (3) Accurately map a cemetery, distinguishing burial sites from one another by subtracting low amplitude data and identifying otherwise unknown burial sites.
- (4) Map out potential leachate plumes from older decaying bodies, possibly linking burial age to signal depth. This is directly applicable to the potential mapping of reservoir fluids.
- (5) Novel use of Schlumberger Petrel™ for viewing a GPR cube using cross-sections and depth slices. The peer-reviewed scientific methodology corroborates the validity of the geoforensics use and the validity of allowing GPR data, analysis, and interpretation to be introduced as evidence in a court of law, particularly for criminal proceedings.
- (6) Provides critical information to the congregation about where excavations could and could not be performed.

1.5.4 Chapter 5 – Joggins GPR Study

The contributions of Chapter 5, entitled “The technical challenges and outcomes of ground-penetrating radar: A site-specific example from Joggins, Nova Scotia” are:

- (1) First conventional ground-penetrating radar survey was tested with the intent of imaging near-surface, dipping strata of the Late Carboniferous Joggins Formation (chosen as a case study for testing concepts) with applicability to subsurface imaging for reservoir characterization.
- (2) The overlying near-surface angular unconformity was successfully imaged, enabling mapping of the approximately 8 m of overlying glacial till (material sourced from the erosion and entrainment of a glacier).
- (3) The challenges of performing a ground-penetrating radar survey in this type of geological environment, such as the overlying clay-rich glacial till, thick overburden, and dipping strata, are highlighted.
- (4) Reveals clearly correlatable links between surface and shallow surface objects and the ground-penetrating radar profiles.
- (5) The preliminary 2D grid survey performed at the former baseball field (lines 45-50) was encouraging and demonstrated potential for a broader survey to delineate the geobody and architectural elements.

1.5.5 Chapter 6 – Tidal Bundles Study

The contributions of Chapter 6, entitled “Episodic Marine Incursions Support a Late Carboniferous Mid-Euramerican Seaway” are:

- (1) Documents for the first time tidal rhythmites in the Late Carboniferous strata of the Joggins Formation and is an example of the delineation of fine-scale baffles and barriers to fluid flow for reservoir characterization studies.
- (2) Provides the first quantitative data of tidal bundles from drill core penetrating the Joggins Formation and adds to the thorough yet relatively small body of work pertaining to tidal bundle research in the Carboniferous.
- (3) Provides evidence for marine and brackish incursions while suggesting the presence of a mid-Euramerican seaway.

1.5.6 Chapter 7 – Cyclostratigraphy Study

The contributions of Chapter 7, titled “Uncovering the Milankovitch Record from a Late Carboniferous Cyclothem Succession in Paleoequatorial Euramerica” are:

- (1) Identification of Milankovitch cycles existing within the Westphalian strata of the Cumberland Subbasin which can facilitate stratigraphic correlation and high-resolution reservoir characterization.
- (2) Determine whether the sedimentary succession intervals were forced by the orbital factors or not.
- (3) Possibility of learning about sedimentation rates.

1.6 Research Timeline

A timeline of my research over the past six years is shown in Figure 1.5. The timeline displays the highlights and major milestones achieved during my time as a PhD student. I attended and presented my research at numerous conferences including three Atlantic Geoscience Colloquiums, one Conjugate Margins Conference, two GeoConventions, and most recently, the GAC-MAC Conference. In addition, I have completed six research papers, which form my dissertation. Of course, my research and methodology were interrupted by the pandemic in 2020 and 2021.

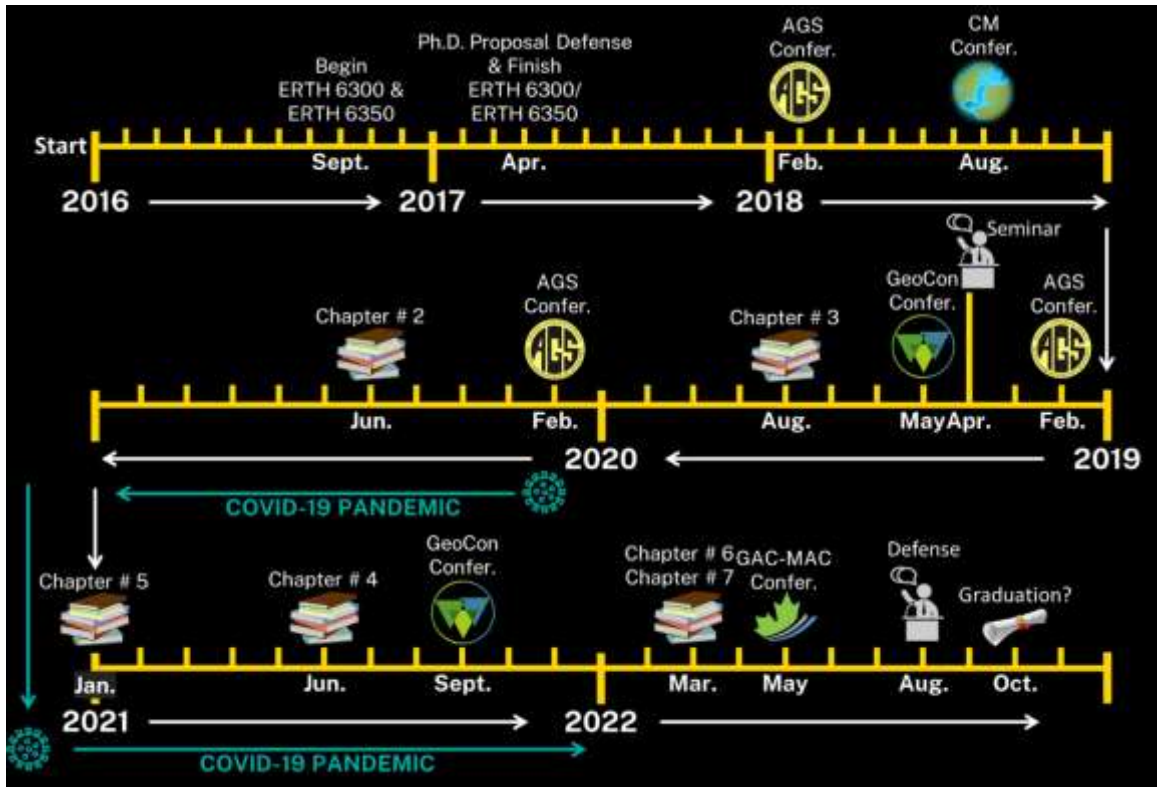


Figure 1.5: Timeline of my research with an emphasis on major milestones achieved.

1.7 References Cited in Chapter 1

Alhumimidi, M.S., Alfarhan, M.S., Cline, J.R., and Aiken, C.L. 2017. Application of a 3D photorealistic model for the geological analysis of the Permian carbonates (Khuff Formation) in Saudi Arabia. *Arabian Journal of Geosciences*, **10**: 112. doi:10.1007/s12517-017-2874-7.

Allen, J. 2016. Numerical Modeling of Salt Tectonics at Rifted Continental Margins. Department of Earth and Environmental Sciences, Dalhousie University, Halifax, Nova Scotia.

Archer, A.W. 1991. Modeling of tidal rhythmites using modern tidal periodicities and implications for short-term sedimentation rates. *In Sedimentary Modeling: Computer Simulations and Methods for Improved Parameter Definition (Bulletin 233)*. Edited by E.K. Franseen and W.L. Watney and C.G. Kendall and W. Ross. Kansas Geological Survey, Lawrence, Kansas. pp. 185-194.

Archer, A.W., Kuecher, G.J., and Kvale, E.P. 1995a. The Role of Tidal-Velocity Asymmetries in the Deposition of Silty Tidal Rhythmites (Carboniferous, Eastern Interior Coal Basin, U.S.A.). *Journal of Sedimentary Research*, **65**: 408-416. doi:10.1306/d42680d6-2b26-11d7-8648000102c1865d.

Archer, A.W., Calder, J.H., Gibling, M.R., Naylor, R.D., Reid, D.R., and Wightman, W.G. 1995b. Invertebrate trace fossils and agglutinated foraminifera as indicators of marine influence within the classic Carboniferous section at Joggins, Nova Scotia, Canada. *Canadian Journal of Earth Sciences*, **32**: 2027-2039. doi:10.1139/e95-156.

Baker, P.L. Fluid, lithology, geometry, and permeability information from ground-penetrating radar for some petroleum industry applications. *In SPE Asia-Pacific Conference*. Perth, Australia 1991. OnePetro.

Bell, W.A. 1912. Joggins Carboniferous section of Nova Scotia. *In Summary Report for 1911*. Geological Survey of Canada. pp. 328-333.

Bellian, J.A., Kerans, C., and Jennette, D.C. 2005. Digital outcrop models: applications of terrestrial scanning lidar technology in stratigraphic modeling. *Journal of Sedimentary Research*, **75**: 166-176. doi:10.2110/jsr.2005.013.

Bellian, J.A., Beck, R., and Kerans, C. 2007. Analysis of hyperspectral and lidar data: Remote optical mineralogy and fracture identification. *Geosphere*, **3**: 491-500. doi:10.1130/GES00097.1.

Bhattacharya, B., Bandyopadhyay, S., Mahapatra, S., and Banerjee, S. 2012. Record of tide-wave influence on the coal-bearing Permian Barakar Formation, Raniganj Basin, India. *Sedimentary Geology*, **267-268**: 25-35. doi:10.1016/j.sedgeo.2012.05.006.

Bingham-Koslowski, N., Grey, M., Pufahl, P., and Ehrman, J.M. 2018. Breaking down Late Carboniferous fish coprolites from the Joggins Formation. *In* 1st Joggins Research Symposium. Atlantic Geoscience Society, Joggins, Nova Scotia.

Boro, H., Rosero, E., and Bertotti, G. 2014. Fracture-network analysis of the Latemar Platform (northern Italy): integrating outcrop studies to constrain the hydraulic properties of fractures in reservoir models. *Petroleum Geoscience*, **20**: 79-92. doi:10.1144/petgeo2013-007.

Bridge, J.S., Alexander, J., Collier, R.E.L., Gawthorpe, R.L., and Jarvis, J. 1995. Ground-penetrating radar and coring used to study the large-scale structure of point-bar deposits in three dimensions. *Sedimentology*, **42**: 839-852. doi:10.1111/j.1365-3091.1995.tb00413.x.

Bryant, I.D., and Flint, S.S. 1993. The geological modelling of hydrocarbon reservoirs and outcrop analogues. *In* The geological modelling of hydrocarbon reservoirs and outcrop analogues. *Edited by* S.S. Flint and I.D. Bryant. Blackwell Scientific Publications, Oxford, UK. pp. 3-20.

Buckley, S.J., Howell, J.A., Enge, H.D., and Kurz, T.H. 2008. Terrestrial laser scanning in geology: data acquisition, processing and accuracy considerations. *Journal of the Geological Society*, **165**: 625-638. doi:10.1144/0016-76492007-100.

Buckley, S.J., Enge, H.D., Carlsson, C., and Howell, J.A. 2010. Terrestrial laser scanning for use in virtual outcrop geology. *The Photogrammetric Record*, **25**: 225-239. doi:10.1111/j.1477-9730.2010.00585.x.

Buhler, P.B., and Grey, M. 2017. Xiphosuran digging traces at the Late Carboniferous Joggins Fossil Cliffs UNESCO World Heritage Site, Nova Scotia, Canada. *Ichnos*, **24**: 179-190. doi:10.1080/10420940.2016.1244055.

Calder, J.H. 1998. The Carboniferous evolution of Nova Scotia. Geological Society, London, Special Publications, **143**: 261-302. doi:10.1144/gsl.Sp.1998.143.01.19.

Calder, J.H., Rygel, M.C., Ryan, R.J., Falcon-Lang, H.J., and Herbert, B.L. 2005. Stratigraphy and sedimentology of early Pennsylvanian red beds at Lower Cove, Nova Scotia, Canada: the Little River Formation with redefinition of the Joggins Formation. *Atlantic Geology*, **41**: 87-102. doi:10.4138/183.

Calder, J.H., Gibling, M.R., Scott, A.C., Davies, S.J., Herbert, B.L., Greb, S.F., and DiMichele, W.A. 2006. A fossil lycopsid forest succession in the classic Joggins section of Nova Scotia: paleoecology of a disturbance-prone Pennsylvanian wetland. *Special Papers - Geological Society of America*, **399**: 169. doi:10.1130/2006.2399(09).

Campbell, D.C. 2011. The Late Cretaceous and Cenozoic Geological History of the Outer Continental Margin off Nova Scotia, Canada: Insights into Margin Evolution from a Mature Passive Margin. *Earth and Environmental Sciences*, Dalhousie University, Halifax, Nova Scotia.

Carpenter, D.K., Falcon-Lang, H.J., Benton, M.J., and Grey, M. 2015. Early Pennsylvanian (Langsettian) fish assemblages from the Joggins Formation, Canada, and their implications for palaeoecology and palaeogeography. *Palaeontology*, **58**: 661-690. doi:10.5061/dryad.b0551.

Carroll, R.L. 1967. Labyrinthodonts from the Joggins Formation. *Journal of Paleontology*, **41**: 111-142.

Casini, G., Hunt, D.W., Mosen, E., and Bounaim, A. 2016. Fracture characterization and modeling from virtual outcrops. *AAPG Bulletin*, **100**: 41-61. doi:10.1306/09141514228.

Chesnel, V., Merino-Tomé, Ó., Fernández, L.P., Villa, E., and Samankassou, E. 2016. Isotopic fingerprints of Milankovitch cycles in Pennsylvanian carbonate platform-top deposits: the Valdorria record, Northern Spain. *Terra Nova*, **28**: 364-373. doi:10.1111/ter.12229.

Chipman, M., Grey, M., and Pufahl, P.K. 2020. Coprolites from a brackish ecosystem in the Pennsylvanian Joggins Formation, Nova Scotia, Canada and their palaeoecological implications. *Palaeogeography, Palaeoclimatology, Palaeoecology*, **538**. doi:10.1016/j.palaeo.2019.109407.

Copeland, M.J. 1959. Coalfields west half Cumberland County, Nova Scotia. *Geological Survey of Canada Memoir* 298. p. 89.

Coughenour, C.L., Archer, A.W., and Lacovara, K.J. 2013. Calculating Earth–Moon system parameters from sub-yearly tidal deposit records: An example from the carboniferous tradewater formation. *Sedimentary Geology*, **295**: 67-76. doi:10.1016/j.sedgeo.2013.08.001.

Davies, D., Williams, B., and Vessell, R. 1992. Models for meandering and braided fluvial reservoirs with examples from the Travis Peak Formation, East Texas. *In* SPE Annual Technical Conference and Exhibition. Society of Petroleum Engineers.

Davies, S.J., and Gibling, M.R. 2003. Architecture of coastal and alluvial deposits in an extensional basin: the Carboniferous Joggins Formation of eastern Canada. *Sedimentology*, **50**: 415-439. doi:10.1046/j.1365-3091.2003.00553.x

Davies, S.J., Gibling, M.R., Rygel, M.C., Calder, J.H., and Skilliter, D.M. 2005. The Pennsylvanian Joggins Formation of Nova Scotia: sedimentological log and stratigraphic framework of the historic fossil cliffs. *Atlantic Geology*, **41**: 87-102. doi:10.4138/182.

Del Sole, L., Antonellini, M., and Calafato, A. 2020. Characterization of sub-seismic resolution structural diagenetic heterogeneities in porous sandstones: Combining ground-penetrating radar profiles with geomechanical and petrophysical in situ measurements (Northern Apennines, Italy). *Marine and Petroleum Geology*, **117**: 1-22. doi:10.1016/j.marpetgeo.2020.104375.

del Strother, P., Gize, A., Hollis, C., and McLean, D. 2021. Bituminous coals on emergent surfaces in an Asbian, lower Carboniferous (Mississippian) limestone succession on the North Wales carbonate platform, UK, and implications for palaeoclimate. *Proceedings of the Yorkshire Geological Society*, **63**: 22. doi:10.1144/pygs2020-006.

DiMichele, W.A., and Falcon-Lang, H.J. 2011. Pennsylvanian 'fossil forests' in growth position (T0 assemblages): origin, taphonomic bias and palaeoecological insights. *Journal of the Geological Society*, **168**: 585-605. doi:10.1144/0016-76492010-103.

Dreyer, T. 1992. Significance of tidal cyclicity for modelling of reservoir heterogeneities in the lower Jurassic Tilje Formation, mid-Norwegian shelf. *Norsk Geologisk Tidsskrift*, **72**: 159-170.

Enge, H.v.D., Buckley, S.J., Rotevatn, A., and Howell, J.A. 2007. From outcrop to reservoir simulation model: Workflow and procedures. *Geosphere*, **3**: 469-490. doi:10.1130/GES00099.1.

Fabuel-Perez, I., Hodgetts, D., and Redfern, J. 2009a. A new approach for outcrop characterization and geostatistical analysis of a low-sinuosity fluvial-dominated succession using digital outcrop models: Upper Triassic Oukaimeden Sandstone Formation, central High Atlas, Morocco. *AAPG Bulletin*, **93**: 795-827. doi:10.1306/02230908102.

Fabuel-Perez, I., Hodgetts, D., and Redfern, J. 2010. Integration of digital outcrop models (DOMs) and high resolution sedimentology-workflow and implications for geological modelling: Oukaimeden Sandstone Formation, High Atlas (Morocco). *Petroleum Geoscience*, **16**: 133-154. doi:10.1144/1354-079309-820.

Falcon-Lang, H.J. 2005. Small cordaitalean trees in a marine-influenced coastal habitat in the Pennsylvanian Joggins Formation, Nova Scotia. *Journal of the Geological Society*, **162**: 485-500. doi:10.1144/0016-764904-080.

Falcon-Lang, H.J. 2006. A history of research at the Joggins Fossil Cliffs of Nova Scotia, Canada, the world's finest Pennsylvanian section. *Proceedings of the Geologists' Association*, **117**: 377-392. doi:10.1016/S0016-7878(06)80044-1.

Falcon-Lang, H.J., Rygel, M.C., Calder, J.H., and Gibling, M.R. 2004. An early Pennsylvanian waterhole deposit and its fossil biota in a dryland alluvial plain setting, Joggins, Nova Scotia. *Journal of the Geological Society*, **161**: 209-222. doi:10.1144/0016-764903-109.

Falcon-Lang, H.J., Benton, M.J., Braddy, S.J., and Davies, S.J. 2006. The Pennsylvanian tropical biome reconstructed from the Joggins Formation of Nova Scotia, Canada. *Journal of the Geological Society*, **163**: 561-576. doi:10.1144/0016-764905-063.

Fang, Q., Wu, H., Wang, X., Yang, T., Li, H., and Zhang, S. 2018. Astronomical cycles in the Serpukhovian-Moscovian (Carboniferous) marine sequence, South China and their implications for geochronology and icehouse dynamics. *Journal of Asian Earth Sciences*, **156**: 302-315. doi:10.1016/j.jseaes.2018.02.001.

Faulkner, S.J., Stimson, M.R., Calder, J.H., and Lucas, S.G. 2017. The first unambiguous pterygote ichnofossil from the Joggins Fossil Cliffs, UNESCO World Heritage Site, Joggins, Nova Scotia, Canada.

Feldman, H.R., Archer, A.W., Kvale, E.P., Cunningham, C.R., Maples, C.G., and West, R.R. 1993. A Tidal Model of Carboniferous Konservat-Lagerstätten Formation. *Palaios*, **8**: 485-498. doi:10.2307/3515022.

Gawthorpe, R.L., Li Collier, R.E., Alexander, J., Bridge, J.S., and Leeder, M.R. 1993. Ground penetrating radar: application to sandbody geometry and heterogeneity studies. Geological Society, London, Special Publications, **73**: 421-432. doi:10.1144/GSL.SP.1993.073.01.24.

Gibling, M.R. 2006. Width and Thickness of Fluvial Channel Bodies and Valley Fills in the Geological Record: A Literature Compilation and Classification. *Journal of Sedimentary Research*, **76**: 731-770. doi:10.2110/jsr.2006.060.

Gibling, M.R., Calder, J.H., Ryan, R., Poll, H.W.v.d., and Yeo, G.M. 1992. Late Carboniferous and Early Permian drainage patterns in Atlantic Canada. *Canadian Journal of Earth Sciences*, **29**: 338-352. doi:10.1139/e92-030.

Godfrey, S., Holmes, R.B., and Laurin, M. 1991. Articulated remains of a Pennsylvanian Embolomere (Amphibia: Anthracosauria) from Joggins, Nova Scotia. *Journal of Vertebrate Paleontology*, **11**: 213-219.

Grammer, G.M., Harris, P.M.M., and Eberli, G.P. 2004. Integration of outcrop and modern analogs in reservoir modeling: overview with examples from the Bahamas. *In* Integration of Outcrop and Modern Analogs in Reservoir Modeling - AAPG Memoir 80. The American Association of Petroleum Geologists, Houston, Texas. pp. 1-22.

Grey, M., and Finkel, Z.V. 2011. The Joggins Fossil Cliffs UNESCO World Heritage site: a review of recent research. *Atlantic Geology*, **47**: 185-200. doi:10.4138/atlgeol.2011.009.

Grey, M., Pufahl, P.K., and Aziz, A.A. 2011. Using Multiple Environmental Proxies to Determine Degree of Marine Influence and Paleogeographical Position of the Joggins Fossil Cliffs, Unesco World Heritage Site. *Palaios*, **26**: 256-263. doi:10.2110/palo.2010.p10-118r.

Hartzell, P., Glennie, C., Biber, K., and Khan, S. 2014. Application of multispectral LiDAR to automated virtual outcrop geology. *ISPRS Journal of Photogrammetry and Remote Sensing*, **88**: 147-155. doi:10.1016/j.isprsjprs.2013.12.004.

Hebert, B.L., and Calder, J.H. 2004. On the discovery of a unique terrestrial faunal assemblage in the classic Pennsylvanian section at Joggins, Nova Scotia. *Canadian Journal of Earth Sciences*, **41**: 247-254. doi:10.1139/e03-096.

Hodgetts, D. 2013. Laser scanning and digital outcrop geology in the petroleum industry: a review. *Marine and Petroleum Geology*, **46**: 335-354. doi:10.1016/j.marpetgeo.2013.02.014.

Holmes, R.B., and Carroll, R.L. 2010. An articulated embolomere skeleton (Amphibia: Anthracosauria) from the Lower Pennsylvanian (Bashkirian) of Nova Scotia. *Canadian Journal of Earth Sciences*, **47**: 209-219. doi:10.1139/E10-008.

Holmes, R.B., Carroll, R.L., and Reisz, R.R. 1998. The first articulated skeleton of *Dendrerpeton acadianum* (Temnospondyli, Dendrerpetontidae) from the Lower Pennsylvanian locality of Joggins, Nova Scotia, and a review of its relationships. *Journal of Vertebrate Paleontology*, **18**: 64-79. doi:10.1080/02724634.1998.10011034.

Howell, J.A., Martinius, A.W., and Good, T.R. 2014. The application of outcrop analogues in geological modelling: a review, present status and future outlook. Geological Society, London, Special Publications, **387**: 1-25. doi:10.1144/SP387.12.

Hower, J.C., Calder, J.H., Eble, C.F., Scott, A.C., Robertson, J.D., and Blanchard, L.J. 2000. Metalliferous coals of the Westphalian A Joggins Formation, Cumberland Basin, Nova Scotia, Canada: petrology, geochemistry, and palynology. *International Journal of Coal Geology*, **42**: 185-206. doi:10.1016/S0166-5162(99)00039-7.

Ielpi, A., Gibling, M.R., Bashforth, A.R., and Dennar, C.I. 2015. Impact of vegetation on Early Pennsylvanian fluvial channels: insight from the Joggins Formation of Atlantic Canada. *Journal of Sedimentary Research*, **85**: 999-1018. doi:10.2110/jsr.2015.50.

Jirásek, J., Opluštil, S., Sivek, M., Schmitz, M.D., and Abels, H.A. 2018. Astronomical forcing of Carboniferous paralic sedimentary cycles in the Upper Silesian Basin, Czech Republic (Serpukhovian, latest Mississippian): New radiometric ages afford an astronomical age model for European biozonations and substages. *Earth-Science Reviews*, **177**: 715-741. doi:10.1016/j.earscirev.2017.12.005.

Jones, R.R., Mccaffrey, K.J., Imber, J., Wightman, R., Smith, S.A., Holdsworth, R.E., Clegg, P., De Paola, N., Healy, D., and Wilson, R.W. 2008. Calibration and validation of reservoir models: the importance of high resolution, quantitative outcrop analogues. Geological Society, London, Special Publications, **309**: 87-98. doi:10.1144/SP309.7.

Keighley, D.G., Calder, J.H., Park, A.F., Pickerill, R.K., Waldron, J.W., Falcon-Lang, H.J., and Benton, M.J. 2008. Discussion on ecology of earliest reptiles inferred from basal Pennsylvanian trackways. *Journal of the Geological Society*, **165**: 983-987. doi:10.1144/0016-76492008-045.

Kelly, T.B., and Wach, G.D. 2020. Analysis of factors influencing the interpretation of a digitally examined fluvial meanderbelt system: Joggins Formation, Nova Scotia. *Canadian Journal of Earth Sciences*, **57**: 524-541. doi:10.1139/cjes-2018-0263.

Kelly, T.B., and Wach, G.D. 2021. Post-Scan Georeferencing of Optech ILRIS-3D Lidar Data from the Joggins Formation Geologic Exposure using ArcGIS for Adjustment.

Kelly, T.B., Wach, G.D., and O'Connor, D.E. 2021a. The technical challenges and outcomes of ground-penetrating radar: A site-specific example from Joggins, Nova Scotia. *AIMS Geosciences*, **7**: 22-55. doi:10.3934/geosci.2021002.

Keogh, K.J., Leary, S., Martinius, A.W., Scott, A.S., Riordan, S., Viste, I., Gowland, S., Taylor, A.M., and Howell, J. 2014. Data capture for multiscale modelling of the Lourinha Formation, Lusitanian Basin, Portugal: an outcrop analogue for the Statfjord Group, Norwegian North Sea. *Geological Society, London, Special Publications*, **387**: 27-56. doi:10.1144/SP387.11.

Kerans, C., Lucia, F.J., and Senger, R. 1994. Integrated characterization of carbonate ramp reservoirs using Permian San Andres Formation outcrop analogs. *AAPG Bulletin*, **78**: 181-216. doi:10.1306/BDF905A-1718-11D7-8645000102C1865D.

King, O.A., and Stimson, M. 2018. Kouphichnium aspodon, a new occurrence of invertebrate traces from the Joggins Fossil Cliffs UNESCO World Heritage Site, Nova Scotia, Canada. *In* 1st Joggins Research Symposium. Atlantic Geoscience Society, Joggins, Nova Scotia.

King, O.A., Stimson, M.R., MacRae, R.A., Calder, J., Hebert, B., and Reid, L. 2019. An ichnotaxonomic and paleoenvironmental study of the xiphosuran ichnogenus Kouphichnium from the UNESCO World Heritage Site Joggins Fossil Cliffs, Nova Scotia, Canada.

Kvale, E.P., Archer, A.W., and Johnson, H.R. 1989. Daily, monthly, and yearly tidal cycles within laminated siltstones of the Mansfield Formation (Pennsylvanian) of Indiana. *Geology*, **17**: 365-368. doi:10.1130/0091-7613(1989)017.

Labourdette, R., and Jones, R.R. 2007. Characterization of fluvial architectural elements using a three-dimensional outcrop data set: Escanilla braided system, South-Central Pyrenees, Spain. *Geosphere*, **3**: 422-434. doi:10.1130/GES00087.1.

Lear, C.H., Anand, P., Blenkinsop, T., Foster, G.L., Gagen, M., Hoogakker, B., Larter, R.D., Lunt, D.J., McCave, I.N., and McClymont, E. 2021. Geological Society of London Scientific Statement: what the geological record tells us about our present and future climate. Geological Society of London.

Maddin, H.C., Mann, A., and Hebert, B. 2020. Varanopid from the Carboniferous of Nova Scotia reveals evidence of parental care in amniotes. *Nat Ecol Evol*, **4**: 50-56. doi:10.1038/s41559-019-1030-z.

Mann, A., Gee, B.M., Pardo, J.D., Marjanović, D., Adams, G.R., Calthorpe, A.S., Maddin, H.C., and Anderson, J.S. 2020. Reassessment of historic ‘microsaurs’ from Joggins, Nova Scotia, reveals hidden diversity in the earliest amniote ecosystem. *Papers in Palaeontology*, **6**: 605-625. doi:10.1002/spp2.1316.

McMechan, G.A., and Soegaard, K. 1998. Sedimentological and geophysical studies of clastic reservoir analogs: Methods, applications and developments of ground-penetrating radar for determination of reservoir geometries in near-surface settings. Final report. Texas Univ., Dallas, TX (United States).

McMechan, G.A., Gaynor, G.C., and Szerbiak, R.B. 1997. Use of ground-penetrating radar for 3-D sedimentological characterization of clastic reservoir analogs. *Geophysics*, **62**: 786-796. doi:10.1190/1.1444188.

Miller, D.J., and Eriksson, K.A. 1997. Late Mississippian Prodeltaic Rhythmites in the Appalachian Basin: A Hierarchical Record of Tidal and Climatic Periodicities. *Journal of Sedimentary Research*, **67**: 653-660. doi:10.1306/d4268608-2b26-11d7-8648000102c1865d.

Minisini, D., Wang, M., Bergman, S.C., and Aiken, C. 2014. Geological data extraction from lidar 3-D photorealistic models: A case study in an organic-rich mudstone, Eagle Ford Formation, Texas. *Geosphere*, **10**: 610-626. doi:10.1130/GES00937.1.

Musial, G., Reynaud, J.-Y., Gingras, M.K., Féliès, H., Labourdette, R., and Parize, O. 2012. Subsurface and outcrop characterization of large tidally influenced point bars of the Cretaceous McMurray Formation (Alberta, Canada). *Sedimentary Geology*, **279**: 156-172. doi:10.1016/j.sedgeo.2011.04.020.

North, C.P., and Prosser, D.J. 1993. Characterization of fluvial and aeolian reservoirs: problems and approaches. Geological Society, London, Special Publications, **73**: 1-6. doi:10.1144/gsl.Sp.1993.073.01.01.

Pardo, J.D., and Mann, A. 2018. A basal aistopod from the earliest Pennsylvanian of Canada, and the antiquity of the first limbless tetrapod lineage. *R Soc Open Sci*, **5**: 181056. doi:10.1098/rsos.181056.

Pranter, M.J., Ellison, A.I., Cole, R.D., and Patterson, P.E. 2007. Analysis and modeling of intermediate-scale reservoir heterogeneity based on a fluvial point-bar outcrop analog, Williams Fork Formation, Piceance Basin, Colorado. *AAPG Bulletin*, **91**: 1025-1051. doi:10.1306/02010706102.

Pranter, M.J., Hewlett, A.C., Cole, R.D., Wang, H., and Gilman, J. 2014. Fluvial architecture and connectivity of the Williams Fork Formation: use of outcrop analogues for stratigraphic characterization and reservoir modelling. Geological Society, London, Special Publications, **387**: 57-83. doi:10.1144/SP387.1.

Prescott, Z.M., Stimson, M.R., Dafoe, L.T., Gibling, M.R., MacRae, R.A., Calder, J.H., and Hebert, B.L. 2014. Microbial mats and ichnofauna of a fluvial-tidal channel in the Lower Pennsylvanian Joggins Formation, Canada. *Palaios*, **29**: 624-645. doi:10.2110/palo.2013.073.

Pringle, J., Howell, J., Hodgetts, D., Westerman, A., and Hodgson, D. 2006. Virtual outcrop models of petroleum reservoir analogues: a review of the current state-of-the-art. *First Break*, **24**: 33-42. doi:10.3997/1365-2397.2006005.

Prokop, J., Pecharová, M., Nel, A., Grey, M., and Hörschemeyer, T. 2017. A remarkable insect from the Pennsylvanian of the Joggins Formation in Nova Scotia, Canada: insights into unusual venation of Brodiidae and nymphs of Megasecoptera. *Journal of Systematic Palaeontology*, **15**: 1051-1065. doi:10.1080/14772019.2017.1283364.

Rafuse, C., and Wach, G. 2011. Reservoir architecture of meanderbelt systems and vegetation density in the Carboniferous using LiDAR imagery. Earth Sciences, Dalhousie University, Halifax, NS.

Rarity, F., Van Lanen, X., Hodgetts, D., Gawthorpe, R., Wilson, P., Fabuel-Perez, I., and Redfern, J. 2014. LiDAR-based digital outcrops for sedimentological analysis: workflows and techniques. Geological Society, London, Special Publications, **387**: 153-183. doi:10.1144/SP387.5.

Reisz, R.R., and Modesto, S.P. 1996. Archerpeton anthracos from the Joggins Formation of Nova Scotia: a microsauro, not a reptile. *Canadian Journal of Earth Sciences*, **33**: 703-709. doi:10.1139/e96-053.

Rotevatn, A., Buckley, S.J., Howell, J.A., and Fossen, H. 2009. Overlapping faults and their effect on fluid flow in different reservoir types: A LIDAR-based outcrop modeling and flow simulation study. *AAPG Bulletin*, **93**: 407-427. doi:10.1306/09300807092.

Rygel, M.C. 2005. Alluvial sedimentology and basin analysis of Carboniferous strata near Joggins, Nova Scotia, Atlantic Canada. Earth Sciences, Dalhousie University, Halifax, NS.

Rygel, M.C., and Shipley, B.C. 2005. "Such a section as never was put together before": Logan, Dawson, Lyell, and mid-Nineteenth-Century measurements of the Pennsylvanian Joggins section of Nova Scotia. *Atlantic Geology*, **41**: 87-102.

Rygel, M.C., and Gibling, M.R. 2006. Natural Geomorphic Variability Recorded in a High-Accommodation Setting: Fluvial Architecture of the Pennsylvanian Joggins Formation of Atlantic Canada. *Journal of Sedimentary Research*, **76**: 1230-1251. doi:10.2110/jsr.2006.100.

Rygel, M.C., Gibling, M.R., and Calder, J.H. 2004. Vegetation-induced sedimentary structures from fossil forests in the Pennsylvanian Joggins Formation, Nova Scotia. *Sedimentology*, **51**: 531-552. doi:10.1111/j.1365-3091.2004.00635.x.

Schwarzacher, W. 1993. *Developments in Sedimentology: Chapter 7 Examples from the Carboniferous*. Elsevier. pp. 107-124.

Scott, A.C. 1998. The legacy of Charles Lyell: advances in our knowledge of coal and coal-bearing strata. Geological Society, London, Special Publications, **143**: 243-260. doi:10.1144/GSL.SP.1998.143.01.18.

Selim, S.S., Wafdy, R., and Khadrah, A.M.A. 2021. Sedimentological analysis and reservoir quality of the early Cenomanian transgressive sandstones, northern Western desert, Egypt. *Journal of Petroleum Science and Engineering*, **197**: 107948. doi:10.1016/j.petrol.2020.107948.

Siddiqui, N.A., Ramkumar, M., Rahman, A.H.A., Mathew, M.J., Santosh, M., Sum, C.W., and Menier, D. 2018. High resolution facies architecture and digital outcrop modeling of the Sandakan formation sandstone reservoir, Borneo: Implications for reservoir characterization and flow simulation. *Geoscience Frontiers*. doi:10.1016/j.gsf.2018.04.008.

SPE Research & Development Committee. 2012. *Grand Challenges Facing the E&P Industry*. Available from <https://www.spe.org/en/industry/globalchallenges/2022>.

Stimson, M., Lucas, S.G., and Melanson, G. 2012. The smallest known tetrapod footprints: *Batrachichnus salamandroides* from the Carboniferous of Joggins, Nova Scotia, Canada. *Ichnos*, **19**: 127-140. doi:10.1080/10420940.2012.685206.

Strasser, A.H., and Heckel, P.H. 2007. Cyclostratigraphy concepts, definitions, and applications. *Newsletters on Stratigraphy*, **42**: 75-114. doi:10.1127/0078-0421/2006/0042-0075.

Tanner, L.H. 2013. A Pennsylvanian Tetrapod Trackway from Joggins, Nova Scotia: The Size Continuum of *Batrachichnus Salamandroides*. *In* *The Carboniferous-Permian Transition: Bulletin 60. Edited by S.G. Lucas and W.A. DiMichele and J.E. Barrick and J.W. Schneider and J.A. Spielmann*. New Mexico Museum of Natural History and Science, Albuquerque, New Mexico. pp. 427-433.

Tape, C.H., Cowan, C.A., and Runkel, A.C. 2003. Tidal-Bundle Sequences in the Jordan Sandstone (Upper Cambrian), Southeastern Minnesota, U.S.A.: Evidence for Tides Along Inboard Shorelines of the Sauk Epicontinental Sea. *Journal of Sedimentary Research*, **73**: 354-366. doi:10.1306/091602730354.

Tatum, D.I., and Francke, J. 2012. Constructing hydrocarbon reservoir analogues of aeolian systems using ground penetrating radar. *Journal of Applied Geophysics*, **81**: 21-28. doi:10.1016/j.jappgeo.2011.09.014.

Teedumae, A., Heldur, N., and Kallaste, T. Sedimentary cyclicality and dolomitization of the Raikkiila Formation in the Nurme drill core (Silurian, Estonia). *In* *Proceedings of the Estonian Academy of Sciences, Geology*. 2004. *Edited by H. Aben and V. Kurnitski*. Estonian Academy Publishers. Vol. 53, pp. 42-62.

Tessier, B., Archer, A.W., Lanier, W.P., and Feldman, H.R. 1995. Comparison of ancient tidal rhythmites (Carboniferous of Kansas and Indiana, USA) with modern analogues. *In* *Tidal Signatures in Modern and Ancient Sediments. Edited by B.W. Flemming and A. Bartholoma*. Wiley-Blackwell, Oxford, UK. pp. 259-271.

Tibert, N.E., and Dewey, C.P. 2006. *Velatomorpha*, a new healdioidean ostracode genus from the early Pennsylvanian Joggins Formation, Nova Scotia, Canada. *Micropaleontology*, **52**: 51-66. doi:10.2113/gsmicropal.52.1.51.

Tibert, N.E., Rygel, M.C., Sanders, S.C., Elrick, S.D., and Nelson, J. 2013. Temporal and spatial distribution of ostracodes across the Pennsylvanian–Permian boundary interval in eastern North America. *International Journal of Coal Geology*, **119**: 93-105. doi:10.1016/j.coal.2013.08.002.

Utting, J., Giles, P.S., and Dolby, G. 2010. Palynostratigraphy of Mississippian and Pennsylvanian rocks, Joggins area, Nova Scotia and New Brunswick, Canada. *Palynology*, **34**: 43-89. doi:10.1080/01916121003620569.

van den Belt, F.J.G., van Hoof, T.B., and Pagnier, H.J.M. 2015. Revealing the hidden Milankovitch record from Pennsylvanian cyclothem successions and implications regarding late Paleozoic chronology and terrestrial-carbon (coal) storage. *Geosphere*, **11**: 1062-1076. doi:10.1130/ges01177.1.

van Lanen, X.M., Hodgetts, D., Redfern, J., and Fabuel-Perez, I. 2009. Applications of digital outcrop models: two fluvial case studies from the Triassic Wolfville Fm., Canada and Oukaimeden Sandstone Fm., Morocco. *Geological Journal*, **44**: 742-760. doi:10.1002/gj.1196.

Waldron, J.W.F., and Rygel, M.C. 2005. Role of evaporite withdrawal in the preservation of a unique coal-bearing succession: Pennsylvanian Joggins Formation, Nova Scotia. *Geology*, **33**: 337-340. doi:10.1130/g21302.1.

Wells, M.R., Allison, P.A., Hampson, G.J., Piggott, M.D., and Pain, C.C. 2005a. Modelling ancient tides: the Upper Carboniferous epi-continental seaway of Northwest Europe. *Sedimentology*, **52**: 715-735. doi:10.1111/j.1365-3091.2005.00718.x.

Wong, C. 2014. Lidar survey of the Joggins Formation in the Coal Mine Point section, Cumberland Basin (Nova Scotia, Canada). BSc Thesis, Department of Earth Sciences, Dalhousie University, Halifax, Nova Scotia.

Yeste, L.M., Henares, S., McDougall, N., García-García, F., and Viseras, C. 2019. Towards the multi-scale characterization of braided fluvial geobodies from outcrop, core, ground-penetrating radar and well log data. In *River to Reservoir: Geoscience to Engineering*. Edited by P.W.M. Corbett and A. Owen and A.J. Hartley and S. Pla-Pueyo and D. Barreto and C. Hackney and S.J. Kape. The Geological Society of London, London, UK. pp. 73-95.

Zatoń, M., Grey, M., and Vinn, O. 2014. Microconchid tubeworms (Class Tentaculita) from the Joggins Formation (Pennsylvanian), Nova Scotia, Canada. *Canadian Journal of Earth Sciences*, **51**: 669-676. doi:10.1139/cjes-2014-0061.

Chapter 2: Post-Scan Georeferencing of Lidar Data from a Geological Exposure Using ArcGIS™ for Adjustment

T.B. Kelly, G.D. Wach, and D.E. O'Connor

This chapter is based on the paper “Post-Scan Georeferencing of LiDAR Data from a Geological Exposure using ArcGIS™ for Adjustment”, by Trevor B. Kelly, Grant D. Wach, and Darragh E. O’Connor is published in the Modern Environmental Science and Engineering journal. The copyright agreement form for this chapter can be found in Appendix A.

2.1 Abstract

With the commonality of lidar increasing in usage amongst a wide array of disciplines, questions will arise regarding how the data is to be used and with what software the data will be visualized, manipulated, and utilized. One question that arises is whether a georeferenced point cloud is required and, if so, should direct georeferencing be performed during a lidar scan or completed post-scan. Georeferencing, in terms of lidar, is the process in which real-world coordinates are assigned to every point in the point cloud such that all data points are grounded where they would be on earth. Lidar scans don't need to be georeferenced; however, for many geological studies, it is particularly important, especially when other types of data are to be integrated. Overall, this can lead to improved geological interpretations. For geological outcrops, such as the cliff face exposed at Joggins, Nova Scotia, the need for georeferenced lidar scans is essential for research relating to the density of the fossilized forest for paleo-reconstruction studies, reservoir heterogeneity, compartmentalization studies, fluvial channel body aspect ratios, or the erosion rate of the cliff face. To save time at the geological exposure, georeferencing is not performed directly by the lidar system, but rather the coordinates from three strategically

placed control points were recorded for post-scan georeferencing. This paper will introduce a workflow detailing the steps to achieve a fully georeferenced point cloud by knowing the ground locations of three targets incorporated into the lidar scan using conventional software, in this case, ArcGIS™.

2.2 Introduction

Light Detection and Ranging (lidar) is used for a variety of applications, including, but not limited to scientific research (e.g., Rotevatn et al. 2008; Rotevatn et al. 2009; Minisini et al. 2014; Sahoo and Gani 2015), law enforcement (e.g., Griggs and Ludwig 1978; Beumier 2012; Wu et al. 2018), surveying (e.g., Xharde et al. 2006; Lim et al. 2013), and construction (e.g., Kwon et al. 2017; Yoon et al. 2017; Puri and Turkan 2020). Current papers published on the topic of georeferencing tend to deal more with the application of mathematical concepts and equipment setup rather than providing a procedural technique for achieving a georeferenced data set (e.g., Schuhmacher and Böhm 2005; Habib et al. 2008; Mohamed and Wilkinson 2009; Olsen et al. 2009; Wilkinson et al. 2010; Llorens et al. 2011; Olsen et al. 2011; Zhang and Shen 2013).

Despite the wide range of uses and different configurations among different disciplines, the premise of operation is similar; a laser pulse is emitted from the unit, travels to some remote target, reflects/refracts off the target, and returns to the detector (Bellian et al. 2005). The two-way travel time (source to target and target to detector) is halved and multiplied by the speed of light to obtain the Z distance. The X and Y positions are determined based on the location of the laser emitter when the pulse exits the instrument (Bellian et al. 2005). In addition to measuring the X, Y, and Z locations of thousands of

pints per second, the lidar instrument also has the capability of measuring the laser/light intensity (I) at each X, Y, and Z location.

In the geoscience discipline, lidar has been a valuable tool for capturing 3D outcrops in point cloud form, from which very detailed sedimentological and stratigraphic interpretations can be carried out. It has been recognized that the resulting intensity values recorded by the lidar unit correlate extremely well to lithology (Figure 2.1), thereby allowing for the determination between sandstone and shale, for example (e.g., Baldrige et al. 2009; Burton et al. 2011). In many instances, it is essential to have a point cloud that is fully georeferenced, which is to say that the points in the point cloud have the same easting, northing, and elevation as they would on earth, instead of being in some generic X, Y, and Z space. For the scans that are performed by researchers of the Dalhousie University Basin and Reservoir Laboratory, the georeferencing of point clouds is carried out post-scan using georeferencing targets, as opposed to direct georeferencing performed during the scan. For this to be successful, three targets (control points) are placed at varying X, Y, and Z locations within the scan zone. The locations of these targets are measured and recorded using a real-time kinematic (RTK) differential global positioning system (DGPS). This helps to alleviate the main disadvantages of direct georeferencing, which are the increased time and precision required for instrument setup (Olsen 2011). Moreover, post-scan georeferencing is particularly useful when the laser scanner does not have built-in GPS capabilities or the built-in GPS capabilities of the laser scanner are not well known, or when there could be potential errors in collecting GPS data directly during the scan, and for multiple scans that will be eventually merged, highly accurate RTK DGPS data is required, which laser scanners do not have as a built-in option.

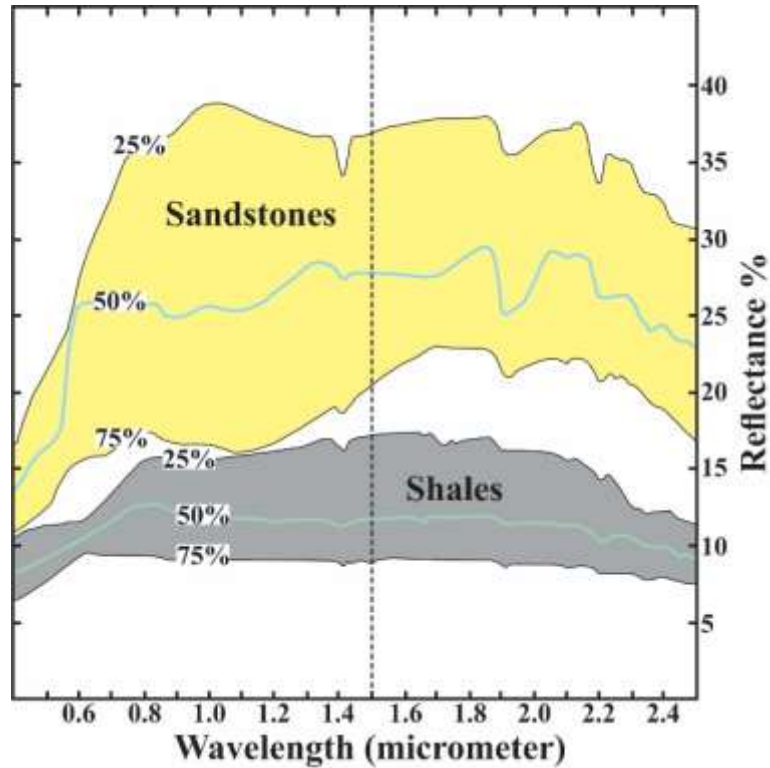


Figure 2.1: A NASA JPL library spectroscopy solid sample data with the median (solid green line) and quartiles for shale (grey) and sandstone (yellow) (after Baldridge et al. 2009; Burton et al. 2011). The dashed line at 1.5 micrometers is the approximate wavelength of terrestrial lidar. At the wavelength of terrestrial lidar, sandstone and shale have a noticeable spectral separability between them (Burton et al. 2011).

The purpose of this technical paper is to introduce a procedure by which georeferencing of point cloud data can be performed using standard and widely available programs and software. The workflow from raw point cloud data to a fully georeferenced data set is broadly divided into four parts: (1) data preparation, (2) creation of point cloud/georeferencing targets shapefiles, (3) point decimation, and (4) point cloud adjustment. This paper will make use of a data set collected in May of 2013 from the Joggins Formation located in the community of Joggins, Nova Scotia.

A fully georeferenced data set allows for a variety of studies, and detailed interpretations can be achieved, such as the determination of coastal erosion rates using multiple georeferenced scans performed over a length of time. Also, the Joggins Formation contains upright, fossilized trees, which is a characteristic that is unique to this site. The

use of successive and georeferenced lidar scans could potentially give researchers the ability to determine the density of the paleo forest that once existed (Figure 2.2). Moreover, a georeferenced point cloud can be easily integrated with other data gathering techniques, such as a ground-penetrating radar survey, for example.

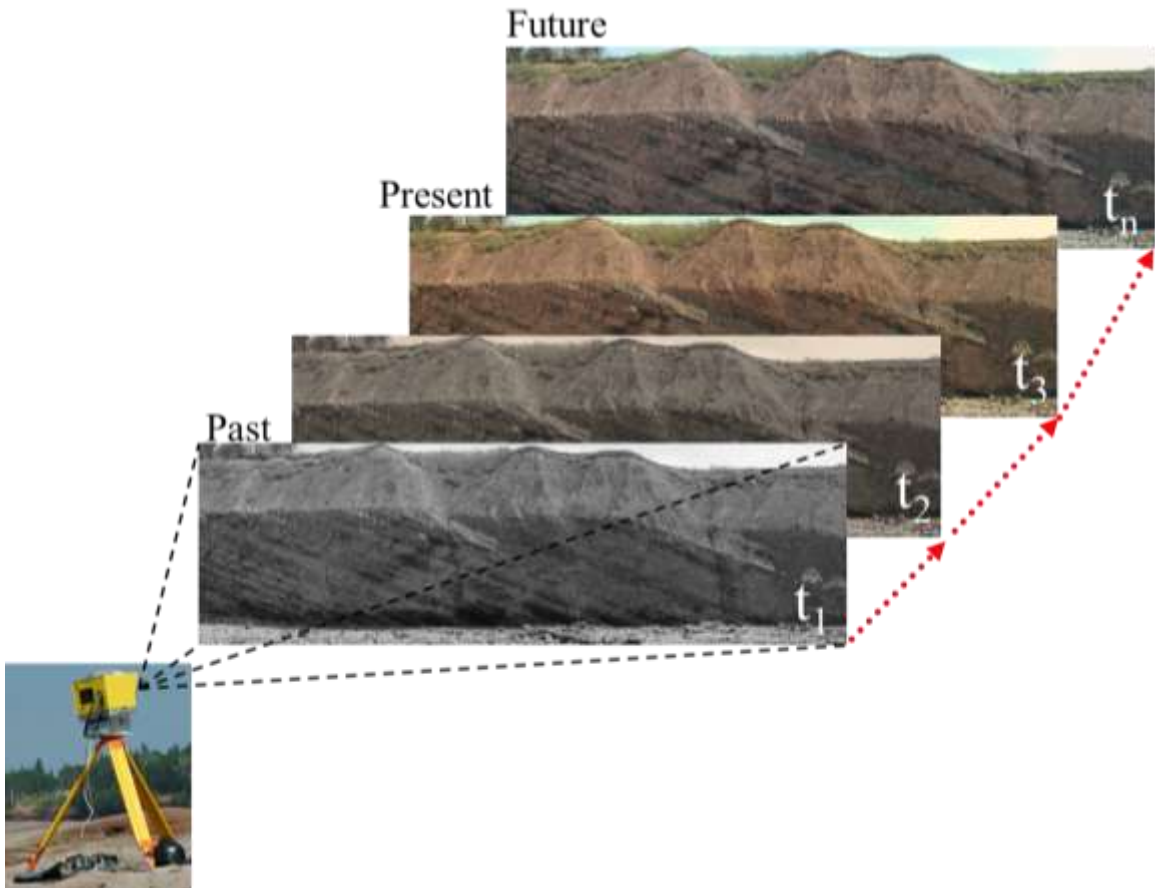


Figure 2.2: Using successive, georeferenced lidar point clouds over some time, a variety of studies could potentially be completed (modified from Wong 2014). These may relate to the paleo forest density or erosion studies.

2.3 Previous Work

The use of lidar in outcrop geology is not a recent trend; however, a search for lidar georeferencing-related outcrop papers does not yield many examples. For that reason, this paper is written out of the need for georeferencing ground-based, static lidar scans using accurate target locations for point cloud adjustment. An article by Schuhmacher and Böhm

(2005) deals with the subjects of sensor- and data-related georeferencing methods. In this paper, seven methods are tested in two separate experiments with the results showing the total accuracy for each method, with the conventional total station setup being the most accurate (Schuhmacher and Böhm 2005).

Habib et al. (2008) performed a comparative, indirect georeferencing analysis in which three sources of control data are investigated: 1) ground control points, 2) lidar patches, and 3) lidar lines. A new method for the absolute orientation of a lidar point cloud was introduced by Mohamed and Wilkinson (2009), in which they placed two antennas on top of a static lidar unit to provide higher data gathering precision for attitude determination. Field survey methods were introduced by Olsen et al. (2009) as ways of georeferencing terrestrial lidar scans completed in a dynamic environment over a significant scan area distance. Wilkinson et al. (2010) present a novel method that utilizes two firmly mounted antennas installed on the optical head of the lidar scanner to determine the absolute positioning of lidar point clouds.

A paper by Llorens et al. (2011) shows how georeferenced information from lidar sensors can have potential benefits for crop management. In their research, they propose a workflow for obtaining a georeferenced canopy map from lidar and paring it with GPS data from a receiver installed atop a tractor. Olsen et al. (2011) discuss the use of a new georeferencing technique with related algorithms for automating 3D point cloud georeferencing of large-scale scans. Zhang and Shen (2013) identify and demonstrate the significant direct georeferencing distortion factors, such as the datum distortion scale and the earth curvature distortion and apply high-precision map projection correction formulas to airborne lidar data for direct georeferencing. While these papers are useful for

determining such things as the optimum equipment setup that will lead to the most accurate data set, they do not present much in the form of a workflow for taking raw data with an arbitrary coordinate system and converting into data that has real-world coordinates.

The Joggins Formation itself has been studied for over 150 years (Grey and Finkel 2011). Much of the research conducted in this area can be grouped into three all-encompassing categories. The first being geology (e.g., sedimentology and stratigraphy); the second being paleobiology (e.g., discovery and taxonomy); and the third being paleoenvironmental reconstructions that incorporate the previous two categories (Grey and Finkel 2011). Grey and Finkel (2011) summarize the bulk of the research within the three categories mentioned above from past to present and provide insight for future work that could arise.

2.4 Study Area

The location of the study area is approximately 230 km north of Halifax, Nova Scotia, in the village of Joggins on the coastline of Chignecto Bay, an inlet of the Bay of Fundy where the tides ebb and flow some 13 meters twice daily (Figure 2.3a). This area was selected due to the continuity and quality of the 2D exposure of the outcrop known as the Joggins Formation, in addition to the ease of access. The section of the scanned outcrop is located just north of Coal Mine Point (Figure 2.3b), which is a sandstone headland composed of more resistant, less erosive rock that displays a significant change in depositional style that is still discussed and debated. The Joggins Fossil Cliffs (Joggins Formation) along with six other conformable formations (Ragged Reef, Springhill Mines, Little River, Boss Point, Claremont, and Shepody) were designated in 2008 as a United Nations Educational, Scientific and Cultural Organization (UNESCO) heritage site,

because of the beautifully exposed and preserved rock layers demonstrating the most complete and comprehensive fossil record of life during the “Coal Age,” a period when lush forests and swamps occurred over much of the World’s tropics (UNESCO 2008).

Joggins and the surrounding area have an extensive history of coal mining, dating back to 1686 and continuing for over 200 years (Falcon-Lang 2009). Intricate underground mine workings were established, with some of the remnants (e.g., mine openings and support timbers) visible within the cliff face. There is also evidence of some of the topside development relating to coal mining in the form of timbers (rail track and support) and steel spikes on the beach between Main Street and the Joggins Fossil Cliffs Centre and remains of a wooden pier that existed for loading coal onto ships during high tide for destinations throughout the Maritimes and New England (Falcon-Lang 2009). The section of the Joggins Formation chosen for scanning does not show evidence of any historical coal mine workings.

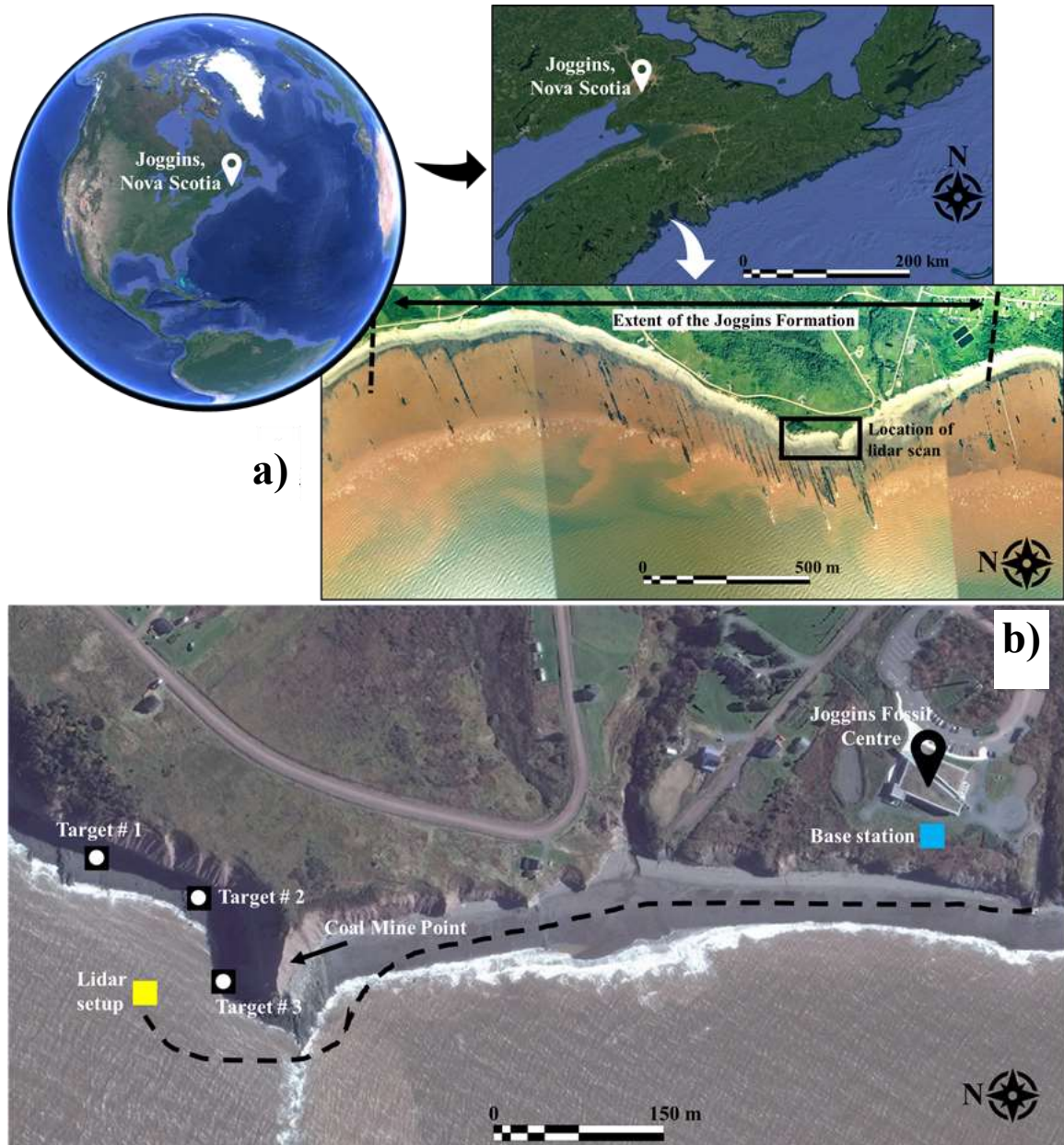


Figure 2.3: Location maps of the Joggins Formation study area. (a) Location map of Joggins, Nova Scotia. The zoomed-in aerial photograph is annotated to show the extent of the Joggins Formation and the location of the lidar scan (after Nova Scotia Department of Natural Resources 2005; Calder and Boon 2007). (b) Aerial photograph of various points of interest. The Joggins Fossil Centre is located near the top right. The blue box just to the south of the centre is the location of the base station. The black dashed line indicates the route that was taken to reach the Coal Mine Point scan area. The lidar setup is indicated by the yellow box in the lower left-hand quadrant of the photograph with the locations of the three target setups shown by a black box with a white circle in the middle.

2.5 Equipment and Methods

2.5.1 *Terrestrial Laser Scanning*

Stationary ground-based laser scanning was achieved by using the tripod-mounted Dalhousie University Basin and Reservoir Laboratory Optech Incorporated Intelligent Laser Ranging and Imaging System (ILRIS) 3D lidar scanner (Figure 2.4) with a scan speed of 2.5 kHz and 2,500 points per second (Optech Incorporated 2006b). Lidar is an exceedingly versatile ground-, air-, and water-based instrument for the remote collection of data and it has been employed comprehensively to an array of disciplines including earth sciences (e.g., Bellian et al. 2005; Bellian et al. 2007; Rotevatn et al. 2009; Moore et al. 2012; Rarity et al. 2014; Grechishnikova 2016; Siddiqui et al. 2018; Zeng et al. 2018). Lidar scanning bombards a surface (in this case, a rock face) with pulsating laser energy and measures the difference in time between the primary pulse emission and the returning signal detection. The emitted laser pulse has a wavelength of 1,535 nm (infrared spectrum). To obtain a reflection, the rock being inundated by laser pulses must be of the type to produce a dielectric discontinuity, allowing the original wave to be reflected to the source.

The section of cliff scanned was chosen because of the abundance of channel bodies. Scanning was completed on a clear, sunny day to avoid various problems, such as the increased reflectivity associated with scanning a wet outcrop and rain droplets. The scan was collected at an average range of approximately 100 m from the cliff face using a 12 mm point spacing in a step-stare scan pattern. The point cloud is an assemblage of approximately 1.4 million points, following decimation of extraneous points; all which contain an 8-bit intensity value between 0 and 255, in addition to a unique X (latitude), Y (longitude), and Z (elevation) value (i.e., each point has an exclusive coordinate).



Figure 2.4: A photograph of the Optech ILRIS-3D lidar scanner setup at Joggins, Nova Scotia (Kelly and Wach 2020). Labelled in this photograph is the laser scanner (1), which was mounted atop the pan/tilt base (2), both of which were connected to a tripod (3). A ruggedized laptop computer (4) was used to adjust scanner settings and initiate the lidar scan. The lidar unit (1 and 2) is powered by a battery pack (5). The dipping strata of the Joggins Formation can be seen in the background. The distance from the lidar setup to the outcrop was approximately 100 m and is indicated by the dashed line.

The lidar system has numerous separate pieces that must be set up in a particular order. The procedure that was used for this scan is as follows:

- (a) setup and level the tripod
- (b) mount the pan/tilt base to the levelled tripod
- (c) mount the lidar scanner on top of the pan/tilt base
- (d) measure the coordinates of the lidar setup using the RTK DGPS
- (e) connect the lidar scanner to the pan/tilt base, the battery pack, and the ruggedized laptop computer using the required connectors and cables
- (f) turn the system on and wait for boot up
- (g) start the specialized software on the laptop computer and connect to the lidar scanner

- (h) set the scan area using the software on the laptop computer and any other desired parameters
- (i) initiate the scan and wait until complete

2.5.2 *Global Positioning System*

The static terrestrial laser scanner was combined with a Real-Time Kinematic (RTK) Differential Global Positioning System (DGPS) (Figure 2.5) to provide location data that was used to georeference the point cloud data set. The purpose of a Real-Time Kinematic Differential Global Positioning System is to apply differential correction techniques that will improve the accuracy of the location data gathered by GPS receivers (Van Sickle 2015). At the study area, the base station was set up over a water well cap on the oceanside (cliffside) of the Joggins Fossil Cliffs Centre, which has been previously surveyed to obtain its coordinates (UTM Zone 20T easting = 387,098.72; northing = 5,061,126.31; elevation = 26.45 m). The transmission antenna was set up next to the base station. Its purpose was to transmit the corrections made by the base station to the rover in real-time. The rover was mounted on an aluminum pole and was carried a maximum distance of ~ 600 m away from the base station/transmission antenna setup. The X, Y, and Z coordinates of each georeferencing target were recorded using the rover mounted RTK DGPS, following their placement inside the lidar scan survey area. This allows for lidar point cloud georeferencing to be completed post-scan in the Basin and Reservoir Laboratory at Dalhousie University.

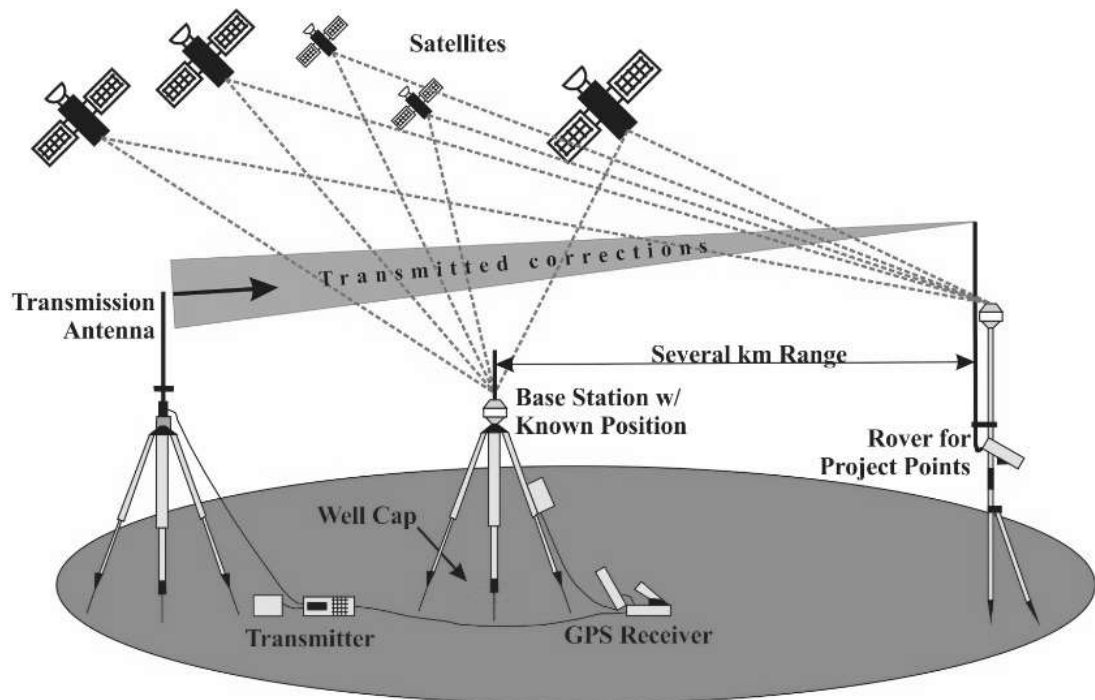


Figure 2.5: Simplified sketch of the global positioning system equipment used to provide a georeferenced lidar data set (after Van Sickle 2015). The base station was erected over a well cap with a known set of coordinates. The transmission antenna was erected next to the base station. The rover was brought to the lidar survey area and utilized for measuring and recording the coordinates of the three lidar survey georeferencing targets.

The RTK DGPS also has numerous separate pieces that must be set up in a particular order. The procedure that was used for this scan is as follows:

- (a) the well cap of known coordinates was located on the backside (cliffside) of the Joggins Fossil Cliffs Centre, and the base station tripod was set up over this well cap and levelled by eye
- (b) place the GPS receiver on the tripod and use the levelling screws to level
- (c) setup the transmission antenna tripod directly adjacent to the base station and level by eye
- (d) mount the transmission antenna on this tripod and extend to its maximum height

- (e) connect the GPS receiver and transmission antenna to their respective power supplies as well as to each other using the required cables and connectors
- (f) record the height of the base station above the well cap and use this value with the known coordinates of the well cap to determine the base stations location
- (g) turn on all the various pieces of equipment, including the rover GPS and make sure both the base station and rover are synced with each other and both are receiving GPS data
- (h) the rover GPS can now be taken to the intertidal zone and used for measuring the locations of the georeferencing targets and the lidar system setup

2.5.3 Georeferencing Targets

Three georeferencing targets were incorporated into the lidar scan area to allow for the resulting point cloud to be georeferenced. A successful lidar scan must include at least three targets placed at varying X, Y, and Z locations so that triangulation can be performed, ensuring accuracy is maximized. The ideal placement for these three targets would be one placed at the top of the section, and the remaining two placed a distance apart on either side of the lidar scan area. However, due to logistics and accessibility, it was not feasible to place a target at the top of the cliff. Therefore, all three targets were placed at varying locations in the intertidal zone (Figure 2.3b).

The targets are made of a 0.5 m by 0.5 m piece of plywood with an outer area covered in black, retro-reflective paint, and an inner circle (approximately 12 cm in diameter) that is white and non-reflective (Figure 2.6a). Targets must be placed such that the black outer area and white inner circle face the lidar unit and can be scanned by the lidar system (Figure 2.6b). When the targets are scanned by the lidar unit, they return a distinct intensity

signature that when combined with the differential GPS readings of the centres of the non-reflective white inner circles, allows for the scans to be georeferenced.



Figure 2.6: Images of the utilized georeferencing targets. (a) image of the lidar georeferencing targets that are placed at varying X, Y, and Z coordinates in front of the cliff face portion to be scanned (Rafuse and Wach 2011). (b) image showing the placement of one of the georeferencing targets on the inter-tidal zone with the cliff and the Joggins Fossil Centre in the background (Rafuse and Wach 2011).

The setup of the three georeferencing targets is quick and straight-forward. The procedure that was used for this scan is as follows:

- (a) three locations a distance apart and at varying elevations within the scan field of view were selected
- (b) a target was placed at each of the three locations, preferably resting against a larger rock for stability
- (c) the RTK DGPS was used to measure the centre of each target

2.6 Data

2.6.1 Lidar/Target Setup Locations

The data consists of an easting, northing, and elevation value for each of the three targets and the lidar setup. The locations of the targets were determined by measuring the

centres of each. The lidar setup location was determined by measuring the approximate centre of the glass lens housing the scanner.

2.6.2 Lidar Point Cloud

The raw lidar data contains over 14.5 million points spread amongst four scan tasks. Some of these points are overlapping, and so can be eliminated. Before working with the raw lidar data, it is first necessary to use the parser software developed by the lidar manufacturer to export file formats that can be used.

2.7 Processing Procedure

The procedure for taking a raw, non-georeferenced lidar point cloud to a fully georeferenced point cloud is divided into four sections, listed here:

- (1) data preparation
- (2) creation of point cloud/georeferencing target shapefiles
- (3) point decimation
- (4) point cloud adjustment

2.7.1 Data Preparation

To prepare the raw lidar intensity data for eventual shapefile creation and subsequent adjustment, a simple workflow was applied. This ensured the point cloud data was in a compatible format for use with ArcGIS™ software. The workflow for accomplishing the data preparation phase is as follows:

- (a) The raw .xyz files were opened using a simple text editor (e.g., Notepad)

(Figure 2.7a). A header line was added across the top corresponding to each column of data. The header line consists of an easting, northing, elevation, and intensity, each separated by one space only, which is the same format as the numerical data below the header.

- (b) The data was displayed with the easting, northing, elevation, and intensity values being separated by only one comma (Figure 2.7b), using the *replace* option found in Notepad.

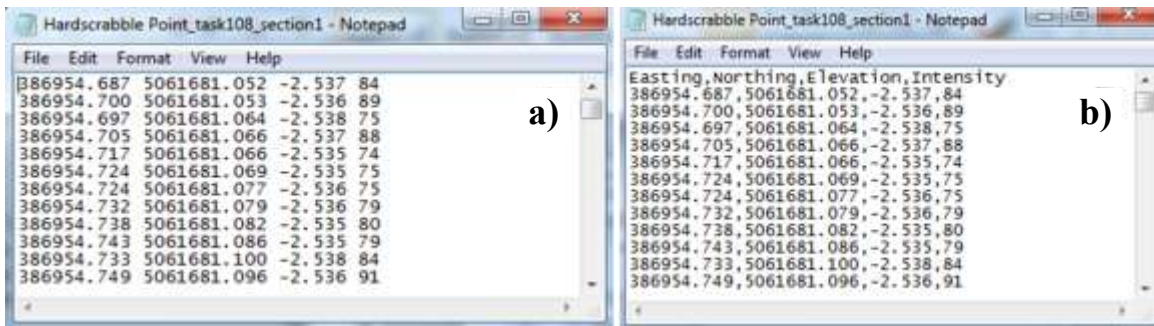


Figure 2.7: Unaltered and altered raw lidar intensity data. (a) Raw lidar intensity data displayed in Notepad. (b) Raw lidar intensity data displayed in Notepad with the addition of a header line and all data separated by one comma.

2.7.2 Shapefile Creation

This section of the workflow utilizes ArcCatalog™, ArcScene™, and ArcMap™ for the creation of shapefiles. The produced shapefiles include the lidar point cloud shapefile, the false coordinate target locations, and the real coordinate target locations. The workflow for accomplishing the *shapefile* creation phase is as follows:

- (a) In ArcCatalog™, use the *File* option from the menu toolbar to *Connect Folder*. Select the folder containing the text file created from the previous Data Preparation workflow. When the folder connects, the text document will be visible under the *Folder Connections* folder in the *Catalog Tree* pane.

- (b) Right-click the text document under *Folder Connections* and select *Create Feature Class from XY Table* (Figure 2.8a). For *Input Fields*, select the proper header description that describes the X Field, Y Field, and Z Field (e.g., easting, northing, and elevation) (Figure 2.8b). Select the *Coordinate System of Input Coordinates* and choose the appropriate coordinate system. For the *Output – Specify output shapefile or feature class*, select the file folder symbol.

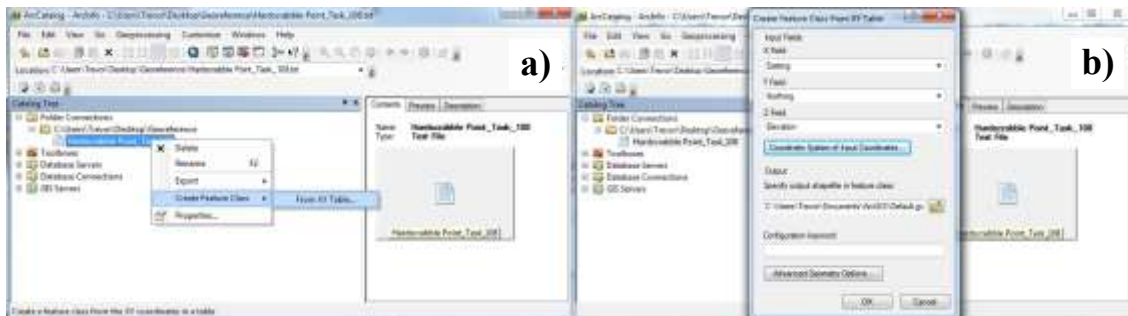


Figure 2.8: The creation of a shapefile from a text document. (a) To create a shapefile from the text document, right-click on the text document, and expand *Create Feature Class*. Select *From XY Table*. (b) A window will open called *Create Feature Class From XY Table*. For the *Input Fields*, select the proper header description that describes the *X Field*, *Y Field*, and *Z Field*. In this case, they are easting, northing, and elevation, respectively.

- (c) The *Saving Data* window will open. Navigate to the folder containing the text document. Be sure that the *Save as type* is selected as being a shapefile and select *Save* and *OK*. In ArcCatalog™, the newly created shapefile is now visible under *Fold Connections* (Figure 2.9).

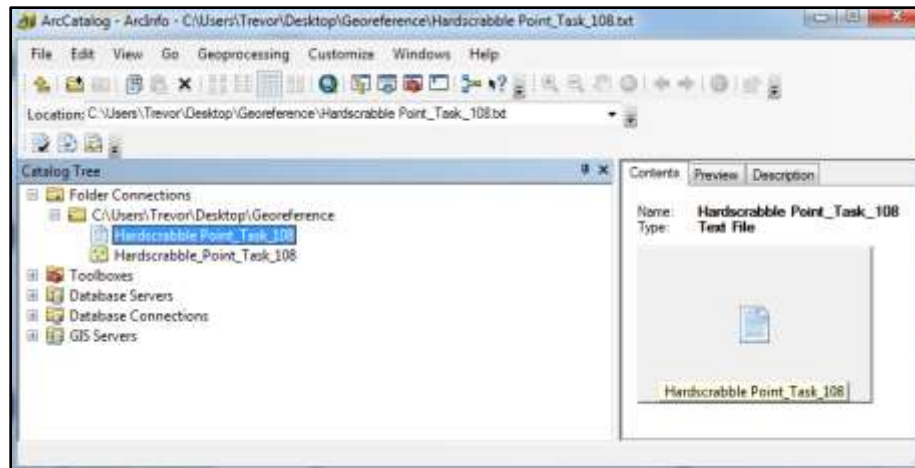


Figure 2.9: A screen capture from ArcCatalog™ showing the newly created shapefile under *Folder Connections* in the *Catalog Tree*.

- (d) Choose a blank map in ArcScene™. Select the *File* drop-down menu and select *Add Data* and *Add Data*. The *Add Data* window will open. Double-click on the *Folder Connections* folder. Select the shapefile and choose *Add*.
- (e) When the shapefile opens, it will be a single colour point cloud (Figure 2.10a). To locate targets, a colour ramp is applied (a set of colours used to represent a range of intensity values). Digital photographs of the scan area will also help locate targets. Right-click on the shapefile and select *Properties*. Select the *Symbology* tab in the *Layer Properties* window and click on *Quantities* and *Graduated Colours*. In the *Fields* section, base the *Value* on *Intensity*. Select a *Colour Ramp* with a broad range of colours and set the *Classes* to at least 10. Click *Apply* and select the *OK* button. The point cloud will display with colour based on intensity (Figure 2.10b). The targets can now be located in the scan.

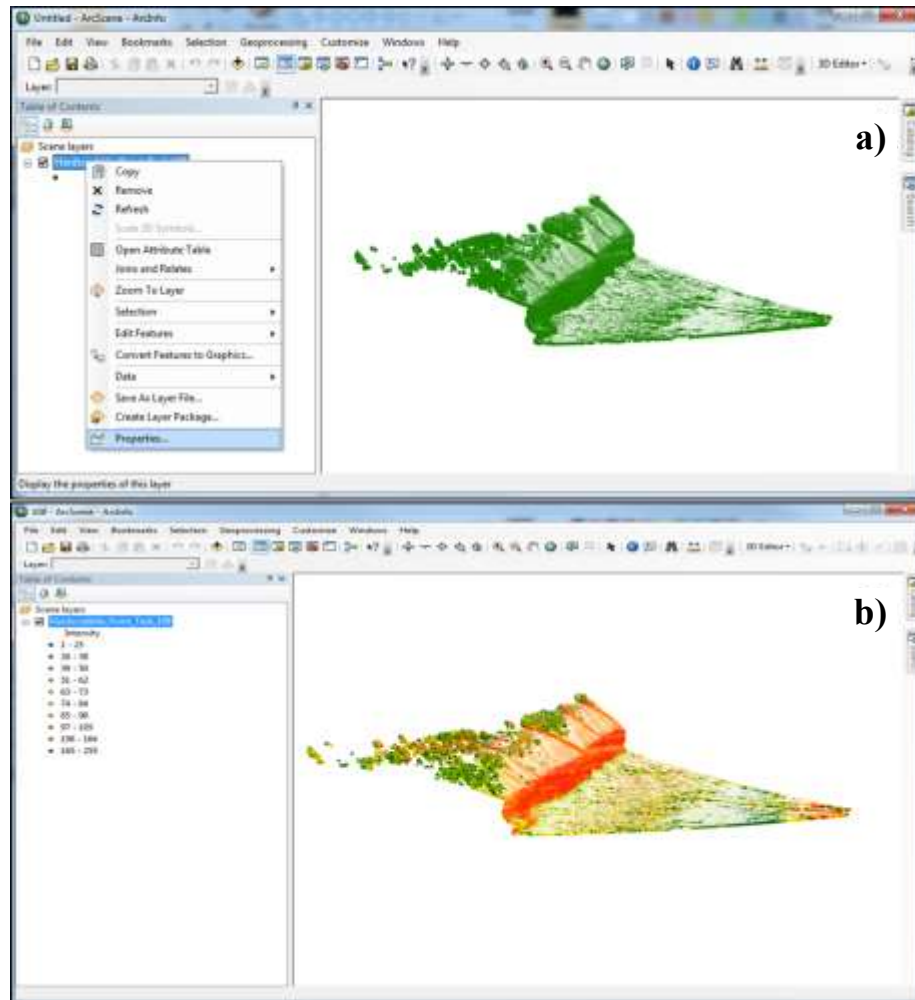


Figure 2.10: Point clouds based on a single colour and on intensity. (a) Initially, the point cloud in ArcScene™ will be displayed in a single colour, which makes ground target locating very difficult. (b) The same image as in A), but with a colour ramp based on intensity applied. Using this intensity-based colour scheme will make ground target locating easier.

- (f) Use the Bitmap images and JPEG images from the raw, unprocessed, and unparsed lidar data in addition to any photographs taken with a camera to help with locating the three georeferencing targets within the point cloud. The targets can be found by using various zoom/pan/tilt options in ArcScene™. The targets appear as a square of high-intensity points. In this case, the target can be seen resting against a boulder, as outlined by the black box (Figure 2.11a). Using the *Identify* tool, click on the point that represents the centre of the target. Record the easting, northing, and elevation from the information that

becomes available. Perform for the remaining two georeferencing targets (Figure 2.11b).

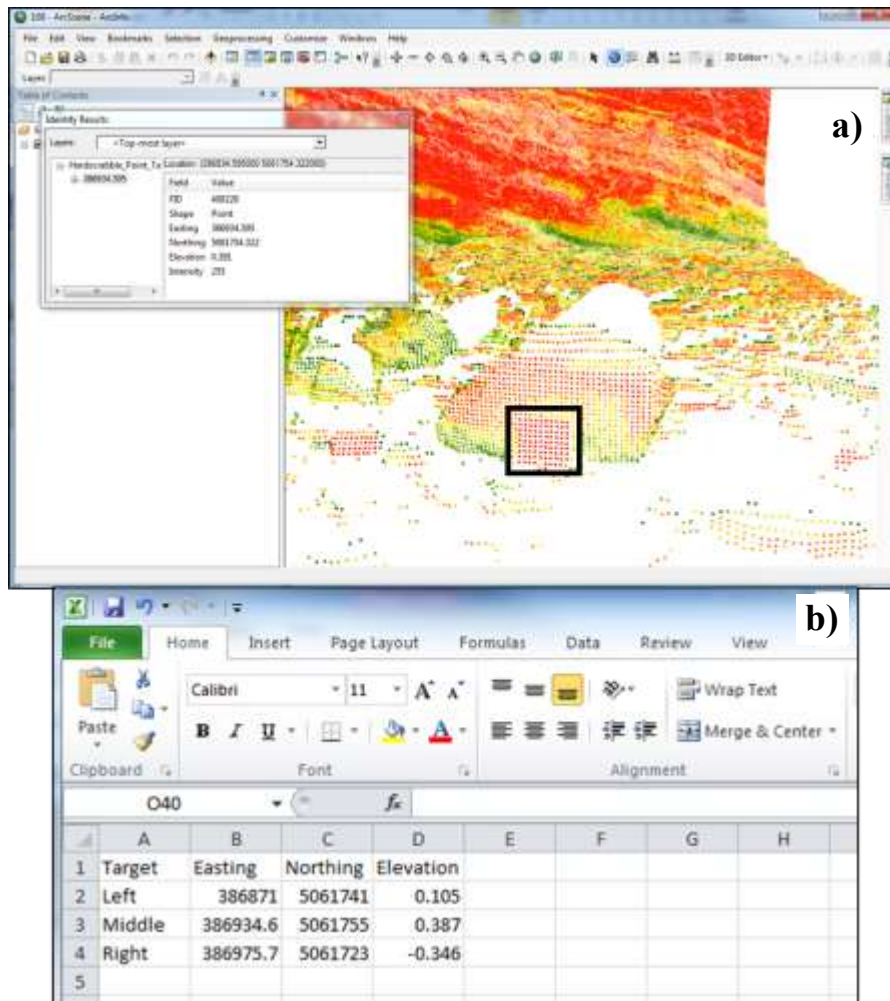


Figure 2.11: Locating the false georeferencing target locations from the intensity-based point cloud. (a) The intensity-based point cloud showing one of the georeferencing targets within the black square. (b) A table recording the false locations of the three georeferencing targets.

- (g) With the three target locations recorded (false locations) open Microsoft Excel and create a simple table (Figure 2.11b). Save the file as a .csv (comma delimited) file within the Georeference named file created back at the start. Make another simple table like the one shown above, but this time input the correct coordinate locations as recorded by the differential global positioning system rover (Figure 2.12). Save it the same way as the previous file.

The image shows a screenshot of a Microsoft Excel spreadsheet. The spreadsheet has a header row with columns labeled A through H. The data is organized as follows:

	A	B	C	D	E	F	G	H
1	Target	Easting	Northing	Elevation				
2	Right	386989.3	5061636	1.036				
3	Middle	387039.7	5061647	3.055				
4	Left	387070	5061705	3.875				
5								

Figure 2.12: A table displaying the correct locations of the three georeferencing targets as measured by the RTK DGPS.

- (h) In ArcCatalog™, refresh the folder to display the new .csv files. The previous steps for creating a shapefile can be applied to the false and real target location files to transform these files into shapefiles.
- (i) Select the *File* drop-down menu in ArcMap™. Choose *Add Data* and *Add Data*. When the window opens, select the three shapefiles, and click *Add* (Figure 2.13a). Note the three points (boxed in green) in the right-hand corner; these are the real-world coordinates that we are trying to get the point cloud to georeference with (Figure 2.13b). The other three points (circled in red) are the incorrect target locations (incorrect because the scan was performed without georeferencing); two of these points are concealed by the point cloud.

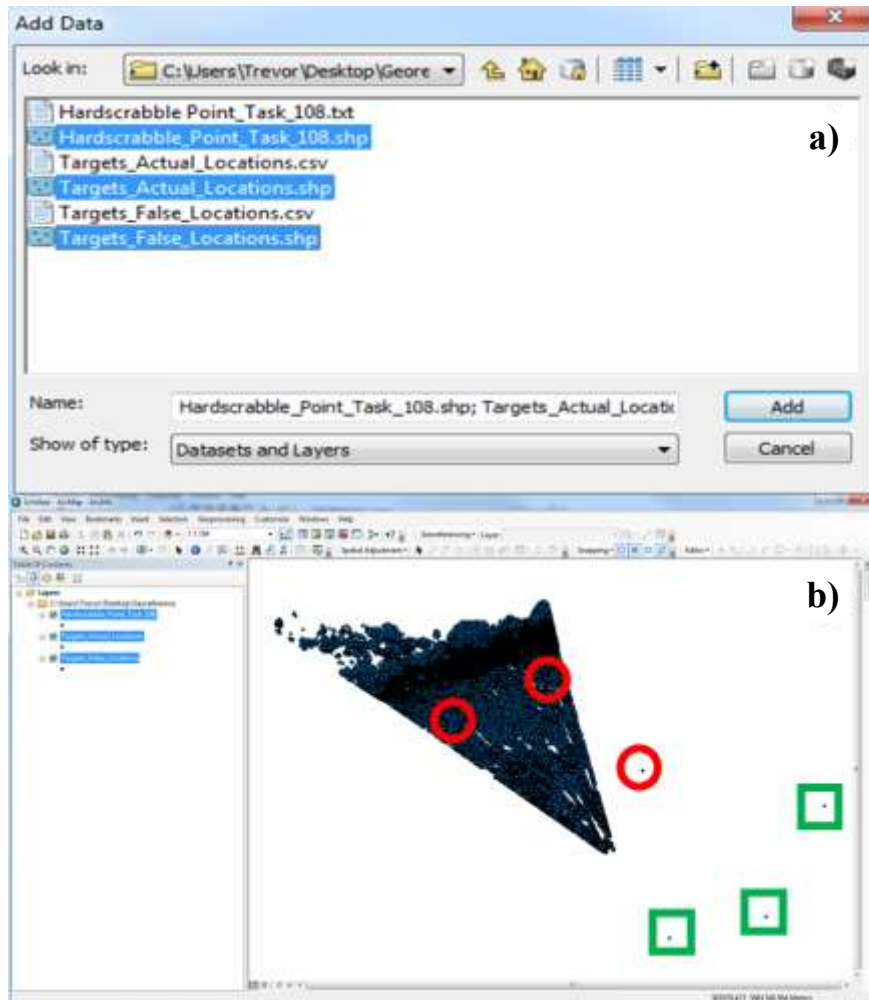


Figure 2.13: The three shapefiles created and displayed. (a) The three shapefiles created in this section. (b) An image that shows the three shapefiles displayed. The point cloud is visible as a triangular-shaped wedge. The false target locations are circled in red, and the real target locations are boxed in green.

2.7.3 Point Decimation

To decrease the processing time and remove points not associated with the outcrop (the focus of concurrent research), many points can be deleted. The points represent objects/areas such as vegetation, infrastructure (e.g., houses, power lines, power poles, etc.), and the intertidal zone, which contains the highest number of erroneous points. The workflow for accomplishing the point decimation phase is as follows:

- (a) The two target locations shapefiles were turned off, leaving only the point

cloud displayed. The *Select by Polygon* tool was used to batch select the points to delete (Figure 2.14a). The chosen points were automatically highlighted in blue (Figure 2.14b). The *Editor* drop-down menu was selected from the *Editor* toolbar, and the *Start Editing* option was chosen.

- (b) Right-click on the point cloud shapefile in the *Table of Contents* and select *Open Attribute Table* (Figure 2.14b). At the bottom of the *Attribute Table*, choose to display only the highlighted points (Figure 2.14b). Right-click on the left-hand edge of the *Attribute Table* and select *Delete Selected*. When finished, the records will be deleted. The *Attribute Table* can be closed.
- (c) Go back to the *Editor* drop-down menu and select *Save Edits*. The process was used several times to shrink the point cloud (Figure 2.14c-d).

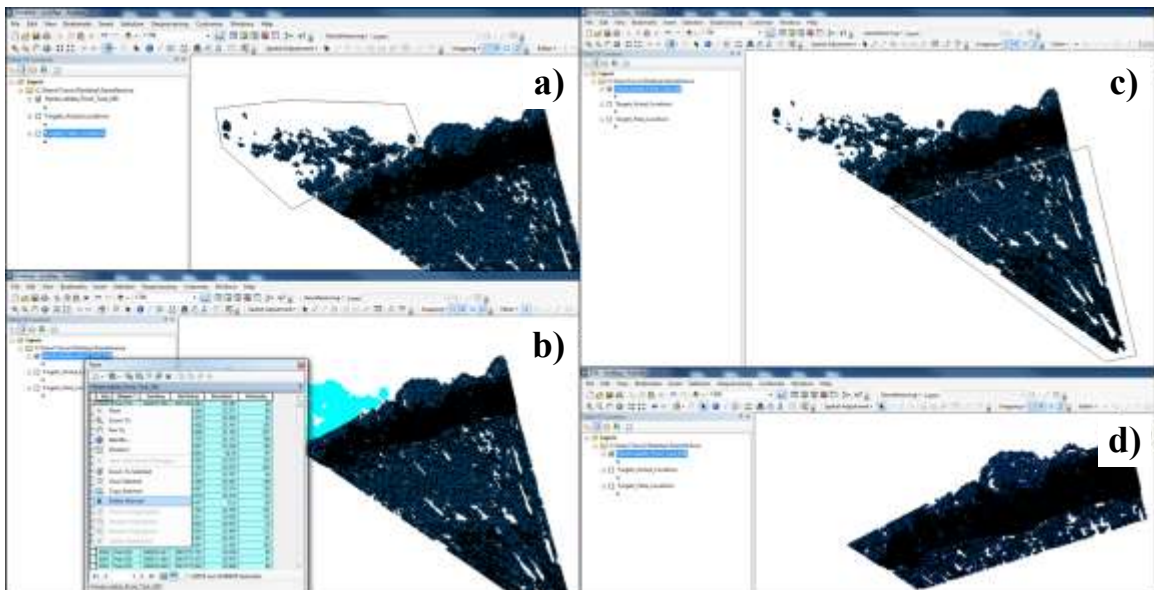


Figure 2.14: The selection of erroneous points from the point cloud. (a) The batch selection of non-useful points from the point cloud using a polygon. (b) The non-useful points are highlighted in the attribute table and can be deleted as a group. (c) The batch selection of the intertidal zone points using a polygon, which for this study is not useful. (d) The final point cloud after the deletion of non-useful points.

2.7.4 Point Cloud Adjustment

The previous workflows relate to preparing the point cloud for georeferencing. The following shows how to take a point cloud with a coordinate system based on the lidar setup to a geodetic coordinate system with each point displaying a unique X, Y, and Z value. The workflow for accomplishing the point cloud adjustment phase is as follows:

- (a) The point cloud shapefile was turned off, leaving the two target location shapefiles visible (Figure 2.15a). The *Start Editing* option was chosen from the *Editor* drop-down menu. Ensure that the *Spatial Adjustment* toolbar is activated and select the *Set Adjust Data* option (Figure 2.15b). The *Choose Input For Adjustment* window will open. Select the *All features in these layers* option and un-check the correct target locations, since they do not need to be georeferenced (Figure 2.15c).

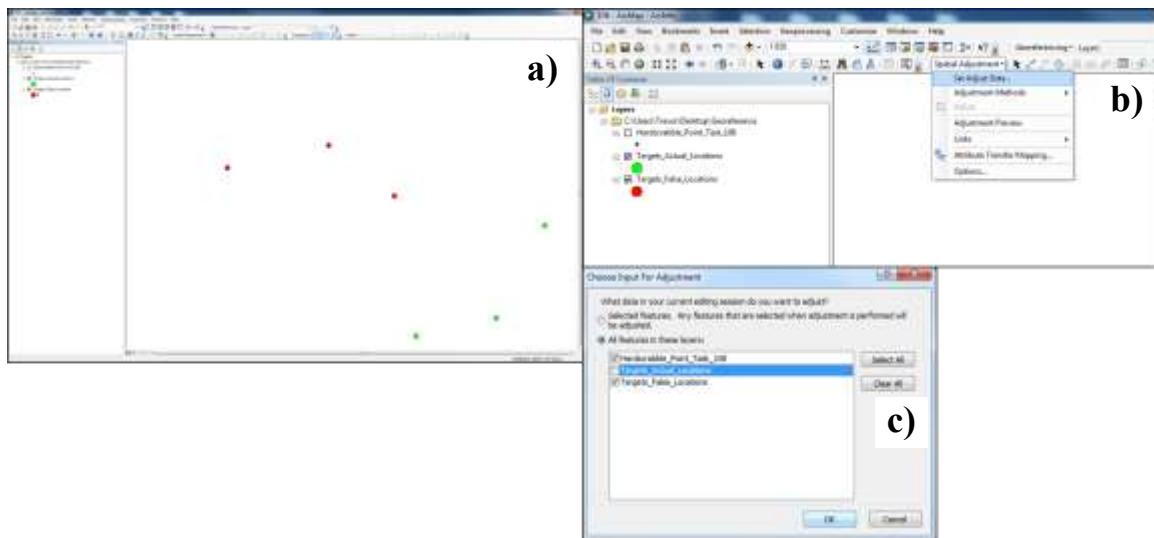


Figure 2.15: The preparation of the point cloud for adjustment. (a) The red points are the incorrect/false georeferencing target locations. The green points are the correct georeferencing target locations, as measured by the RTK DGPS. (b) To adjust the incorrect georeferencing target locations and the point cloud, the *Set Adjust Data* must be selected from the *Spatial Adjustment* toolbar. (c) To adjust the data, only choose the point cloud and the false georeferencing target locations.

(b) In the *Spatial Adjustment* drop-down menu, the *Transformation – Affine* option from the *Adjustment Methods* was chosen (Figure 2.16a). Select the *New Displacement Link* on the *Spatial Adjustment* toolbar (Figure 2.16b). Select one of the false location points, which will snap to that point, then select the point that corresponds to the position where that point should be. This can be completed for the remaining two locations (Figure 2.16c). Click on the *Spatial Adjustment* drop-down menu again and click on *Adjust*. When the adjustment is complete, select the *Editor* drop-down menu and choose *Save Edits*. The red points are not visible because they are overlain by the true target locations (green points). Turn the point cloud shapefile on (Figure 2.17). The point cloud should now be georeferenced.

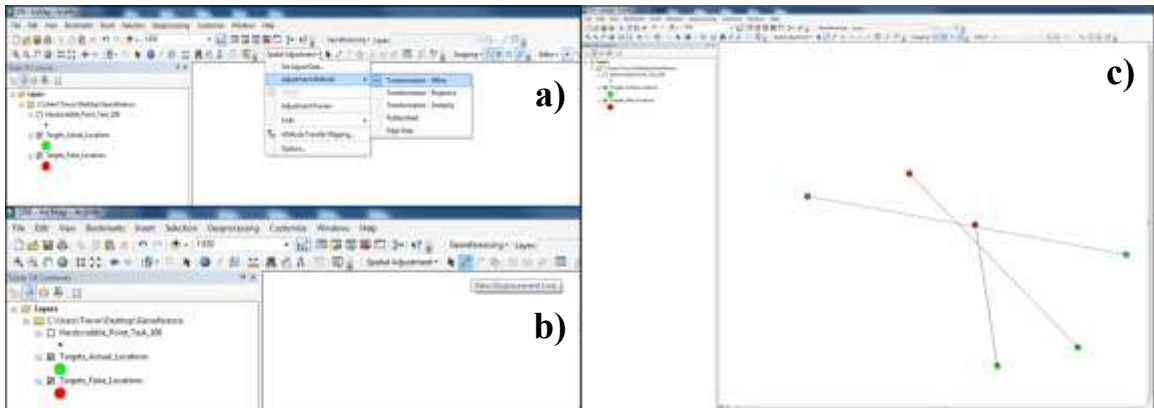


Figure 2.16: The transformation of the point cloud data to its proper location. (a) The *Transformation – Affine* was chosen from the *Adjustment Methods* of the *Spatial Adjustment* tab. (b) The location of the *New Displacement Link* highlighted in blue. (c) The image shows how the points will be shifted.

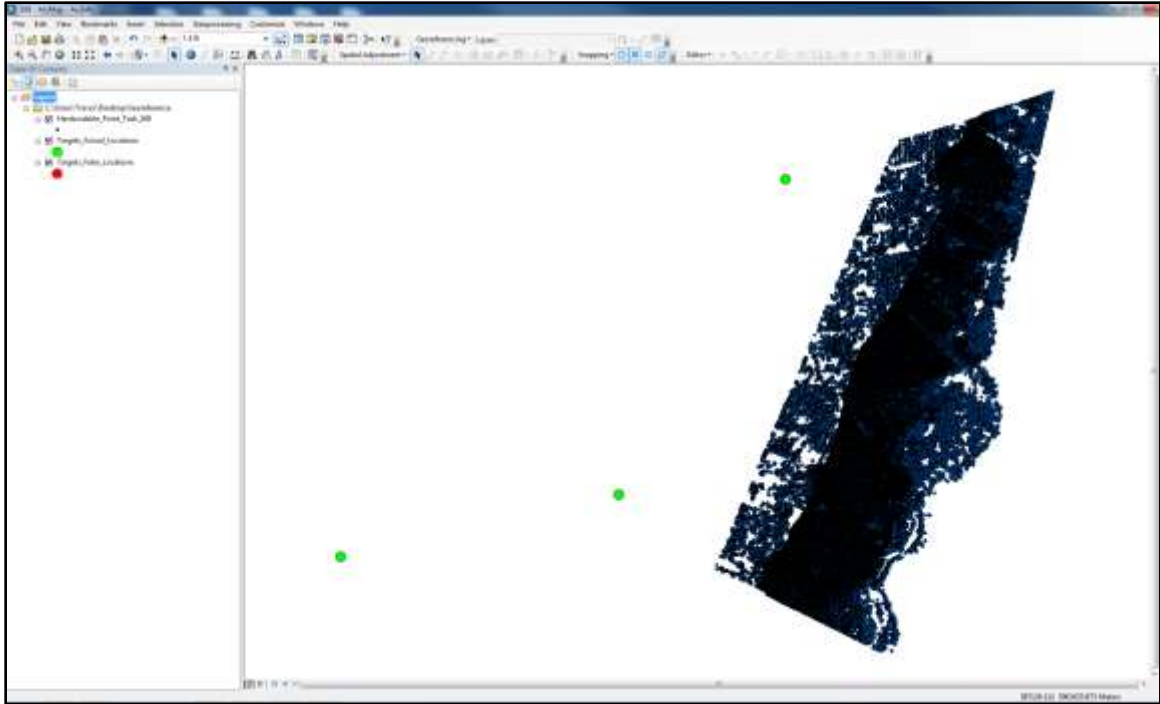


Figure 2.17: An image showing the adjusted point cloud and false georeferencing target locations (which are overlain by the correct georeferencing target location points (green points)).

- (c) With the point cloud shifted to its real-world coordinates, the *Attribute Table* can now be updated to display the new values for easting and northing. This is done by selecting the *Geoprocessing* drop-down menu and choosing *ArcToolbox*. In the *ArcToolbox* window that opens, expand the *Data Management Tools* option and expand the *Features* category. Select the *Add XY Coordinates* option. In the *Add XY Coordinates* window, click on the drop-down menu on the *Input Features* selection. Select the point cloud shapefile and click the *OK* button.
- (d) When the new coordinates have been written to the *Attribute Table* (Figure 2.18), there should now be four new columns (*Point_X*, *Point_Y*, *Point_Z*, and *Point_M*). With the *Attribute Table* still open, it is now possible to export the data for use with other software. Click on the drop-down menu and select the

Export option. When the *Export Data* window opens, click on the *Output* table file. Save the exported table to the folder created back at that start containing all the text files and shapefiles.

FID	Shape	Easting	Northing	Elevation	Intensity	POINT_X	POINT_Y	POINT_Z	POINT_M
0	Point ZM	386886.267	5061762.162	1.07	86	387076.534663	5061679.20835	1.07	1
1	Point ZM	386886.379	5061762.334	1.076	84	387076.593116	5061679.01368	1.076	1
2	Point ZM	386886.404	5061762.396	1.078	82	387076.624071	5061678.95526	1.078	1
3	Point ZM	386886.581	5061762.294	1.073	49	387076.432878	5061678.88462	1.073	1
4	Point ZM	386878.984	5061760.03	1.089	89	387079.600705	5061686.12757	1.089	1
5	Point ZM	386879.394	5061760.273	1.095	87	387079.521388	5061685.66008	1.095	1
6	Point ZM	386879.563	5061760.191	1.097	77	387079.35051	5061685.58288	1.097	1
7	Point ZM	386879.665	5061760.179	1.09	77	387079.275817	5061685.51251	1.09	1
8	Point ZM	386879.575	5061760.369	1.099	43	387079.477819	5061685.46086	1.099	1
9	Point ZM	386879.872	5061760.163	1.096	43	387079.130569	5061685.36441	1.096	1
10	Point ZM	386879.864	5061760.265	1.094	38	387079.213087	5061685.30586	1.094	1
11	Point ZM	386880.222	5061760.46	1.099	63	387079.130797	5061684.90856	1.099	1
12	Point ZM	386880.221	5061760.556	1.103	84	387079.204263	5061684.84846	1.103	1
13	Point ZM	386880.32	5061760.548	1.106	100	387079.134533	5061684.77785	1.106	1
14	Point ZM	386882.017	5061760.857	1.109	112	387078.27768	5061683.28466	1.109	1
15	Point ZM	386883.903	5061761.611	1.124	93	387077.636854	5061681.36486	1.124	1

Figure 2.18: The updated attribute table showing the four new columns.

It is now possible to open the data table in a data editing program like Microsoft Excel and delete all the irrelevant columns of data (keep new X, Y, and Z coordinates and the corresponding intensity values). For the example used in this paper, the relevant data were the updated eastings and northings, as well as the elevation and intensity. Also, of importance here is to realize that the point cloud used for the demonstration of this workflow is just one of four sections that make up the scanned area of the cliff face. The remaining three sections of the scan will also have to undergo a similar workflow to georeference them.

2.8 Results

Through the successful application of the procedure on the Joggins Formation lidar

data set, the point cloud was significantly reduced from a cumbersome and processing-intensive, several million individual points to a manageable 1.4 million points. Initially, the point cloud contained millions of erroneous points representing the intertidal area, vegetation on the top of the cliff, and even some structures (houses, power lines, etc). Each of the points that comprise the point cloud has been fully georeferenced with unique easting, northing, and elevation values because of the combined usage of georeferencing targets and an RTK DGPS. Examples of the georeferenced point cloud are shown in Figure 2.19, Figure 2.20, and Figure 2.21. This merged point cloud is now available for several studies relating to heterogeneity, coastal erosion, and ancient forest density, to name a few.

With the successful completion of the workflow described herein, it is possible to have a fully georeferenced point cloud that displays the relevant points only with all erroneous points decimated and thus, lessening processing times and making interpretations easier. Initially, the point cloud contained a large number of intertidal points, vegetation on the top of the cliff, and even some structures (houses, power lines, etc). With all these points removed, the result is a cleaned point cloud that is ready for interpretation.

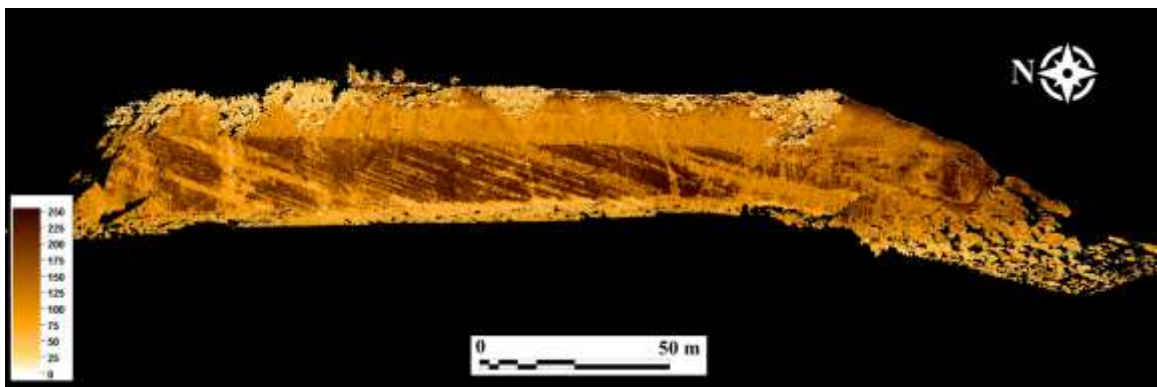


Figure 2.19: Petrel™ E & P Software screen capture showing the point-decimated, fully georeferenced point cloud of the Joggins Formation cliff face. This image is a composition of the point cloud shown in the preceding workflow, along with the other three other scan sections merged. The colours are based on the lidar intensity with log sand, and shale colour ramp applied.

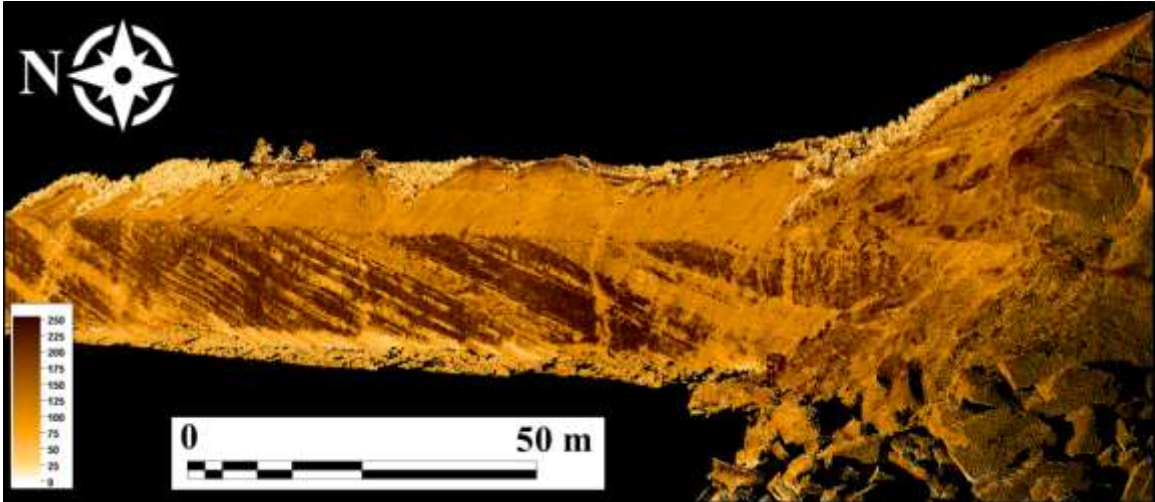


Figure 2.20: Petrel E & P Software screen capture showing a view looking along the cliff face from the north at Coal Mine to the south.

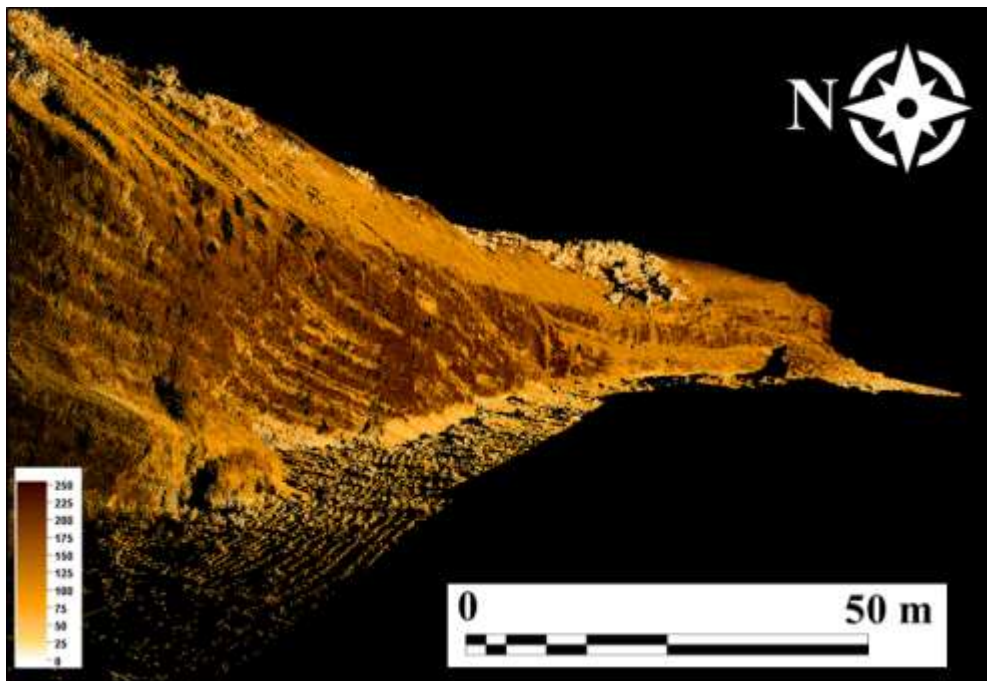


Figure 2.21: Petrel™ E & P Software screen capture showing a view looking down the cliff face from the north to the south at Coal Mine Point. Notice that only a small number of points representing the intertidal area were left for reference.

2.9 Discussion and Conclusions

The ideas presented in this paper detail one method of performing post-scan georeferencing analysis on a large geological outcrop section that has been scanned by a

static terrestrial lidar scanner and paired with an RTK DGPS and control points. The application of commonly available software ensures that the methods can be applied consistently and efficiently with repeatable results. For lidar scans that must be performed in a relatively short amount of time (in this case due to tides), georeferencing post-scan has been shown to be a viable option. Post-scan georeferencing is advantageous when the laser scanner does not have built-in GPS capabilities or the built-in GPS capabilities of the laser scanner is not well known. Additionally, there could be potential errors in collecting GPS data directly during the scan, so using targets could serve as a backup. For multiple scans that will be eventually merged, highly accurate RTK DGPS data is required, which laser scanners do not have as a built-in option.

At Joggins and many other coastal cliffs that are subject to the rising and falling of tides, the most efficient use of time should be the collection of data. The time required to perform all the steps outlined in the workflow is rather short, depending on the processing capability of the computer workstation being utilized. Accurately georeferenced data are particularly important for time series data sets in which the observation of real changes over a certain period is the goal. The uniqueness of Joggins Formation, with its fossilized, upright trees, offers researchers the possibility of studying paleo forest density using successive and georeferenced lidar scans taken over some time. Additionally, a georeferenced point cloud can be easily integrated with other data gathering techniques, such as a ground-penetrating radar survey, for example.

2.10 Acknowledgments

This work was supported by the Nova Scotia Offshore Development Fund and the Nova Scotia Government. Schlumberger is acknowledged for providing the Petrel™

software used to visualize and manipulate the point cloud data. We want to thank Dr. Lawrence Plug of the Dalhousie University Department of Earth Sciences for allowing the use of the real-time kinematic differential global positioning system equipment. We also want to thank Johnathan Thibodeau for his field assistance and for constructing the georeferencing targets. Finally, the members of the Dalhousie University Basin and Reservoir Laboratory are acknowledged for their help with the fieldwork to collect the data used in this research.

2.11 References Cited in Chapter 2

Baldrige, A.M., Hook, S.J., Grove, C.I., and Rivera, G. 2009. The ASTER spectral library version 2.0. *Remote Sensing of Environment*, **113**: 711-715. doi:10.1016/j.rse.2008.11.007.

Bellian, J.A., Kerans, C., and Jennette, D.C. 2005. Digital outcrop models: applications of terrestrial scanning lidar technology in stratigraphic modeling. *Journal of Sedimentary Research*, **75**: 166-176. doi:10.2110/jsr.2005.013.

Bellian, J.A., Beck, R., and Kerans, C. 2007. Analysis of hyperspectral and lidar data: Remote optical mineralogy and fracture identification. *Geosphere*, **3**: 491-500. doi:10.1130/GES00097.1.

Beumier, C. Vehicle Speed Estimation from Two Images for LIDAR Second Assessment. *In Proceedings of the International Conference on Computer Vision Theory and Applications (VISAPP-2012)*. Rome, Italy 2012. Vol. 1, pp. 381-386.

Burton, D., Dunlap, D.B., Wood, L.J., and Flaig, P.P. 2011. Lidar Intensity as a Remote Sensor of Rock Properties. *Journal of Sedimentary Research*, **81**: 339-347. doi:10.2110/jsr.2011.31.

Calder, J.H., and Boon, J. 2007. Joggins Fossil Cliffs: Property Nominated for Inscription on the World Heritage List. Nova Scotia Department of Natural Resources, Mineral Resources Branch, Halifax, NS. pp. Open File Map ME 2007-2001.

Falcon-Lang, H.J. 2009. Earliest history of coal mining and grindstone quarrying at Joggins, Nova Scotia, and its implications for the meaning of the place name “Joggins”. *Atlantic Geology*, **45**: 1-20. doi:10.4138/atlgeol.2009.001.

Grechishnikova, A. 2016. Integrated application of a high-resolution LIDAR outcrop survey of an unconventional Niobrara Reservoir, Denver Basin, Colorado. *First Break*, **34**: 65-71. doi:10.3997/1365-2397.34.5.84449.

Grey, M., and Finkel, Z.V. 2011. The Joggins Fossil Cliffs UNESCO World Heritage site: a review of recent research. *Atlantic Geology*, **47**: 185-200. doi:10.4138/atlgeol.2011.009.

Griggs, M., and Ludwig, C.B. 1978. Legal aspects of remote sensing and air enforcement. *Journal of the Air Pollution Control Association*, **28**: 119-122. doi:10.1080/00022470.1978.10470578.

Habib, A., Jarvis, A., Kersting, A., and Alghamdi, Y. Comparative analysis of georeferencing procedures using various sources of control data. *In* 21st ISPRS Proceedings. Beijing, China 2008. *Edited by* J. Chen and J. Jiang and S. Nayak. International Society for Photogrammetry and Remote Sensing. Vol. XXXVII, pp. 1147-1152.

Kelly, T.B., and Wach, G.D. 2020. Analysis of factors influencing the interpretation of a digitally examined fluvial meanderbelt system: Joggins Formation, Nova Scotia. *Canadian Journal of Earth Sciences*, **57**: 524-541. doi:10.1139/cjes-2018-0263.

Kwon, S., Park, J.-W., Moon, D., Jung, S., and Park, H. 2017. Smart merging method for hybrid point cloud data using UAV and LIDAR in earthwork construction. *Procedia engineering*, **196**: 21-28. doi:10.1016/j.proeng.2017.07.168.

Lim, S., Thatcher, C.A., Brock, J.C., Kimbrow, D.R., Danielson, J.J., and Reynolds, B.J. 2013. Accuracy assessment of a mobile terrestrial lidar survey at Padre Island National Seashore. *International Journal of Remote Sensing*, **34**: 6355-6366. doi:10.1080/01431161.2013.800658.

Llorens, J., Gil, E., Llop, J., and Queralto, M. 2011. Georeferenced LiDAR 3D vine plantation map generation. *Sensors (Basel)*, **11**: 6237-6256. doi:10.3390/s110606237.

Minisini, D., Wang, M., Bergman, S.C., and Aiken, C. 2014. Geological data extraction from lidar 3-D photorealistic models: A case study in an organic-rich mudstone, Eagle Ford Formation, Texas. *Geosphere*, **10**: 610-626. doi:10.1130/GES00937.1.

Mohamed, A., and Wilkinson, B. 2009. Direct georeferencing of stationary LiDAR. *Remote sensing*, **1**: 1321-1337. doi:10.3390/rs1041321.

Moore, J., Taylor, A., Johnson, C., Ritts, B.D., and Archer, R. 2012. Facies analysis, reservoir characterization, and LIDAR modeling of an Eocene lacustrine delta, Green River Formation, southwest Uinta Basin, Utah. *In* Lacustrine sandstone reservoirs and hydrocarbon systems: AAPG Memoir 95. *Edited by* O.W. Baganz and Y. Bartov and K. Bohacs and D. Nummedal. The American Association of Petroleum Geologists, Houston, Texas. pp. 183-208.

Nova Scotia Department of Natural Resources. 2005. Aerial Photography - 2005 Colour Photographs.

Olsen, M.J. 2011. Putting the pieces together: laser scan geo-referencing. *LiDAR Magazine*, **1**.

Olsen, M.J., Johnstone, E., Driscoll, N., Ashford, S.A., and Kuester, F. 2009. Terrestrial laser scanning of extended cliff sections in dynamic environments: Parameter analysis. *Journal of Surveying Engineering*, **135**: 161-169. doi:10.1061/(ASCE)0733-9453(2009)135:4(161).

Olsen, M.J., Johnstone, E., Kuester, F., Driscoll, N., and Ashford, S.A. 2011. New automated point-cloud alignment for ground-based light detection and ranging data of long coastal sections. *Journal of Surveying Engineering*, **137**: 14-25. doi:10.1061/(ASCE)SU.1943-5428.0000030.

Optech Incorporated. 2006b. ILRIS-3D Operation Manual.

Puri, N., and Turkan, Y. 2020. Bridge construction progress monitoring using lidar and 4D design models. *Automation in Construction*, **109**: 1-15. doi:10.1016/j.autcon.2019.102961.

Rafuse, C., and Wach, G. 2011. Reservoir architecture of meanderbelt systems and vegetation density in the Carboniferous using LiDAR imagery. Earth Sciences, Dalhousie University, Halifax, NS.

Rarity, F., Van Lanen, X., Hodgetts, D., Gawthorpe, R., Wilson, P., Fabuel-Perez, I., and Redfern, J. 2014. LiDAR-based digital outcrops for sedimentological analysis: workflows and techniques. Geological Society, London, Special Publications, **387**: 153-183. doi:10.1144/SP387.5.

Rotevatn, A., Torabi, A., Fossen, H., and Braathen, A. 2008. Slipped deformation bands: A new type of cataclastic deformation bands in Western Sinai, Suez rift, Egypt. *Journal of Structural Geology*, **30**: 1317-1331. doi:10.1016/j.jsg.2008.06.010.

Rotevatn, A., Buckley, S.J., Howell, J.A., and Fossen, H. 2009. Overlapping faults and their effect on fluid flow in different reservoir types: A LIDAR-based outcrop modeling and flow simulation study. *AAPG Bulletin*, **93**: 407-427. doi:10.1306/09300807092.

Sahoo, H., and Gani, N.D. 2015. Creating three-dimensional channel bodies in LiDAR-integrated outcrop characterization: A new approach for improved stratigraphic analysis. *Geosphere*, **11**: 777-785. doi:10.1130/GES01075.1.

Schuhmacher, S., and Böhm, J. Georeferencing of terrestrial laserscanner data for applications in architectural modeling. *In* Proceedings of the ISPRS Working Group V/4 Workshop 3DARCH "Virtual Reconstruction and Visualization of Complex Architectures". Mestre-Venice, Italy, August 22-24 2005, pp. 1-7.

Siddiqui, N.A., Ramkumar, M., Rahman, A.H.A., Mathew, M.J., Santosh, M., Sum, C.W., and Menier, D. 2018. High resolution facies architecture and digital outcrop modeling of the Sandakan formation sandstone reservoir, Borneo: Implications for reservoir characterization and flow simulation. *Geoscience Frontiers*. doi:10.1016/j.gsf.2018.04.008.

UNESCO. 2008. World Heritage List - Joggins Fossil Cliffs. Available from whc.unesco.org/en/list/1285/ [accessed September 6 2018].

Van Sickle, J. 2015. *GPS for Land Surveyors*. CRC Press.

Wilkinson, B.E., Mohamed, A.H., Dewitt, B.A., and Seedahmed, G.H. 2010. A novel approach to terrestrial LiDAR georeferencing. *Photogrammetric Engineering & Remote Sensing*, **76**: 683-690. doi:10.14358/PERS.76.6.683.

Wong, C. 2014. Lidar survey of the Joggins Formation in the Coal Mine Point section, Cumberland Basin (Nova Scotia, Canada). BSc Thesis, Department of Earth Sciences, Dalhousie University, Halifax, Nova Scotia.

Wu, B.-T., Li, P.-C., Chen, J.-H., Li, Y.-J., and Fan, Y.-C. 3D Environment Detection Using Multi-View Color Images and LiDAR Point Clouds. *In* 2018 IEEE International Conference on Consumer Electronics-Taiwan (ICCE-TW). 2018. IEEE, pp. 1-2.

Xharde, R., Long, B.F., and Forbes, D.L. 2006. Accuracy and limitations of airborne LiDAR surveys in coastal environments. *In* International Geoscience and Remote Sensing Symposium, Denver, CO. pp. 2412-2415.

Yoon, S., Wang, Q., and Sohn, H. Optimal Placement of Precast Bridge Deck Slabs with respect to Precast Girders using LiDAR. *In* 34th International Symposium on Automation and Robotics in Construction (ISARC 2017). 2017. Vilnius Gediminas Technical University, Department of Construction Economics. Vol. 34, pp. 879-886.

Zeng, Q., Lu, W., Zhang, R., Zhao, J., Ren, P., and Wang, B. 2018. LIDAR-based fracture characterization and controlling factors analysis: An outcrop case from Kuqa Depression, NW China. *Journal of Petroleum Science and Engineering*, **161**: 445-457. doi:10.1016/j.petrol.2017.12.002.

Zhang, Y., and Shen, X. 2013. Direct georeferencing of airborne LiDAR data in national coordinates. *ISPRS Journal of Photogrammetry and Remote Sensing*, **84**: 43-51. doi:10.1016/j.isprsjprs.2013.07.003.

Chapter 3: Analysis and Factors Influencing the Interpretation of a Digitally Examined Fluvial Meanderbelt System: Joggins Formation, Nova Scotia

T.B. Kelly and G.D. Wach

This chapter is based on the paper “Analysis of Factors Influencing the Interpretation of a Digitally Examined Fluvial Meanderbelt System: Joggins Formation, Nova Scotia”, by Trevor B. Kelly and Grant D. Wach and is published in the Canadian Journal of Earth Sciences. The copyright agreement form for this chapter can be found in Appendix A.

3.1 Abstract

Clastic reservoir exploration, development, and exploitation can be inherently complex with conventional recovery largely dependent on trap size and shape, column height, and development strategy. Reservoir architecture, such as the geometry of sand bodies and interlayered clayey/silty baffles and barriers are also extremely important to recognize and comprehend. Numerous data collection techniques/methods are widely available for helping to enrich reservoir outcrop analogue data extraction from well-scale to seismic scale. This integrated study uses the inherited, combined data from a localized light detection and ranging survey, measurements taken from a portable handheld spectrometer and air permeameter, in addition to total (or absolute) porosity measurements from thin sections to assist with the analysis of components influencing the interpretation of a digitally analyzed fluvial meanderbelt system outcrop. The purpose is not to perform a detailed reservoir characterization or to model a potential reservoir, but rather to study a section of a reservoir analogue and apply reservoir geology with integrated data collection techniques to highlight potential benefits and shortcomings of this type of approach. A point cloud survey generated from light detection and ranging, coupled with other tools including a portable handheld spectrometer and permeameter, supplements data from the

light detection and ranging scan and increases the confidence of interpretations. Spectrometer measurements recorded at the outcrop are used to generate a pseudo-gamma log. Handheld air permeameter measurements give a sense of the permeability of corresponding lithologies as well as the variability in permeability of the reservoir both laterally and vertically. Light detection and ranging also provides important information regarding rock properties. The high detail of the outcrop images is used for the assessment of reservoir characteristics. Reservoir data leads to an increased understanding of subsurface reservoirs, particularly of the fluvial meanderbelt type. This study shows the importance and drawbacks of a combined digital data collection approach for the analysis of a sedimentary outcrop.

3.2 Introduction

Meandering fluvial systems form important petroleum-producing reservoirs (e.g., Widuri field in the Java Sea, Little Creek field in Mississippi, and the Daqing field in China) that can be straightforward or complex to produce. In the petroleum industry, it is normal to perform detailed outcrop studies, particularly when a new type of reservoir is being developed that has not previously been drilled and apply any analogous outcrop data and results to the subsurface reservoir. The distribution and flow of petroleum fluids are controlled by the architecture of the depositional system as well as the internal fabric and geometry of sedimentary features (North and Prosser 1993). To characterize the reservoir and understand and predict the flow and distribution of petroleum fluids, the architectural variability and geological discontinuities need to be defined (Figure 3.1). Seismic imaging only resolves the larger-scale architectural features (North and Prosser 1993). Well data offer higher resolution but is widely-spaced within a reservoir (North and Prosser 1993).

Therefore, available subsurface data pertaining to a petroleum reservoir are incomplete concerning the spatial and architectural relationships of sandstone bodies (van Lanen et al. 2009). This results in the creation of highly interpretive geological models of subsurface reservoirs that may not be representative of the actual reservoir (van Lanen et al. 2009).

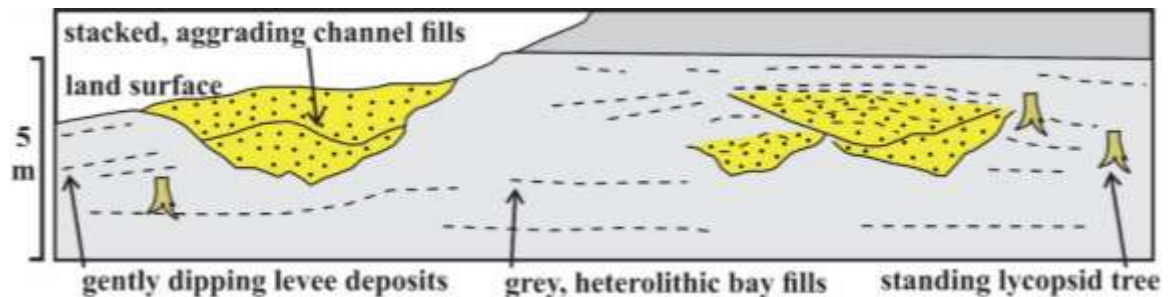


Figure 3.1: Schematic illustration showing the stacked, aggrading channel systems of the Joggins Formation and associated elements (modified from Gibling 2006). The sandbodies are also classified as geobodies, with their internal structures being the architectural elements.

To help fill these gaps of subsurface reservoir architecture, it is often necessary to study modern fluvial meanderbelt systems and ancient fluvial meanderbelt systems from geological outcrops (e.g. Davies et al. 1992; Grammer et al. 2004). Depositional environments with similar characteristics to subsurface petroleum reservoirs over a broad range of scales (seismic to log) provide three-dimensionality and data continuity. Advances in outcrop study over the past two decades have increased the cost efficiency and volume of data that can be collected by means of portable digital field equipment, e.g. the combination of a differential global positioning system with a statically positioned terrestrial laser scanner, known as light detection and ranging (lidar), for the rapid acquisition of spatial data (e.g. Bellian et al. 2005; Pringle et al. 2006; Buckley et al. 2010; Hodgetts 2013; Rarity et al. 2014).

Digital field techniques for the study of outcrops has increased as geoscientists recognize the benefits of these applications either as standalone techniques or integrated with other digital field techniques (e.g. portable handheld spectrometer and air

permeameter) and traditional field techniques (e.g. outcrop measurement logging and thin section analysis). Studies that have examined the most efficient way to capture, visualize, and quantify the data from digital field techniques include Bellian et al. (2005); Enge et al. (2007); Buckley et al. (2008); Hodgetts (2013); Hartzell et al. (2014); Howell et al. (2014). Other applications of digital field techniques include those relating to structural and sedimentological studies (e.g. Bellian et al. 2007; Labourdette and Jones 2007; Fabuel-Perez et al. 2009a; Rotevatn et al. 2009; van Lanen et al. 2009; Fabuel-Perez et al. 2010; Keogh et al. 2014; Minisini et al. 2014; Casini et al. 2016; Alhumimidi et al. 2017).

This paper uses the Late Carboniferous (Pennsylvanian) meandering fluvial system outcrop at Joggins, Nova Scotia, to 1) demonstrate methodology for the integration and modelling of data; 2) demonstrate the architectural complexity of a fluvial meanderbelt system; 3) de-risk production from fluvial reservoirs by providing real data and information on reservoir parameters; 4) offer a range of architectural data on fluvial reservoirs and 5) illustrate how traditional field data has been collected and is integrated with modern field data. Other studies of Carboniferous-aged, fluvial meanderbelt examples include the Rocky Ridge Field in North Dakota (Hastings 1990) and the Sorrento Field in Colorado (Sonnenberg et al. 1991; Blott et al. 1999). Additionally, the applications and benefits of these integrated techniques are discussed to show how the analyzing techniques aid in better using the full digital data sets to obtain geostatistical information and improve our understanding of these fluvial systems. Lidar, spectrometer, permeameter, and thin sections provide the opportunity for increased interpretation reliability.

3.3 Study Area

The study area is located 230 km north of Halifax, Nova Scotia, by the village of Joggins on the shores of Chignecto Bay, an inlet of the Bay of Fundy where the tides rise and fall 13 meters twice daily (Figure 3.2). It was selected based on its ease of access and the continuity and quality of the 3D exposure of the outcrop belonging to the Joggins Formation.



Figure 3.2: The Joggins Formation outcrop as viewed by a merged set of aerial photographs from 2005, prior to the construction of the Joggins Fossil Centre (Nova Scotia Department of Natural Resources 2005; Calder and Boon 2007).

The section of the outcrop scanned is located just to the north of Coal Mine Point (Figure 3.3), which is a sandstone promontory of more resistant rock. The Joggins Formation along with six other conformable formations (Ragged Reef, Springhill Mines, Little River, Boss Point, Claremont and Shepody) were designated in 2008 as a United Nations Educational, Scientific and Cultural Organization (UNESCO) heritage site because of the superbly exposed and preserved rock layers representing the most complete and comprehensive fossil record of life during the “Coal Age”, a time when lush forests and swamps covered much of the Earth's paleotropical latitudes (UNESCO 2008).



Figure 3.3: Digital photograph of the section of Joggins Formation scanned by lidar. Coal Mine Point is the headland on the right-hand side of the photograph.

3.4 Geological Setting

The Cumberland Subbasin is one of ten subbasins that underlie both onshore and offshore portions of the Maritimes Basin (Figure 3.4). The Cumberland Subbasin is approximately 4,500 km² and bounded by faults (Ryan et al. 1987; RPS Energy 2010). Covering large tracts of northwestern Nova Scotia, and to a much lesser extent, areas of southern New Brunswick, the Cumberland Subbasin is situated between the Caledonia Highlands and Westmorland Uplift to the west, the Cobequid Highlands to the south and the Antigonish Highlands to the east (Ryan and Boehner 1994; RPS Energy 2010). The Cumberland Subbasin is known for its plentiful coal deposits of which numerous seams and old mine workings can be seen in the Joggins Formation.

The Cumberland and Mabou groups form a continuous and conformable 14.7 km long outcrop (Figure 3.5) along the coast of Chignecto Bay (Grey and Finkel 2011). Browne and Plint (1994) mention that the margins of the subbasin include the North Fault to the south, the Caledonia-Dorchester fault system to the north and the Harvey-Hopewell Fault to the west. Martel (1987) suggests the northwestern basin limits may be delineated by a basement horst that formed along the Hastings Fault.

The basin contains a series of synclines with the larger examples being the Athol, Tatamagouche, Scotsburn, Amherst, and Wallace, along with two diapiric anticlines

known as the Claremont-Malagash and Minudie anticlines, both of which are enclosed by the synclinal series (Ryan and Boehner 1994). Ryan and Boehner (1994) claim that the structural features contained within the Cumberland Subbasin are related to basin development features, including growth faults, strike-slip faults, and major synclines. These features are either unrelated or indirectly associated with evaporate tectonics and salt structures such as diapirs, domes, diapiric anticlines, and salt movement-related folds and faults. The Cumberland Subbasin is classified as a salt-withdrawal basin with syndepositional slump features indicative of syndepositional movement of salt.

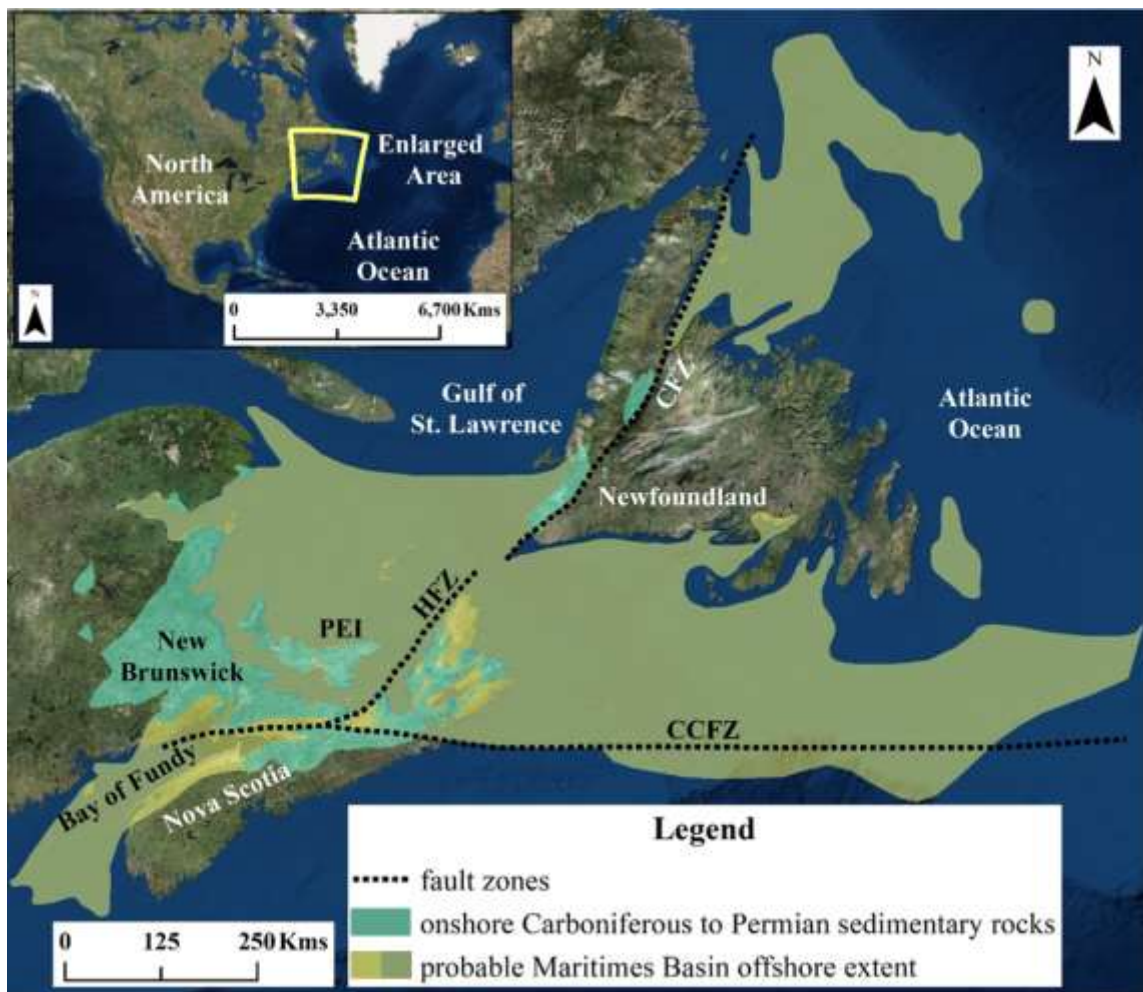


Figure 3.4: The extent of the Maritimes Basin of Eastern Canada showing the onshore distribution of Carboniferous to Permian outcrops. The fault zones are as follows: CCFZ, Cobequid-Chedabucto Fault Zone; CFZ, Cabot Fault Zone; HFZ, Hollow Fault Zone (Allen et al. 2013).

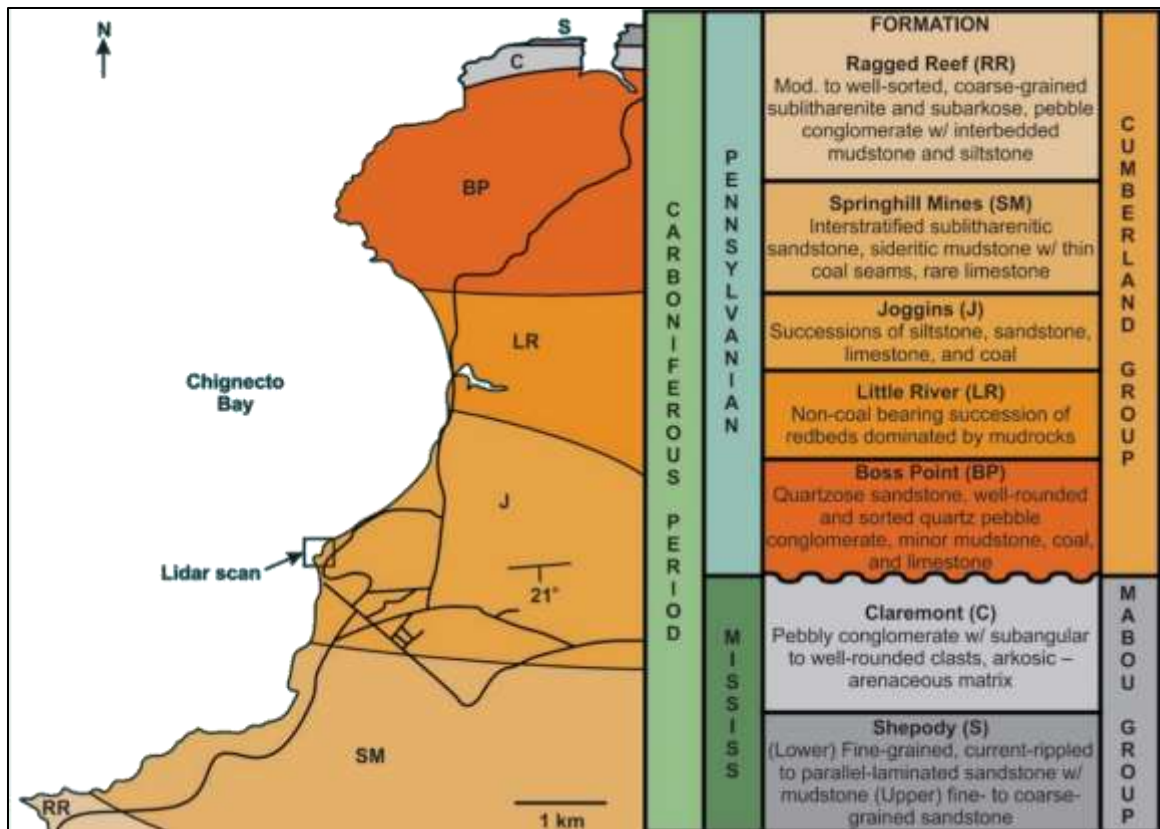


Figure 3.5: Simplified plan view showing the Joggins Fossil Cliffs geology (modified from Grey and Finkel 2011).

3.5 Sedimentology and Stratigraphy

The Joggins Formation is 915.5 m thick and is divided into 14 cycles, each characterized by limestone, coal, or fossiliferous mudstone at their base (Davies and Gibling 2003; Davies et al. 2005). These cycles are grouped into three distinct stratigraphic facies; well-drained and poorly-drained floodplain facies and open-water facies (Davies and Gibling 2003).

The well-drained facies contain reddish-coloured siltstone, mudstone, and sandstone with the occurrence of small-scale channel sandstones and carbonate nodules. Within the well-drained alluvial plain deposits occur thin grey-green layers with millimeter-scale coal laminae, probably the result of alternating high and low water table conditions (Davies and

Gibling 2003). Channel bodies are comprised of red and grey sandstone and mudstone with conglomerate and are narrow (~ 1 m) with a maximum thickness of 6 m (Davies et al. 2005; Rygel 2005). The most likely environments of deposition were well-drained alluvial plains containing anastomosing channels (Davies and Gibling 2003).

The poorly-drained facies contain mainly sandstone and green/grey mudstone hosting rare sub-meter thick coal seams (the target of historical coal mining), carbonaceous mudstone and minor limestone containing siderite nodules (Davies et al. 2005). The famous fossilized trees occur within the thicker sandstone and mudstone beds and may be up to 6 m in height according to recent measurements (Calder et al. 2006). Channel bodies are typically between 1 to 3 m thick and are a regular occurrence, although there are larger channel bodies up to 9 m thick (Davies et al. 2005). The poorly-drained facies are interpreted to have been deposited in a coastal wetland or deltaic plain environment with high rainfall and humidity, similar to the Mississippi Delta (Davies and Gibling 2003; Davies et al. 2005).

The open-water (marine) facies contain organic-rich, well-cemented limestone or “clam coals” as they are locally known due to their dark grey appearance and presence of bivalve fossils (Davies et al. 2005). The limestone is overlain by laminated siltstone, which contains disk-shaped siderite nodules. The siltstones are capped with a few meters of sharp-based sheet sandstones that show evidence of channel downcutting and contain such features as ripple cross-laminations and mud drapes (Davies et al. 2005). The open-water facies are interpreted as having been deposited in a basin-wide, brackish (restricted marine) environment that was equivalent to the modern Baltic Sea with its variable salinity and somewhat enclosed attributes (Grasshoff 1975; Davies et al. 2005).

The Joggins Formation coal beds have been the subject of studies pertaining to their deposition, composition, and hydrocarbon potential, with the findings summarized by Grey and Finkel (2011). Dawson (1854) estimated that the formation contained a minimum of 45 coal beds with varying thicknesses from less than a centimeter to meter-scale. The organic maturation of the Joggins Formation, based on vitrinite reflectance from surface exposures ranges from 0.67 % to 0.7 %, or qualitatively low (Mukhopadhyay et al. 1991). The coals contain liptinite macerals with Type II-III kerogen, indicating condensate-gas prone source rocks with hydrogen index values ranging from 250-300 mg HC/g total organic content (Mukhopadhyay et al. 1991). Gibling and Kalkreuth (1991) also reported good to very good source rock potential but concluded the coal beds were too thin for economically viable hydrocarbon volumes.

3.6 Methods

A variety of common field measurement equipment was used for data collection. This included a terrestrial laser scanner paired with a global positioning system, a portable handheld gamma ray spectrometer, a portable handheld air permeameter, and hand samples to allow for digital image porosity analysis. The terrestrial laser scanning was performed by the authors. Measurements taken using the spectrometer and air permeameter were performed by colleagues.

3.6.1 Terrestrial Laser Scanning

Static terrestrial laser scanning was completed using the Dalhousie University Basin and Reservoir Laboratory Optech Incorporated Intelligent Laser Ranging and Imaging

System (ILRIS) 3D lidar scanner (Figure 3.6) with a scan speed of 2.5 kHz and 2,500 points per second. (Optech Incorporated 2006b).



Figure 3.6: An image of the Optech ILRIS-3D lidar scanner setup. In this image, the laser scanner (1) is mounted atop the pan/tilt base (2), both of which are connected to a tripod (3). A ruggedized laptop (4) is used to adjust scanner settings and initiate a scan. The lidar unit (1 and 2) are powered by a battery pack (5). The tilted strata of the Joggins Formation can be seen in the background. The distance from the lidar setup to the face of the outcrop is approximately 100 m and indicated by the dashed yellow line.

Lidar is a highly versatile ground-, air- and water-based tool for the remote collection of data and it has been applied extensively to a variety of disciplines including earth sciences (e.g. Bellian et al. 2005; Bellian et al. 2007; Rotevatn et al. 2009; Moore et al. 2012; Rarity et al. 2014; Grechishnikova 2016; Siddiqui et al. 2018; Zeng et al. 2018). Lidar scanning bombards a surface with laser pulses and measures the gap in time between the initial pulse emission and the returning signal detection. The emitted laser pulse has a wavelength of 1,535 nm (infrared spectrum). For a reflection to be obtained, the rock being bombarded by laser pulses must be of the type to produce a dielectric discontinuity, thereby allowing the original wave to be reflected to the source.

The section of the cliff was chosen for scanning because of the abundance of channel bodies, quality, and access. The scan was performed on a sunny, clear day to avoid various problems such as the increased reflectivity associated with scanning a wet outcrop and rain droplets. The scan was collected at an average range of 100 m from the cliff face at a 12 mm point spacing in a step-stare scan pattern. The point cloud is an assemblage of approximately 1.4 million points following the decimation of irrelevant points; all which contain an 8-bit intensity value between 0 and 255, in addition to a unique X (latitude), Y (longitude), and Z (elevation) value (i.e., each point has an exclusive coordinate).

The point cloud is georeferenced to provide all points in the point cloud with real-world coordinates. To perform this task, at least three georeferencing targets must be placed at varying X, Y, and Z locations to allow for triangulation. Preferably, placement of the three targets would include one at the top of the section and two at a distance on either side of the lidar unit. The targets consist of a piece of plywood cut into a 0.5 m by 0.5 m square with an outer area covered in black, retro-reflective paint and an inner circle (approximately 12 cm in diameter) that is white and non-reflective. The targets are placed in such a way that the black outer area and white inner circle face the lidar unit. When scanned by the lidar unit, the targets return a distinct signature that when combined with the global positioning system readings of the centers of the non-reflective white inner circles allows for the scans to be georeferenced.

3.6.2 Global Positioning System

Static terrestrial laser scanning was paired with a Real-Time Kinematic (RTK) differential Global Positioning System (DGPS) (Figure 3.7) for obtaining a fully georeferenced data set. A Real-Time Kinematic differential Global Positioning System

applies differential correction techniques to improve the accuracy of location data that is gathered using GPS receivers (Van Sickle 2015). The base station was erected over a well cap on the backside (cliffside) of the Joggins Fossil Cliffs Centre that has known surveyed coordinates (UTM Zone 20T Easting = 387,098.72; Northing = 5,061,126.31; Elevation = 26.453 m). The transmission antenna was set up next to the base station to transmit the corrections made by the base station to the rover in real-time as they become available. The rover was mounted on an aluminum pole and positioned ~ 0.5 km away from the base station/transmission antenna setup. Following the placement of georeferencing targets within the lidar scan survey area, the X, Y, and Z coordinates of each target were recorded. This allows for georeferencing of the lidar point cloud to be completed post-scan in the Basin and Reservoir Laboratory at Dalhousie University.

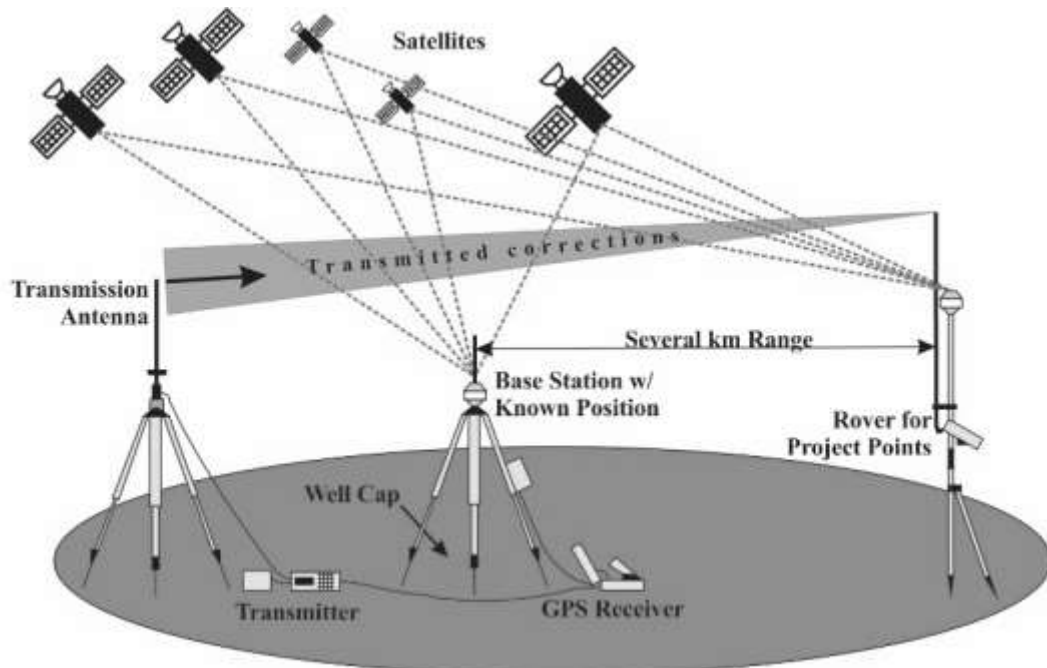


Figure 3.7: Simplified sketch of the global positioning equipment used to provide a georeferenced lidar data set (modified from Van Sickle 2015). The base station was set up over a well cap with a known set of coordinates. The transmission antenna was erected next to the base station. The rover was taken to the lidar survey area for use with measuring the coordinates of the three lidar survey markers.

3.6.3 *Portable Handheld Gamma Ray Spectrometer*

Measurements were taken using a Science Applications International Corporation Exploranium – Radiation Detection Systems GR-130 miniSPEC spectrometer with a 74 cm³ thallium-activated sodium-iodide [NaI (Ti)] detector (Exploranium - Radiation Detection Systems 2001). The spectrometer has numerous functions, and for this study, the gamma ray scintillometer survey function was used by selecting the survey mode from the main menu list. A gamma ray scintillometer is used to measure the radioactive content of a rock sample by measuring the amount of uranium (U), thorium (Th) and potassium (K). Readings are taken at regular intervals by merely placing the device against the rock surface and recording the value displayed. Gamma rays are detected when they encounter the sodium iodide crystal within the instrument, resulting in the emission of free electrons and light energy, which are converted into electrical pulses. The stronger the gamma rays encountered, the larger the produced electrical pulse response will be within the instrument. The number of pulses or counts is proportional to the amount of radioactive material. The device displays the current count rate in the form of counts per second (cps).

Typically, finer-grained lithologies, such as siltstones and mudstones, will contain abundant concentrations of radioactive elements when compared to sandstones. The finer-grained lithologies contain clay minerals (abundant with K), which have large interlayer spacings in their crystal structures, allowing U and Th also to fit in. Sandstones generally have low radioactive content because they have characteristically high amounts of quartz that has very low radioactive element uptake in its crystal lattice. Sandstones are subject to increased working and re-working during transport, meaning that typically the higher the mineralogical maturity, the lower the radioactive content. On a gamma ray log trace,

sandstone will usually display lower values; mudstone will typically display higher values. This allows for the recognition of subtle variations in clay content within the sandstone bodies. Gamma ray counts can be used to determine baffles and barriers to fluid flow in a reservoir. This portable spectrometer was used at 30 different stratigraphic levels along the base of the studied section. At each of the locations, the sampling time was typically 5 seconds (a few were 6 seconds; one was 7 seconds), with a reading recorded every second. The sampling time was arbitrary. Measurement locations were based on changes in lithology and the nature of the contacts rather than a set interval. Values were also recorded from eight collected hand samples as well as 51 fallen sandstone blocks along the section and the base of Coal Mine Point. The fallen blocks represented material that was at too high an elevation in the cliff to reach.

3.6.4 Portable Handheld Air Permeameter

A factory-calibrated portable handheld air permeameter was used to indirectly measure the in-situ permeability of sandstone at different outcrop locations. A total of 24 in-situ measurements were made on rocks representing the well-drained and poorly drained facies associations. The dipping strata allowed values to be recorded along the entire stratigraphic interval. Data was collected using a New England Research Incorporated TinyPerm II Portable Air Permeameter (mini-permeameter), which resembles an elaborate bicycle pump and allows for the indirect, non-invasive, and non-destructive measurement of rock matrix permeability (New England Research 2013). This type of air permeameter has been successfully applied to numerous geologically-related studies around the world representing numerous depositional environments (e.g. Huysmans et al. 2008; Rotevatn et al. 2008; Fossen 2010; Fossen et al. 2011; Rogiers et al. 2011; Pessemiers et al. 2012;

Torabi 2012; Haffen et al. 2013; Rogiers et al. 2013; Antonellini et al. 2014; Magnabosco et al. 2014; Rogiers et al. 2014; Morgan and Murray 2015; O'Connor 2016; Raduha et al. 2016).

The instrument has a detection range from 10 millidarcys to 10 darcys (New England Research 2013). To record the permeability of a (rock) specimen, the pump is first fully extended. The user applies pressure to a 22 mm diameter rubber nozzle with an inlet/outlet diameter of 9 mm (an area of 63.62 mm²), which is held tightly against a relatively flat rock surface and the plunger handle is fully depressed to its lock position (Huysmans et al. 2008). Air from the chamber is forced into the rock surface with a microcontroller unit monitoring the plunger volume and transient vacuum pulse at the surface of the contacted sample. The microcontroller uses signal processing to compute the response function of the instrument/sample system (Rotevatn et al. 2008). The resulting values displayed on the microcontroller can be correlated to a permeability value in millidarcys using a calibration chart, with the correlation between permeameter values displayed on the microcontroller screen and the resulting permeability being linear (Figure 3.8). The higher values correspond to lower permeabilities and vice versa. Permeability was given a rank (

Table 3.1) originally by Levorsen (1954) and modified by Nabawy et al. (2009).

The TinyPerm II was calibrated in 2007 at Dr. Alastair Ruffell's laboratory at Queens University in Belfast, Ireland using a sandstone block of known permeability. The values were excellent and within all error measurements.

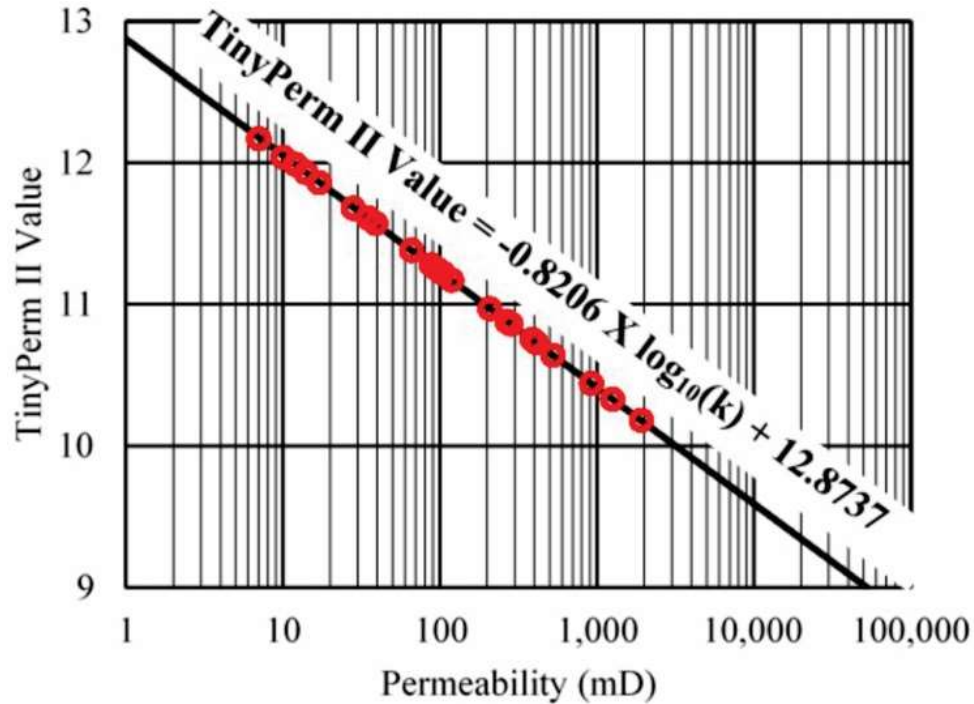


Figure 3.8: The permeability calibration chart used to correlate a TinyPerm II value (Y-axis) with corresponding permeability. The red points indicate the measured data points. The black line is the trendline with corresponding equation of the line.

Table 3.1: Permeability ranking (Levorsen 1954; Nabawy et al. 2009).

Rank	Fair	Good	Very Good	Excellent
Range	$1 < k \leq 10$ md	$10 < k \leq 100$ md	$100 < k \leq 1000$ md	$1000 < k$

3.6.5 Digital Image Porosity Analysis

There are several quantitative aspects of porosity that can be measured and calculated; all relating to different pore spaces. For this study, total (or absolute) porosity was measured. The total porosity is the summation of effective and ineffective porosity (all void spaces), which are related to measurements of interconnected and isolated pores, respectively (Magnabosco et al. 2014).

Digital image porosity analysis was carried out by use of an Olympus BX51 polarizing microscope on thin sections made from gathered hand samples. The thin sections were stained with a blue dye, such that any pores would exhibit a blue colour. The microscope was fitted with a camera to allow for digital images to be captured on the

connected desktop computer using the Olympus Digital Projection Controller software. The digital images were imported, one by one, into Image-Pro Plus. The software allowed for the manual selection of porosity. For contrast, the blue-dyed areas representing porosity were coloured in yellow, grains were coloured in blue, and cement was coloured in brown.

Apart from porosity, the grain area percentage and cement area percentage were also measured. Three area percentages were calculated; void area, grain area, and cement area, each of which were given a unique colour. The software scanned each image and estimated a total percentage value based on the area defined by each colour. The resulting porosity values were then given a rank, following that originally published by Levorsen (1954) and modified by Nabawy et al. (2009) (Table 3.2).

Table 3.2: Porosity ranking (Levorsen 1954; Nabawy et al. 2009).

Rank (%)	Negligible (%)	Poor (%)	Fair (%)	Good (%)	Very Good (%)	Excellent (%)
Negligible	$0 < \phi \leq 5$	$5 < \phi \leq 10$	$10 < \phi \leq 15$	$15 < \phi \leq 20$	$20 < \phi \leq 25$	$25 < \phi$

3.7 Errors and Uncertainty

3.7.1 Terrestrial Laser Scanning

According to the manufacturer, Optech Incorporated (2006a), the lidar scanner used for this study has a raw range accuracy of 7 mm at 100 m from target and a raw positional accuracy of 8 mm at 100 m from the target. A major limitation of lidar imaging is the inerrant data gaps that occur from overhangs, notches, and promontories (e.g. Xharde et al. 2006; Sturzenegger et al. 2007). At the study area, these features result from shore-based processes that include wave action and freeze-thaw cycles along exposed rock faces. To decrease data gaps, it is often necessary to scan the same outcrop region multiple times from different locations and angles (Sturzenegger et al. 2007). For this study, only one scan

from one location was completed. As a result, data gaps are present when the outcrop point cloud is viewed at an angle other than perpendicular from the scanner setup location. This has the effect of creating areas with no point cloud detail around overhangs, notches, and promontories, but is not detrimental to this study.

Lichti and Harvey (2002) and Sturzenegger et al. (2007) also suggest that rock mass reflectivity is affected by surface water, leading to a decrease in the laser scanning range. Lichti and Harvey (2002) showed that a scanning distance of 3 m, the intensity increased if the reflecting surface was wet, while at 53 m, the intensity decreased for a wet reflecting surface. Sturzenegger et al. (2007) noticed this phenomenon when scanning an outcrop with groundwater seeping from fractures and noted the difference in reflectivity between the dry and wet areas. This is of importance for this study since approximately 14 m of the outcrop is underwater twice a day. For that reason, any outcrop studies done at this location must be efficient. The lidar scan was done while the tide was in full retreat; meaning the equipment was transported, setup, and initialized as soon as the intertidal area was exposed. So, this scan was performed on an outcrop that was wet or at least partially so. It is not known to what extent or magnitude the wet outcrop had on the acquired data.

3.7.2 *Global Positioning System*

The RTK DGPS had a positional accuracy of approximately +/- 2 cm (Van Sickle 2015). As discussed earlier, the base station was set up over a well cap with previously (circa 2008) surveyed coordinates. Not much is known about the survey of the base station (well cap) coordinates, other than it was done using the same high accuracy survey instruments. It is therefore assumed that the coordinates of the well cap are accurate to within +/- 2 cm.

3.7.3 *Portable Handheld Gamma Ray Spectrometer*

According to Exploranium - Radiation Detection Systems (2001), the spectrometer contains a glass vial as part of its inner workings and is sensitive to humidity and temperature, which affects the accuracy of measurements. To ensure accuracy is maintained when collecting data, the instrument contains a cesium-137 chip for calibration (Exploranium - Radiation Detection Systems 2001). The manufacturer of the spectrometer lists the normalized standard error as 2.25 (Exploranium - Radiation Detection Systems 2001).

3.7.4 *Portable Handheld Air Permeameter*

Several operational errors are possible when measuring permeability, especially in-situ. The most significant error is the tightness of the seal between the rubber nozzle of the permeameter and the rock surface (Magnabosco et al. 2014). This seal between instrument and rock is influenced mainly by the pressure of the seal against the surface, the angle at which the tip of the probe contacts the rock surface, and the roughness of the rock surface (Brown and Smith 2013; Filomena et al. 2014).

Measurements are also sensitive to full or partial sample water saturation, which is of importance for this study because of the rise and fall of the tides at the study area (Brown and Smith 2013). These tides cover the outcrop well above the height at which measurements were taken. Air permeameter measurements have a small area of investigation, so results may not be representative for the entire layer because permeability can have a wide range of values, several orders of magnitude in some instances, in less than a meter (Brown and Smith 2013). Magnabosco et al. (2014) observed that the seal

between the sample and the instrument at low temperatures (cold) was less than at higher temperatures, which they attributed to the lack of flexibility in the rubber nozzle of the device at lower temperatures. Filomena et al. (2014) assessed the accuracy of gas-driven permeability measurements using a variety of probe-type permeameter, such as the TinyPerm II and determined that measured permeabilities were 34 to 41 % (average of ~ 37 %) lower for unconfined samples than core plugs. De Boever et al. (2016) was able to show that permeability measurements made with a TinyPerm II corresponded very well with the Lattice-Boltzmann method for determining permeability with measurements typically in the same order of magnitude.

For this study, no samples were taken for core plug permeability analysis. There are also no other outcrop studies of the Joggins Formation that have determined permeabilities from an air permeameter or from laboratory measured core plugs; hence, there is no way of comparing current permeability values from this study to other known permeabilities. Quantification of the uncertainty associated with this instrument at the study area is not possible given current data.

3.7.5 Digital Image Porosity Analysis

Porosity results can vary significantly across a single thin section and within an outcrop, can vary by an order of magnitude in under a meter (Brown and Smith 2013). During the preparation of a thin section for digital image porosity analysis, holes may inadvertently be created in the thin section. As a result, these holes in the thin section may unknowingly be counted as porosity, thereby increasing the total porosity value.

3.8 Results and Discussion

3.8.1 Gamma Ray Logs

The total gamma radiation for the studied section (Table 3.3 and Figure 3.9) varied from 82 cps for trough-cross stratified, thinly bedded medium-grained sandstone, to 256 cps for mudstone with average values from 93 cps to 255 cps. Gamma ray values were recorded at 25 stops along the base of the outcrop (Figure 3.9) at and near Coal Mine Point, with five measurements per stop along the outcrop. A pseudo gamma ray log based on these measurements from each stop was constructed (Figure 3.10) using the technique described by Slatt et al. (1992).

Table 3.3: Average gamma ray measurements within the area scanned by lidar acquired 100 m to the north of Coal Mine Point up to and including the large meandering channel body at Coal Mine Point.

Site	GR (cps)	Description
1A	166	host sst with shale rip-up clasts; f.g. to m.g. sst; angular to subangular clasts (up to 4 cm)
1B	196	base of sst channel body from 1A above
1C	172	ancient tree trunk, replaced by sst and found within 1A above
2	182	f.g. to m.g. sst
3	249	grey, silty- sst; small, blocky and fissile; scintillometer detector sounded, indicating uranium
4	222	massive siltstone bed (~ 30 cm in thickness)
5	203	v.f.g. sandy siltstone
6	62	current rippled sst; trace fossils on surface
7	224	slightly sandy siltstone with iron-pyrite nodules (up to 5 cm)
8	198	f.g. to m.g. sst
9	231	red to grey interbedded siltstone
10	189	parallel laminated f.g. sst; some ripples; slightly silty
11	210	red to grey v.f.g. sst; current ripples
12	246	dark grey; small blocky; silty clay
13	202	silty v.f.g. sst
14	227	small, blocky, sandy siltstone
15	216	red claystone; forms part of a channel body along with location 16 and 17
16	203	intershale (10 cm thick); forms part of a channel body along with location 15 and 17
17	181	sst; forms part of a channel body along with location 15 and 16
18	261	m.g.; small blocky; silty clay sst
19	181	v.f.g. to f.g. sst with 30-50 cm beds; capped with small 1 x 5m (w x h) channels
20	220	v.f.g. to f.g. silty sst
21	203	v.f.g. silty sst
22	181	v.f.g. silty sst
23	235	m.g.; grey; silty clay; blocky
24	211	coal; 15 cm
25	198	f.g. sst with fine-laminations of grey-silty claystone (cm scale)
26	97	massive m.g. sst; located near large meandering channel body at Coal Mine Point
27	93	trough-cross; thin beds; m.g. sst; located near large meandering channel body at Coal Mine Point
28	98	massive m.g. sst; located near large meandering channel body at Coal Mine Point

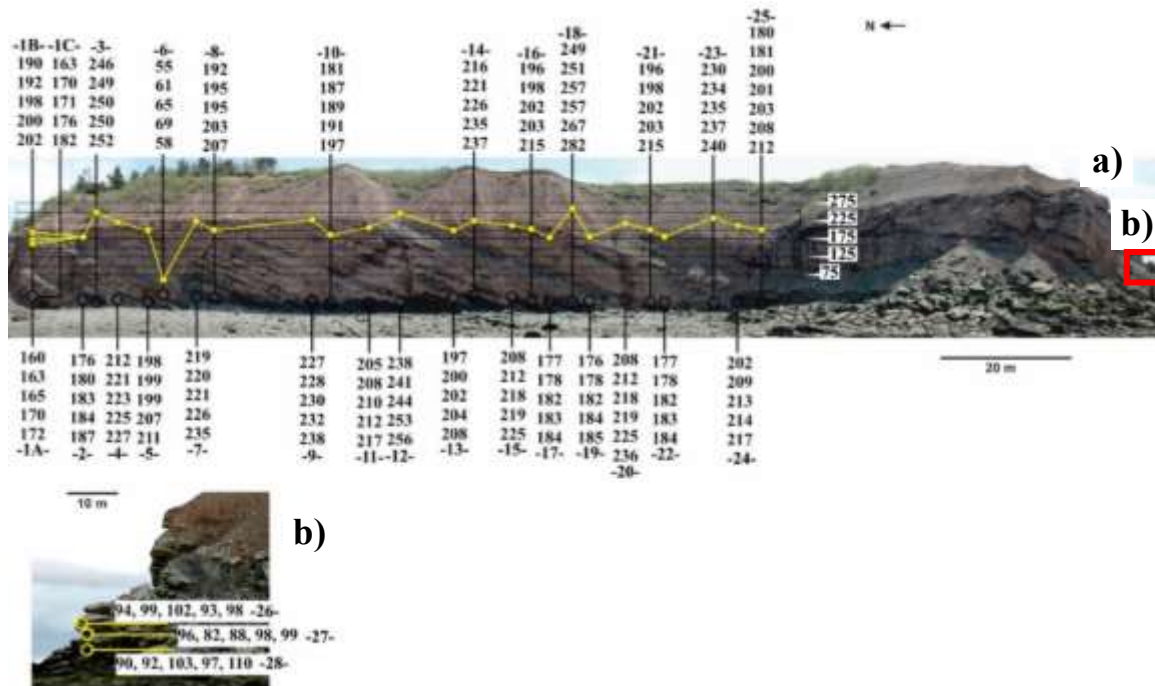


Figure 3.9: The location of spectrometer measurements along the studied section. (a) Location of 27 spectrometer measurements along the exposed outcrop scanned by lidar. Measurements were recorded north of Coal Mine Point. (b) Location of 3 spectrometer measurements taken on fallen blocks from the large meandering channel sandstone body, on the south of Coal Mine Point.

The higher gamma ray values are associated with mudstone, and lower values are associated with the sandstone bodies. The relationship of the sandstone bodies (lower cps) and mudstone layers (higher cps) with the pseudo gamma ray log is apparent when the pseudo gamma ray log and stratigraphic section by Rygel (2005) are correlated. The higher gamma ray values documented from the red mudstone beds probably reflect the presence of potassium-feldspar or U, Th, and K-bearing heavy minerals. These mudstones are not visibly rich in organic matter, so any contribution to the high gamma count can be ruled out. Examples of sandstones with high gamma ray readings also occur, likely for the same reasons as the red mudstone beds and/or because of the presence of extra-basinal clasts, where a sandstone contains intraformational mudstone rip-up clasts, thus skewing the gamma ray spectrometer readings to higher values. This is an important consideration and

cannot be discerned from subsurface data unless interpreted on image logs (Nickerson 2010).

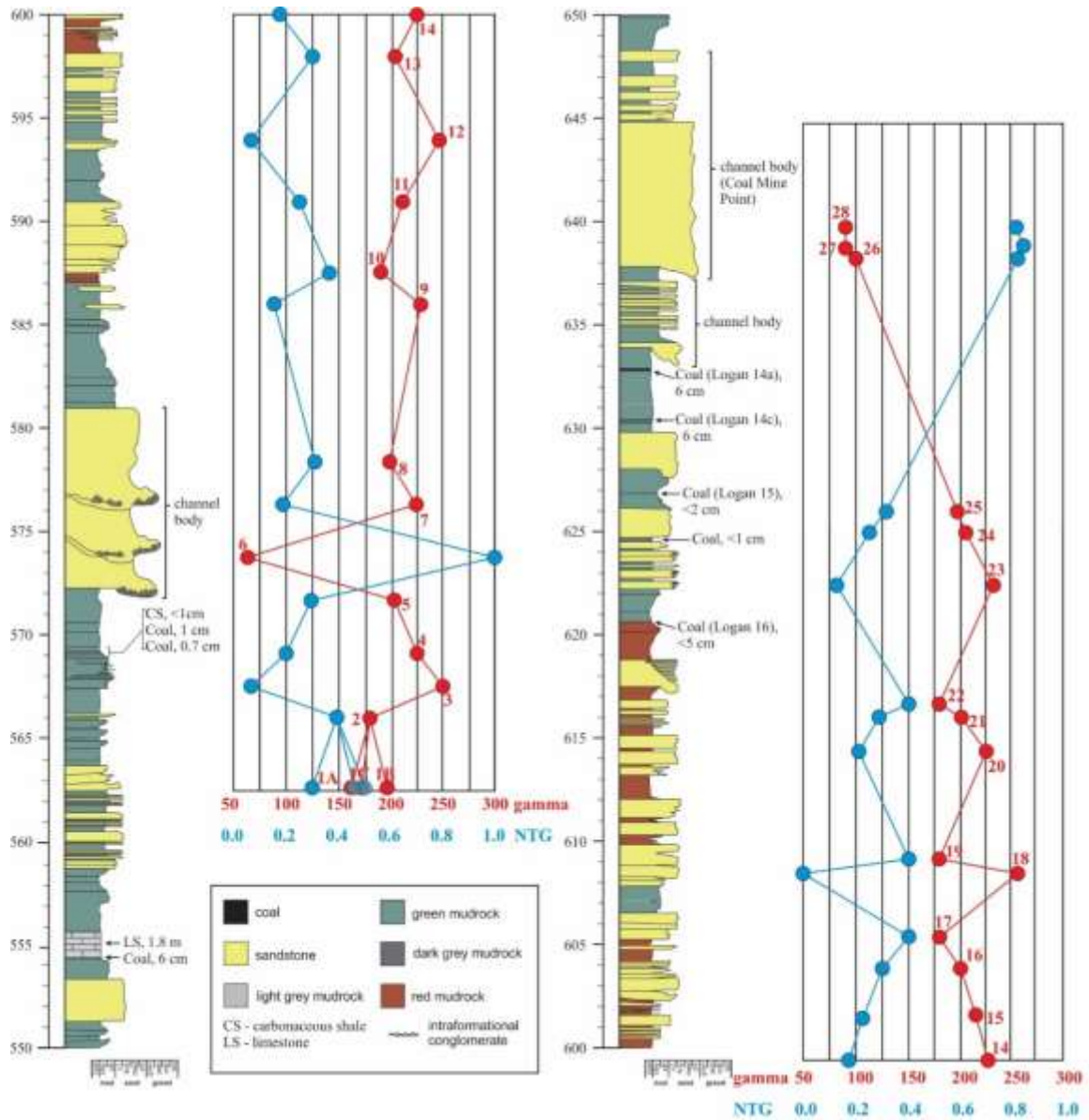


Figure 3.10: Measured section with gamma ray (red) and NTG (blue) curves (after Rygel 2005).

Gamma ray spectrometer readings were recorded on fifty-one visually homogenous sandstone blocks eroded from the cliff face. A total of 5 measurements at the same location were collected for each sandstone block (255 total measurements). The sandstone blocks were chosen randomly and surveyed to determine the variability in gamma counts within

the sandstone. The range of gamma ray values amongst the fallen blocks was not significant, suggesting they have similar compositional characteristics. Readings ranged from 97 cps to 195 cps with average values ranging from 109 cps to 163 cps. The average value for all 255 measurements was 136 cps. The increased values suggest the presence of radioactive elements linked to variably finer grained lithologies and a variable radioactive grain content containing feldspar and other heavy minerals, as seen from thin sections. The heavy minerals were not identified specifically other than recognizing that they were typically black in colour and opaque. Eight hand samples were analyzed with the spectrometer for a total of 60 seconds, providing 60 readings for each sample. The average gamma value for the sandstone, limestone, and coal lithologies is approximately 130 cps for each (Table 3.4).

Table 3.4: Gamma ray measurements from eight hand samples from the Joggins Formation study area.

Hand Sample	Lithology	Gamma Ray Counts (minimum value)	Gamma Ray Counts (maximum value)
GW101-2013TK	sandstone	115	155
GW102-2013TK	sandstone	116	151
GW103-2013TK	sandstone	118	149
GW104-2013TK	coal	111	154
GW105-2013TK	limestone	113	143
GW106-2013TK	sandstone	120	143
GW107-2013TK	sandstone	112	145
GW108-2013TK	sandstone	112	142

3.8.2 Net-To-Gross (NTG) – Scaling Gamma Ray Log

The gamma ray data set for the measured section (Figure 3.9) indicates that values lower than 93 cps are 100 % sandstone, whereas gamma ray values greater than 255 cps are indicative of 100 % mudstone.

$$NTG_{GR} = 1 - \frac{(GR_{value} - GR_{sand\ cutoff})}{(GR_{shale\ cutoff} - GR_{sand\ cutoff})} = 1 - \frac{(GR_{value} - 93)}{162} \dots \dots \dots (1)$$

The average net-to-gross ratio for the measured section (study area) by Rygel (2005) (Figure 3.10) was calculated to be 0.478. Although the NTG is nearly 50 %, it gives an erroneous calculation of reservoir quality and continuity because the sandstone is not a thick, homogenous unit. The sandstone is divided up into beds of variable thickness separated by thin (cm-scale) to thick (dm scale) beds of mudstone and coal that act as baffles and barriers to fluid migration.

3.8.3 *Permeability*

Permeameter values were collected on eight fresh sandstone blocks eroded from the cliff face (Table 3.5). Permeability values ranged from 66 to 1,917 md, which range from good to excellent. Permeameter measurements were also recorded along the cliff face. A total of 10 samples were tested. Values ranged from 7 md to 410 md, which is considered fair to very good following Levorsen (1954) and Nabawy et al. (2009). Permeameter values are summarized in Table 3.5 and plotted on Figure 3.12.

Table 3.5: Air permeameter values with their corresponding permeability value. Samples 1 to 8 were collected from random, fallen blocks near the base of Coal Mine Point; samples 9 to 24 are described in more detail, consisting of fallen blocks and direct measurements made on the cliff face near Coal Mine Point. Results are plotted in Figure 3.11.

Sample #	Lithology	TinyPerm Value	Permeability (md)
1x	Sandstone (near base of Coal Mine Point)	10.64	527
2x	Sandstone (near base of Coal Mine Point)	11.38	66
3x	Sandstone (near base of Coal Mine Point)	10.86	284
4x	Sandstone (near base of Coal Mine Point)	10.75	387
5x	Sandstone (near base of Coal Mine Point)	10.33	1,258
6x	Sandstone (near base of Coal Mine Point)	10.44	924
7x	Sandstone (near base of Coal Mine Point)	10.18	1,917
8x	Sandstone (near base of Coal Mine Point)	10.88	269
9x	Fallen, blocky, silty-sandstone; horizontal	11.28	88
10x	Same as above; vertical	12.04	10
11x	Fallen, grey, sandy-siltstone; vertical	11.99	12
12x	Same as above; horizontal	11.57	39
13x	Large fossilized tree trunk, red-brown	12.17	7
14x	Fine-grained massive sandstone; horizontal	11.61	35
15x	Same as above; vertical	11.68	28
16x	Fine lower sandstone; vertical	11.23	101
17x	Same as above; horizontal	11.22	104
18x	Very fine upper shale; vertical	11.86	17
19x	Very fine upper shale	11.17	119
20x	Coal bed on safe outcrop; horizontal	11.25	95
21x	Same as above; vertical	11.93	14
22x	Large sandstone bedset; horizontal	10.88	269
23x	Same as above but with climbing ripples	10.73	410
24x	Conglomerate; horizontal	10.97	209

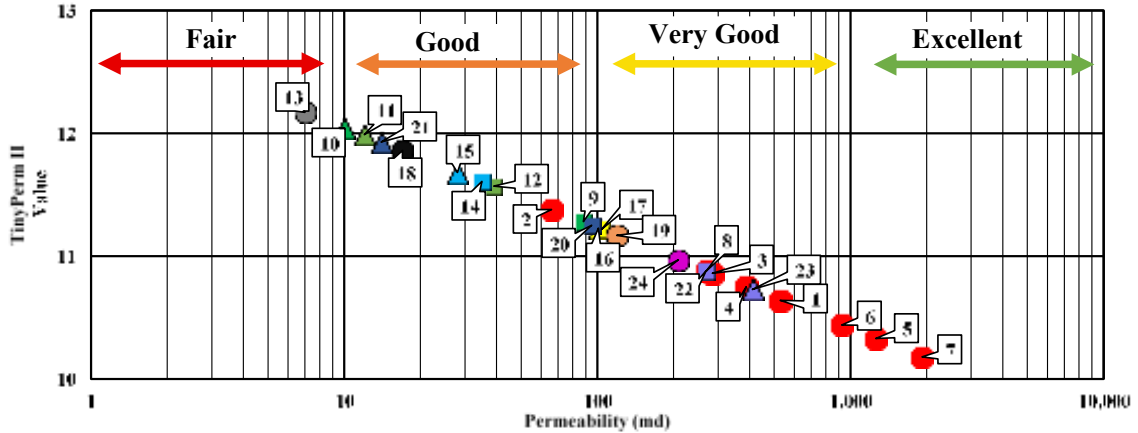


Figure 3.11: Values as from Table 3.5 plotted with the rank (after Levorsen 1954; Nabawy et al. 2009). All data points are labelled with their respective sample number. Samples 1 to 8 are shown in red. Samples 9 to 24 are uniquely labelled by shape and colour. Squares represent the sample being measured in a horizontal sense (the way it would have been deposited originally). Triangular points represent the sample being measured in a vertical sense (in relation to the way it would have originally been deposited).

These values exhibit a wide range, especially the first eight samples measured near the base of Coal Mine Point. Sample 5 and sample 7 occupy the excellent range (1,000 md and over) and represent a sizeable meandering channel body (point bar) at Coal Mine Point. The permeability data displays a wide range of measured values representing different lithologies, but also a large variation within the sandstones, with variations in permeability in both the horizontal and vertical sense (with respect to bedding) (Figure 3.12). This demonstrates lateral and vertical heterogeneity. The permeability measurements are another indicator of the complexity of the Joggins Formation and other fluvial reservoirs in terms of reservoir heterogeneity.

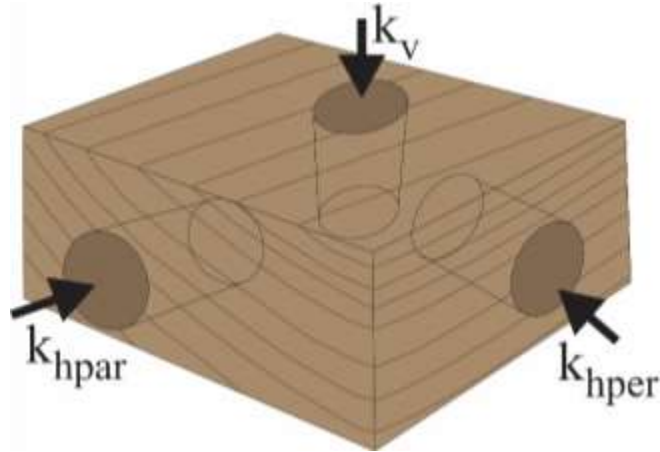


Figure 3.12: Schematic illustration representing a cross-laminated or cross-bedded sandstone showing different core plug orientations and associated permeability (k) measurement nomenclature (modified from Meyer and Krause 2006). The $k(v)$ is vertical permeability, $k(hpar)$ is horizontal permeability parallel to the strike of the cross-bedding/cross-laminations and $k(hper)$ is horizontal permeability perpendicular to the strike of the cross-bedding/cross-laminations.

3.8.4 Porosity – Digital Analysis

The total porosity results obtained from the thin sections and image analysis software indicate representative lithologies had average porosity values ranging from 0.9 % (negligible) to 7.4 % (poor). Porosity was measured at numerous areas of each thin section as total porosity. The porosity exhibited by the samples is intergranular as it exists between grains. The total porosity analysis shows the percentage of cement is greater than initially predicted visually and the cement is primarily ankerite. A summary of the cement area, grain area, and porosity of each of the six sandstone lithologies is presented (Table 3.6).

Table 3.6: Calculated average porosity, cement, and grain area values based on image analysis of representative photomicrographs for each of the sandstone hand samples.

Sample #	Cement Area (%)	Grain Area (%)	Porosity (%) and Rank
GW101-2013TK	29.2	69.1	1.7 (Negligible)
GW102-2013TK	23.1	69.5	7.4 (Poor)
GW103-2013TK	37.8	59.5	2.8 (Negligible)
GW106-2013TK	25.5	70.4	4.1 (Negligible)
GW107-2013TK	39.6	59.6	0.9 (Negligible)
GW108-2013TK	41.6	56.4	2.0 (Negligible)

Figure 3.13 and Figure 3.14 are examples of photomicrographs. Both samples are sandstones, with calculated porosity values of approximately 3 %. The range of porosity values measured for each thin section is plotted in Figure 3.15.

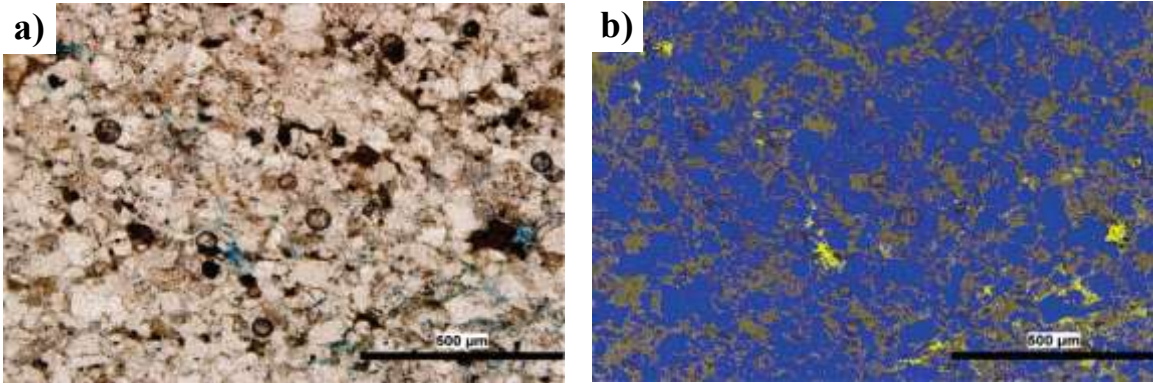


Figure 3.13: Photomicrographs of thin section GW102-2013TK-1. (a) Photomicrograph of thin section GW102-2013TK-1 (at 10X) in normal light with porosity shown in blue (dye). (b) Photomicrograph of thin section GW102-2013TK-1, but with porosity shown in yellow, grains as blue and cement as brown. The porosity is 3.0 %.

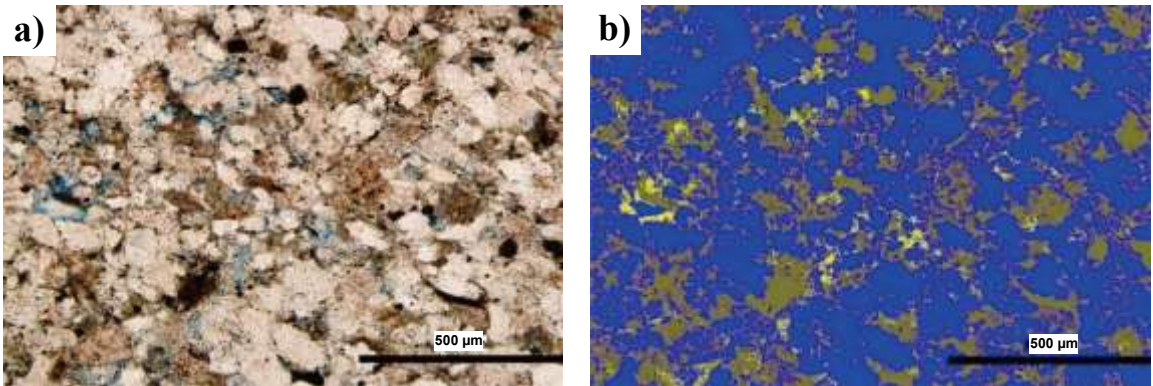


Figure 3.14: Photomicrographs of thin section GW106-2013TK-6. (a) Photomicrograph of thin section GW106-2013TK-6 (at 10X) in normal light with porosity shown in blue (dye). (b) Photomicrograph of thin section GW106-2013TK-6, but colourized to show porosity in yellow, grains as blue and cement as brown. The porosity is 3.4 %.

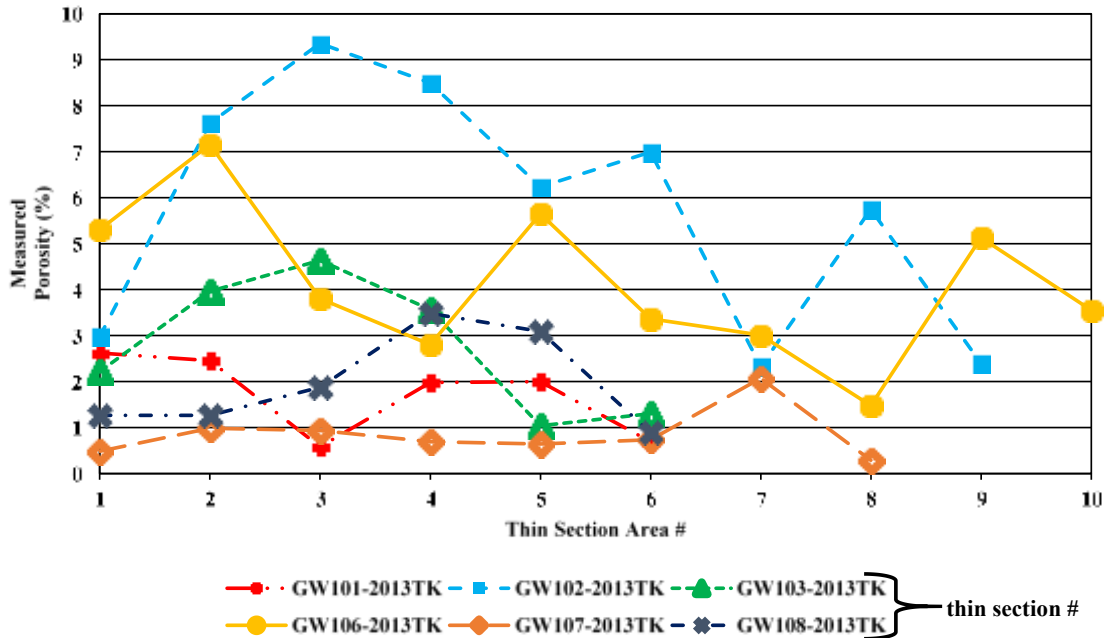


Figure 3.15: The variation in calculated porosity for each thin section of each sandstone sample. Thin section 10 for sample GW102-2013TK was not included because it was determined to be an outlier. The coal (GW104-2013TK) and limestone (GW105-2013TK) samples were not plotted.

3.8.5 Architectural Element Variability and Reservoir Connectivity

The lidar images show the lateral variations in sandstone body thickness observed at the outcrop. The characteristics of a good reservoir rock can change drastically across short distances (few meters or less) because of factors such as the pinch and swell nature of sandstone bodies. The variability in thickness of these sandstone bodies is just one of the numerous complexities that must be considered when attempting to understand reservoir rocks. The variable bed lithology can be discerned in the lidar images through correlation with the outcrop photographs. Sandstone beds are present between low permeability layers, including coal, mudstone, and sandy mudstone. These deposits vary widely in their thickness from 2 to 10 m for some of the thicker sandstone bodies to 2 to 5 cm for some of the coal strata. These analogous outcrop observations illustrate the various parameters that can affect production from meandering fluvial reservoirs.

Lithologies can be recognized by displaying the point cloud using a colour scheme where the dark brown colours (Figure 3.16, Figure 3.17 and Figure 3.18) represent sandstone and the light brown colours represent finer-grained lithologies, such as the mudstone and siltstone. Additionally, the light brown colours can represent areas that are extremely water wet or clay-rich, indicating permeability as well as the loose, unconsolidated Quaternary glacial till which lie unconformably over the tilted strata of the Joggins Formation. In other words, the hotter intensities (dark brown) correlate strongly with the higher reflectivity units.

Calibration of the point cloud for sandstone helps to clarify a variety of reservoir attributes. Figure 3.16 is a view of the entire point cloud showing the degree of reservoir compartmentalization, apart from the massive sandstone of Coal Mine Point and the sharp contact between the Joggins Formation and the overlaying Quaternary sediments. In Figure 3.16 and all other succeeding images, the alternating lithologies are well defined. Low permeability pathways and impermeable layers (baffles and barriers) to fluid flow, as well as permeable channel sandstones demonstrate a wide variation in permeability from 7 to 1,917 md within the Joggins Formation. Migration of fluids within a sandstone unit of the Joggins Formation is reduced by a low permeability zone within that bed. The finer-grained lithologies such as the mudstone, coal, and siltstone, serve as barriers to fluid migration, presumably with crossflow only occurring along fractures or small faults.

Within the interbedded zones, we can identify false connectivity (Figure 3.17 and Figure 3.18) from the lidar images caused when sandstone is eroded and accumulates on areas of the rough cliff face, which masks the true lithology and leads to an increased net-to-gross ratio. The gamma ray signature can be used with primary observations of facies to

help differentiate low gamma ray reservoirs (sandstone) from high response barriers and baffles (mudstone/coal). Gamma ray values (cps) combined with digital photography, corrects the interpretation of recorded intensity data from lidar. Assessment of reservoir connectivity at the outcrop scale using the DOM indicates poor reservoir connectivity. Connected sandstone bodies are important for hydrocarbon reservoirs or aquifers as it effects reservoir production.



Figure 3.16: The generated point cloud cliff section viewed from the West. A colour scale has been applied based on the intensity of the reflected light, which ranges between 0 and 255. The lower intensity values correlate with the finer-grained, quartz-poor lithologies and unconsolidated sediments. The higher intensity values correlate with the good quality quartz sandstone, as well as vegetation and sandstone-rich mine tailings.



Figure 3.17: Close-up view of the generated digital point cloud looking from the West. This view shows the highly compartmentalized nature of the Joggins Formation outcrop with the lower intensity values (see intensity scale) correlating with the finer-grained, quartz-poor sandstones, mudstones, and unconsolidated sediments and the higher intensity values correlating with the good quality quartz sandstone.

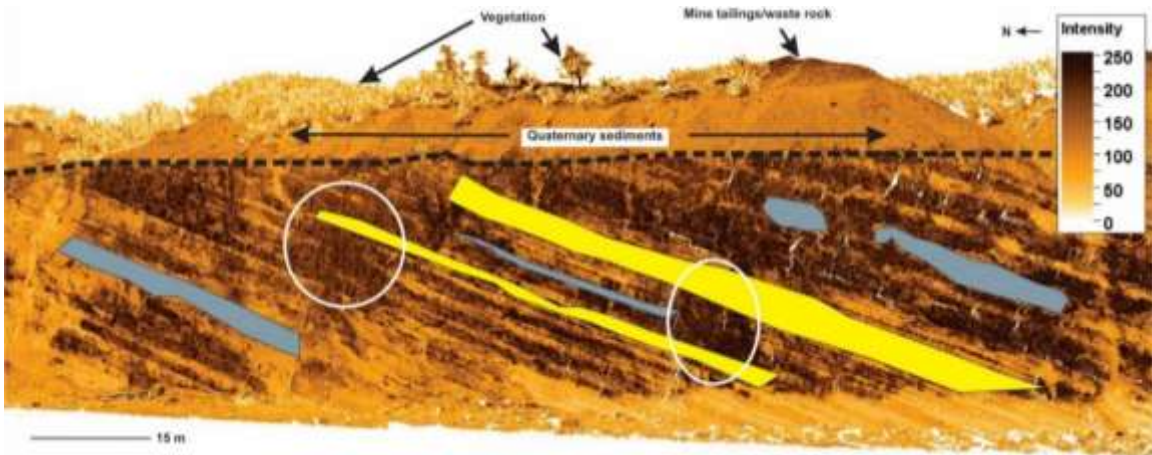


Figure 3.18: Close-up view of the generated digital point cloud looking from the West showing numerous interpreted features. In general, the higher quality quartz sandstone appears as the darker intensity colours, while the finer-grained material, such as mudstone appear as the lighter intensity colours. Where the sandstone has eroded and accumulated on small promontories (areas outlined by the white) along the cliff face to mask the true lithology and appear as though the area is entirely good quality sandstone. The unconformity between the dipping Joggins Formation strata and the overlying Quaternary sediments (poorly sorted glacial till/clay to boulder size) is visible. Examples of the good quality sandstone (yellow) are shown as are examples of the finer-grained lithologies (grey).

3.8.6 *Quantitative Data Summary and Discussion*

The quantitative data are presented in Table 3.7. These data could be useful for creating a low-resolution 3D block model where the lidar point cloud serves as the starting point for building the geomodel because changes in lithology can be traced and baffles/barriers can be easily distinguished. The pseudo-gamma ray curve helps to distinguish between sandstone and mudstone. The porosity and permeability data can be used to populate the simple model to allow for basic fluid flow simulations to be run using oil, gas, water, or a combination.

Additionally, carbon dioxide can be used as a simulation fluid since carbon capture and storage are becoming more prevalent. These simulations would help show the flow dynamics within a fluvial meanderbelt system but could potentially be useful for other analogues. Furthermore, the data provide insight into sandstone/mudstone contact architecture and permeability/porosity distributions.

Numerous benefits and problems are recognized in this study. One obvious benefit is how well the lidar intensity correlates with lithology. Also, the study provides a sense of the requirements for data collection versus the size of the outcrop study area. Using the current data to create a geomodel would produce a low-resolution example. A higher density of data is needed for high-resolution models.

One of the problems is the study area was too large for the amount of data collected. For this study to be truly useful and comparable to modern studies, it needs to be completed, in 3D, at far more detail and carried through to the modeling stage. Another issue relates to the measurement of permeability and porosity. There is no laboratory-measured permeability to compare with air permeameter measurements of permeability, and there is no laboratory-measured porosity to compare with thin section measurements of porosity.

To improve upon similar studies in the future, it is recommended that the study area be decreased in size and the quantity of data be increased. This would involve selecting one or more areas on the outcrop with a clean, flat surface and perhaps setting up a meter by meter-sized study area, whereby a grid could be superimposed and air permeameter and gamma ray spectrometer measurements could be recorded at regular intervals both horizontally and vertically. A detailed description of the variation in grain size, sorting, roundness, sedimentary structures, etc. would also yield valuable reservoir rock information. A highly detailed lidar scan (e.g., 1 mm spacing) of the surface would further help to show variations in quartz abundance and sedimentary structure relations. Numerous core plugs could be collected for porosity and permeability analysis in a laboratory to corroborate values measured at the outcrop and in thin sections. This would result in a higher resolution study, albeit at a smaller scale, that offers more details relating to

reservoir characterization, such as the internal architecture and heterogeneity. This information could be used to create a high-resolution 3D geomodel of a small outcrop section populated with closely spaced porosity and permeability data that could be simulated.

Table 3.7: Summary of the measurements and descriptions completed in the study area.

Geobody/A.E.	Site/ Sample	Facies	ϕ	k (md)	GR (cps)	Int.
-	1A	sst with shale clasts	-	-	166	175
channel base	1B	sst	-	-	196	255
tree trunk	1C	sst	-	-	172	155
-	2	sst	-	-	182	120
-	3	silty- sst	-	-	249	77
-	4	massive siltstone	-	-	222	169
-	5	sandy siltstone	-	-	203	124
ripples	6	current rippled sst	-	-	62	226
-	7	sandy siltstone	-	-	224	105
-	8	sst	-	-	198	103
-	9	interbedded siltstone	-	-	231	187
ripples	10	slightly silty sst	-	-	189	114
ripples	11	current rippled sst	-	-	210	227
-	12	silty clay	-	-	246	173
-	13	silty sst	-	-	202	206
-	14	sandy siltstone	-	-	227	96
channel body	15	claystone	-	-	216	208
channel body	16	shale	-	-	203	200
channel body	17	sst	-	-	181	174
-	18	silty clay sst	-	-	261	104
channel body	19	sst	-	-	181	119
-	20	silty sst	-	-	220	95
-	21	silty sst	-	-	203	89
-	22	silty sst	-	-	181	255
-	23	silty clay	-	-	235	182
-	24	coal	-	-	211	255
-	25	sst with silty claystone	-	-	198	115
channel body	26	sst	-	-	97	158
channel body	27	sst	-	-	93	255
channel body	28	sst	-	-	98	204
-	GW101-2013TK	sst (hand sample)	1.7	-	~130	-
-	GW102-2013TK	sst (hand sample)	7.4	-	~130	-
-	GW103-2013TK	sst (hand sample)	2.8	-	~130	-
-	GW104-2013TK	coal (hand sample)	-	-	~130	-
-	GW105-2013TK	lst (hand sample)	-	-	~130	-
-	GW106-2013TK	sst (hand sample)	4.1	-	~130	-

Geobody/A.E.	Site/ Sample	Facies	ϕ	k (md)	GR (cps)	Int.
-	GW107-2013TK	sst (hand sample)	0.9	-	~130	-
-	GW108-2013TK	sst (hand sample)	2.0	-	~130	-
channel base	1x	sst (base of Coal Mine Point)	-	527	-	-
channel base	2x	sst (base of Coal Mine Point)	-	66	-	-
channel base	3x	sst (base of Coal Mine Point)	-	284	-	-
channel base	4x	sst (base of Coal Mine Point)	-	387	-	-
channel base	5x	sst (base of Coal Mine Point)	-	1,258	-	-
channel base	6x	sst (base of Coal Mine Point)	-	924	-	-
channel base	7x	sst (base of Coal Mine Point)	-	1,917	-	-
channel base	8x	sst (base of Coal Mine Point)	-	269	-	-
-	9x	fallen, blocky, silty-sst; horizontal	-	88	-	-
-	10x	fame as above; vertical	-	10	-	-
-	11x	fallen, grey, sandy-siltstone; vertical	-	12	-	-
-	12x	same as above; horizontal	-	39	-	-
tree trunk	13x	fossilized tree trunk, red-brown	-	7	-	-
-	14x	fine-grained massive sst; horizontal	-	35	-	-
-	15x	same as above; vertical	-	28	-	-
-	16x	fine lower sst; vertical	-	101	-	-
-	17x	same as above; horizontal	-	104	-	-
-	18x	very fine upper shale; vertical	-	17	-	-
-	19x	very fine upper shale	-	119	-	-
-	20x	coal bed on safe outcrop; horizontal	-	95	-	-
-	21x	same as above; vertical	-	14	-	-
-	22x	large sst bedset; horizontal	-	269	-	-
ripples	23x	same as above with climbing ripples	-	410	-	-
-	24x	conglomerate; horizontal	-	209	-	-

3.8.7 Geobody Analysis

In geoscience field studies, lidar has been a useful tool for capturing 3D outcrops in point cloud form, from which detailed sedimentological and stratigraphic interpretations can be performed. It has been recognized that the resulting intensity values recorded by the lidar unit correlate extremely well to lithology (Figure 2.1), thereby allowing for the determination between sandstone and shale, for example (e.g., Baldrige et al. 2009; Burton et al. 2011). The Joggins Formation is an example where this lidar intensity correlation to lithology concept is visible, allowing for the understanding of the controls of lateral facies on fluid flow and geobody analysis (Figure 3.19).

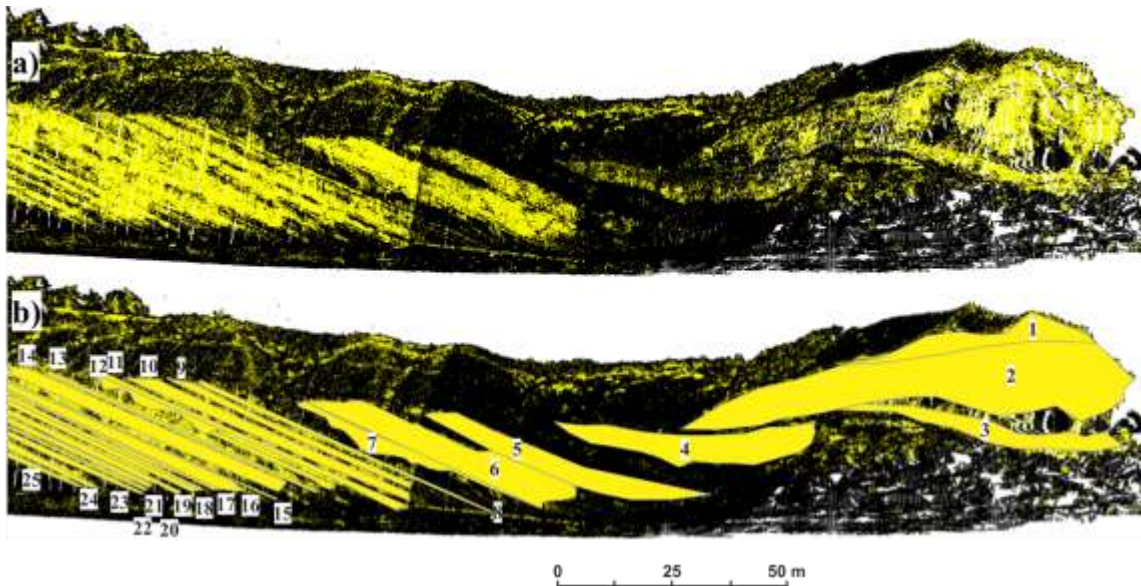


Figure 3.19: The lidar generated point cloud of the Joggins Formation outcrop viewed from the West. The point cloud has been colourized to show the sandstone geobodies in yellow. Coal Mine Point is located on the right-hand side and comprises multi-story channel complex (numbers 1 through 3) with scoured basal contacts. A digital photograph of this section is shown in Figure 3.3. a) The uninterpreted point cloud. b) the interpreted point cloud with sandstone geobodies shown in yellow and numbered from 1 to 24.

The sandstone geobodies are easily visualized in the high-resolution lidar point cloud image shown in Figure 3.19. These geobodies are represented by yellow polygons and are either multi-story channels with scoured bases or sheet sandstones. The distinction between these sandstone geobody types is particularly important for reservoir heterogeneity studies because multi-story channels typically form due to episodes of cut and fill, thereby creating potential baffles where thin shale drapes occur between sands. Sheet sands may form from a variety of processes, including overbank deposits, waning flow of channel deposition, and distal flood events. In the Joggins Formation they typically are well sorted fine-grained sandstones. Stacked sheet sands are usually separated by form baffles formed by finer grained siltstone. Even sand-on-sand contact or thin shale drapes occurring between sands can exhibit thin baffles that would not be visible in subsurface seismic or petrophysical data when delineating reservoirs for production of injection operations.

Mapping the outcrop with the lidar data allows the fluid flow paths to be delineated (Figure 3.20). Flow would be laterally and vertically through individual sandstone geobodies, while thin shale drapes between stacked sheet sands and multi-story channels would act as a baffle. The thicker shale intervals would act as barriers to fluid flow. A summary of the sandstone geobody types, width, and thickness are listed in Table 3.8. Note the width is a minimum estimate as it is possible that some of the sandstone geobodies are wider than measured from the lidar image because they might be penetrating beneath the beach face, obscured by erosional material from above, or have been truncated by the angular unconformity that occurs at the top of the formation with the overlying Quaternary sediments.

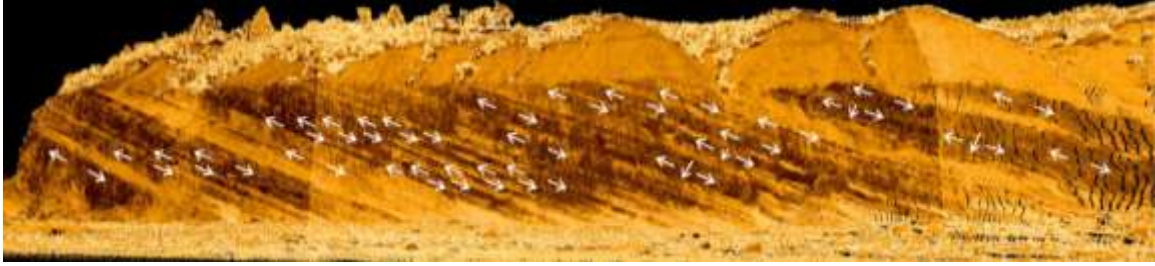


Figure 3.20: The generated point cloud section viewed from the West showing fluid flow lines in white.

Table 3.8: Summary of the geobody number, geobody type, width, and thickness as measured from Figure 3.19.

Geobody #	Geobody Type	Width (m)	Thickness (m)
1	multi-story channel/scoured base	22.3	4.5
2	multi-story channel/scoured base	58.8	9.5
3	multi-story channel/scoured base	22.6	1.8
4	multi-story channel/scoured base	57.3	4.3
5	multi-story channel	51.6	3.1
6	multi-story channel	40.7	4.3
7	multi-story channel/scoured base	48.5	3.5
8	sheet sands	51.9	1.2
9	sheet sands	51.2	2.1
10	sheet sands	51.9	3.4
11	sheet sands	51.7	1.5
12	multi-story channel/scoured base	51.5	2.4
13	sheet sands	51.2	1.4
14	sheet sands	51.1	4.5
15	sheet sands	51.9	1.1
16	sheet sands	51.7	3.0
17	sheet sands	51.6	1.1
18	sheet sands	51.0	1.4
19	sheet sands	51.1	2.0
20	sheet sands	51.3	1.6
21	sheet sands	51.4	1.4
22	sheet sands	51.7	1.6
23	sheet sands	51.8	1.8
24	sheet sands	51.6	1.7
25	sheet sands	51.5	1.5

3.8.8 Outcrop to Core Correlation

Outcrop data provides excellent information on the vertical and lateral facies relationships that can be applied to seismic, petrophysical, and core data. The borehole history report and the drill core show that the borehole intersected six major coal seams.

From youngest to oldest, the seams are the Joggins, Queen, Rector, Jubilee, Kimberly, and Forty Brine. The measured section by Davies et al. (2005) identifies the Joggins, Queen, Kimberly, Forty Brine, and Fundy seams in the outcrop. A correlation was performed using the coal seams present in the hole and the outcrop (Joggins, Queen, Kimberly, and Forty Brine). A summary of the coal seam intervals and coal thicknesses in the borehole and the outcrop are shown in Table 3.9. The visual correlation between the borehole and the outcrop is shown in Figure 3.21.

Table 3.9: Summary of coal seam intervals and thicknesses from borehole and outcrop. Borehole intervals are from REI Nova Scotia (1995), and outcrop intervals are from Rygel (2005).

Coal Seam	Interval (m)		Coal Thickness (cm)	
	Borehole ¹	Outcrop ²	Borehole	Outcrop
Joggins	820.11 – 823.03	804.20 – 807.45	119	150
Queen	839.70 – 842.22	778.95 – 781.90	114	38
Rector	879.87 – 880.23	–	28	–
Jubilee	924.59 – 925.31	–	72	–
Kimberly	976.64 – 980.05	630.20 – 632.40	112	22
Forty Brine	1,055.44 – 1,060.17	545.80 – 547.30	153	72
Fundy	–	419.60 – 420.70	–	85

Notes: 1 – measurements are based on depth down the borehole; 2 – measurements are based on distance from the start of the Joggins Formation at Lower Cove

The REI-B2-1 borehole penetrates a portion of the Joggins Formation and allows the borehole to be stratigraphically placed within the outcrop at the Joggins coastal section, which displays the Joggins Formation in its entirety. Over the last two centuries, several researchers have performed partial or complete measured sections of the Joggins Formation outcrop interval (e.g., Logan 1845; Davies et al. 2005). Using the most recent section by Davies et al. (2005) that defines the cycles based on variations in lithology determined by interpretation of “well-drained” and “poorly-drained” sub-environments, it became possible to correlate between the borehole and the outcrop using major coal seams that occur in both (Figure 3.21). The measured section indicates the locations of five major coal

seams along the outcrop. From youngest to oldest, the five seams are the Joggins, Queen, Kimberly, Forty Brine, and Fundy.

Six major coal seams are in the borehole interval of the Joggins Formation (Figure 3.21). From youngest to oldest, the six seams are the Joggins, Queen, Rector, Jubilee, Kimberly, and Forty Brine. The additions of the Rector and Jubilee coal seams in the borehole interval demonstrate that not all coal seams are laterally continuous across the region and that caution must be taken when stratigraphically mapping the coal intervals or using them as datums, not only in the Joggins Formation of Cumberland Basin, but other subsurface studies worldwide in similar depositional systems. The Fundy coal seam was not visible in the borehole interval because it occurs deeper in the Joggins Formation than the borehole penetrates or pinched out further seaward. Regardless, the four coal seams known as the Joggins, Queen, Kimberly, and Forty Brine are consistent between the two and were used to place the borehole sediments with those from the outcrop stratigraphically. It is well-known that coal seams can have a large thickness variability, both locally and regionally (e.g., Ryer and Langer 1980; Ghosh 1987; Nalendra et al. 2017; Jangara and Ozturk 2021). These thickness changes are also evident in the Joggins Formation coal seams (e.g., Copeland 1959).

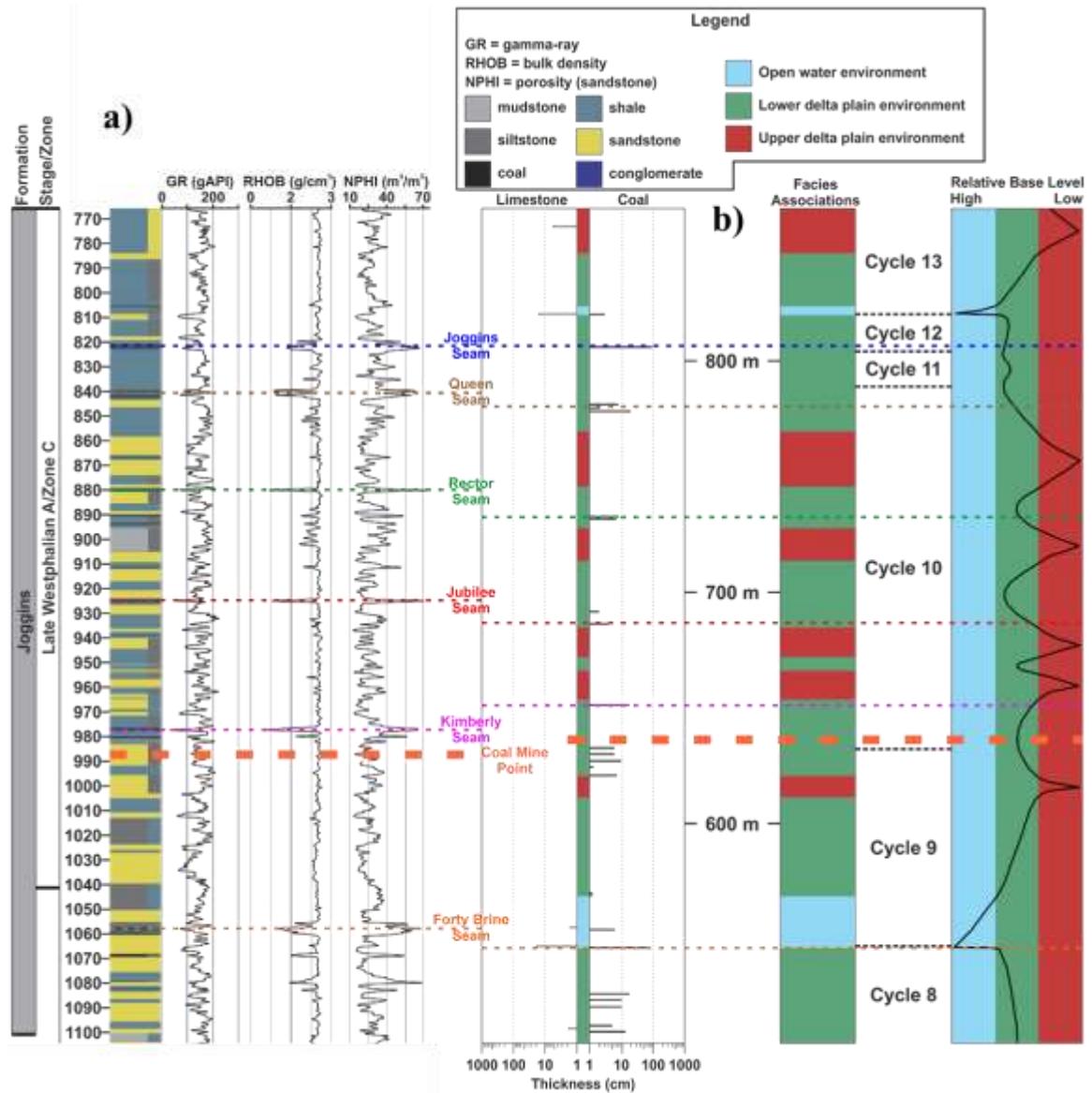


Figure 3.21: A correlation of major coal seams between the REI-B2-1 borehole and the outcrop, which is shown according to the three facies associations interpreted at Joggins. a) Summary lithology log of the Joggins Formation interval from the borehole. The gamma-ray, density, and porosity curves have also been plotted. The major coal seams are also labelled. b) Summary log for the complete Joggins Formation, displaying cycles, facies assemblages, location, and thickness of coal and limestone beds, and relative base-level curve (Davies et al. 2005).

3.8.9 Drill Core Analysis

Rigorous and detailed examination of the continuous Joggins Formation drill core interval can provide critical information regarding reservoir heterogeneity and baffles and barriers to fluid flow. Detailed core description also has the potential of providing high-

resolution details than what is possible from outcrop alone. Parameters including thickness, grain size, sedimentary structures, accessories, such as fossils and diagenetic features, lithologies, and the nature of contacts were recorded. The Joggins outcrop has been the focus of virtually all research conducted on the Joggins Formation, whereas the core data has not been incorporated into studies providing depositional facies information, critical for reservoir characterization studies.

Continuous cores have several advantages over outcrop exposures for environment of deposition interpretation. These advantages are listed by Weimer and Tillman (1980) and include: 1) not restricted to stratigraphic unit outcrop positions, 2) often provide a more complete section of the stratigraphic unit, 3) enhanced preservation of contacts between units having significantly dissimilar resistances to weathering, 4) improved preservation of delicate primary and soft sediment deformation structures in shale and siltstone units, 5) better preservation of trace fossils, 6) ability to attain material for petrographic study below the groundwater table, and 7) allow comparison of lithologic properties with petrophysical properties and wireline log responses. These advantages, however, are offset by the absence of a three-dimensional view and the inability to observe lateral facies changes and large-scale sedimentary features directly (Weimer and Tillman 1980).

Representative examples of the drill core from the Joggins Formation are shown in Figure 3.22 and Figure 3.23. Figure 3.22 shows a consecutive interval of six boxes (264-269), ranging from a depth of 971.90 m to 997.60 m. Figure 3.23 shows a consecutive interval of six boxes (270-275), ranging from a depth of 997.60 m to 1,023.30 m. The drill core images of the Joggins Formation are shown in Appendix D and the subsequent core description is shown in Appendix E.

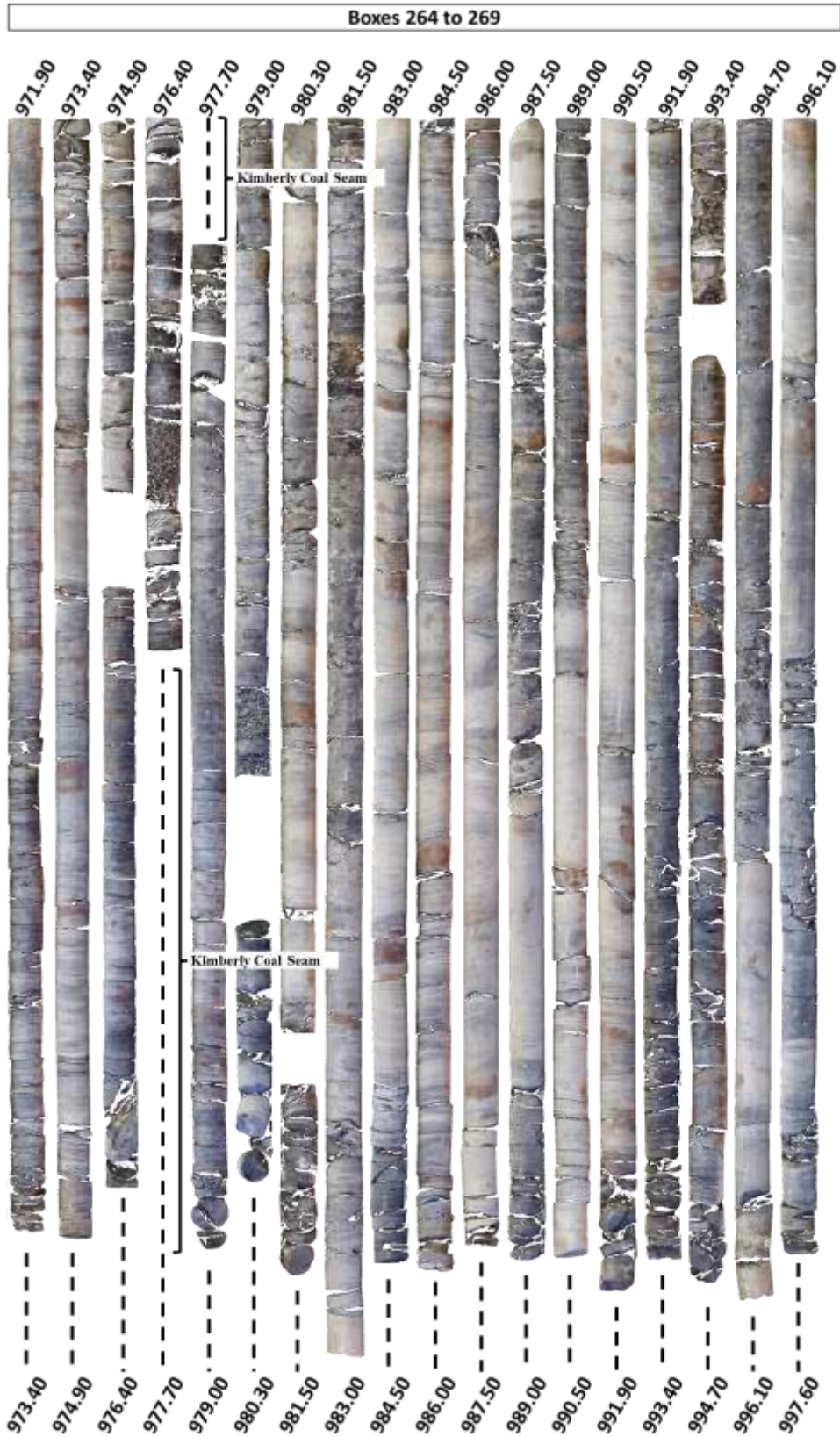


Figure 3.22: Representative core photographs (from the REI-B2-1 borehole) of the Joggins Formation. The photographs show a total of six boxes of consecutive core from 971.90 m to 997.60 m.

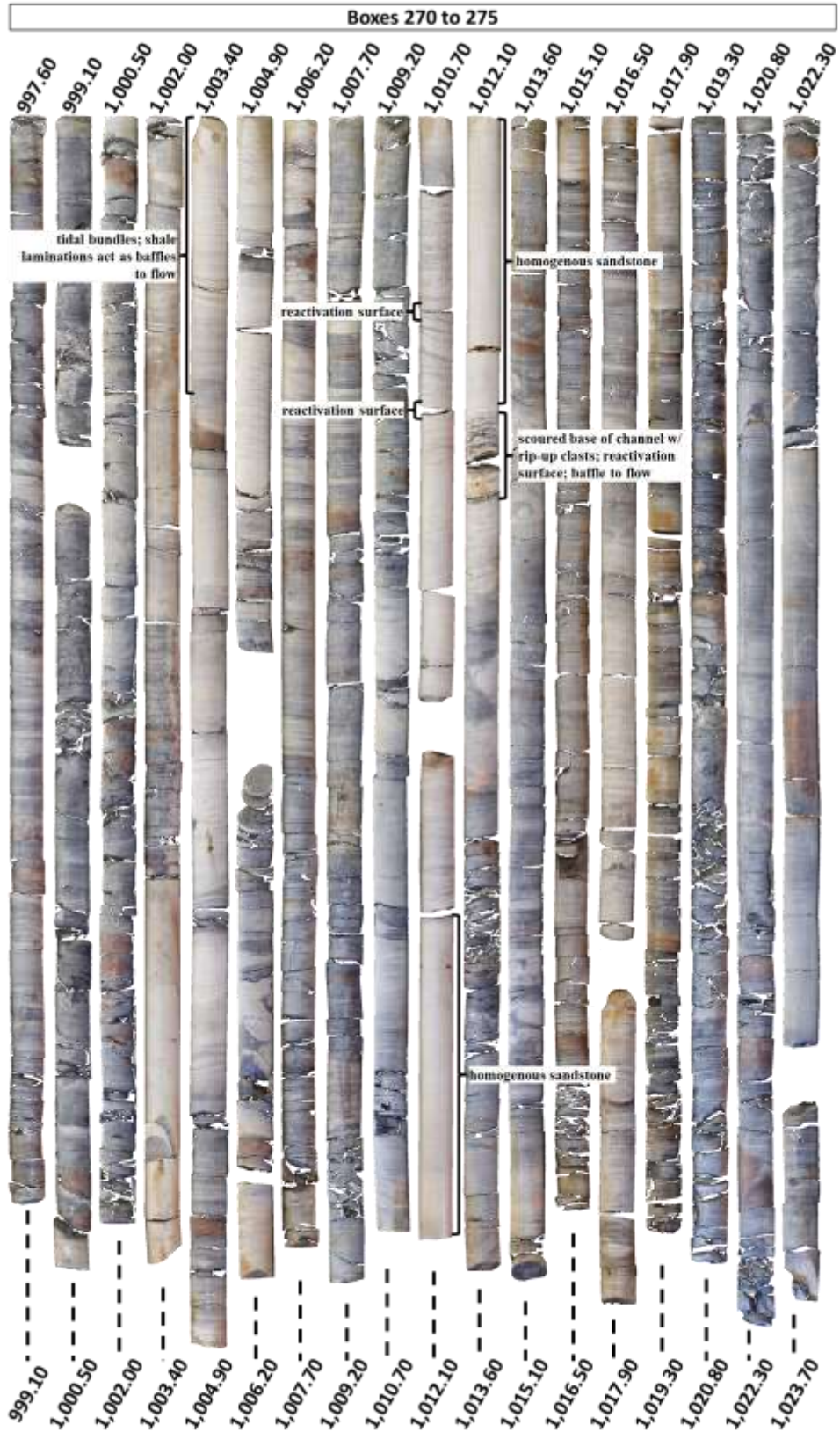


Figure 3.23: Representative core photographs (from the REI-B2-1 borehole) of the Joggins Formation. The photographs show a total of six boxes of consecutive core from 997.60 m to 1,023.70 m.

The drill core interval of the Joggins Formation ranges from a depth of (765 m to 1,101.5 m). It was not possible to complete a thorough description of the complete 336.50 m of core due to access limitations to the Core Facility brought on by the pandemic restrictions to government buildings. However, it is possible to portray the importance of drill core to the overall understanding of reservoir characterization, heterogeneity, architectural elements, and baffles and barriers. Reactivation surfaces are apparent throughout the interval, noted where the dip angle of the laminae or beds changes. These surfaces are also permeability baffles. An example of rip-up clasts occurring at the scoured base of a channel also suggests a reactivation surface, which acts as a baffle to fluid flow.

The Joggins Formation in outcrop and core provides an unrivalled example where lithology variability (lithofacies) constrained by depositional setting and sub environments, demonstrate the controls on stratigraphic correlations permeability baffles and barriers to fluid flow and geobody analysis. These analyses address three of the reservoir engineering challenges identified by the SPE Research & Development Committee (2012); higher resolution subsurface imaging, demonstration of controls limiting increased recovery, and carbon capture, utilization, and storage capacity.

3.9 Conclusions

1. Gamma ray spectrometry reveals a wide range of values, which are expected from the complex stacking of variable bed lithology of the interbedded strata. It re-iterates the usefulness of gamma ray spectrometry for aiding with lithology contrasts in complex geology but cannot selectively measure and identify reservoir heterogeneity such as clast variability.

2. Outcrop permeability data varies widely from 7 md to approximately 2,000 md. The variability in outcrop permeability is not simply the result of a change in lithology between beds; rather, permeability appears to vary within individual beds, because of subtle changes in lithology and composition. This relates back to the interbedded nature of the strata in the outcrop.
3. Lidar can be a highly useful tool to characterize the heterogeneity of an outcrop because of its high resolution and high detail of the resulting generated point cloud. The intensity of the reflected light from the rock outcrop that is measured by the lidar system has the added benefit of being a proxy for lithology, at least for an outcrop that displays such widely varying and alternating rock strata, such as at Joggins. For a more lithologically homogenous outcrop, it may be more challenging to extract information from a high-resolution point cloud.
4. Reservoir characterization and heterogeneity studies are further improved when lidar is paired with more traditional approaches of measurement, such as the use of gamma ray spectrometry and an air permeameter. Considering the overall studied section, reservoir heterogeneity of the Joggins Formation is stratigraphically controlled with variations in alternating lithology being the apparent reason. Single beds within that overall studied section further exhibit vertical and horizontal heterogeneity because of lithological changes within them or changes in grain size, which do occur. It is also likely that sedimentary structures play a role in reservoir heterogeneity within single beds.

3.10 Acknowledgments

The authors would like to thank the members of the Dalhousie University Basin and Reservoir Laboratory for providing field assistance and data collection. We are appreciative of Dr. Yawooz Kettanah for training on the proper use of the microscope and software necessary to perform the digital image porosity analysis. Thanks to Dr. Lawrence Plug for allowing the use of his differential global positioning system equipment, to Gordon Brown for preparing thin sections and the folks at the Joggins Fossil Center for accommodating us during a busy time of year. The authors also acknowledge Ellen and Neil Watson, as well as the associate editor and an anonymous reviewer for their constructive suggestions and feedback.

3.11 References Cited in Chapter 3

Alhumimidi, M.S., Alfarhan, M.S., Cline, J.R., and Aiken, C.L. 2017. Application of a 3D photorealistic model for the geological analysis of the Permian carbonates (Khuff Formation) in Saudi Arabia. *Arabian Journal of Geosciences*, **10**: 112. doi:10.1007/s12517-017-2874-7.

Allen, J.P., Fielding, C.R., Rygel, M.C., and Gibling, M.R. 2013. Deconvolving Signals of Tectonic and Climatic Controls From Continental Basins: An Example From the Late Paleozoic Cumberland Basin, Atlantic Canada. *Journal of Sedimentary Research*, **83**: 847-872. doi:10.2110/jsr.2013.58.

Antonellini, M., Cilona, A., Tondi, E., Zambrano, M., and Agosta, F. 2014. Fluid flow numerical experiments of faulted porous carbonates, Northwest Sicily (Italy). *Marine and Petroleum Geology*, **55**: 186-201. doi:10.1016/j.marpetgeo.2013.12.003.

Baldrige, A.M., Hook, S.J., Grove, C.I., and Rivera, G. 2009. The ASTER spectral library version 2.0. *Remote Sensing of Environment*, **113**: 711-715. doi:10.1016/j.rse.2008.11.007.

Bellian, J.A., Kerans, C., and Jennette, D.C. 2005. Digital outcrop models: applications of terrestrial scanning lidar technology in stratigraphic modeling. *Journal of Sedimentary Research*, **75**: 166-176. doi:10.2110/jsr.2005.013.

Bellian, J.A., Beck, R., and Kerans, C. 2007. Analysis of hyperspectral and lidar data: Remote optical mineralogy and fracture identification. *Geosphere*, **3**: 491-500. doi:10.1130/GES00097.1.

Blott, J.E., Davis, T.L., and Benson, R.D. 1999. Morrow sandstone reservoir characterization: A 3-D multicomponent seismic success. *The Leading Edge*, **18**: 394-397. doi:10.1190/1.1438305.

Brown, S., and Smith, M. 2013. A transient-flow syringe air permeameter. *Geophysics*, **78**: 307-313.

Browne, G.H., and Plint, G.A. 1994. Alternating braidplain and lacustrine deposition in a strike-slip setting: The Pennsylvanian Boss Point Formation of the Cumberland Basin, Maritime Canada. *Journal of Sedimentary Research*, **64**: 40-59. doi:10.1311/JSE.1994.0640040.

Buckley, S.J., Howell, J.A., Enge, H.D., and Kurz, T.H. 2008. Terrestrial laser scanning in geology: data acquisition, processing and accuracy considerations. *Journal of the Geological Society*, **165**: 625-638. doi:10.1144/0016-76492007-100.

Buckley, S.J., Enge, H.D., Carlsson, C., and Howell, J.A. 2010. Terrestrial laser scanning for use in virtual outcrop geology. *The Photogrammetric Record*, **25**: 225-239. doi:10.1111/j.1477-9730.2010.00585.x.

Burton, D., Dunlap, D.B., Wood, L.J., and Flaig, P.P. 2011. Lidar Intensity as a Remote Sensor of Rock Properties. *Journal of Sedimentary Research*, **81**: 339-347. doi:10.2110/jsr.2011.31.

Calder, J.H., and Boon, J. 2007. Joggins Fossil Cliffs: Property Nominated for Inscription on the World Heritage List. Nova Scotia Department of Natural Resources, Mineral Resources Branch, Halifax, NS. pp. Open File Map ME 2007-2001.

Calder, J.H., Gibling, M.R., Scott, A.C., Davies, S.J., Herbert, B.L., Greb, S.F., and DiMichele, W.A. 2006. A fossil lycopsid forest succession in the classic Joggins section of Nova Scotia: paleoecology of a disturbance-prone Pennsylvanian wetland. *Special Papers - Geological Society of America*, **399**: 169. doi:10.1130/2006.2399(09).

Casini, G., Hunt, D.W., Mosen, E., and Bounaim, A. 2016. Fracture characterization and modeling from virtual outcrops. *AAPG Bulletin*, **100**: 41-61. doi:10.1306/09141514228.

Copeland, M.J. 1959. Coalfields west half Cumberland County, Nova Scotia. Geological Survey of Canada Memoir 298. p. 89.

Davies, D., Williams, B., and Vessell, R. 1992. Models for meandering and braided fluvial reservoirs with examples from the Travis Peak Formation, East Texas. *In* SPE Annual Technical Conference and Exhibition. Society of Petroleum Engineers.

Davies, S.J., and Gibling, M.R. 2003. Architecture of coastal and alluvial deposits in an extensional basin: the Carboniferous Joggins Formation of eastern Canada. *Sedimentology*, **50**: 415-439. doi:10.1046/j.1365-3091.2003.00553.x

Davies, S.J., Gibling, M.R., Rygel, M.C., Calder, J.H., and Skilliter, D.M. 2005. The Pennsylvanian Joggins Formation of Nova Scotia: sedimentological log and stratigraphic framework of the historic fossil cliffs. *Atlantic Geology*, **41**: 87-102. doi:10.4138/182.

Dawson, J.W. 1854. On the coal-measures of the South Joggins, Nova Scotia. *Quarterly Journal of the Geological Society*, **10**: 1-42.

De Boever, W., Bultreys, T., Derluyn, H., Van Hoorebeke, L., and Cnudde, V. 2016. Comparison between traditional laboratory tests, permeability measurements and CT-based fluid flow modelling for cultural heritage applications. *Sci Total Environ*, **554-555**: 102-112. doi:10.1016/j.scitotenv.2016.02.195.

Enge, H.v.D., Buckley, S.J., Rotevatn, A., and Howell, J.A. 2007. From outcrop to reservoir simulation model: Workflow and procedures. *Geosphere*, **3**: 469-490. doi:10.1130/GES00099.1.

Exploranium - Radiation Detection Systems. 2001. GR-130 MiniSPEC User Manual (Revision 15.1).

Fabuel-Perez, I., Hodgetts, D., and Redfern, J. 2009a. A new approach for outcrop characterization and geostatistical analysis of a low-sinuosity fluvial-dominated succession using digital outcrop models: Upper Triassic Oukaimeden Sandstone Formation, central High Atlas, Morocco. *AAPG Bulletin*, **93**: 795-827. doi:10.1306/02230908102.

Fabuel-Perez, I., Hodgetts, D., and Redfern, J. 2010. Integration of digital outcrop models (DOMs) and high resolution sedimentology-workflow and implications for geological modelling: Oukaimeden Sandstone Formation, High Atlas (Morocco). *Petroleum Geoscience*, **16**: 133-154. doi:10.1144/1354-079309-820.

Filomena, C.M., Hornung, J., and Stollhofen, H. 2014. Assessing accuracy of gas-driven permeability measurements: a comparative study of diverse Hassler-cell and probe permeameter devices. *Solid Earth*, **5**: 1-11. doi:10.5194/se-5-1-2014.

Fossen, H. 2010. Deformation bands formed during soft-sediment deformation: Observations from SE Utah. *Marine and Petroleum Geology*, **27**: 215-222. doi:10.1016/j.marpetgeo.2009.06.005.

Fossen, H., Schultz, R.A., and Torabi, A. 2011. Conditions and implications for compaction band formation in the Navajo Sandstone, Utah. *Journal of Structural Geology*, **33**: 1477-1490. doi:10.1016/j.jsg.2011.08.001.

Ghosh, R. 1987. The variation in thickness and composition of coal seams and its use in interpretation of palaeocurrents—A case study from the Raniganj Coalfield, West Bengal, India. *International Journal of Coal Geology*, **9**: 209-220. doi:10.1016/0166-5162(87)90046-2.

Gibling, M.R. 2006. Width and Thickness of Fluvial Channel Bodies and Valley Fills in the Geological Record: A Literature Compilation and Classification. *Journal of Sedimentary Research*, **76**: 731-770. doi:10.2110/jsr.2006.060.

Gibling, M.R., and Kalkreuth, W.D. 1991. Petrology of selected carbonaceous limestones and shales in Late Carboniferous coal basins of Atlantic Canada. *International Journal of Coal Geology*, **17**: 239-271. doi:10.1016/0166-5162(91)90034-G.

Grammer, G.M., Harris, P.M.M., and Eberli, G.P. 2004. Integration of outcrop and modern analogs in reservoir modeling: overview with examples from the Bahamas. *In* Integration of Outcrop and Modern Analogs in Reservoir Modeling - AAPG Memoir 80. The American Association of Petroleum Geologists, Houston, Texas. pp. 1-22.

Grasshoff, K. 1975. The hydrochemistry of landlocked basins and fjords. *Chemical oceanography*, **2**: 455-597.

Grechishnikova, A. 2016. Integrated application of a high-resolution LIDAR outcrop survey of an unconventional Niobrara Reservoir, Denver Basin, Colorado. *First Break*, **34**: 65-71. doi:10.3997/1365-2397.34.5.84449.

Grey, M., and Finkel, Z.V. 2011. The Joggins Fossil Cliffs UNESCO World Heritage site: a review of recent research. *Atlantic Geology*, **47**: 185-200. doi:10.4138/atlgeol.2011.009.

Haffen, S., Geraud, Y., Diraison, M., and Dezayes, C. 2013. Determination of fluid-flow zones in a geothermal sandstone reservoir using thermal conductivity and temperature logs. *Geothermics*, **46**: 32-41. doi:10.1016/j.geothermics.2012.11.001.

Hartzell, P., Glennie, C., Biber, K., and Khan, S. 2014. Application of multispectral LiDAR to automated virtual outcrop geology. *ISPRS Journal of Photogrammetry and Remote Sensing*, **88**: 147-155. doi:10.1016/j.isprsjprs.2013.12.004.

Hastings, J.O. 1990. Coarse-grained meander-belt reservoirs, Rocky Ridge field, North Dakota. *In Sandstone Petroleum Reservoirs*. Springer. pp. 57-84.

Hodgetts, D. 2013. Laser scanning and digital outcrop geology in the petroleum industry: a review. *Marine and Petroleum Geology*, **46**: 335-354. doi:10.1016/j.marpetgeo.2013.02.014.

Howell, J.A., Martinius, A.W., and Good, T.R. 2014. The application of outcrop analogues in geological modelling: a review, present status and future outlook. Geological Society, London, Special Publications, **387**: 1-25. doi:10.1144/SP387.12.

Huysmans, M., Peeters, L., Moermans, G., and Dassargues, A. 2008. Relating small-scale sedimentary structures and permeability in a cross-bedded aquifer. *Journal of Hydrology*, **361**: 41-51. doi:10.1016/j.jhydrol.2008.07.047.

Jangara, H., and Ozturk, C.A. 2021. Longwall top coal caving design for thick coal seam in very poor strength surrounding strata. *International Journal of Coal Science & Technology*, **8**: 641-658.

Keogh, K.J., Leary, S., Martinius, A.W., Scott, A.S., Riordan, S., Viste, I., Gowland, S., Taylor, A.M., and Howell, J. 2014. Data capture for multiscale modelling of the Lourinha Formation, Lusitanian Basin, Portugal: an outcrop analogue for the Statfjord Group, Norwegian North Sea. Geological Society, London, Special Publications, **387**: 27-56. doi:10.1144/SP387.11.

Labourdettes, R., and Jones, R.R. 2007. Characterization of fluvial architectural elements using a three-dimensional outcrop data set: Escanilla braided system, South-Central Pyrenees, Spain. *Geosphere*, **3**: 422-434. doi:10.1130/GES00087.1.

Levorsen, A.I. 1954. *Geology of Petroleum*. W.H. Freeman Company, San Francisco, California.

Lichti, D.D., and Harvey, B.R. 2002. The Effects of Reflecting Surface Material Properties on Time-of-Flight Laser Scanner Measurements. *In* Symposium on Geospatial Theory, Processing and Applications, Ottawa, ON. p. 9.

Logan, W.E. 1845. A section of the Nova Scotia coal measures as developed at Joggins on the Bay of Fundy, in descending order, from the neighbourhood of the west Ragged Reef to Minudie, reduced to vertical thickness. *Journals of the Legislative Assembly of the Province of Canada*, **4**: 28-45.

Magnabosco, C., Braathen, A., and Ogata, K. 2014. Permeability model of tight reservoir sandstones combining core-plug and Miniperme analysis of drillcore; Longyearbyen CO2 Lab, Svalbard. *Norwegian Journal of Geology*, **94**: 189-200.

Martel, T.A. 1987. Seismic Stratigraphy and Hydrocarbon Potential of the Strike-Slip Sackville Sub-Basin, New Brunswick. *In* Memoir 12 - Sedimentary basins and basin-forming mechanisms. *Edited by* C. Beaumont and A.J. Tankard. Atlantic Geoscience Society, Halifax. pp. 319-334.

Meyer, R., and Krause, F.F. 2006. Permeability anisotropy and heterogeneity of a sandstone reservoir analogue: An estuarine to shoreface depositional system in the Virgelle Member, Milk River Formation, Writing-on-Stone Provincial Park, southern Alberta. *Bulletin of Canadian Petroleum Geology*, **54**: 301-318. doi:10.2113/gscpgbull.54.4.301.

Minisini, D., Wang, M., Bergman, S.C., and Aiken, C. 2014. Geological data extraction from lidar 3-D photorealistic models: A case study in an organic-rich mudstone, Eagle Ford Formation, Texas. *Geosphere*, **10**: 610-626. doi:10.1130/GES00937.1.

Moore, J., Taylor, A., Johnson, C., Ritts, B.D., and Archer, R. 2012. Facies analysis, reservoir characterization, and LIDAR modeling of an Eocene lacustrine delta, Green River Formation, southwest Uinta Basin, Utah. *In* Lacustrine sandstone reservoirs and hydrocarbon systems: AAPG Memoir 95. *Edited by* O.W. Baganz and Y. Bartov and K. Bohacs and D. Nummedal. The American Association of Petroleum Geologists, Houston, Texas. pp. 183-208.

Morgan, B.C., and Murray, K.E. 2015. Characterizing Small-Scale Permeability of the Arbuckle Group, Oklahoma. Oklahoma Geological Survey, Norman, Ok.

Mukhopadhyay, P.K., Hatcher, P., and Calder, J.H. 1991. Hydrocarbon generation of coal and coaly shale from fluvio-deltaic and deltaic environments of Nova Scotia and Texas. *Organic Geochemistry*: 17,765-783.

Nabawy, B.S., Rochette, P., and Géraud, Y. 2009. Petrophysical and magnetic pore network anisotropy of some cretaceous sandstone from Tushka Basin, Egypt. *Geophysical Journal International*, **177**: 43-61. doi:10.1111/j.1365-246X.2008.04061.x.

Nalendra, S., Kuncoro, B., and Burhanudin, A. Thickness variation of Coal Seams in Loa Janan Anticline: Implication for Exploration and Mining Activities. *In Natural Resources and Infrastructure Development for National Sovereignty*. Malang, Indonesia 2017. *Edited by D. Ralanarko*. Indonesian Association of Geophysicist.

New England Research. 2013. TinyPerm II: Portable Air Permeameter User's Manual. San Ramon, California.

Nickerson, J.D. 2010. Architecture and Geometry of Braided Channel Complex in the Triassic Wolfville Formation. Earth Sciences, Dalhousie University, Halifax, NS.

North, C.P., and Prosser, D.J. 1993. Characterization of fluvial and aeolian reservoirs: problems and approaches. *Geological Society, London, Special Publications*, **73**: 1-6. doi:10.1144/gsl.Sp.1993.073.01.01.

Nova Scotia Department of Natural Resources. 2005. Aerial Photography - 2005 Colour Photographs.

O'Connor, D. 2016. Facies Distribution, Fluvial Architecture, Provenance, Diagenesis, and Reservoir Quality of Synrift Successions from the Breakup of Pangea: Examples from the Fundy Basin and Orpheus Graben. Earth Sciences, Dalhousie University, Halifax, NS.

Optech Incorporated. 2006a. Optech ILRIS-3D, Vaughan, ON.

Optech Incorporated. 2006b. ILRIS-3D Operation Manual.

Pessemiers, M., Huysmans, M., Peeters, L., Batelaan, O., and Dassargues, A. 2012. Relationship between sedimentary features and permeability at different scales in the Brussels Sands. *Geologica Belgica*, **15**: 156-164.

Pringle, J., Howell, J., Hodgetts, D., Westerman, A., and Hodgson, D. 2006. Virtual outcrop models of petroleum reservoir analogues: a review of the current state-of-the-art. *First Break*, **24**: 33-42. doi:10.3997/1365-2397.2006005.

Raduha, S., Butler, D., Mozley, P.S., Person, M., Evans, J., Heath, J.E., Dewers, T.A., Stauffer, P.H., Gable, C.W., and Kelkar, S. 2016. Potential seal bypass and caprock storage produced by deformation-band-to-opening-mode-fracture transition at the reservoir/caprock interface. *Geofluids*, **16**: 752-768. doi:10.1111/gfl.12177.

Rarity, F., Van Lanen, X., Hodgetts, D., Gawthorpe, R., Wilson, P., Fabuel-Perez, I., and Redfern, J. 2014. LiDAR-based digital outcrops for sedimentological analysis: workflows and techniques. Geological Society, London, Special Publications, **387**: 153-183. doi:10.1144/SP387.5.

REI Nova Scotia. 1995. The Coring and Logging of REI-B2-1. Halifax, Nova Scotia.

Rogiers, B., Beerten, K., Smeekens, T., and Mallants, D. 2011. Air permeability measurements on Neogene and Quaternary sediments from the Campine area: using outcrop analogues for determining hydrodynamic aquifer properties. Belgian Nuclear Research Centre: 23.

Rogiers, B., Beerten, K., Smeekens, T., Mallants, D., Gedeon, M., Huysmans, M., Batelaan, O., and Dassargues, A. 2013. The usefulness of outcrop-analogue air-permeameter measurements for analysing aquifer heterogeneity: testing outcrop hydrogeological parameters with independent borehole data. *Hydrology and Earth System Sciences*, **17**: 5155-5166. doi:10.5194/hess-17-5155-2013.

Rogiers, B., Winters, P., Huysmans, M., Beerten, K., Mallants, D., Gedeon, M., Batelaan, O., and Dassargues, A. 2014. High-resolution saturated hydraulic conductivity logging of borehole cores using air permeability measurements. *Hydrogeology Journal*, **22**: 1345-1358. doi:10.1007/s10040-014-1144-y.

Rotevatn, A., Torabi, A., Fossen, H., and Braathen, A. 2008. Slipped deformation bands: A new type of cataclastic deformation bands in Western Sinai, Suez rift, Egypt. *Journal of Structural Geology*, **30**: 1317-1331. doi:10.1016/j.jsg.2008.06.010.

Rotevatn, A., Buckley, S.J., Howell, J.A., and Fossen, H. 2009. Overlapping faults and their effect on fluid flow in different reservoir types: A LIDAR-based outcrop modeling and flow simulation study. *AAPG Bulletin*, **93**: 407-427. doi:10.1306/09300807092.

RPS Energy. 2010. Screening of Potential CO₂ Storage Sites Onshore Nova Scotia. Carbon Capture and Storage Research Consortium of Nova Scotia

Ryan, R.J., and Boehner, R.C. 1994. Geology of the Cumberland Basin, Cumberland, Colchester and Pictou Counties, Nova Scotia - Memoir 10. *Edited by* Mines and Energy Branch - Department of Natural Resources. Department of Natural Resources, Halifax.

Ryan, R.J., Calder, J.H., Donohoe Jr., H.V., and Naylor, R. 1987. Late Paleozoic Sedimentation and Basin Development Adjacent to the Cobequid Highlands Massif, Eastern Canada. *In* Memoir 12 - Sedimentary basins and basin-forming mechanisms. *Edited by* C. Beaumont and A.J. Tankard. Atlantic Geoscience Society, Halifax. pp. 311-317.

Ryer, T.A., and Langer, A.W. 1980. Thickness change involved in the peat-to-coal transformation for a bituminous coal of Cretaceous age in central Utah. *Journal of Sedimentary Research*, **50**.

Rygel, M.C. 2005. Alluvial sedimentology and basin analysis of Carboniferous strata near Joggins, Nova Scotia, Atlantic Canada. Earth Sciences, Dalhousie University, Halifax, NS.

Siddiqui, N.A., Ramkumar, M., Rahman, A.H.A., Mathew, M.J., Santosh, M., Sum, C.W., and Menier, D. 2018. High resolution facies architecture and digital outcrop modeling of the Sandakan formation sandstone reservoir, Borneo: Implications for reservoir characterization and flow simulation. *Geoscience Frontiers*. doi:10.1016/j.gsf.2018.04.008.

Slatt, R.M., Jordan, D.W., D'Agostino, A.E., and Gillespie, R.H. 1992. Outcrop gamma-ray logging to improve understanding of subsurface well log correlations. *Geological Society, London, Special Publications*, **65**: 3-19. doi:10.1144/GSL.SP.1992.065.01.02.

Sonnenberg, S.A., McKenna, D.J., and McKenna, P.J. 1991. Sorrento Field--USA Denver Basin, Colorado.

SPE Research & Development Committee. 2012. Grand Challenges Facing the E&P Industry. Available from <https://www.spe.org/en/industry/globalchallenges/2022>.

Sturzenegger, M., Yan, M., Stead, D., and Elmo, D. Application and limitations of ground-based laser scanning in rock slope characterization. *In* 1st Canada-US Rock Mechanics Symposium. Vancouver, BC 2007, pp. 29-36.

Torabi, A. 2012. Heterogeneity within deformation bands in sandstone reservoirs. *In* 46th US Rock Mechanics / Geomechanics Symposium, Chicago, IL.

UNESCO. 2008. World Heritage List - Joggins Fossil Cliffs. Available from whc.unesco.org/en/list/1285/ [accessed September 6 2018].

van Lanen, X.M., Hodgetts, D., Redfern, J., and Fabuel-Perez, I. 2009. Applications of digital outcrop models: two fluvial case studies from the Triassic Wolfville Fm., Canada and Oukaimeden Sandstone Fm., Morocco. *Geological Journal*, **44**: 742-760. doi:10.1002/gj.1196.

Van Sickle, J. 2015. GPS for Land Surveyors. CRC Press.

Weimer, R.J., and Tillman, R.W. 1980. Tectonic influence on deltaic shoreline facies, Fox Hills Sandstone, West-central Denver Basin. Professional Contributions of the Colorado School of Mines. Colorado School of Mines, Golden, CO.

Xharde, R., Long, B.F., and Forbes, D.L. 2006. Accuracy and limitations of airborne LiDAR surveys in coastal environments. *In* International Geoscience and Remote Sensing Symposium, Denver, CO. pp. 2412-2415.

Zeng, Q., Lu, W., Zhang, R., Zhao, J., Ren, P., and Wang, B. 2018. LIDAR-based fracture characterization and controlling factors analysis: An outcrop case from Kuqa Depression, NW China. *Journal of Petroleum Science and Engineering*, **161**: 445-457. doi:10.1016/j.petrol.2017.12.002.

**Chapter 4: A Novel Approach to 3D Modelling Ground-Penetrating Radar
(GPR) Data – A Case Study of a Cemetery and Applications for Criminal
Investigation**

T.B. Kelly, M.N. Angel, D.E. O'Connor, C.C. Huff, L. Morris, and G.D. Wach

This chapter is based on the paper “A Novel Approach to 3D Modelling Ground-Penetrating Radar (GPR) Data – A Case Study of a Cemetery and Applications for Criminal Investigation”, by Trevor B. Kelly, Max N. Angel, Darragh E. O'Connor, Cambria C. Huff, Lauren E. Morris, and Grant D. Wach and is published in the Forensic Science International journal. The copyright agreement form for this chapter can be found in Appendix A.

4.1 Abstract

Ground-penetrating radar (GPR) is an established geophysical technique used extensively for the accurate reconstruction of the shallow (< 10 m) subsurface. Reconstructions have largely been completed and presented as 2D vertical and horizontal planes, leaving limited visualization of subsurface 3D shapes and their spatial relationships. With technological advancements, particularly the availability and integration of various software platforms, 3D modelling of GPR data is now emerging as the new standard. However, despite these developments, there remains an inadequate examination and testing of these techniques, particularly in determining if their application is beneficial and warranted. In this study we conducted a GPR grid survey on a churchyard cemetery to generate and evaluate 2D and 3D-modelled reconstructions of the cemetery burial sites. Data collection and processing was completed using a Sensors and Software Incorporated pulseEKKO™ Pro SmartCart GPR system and EKKO_Project™ software, respectively. The modelling component was achieved using Schlumberger's Petrel™ E & P software platform, which is tailored to the petroleum industry. The subsurface patterns present in the 2D and 3D models closely

matched the cemetery plot plan, validating our data collection, processing, and modelling methods. Both models were adequate for 2D horizontal visualization of reflection patterns at any specific depth. The 3D model was used to identify the presence of a companion burial plot (stacked caskets) and possible leachate plumes below and encircling burial sites, both of which were not evident in the 2D model, highlighting the benefits of 3D modelling when discerning subsurface objects. We expect our findings to be of value to similar GPR studies, with particular significance to geoforensic studies and criminal investigations.

4.2 Introduction

Objects in the subsurface are obscured by sediments, but GPR helps to elucidate and investigate these objects. While 2D GPR allows for the detection of objects and their depth, 3D GPR goes further and allows for interpretations such as the lateral extent and shape of objects to be made. The use of 3D visualization software became possible nearly three decades ago and while GPR use has grown significantly in its applicability, 3D visualization applied to GPR has not been universally adopted or incorporated into forensic sciences. 2D surface-parallel depth slices have become the accepted standard for displaying 3D environments and this can result in the misinterpretation of the 3D nature and spatial relationships of complex subsurface objects. When 3D visualization is used, it is done either by forming a wide grid of GPR radargrams, or by constructing large 3D models encompassing all data where only the data on the extremities are viewable, blocking any innerworkings of the target area (Aziz et al. 2016; Fernández-Álvarez et al. 2017). By subtracting low-amplitude signals representative of undisturbed soil, proper 3D visualization can maximize accuracy and provide a more intuitive visual representation of data.

GPR is a non-destructive, non-invasive remote sensing method that is highly versatile for use with several different disciplines for the imaging and study of the shallow subsurface (Neal and Roberts 2000; Neal 2004). It accomplishes this through the detection of electrical discontinuities by the generation, propagation, reflection, and reception of pulsed high-frequency electromagnetic energy (Neal and Roberts 2000; Neal 2004). These discontinuities are directly related to water saturation, salinity, porosity, and mineralogical variations (Møller and Anthony 2003; Jol 2009). Ideal GPR results are typically achieved from clean, quartzose-rich clastic sediments that contain no clays or silts (Jol and Smith 1991; Smith and Jol 1992). Signal attenuation is a real concern when performing a GPR survey, with problems arising from concentrations of silt, clay, caliche, and moist saline conditions (Beres Jr. and Haeni 1991; Jol and Smith 1991; Smith and Jol 1992).

GPR has been applied successfully in numerous disciplines and environments including, but not limited to, utility locating (Lester and Bernold 2007; Thomas et al. 2009; Ni et al. 2010), forensic/law enforcement (Roark et al. 1998; Schultz 2007; Billinger 2009; Ruffell et al. 2009; Barone et al. 2015; Fernández-Álvarez et al. 2016), infrastructure (Maser 1996; Maierhofer 2003; Lalagüe 2015), mining/quarrying (Botelho and Mufti 1998; Ralston and Hainsworth 1999; Strange et al. 2005; Porsani et al. 2006; Kadioglu 2008; Rafezi et al. 2015), geotechnical/environmental (Daniels et al. 1992; Pettersson and Nobes 2003; Yelf 2007; Hamzah et al. 2009; Benedetto et al. 2012; Venkateswarlu and Tewari 2014), archaeological (Fernández-Álvarez et al. 2016; Imposa et al. 2018; Qin et al. 2018), military (Ho and Gader 2002; Varela-Ortiz et al. 2013; Kumlu and Erer 2019), agriculture/forestry (Yoder et al. 2001; Butnor et al. 2003; Huisman et al. 2003; Zenone et al. 2008; Lorenzo et al. 2010; Liu et al. 2018), and ice/snow (Arcone 1996; Vaughan et al.

1999; Pälli et al. 2002; Lundberg et al. 2006; De Pascale et al. 2008; Mitterer et al. 2011). Detecting foreign objects or regions in the subsurface has a near endless range of applications if accuracy of data collection and modelling can be optimized. Criminal investigations, when searching for human remains or objects relating to crime is one use which we believe could strongly benefit from optimized GPR use. GPR paired with 3D visualization could be especially useful in the example of mass graves, where any representative data is in the form of an amorphous blob. The study of mass graves is ongoing, and GPR, as well as ERT, are the commonly used methods for their study. In a study comparable to ours, Rubio-Melendi et al. (Rubio-Melendi et al. 2018) utilizes 3D modelling of ERT data to map out a mass grave in Spain which proved effective, however, stopped at 2D modelling when it came to their GPR visualization (Rubio-Melendi et al. 2018). The techniques we demonstrate in this study show how greater resolution of buried remains can be accomplished. Greater resolution will allow for further data interpretation and manipulation not necessarily possible in 2D visualization (Di Prima et al. 2020).

We hope to demonstrate a unique workflow method to optimally visualize data in 3D, as to hopefully set a new standard for future modelling of GPR surveys in criminal investigation geoforensics and beyond. With the processing of EKKO_Project™ Software from Sensors and Software and the accurate finite-element modelling in Petrel™ software from Schlumberger, we can remove irrelevant data in order to build a 3D model displaying precise and pertinent data, lending a better understanding of the subsurface. The GPR was used to map out the burial sites, identifying any abnormal forensic facies up to 4 m in depth. This survey takes place in a cemetery with tombstones, plot plans, and different types of burial sites and practices (single-casket, multi-casket, and urns). Tombstones and plot plans

indicate exact burial locations and age of burial sites. The plot plans also contain unmarked but known burial sites. These are sites indicated on plot plans and confirmed by the cemetery warden but have no tombstones or indication of a burial site in the field. Satellite images are also useful in locating exact locations of known burial sites. This supplementary information allows us to fact-check data, thus testing the strength of our 3D modelling method. It also allows us to examine if any relationship is discernible between age and size of burial and the signal it generates.

4.3 Study Area and Site Characterization

The study area is located at 1231 Highway # 1 ($44^{\circ} 55' 23.8893''$ north and $63^{\circ} 53' 32.2534''$ west), in the community of Lakelands, Hants County, Nova Scotia, Canada, approximately 44 km northwest of the capital of Halifax, Nova Scotia (Figure 4.1). The site consists of a nearly cleared piece of land with mixed trees bordering the edges of the property. The property contains a large gravel parking lot, a shed, a small gathering hall, and the church itself. The church sits atop a concrete block foundation with a furnace room adjacent to the basement (Risk 2020). The church was originally built in 1845 by Richard Uniacke for his family and their community. It was built on a stone foundation but was raised onto a new concrete foundation in 2008. There is also a dug water well on the property with the water level occurring at approximately 18 m below the top of the well (Risk 2020). The cemetery contains many burial plots (Figure 4.2), some of which are utilized. Burial plots that are being utilized are noted by a headstone. There are a few trees and bushes growing within the cemetery area.

The climate of the region is classified as humid temperate with long and cold winters and short and warm summers (Cann et al. 1954). The approximate mean annual

temperature and precipitation is 6°C and 1,100 mm, respectively (Cann et al. 1954). During the month of July, when fieldwork was conducted, the average precipitation is typically 110 mm (Cann et al. 1954). However, July of 2019 was a particularly dry month which saw only 48.4 mm of total rainfall for the month, less than half of what is considered to be normal (Figure 4.3) (Environment Canada 2020). Only ten days in July had rainfall values and no precipitation occurred on the day of the fieldwork (Environment Canada 2020).

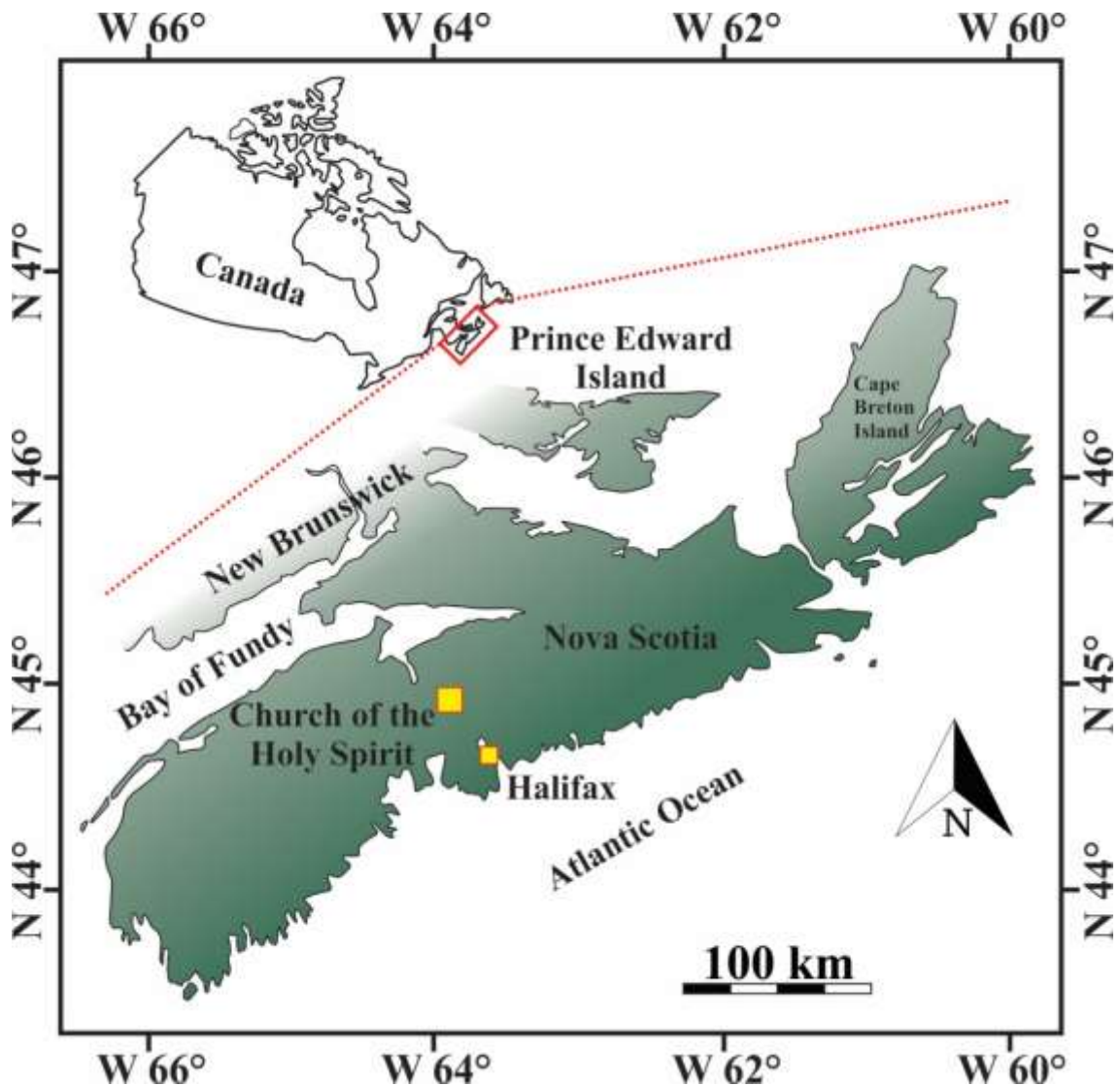


Figure 4.1: Overview of study location.

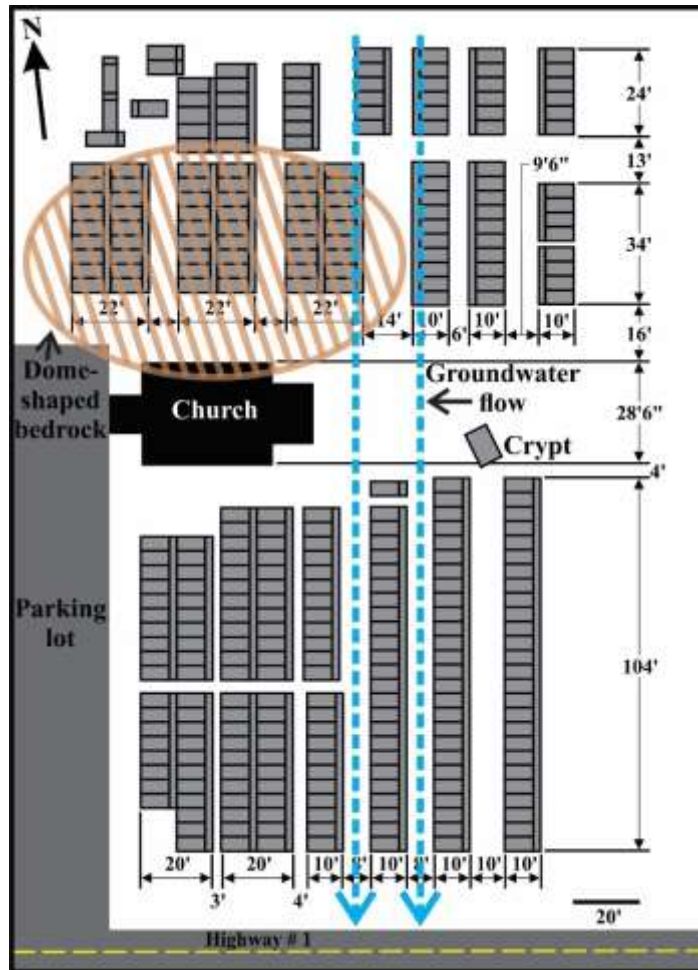


Figure 4.2: Plan view sketch of the study area showing the approximate location of the dome-shaped bedrock feature (hatch patterned oval) to the north of the church. The dashed blue line indicates the direction of groundwater flow.

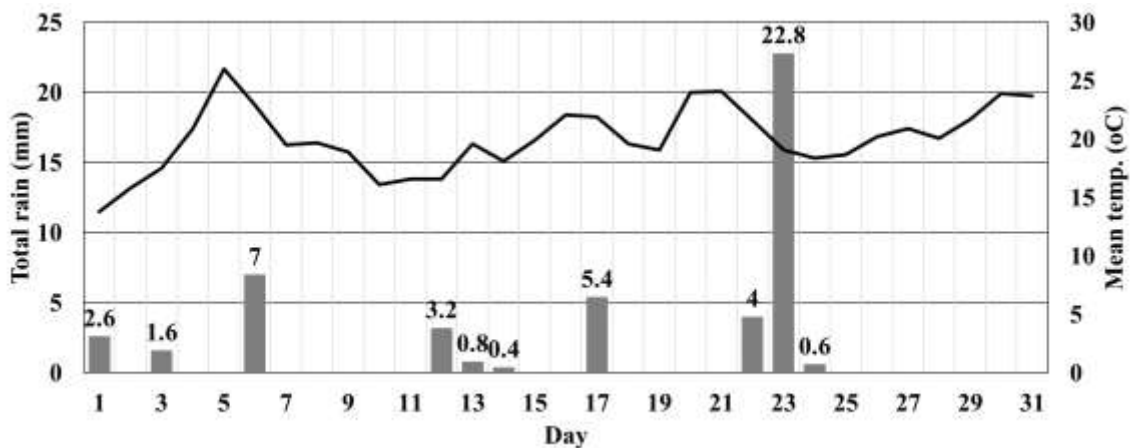


Figure 4.3: A graph showing the total precipitation and mean temperature for the month of July 2019 (Environment Canada 2020). The histogram plot indicates the daily precipitation, with values indicated. The line graph indicates the mean daily temperature.

4.4 Burial Practices and Decomposition Rates

Funeral and burial practices were variable in Nova Scotia throughout the 1800s and 1900s. In rural locations, a practice Poulter (2011) refers to as community funerals were common, where the community of the deceased prepared the body, built a six-sided wooden coffin, and buried the individual once decay had begun thus proving the person was indeed deceased (Poulter 2011). Ice was used to slow decay so that the community could gather for a wake (MacDonald 2020). However, Poulter (2011) states that as early as 1909, embalming was available and practiced in certain parts of the province. Though not readily available in rural areas, the practice of embalming a body increased in popularity throughout the twentieth century until it became standard practice. For example, an embalmer was sent out with the crew assigned to retrieve the bodies from the site of the tragic Titanic sinking (Bier 2018). Embalming techniques were variable, though arsenic was typically heavily employed, and embalming factored heavily into the professionalization of funeral directors (Doughty 2019).

Despite the availability of embalming, Nova Scotia was slower to adopt embalming and other practices that are now considered traditional than the US and other Canadian provinces (MacDonald 2020). Furthermore, establishing a single funeral practice is complicated as different communities had different traditions and standard practices regarding death, preservation, burial, and record keeping. What is more, not all bodies were regarded as equal or worthy of preservation and burial; lower-class individuals were not likely to receive the same treatment as upper-class individuals upon their demise. For instance, the majority of lower-class passengers who perished in the Titanic sinking were buried at sea as they were not deemed worth embalming and bringing back to land for a

funeral (Bier 2018). Though a single practice cannot be established, in investigating funerary traditions in Cape Breton, MacDonald (2020) notes that the Scottish Gaels, French Acadians, and Mi'kmaq First Nation shared "essential elements" (pg. 2) in funerary practices, though the particulars varied based on the community and class. Though there was a certain amount of improvisation, pine and spruce were typically reserved to build coffins which were sometimes polished with alder ashes and tallow (MacDonald 2020). The Provincial Archives of Nova Scotia house several photographs of funerals from the 1800s and 1900s. Both coffins and caskets are used, and though it is difficult to say with any certainty, the coffins or caskets appear to be relatively simple wooden structures.

While using a coffin or a casket is less relevant, the materials used would likely impact the rate of decay as some materials would impede insect activity more readily and for longer than other types. Poulter (2011) notes that while the majority of caskets and coffins were wooden, metal coffins were also used. In 1848, the Fisk Airtight Coffin was patented, a cast iron coffin that was shaped to the body (Doughty 2015). Furthermore, The Most Holy Trinity Cemetery in Brooklyn, New York, founded 1851, used entirely metal grave markers (Atlas Obscura 2020), indicating that metal was readily available in the funeral business in the 1800s. Given Nova Scotia's climate, wood would decay more rapidly than metal, thus resulting in more rapid body decomposition. The Fisk Airtight Coffin and models similar to it would especially impede decomposition; as the name indicates, the body would be deprived of the conditions required for decomposition to take place. In an article published in *The Guardian*, Costandi (Costandi 2015) states that decay begins only a matter of minutes after death, though embalming delays visible decomposition for a time to allow family and friends the opportunity to see the deceased

as they were in life during the viewing and/or funeral. Though decay begins soon after death, there are numerous factors that impact the overall rate of decomposition that vary between individuals and environments. Hot, arid climates are more likely to produce mummification than full decay whereas water-rich environments are more likely to speed up the decay process. Fiedler et al. (2004) state that under ideal conditions, a corpse will take three to twelve years to decompose into a skeletal state. Funeral Guide (Funeral Guide 2016), a United Kingdom based funeral resource, elaborates, saying an unembalmed body buried at six feet will take eight to twelve years to skeletonize. An embalmed body will take longer, though how long is subject to the climate, soil type(s), and casket/casket materials.

While the exact rate of decomposition in traditionally buried bodies seems to be unknown, there is consensus that other factors, such as the formation of adipocere (grave wax) can also hinder or even indefinitely delay decomposition (Fiedler et al. 2004; The Australian Museum 2020). Adipocere formation can cause bodies that have been buried for the same length of time to be at different stages of decomposition as the waxy substance preserves the corpse (Fiedler et al. 2004). Though adipocere may not form on each corpse, it can accumulate in the soils and spread to surrounding gravesites, thus hindering the decomposition of other bodies for 20 to 40 years (Doughty 2018).

4.5 Geological Background

4.5.1 Surficial Geology

Surficial geology impacts the ability to properly collect data during GPR surveys. For example, high clay content will attenuate a GPR signal faster than a coarser grained

material (Doolittle and Bellantoni 2010), making it difficult to properly image human remains and other objects related to criminal cases. A comprehensive soil survey of Hants County by Cann et al. (Cann et al. 1954), states that the soil in the study area belongs to the Halifax soil series (Figure 4.4a). This provided a preliminary assessment of the study area, indicating any areas containing soil that could attenuate the GPR signals faster, thus being unsuitable for a survey.

The Halifax soil series represents approximately 6 % of Hants County soils with soil profiles that range from a few centimeters to approximately one meter (Cann et al. 1954) (Figure 4.4a). This soil has typically good drainage with numerous poorly drained depressions. It can also be stony (Cann et al. 1954). Overall, the soil is a light brown sandy loam over a yellowish-brown sandy loam, derived from glacial till. The parent material for this soil type is a greyish brown sandy loam derived from hard sandstone, slate, and quartzite. Granitic boulders and glacial erratics are possibly present. Forest vegetation comprises white spruce, maple, birch, and pine on the better drained areas, and black spruce, hemlock and poplar on the more poorly drained sites (Cann et al. 1954). A representative profile is described in Table 4.1.

Table 4.1: Representative soil profile for the study area (Cann et al. 1954).

Horizon	Depth (cm)	Description
A ₀	0 – 5	Loose; primarily litter and decomposing organic matter
A ₁	5 – 10	Loose; pinkish-grey sandy loam; fine platy structure; cobbles
B ₁	10 – 35	Loose; strong brown sandy loam; good root development; cobbles
B ₂	35 – 75	Slightly firm; yellow-brown sandy loam; some roots; friable; cobbles
C	75+	Moderately firm; grey-brown gravelly sandy loam; friable; stones and cobbles

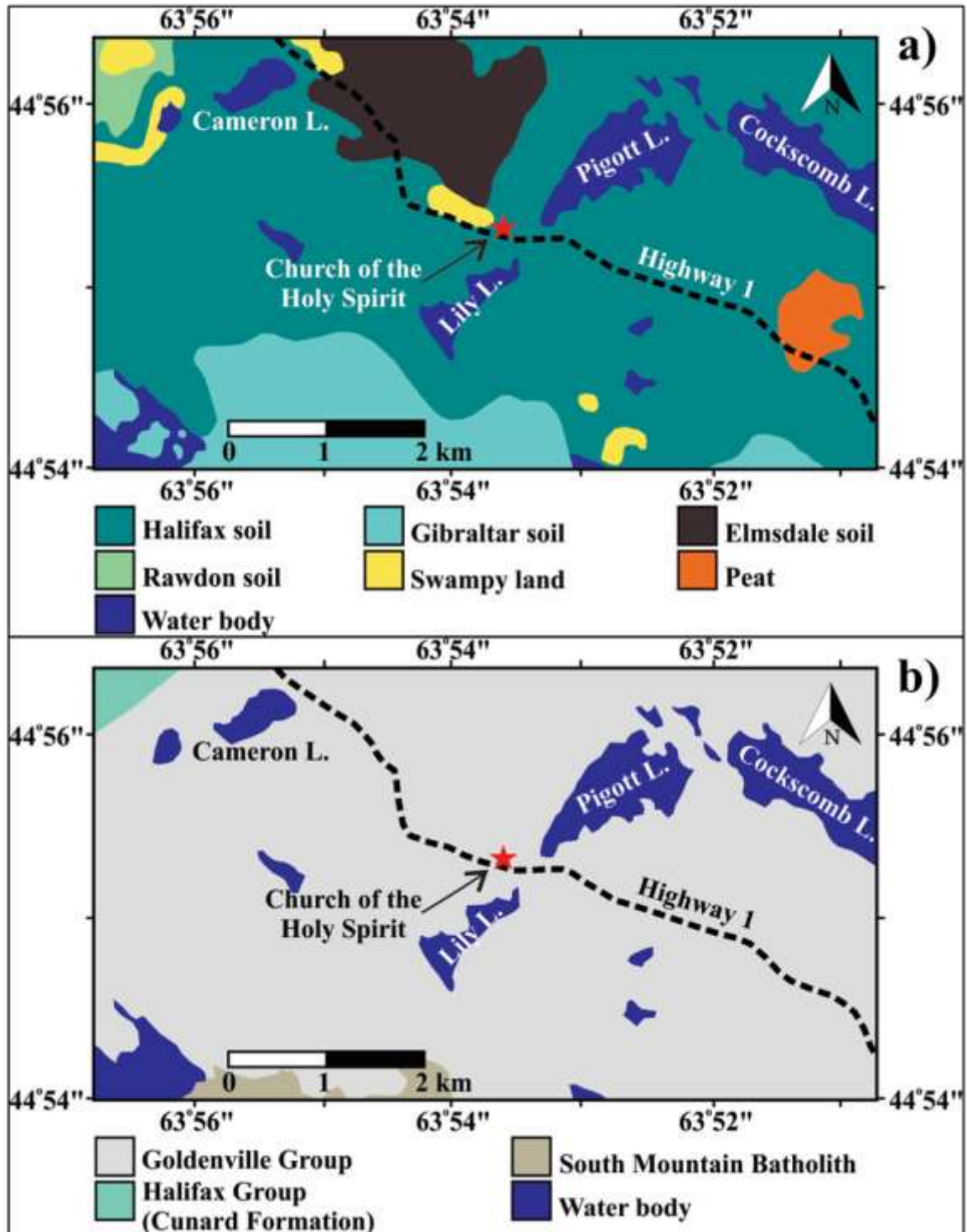


Figure 4.4: Soil profile and bedrock geology maps of the study area. (a) Close-up view of the soil profile map of Nova Scotia showing the study area with a red star. The soil in the study area is represented by the dark green colour and is the Halifax soil series (modified from Cann et al. 1954). (b) Close-up view of the geological map of Nova Scotia showing the study area with a red star. The study area lies on Goldenville Group rocks (COG), with some South Mountain Batholith (Dgd) lying to the south (modified from Keppie 2000).

The texture throughout the profiles is usually a sandy loam. The soils are typically unsuitable for agriculture due to excessive stoniness and discontinuous distribution of well-drained soils (some areas with poorly drained depression). The porous nature of the soil makes it well suited to the forest environment (Cann et al. 1954). The poor drainage of water from the cemetery was of concern as high water content could attenuate the GPR signal (Fiedler et al. 2009), however imaging was still able to be carried out. A summary of the soil profile is tabulated in Table 4.2.

Table 4.2: Summary of the soil profile at the study area (Cann et al. 1954).

Soil Series	Symbol	Description	Parent Material	Topo.	Drainage
Halifax	Hx-P	Light brown sandy loam over yellowish brown sandy loam; fairly stony	Greyish brown sandy loam till derived from hard sandstone, slate, and quartzite	Rolling to hilly	Good, with numerous poorly-drained depressions; stony/boulders

4.5.2 *Bedrock Geology*

The study area lies on top of Goldenville Group bedrock, which is comprised of massive grey to greenish-grey quartzose sandstones, generally poorly sorted, with chlorite-rich matrix, interbedded with generally subordinate grey to black slate (Figure 4.4b). The rocks have been regionally metamorphosed to greenschist and, locally, amphibolite facies. Gold-bearing quartz veins occur at many localities. The sandstones are believed to have been deposited by turbidity currents and related processes. The Goldenville Group is part of the encompassing Meguma Supergroup, which also includes the Halifax Group, which is dominated by slates and sheared siltstones with minor sandstones. The Goldenville Group is lower and overlain by the Halifax Group. From soil probe testing in the cemetery,

it appears the bedrock is rather shallow on the north side of the church (which is outside of the GPR survey area) and forms a dome-like structure (Figure 4.2) that is 18 m wide by 23 m, oriented parallel to Highway # 1 and extending beneath the church (Risk 2020).

4.6 Equipment and software

4.6.1 Ground-Penetrating Radar

A Sensors and Software Incorporated pulseEKKO™ Pro SmartCart GPR system (Figure 4.5) was used to map the subsurface of the cemetery and identify any radar facies that appeared abnormal, indicating remains or other foreign objects. It is owned and operated by the Dalhousie University Basin and Reservoir Laboratory. This highly durable, self-contained system has 4-wheels to allow for the rapid and continuous collection of data. The system includes a GPS rover receiver (not used for this study), a transmitting and receiving antennae, a digital video logging screen, and a power unit for the screen and antennae. A built-in odometer serves as the triggering method for the survey.

The transmitting and receiving antennae were oriented parallel to each other and perpendicular to the line direction. The 200 MHz antennae with a separation of 0.5 m was used for all lines. This frequency was chosen because the specifications suggested a depth of penetration and resolution sufficient for subsurface cemetery imaging. These results are corroborated by Schultz et al. (Schultz et al. 2012) and Aziz et al. (Aziz et al. 2016) in their investigations. The 200 MHz antennae have a length of 0.5 m and a step size of 0.1 m. The time window is 100 ns and there are 250 points per trace. The sampling interval is 400 picoseconds (ps), and the transmitter pulsar voltage is 1,000 volts. The imaging of the cemetery was captured to a depth of approximately 90 ns two-way travel time (TWT),

corresponding to a depth of approximately 4.5 m. Based on the soil types present in this area, the dielectric permittivity (K) is between 20 (wet sandy soil) and 30 (sandy loam soil).

Prior to onsite data collection, the Sensors and Software Incorporated pulseEKKO™ Pro SmartCart's odometer-trigger was calibrated. Calibration was completed using the following steps: 1) laying a 10 m long measuring tape along a flat surface, 2) selecting the 10 m length odometer calibration option on the GPR system, and 3) walking the SmartCart from the 0 m mark to the 10 m mark. This ensured that electromagnetic pulses would be emitted every 10 cm during data collection and that the length of each collected line was captured in its associated metadata. Prior to collection of each GPR line, the GPS location and the compass orientation of the line were measured. Each collected GPR line had a length, a GPS starting location, and an orientation, all of which could be used to georeference each GPR line. No topographic corrections were included in this project. However, due to the generally flat surface and relatively small survey area, there is minimal topographic variation to be corrected for.

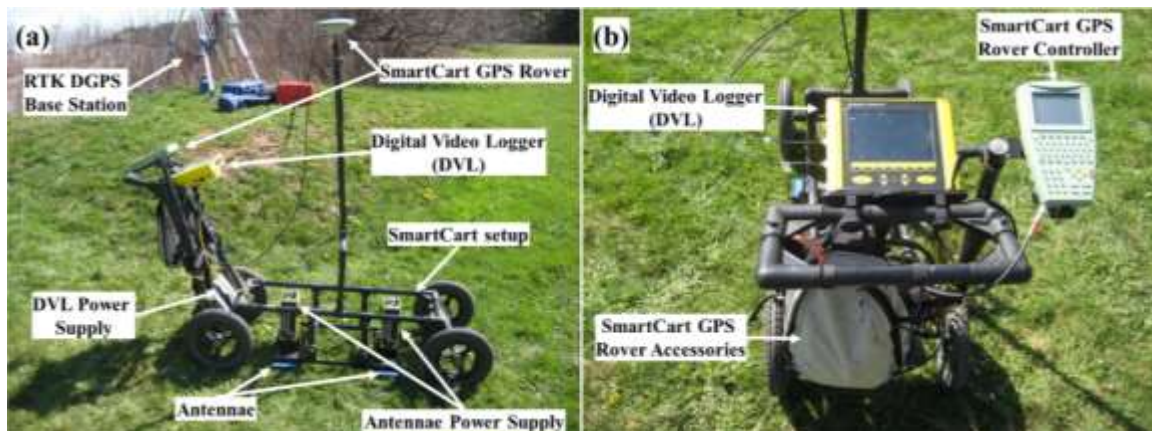


Figure 4.5: A typical GPR cart setup consists of many separate components (Kelly et al. 2021a). (a) The SmartCart setup with the relevant components labelled. (b) The operators view of the SmartCart with various labelled components. For this study, the GPS equipment was not utilized.

4.6.2 *EKKO_Project™ GPR Software*

Once the GPR data has been collected in the field, specialized GPR software is used to organize, view, edit, process and plot the GPR data (Sensors and Software Inc. 2018a). The GPR software utilized for this study was EKKO_Project™, which is produced by Sensors and Software Incorporated and consists of a basic program with optional, add-on modules (Sensors and Software Inc. 2018a). The software stores the data as .gpz files, which are automatically exported from the GPR data collection equipment and they allow additional files, such as GPS, topography, photos, notes, etc. to also be stored in the .gpz file as well (Sensors and Software Inc. 2018a).

4.6.3 *Petrel™ E & P Software*

Petrel™ is a software platform developed by Schlumberger primarily for use in the exploration (e.g., seismic) and production (e.g., monitoring surveillance) sectors of the petroleum industry (Schlumberger 2014). Within this software, a user can perform a variety of tasks, including but not limited to interpreting seismic data, performing well correlation, building reservoir models, visualizing reservoir simulation results, calculating volumes, producing maps and designing development strategies for the maximization of reservoir exploitation (Schlumberger 2014). For this study, the finite-element modelling that can be performed in the Petrel™ software was used to build a 3D model displaying precise and pertinent data, offering a better understanding of the subsurface.

4.7 Fieldwork and Survey Area

Fieldwork was conducted on July 30th, 2019. The survey area consisted of the 30 m by 40 m (1,200 m²) southern section of the cemetery, which surrounds the church. The area immediately north of the church is relatively flat, while the area to the east and south are slightly sloped away from the church towards Highway # 1. This localized survey was conducted on a grass surface and resulted in a total of 40 separate radargrams (total distance of 1,352.5 m); 25 oriented north-south and 15 oriented east-west (Figure 4.6). Line spacing was approximately 1 m and was adjusted for headstone locations and other surficial features that had to be avoided.

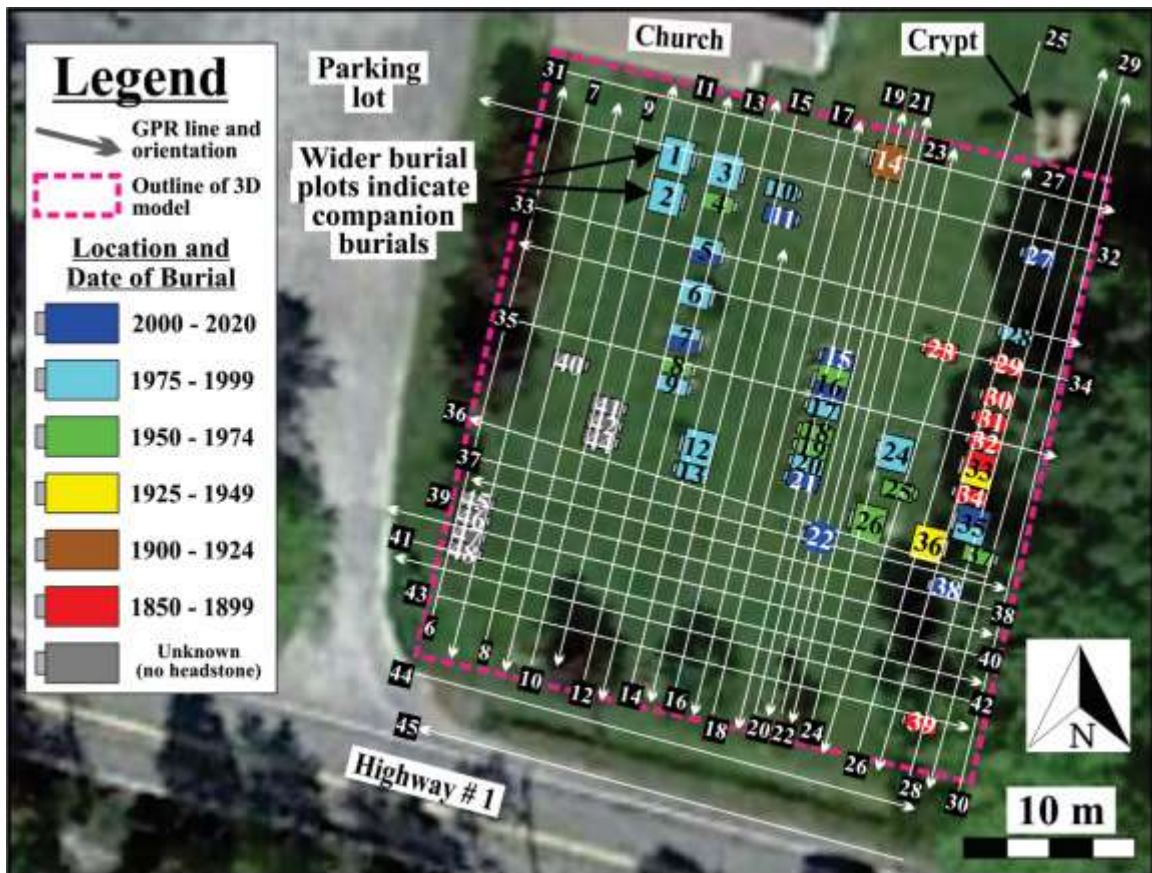


Figure 4.6: Close-up view of the study location, indicating grave site locations and ages, location, and number of each GPR line, and outline of the model (Google 2020). GPR lines 6 to 30 are oriented N-S, while lines 31 to 45 are oriented E-W.

4.8 Data Processing

Processing of the GPR data was completed using EKKO_Project™ software from Sensors and Software. GPR radargrams were geo-referenced. Standard filters and gains (dewow, average background subtraction, and amplitude gains) were applied to the GPR radargrams to remove signal noise, and best display the data. The processing of the GPR data typically follows three main phases, as outlined by Szymczyk and Szymczyk (2013) and includes; 1) the determination of an appropriate processing workflow, 2) the determination of the appropriate parameters and inputs for each step of the workflow, and 3) a review of the output for each processing step and the correction of any issues as a result of improper input parameters. For this study, the application of the dewow filter, the spreading and exponential calibrated compensation (SEC2) gain, and the background subtraction filter produced the clearest subsurface images.

The dewow time filter was first applied to each radargram to remove of the initial DC component and low-frequency, slowly decaying ‘wow’, while preserving the high frequency signal (Sensors and Software Inc. 2018b). These can be produced by several factors, but are primarily the result of early wave arrivals, dynamic range limitations on instrumentation, and/or inductive coupling effects (Sensors and Software Inc. 2018b).

The SEC2 gain was used to counteract the spherical spreading losses and the exponential ohmic energy dissipation in the GPR lines (Sensors and Software Inc. 2018b). The input parameters necessary for this gain are an attenuation value for the substrate (ground), a beginning value to be added to the exponential gain function and a maximum value for the gain (Sensors and Software Inc. 2018b). The average time-amplitude graph for each trace was examined both before and after the application of the gain to ensure it

was appropriately employed as explained by Annan (2009). Each line had unique attenuation, start and maximum values. The values for attenuation ranged between 1.54 and 3.80 dB/m with a mean of 2.13 dB/m. The start gain values ranged from 0.53 to 1.04 with an average of 0.73. The maximum gain values used varied from 24.00 to 67.00 with a mean of 38.85.

The background subtraction filter applies a moving average background subtraction to the data set, which has the effect of enhancing dipping events, such as hyperbolas from point sources like coffins (Sensors and Software Inc. 2018b). The two parameters associated with this filter are the filter width (the width of the moving-average window added in the spatial trace-differencing filter) and the type (the shape of the filter used to calculate the moving-average trace) (Sensors and Software Inc. 2018b). For this study, a filter width equal to the length of each line was used and a rectangular type was applied.

4.9 Model Building and Results

The completion of the GPR survey resulted in 40 unique radargrams, with 25 oriented approximately north-south and 15 oriented approximately east-west. The accurate records kept by the church, along with the headstones allow for a definitive correlation between the hyperbolic features observed in the radargrams and locations of burial sites. The processed radargrams were exported from EKKO_Project™ into Petrel™ and interpolated to make 2D depth slices of the subsurface every 10 cm for a total of 4 m (Figure 4.7), which were displayed with reflectivity amplitude (absolute) strength. The interpolation method in Petrel™ involved importing the 2D GPR cross-sections (as shown in Figure 4.6) and linearly interpolating data into the gaps between adjacent GPR lines to create a solid 3D volume. This method is common for displaying and understanding the 3D shape and spatial

relationship of buried objects. It is the high-resolution processed data that allows for casket identification, particularly in the case of stacked caskets with human remains.

In the GPR literature, 3D models are typically displayed in one or a combination of four different ways (summarized in Figure 4.8); 1) the 3D model is sliced into a single plane (e.g., Leucci and Negri 2006), leading to difficulties when trying to interpret the 3D shape and spatial relationship of subsurface objects (Figure 4.8a), 2) the 3D model is sliced in each of the three model planes (x, y, and z) (e.g., Giannopoulos 2005), which again, only provides a partial understanding of the 3D shape and spatial relationship of subsurface objects (Figure 4.8b), 3) a partial transparency filter (e.g., Kadioglu and Daniels 2008) is applied to the low amplitude reflection signals in the 3D model, which makes depth relationships between buried objects very difficult (Figure 4.8c), and 4) a complete transparency filter (e.g., Kadioglu and Ulugergerli 2012; Kadioglu 2013) is applied on the low amplitude reflection signals, which also makes depth relationships between buried objects difficult (Figure 4.8d).

Using Petrel™ software, depth slices (Figure 4.7) were generated and a 3D model was created (Figure 4.8 and Figure 4.9). High-amplitude signals are visible where known graves occur, and in various other locations. Figure 4.9 displays the range in both depth and strength of the higher amplitude signals as well. Where unidentified and unmarked burial sites (indicated by grey rectangles in Figure 4.6) occur in the west and southwest regions of the cemetery, high reflection amplitudes are produced.

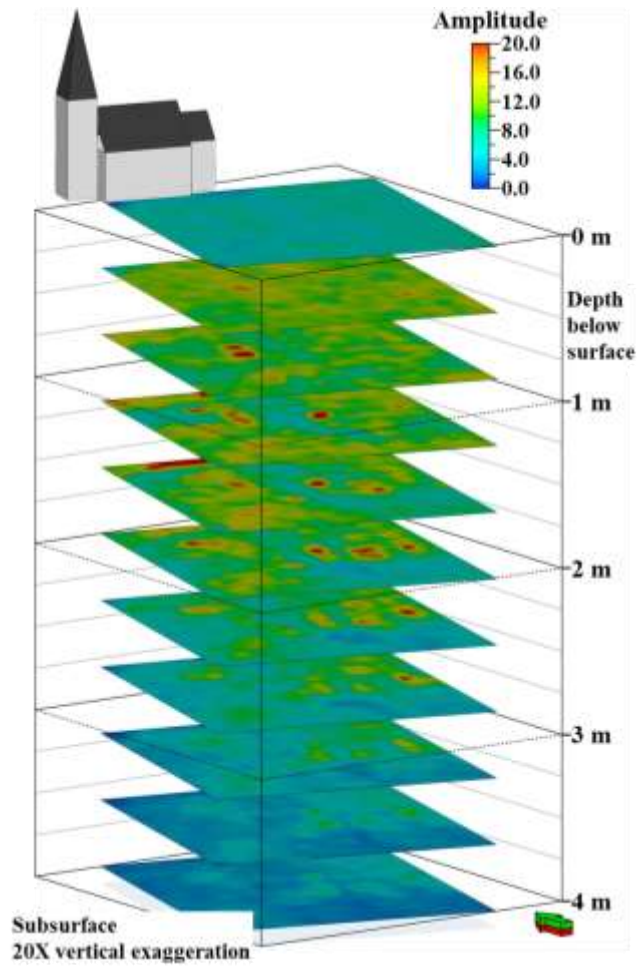


Figure 4.7: A series of 2D depth slices showing reflectivity amplitude (absolute) strength to a depth of 4 m. This is a typical method used for displaying and attempting to understand the 3D shape and spatial relationship of buried objects. Please note - the subsurface is 20X vertical exaggeration.

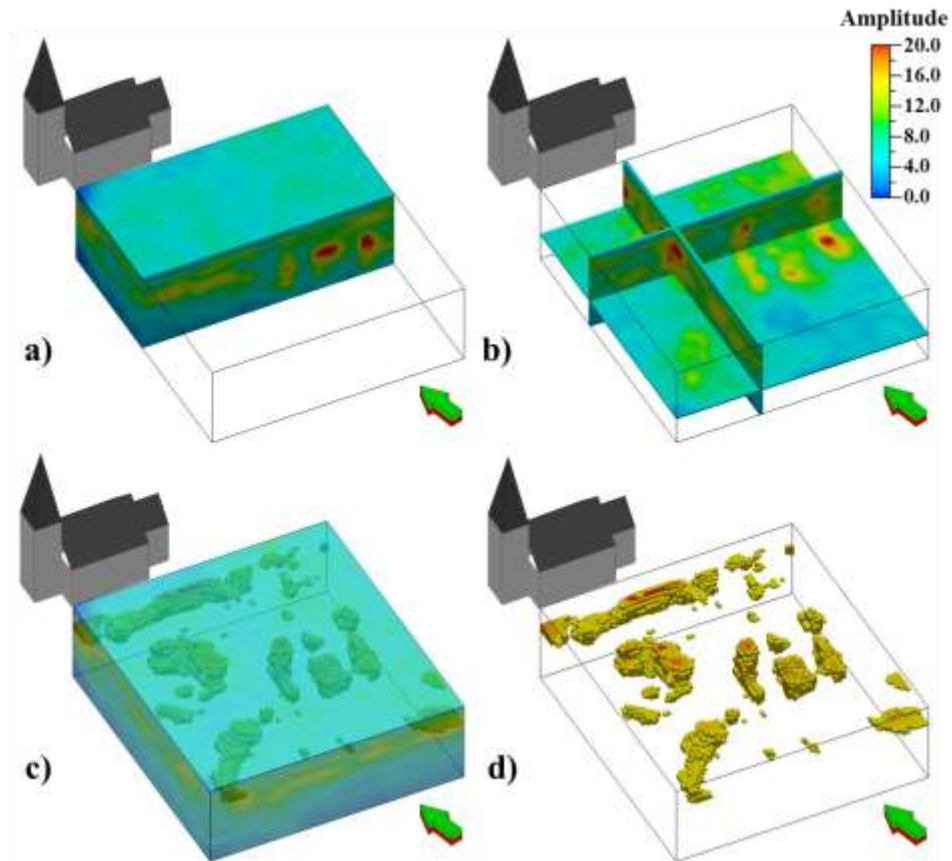


Figure 4.8: Various ways previous 3D models have been displayed in the GPR literature and the issues with each type of display. (a) Slicing the 3D model in a single plane does not resolve the 3D shape or spatial relationship of subsurface objects. (b) Slicing the 3D model in each of the three model planes (x, y, and z) only provides a partial understanding of shape and spatial relationships of subsurface objects. (c) Using a partial transparency filter on the low amplitude reflection signals makes it difficult to understand the depth of objects relative to one another. (d) Using a complete transparency filter on the low amplitude reflection signals also causes difficulties in understanding the depth of objects relative to one another.

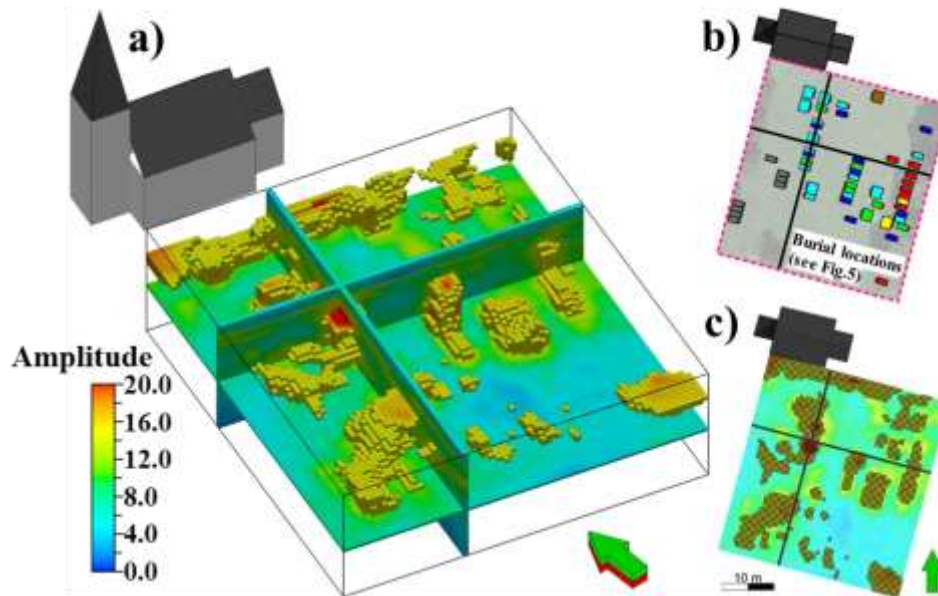


Figure 4.9: A 3D render of the model created from the GPR data. (a) Here we combine the 3D display techniques of Figure 4.8b and d. By using a transparency filter to remove the lowest amplitude reflection signal, the high amplitude reflections remain, which are displayed as the 3D blocks. These show the shape and size of the subsurface buried objects. By adding the 2D cross-sections and depth slice, we can better understand the spatial relationships between each of the objects. (b) A top-down view of the cross-sections relative to the location of the burial sites. (c) A top-down view of the cross-sections and depth slice. Several high amplitude reflections are present in the southwest most part of the model. These are likely the site of unmarked (and significantly older) burials. There are also no high amplitude reflection signals from burial sites 35 to 38, suggesting that no casket is present.

Depth slices and cross sections from the 3D model of the cemetery are displayed based on amplitude reflectivity (Figure 4.10). The high amplitude shades of red and yellow are indicative of buried objects. It was determined that a combination of Figure 4.8b and d provided the most comprehensive 3D render of the model collected from the study area (Figure 4.9). Using a transparency filter to remove the low amplitude reflection signal component, the high amplitude reflections remain, which are displayed as the 3D blocks (Figure 4.9). These show the shape and size of the buried objects. With the addition of the 2D cross-sections and depth slice, the interpretations between spatial relationships and objects can be improved.

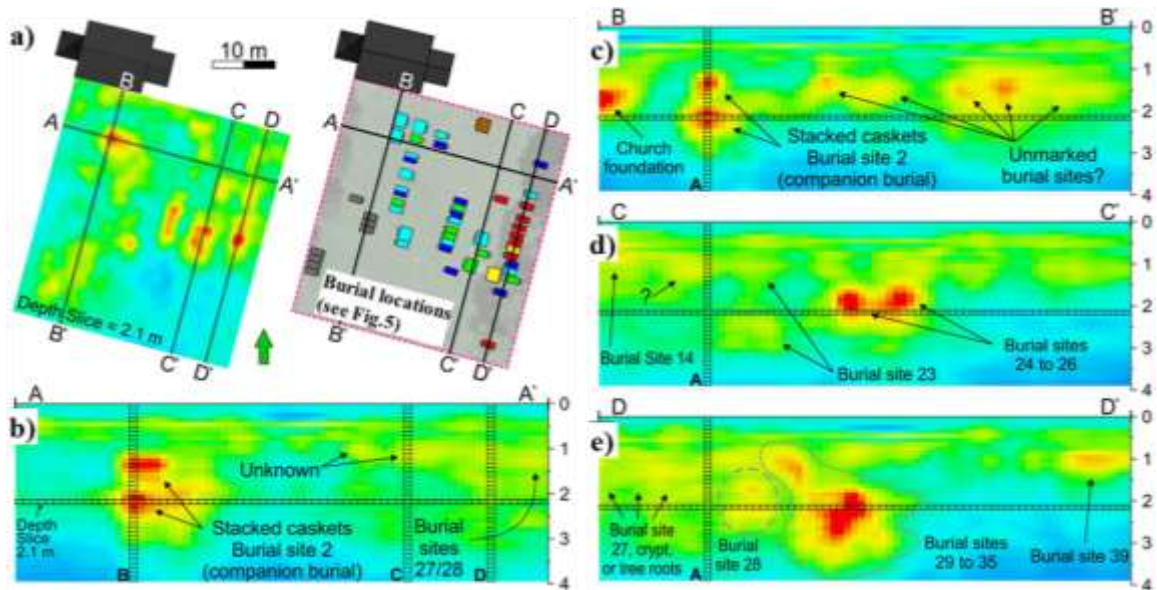


Figure 4.10: Depth slices and cross sections from the 3D model. (a) (left) A horizontal depth slice at 2.1 m depth and the location of 4 cross sections from the 3D model. Red and yellow colours are indicative of potential buried objects. (right) A surface overview of the model showing the location of graves relative to the 4 cross sections from the model. (b) Cross section A to A' - An east-west oriented cross section. The horizontal and vertical lines comprised of black outlined rectangles are the location of the depth slice and other cross section lines. In this cross section we can see stacked caskets (burial site 2) shown by the vertically stacked red amplitude signals. To the right of this we have a series of lower yellow amplitude signals, indicating the possibility of a buried object or a buried object adjacent but outside of this plane. (c) Cross section B to B' - The high amplitude signal to the left of this image is likely due to the rock/cement foundation of the church. The stacked red amplitude signals show the stacked caskets from burial site 2. A series of strong yellow to moderate red coloured reflections to the right are the location of the unmarked burial sites. These reflections appear to be between 1 to 2 m depth, like many of the other burial sites in this cemetery. (d) Cross section C to C'. The weak red to strong yellow colours apparent on the left side of the image are amplitude reflections caused by caskets adjacent to but outside of the cross-section plane. The distinct red coloured amplitude reflections in the middle of the cross-section clearly display the adjacent burial sites from burial sites 24 to 26. (e) Cross-section D to D'. The weak red to strong yellow colours on the left side of the image are caused by burial sites 27, the adjacent crypt, or possibly tree roots from adjacent trees lining the eastern most part of the cemetery. The center of this image shows a large red-yellow amplitude reflection that encompasses many of the burial sites from 28 to 35. These are the oldest burial sites from this cemetery, and less is known about the standard and specifications on how these bodies were buried. It is possible that through decay and decomposition that the once separate and distinct gravesites have now become indistinguishable from one another. To the far right we can see reflection amplitudes from burial site 39.

By integrating both the radargrams, collected from the GPR and the 3D model, it is possible to reach an intuitive understanding of the subsurface. A comparison between an unprocessed radargram, processed radargram, and a cross section through the 3D model at the approximate location of the radargram is shown in Figure 4.11 to Figure 4.16. Examples of north-south oriented lines are shown in Figure 4.11, Figure 4.12, and Figure 4.13.

Examples of east-west oriented lines are shown in Figure 4.14, Figure 4.15, and Figure 4.16.

Figure 4.11 displays an unprocessed radargram (top) and processed radargram (middle) of GPR line 13, as well as a cross section (bottom) through the 3D model at the approximate location of GPR line 13. The line starts near the corner of the church and ends near some trees and the ditch to the south of the property. The line traverses over burials 3 to 9 and is near burials 12 and 13. The unprocessed radargram of line 13 displays noticeable hyperbolic tops at positions ~ 9 m and ~ 14 m. Fainter hyperbolic features occurring along the entire line length but dissipate at approximately 2.5 m depth.

The processed radargram of line 13 (Figure 4.11) shows the two hyperbolic features at ~ 9 m and ~ 14 m more clearly, which correspond to the locations of burials 3 to 9. Additionally, the hyperbolic features are clearer across the entire length of the line and are also visible to ~ 4 m depth.

A cross-section through the 3D model at the approximate location of line 13 (Figure 4.11) portrays three zones of moderate-to-high amplitude. The high amplitude area at the start of the line (position 0 m to ~ 2 m) suggests a response from the line beginning very close to the church. The high amplitude region between positions ~ 5 m to ~ 16 m correlates with the locations of burials 3 to 9. The high amplitude zone between positions ~ 22 m and ~ 26 m is weaker and smaller in size but corresponds to the locations of burials 12 and 13. In the area of burials 3 to 9, there are well-defined hyperbolas visible in the radargram.

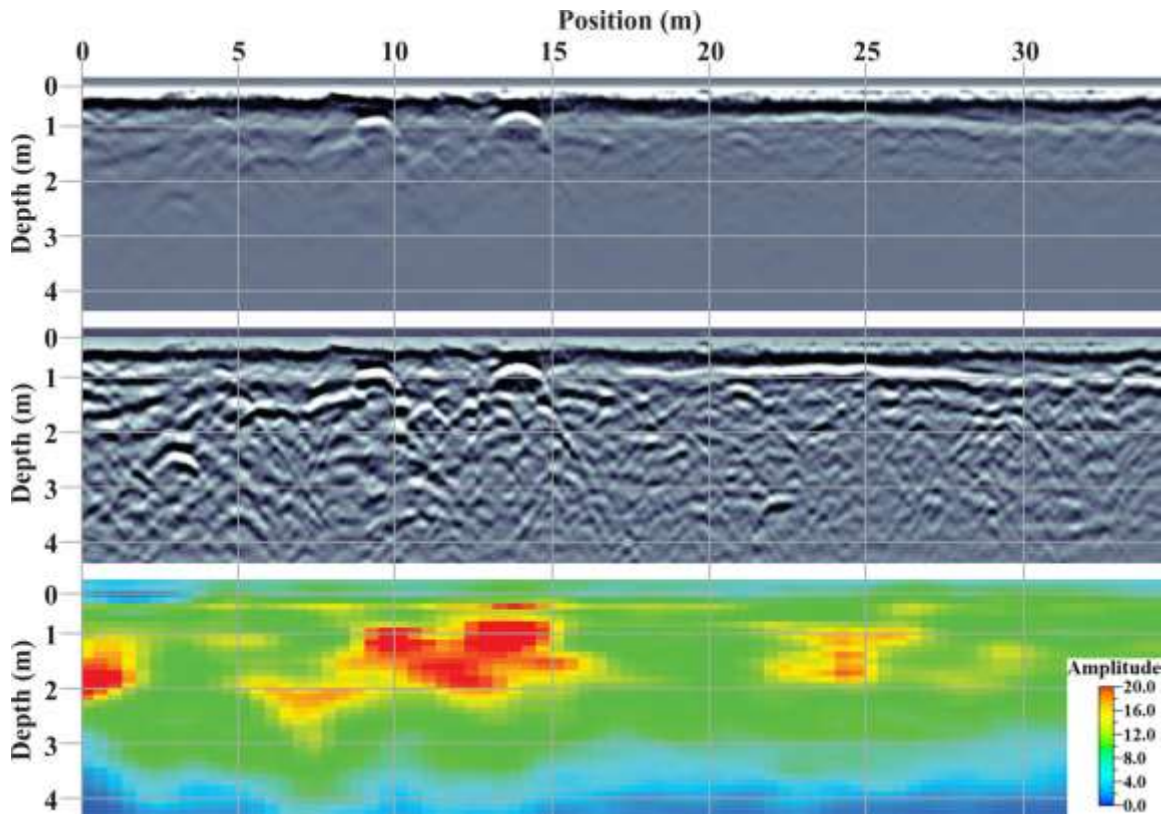


Figure 4.11: An example showing results from the north to south oriented line 13. (Top) The unprocessed radargram of line 13 showing pronounced hyperbolic tops at ~ 9 m and ~ 14 m. (Middle) The processed radargram of line 13 showing clearer and more abundant hyperbolas between position ~ 4 m and ~ 16 m, which corresponds to the locations of burials 3 to 9. (Bottom) A cross-section through the 3D model at the approximate location of line 13. Three zones of high amplitude are visible within this cross-section. The high amplitude area at the start of the line (position 0 m to ~ 2 m) suggests the response is the result of beginning the line very close to the church. The high amplitude area from ~ 5 m to ~ 16 m corresponds to the locations of burials 3 to 9. The high amplitude zone between ~ 22 m and ~ 26 m is weaker and smaller in size, but most likely corresponds to burials 12 and 13.

Figure 4.12 shows an unprocessed radargram (top) and processed radargram (middle) of GPR line 19, as well as a cross section (bottom) through the 3D model at the approximate location of GPR line 19. Line 19 starts in the north close to burial 14 and ends in the south near the vicinity of some trees and the ditch at the edge of the property. The unprocessed radargram of line 19 shows hyperbolic reflectors throughout the length of the line, with more noticeable clusters occurring between positions ~ 2 m and ~ 4 m and again between ~ 15 m and ~ 22 m. The reflectors generally dissipate below 3 m depth.

The processed radargram of line 19 shows the hyperbolic reflectors more clearly to a depth of ~ 4 m and occurring the entire length of the line. Hyperbolic reflectors are clear and more abundant between positions ~ 2 m and ~ 4 m and again between ~ 15 m and ~ 22 m. These positions correspond to the location of burial 14 and the locations of burials 15 to 21, respectively. Between positions ~ 32 m and ~ 35 m there are smaller, less pronounced hyperbolas perhaps from being close to vegetation (roots).

A cross-section through the 3D model at the approximate location of line 19 suggests three distinct zones of high amplitude. The high amplitude area near the start of the line (position ~ 2 m to ~ 4 m) suggests the response is from burial 14. The high amplitude area from ~ 14 m to ~ 21 m corresponds to the locations of burials 15 to 21. The moderate amplitude zone between ~ 30 m and ~ 35 m is weaker in size, but the location near the end of the line suggests vegetation (roots) may have contributed to the response.

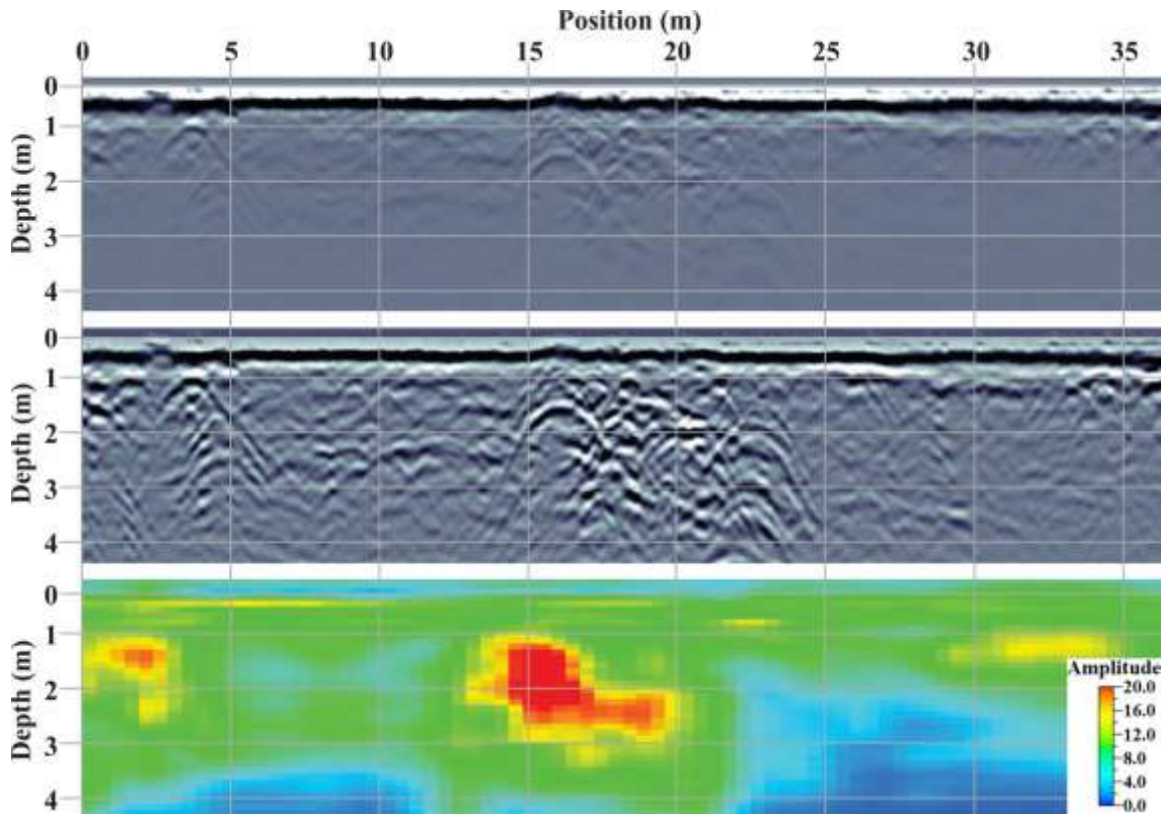


Figure 4.12: An example showing results from the north to south oriented line 19. (Top) The unprocessed radargram of line 19 showing hyperbolic reflectors between ~ 2 m and ~ 4 m and again between ~ 15 m and ~ 22 m. (Middle) The processed radargram of line 19 showing clearer and more abundant hyperbolas between ~ 2 m and ~ 4 m and again between ~ 15 m and ~ 22 m. These correspond to the location of burial 14 and the locations of burials 15 to 21, respectively. Between position ~ 32 m and ~ 35 m there are smaller, less pronounced hyperbolas perhaps from the line being close to vegetation (roots). (Bottom) A cross-section through the 3D model at the approximate location of line 19. Three zones of high amplitude are visible within this cross-section. The high amplitude area at the start of the line (position ~ 2 m to ~ 4 m) suggests the response is the result of burial 14. The high amplitude area from ~ 14 m to ~ 21 m corresponds to the locations of burials 15 to 21. The moderate amplitude zone between ~ 30 m and ~ 35 m is weaker in size, but the location near the end of the line suggests the result is from vegetation (roots) that was nearby.

Figure 4.13 presents an unprocessed radargram (top) and processed radargram (middle) of GPR line 27, as well as a cross section (bottom) through the 3D model at the approximate location of GPR line 27. Line 27, which runs from north to south, starts near the crypt and crosses burial 27, burials 28 to 38. It almost traverses over burial 39 as well. The line is also located near the tree line along the eastern edge of the property. The unprocessed radargram of line 27 shows very faint indications of hyperbolic reflectors along the entire length, but these dissipate at a depth of approximately 3 m. The processed

radargram of line 27 displays a clearer picture of hyperbolas throughout the length of the line, but these are not as pronounced as line 13 or line 19, for example. This radargram is more chaotic looking with abundant, different sized reflectors and lots of overlapping.

A cross-section through the 3D model at the approximate location of line 27 suggests two regions of interest. There is a moderate to high amplitude region from ~ 0 m to ~ 18 m, which corresponds well with the locations of burials 27 to 38. Perhaps the moderate amplitude regions are related to leachate plumes emanating from the burial. Another moderately high amplitude region occurs between ~ 30 m and ~ 35 m, which potentially corresponds to the location of burial 39 near the end of the line.

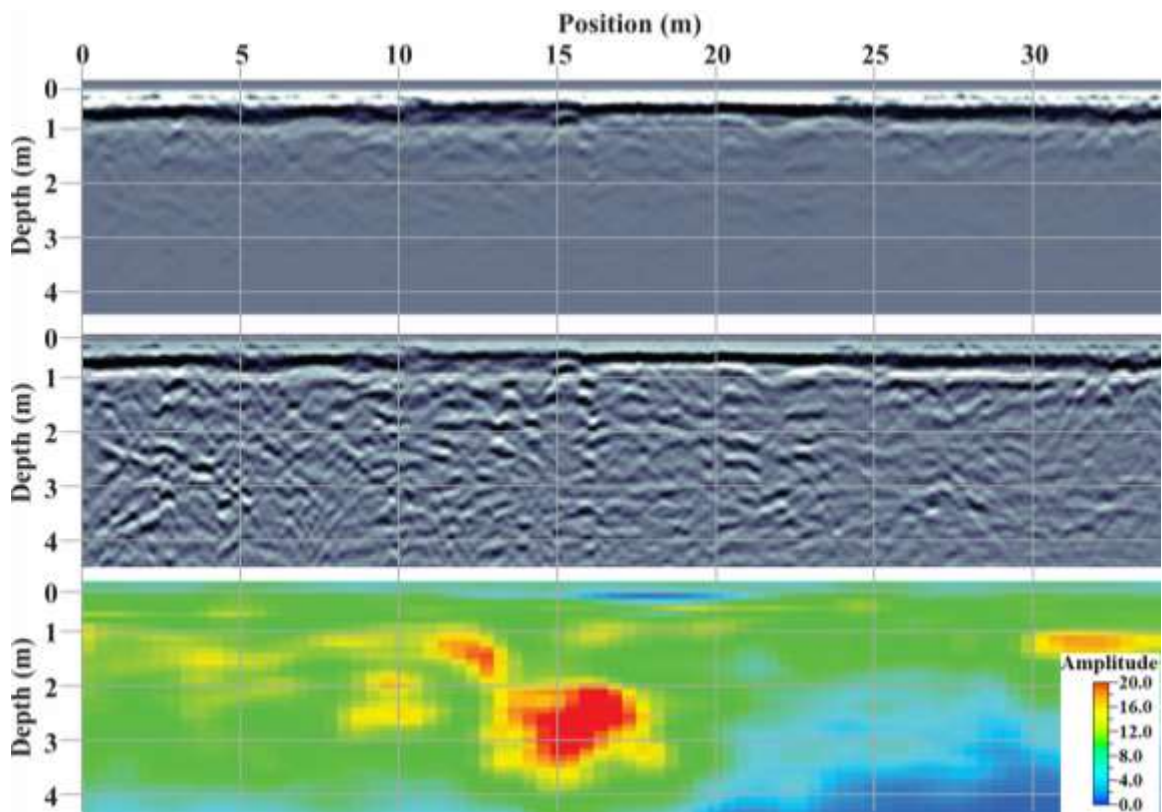


Figure 4.13: An example showing results from the north to south oriented line 27. (Top) The unprocessed radargram of line 27 showing faint indications of hyperbolic reflectors along the entire length. (Middle) The processed radargram of line 27 showing hyperbolas present throughout, but not as pronounced line 13 or line 19, for example. This radargram is chaotic looking with abundant, different sized reflectors overlapping. (Bottom) A cross-section through the 3D model at the approximate location of line 27. There is a moderate to high amplitude region from ~ 0 m to ~ 18 m, which corresponds well with the locations of burials 27 to 38. Another moderately high amplitude region occurs between ~ 30 m and ~ 35 m, which potentially corresponds to the location of burial 39 near the end of the line.

Figure 4.14 displays an unprocessed radargram (top) and processed radargram (middle) of GPR line 32, as well as a cross section (bottom) through the 3D model at the approximate location of GPR line 32. Line 32 starts near the edge of the tree line in the east and ends near edge of the parking lot to the west. It crosses or comes very near burials 1, 3, 10, and 27. The unprocessed radargram of line 32 reveals hyperbolic reflectors throughout the entire length of the line but dissipating below 3 m depth.

The processed radargram of line 32 displays the hyperbolic reflectors more clearly, with what appears to be three regions of interest. These regions are between ~ 0 m and ~ 10 m, ~ 17 m to ~ 24 m, and ~ 26 m to ~ 35 m. These regions could correspond with burials 1, 3, 10, 14, and 27. A cross-section through the 3D model at the approximate location of line 32 suggests 4 regions of high amplitude, with additional moderate amplitude areas. The region between position ~ 0 m and ~ 2.5 m is well into the tree line and could correlate to some unknown buried object (e.g., rock or metal object). It is possible it may also be an unmarked burial site. The region between ~ 4 m and ~ 7.5 m correlate nicely with the location of burial 27.

A cross-section through the 3D model shows a moderate amplitude region/pinch-out between ~ 7.5 m and ~ 10 m. This pinch-out may suggest the presence of a leachate plume emanating from this burial location. The region between ~ 14 m and ~ 24 m correlates with the locations of burials 10, 3, and 1. The moderate amplitude region between ~ 25 m and ~ 31 m occurs in the treed area near the edge of the cemetery/parking lot. This is likely due to the presence of vegetation (e.g., trees and associated root systems). The high amplitude regions at ~ 5 m and ~ 15 m have moderate amplitude tails, perhaps suggesting the presence of leachate plumes emanating from the burials.

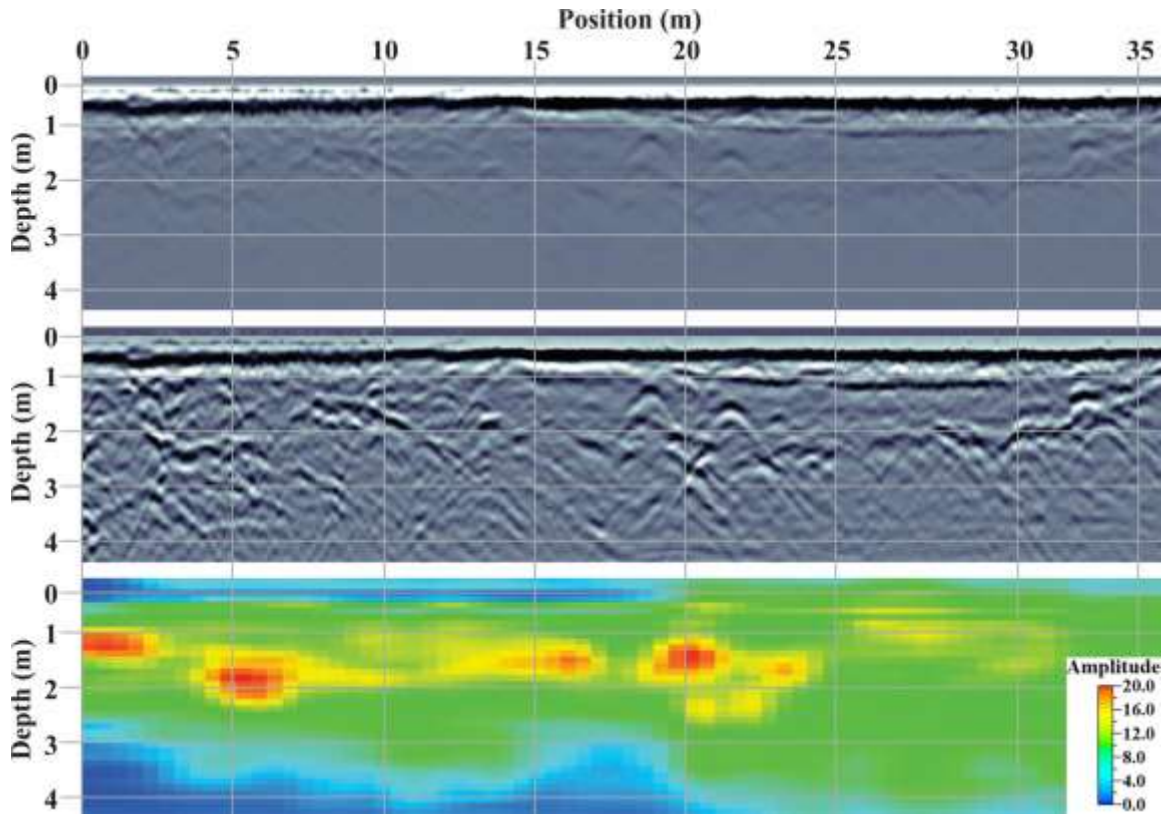


Figure 4.14: An example showing results from the east to west oriented line 32. (Top) The unprocessed radargram of line 32 showing faint indications of hyperbolic reflectors along the entire length. (Middle) The processed radargram of line 32 showing clearer and more abundant hyperbolas between ~ 0 m and ~ 10 m, ~ 17 m to ~ 24 m, and ~ 26 m to ~ 35 m. These regions could correspond with burials 1, 3, 10, 14, and 27. (Bottom) A cross-section through the 3D model at the approximate location of line 32. Four regions of high-to-moderate amplitude, and one moderate amplitude area is visible within this cross-section. The region between position ~ 0 m and ~ 2.5 m could correlate to some unknown buried object (e.g., rock or metal object) or it may be an unmarked burial site. The region between ~ 4 m and ~ 7.5 m correlate nicely with the location of burial 27. The moderate amplitude region/tail between ~ 7.5 m and ~ 10 m may show the presence of a leachate plume. The region between ~ 14 m and ~ 24 m correlates with the locations of burials 10, 3, and 1. The moderate amplitude region between ~ 25 m and ~ 31 m occurs in the treed area near the edge of the cemetery/parking lot and is likely due to the presence of vegetation (e.g., trees and associated root systems).

Figure 4.15 displays an unprocessed radargram (top) and processed radargram (middle) of GPR line 35, as well as a cross section (bottom) through the 3D model at the approximate location of GPR line 35. Line 35 starts near the edge of the parking lot and ends near the tree line at the eastern edge of the property. It traverses across burials 8, 16, 17, and 32. The unprocessed radargram of line 35 indicates abundant yet faint hyperbolic reflectors throughout the entirety of the line, but they do dissipate below 3 m depth.

The processed radargram of line 35 portrays the hyperbolic reflectors more clearly and with greater abundance. The processed radargram suggests three regions of interest: a region at ~ 10 m, a region at ~ 17 m to ~ 20 m, and a region at ~ 28 to ~ 30 m. There are also some features that suggest horizons within the profile, particularly from position ~ 0 m to ~ 13 m at 1 m and 1.5 m depth, respectively.

A cross-section through the 3D model at the approximate location of line 35 shows the three zones of high amplitude more vividly. The high amplitude area at position ~ 9 m to ~ 12 m corresponds to the location of burial 8. The high amplitude area from ~ 17 m to ~ 21 m corresponds to the location of burials 16 and 17. The moderate amplitude zone between ~ 27 m and ~ 30 m is weaker but does correspond with the location of burial 32.

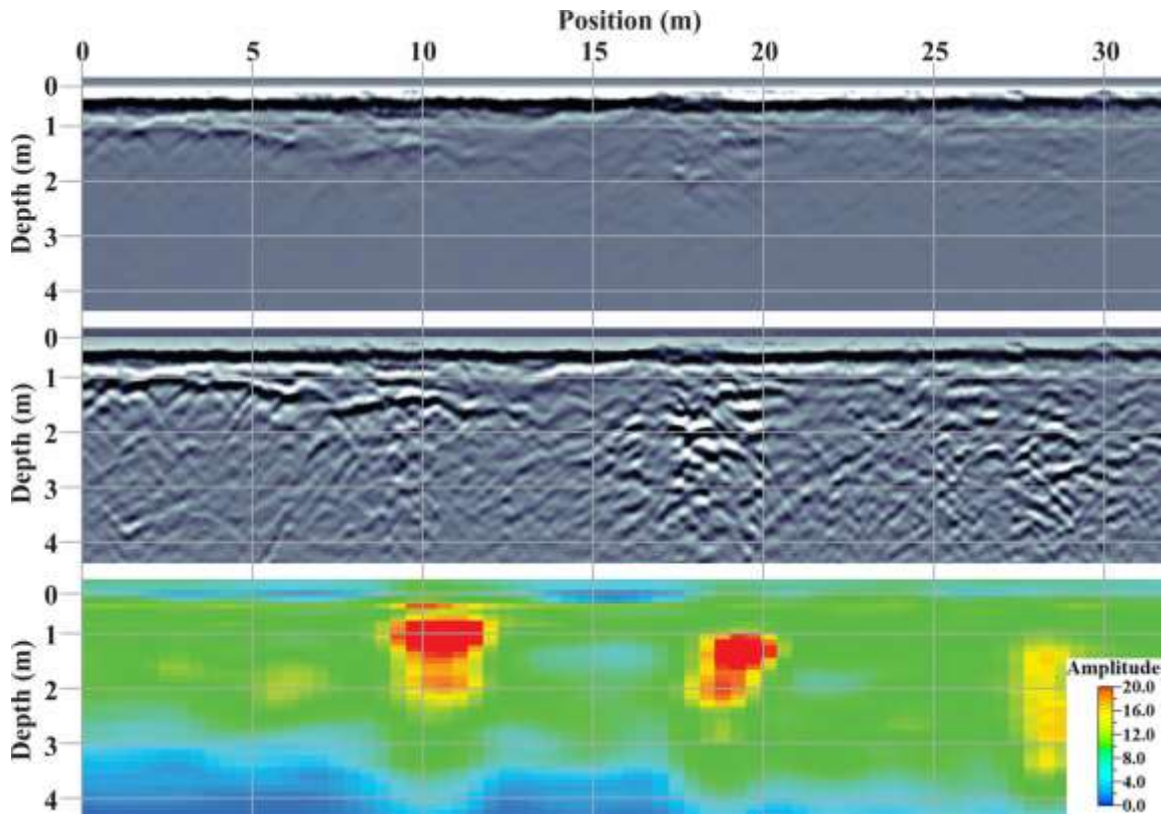


Figure 4.15: An example showing results from the west to east trending line 35. (Top) The unprocessed radargram of line 35 showing abundant faint hyperbolic reflectors. (Middle) The processed radargram of line 35 showing clearer and more abundant hyperbolas. This image suggests three regions of interest, a region at ~ 10 m, a region at ~ 17 m to ~ 20 m, and a region at ~ 28 to ~ 30 m. (Bottom) A cross-section through the 3D model at the approximate location of line 35. Three zones of high amplitude are visible within this cross-section. The high amplitude area at position ~ 9 m to ~ 12 m corresponds to the location of burial 8. The high amplitude area from ~ 17 m to ~ 21 m corresponds to the location of burials 16/17. The moderate amplitude zone between ~ 27 m and ~ 30 m is weaker but does correspond with the location of burial 32.

Figure 4.16 displays an unprocessed radargram (top) and processed radargram (middle) of GPR line 40, as well as a cross section (bottom) through the 3D model at the approximate location of GPR line 40. Line 40 starts near the edge of the tree line in the east and ends near edge of the parking lot to the west. The unprocessed radargram displays abundant faint hyperbolic reflectors across the entire length of the line, but these dissipate after 2.5 m depth.

The processed radargram of line 40 shows a clearer visual of the hyperbolas occurring along the line. This image suggests a region of interest between ~ 19 m and ~ 33

m. This corresponds to the location of burials 46 and 47, which have no surface marker present.

A cross-section through the 3D model at the approximate location of line 40 indicates a moderate to high amplitude region between ~ 22 m and ~ 29 m, corresponding to the locations of burials 46 and 47.

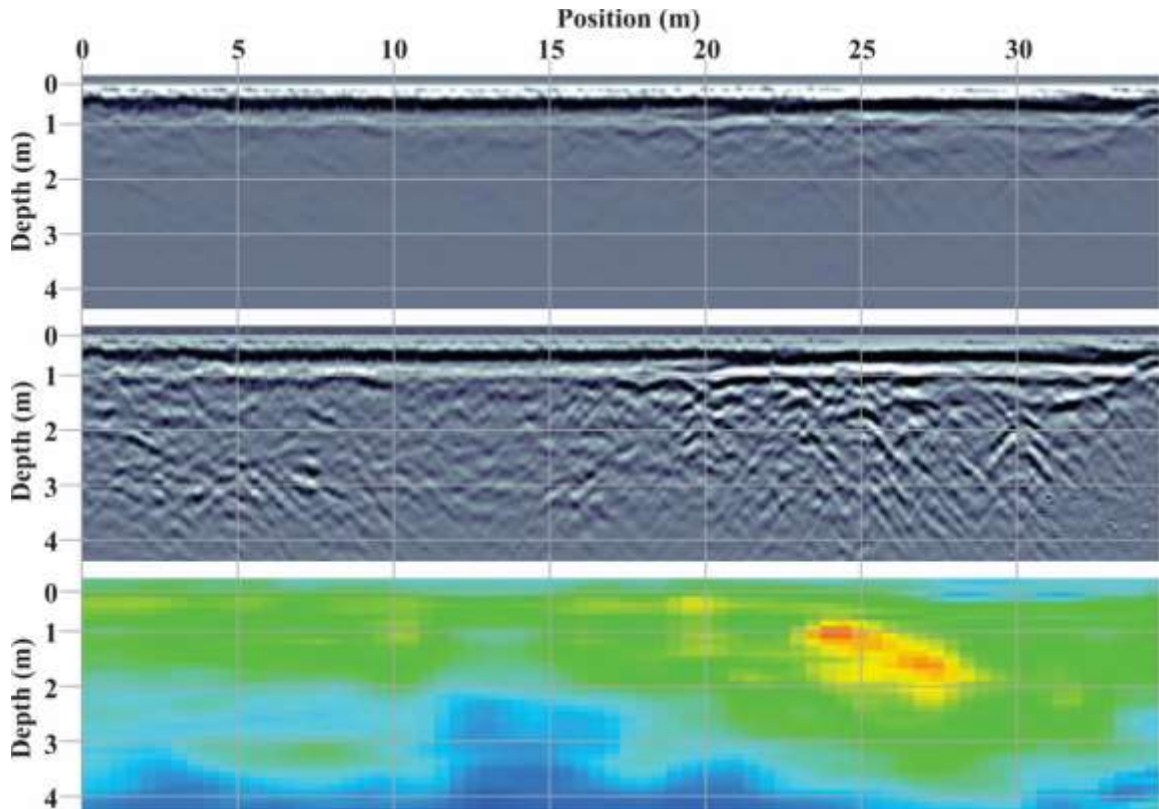


Figure 4.16: An example showing results from the east to west trending line 40. (Top) The unprocessed radargram of line 40. Abundant faint hyperbolic reflectors occur between ~ 17 m and the end of the line. (Middle) The processed radargram of line 40 showing a clearer image of the hyperbolas. This image suggests a region of interest between ~ 19 m and ~ 33 m. This corresponds to the location of burials 46 and 47, which have no surface marker present. (Bottom) A cross-section through the 3D model at the approximate location of line 40. The moderate to high amplitude region between ~ 22 m and ~ 29 m corresponds to the location of burials 46 and 47.

4.10 Discussion

Through the interpretation of processed 2D radargrams, burial sites in the cemetery are visible in the form of hyperbolic reflectors (Figure 4.11 to Figure 4.16). They can also be detected through the evaluation of individual reflection amplitude depth-slices (e.g.,

Figure 4.7). Alternatively, a 3D model provides an in-depth view of the interior architecture of the cemetery (Figure 4.8 and Figure 4.9). In this study, the areas of high amplitude (yellows and reds) data within the 3D model correlate extremely well with the locations of known burials. Through the removal of low amplitude (greens and blues) data, leaving only the relevant data (burial locations), a significantly more accurate representation of the cemetery burial layout is presented.

The unmarked known burial sites are more enigmatic (those colored grey in Figure 4.6). These are in the west-southwest region of the cemetery (sites 40 to 4 in Figure 4.6). Their locations do not correspond perfectly with high-amplitude signals, but it is possible that the locations of some burial sites in the cemetery are poorly estimated. Even if these southwestern-most unmarked burial sites were located slightly to the east, they would not fulfill the entire area containing these signals.

High-amplitude signals are visible across the whole of the southern edge of the surveyed grid, possibly corresponding to boulders or roots at the edge of the property. A recent study by Kelly et al. (2021a) shows the response that can be produced from vegetation (e.g., trees and roots). There are also high-amplitude signals at the northern border of the cemetery, which we attribute to the steel oil furnace used for heating, or the original stone foundation of the church. Further than just identifying locations of burial sites, our 3D model enables us to visualize additional information about the subsurface.

The 3D model also allows for depth interpretations, with the variation in burial depths potentially related to age. This study suggests that the modern burials are typically at a depth of 1 to 2 m. The older burials (red boxes in Figure 4.6) seems to have variable depths. For example, in Figure 4.13, the moderately high amplitude region that corresponds to

burial 39 occurs down to a depth of approximately 1.5 m, while in Figure 4.15, the high amplitude region that corresponds to burial 32 occurs down to a depth of approximately 3.5 m.

As time progresses in the wet reducing environment of certain burial sites, Fe and Mn can be mobilized and leach into the underlying soil (Breuning-Madsen et al. 2001). This can cause hard, cemented layers to form in the soil under the burial site (Breuning-Madsen et al. 2001). The presence of hardened layers below the burial site can then generate a deeper high-amplitude signal in the radargram. Pringle et al. (2012b) similarly suggest that a relict conductive ‘leachate’ plume formed below and around a decaying body can be imaged. This could explain the deep higher-amplitude responses and serves more as anecdotal evidence of the additional information optimized 3D modelling can provide.

Figure 4.10 displays stronger signal amplitudes at certain known sites of stacked caskets, such as the area indicated on Figure 4.10 in the northwest quadrant. The area indicated contains several caskets and urns, the highest concentrated area in the cemetery. While not every burial site containing more than one casket is distinguishable by amplitude signal strength, those areas of highest concentration are discernable.

Areas with unexpectedly high-amplitude signals could represent unmarked graves, but also could be granitic glacial boulders or other foreign artifacts. Figure 4.10 also clearly indicates rows of confirmed burial sites along the eastern side of the cemetery, the furnace or foundation on the north side of the cemetery, and the areas containing unmarked and unidentified burial sites on the western portion of the cemetery. When low-amplitude cut-offs are applied, the vertical and horizontal extent of human remains, and other objects is clear. This is extremely valuable for locating evidence or human remains relating to

criminal cases while also helping to reduce unforeseen costs associated with misidentification of 3D objects during retrieval.

There is evidence to suggest at least the possibility of leachate plumes (Figure 4.17) being identified using the data and methods from this study, particularly when examining the 2D cross sections from the model. Numerous studies have employed the use of GPR for identifying and delineating leachate plumes in the subsurface such as from landfills (e.g., Reyes-López et al. 2008), contaminated hydrocarbon sites (e.g., Atekwana et al. 2000), and clandestine grave sites (e.g., Pringle et al. 2012a), which is most pertinent to this study. Many of the modern burial sites (e.g., those on the northwest and central parts of the cemetery) provide GPR reflection signals that are constrained to high amplitude circular centers with narrow or thin rings of diminishing amplitude (Figure 4.10b, c, and d). However, the oldest burials located on the eastern portion of the cemetery, and the unmarked burials identified on the southwestern most corner of the cemetery (which are probably also 100+ years old), contain amorphous shaped centers with broad, slowly diminishing outward amplitudes (Figure 4.10b and e). This is likely due to extended decay and decomposition of the human remains in the oldest burial sites and that the remnants of this decay have leached both laterally and downward at these burial site locations. While GPR has been used successfully in the literature to aid with the identification and delineation of subsurface plumes, integrating it with other traditional (e.g., groundwater and soil geochemistry) and geophysical techniques (e.g., electrical resistivity tomography) is required to definitively understand the scope of the subsurface plumes.

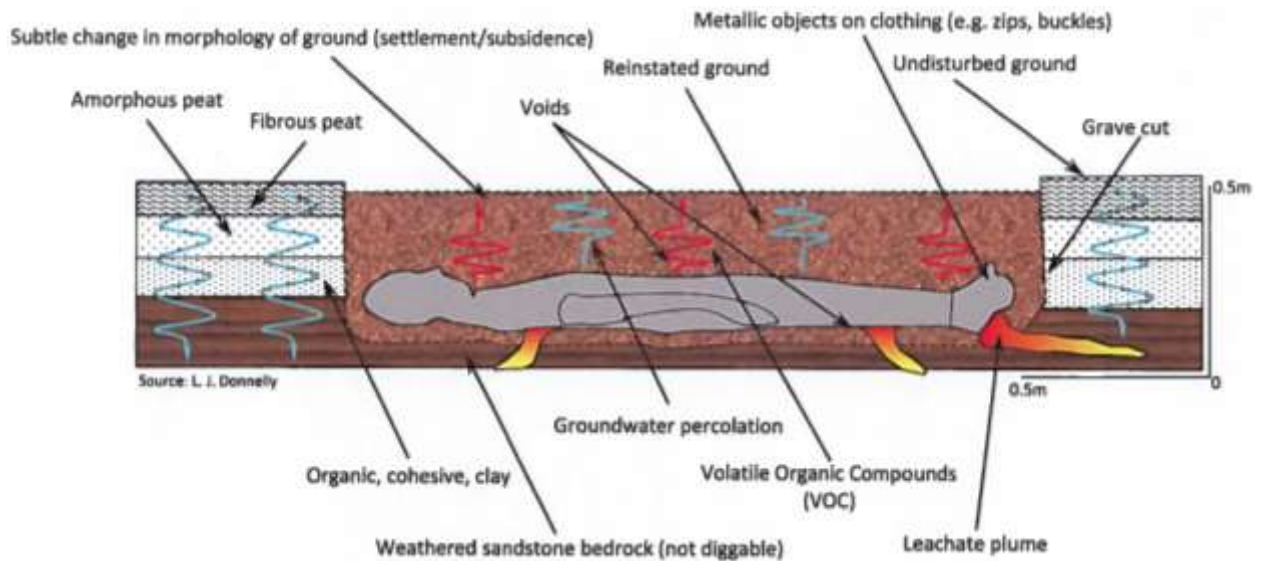


Figure 4.17: Theoretical geological model for a GPR imaged grave (Donnelly 2002; Donnelly and Harrison 2015).

This is a summary of how this 3D visualization technique can provide deeper insight into data than 2D radargrams or rudimentary 3D models (see Figure 4.8 for examples of how 3D GPR models are typically illustrated). Simply evaluating 2D radargrams leaves a lot to the imagination and this is still a technique widely used in basic GPR projects. Other 3D visualizations, such as those by Fernández-Álvarez et al. (2017) and Aziz et al. (2016), also do not allow for optimal visualization of the inner workings of their target areas. By filtering out low-amplitude signals, one can view solely the relevant data. This is especially relevant in fields such as forensic science where human remains are the targets. Human remains are reasonably small compared to other targets in GPR survey. Misidentification can be detrimental to a criminal investigation, making optimal visualization a top priority. The possibility of relating burial depth to time of interment should be investigated further, as it could also potentially be a useful tool for Forensic Science projects relating to human remains.

Well established workflows relating to geoforensic investigations have been suggested and applied in a variety of environments around the world (e.g., Donnelly and Harrison 2010; Donnelly 2012; Pringle et al. 2012b; Donnelly 2013; Donnelly and Harrison 2015, 2017). The applied workflow for this study and for other criminal investigations carried out by the Basin and Reservoir Laboratory is shown in Figure 4.18 and incorporates some of the ideas previously suggested. It briefly outlines the various steps in site identification, fieldwork, processing, and model building. Rubio-Melendi et al. (2018) and Fernández-Álvarez et al. (2017) also stress the importance of desk study and site description in their studies, especially in the case of identifying otherwise unknown locations of human remains. Future work related to this type of study could focus further upon the shapes of the moderate-to-high amplitude responses shown in the 3D model. It may also be a possibility to correlate between the amplitude response from the 3D model and the different types of casket/coffin materials. In other words, the type of material (i.e., wood versus metal) may cause a higher amplitude response in the 3D model.

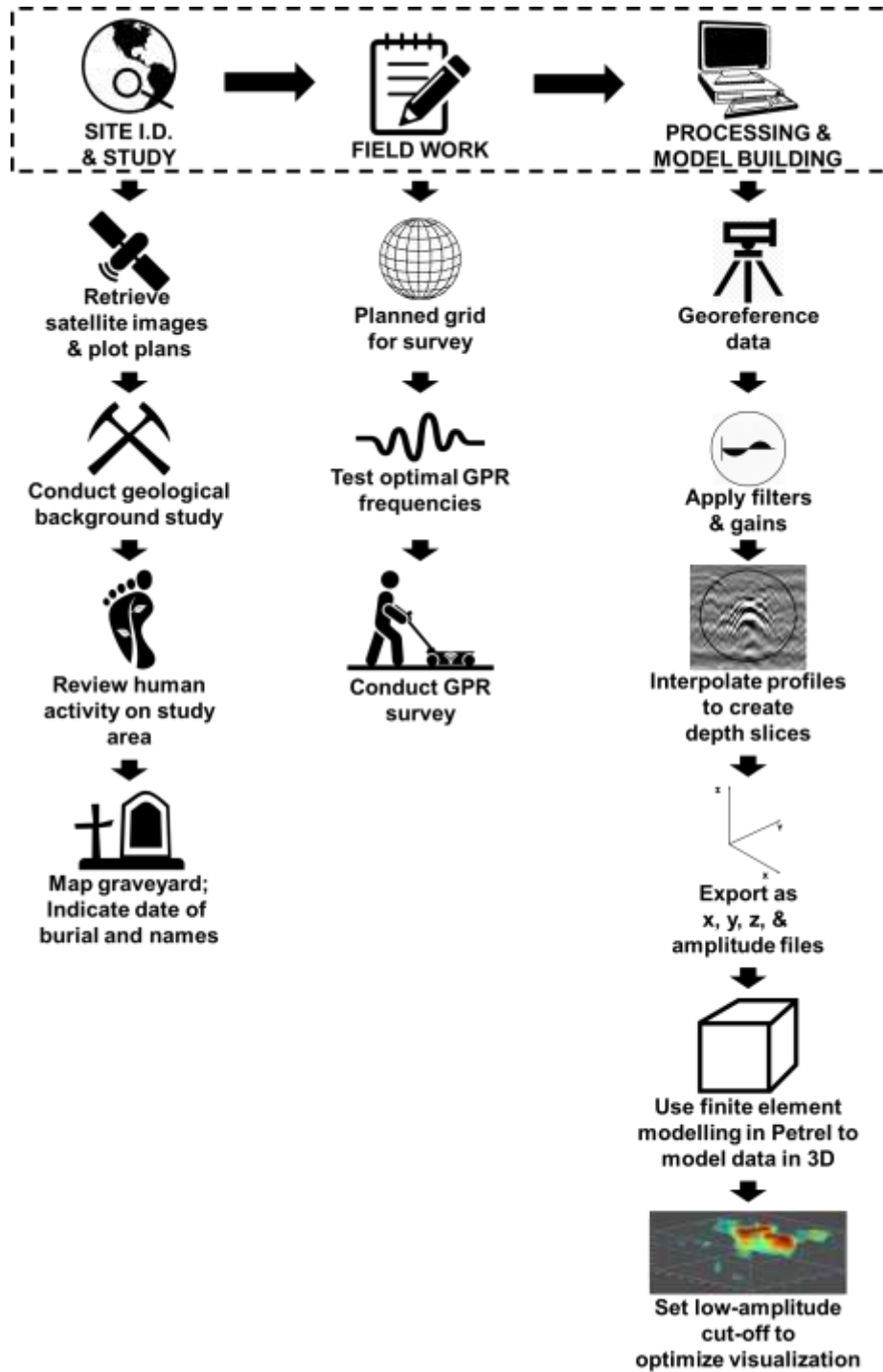


Figure 4.18: A generalized workflow for this case study from site identification through to 3D modelling.

4.11 Conclusions

Near-surface geophysical imaging has been employed since the 1960's and in recent decades has grown extensively in its uses and applications. Although it is a widely utilized tool, the modelling of data needs an update, with high applicability to criminal investigation involving human remains, but beyond that as well. In this paper we evaluate the use of 2D and 3D modelling in GPR studies, and how for the most part these methods can be improved upon. We provide a workflow for an optimized 3D model accurately outlining the burial site distribution and depth of burial for each site. This case study demonstrates this modelling method's ability to easily visualize relevant inner workings of the study area, including depths and sizes of burial sites. It also shows the added benefit of the 3D model.

Through the integration of the workflow (Figure 4.18) and 3D modelling method, we have demonstrated that the results are able to (1) accurately map a cemetery, distinguishing burial sites from one another by subtracting low amplitude data; (2) identify otherwise unknown burial sites; (3) map out potential leachate plumes from older decaying bodies possibly linking burial age to signal depth and; (4) create an overall more intuitive, easily manipulatable, 3D model to optimize visualization. This is possible through a scrutinizing site study, testing equipment for optimal data acquisition, and a novel 3D modelling method using finite-element modelling in Petrel™ software from Schlumberger. We hope that the methods presented from this case study will show the benefit of 3D GPR modelling in the forensic science community and beyond.

4.12 Acknowledgements

We would like to thank Reverend Jack Risk, John Brooks, and Blaine Fisher from the Church of the Holy Spirit for the information they provided and their assistance on site. We would like to thank members of the Dalhousie University Basin and Reservoir Laboratory for their help with data collection and report writing. We are grateful to Schlumberger Limited for their Petrel™ software donation to Dr. Grant Wach of the Dalhousie University Basin and Reservoir Laboratory. The feedback received from Drs. Laurence Donnelly, Alastair Ruffell, and Shari Forbes of the IFG (Institute for Forensic Geology) were helpful and greatly appreciated. The online seminar conducted by Greg Johnston of Sensors and Software Inc. provided valuable information regarding GPR data collection, interpretation, and processing. We also acknowledge Christian Jackowski, the editorial manager for Forensic Science International and the anonymous reviewers for their comments.

4.13 References Cited in Chapter 4

Annan, A.P. 2009. Electromagnetic Principles of Ground-Penetrating Radar Theory. *In* Ground Penetrating Radar Theory and Applications. *Edited by* H.M. Jol. Elsevier Science, Amsterdam, The Netherlands. pp. 3-40.

Arcone, S.A. 1996. High resolution of glacial ice stratigraphy: a ground-penetrating radar study of Pegasus Runway, McMurdo Station, Antarctica. *Geophysics*, **61**: 1653-1663. doi:10.1190/1.1444084.

Atekwana, E.A., Sauck, W.A., and Werkema Jr, D.D. 2000. Investigations of geoelectrical signatures at a hydrocarbon contaminated site. *Journal of Applied Geophysics*, **44**: 167-180. doi:10.1016/S0926-9851(98)00033-0.

Atlas Obscura. 2020. Most Holy Trinity Cemetery, Brooklyn, New York: A burial ground of rusting metal grave markers. Available from <https://www.atlasobscura.com/places/most-holy-trinity-cemetery>.

Aziz, A.S., Stewart, R.R., Green, S.L., and Flores, J.B. 2016. Locating and characterizing burials using 3D ground-penetrating radar (GPR) and terrestrial laser scanning (TLS) at the historic Mueschke Cemetery, Houston, Texas. *Journal of Archaeological Science: Reports*, **8**: 392-405. doi:10.1016/j.jasrep.2016.06.035.

Barone, P.M., Di Maggio, R.M., and Ferrara, C. 2015. Not necessarily buried bodies: forensic GPR investigations from criminal to civil justice. *In* 8th International Workshop on Advanced Ground Penetrating Radar (IWAGPR). 2015. IEEE, pp. 1-4.

Benedetto, A., Benedetto, F., and Tosti, F. 2012. GPR applications for geotechnical stability of transportation infrastructures. *Nondestructive Testing and Evaluation*, **27**: 253-262. doi:10.1080/10589759.2012.694884.

Beres Jr., M., and Haeni, F.P. 1991. Application of ground-penetrating-radar Methods in Hydrogeologic Studies. *Groundwater*, **29**: 375-386. doi:10.1111/j.1745-6584.1991.tb00528.x.

Bier, J. 2018. Bodily circulation and the measure of a life: Forensic identification and valuation after the Titanic disaster. *Social Studies of Science*, **48**: 635-662. doi:10.1177/0306312718801173.

Billinger, M.S. 2009. Utilizing ground penetrating radar for the location of a potential human burial under concrete. *Canadian Society of Forensic Science Journal*, **42**: 200-209. doi:10.1080/00085030.2009.10757607.

Botelho, M.A., and Mufti, I.R. 1998. Exploitation of limestone quarries in Brazil with depth migrated ground-penetrating radar data. *In* SEG Technical Program Expanded Abstracts 1998. Society of Exploration Geophysicists pp. 836-839.

Breuning-Madsen, H., Holst, M.K., and Rasmussen, M. 2001. The chemical environment in a burial mound shortly after construction—an archaeological–pedological experiment. *Journal of Archaeological Science*, **28**: 691-697. doi:10.1006/jasc.1999.0570.

Butnor, J.R., Doolittle, J., Johnsen, K.H., Samuelson, L., Stokes, T., and Kress, L. 2003. Utility of ground-penetrating radar as a root biomass survey tool in forest systems. *Soil Science Society of America Journal*, **67**: 1607-1615. doi:10.2136/sssaj2003.1607.

Cann, D.B., Hilchey, J.D., and Smith, G.R. 1954. Nova Scotia Soil Survey: Soil Survey of Hants County, Nova Scotia. Nova Scotia Department of Agriculture, Truro, Nova Scotia.

Costandi, M. 2015. Life after death: The science of human decomposition. Available from <https://www.theguardian.com/science/neurophilosophy/2015/may/05/life-after-death>.

Daniels, J.J., Roberts, R., and Vendl, M. 1992. Site studies of ground penetrating radar for monitoring petroleum product contaminants. *In* Symposium on the Application of Geophysics to Engineering and Environmental Problems. 1992. Society of Exploration Geophysicists, pp. 597-609.

De Pascale, G.P., Pollard, W.H., and Williams, K.K. 2008. Geophysical mapping of ground ice using a combination of capacitive coupled resistivity and ground-penetrating radar, Northwest Territories, Canada. *Journal of Geophysical Research: Earth Surface*, **113**. doi:10.1029/2006JF000585.

Di Prima, S., Winiarski, T., Angulo-Jaramillo, R., Stewart, R.D., Castellini, M., Abou Najm, M.R., Ventrella, D., Pirastru, M., Giadrossich, F., and Capello, G. 2020. Detecting infiltrated water and preferential flow pathways through time-lapse ground-penetrating radar surveys. *Science of The Total Environment*: 138511. doi:10.1016/j.scitotenv.2020.138511.

Donnelly, L.J. 2002. How forensic geology helps solve crime. Record of presentation on Forensic Geology and the Moors Murders to the House of commons, Westminster Palace, on 12th March.

Donnelly, L.J. 2012. Use of geology in forensic science: Search to locate burials. *Encyclopaedia of Quaternary Science*. Elsevier.

Donnelly, L.J. 2013. The Applications of Forensic Geology & Geophysics for Police and Law Enforcement Ground Searches. *In* Second EAGE International Conference on Engineering Geophysics. 2013. European Association of Geoscientists & Engineers, pp. cp-368-00049.

Donnelly, L.J., and Harrison, M. 2010. Development of geoforensic strategy & methodology to search the ground for an unmarked burial or concealed object. *Emergency Global Barclay media Limited*: 30-35.

Donnelly, L.J., and Harrison, M. 2015. A collaborative methodology for ground searches by a forensic geologist and law enforcement (police) officer: detecting evidence related to homicide, terrorism and organized crime. *In* International Conference on Engineering Geophysics, Al Ain, United Arab Emirates. 2015. Society of Exploration Geophysicists, pp. 88-95.

Donnelly, L.J., and Harrison, M. 2017. Ground searches for graves and buried targets related to homicide, terrorism and organised crime. *Journal of International Geoscience*, **40**: 106-117. doi:10.18814/epiiugs/2017/v40i2/017012.

Doolittle, J.A., and Bellantoni, N.F. 2010. The search for graves with ground-penetrating radar in Connecticut. *Journal of Archaeological Science*, **37**: 941-949. doi: 10.1016/j.jas.2009.11.027.

Doughty, C. 2015. Morbid minute: Coffins vs. caskets. Available from <https://www.youtube.com/watch?v=nUaqKZnClGQ>.

Doughty, C. 2018. Adipocere aka grave wax. Available from <https://www.youtube.com/watch?v=gi0Gi0sqXwg>.

Doughty, C. 2019. We recreated a Victorian funeral. Available from <https://www.youtube.com/watch?v=0OIF-EtoGBo>.

Environment Canada. 2020. Daily Data Report for July 2019: Halifax Stanfield International Airport. Available from https://climate.weather.gc.ca/climate_data/daily_data_e.html?StationID=50620&timeframe=2&StartYear=1840&EndYear=2020&Day=5&Year=2019&Month=7.

Fernández-Álvarez, J.-P., Rubio-Melendi, D., Martínez-Velasco, A., Pringle, J.K., and Aguilera, H.-D. 2016. Discovery of a mass grave from the Spanish Civil War using Ground Penetrating Radar and forensic archaeology. *Forensic science international*, **267**: 10-17. doi:10.1016/j.forsciint.2016.05.040.

Fernández-Álvarez, J.-P., Rubio-Melendi, D., Castillo, J.A.Q., González-Quirós, A., and Cimadevilla-Fuente, D. 2017. Combined GPR and ERT exploratory geophysical survey of the Medieval Village of Pancorbo Castle (Burgos, Spain). *Journal of Applied Geophysics*, **144**: 86-93. doi:10.1016/j.jappgeo.2017.07.002.

Fiedler, S., Schneckenberger, K., and Graw, M. 2004. Characterization of soils containing adipocere. *Archives of environmental contamination and toxicology*, **47**: 561-568. doi:10.1007/s00244-004-3237-4.

Fiedler, S., Illich, B., Berger, J., and Graw, M. 2009. The effectiveness of ground-penetrating radar surveys in the location of unmarked burial sites in modern cemeteries. *Journal of Applied Geophysics*, **68**: 380-385. doi:10.1016/j.jappgeo.2009.03.003.

Funeral Guide. 2016. What is embalming? A guide to the embalming process. Available from <https://www.funeralguide.co.uk/help-resources/arranging-a-funeral/funeral-guides/what-is-embalming>.

Giannopoulos, A. 2005. Modelling ground penetrating radar by GprMax. *Construction and Building Materials*, **19**: 755-762. doi:10.1016/j.conbuildmat.2005.06.007.

Google. 2020. Google Earth Satellite Image. Google.

Hamzah, U., Samsudin, A.R., and Ismail, M.A. 2009. Geoelectrical resistivity and ground penetrating radar techniques in the study of hydrocarbon-contaminated soil. *Sains Malaysiana*, **38**: 305-311.

Ho, K., and Gader, P.D. 2002. A linear prediction land mine detection algorithm for hand held ground penetrating radar. *IEEE Transactions on Geoscience and Remote Sensing*, **40**: 1374-1384. doi:10.1109/TGRS.2002.800276.

Huisman, J.A., Hubbard, S.S., Redman, J.D., and Annan, A.P. 2003. Measuring soil water content with ground penetrating radar: A review. *Vadose zone journal*, **2**: 476-491. doi:10.2136/vzj2003.4760.

Imposa, S., Grassi, S., Patti, G., and Boso, D. 2018. New data on buried archaeological ruins in Messina area (Sicily-Italy) from a ground penetrating radar survey. *Journal of Archaeological Science: Reports*, **17**: 358-365. doi:10.1016/j.jasrep.2017.11.031.

Jol, H.M. 2009. *Ground Penetrating Radar Theory and Applications*. Elsevier Science, Oxford.

Jol, H.M., and Smith, D.G. 1991. Ground penetrating radar of northern lacustrine deltas. *Canadian Journal of Earth Sciences*, **28**: 1939-1947. doi:10.1139/e91-175.

Kadioglu, S. 2008. Photographing layer thicknesses and discontinuities in a marble quarry with 3D GPR visualisation. *Journal of Applied Geophysics*, **64**: 109-114. doi: 10.1016/j.jappgeo.2008.01.001.

Kadioglu, S. 2013. Transparent 2D/3D Half Bird's-Eye View of Ground Penetrating Radar Data Set in Archaeology and Cultural Heritage. *In* *Imaging and Radioanalytical Techniques in Interdisciplinary Research - Fundamentals and Cutting Edge Applications*. Edited by F. Kharfi. Intechopen, Rijeka, Croatia. p. 204.

Kadioglu, S., and Daniels, J.J. 2008. 3D visualization of integrated ground penetrating radar data and EM-61 data to determine buried objects and their characteristics. *Journal of Geophysics and Engineering*, **5**: 448-456. doi:10.1088/1742-2132/5/4/008.

Kadioglu, S., and Ulugergerli, E.U. 2012. Imaging karstic cavities in transparent 3D volume of the GPR data set in Akkopru dam, Mugla, Turkey. *Nondestructive Testing and Evaluation*, **27**: 263-271. doi:10.1080/10589759.2012.694885.

Kelly, T.B., Wach, G.D., and O'Connor, D.E. 2021a. The technical challenges and outcomes of ground-penetrating radar: A site-specific example from Joggins, Nova Scotia. *AIMS Geosciences*, **7**: 22-55. doi:10.3934/geosci.2021002.

Keppie, J.D. 2000. Geological Map of the Province of Nova Scotia. Nova Scotia Department of Natural Resources: Minerals and Energy Branch, Halifax, Nova Scotia.

Kumlu, D., and Erer, I. 2019. Clutter removal techniques in ground penetrating radar for landmine detection: A Survey. *In* *Operations Research for Military Organizations*. IGI Global. pp. 375-399.

Lalagüe, A. 2015. Use of ground penetrating radar for transportation infrastructure maintenance.

Lester, J., and Bernold, L.E. 2007. Innovative process to characterize buried utilities using ground penetrating radar. *Automation in Construction*, **16**: 546-555. doi:10.1016/j.autcon.2006.09.004.

Leucci, G., and Negri, S. 2006. Use of ground penetrating radar to map subsurface archaeological features in an urban area. *Journal of Archaeological Science*, **33**: 502-512. doi:10.1016/j.jas.2005.09.006.

- Liu, X., Dong, X., Xue, Q., Leskovar, D.I., Jifon, J., Butnor, J.R., and Marek, T. 2018. Ground penetrating radar (GPR) detects fine roots of agricultural crops in the field. *Plant and soil*, **423**: 517-531. doi:10.1007/s11104-017-3531-3.
- Lorenzo, H., Pérez-Gracia, V., Novo, A., and Armesto, J. 2010. Forestry applications of ground-penetrating radar. *Forest Systems*, **19**: 5-17.
- Lundberg, A., Richardson-Näslund, C., and Andersson, C. 2006. Snow density variations: consequences for ground-penetrating radar. *Hydrological Processes: An International Journal*, **20**: 1483-1495. doi:10.1002/hyp.5944.
- MacDonald, S.Y. 2020. With Respect to the Dead: Reconstructing a Historic View of Death in Gaelic Nova Scotia. *Genealogy*, **4**: 66. doi:10.3390/genealogy4020066.
- Maierhofer, C. 2003. Nondestructive evaluation of concrete infrastructure with ground penetrating radar. *Journal of Materials in Civil Engineering*, **15**: 287-297.
- Maser, K.R. 1996. Condition assessment of transportation infrastructure using ground-penetrating radar. *Journal of infrastructure systems*, **2**: 94-101. doi:10.1061/(ASCE)1076-0342(1996)2:2(94).
- Mitterer, C., Heilig, A., Schweizer, J., and Eisen, O. 2011. Upward-looking ground-penetrating radar for measuring wet-snow properties. *Cold regions science and technology*, **69**: 129-138. doi:10.1016/j.coldregions.2011.06.003.
- Møller, I., and Anthony, D. 2003. A GPR study of sedimentary structures within a transgressive coastal barrier along the Danish North Sea coast. *Geological Society, London, Special Publications*, **211**: 55-65. doi:10.1144/gsl.Sp.2001.211.01.05.
- Neal, A. 2004. Ground-penetrating radar and its use in sedimentology: principles, problems and progress. *Earth-Science Reviews*, **66**: 261-330. doi:10.1016/j.earscirev.2004.01.004.
- Neal, A., and Roberts, C.L. 2000. Applications of ground-penetrating radar (GPR) to sedimentological, geomorphological and geoarchaeological studies in coastal environments. *Geological Society, London, Special Publications*, **175**: 139-171. doi:10.1144/gsl.Sp.2000.175.01.12.

Ni, S.-H., Huang, Y.-H., Lo, K.-F., and Lin, D.-C. 2010. Buried pipe detection by ground penetrating radar using the discrete wavelet transform. *Computers and Geotechnics*, **37**: 440-448. doi:10.1016/j.compgeo.2010.01.003.

Pälli, A., Kohler, J.C., Isaksson, E., Moore, J.C., Pinglot, J.F., Pohjola, V.A., and Samuelsson, H. 2002. Spatial and temporal variability of snow accumulation using ground-penetrating radar and ice cores on a Svalbard glacier. *Journal of Glaciology*, **48**: 417-424. doi:10.3189/172756502781831205.

Pettersson, J.K., and Nobes, D.C. 2003. Environmental geophysics at Scott Base: ground penetrating radar and electromagnetic induction as tools for mapping contaminated ground at Antarctic research bases. *Cold regions science and technology*, **37**: 187-195. doi:10.1016/S0165-232X(03)00037-5.

Porsani, J.L., Sauck, W.A., and Júnior, A.O. 2006. GPR for mapping fractures and as a guide for the extraction of ornamental granite from a quarry: A case study from southern Brazil. *Journal of Applied Geophysics*, **58**: 177-187. doi:10.1016/j.jappgeo.2005.05.010.

Poulter, G. 2011. What's traditional about "the traditional funeral"? Funeral rituals and the evolution of the funeral industry in Nova Scotia. *Journal of the Canadian Historical Association/Revue de la Société historique du Canada*, **22**: 133-159. doi:10.7202/1008960ar.

Pringle, J.K., Jervis, J.R., Hansen, J.D., Jones, G.M., Cassidy, N.J., and Cassella, J.P. 2012a. Geophysical monitoring of simulated clandestine graves using electrical and ground-penetrating radar methods: 0–3 years after burial. *Journal of Forensic Sciences*, **57**: 1467-1486. doi:10.1111/j.1556-4029.2012.02151.x.

Pringle, J.K., Ruffell, A., Jervis, J.R., Donnelly, L., McKinley, J., Hansen, J., Morgan, R., Pirrie, D., and Harrison, M. 2012b. The use of geoscience methods for terrestrial forensic searches. *Earth-Science Reviews*, **114**: 108-123. doi:10.1016/j.earscirev.2012.05.006.

Qin, T., Zhao, Y., Lin, G., Hu, S., An, C., Geng, D., and Rao, C. 2018. Underwater archaeological investigation using ground penetrating radar: A case analysis of Shanglinhu Yue Kiln sites (China). *Journal of Applied Geophysics*, **154**: 11-19. doi:10.1016/j.jappgeo.2018.04.018.

Rafezi, H., Novo, A., and Hassani, F.P. 2015. An investigation into application of Ground Penetrating Radar (GPR) in surface mining. *In* Symposium on the Application of Geophysics to Engineering and Environmental Problems 2015. 2015. Society of Exploration Geophysicists and Environment and Engineering Geophysical Society, pp. 54-60.

Ralston, J.C., and Hainsworth, D.W. Application of ground penetrating radar for coal depth measurement. *In* 1999 IEEE International Conference on Acoustics, Speech, and Signal Processing. Proceedings. ICASSP99 (Cat. No. 99CH36258). 1999. IEEE. Vol. 4, pp. 2275-2278.

Reyes-López, J.A., Ramírez-Hernández, J., Lázaro-Mancilla, O., Carreón-Diazconti, C., and Garrido, M.M.-L. 2008. Assessment of groundwater contamination by landfill leachate: A case in México. *Waste Management*, **28**: S33-S39. doi:10.1016/j.wasman.2008.03.024.

Risk, J. 2020. Church of the Holy Spirit Information. *Edited by* G. Wach, Halifax, Nova Scotia.

Roark, M.S., Strohmeyer, J., Anderson, N., Shoemaker, M., and Oppert, S. 1998. Applications of the ground-penetrating radar technique in the detection and delineation of homicide victims and crime scene paraphernalia. *In* 11th EEGS Symposium on the Application of Geophysics to Engineering and Environmental Problems. 1998. European Association of Geoscientists & Engineers, pp. cp-203-00112.

Rubio-Melendi, D., Gonzalez-Quirós, A., Roberts, D., García, M.d.C.G., Domínguez, A.C., Pringle, J.K., and Fernández-Álvarez, J.-P. 2018. GPR and ERT detection and characterization of a mass burial, Spanish Civil War, Northern Spain. *Forensic science international*, **287**: e1-e9.

Ruffell, A., McCabe, A., Donnelly, C., and Sloan, B. 2009. Location and assessment of an historic (150–160 years old) mass grave using geographic and ground penetrating radar investigation, NW Ireland. *Journal of Forensic Sciences*, **54**: 382-394.

Schlumberger. 2014. 2014 Petrel Fundamentals: Training and Exercise Guide. Schlumberger, Houston, Texas.

Schultz, J.J. 2007. Using ground-penetrating radar to locate clandestine graves of homicide victims: forming forensic archaeology partnerships with law enforcement. *Homicide Studies*, **11**: 15-29. doi:10.1177/1088767906296234.

Schultz, J.J., Grasmueck, M., Weger, R., Muztaza, N.M., Saidin, M.M., Azwin, I.N., Saad, R., Kofun, H., and Leucci, G. 2012. Detecting buried remains using ground penetrating radar. U.S. Department of Justice.

Sensors and Software Inc. 2018a. EKKO_Project: User's Manual, Mississauga, Ontario.

Sensors and Software Inc. 2018b. EKKO_Project: Processing Module Users Guide.

Smith, D.G., and Jol, H.M. 1992. Ground-penetrating radar investigation of a Lake Bonneville delta, Provo level, Brigham City, Utah. *Geology*, **20**: 1-4. doi:10.1130/0091.

Strange, A.D., Ralston, J.C., and Chandran, V. Application of ground penetrating radar technology for near-surface interface determination in coal mining. *In Proceedings.(ICASSP'05). IEEE International Conference on Acoustics, Speech, and Signal Processing, 2005. 2005. IEEE. Vol. 5, pp. v/701-v/704 Vol. 705.*

Szymczyk, M., and Szymczyk, P. 2013. Preprocessing of GPR data. *Image Processing and Communications*, **18**: 83-90. doi:10.2478/v10248-012-0082-3.

The Australian Museum. 2020. Decomposition - Body Changes. Available from <https://australian.museum/about/history/exhibitions/death-the-last-taboo/decomposition-body-changes/2020>].

Thomas, A.M., Rogers, C.D.F., Chapman, D.N., Metje, N., and Castle, J. 2009. Stakeholder needs for ground penetrating radar utility location. *Journal of Applied Geophysics*, **67**: 345-351. doi:10.1016/j.jappgeo.2008.07.006.

Varela-Ortiz, W., Cintrón, C.Y.L., Velázquez, G.I., and Stanton, T.R. 2013. Load testing and GPR assessment for concrete bridges on military installations. *Construction and Building Materials*, **38**: 1255-1269. doi:10.1016/j.conbuildmat.2010.09.044.

Vaughan, D.G., Corr, H.F.J., Doake, C.S.M., and Waddington, E.D. 1999. Distortion of isochronous layers in ice revealed by ground-penetrating radar. *Nature*, **398**: 323-326. doi:10.1038/18653.

Venkateswarlu, B., and Tewari, V.C. 2014. Geotechnical applications of ground penetrating radar (gpr). *Jour. Ind. Geol. Cong*, **6**: 35-46.

Yelf, R.J. 2007. Application of ground penetrating radar to civil and geotechnical engineering. *Electromagnetic Phenomena*, **7**: 18.

Yoder, R.E., Freeland, R.S., Ammons, J.T., and Leonard, L.L. 2001. Mapping agricultural fields with GPR and EMI to identify offsite movement of agrochemicals. *Journal of Applied Geophysics*, **47**: 251-259.

Zenone, T., Morelli, G., Teobaldelli, M., Fischanger, F., Matteucci, M., Sordini, M., Armani, A., Ferrè, C., Chiti, T., and Seufert, G. 2008. Preliminary use of ground-penetrating radar and electrical resistivity tomography to study tree roots in pine forests and poplar plantations. *Functional Plant Biology*, **35**: 1047-1058. doi:10.1071/FP08062.

Chapter 5: The Technical Challenges of Ground-Penetrating Radar: A Case Study from the Joggins Formation, Joggins, Nova Scotia

T.B. Kelly, G.D. Wach, and D.E. O'Connor

This chapter is based on the paper “The Technical Challenges and Outcomes of Ground-Penetrating Radar: A Site-Specific Example from Joggins, Nova Scotia”, by Trevor B. Kelly, Grant D. Wach, and Darragh E. O'Connor and is published in the American Institute of Mathematical Sciences (AIMS) Geoscience's journal. The copyright agreement form for this chapter can be found in Appendix A.

5.1 Abstract

The Carboniferous Joggins Formation is known for its complete succession of fossil-rich, coal-bearing strata, deposited in a fluvial meanderbelt depositional setting. Hence, the Joggins Formation outcrop is an excellent analogue for studying the 2D geological complexities associated with meanderbelt systems. In this research, a conventional ground-penetrating radar system was tested with the intent of imaging near-surface, dipping, strata of the Joggins Formation (potentially with subsequent repeats as annual erosion provides new visual calibrations). The survey was unsuccessful in its primary goal, and for future reference we document the reasons here. However, the overlying near-surface angular unconformity was successfully imaged enabling mapping of the approximately 8 m of overlying glacial till. A successful outcome would have allowed observations from the 2D outcrop to be extended into 3D space and perhaps lead to an increased understanding of the small (e.g., bedform baffles and barriers) and large (e.g., channel bodies) scale architectural elements, meanderbelt geometry, and aspect ratios. The study comprises a 42-line, 3.46 km ground-penetrating radar survey using a Sensors and Software pulseEKKO Pro SmartCart system. It was combined with a real-time kinematic differential global

positioning system for the georeferencing of survey lines. The 50 MHz antenna frequency, with a 1 m separation, was chosen to maximize the depth of penetration, while still maintaining a reasonable resolution. The results show that many of the lines are contaminated with diffraction hyperbolae, possibly caused from buried objects near or under the survey lines or surface objects near the survey lines. A total of thirteen unique radar reflectors are described and interpreted from this work. The thick clay-rich soil overlying the Joggins Formation probably contributed to significant signal attenuation and the nature of the Carboniferous strata (dip of the beds, pinching and swelling of the beds, bed thickness, etc.) also contributed to imaging difficulties.

5.2 Introduction

The use of 2D siliclastic outcrops for the study of reservoir analogues provides a wealth of knowledge relating to the interwell scale geometrical and petrophysical heterogeneities within a depositional system, which ultimately control permeability and porosity, and thus, the mobility and capacity of reservoir fluids (McMechan et al. 1997). Ideally, the 2D outcrop would be extended into the third dimension to allow for the development of a continuous model that would further help with interpretations. The issue that one is then faced with is how to best fill in the region behind the outcrop to create a 3D model (Knight et al. 1997). One such method that has the potential of providing this data is ground-penetrating radar (GPR); a near-surface geophysical technique that can provide high-resolution images of ancient and modern sedimentary sequences, which can be used to improve the understanding of small (e.g., bedform baffles and barriers) to large (e.g., channel bodies) scale architectural elements, meanderbelt geometry, and aspect ratios, just to name a few (Smith and Jol 1992; Knight et al. 1997; McMechan et al. 1997;

Møller and Anthony 2003; Kostic and Aigner 2007; Rey et al. 2013; Barboza et al. 2014; Lanzarone et al. 2016; Dillenburg et al. 2017; Leandro et al. 2019; Dillenburg et al. 2020).

GPR is a non-invasive and non-destructive remote sensing geophysical technique that is highly useful and versatile utilized in several different disciplines for the imaging and subsequent study of the shallow subsurface (e.g., Neal and Roberts 2000; Neal 2004). It accomplishes this through the detection of electrical discontinuities by the generation, propagation, reflection, and reception of pulsed high-frequency electromagnetic energy (e.g., Neal and Roberts 2000; Neal 2004). These discontinuities are directly related to water saturation, salinity, porosity, and mineralogical variations (Møller and Anthony 2003; Jol 2009). Ideal GPR results are typically achieved from clean, quartzose-rich clastic sediments that contain no clays or silts (e.g., (e.g., Jol and Smith 1991; Smith and Jol 1992). Signal attenuation is a real concern when performing a GPR survey, with problems arising from concentrations of silt, clay, caliche, and moist saline conditions (e.g., Beres Jr. and Haeni 1991; Jol and Smith 1991; Smith and Jol 1992).

Here we provide the first comprehensive results from a primarily road-based GPR survey. In this study, a total of 42 GPR lines were collected over the Carboniferous-aged Joggins Formation of northern Nova Scotia, Canada, using one set of 50 MHz antennae arranged as a transmitter/receiver pair. The GPR system was combined with a Real-Time Kinematic (RTK) Differential Global Positioning System (DGPS) to provide a fully georeferenced group of survey lines with positional accuracy of approximately ± 2 cm (Van Sickle 2015). The goals of this survey were to image the dipping conformable strata of the fluvial-dominated Joggins Formation to identify sedimentary structures that could be correlated with a previously obtained lidar survey of the cliff face. This work was

performed with the aim of providing constraining data on the reservoir architecture of the Carboniferous fluvial meanderbelt system of the Joggins Formation in 3D (outcrop + GPR).

The results of the GPR study were to be used as inputs to stochastic models of the Joggins Formation with the purpose of understanding the inherent reservoir heterogeneity sensitivities of the analogous reservoir. The four main geometric measures include channel depth, channel width, sandstone thickness and channel-belt width. From those, four aspect ratios can be calculated, (1) channel depth versus sandstone thickness, (2) channel depth versus channel width, (3) channel-belt width versus channel depth, and (4) channel-belt width versus channel width. Gibling (2006) documents the width and thickness of fluvial channel bodies from the geological record, including those measured from the 2D outcrop exposure of the Joggins Formation.

Additionally, this study was carried out to test the applicability of the GPR system to provide high-resolution imaging of the dipping strata of the Joggins Formation, with the possibility that these images could be integrated with other outcrop (e.g., lidar) and subsurface data (e.g., drill core, well logs). The majority of the GPR data show strong diffraction hyperbolae, which is likely the result of above ground and subsurface objects. These objects could not be bypassed since most of the GPR lines were conducted on gravel/dirt roads traversing on top of the Joggins Formation strata. The objects that contaminate the radargrams must be understood and differentiated from the true sedimentary structures that were the purpose of this survey. There are also many other items that were unique to this survey that could potentially result in the radargrams being contaminated.

A search of previous research related to the Joggins Formation yields a vast number of publications that are either written directly about the Joggins Formation or mention the Joggins Formation in some capacity (e.g., Davies and Gibling 2003; Rygel et al. 2004; Davies et al. 2005; Calder et al. 2006; Gibling 2006; Calder and Boon 2007). According to a recent publication by Grey and Finkel (2011), the bulk of the research occupies one of three major categories; a general geology category that includes sedimentology and stratigraphy publications (e.g., Davies and Gibling 2003; Davies et al. 2005; Waldron and Rygel 2005; Rygel and Gibling 2006); a paleobiology category that includes taxonomic discoveries and descriptions (e.g., Carroll 1967; Archer et al. 1995b; Reisz and Modesto 1996; Tibert and Dewey 2006; Carpenter et al. 2015); and a paleoecology category (e.g., Brand 1994; Calder et al. 2006).

Despite the abundant research carried out in this area, there is a lack of research into the subsurface imaging of the Joggins Formation, particularly those that utilize ground penetrating radar. The exception dating back to the early 1960's, until approximately 2008, when numerous 2D seismic lines were collected in the onshore Cumberland Subbasin for the purpose of hydrocarbon resources exploration. In addition, several petroleum boreholes were drilled to test areas and structures of potential interest. Some of these wells penetrated the Joggins Formation strata. The Athol Syncline was the focus of a regional seismic study and appeared to show evidence of rapid subsidence within the Cumberland Subbasin resulting from Mississippian salt withdrawal at depth, allowing for thick sediment accumulations and preservation (Waldron and Rygel 2005).

5.3 Study Area

The community of Joggins is located approximately 230 km north of Halifax, Nova Scotia. Joggins and the corresponding outcrop lie alongside Chignecto Bay, a smaller bay within the grander Bay of Fundy. In this area, the tides ebb and flow some 13 m with each tidal cycle (Figure 5.1). The mean annual temperature is approximately 6.0 °C, and the mean annual precipitation is 1154.8 mm. The ease of access, continuity and quality of the Joggins Formation exposure and the numerous road/grass surfaces over which a GPR survey could be completed are the main reasons behind its selection as a study site. The Joggins Fossil Cliffs (Joggins Formation) were nominated in 2008 as a United Nations Educational, Scientific and Cultural Organization (UNESCO) heritage site, together with six additional conformable formations (Ragged Reef, Springhill Mines, Little River, Boss Point, Claremont and Shepody) because of the exceptionally well-preserved rock outcrops and fossil assemblages that document life during the “Coal Age”, a time when fertile forests and wetlands occupied the World’s tropics (UNESCO 2008).

Joggins and the nearby area have seen extensive coal mining that dates back to 1686 (Falcon-Lang 2009), continuing intermittently for over 200 years. During that time, elaborate underground mine workings were created, with many of the remnants (e.g., mine opening supports and railway line support timbers) visible in the cliff face from the intertidal zone (e.g., Rust et al. 1985; Falcon-Lang 2009; Quann et al. 2010). The surface development was also substantial, with timbers (rail track and support) and steel spikes still visible on the intertidal zone between Main Street and the Joggins Fossil Cliffs center. The remains of a wooden pier that existed for the load-out of coal onto ships during high tide for destinations throughout the Maritimes and New England (Falcon-Lang 2009). The

ground over which the GPR survey was conducted, has seen extensive, human-related activity, which needs to be accounted for when interpreting the data.

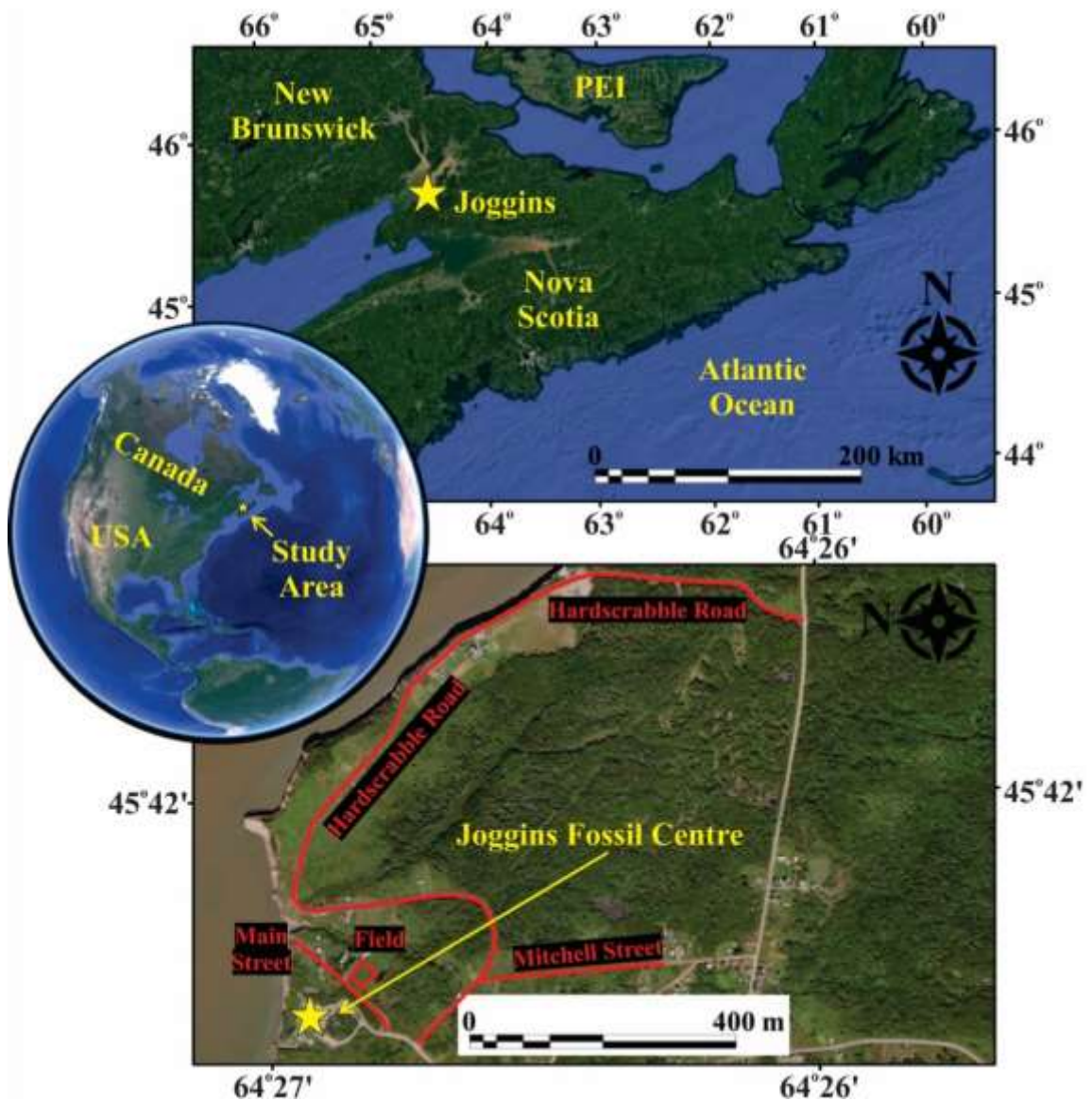


Figure 5.1: Location map of Joggins, Nova Scotia. GPR data was collected from the areas outlined with red (basemap from Google Maps 2020).

5.4 Geological Background

5.4.1 Overburden Geology

Overburden (soil and glacial till) geology is important for GPR studies because of the direct impact it has on data collection, especially when attempting to image underlying bedrock. A review of borehole reports from the area describes the overburden as ranging in thickness from 1.5 to 20.1 m (average of 6.4 m). In the study area, the Joggins Formation is overlain by glacial till with a developed soil horizon on top for a total thickness of approximately 8 m (Figure 5.2). Joggins soils are grayish-brown, moderately fine-textured, and stony with poor internal drainage (e.g., Nowland and MacDougall 1973; Keys et al. 2010). The “A” horizon is at least 15 cm thick and characterized by pale gray to pale brown sandy loam and sandy clay loam with yellowish mottling, an indication of extended saturation and gleying (e.g., Nowland and MacDougall 1973; Keys et al. 2010). Underlying is a 10 to 25 cm thick yellowish and reddish interval of mottled material with a dullish brown matrix, manganese dioxide (MnO_2) concretions and considerable free iron accumulation. The remaining “B” horizon begins at approximately 30 cm and continues to 60 cm depth. It is a compact, dense sandy clay loam with a weakening mottled texture and brown to dark grayish brown matrix (Nowland and MacDougall 1973). Thin clay lines most of the voids, resulting in a low permeability zone. The underlying “C” horizon is also clay-rich, dense, and dull reddish-brown to grayish-brown with rare mottling. The detailed soil horizon characteristics are described by Nowland and MacDougall (1973).

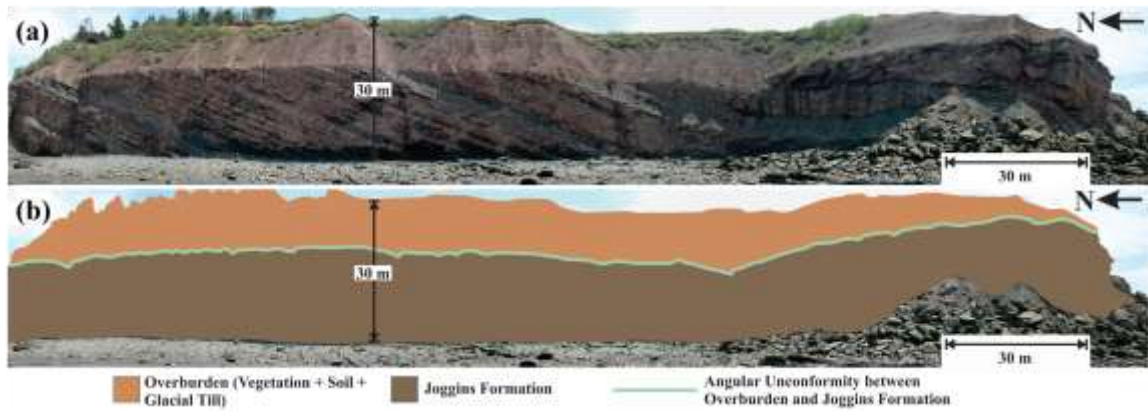


Figure 5.2: Uninterpreted and interpreted images of the Joggins Formation study area. (a) An uninterpreted photograph of a section of the Joggins Formation showing the promontory on the left known as Coal Mine Point. (b) The same photograph as the top, except with some simple interpretation. The orange at the top indicates the portion known as overburden composed of vegetation, soil, and primarily glacial till. The brown area below the orange is the Joggins Formation. The green line between the two areas indicates the location of the well-defined angular unconformity.

Glacial till is defined as a mass of unsorted debris deposited by a glacier and consisting of grain sizes ranging from boulders to clay (Prothero and Schwab 2003). The glacial till on which these soil horizons were formed is a grayish, silty clay loam that originated from the fine-grained grey and red sandstones, shales and mudstones of the Carboniferous coal measure beds (Nowland and MacDougall 1973). A more recent study by Stea and Finck (1986) names the till in this location as the Joggins Till. It is described as being a sandy silt that is dark yellowish-brown in colour with clasts composed of grey sandstones, shales, mudstones, and minor red sandstones and shales, limestone and coal (Stea and Finck 1986).

5.4.2 *Bedrock Geology*

The Maritimes Basin is comprised of ten onshore/offshore subbasins, of which the Cumberland Subbasin is one (Figure 5.3). It hosts numerous, well-known coal deposits, of which numerous seams and their associated mine workings are visible from the intertidal zone. The Joggins Formation is part of the Cumberland Group and with the Mabou Group

forms a continuous 14.7 km long outcrop (Figure 5.4) along the coast of Chignecto Bay (Grey and Finkel 2011). At approximately 4500 km², the Cumberland Subbasin is a fault-bounded depocenter containing some 7000 m of Late Devonian to Early Permian sediment (e.g., Ryan et al. 1987; RPS Energy 2010). The subbasin occurs over areas of northwestern Nova Scotia and to a minor extent, regions of southern New Brunswick. It is positioned to the south by the Cobequid Mountains, to the west by the Caledonian Highlands and Westmorland Uplift, and to the east by the Antigonish Highlands ((e.g., Ryan and Boehner 1994; RPS Energy 2010)). It is suggested by Browne and Plint (1994) that the subbasin margins are comprised to the south by the North Fault, to the north by the Caledonia-Dorchester fault system, and to the west by the Harvey-Hopewell Fault. The northwestern basin margins, as suggested by Martel (1987) are characterized by a laterally trending basal horst along the Hastings Fault.

A sequence of synclines occur in the basin, with the more significant examples being the Amherst, Athol, Scotsburn, Tatamagouche, and Wallace, in addition to a couple diapirism-related anticlines known as the Claremont-Malagash and Minudie, both being encircled by the aforementioned synclinal sequence (Ryan and Boehner 1994). According to Ryan and Boehner (1994) the Cumberland Subbasin structural elements are correlated with basin growth features and include major synclines as well as growth and strike-slip faults. Those structural elements are either unrelated to or are indirectly related to salt tectonics and their related salt structures such as diapiric anticlines, diapirs, domes, and folds/faults related to salt movement (Ryan and Boehner 1994). The Cumberland Subbasin is considered a salt-withdrawal basin with both the slump features and movement of salt occurring concurrently with basin deposition.

The Joggins Formation has been interpreted to contain three stratigraphic facies; a well-drained floodplain facies that includes reddish siltstone, mudstone and sandstone with minor greyish mudstone, rare coal and limestone beds; a poorly-drained floodplain facies comprised of interbedded deposits of sand-poor and sand-rich beds, green/grey mudstone associated with coal, carbonaceous shale, and minor limestone; and an open-water facies (marine deposits) of sandstones and siltstones with thin limestone (Davies and Gibling 2003). The strata dip to the south at approximately 21°.

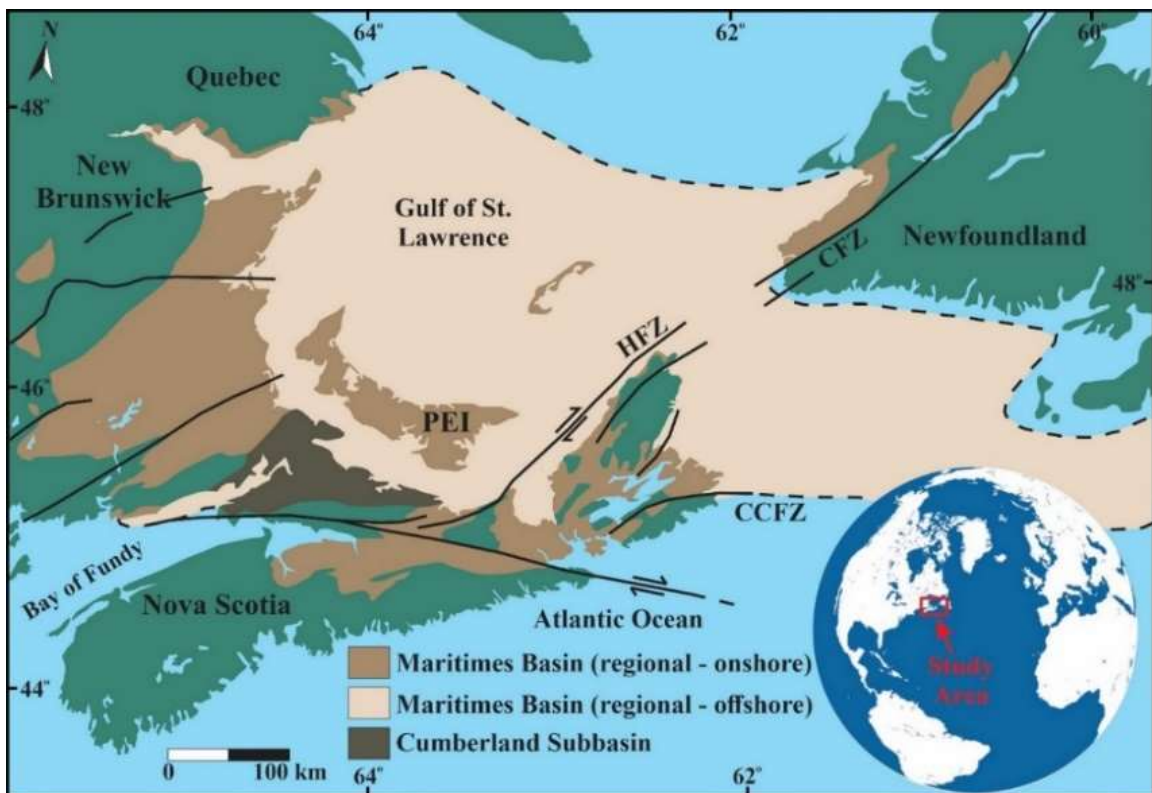


Figure 5.3: Map of the onshore/offshore regional Maritimes Basin. The Cumberland Subbasin is also included in the Maritimes Basin but has been separately highlighted. The three major fault zones are as follows: CCFZ, Cobequid-Chedabucto Fault Zone; CFZ, Cabot Fault Zone; and HFZ, Hollow Fault Zone (modified from (modified from Gibling et al. 1992; Rygel 2005; Allen et al. 2013; Kelly and Wach 2020). The acronym “PEI” stands for Prince Edward Island.

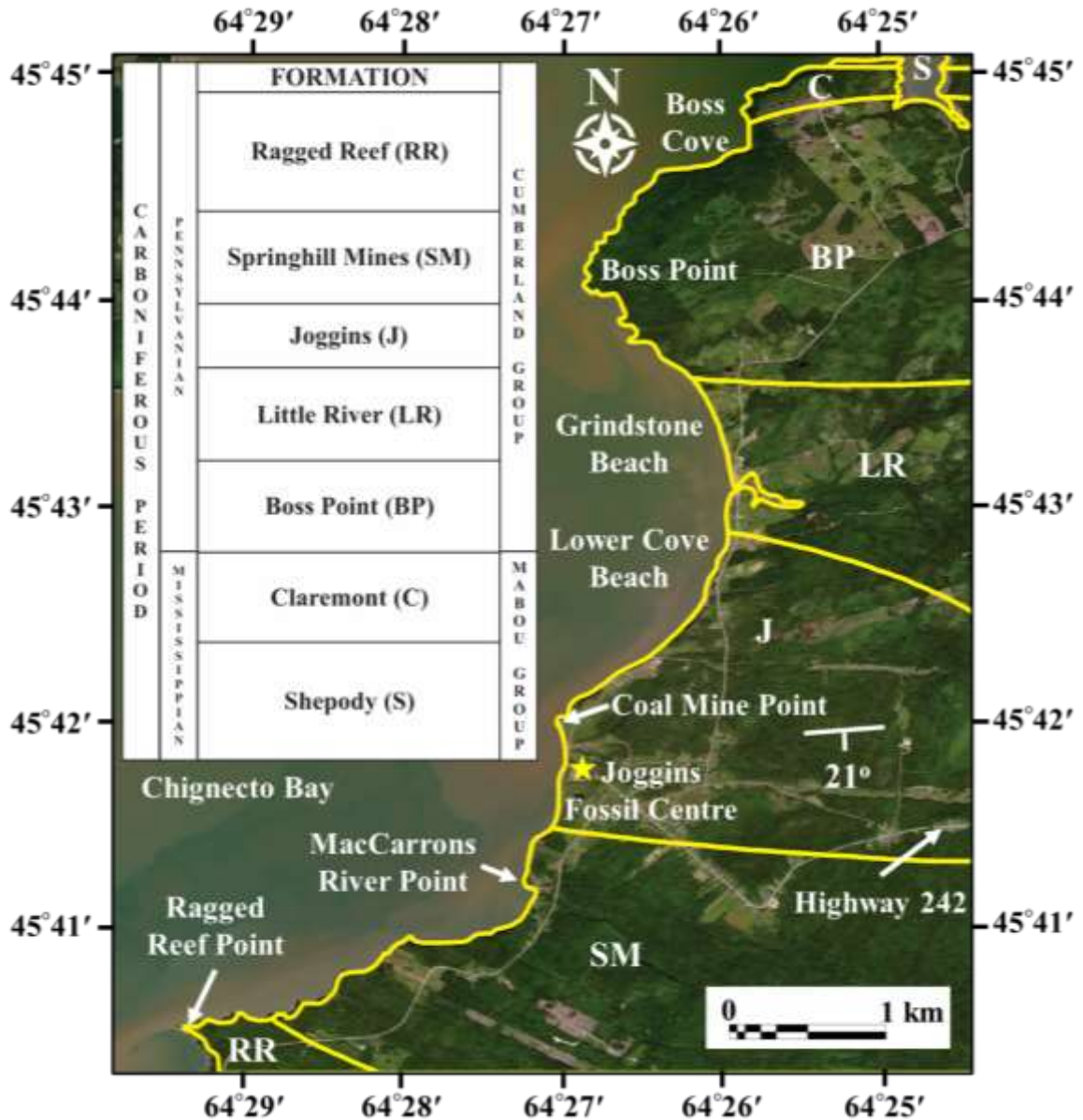


Figure 5.4: Plan view showing the Carboniferous Joggins Fossil Cliffs geology (modified from Grey and Finkel 2011; Google Maps 2020). The stratigraphic column shows the geological formations with their relative ages. The formations, from both the Cumberland Group and Mabou Group, make up the 14.7 km of coastline that is recognized as a UNESCO World Heritage Site.

5.5 Equipment and Methods

To achieve the research objectives of this study, a GPR and RTK DGPS system was used. To assist with GPR interpretation, data gathering was paired with an RTK DGPS to precisely georeference the GPR data. The Joggins Formation outcrop along the shoreline

also provides a valuable 2-D view, while the GPR attempts to add the 3rd dimension. The outcrop study of the Joggins Formation helps to characterize and confirm the sedimentology and the internal architecture of the fluvial outcrop, particularly at smaller scales, which the GPR imaging is unable to resolve.

A Sensors and Software Incorporated pulseEKKO Pro SmartCart GPR system (Figure 5.5) was used for this study and supplied by the Dalhousie University Basin and Reservoir Laboratory. The cart is highly durable and has 4-wheels to provide the rapid and continuous collection of data in open areas. The cart is a self-contained system that includes the GPS rover receiver, transmitting and receiving antennae, digital video logging screen, and power supplies for the screen and antennae. The triggering method for the GPR survey is the built-in odometer. The transmitting and receiving antennae were oriented perpendicular to the line profile direction.

The 50 MHz antennae with the standard transmitter/receiver configuration and a separation of 1.0 m was used for all lines. It was chosen because the specifications suggested a depth of penetration and resolution sufficient for Joggins Formation imaging. The 50 MHz antennae have a length of 2 m and a nominal spatial resolution length of at most 0.5 m. The step size is 0.1 m, the time window is 400 ns and there are 250 points per trace. The sampling interval is 1600 picoseconds (ps). The transmitter pulsar voltage is 1000 volts. The assumed velocity was 0.100 m/ns, which is between the value for wet clay and dry clay. The imaging of the Joggins Formation is captured to a depth of approximately 300 ns two-way travel time (TWT), corresponding to a depth of roughly 17.0 m. Setup parameters are listed in Table 5.1.

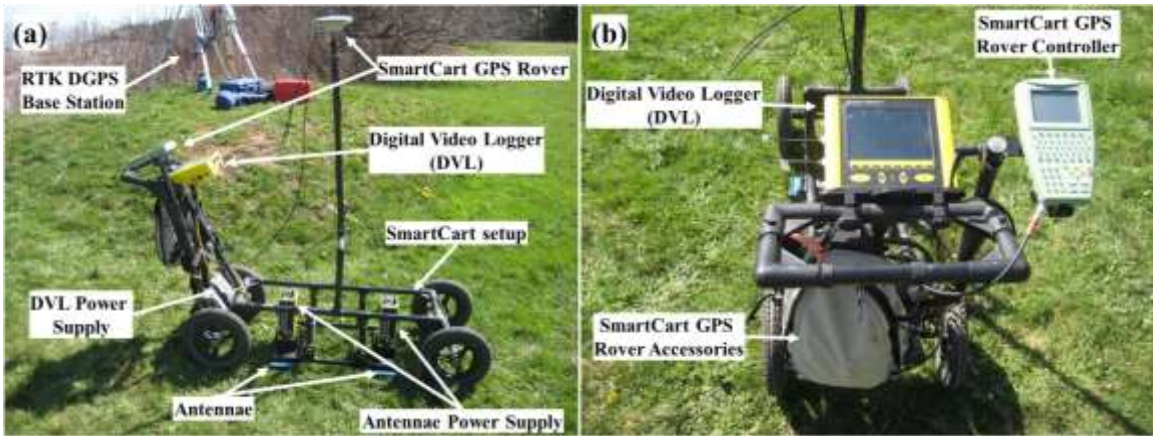


Figure 5.5: The overall GPR SmartCart setup. (a) The typical sideview of the GPR SmartCart setup with many of the features labelled. (b) The view from the operator's position looking at the GPR SmartCart. The operator has a clear view of the digital video logger (DVL) and the RTK DGPS rover controller. Note: the images show the setup with the 200 MHz antennae and not the 50 MHz antennae used for data collection.

The GPR system was paired with a RTK DGPS to provide a fully georeferenced group of survey lines with positional accuracy of approximately ± 2 cm (Van Sickle 2015). The survey incorporated a Leica GPS1200+ Series High Performance Global Navigation Satellite System (GNSS) to apply differential corrections and broadcast accurate location data to the rover receiver. The GPS system consisted of a base station and a transmission antenna used to transmit corrections from the base station to the rover receiver in real-time (Figure 5.6). The rover receiver was mounted to the midpoint of the GPR cart. The base station was placed over a drilled water well with established surveyed coordinates (UTM Zone 20T; Easting = 387,098.72; Northing = 5,061,126.31; Elevation = 26.453 m) at the rear (water side) of the Joggins Fossil Cliffs Centre. As the GPR cart is pushed along a survey line, the rover receiver acquires GPS coordinates and the wander or drift that is recorded by the base station is subtracted in real-time from the coordinates recorded by the GPR cart. The corrected points are then recorded into the radargram.

Table 5.1: Summary table of GPR system setup parameters.

Parameter	Value/Description
<i>GPR Parameters</i>	
Antenna Frequency	50.0 MHz
Antenna Separation	1.000 m
Assumed Velocity	0.100 m/ns
	0.328 ft/ns
Time Window	400.00 ns
Number of Points	250
Sample Interval	1.60 ns
System Stacking	32
Pulsar Settings	Auto PRO
<i>Survey Parameters</i>	
Start Position	0.00 m
Antenna Step Size	0.100 m
Position Units	Metric
Survey Type	Reflection
<i>Acquisition Control Parameters</i>	
Triggering Method	Odometer
Trace Delay	0.0 sec
Odometer Calibration	1045.75 forward
Beeper Active	None
Data Storage	Removable
GPS Usage	Every Trace
GPS Baud Rate	19200
GPS Transfer Bits	1s 8d N
GPS End String	\$GPRMC
<i>Display Parameters</i>	
Trace Type	Grey Scale
Trace Spacing	8 pixels
Gain Type Applied	SEC

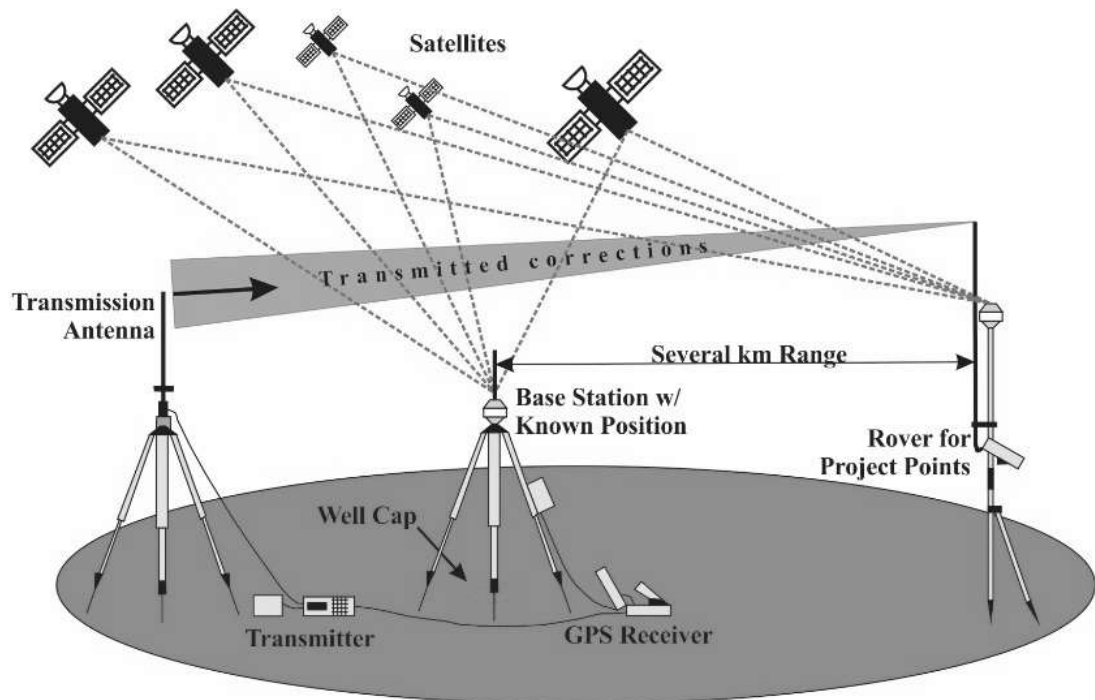


Figure 5.6: Sketch of the global positioning system equipment used to provide a fully georeferenced ground-penetrating radar data set (modified from Van Sickle 2015; Kelly and Wach 2020). The base station was assembled over a drilled water well with known coordinates. The transmission antenna was placed adjacent to the base station. The rover was mounted on the GPR SmartCart for providing survey line locational coordinates.

The processing workflow follows three main tasks; the first being the selection of an acceptable GPR data processing workflow; the second being the selection of the appropriate parameters and inputs for each processing step, where required (the dewow filter does not have any inputs, it is simply applied or not applied); and finally, the observation of end results for each processing step and the correction of any issues caused by an incorrect parameter (Szymczyk and Szymczyk 2013). EKKO_Project™ software was used for editing, processing, and viewing the GPR data. The software was developed by Sensors and Software Incorporated and is a professional “software version that allows for data plotting, editing and full processing routines including spatial and temporal filters, migration, instantaneous attributes, amplitude spectra, CMP velocity analysis and more.” All GPR data were post-processed. Processing was performed using iterations paired with

descriptions of how and when each processing technique should be applied. Processes were applied individually and in conjunction with other processes until the radargram was sufficient for interpretation.

The GPS data was collected concurrently with the GPR data on the Sensors and Software Digital Video Logger (DVL) and was added to the GPR data using the file that recorded GPS positions at regular trace intervals. The GPS data was stored as the GGA (Global Positioning System Fix Data) format, which is a standard format recognized by the National Marine Electronics Association. The GPS data was converted to UTM coordinates and the step-size re-calculated. Topographic correction of the GPR data along the survey lines was performed using the EKKO_Project™ software. The topographic variation along the survey areas is shown on the inset elevation profile plot in Figure 5.7.

Signal saturation correction or dewow is a type of time filter and was applied to each trace for the removal of the initial DC component and low-frequency, slowly decaying “wow” (Annan 2003; Dojack 2012). This is caused by the arrival of early waves, dynamic range limitations on instrumentation, and/or inductive coupling effects and becomes superimposed on the high frequency reflections (Annan 2003; Dojack 2012). It is typically almost always applied and is usually the first process applied.

To compensate for the spreading and attenuation of the propagating wave front, the Spreading and Exponential Compensation (SEC) gain was used to apply the exponential gain (approximately $1/r^2$) that compensates for the spreading and attenuation of the propagating wave front. The input parameters necessary for this gain are an attenuation value for the substrate, a beginning value to be added to the exponential gain function and a maximum value for the gain. The average time-amplitude plot for each trace was

examined both before and after the application of the gain to ensure it was properly applied as described by Annan (1999). Each line had unique attenuation, start and maximum values. The values for attenuation ranged between 2.08 and 5.31 dB/m with an average of 3.63 dB/m. The start gain value ranged from 0.62 to 1.44 with an average of 0.92. The maximum gain value applied ranged from 32 to 222 with an average of 123.79.

5.6 Survey Area

A localized GPR survey was carried out along 3 gravel roads and one grassy field over the Joggins Formation (Figure 5.7). The four areas are Hardscrabble Road, Main Street, a grassy area adjacent to Main Street, and Mitchell Street (Figure 5.9). The GPR survey conducted on Hardscrabble Road consisted of 31 lines (lines 09–39) between elevations ranging from 17 to 48 m above sea level for a total distance of approximately 2500 m. A representative image of Hardscrabble Road can be seen in Figure 5.9a. The GPR survey conducted on Mitchell Street consisted of 1 line (line 51) between elevations ranging from 31 to 43 m above sea level for a total distance of approximately 434 m. A representative image of Mitchell Street can be seen in Figure 5.9b. The GPR survey conducted on the grassy field adjacent to Main Street consisted of 5 lines (lines 45–50) between elevations ranging from 24 to 27 m above sea level for a total distance of approximately 236 m. A representative image of the grassy area adjacent to Main Street can be seen in Figure 5.9c. The GPR survey conducted on Main Street consisted of 5 lines (lines 40–44) between elevations ranging from 19 to 31 m above sea level for a total distance of approximately 307 m. A representative image of Main Street can be seen in Figure 5.9d. In summary, the GPR survey consisted of a total of 42 lines over the Joggins Formation between elevations from 16.97 m to 47.47 m above sea level for a total distance

of approximately 3500 m (Figure 5.7; Table 5.2). The roads are primarily non-linear, so the survey was completed using numerous short straight-line segments.

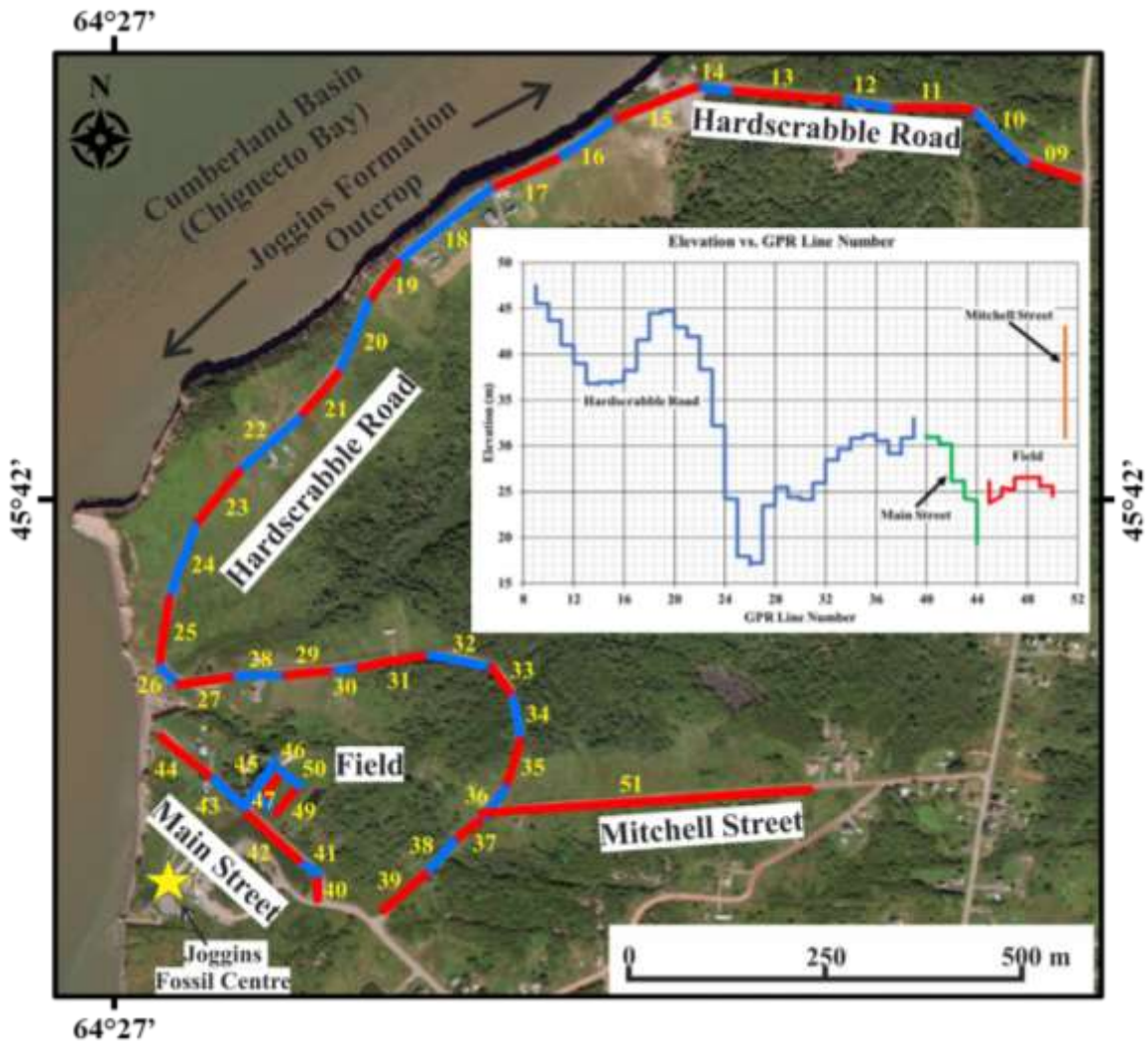


Figure 5.7: A satellite image of the study area showing GPR line locations with contrasting blue and red lines (basemap from Google Maps 2020). The inset graph plots the survey elevation profile.

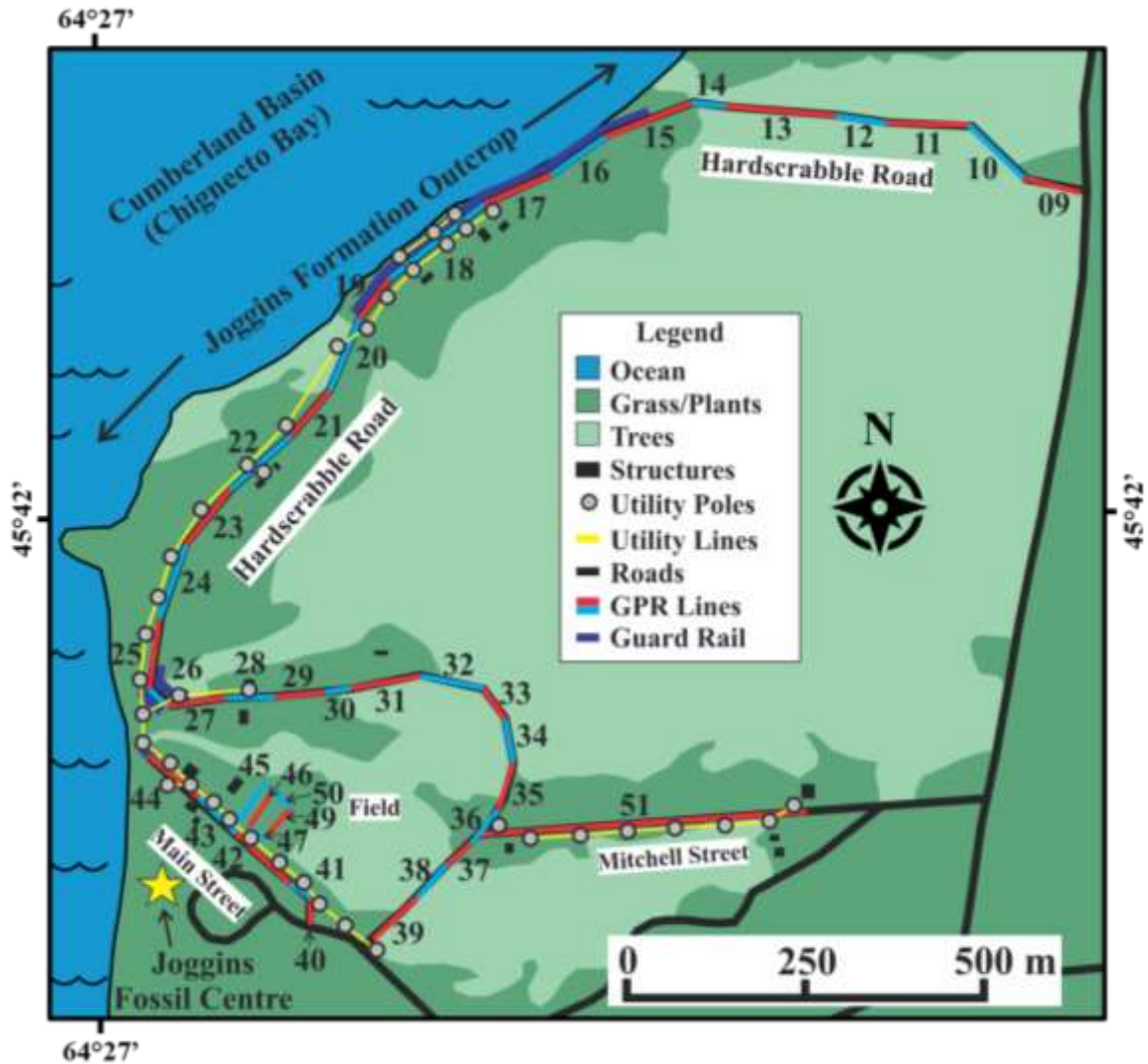


Figure 5.8: A plan view sketch of the study area showing the GPR lines in relation to surficial features (basemap from Google Maps 2020).

The GPR survey areas are sparsely populated; however, there are an abundance of surficial features, both human-made and natural, that may have varying effects on the quality of the GPR data collected. Many of the surficial features and objects that occur adjacent to or in the vicinity of GPR data collection are shown in Figure 5.8b. Residential dwellings are generally well-spread out, but are in certain areas along Hardscrabble Road, Main Street, and Mitchell Street. Along with these dwellings is the associated infrastructure, mainly utility poles, and power lines, which do occur in abundance adjacent

to the three road surfaces surveyed. The infrastructure also includes steel guard rails with wooden posts along the road areas that closely border the cliff edge. Areas of vegetation (e.g., grass, plants, and trees) are also located along the flanks of the roads where the GPR surveys were completed on. Due to the variation in surficial features along the GPR survey lines, it may be possible to look for subtle changes in the reflection profiles and correlate the response to a particular feature.

Table 5.2: A summary of the 42 GPR lines collected at Joggins.

Line	Line Length (m)	# Traces	Min Elev. (m)	Max Elev. (m)
Line09 ¹	71.5	144.0	45.55	47.47
Line10 ¹	100.5	202.0	43.69	45.51
Line11 ¹	107.5	216.0	41.01	43.68
Line12 ¹	67.5	136.0	39.02	40.98
Line13 ¹	145.5	292.0	36.79	38.99
Line14 ¹	44.0	89.0	36.73	36.96
Line15 ¹	120.5	242.0	36.69	37.01
Line16 ¹	87.0	175.0	37.03	38.22
Line17 ¹	95.0	191.0	38.22	41.56
Line18 ¹	156.5	314.0	41.57	44.49
Line19 ¹	65.0	131.0	44.49	44.85
Line20 ¹	102.0	205.0	42.95	44.74
Line21 ¹	79.0	159.0	41.93	42.97
Line22 ¹	105.0	211.0	38.33	41.92
Line23 ¹	93.0	187.0	32.20	38.31
Line24 ¹	100.5	202.0	24.23	32.18
Line25 ¹	92.0	185.0	17.93	24.18
Line26 ¹	34.0	69.0	16.97	17.90
Line27 ¹	77.0	155.0	17.20	23.45
Line28 ¹	64.5	130.0	23.47	25.48
Line29 ¹	65.5	132.0	24.38	25.48
Line30 ¹	33.0	67.0	24.12	24.40
Line31 ¹	93.0	187.0	24.09	25.93
Line32 ¹	84.0	169.0	25.94	28.48
Line33 ¹	49.5	100.0	28.45	29.62
Line34 ¹	56.5	114.0	29.61	30.85
Line35 ¹	66.5	134.0	30.79	31.19
Line36 ¹	54.5	110.0	30.52	31.31

Continued on next page

Line	Line Length (m)	# Traces	Min Elev. (m)	Max Elev. (m)
Line37 ¹	43.5	88.0	29.14	30.53
Line38 ¹	57.0	115.0	29.06	30.85
Line39 ¹	73.5	148.0	30.88	33.00
Line40 ²	34.5	70.0	30.94	31.18
Line41 ²	31.0	63.0	30.20	30.97
Line42 ²	98.0	197.0	26.11	30.20
Line43 ²	62.0	125.0	24.27	26.17
Line44 ²	81.0	163.0	19.32	24.02
Line45 ³	72.5	146.0	23.76	26.09
Line46 ³	53.0	107.0	24.52	25.43
Line47 ³	33.5	68.0	25.14	26.51
Line49 ³	46.5	94.0	25.51	26.57
Line50 ³	30.5	62.0	24.50	25.60
Line51 ⁴	433.5	868.0	30.90	43.04

¹-lines collected on Hardscrabble Road;

²-lines collected on Main Street;

³-lines collected on a grassy area adjacent to Main Street;

⁴-line collected on Mitchell Street.

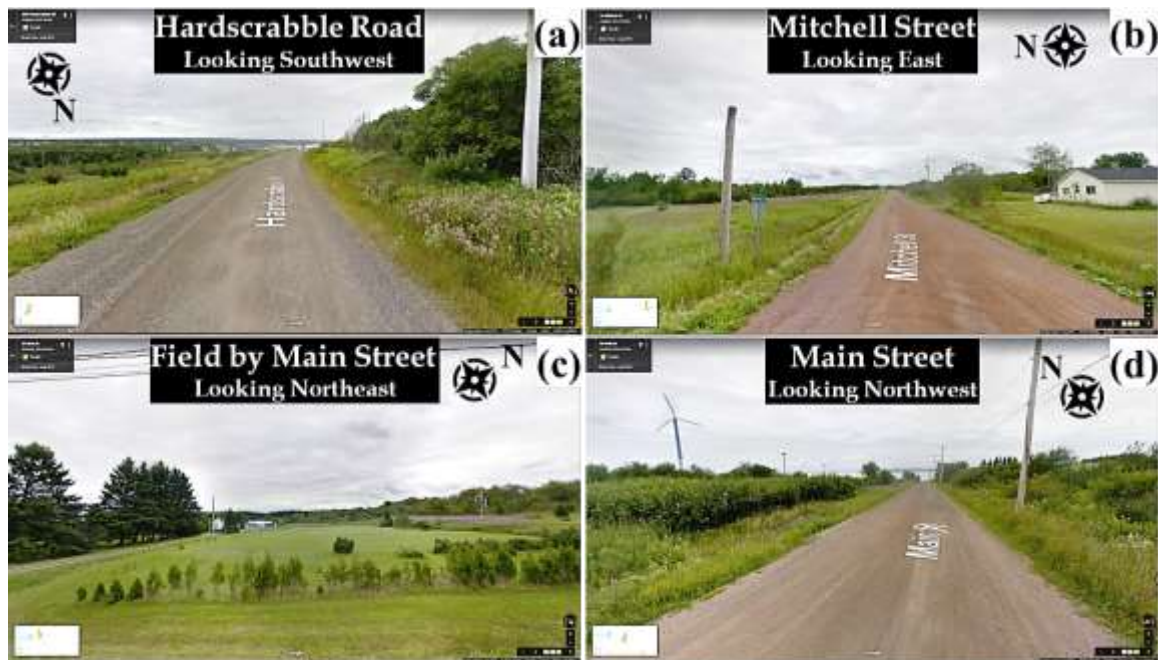


Figure 5.9: Representative images of the four GPR survey areas. The four areas over which GPR surveying was done includes (a) Hardscrabble Road, (b) Mitchell Street, (c) a grassy area adjacent to Main Street, and (d) Main Street (Google 2013).

5.7 Results

5.7.1 *Processed Radargrams*

The completion of the GPR survey at Joggins, Nova Scotia resulted in 42 unique radargrams across three road surfaces (Hardscrabble Road, Main Street, and Mitchell Street) and a grassy area adjacent to Main Street. The 42 processed radargrams are displayed in Figure 5.10. All radargrams have an initial high amplitude, thick, horizontally continuous reflector. It always occurs at the top of the radargram and follows the topography of the individual survey line.

In addition, all radargrams display a second high amplitude, thick, primarily horizontally continuous reflector that is always below the primary top reflector. It too will generally follow the topography of the individual survey line, but can be discontinuous. Numerous radargrams contain high amplitude, sharp, concave downwards reflectors that have a consistent shape and are either overlapping or have a consistent spacing. In general, coherent reflectors are absent below approximately 6 to 8 m depth. The resulting reflectors that are visible in the radargrams are summarized in the following radar reflectors section and in Figure 5.11. In total, 13 radar reflectors are described and interpreted.

5.7.2 *Radar Reflectors*

Selected results from four areas surveyed across the Joggins Formation are presented here. The variability in surficial features along the various surveys results in reflectors that can be correlated nicely to these features. A total of thirteen unique radar reflectors have been identified from the GPR data and are briefly summarized (Figure 5.11). RR1 is a high amplitude, thick reflection and is the first signal measured by the receiver and occurs in all

42 collected radargrams. It is continuous for the complete length of each radargram and is followed by a low amplitude signal. It follows the natural topography of the GPR survey line. There are no other features that occur with this reflector. RR2 is a high amplitude, thick reflection and is the second signal measured by the receiver and occurs in all 42 collected radargrams. It is typically continuous for the complete length of each radargram, although it can be discontinuous in several lines. It is followed by a low amplitude signal. It follows the natural topography of the GPR survey line. This reflector is affected by the subsurface and surficial features. Reflectors RR3 is characterized by a thin, high amplitude reflection, followed by a lower amplitude signal. This reflector occurs at approximately 8 m depth in the radargrams it occurs in, which is consistent with the approximate depth of the overburden in the area. The RR4 reflector is common throughout the radargrams. It is characterized by regularly spaced; high amplitude followed by low amplitude concave downwards reflectors. They have a consistent shape and are sharply outlined.

The RR5 reflector is also common throughout the radargrams. It is characterized by irregularly spaced; high amplitude followed by low amplitude concave downwards reflectors. They have a less consistent shape and are not as sharply outlined as the RR4 reflector. reflector RR6 is not common throughout the radargrams and is characterized by a break in the second thick, high amplitude reflector. The RR7 reflector is characterized by high amplitude, repeating, and parallel reflectors that reverberate throughout the radargram. The RR8 reflector is reflection-free. There are no coherent reflectors observed in the radargrams. RR9 is a thick, high amplitude, concave downwards reflection that only appears to be visible in a couple of radargrams. It is associated with the high amplitude, thick, continuous reflector (RR2). RR10 is a high amplitude, thick, and discontinuous

reflector that occurs below RR2. It displays an undulating profile and is only visible in a single radargram. RR11 is a continuous, upright, high/low amplitude reflector that mimics a teepee shape. It is very-well defined and sharp. It occurs in only five radargrams. RR12 is a vertical, mottled high and low amplitude reflector that is only visible in a single radargram. The features are not continuous throughout the whole radargram. RR13 is a small, near-surface, high amplitude reflector. It is concave downwards and sharp with a consistent shape. They are associated with RR2.

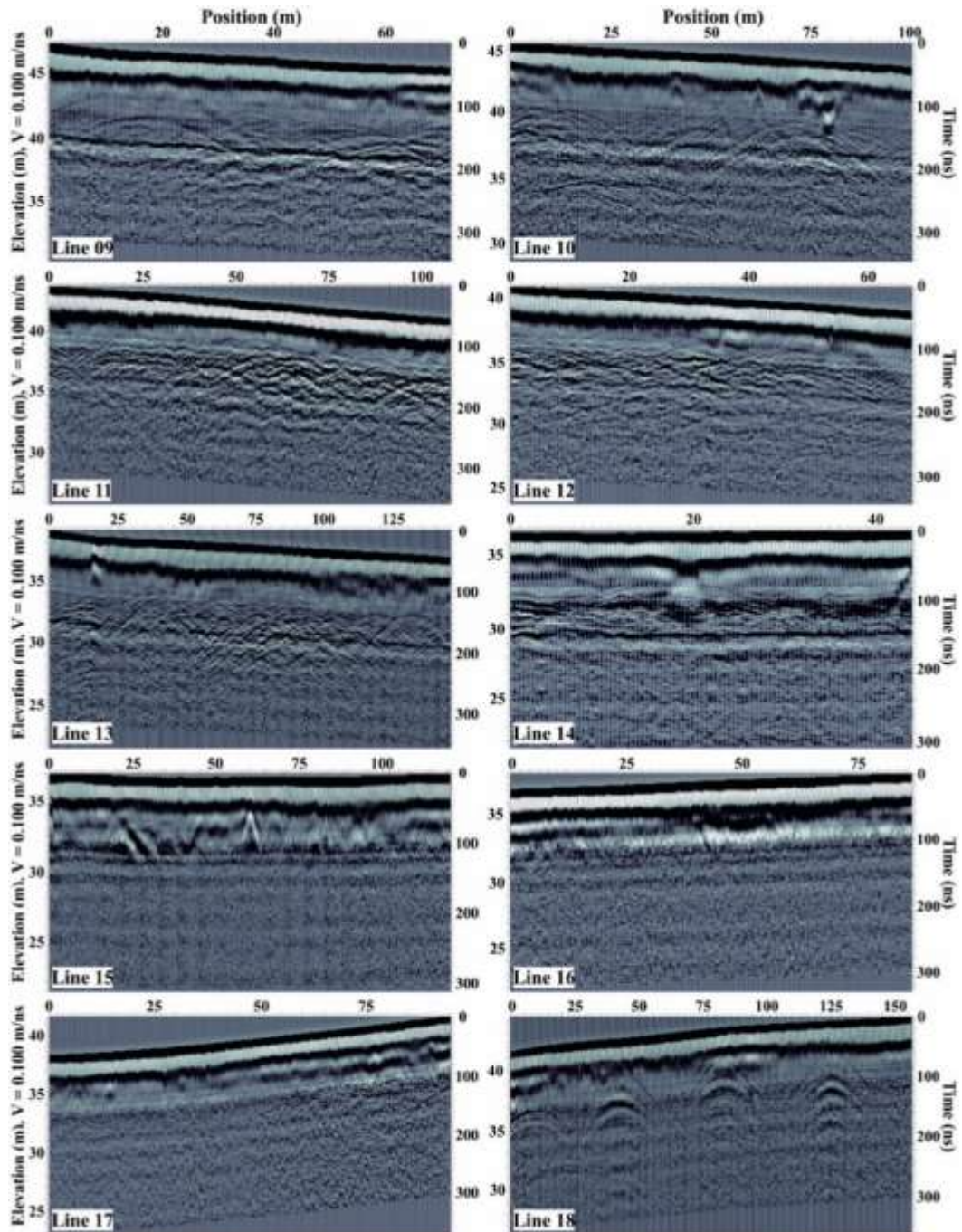


Figure 5.10: Radargrams for lines 09 to 18 inclusive with position on the upper abscissa, elevation on the left ordinate and time on the right ordinate. Radargrams for lines 19 to 28 inclusive with position on the upper abscissa, elevation on the left ordinate and time on the right ordinate. Radargrams for lines 29 to 38 inclusive with position on the upper abscissa, elevation on the left ordinate and time on the right ordinate. Radargrams for lines 39 to 51 inclusive with position on the upper abscissa, elevation on the left ordinate and time on the right ordinate.

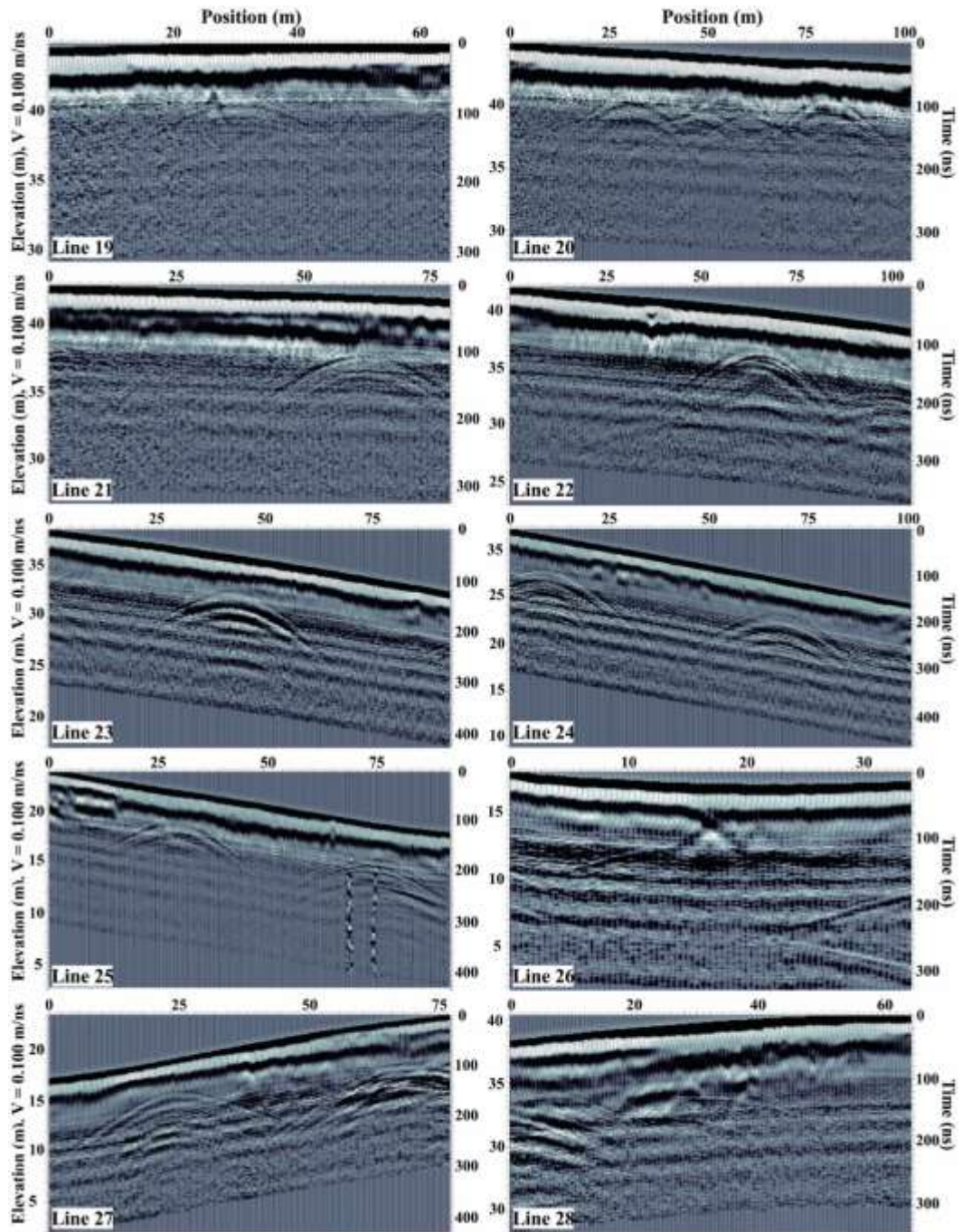


Figure 5.9: Continued.

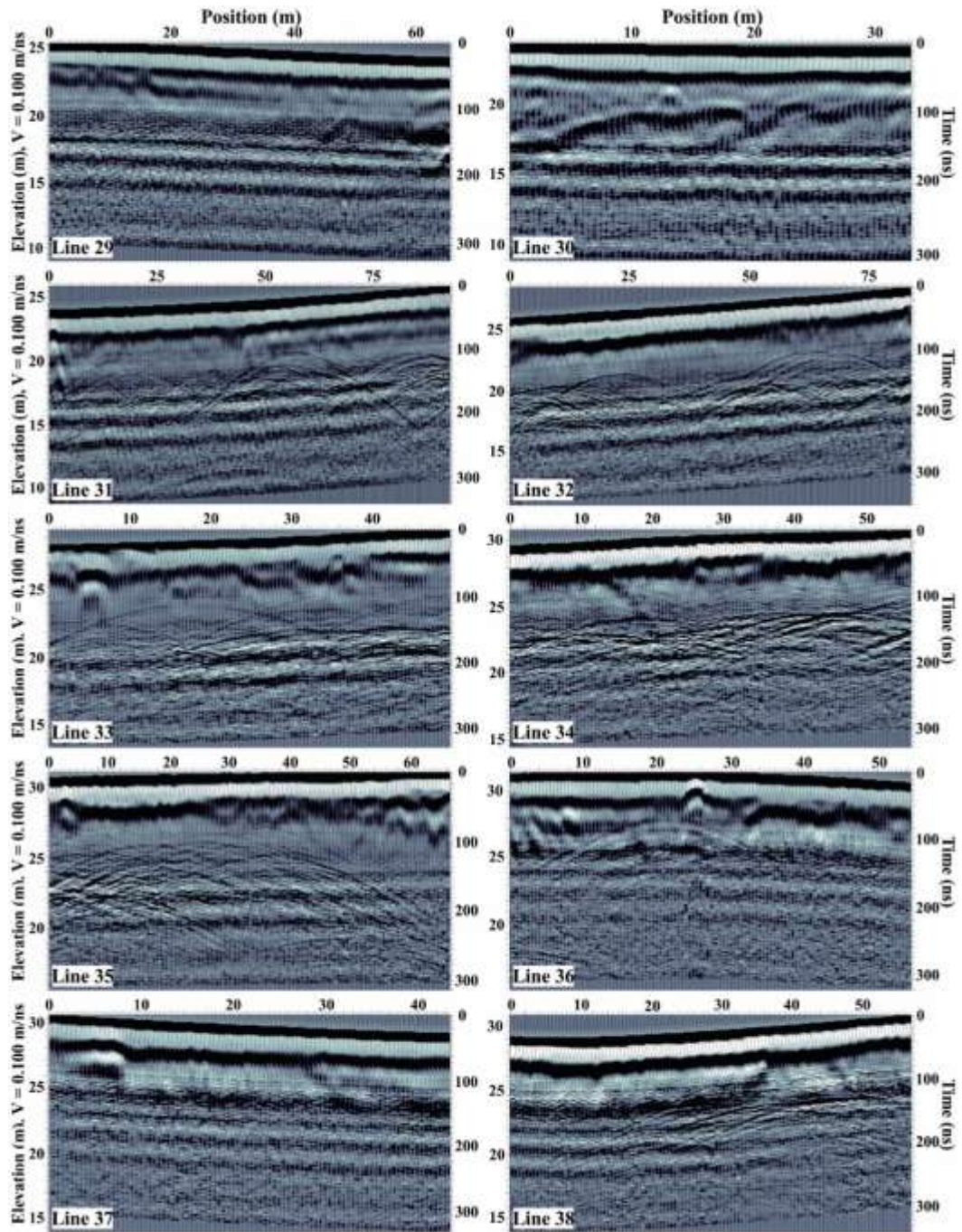


Figure 5.9: Continued.

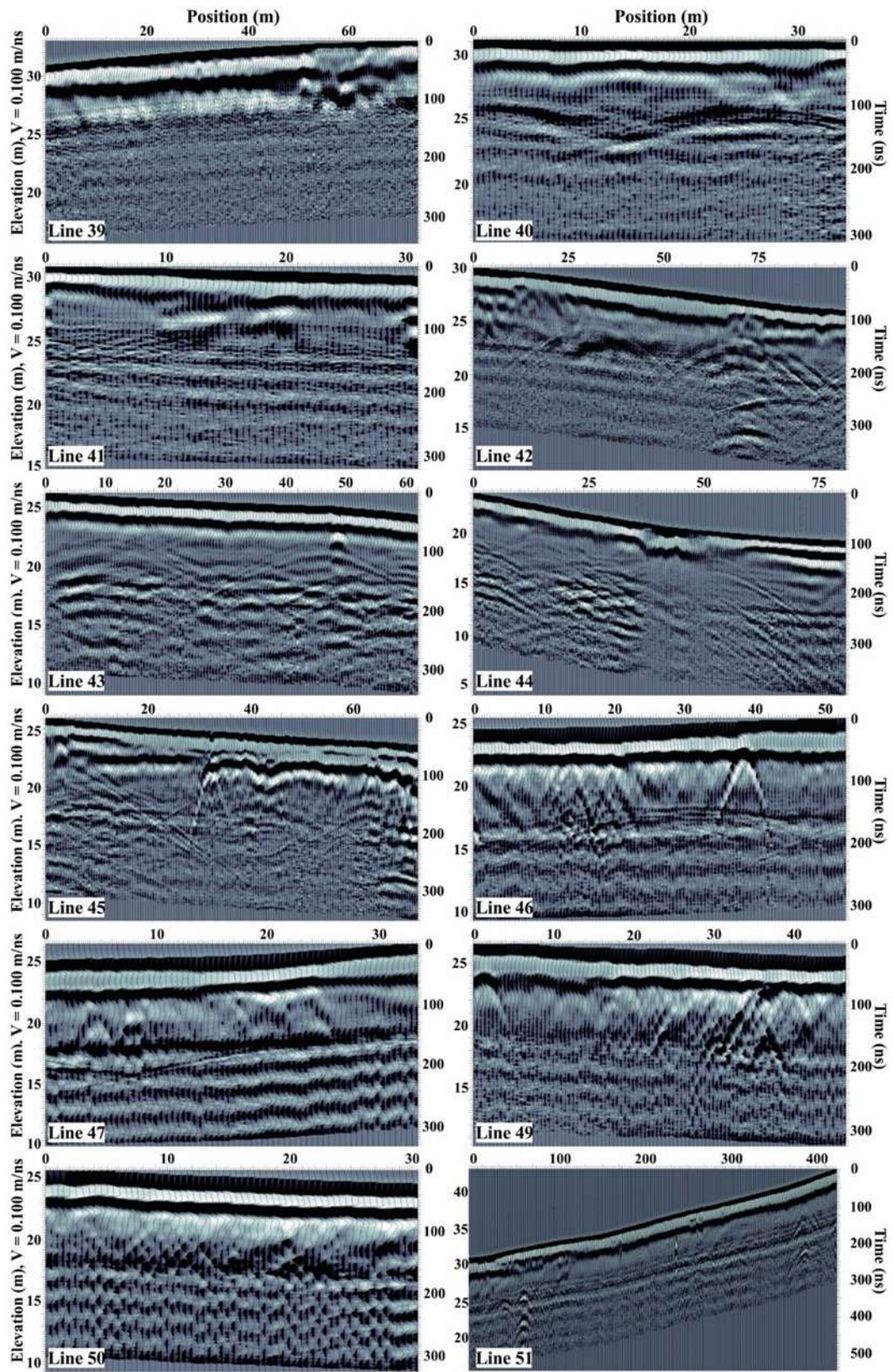


Figure 5.9: Continued.

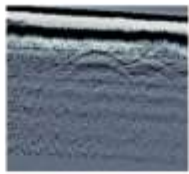

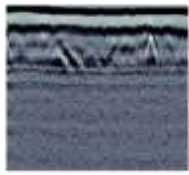


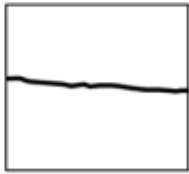
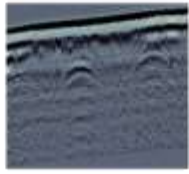
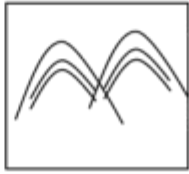



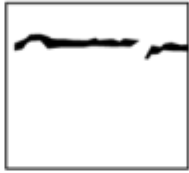

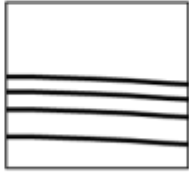
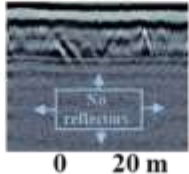
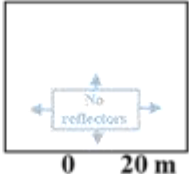
Radar Reflectors	GPR Example	GPR Interpretation	Associated Lines
RR1- High amplitude, thick, continuous reflector; always at top of profile			All (Hardscrabble Road, Main Street, grassy area off Main Street, and Mitchell Street)
RR2- High amplitude, thick, continuous reflector; always below primary top reflector			All (Hardscrabble Road, Main Street, grassy area off Main Street, and Mitchell Street)
RR3- High amplitude followed by low amplitude reflector; continuous; occurs at 6 to 8 m depth			9, 10, 11, 13, 14, 15, 29 (Hardscrabble Road); 51 (Mitchell Street)
RR4- Regularly spaced, high amplitude, sharp, concave downwards reflector; consistent shape			18, 19, 20, 21, 22, 23, 24, 25, 27, 36 (Hardscrabble Road); 42, 43, 44 (Main Street); 51 (Mitchell Street)
RR5- Irregularly spaced, high amplitude sharp, concave downwards reflector; inconsistent shape			9, 10, 11, 12, 13, 15, 20, 27, 31, 32, 33, 34, 35 (Hardscrabble Road); 51 (Mitchell Street)
RR6- Break in the high amplitude, thick, continuous reflector; always below primary top reflector			27, 39 (Hardscrabble Road); 45 (grassy area off Main Street)
RR7- High amplitude repeating reflector; reverberations			All (Hardscrabble Road, Main Street, grassy area off Main Street, and Mitchell Street)
RR8- Coherent reflectors are absent			All (Hardscrabble Road, Main Street, grassy area off Main Street, and Mitchell Street)

Figure 5.11: Radar reflectors identified in the 42 radargrams from Joggins. The radar reflectors and description, a GPR example from the data collected, the outline interpretation of that feature, and the associated lines the feature occurs in are shown.

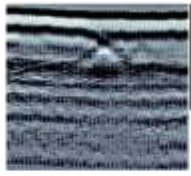





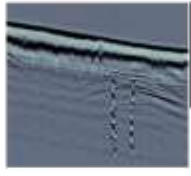
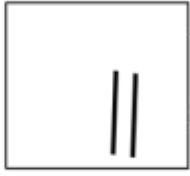
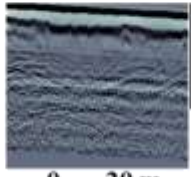

Radars Reflectors	GPR Example	GPR Interpretation	Associated Lines
RR9 - High amplitude, thick, concave downwards reflector; occurs with the high amplitude, thick, reflector that occurs below the primary top reflector			14, 26 (Hardscrabble Road)
RR10 - High amplitude, thick, reflector; discontinuous			30 (Hardscrabble Road)
RR11 - Continuous, upright, high/low amplitude reflector; mimic a teepee shape; very defined, sharp			15 (Hardscrabble Road); 45, 46, 47, 49 (grassy area off Main Street)
RR12 - Vertical high and low amplitude reflector; not continuous throughout the whole profile			25 (Hardscrabble Road)
RR13 - Small scale, near-surface, high amplitude sharp, concave downwards reflector; consistent shape			9, 10, 17, 18, 21, 24, 25, 35 (Hardscrabble Road)

Figure 5.10: Continued.

5.8 Discussion

RR1 is defined as the direct air wave. This high amplitude reflection is the first signal measured by the receiver and occurs in all 42 collected radargrams. It is continuous for the complete length of each radargram and is followed by a low amplitude signal. Typical examples of this radar reflector can be seen in all radargrams, including radargrams 31 and 37 (Figure 5.12). Since the radargrams have all been georeferenced, the direct air wave follows the topography.

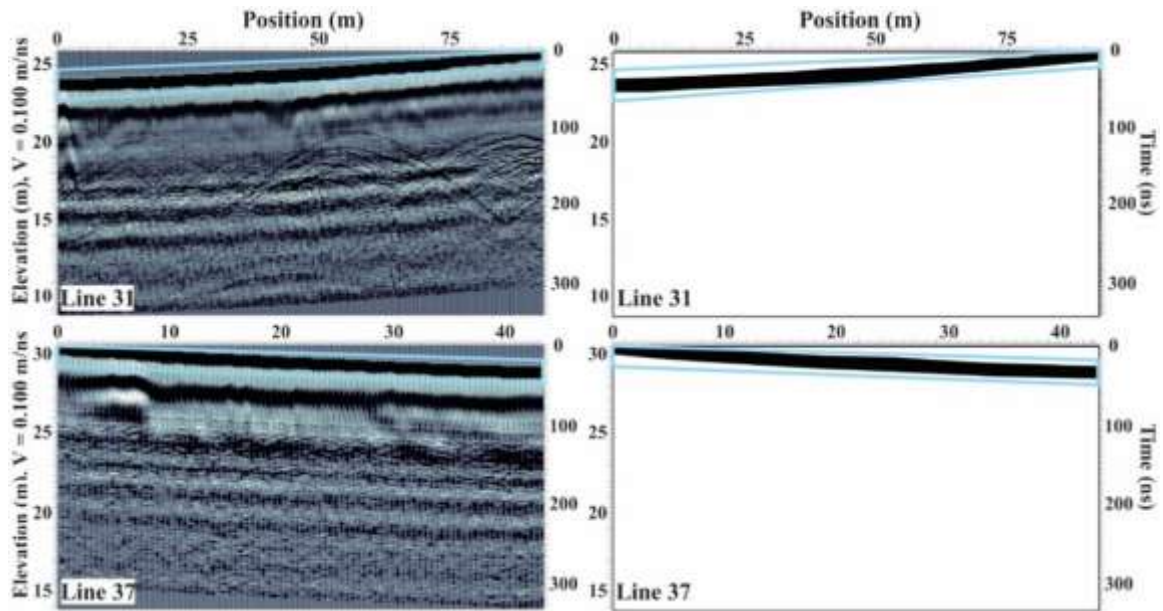


Figure 5.12: Uninterpreted and interpreted radargrams of lines 31 and 37 showing examples of radar reflector 1, which is interpreted to represent the direct air wave.

RR2 is defined as the direct ground wave. This high amplitude reflection is the second signal measured after the direct air wave and is also present in all 42 radargrams. The majority of the radargrams display a continuous direct ground wave, except for lines 27, 39, and 45 in which they are discontinuous. Typical examples of this radar reflector can be seen in all radargrams, including radargrams 31 and 43 (Figure 5.13). The undulating nature of the ground wave highlights the small topographic changes that occur over the lengths of each GPR line segment.

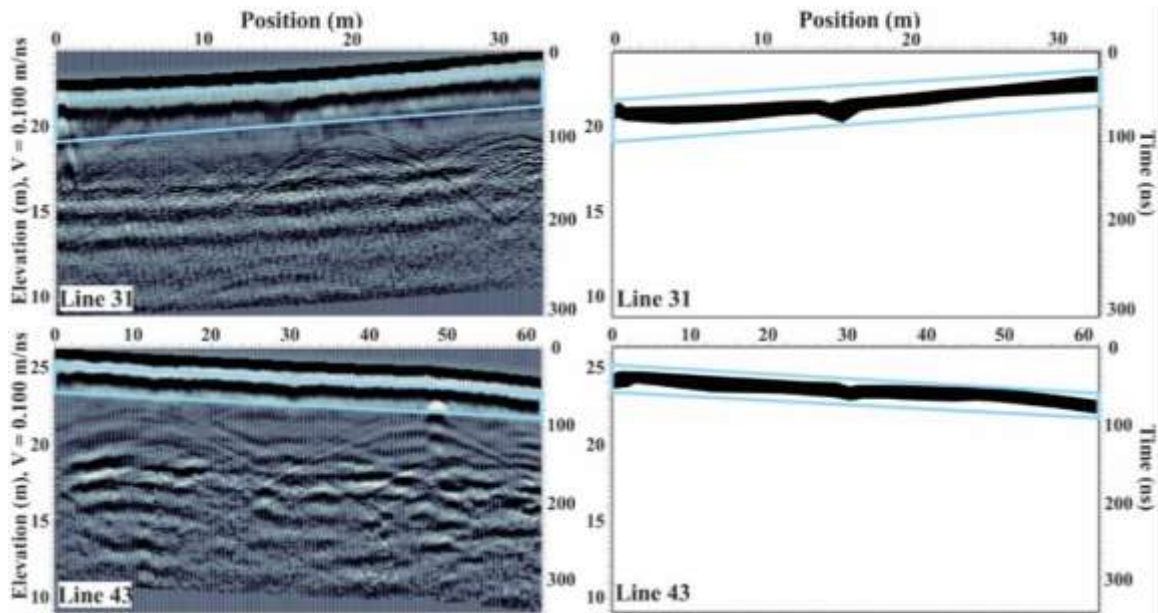


Figure 5.13: Uninterpreted and interpreted radargrams of lines 31 and 43 showing examples of radar reflector 2, which is interpreted to represent the direct ground wave.

RR3 is interpreted to represent the angular unconformity contact between the Carboniferous-aged Joggins Formation and the overlying Quaternary-aged glacial till and soil cover. The sharpness of the contact as well as the depth it is occurring at (6 to 8 m) are the main reasons for this interpretation. Curiously though, this reflector is not present in all radargrams, even though all survey lines were completed on top of overburden overlying the Joggins Formation. Examples of this radar reflector can be seen in several radargrams, including radargrams 09 and 13 (Figure 5.14).

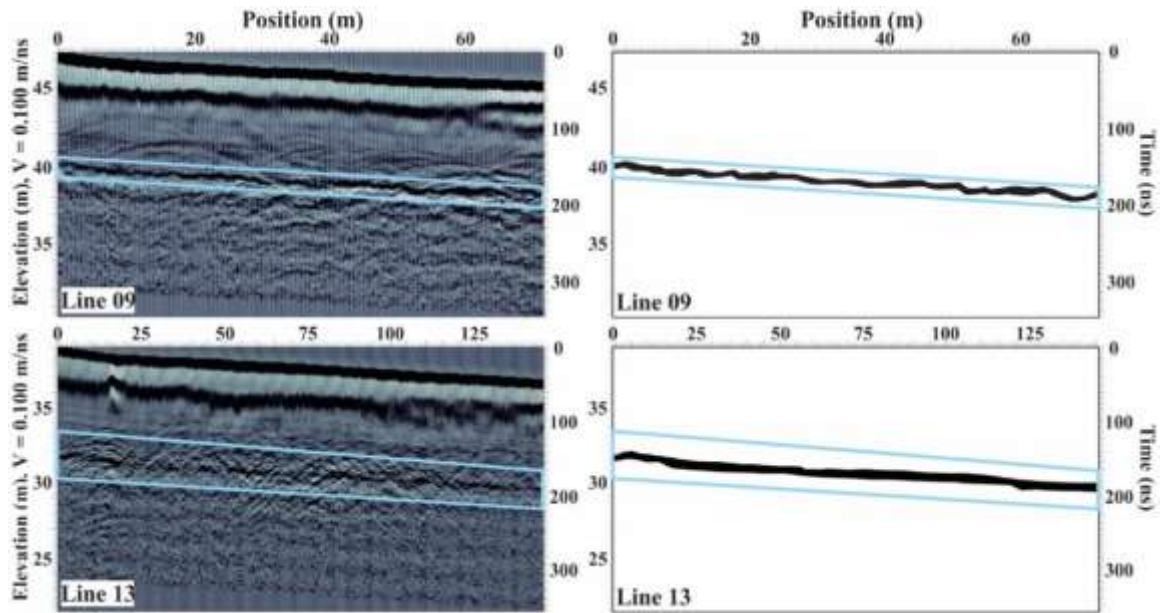


Figure 5.14: Uninterpreted and interpreted radargrams of lines 09 and 13 showing examples of radar reflector 3, which is interpreted to represent the angular unconformity contact.

The RR4 reflector correlates to utility poles that are erected at certain locations adjacent to the road surfaces. Several radargrams were recorded along road surfaces that have regularly spaced wooden utility poles located less than 10 m from the centerline of the road. The data from these lines show regularly spaced, clear, and sharp, concave downwards reflectors whose locations match those of the utility poles along the survey lines. Typical examples of this radar reflector can be seen in several radargrams, including radargrams 18 and 23 (Figure 5.15).

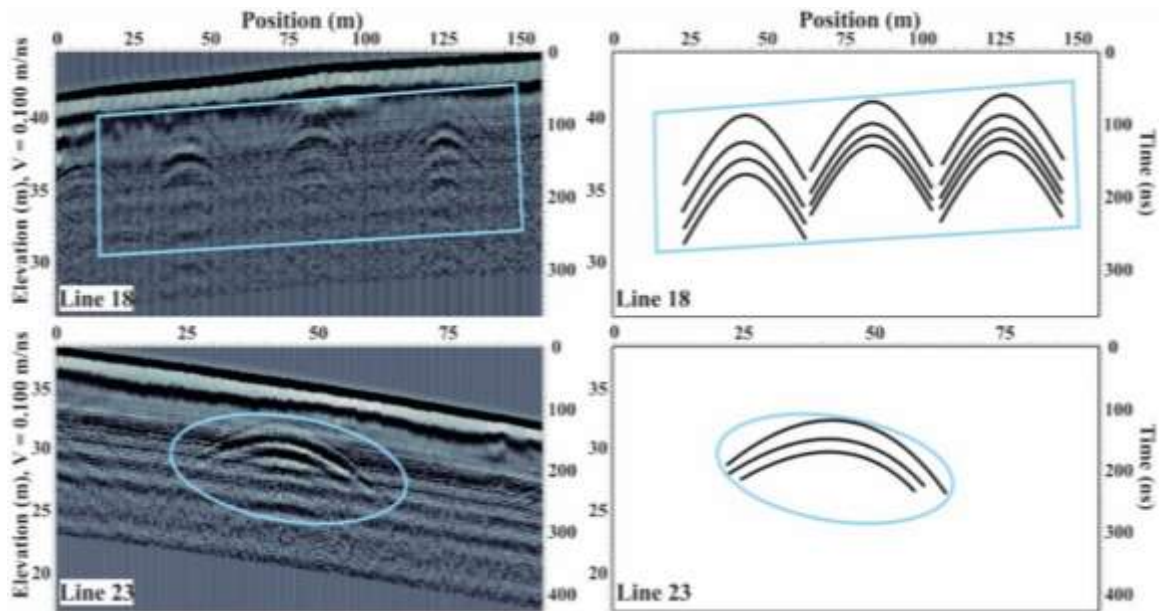


Figure 5.15: Uninterpreted and interpreted radargrams of lines 18 and 23 showing examples of radar reflector 4, which is interpreted to represent the utility poles adjacent to the road surfaces.

The RR5 reflector is also composed of concave downwards reflectors. However, these reflectors are noticeably different when compared to the utility poles described by RR4. Through careful examination of the radargrams, it was determined that RR5 represent trees. In contrast to the regularly spaced utility poles giving regular and clear diffraction hyperbolae, trees on the other hand produce hyperbolae that are randomly occurring and are overlapping. This theory was tested by viewing the GPR lines that did not have power line infrastructure located next to the road surface, but did have abundant, randomly occurring trees. Representative examples of this radar reflector can be seen in radargrams 10 and 32 (Figure 5.16).

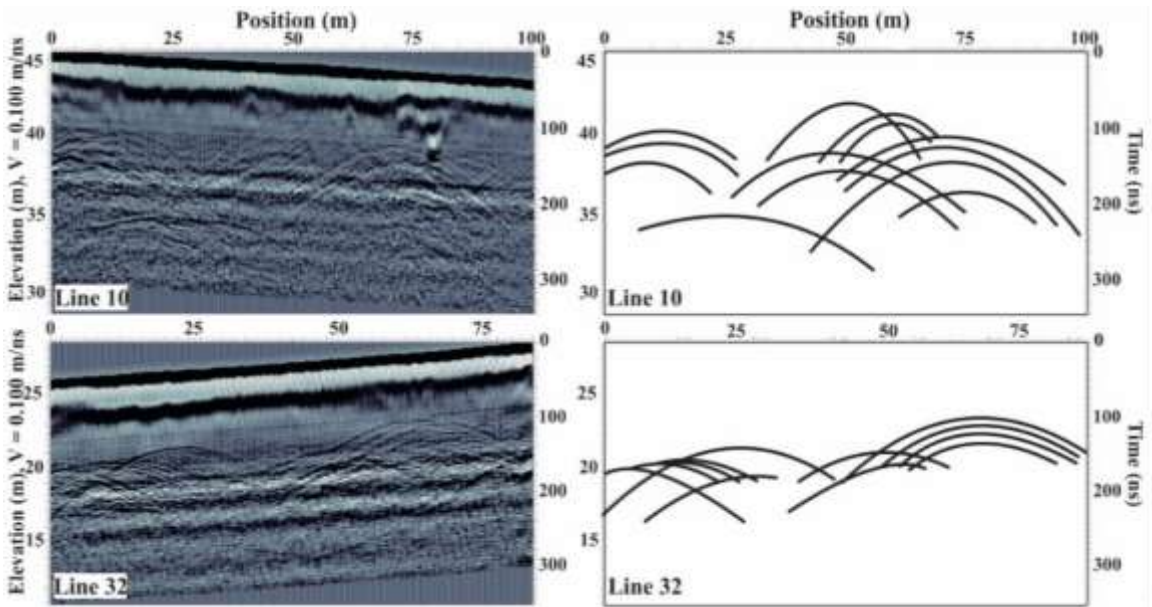


Figure 5.16: Uninterpreted and interpreted radargrams of lines 10 and 32 showing examples of radar reflector 5, which is interpreted to represent the reflections caused by trees adjacent to the road surfaces.

The RR6 reflector is rarely observed in the radargrams. The survey lines where this reflector becomes discontinuous are also the areas where the GPR has passed beneath a power line. It can therefore be surmised that overhead power lines can cause a brief break in the direct ground wave. Typical examples of this radar reflector can be seen in radargrams 27 and 39 (Figure 5.17).

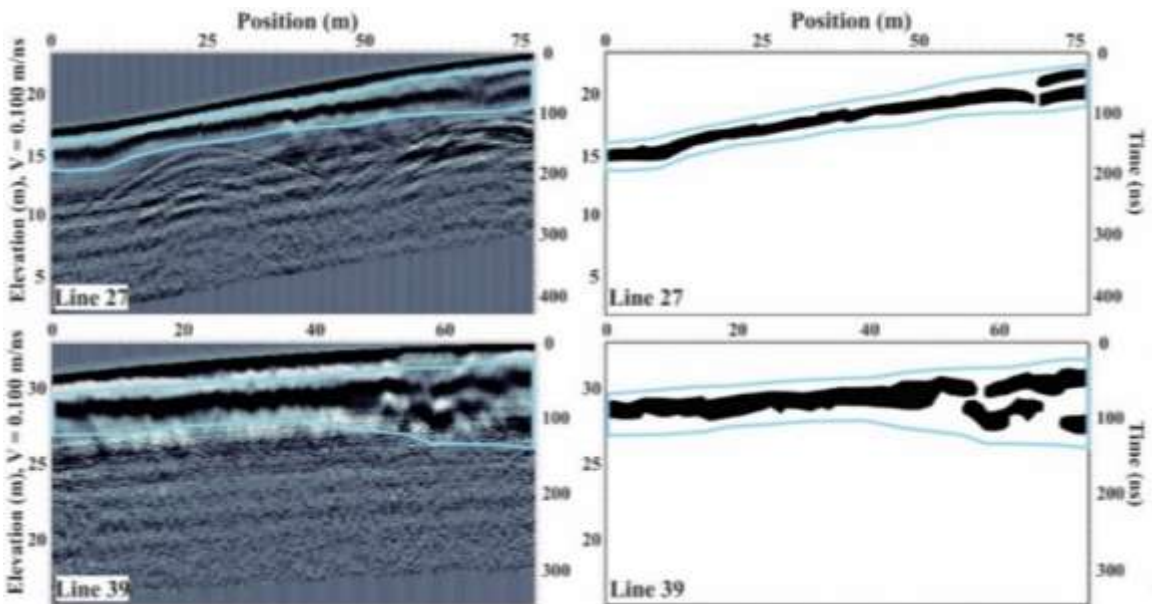


Figure 5.17: Uninterpreted and interpreted radargrams of lines 27 and 39 showing examples of radar reflector 6, which shows the direct ground wave becoming discontinuous when the GPR survey passes beneath a power line.

The RR7 reflector represent multiples or reverberations of the electromagnetic energy, probably as a result of the clay-rich soil and glacial till. These types of reflectors occur throughout all the radargrams, although they may be subtle. Representative examples of this radar reflector are shown in radargrams 29 and 31 (Figure 5.18).

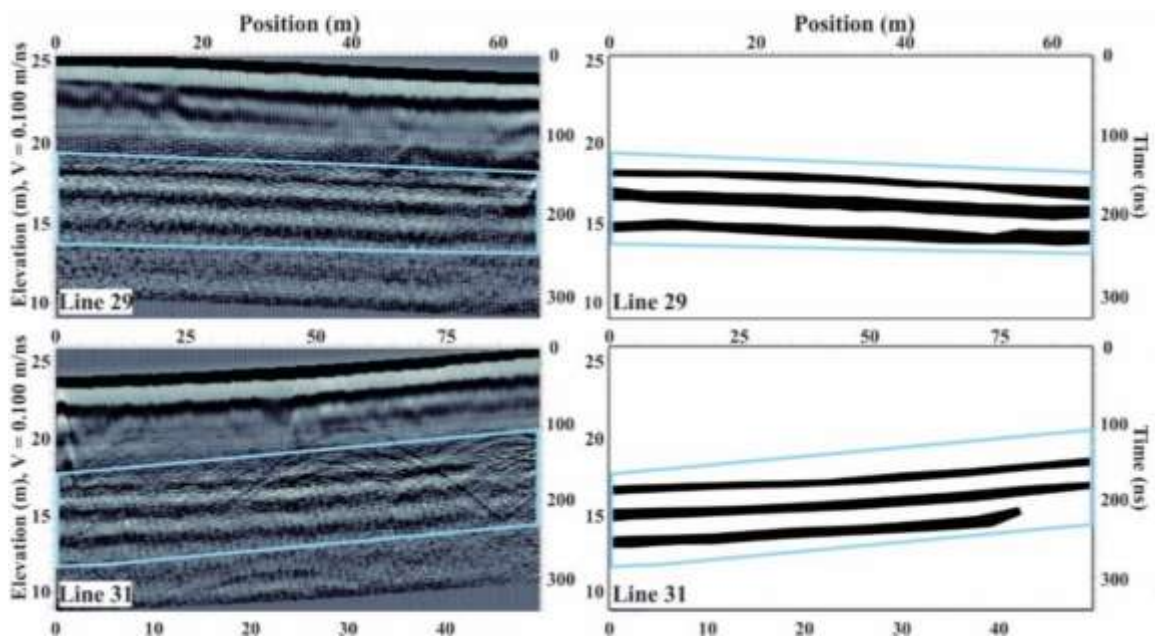


Figure 5.18: Uninterpreted and interpreted radargrams of lines 29 and 31 examples of radar reflector 7, which shows multiples or reverberations within the data.

We interpret the RR8 reflector as areas where the GPR signal has been attenuated. This typically signifies either a lithological unit that is massive and homogenous, the presence of dissolved minerals in groundwater with highly conductive properties, and/or the presence of clay-rich sediments (e.g., (e.g., Heteren et al. 1998; Ékes and Friele 2003)). In this study, it was determined that the attenuation was caused by the overlying clay-rich glacial till and soil. This reflector makes up the majority of all radargrams and is widespread among all 42 radargrams, indicating that at least locally, the clay-rich glacial till and soil are probably

present. Typical examples of the attenuated signal can be seen in radargrams 19 and 20 (Figure 5.19).

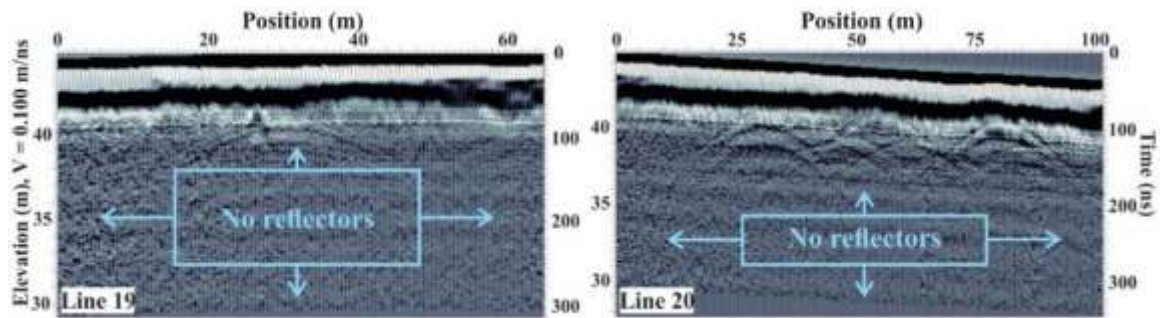


Figure 5.19: Uninterpreted radargrams of lines 19 and 20 showing examples of radar reflector 8, which show examples of the attenuated GPR signals.

The RR9 reflector is rarely observed in the radargrams but is interpreted to represent culverts that are installed beneath the road surface. Typical examples of this radar reflector can be observed in radargrams 14 and 26 (Figure 5.20) It was not observed if a culvert actually exists beneath the line 14 road segment of Hardscrabble Road; however, one was observed beneath the segment of Hardscrabble Road traversed by line 26.

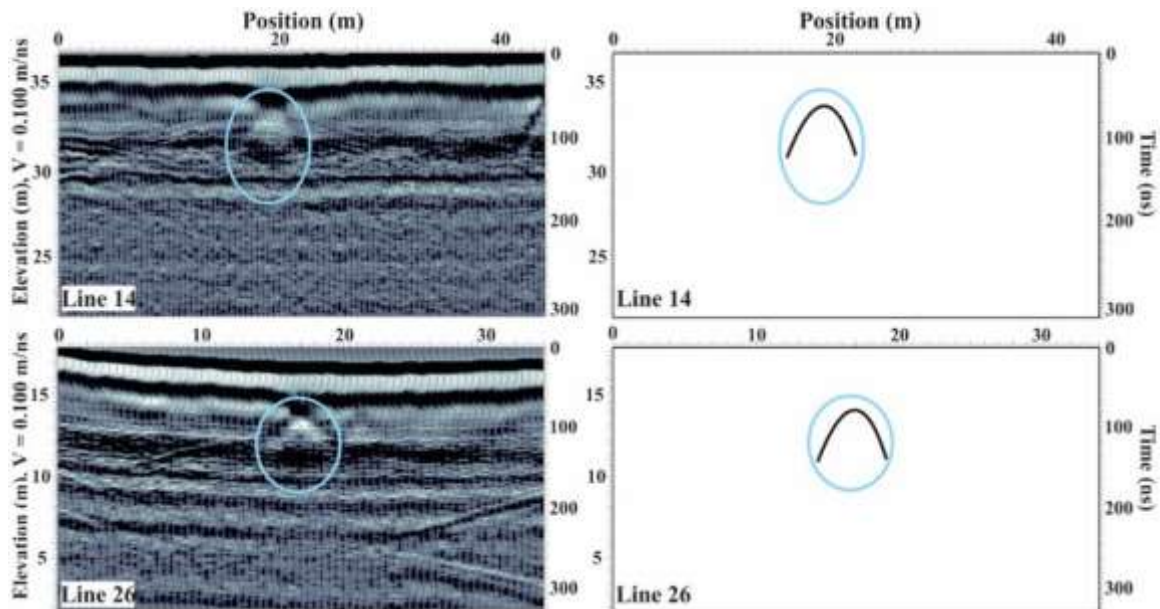


Figure 5.20: Uninterpreted and interpreted radargrams of lines 14 and 26 showing examples of radar reflector 9, which is interpreted to represent culverts beneath the roadway.

RR10 is interpreted to represent the undulating angular unconformity contact between the Carboniferous-aged Joggins Formation and the overlying Quaternary-aged glacial till and soil cover. The sharpness of the contact as well as the depth it is occurring at (6 to 8 m) are the main reasons for this interpretation. The lone example of this radar reflector can be seen in radargram 30 (Figure 5.21).

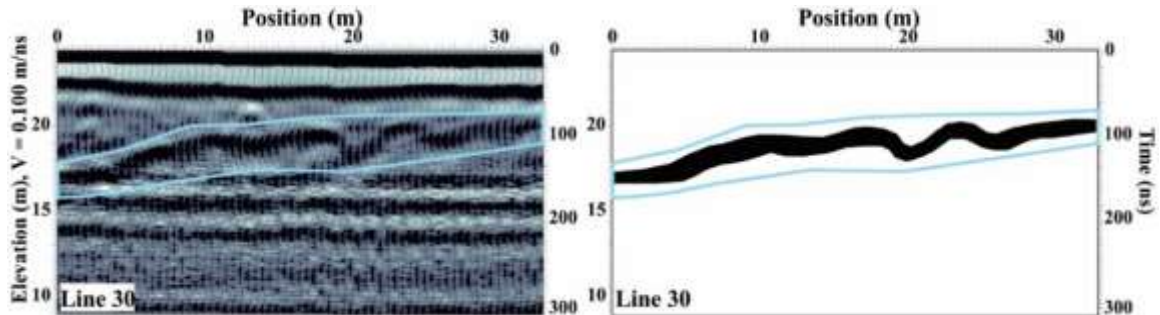


Figure 5.21: Uninterpreted and interpreted radargram of line 30 showing examples of radar reflector 10, which has been interpreted to represent the undulating angular unconformity contact.

RR11 is interpreted to represent small diameter metal pipes or boulders. The only instance of this type of reflector on a road surface was line 15 across Hardscrabble Road. The remainder of these reflectors were found occurring in the grassy area adjacent to Main Street. Typical examples of this radar reflector can be seen in radargrams 45 and 46 (Figure 5.22).

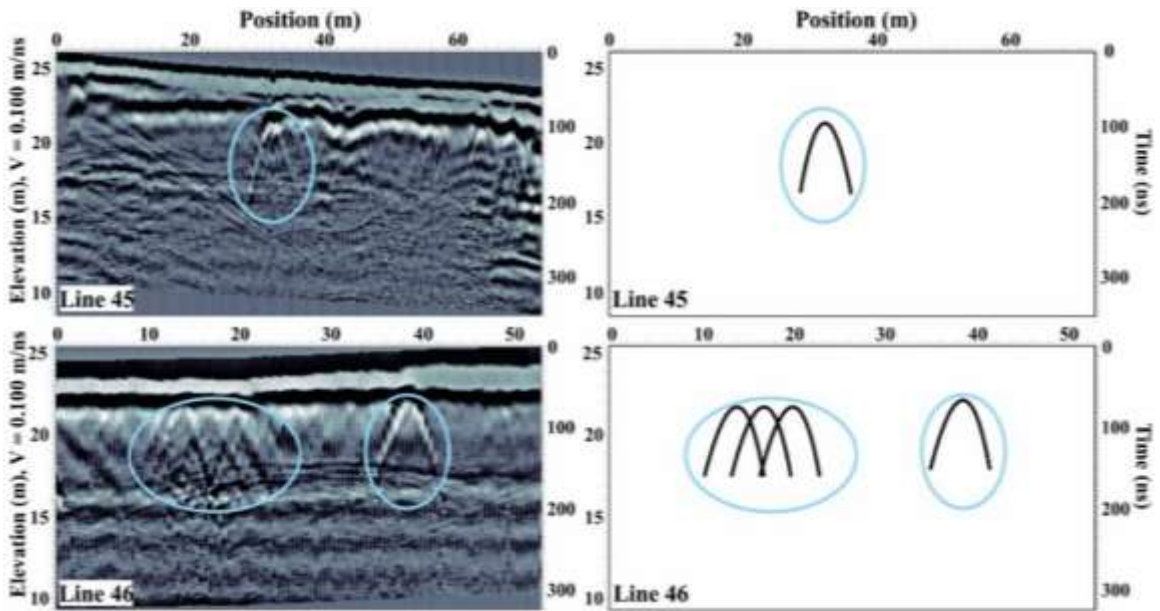


Figure 5.22: Uninterpreted and interpreted radargrams of lines 45 and 46 showing examples of radar reflector 11, which is interpreted to represent metal pipes and/or boulders.

RR12 is interpreted to be two instances where data skips occurred (not collected at a trace location). These two vertical features are not related to any subsurface features. The sole example of this radar reflector can be seen in radargram 25 (Figure 5.23). Despite these two instances of non-signal, there are noticeable repeating hyperbolae occurring in the background, which correlates to the wooden utility pole at position 75 m near the end of the line.

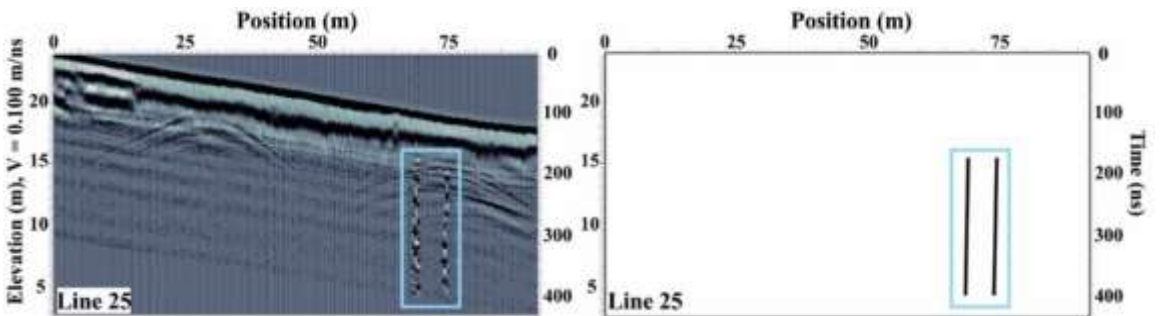


Figure 5.23: Uninterpreted and interpreted radargram of line 25 showing examples of radar reflector 12, which has been interpreted to represent data skips.

RR13 is interpreted to represent the locations of boulders and are associated with the RR2 radar reflector (direct ground wave). Since the area does contain several meters of

glacial till, it would be reasonable to assume that larger rocks are present beneath the areas traversed with the GPR. Typical examples of this radar reflector can be seen in radargrams 09 and 10 (Figure 5.24).

Performing a GPR survey as it was done over the Joggins Formation presented a number of challenges. In the 42 radargrams that were gathered over the study area, it does not appear that any contain reflections that would be considered those of the Joggins Formation. The most probable culprit for the failure in imaging the Joggins Formation strata is the thick clay-rich soil and glacial till overburden that would have greatly attenuated (radar reflector 8) the transmitted energy in the subsurface.

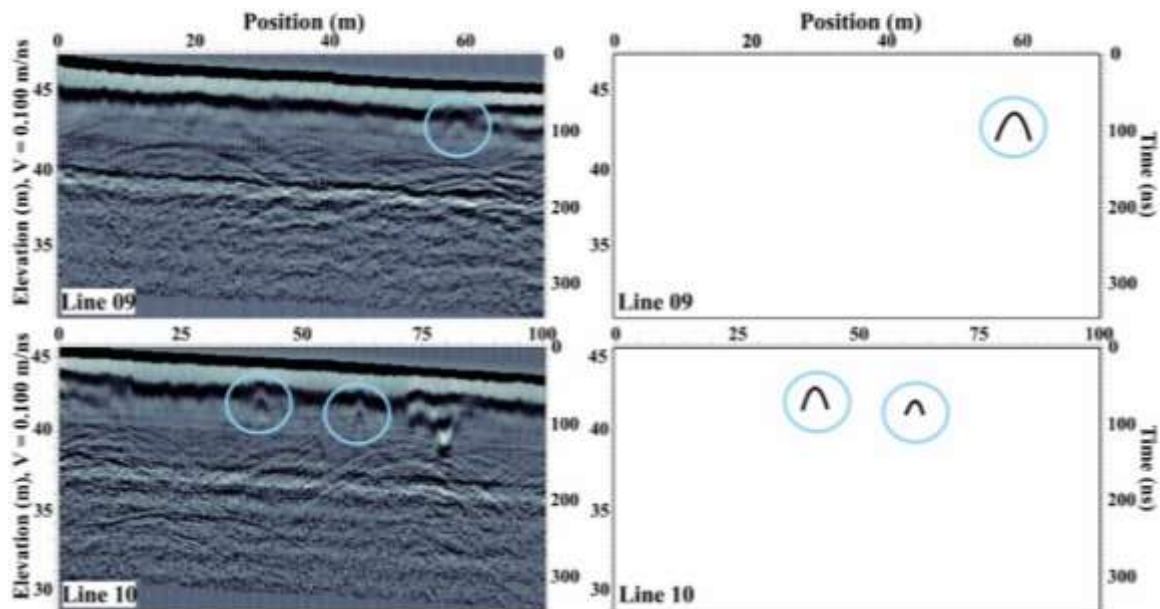


Figure 5.24: Uninterpreted and interpreted radargrams of lines 09 and 10 showing examples of radar reflector 13, which is interpreted to represent boulders.

Another probable culprit is the Joggins Formation itself. It is well known from viewing the outcrop on the intertidal area that the strata dip at a constant 21° and are highly variable with respect to both lithology and thickness. Sedimentary beds of a certain thickness would not be visible since they are below the resolution of the antennae used. Furthermore, the beds are composed of a wide range of lithologies, from clay-sized

particles up to gravel-sized particles; thus, the individual beds themselves could be contributing to attenuation as well. Power lines run along the edge of the roads that were surveyed, which may result in some problems. At certain sections of the survey, the GPR was near the cliff edge. This could translate into some edge effects in the radargrams.

The GPR data are contaminated to varying degrees by above-ground objects. Several lines were recorded along road surfaces that have regularly spaced wooden utility poles located less than 10 m from the centerline of the road. The data from these lines show regularly spaced and crisp/clear hyperbolae that correlate with the locations of the utility poles along the survey lines. Typical examples are shown in with radar reflector 4. The positions of these hyperbolae correspond with the above-ground positions of two utility poles along the survey line. These similar types of diffraction hyperbolae occur from lines 18 to 25, 27, and 36 collected on Hardscrabble Road, Line 51 collected on Mitchell Street, and lines 42 to 44 collected on Main Street; all of which have power line infrastructure.

In contrast to the regularly spaced utility poles giving regular and clear diffraction hyperbolae, trees on the other hand also cause a similar phenomenon in the radargrams, except that the hyperbolae occur randomly and are overlapping. This theory was tested by viewing the GPR lines that did not have power line infrastructure located next to the road surface, but did have abundant, randomly occurring trees. Typical examples are shown in radar reflector 5, which displays abundant, irregularly spaced and overlapping hyperbolae. Similar diffraction hyperbolae occur in lines 9 to 13 and 31 to 35 on Hardscrabble Road, and Line 43 on Main Street.

In a few instances, a power line will cross over Hardscrabble Road or Main Street. When this occurs, a noticeable feature can be observed in the radargrams (radar reflector

6). The clear and crisp reflectors that are typical with the utility poles become more chaotic. This would infer that the power lines passing overhead do influence the GPR signals.

5.9 Conclusions

In this study, we have utilized GPR in an attempt to image the internal geometry and architecture of the Joggins Formation and thus, aid with extending the 2D outcrop into 3D by way of modeling the larger scale features. Through iterations of GPR processing techniques and examination of the resulting radargrams, it can be concluded that the survey was unsuccessful in showing Joggins Formation structures and internal architecture. This is likely the result of a combination of factors, with the dominant one being the thick, highly conductive nature of the clay-rich glacial till/overburden. Unfortunately, it was determined that numerous difficulties relating to both the Joggins Formation itself and the area over which the GPR data was collected made any imaging of the Joggins Formation non-occurrence. The imaging issues that are directly related to the Joggins Formation most likely include (1) dipping beds cause increased refraction, unlike a horizontal or nearly horizontal bed, (2) the scale of the beds is too fine for the GPR configuration used for individual beds; at best, it could only image the thicker beds, and (3) the abundant jointing and fracturing visible in the outcrop exposure probably permeates throughout the subsurface, thereby compounding imaging problems. It is possible that lower frequency antennae could have provided a depth of penetration sufficient to image the Joggins Formation; however, the resolution would have been affected and the likelihood of being able to interpret the dipping strata would have been compromised. Greater success might have resulted if GPR surveying was conducted in an area with thinner overburden.

A variety of overburden and surface/subsurface objects may also affect the GPR data collection. Some of the most likely issues include (1) the soil and glacial till making up the overburden layer are clay-rich, thereby leading to signal attenuation, (2) the compacted road surface also has clay materials, in addition to other materials which would also enhance signal attenuation, (3) metallic/wooden objects either exposed at the surface or buried will create additional artifacts in the radargrams. These objects include galvanized steel guard rails, overhead power lines and their associated infrastructure, traffic signage, and cars parked in driveways or passing the GPR equipment while collecting data. Other potential issues that may hamper efforts include the uneven terrain the data was collected on and whether there are GPR data collection issues near the edge of a vertical cliff face. The effects of surface objects, such as trees and utility lines are well-documented as being the culprits of many diffraction hyperbolae seen in the radargrams.

Despite the lack of subsurface imaging from the Joggins Formation, significant insight was gained as to the limitations of the GPR application in this type of environment. There was also some moderate success in imaging the angular unconformity, which was apparent in several radargrams. Perhaps the imaging of the unconformity was related to variations in overburden thickness and/or clay content. Although the primary objective of imaging the Joggins Formation was unsuccessful, it nevertheless increased our knowledge concerning the true impact of clay-rich overburden sediments on bedrock imaging, in addition to the impacts that surface features can cause on GPR data collection. The knowledge gained from this study can be utilized in future GPR surveys, particularly with respect to geoforensic studies where the study areas contain similar surface infrastructure (e.g., utility poles, power lines, etc.). This study also demonstrates the usefulness of

shallow subsurface GPR for geohazard assessments. It is important to reiterate that this was the site of extensive past coal mining efforts with well-developed surface infrastructure. Therefore, the area probably contains an abundance of erratic metal objects, large boulders, etc., that would have an influence on the generated radargrams.

5.10 Acknowledgments

This work was made possible by the Dalhousie University Basin and Reservoir Laboratory and its members. We are grateful to Bill Richards for providing helpful suggestions and sound advice for improving this paper. We also acknowledge Dr. Lawrence Plug for allowing the use of his GPS equipment. We thank the anonymous reviewers for their suggestions and comments.

5.11 References Cited in Chapter 5

Allen, J.P., Fielding, C.R., Rygel, M.C., and Gibling, M.R. 2013. Deconvolving Signals of Tectonic and Climatic Controls From Continental Basins: An Example From the Late Paleozoic Cumberland Basin, Atlantic Canada. *Journal of Sedimentary Research*, **83**: 847-872. doi:10.2110/jsr.2013.58.

Annan, A.P. Practical Processing of GPR Data. *In* Second Government Workshop on Ground Penetrating Radar. 1999. Sensors and Software Inc., pp. 1-18.

Annan, A.P. 2003. Ground Penetrating Radar Principles, Procedures & Applications. Sensors and Software Inc. pp. 1-286.

Archer, A.W., Calder, J.H., Gibling, M.R., Naylor, R.D., Reid, D.R., and Wightman, W.G. 1995b. Invertebrate trace fossils and agglutinated foraminifera as indicators of marine influence within the classic Carboniferous section at Joggins, Nova Scotia, Canada. *Canadian Journal of Earth Sciences*, **32**: 2027-2039. doi:10.1139/e95-156.

Barboza, E.G., Rosa, M.L.C.C., Dillenburg, S.R., da Silva, A.B., and Tomazelli, L.J. 2014. Stratigraphic analysis applied on the recognition of the interface between marine and fluvial depositional systems. *Journal of Coastal Research*, **70**: 687-692. doi:10.2112/SI70-116.1.

Beres Jr., M., and Haeni, F.P. 1991. Application of ground-penetrating-radar Methods in Hydrogeologic Studies. *Groundwater*, **29**: 375-386. doi:10.1111/j.1745-6584.1991.tb00528.x.

Brand, U. 1994. Continental hydrology and climatology of the Carboniferous Joggins Formation (lower Cumberland Group) at Joggins, Nova Scotia: evidence from the geochemistry of bivalves. *Palaeogeography, Palaeoclimatology, Palaeoecology*, **106**: 307-321. doi:10.1016/0031-0182(94)90016-7.

Browne, G.H., and Plint, G.A. 1994. Alternating braidplain and lacustrine deposition in a strike-slip setting: The Pennsylvanian Boss Point Formation of the Cumberland Basin, Maritime Canada. *Journal of Sedimentary Research*, **64**: 40-59. doi:10.1073-1318/94/0B64-40/\$03.0.

Calder, J.H., and Boon, J. 2007. Joggins Fossil Cliffs: Property Nominated for Inscription on the World Heritage List. Nova Scotia Department of Natural Resources, Mineral Resources Branch, Halifax, NS. pp. Open File Map ME 2007-2001.

Calder, J.H., Gibling, M.R., Scott, A.C., Davies, S.J., Herbert, B.L., Greb, S.F., and DiMichele, W.A. 2006. A fossil lycopsid forest succession in the classic Joggins section of Nova Scotia: paleoecology of a disturbance-prone Pennsylvanian wetland. *Special Papers - Geological Society of America*, **399**: 169. doi:10.1130/2006.2399(09).

Carpenter, D.K., Falcon-Lang, H.J., Benton, M.J., and Grey, M. 2015. Early Pennsylvanian (Langsettian) fish assemblages from the Joggins Formation, Canada, and their implications for palaeoecology and palaeogeography. *Palaeontology*, **58**: 661-690. doi:10.5061/dryad.b0551.

Carroll, R.L. 1967. Labyrinthodonts from the Joggins Formation. *Journal of Paleontology*, **41**: 111-142.

Davies, S.J., and Gibling, M.R. 2003. Architecture of coastal and alluvial deposits in an extensional basin: the Carboniferous Joggins Formation of eastern Canada. *Sedimentology*, **50**: 415-439. doi:10.1046/j.1365-3091.2003.00553.x

Davies, S.J., Gibling, M.R., Rygel, M.C., Calder, J.H., and Skilliter, D.M. 2005. The Pennsylvanian Joggins Formation of Nova Scotia: sedimentological log and stratigraphic framework of the historic fossil cliffs. *Atlantic Geology*, **41**: 87-102. doi:10.4138/182.

Dillenburg, S.R., Barboza, E.G., Rosa, M.L.C., Caron, F., and Sawakuchi, A.O. 2017. The complex prograded Cassino barrier in southern Brazil: Geological and morphological evolution and records of climatic, oceanographic and sea-level changes in the last 7–6 ka. *Marine Geology*, **390**: 106-119. doi:10.1016/j.margeo.2017.06.007.

Dillenburg, S.R., Hesp, P.A., Keane, R., da Silva, G.M., Sawakuchi, A.O., Moffat, I., Barboza, E.G., and Bitencourt, V.J. 2020. Geochronology and evolution of a complex barrier, Younghusband Peninsula, South Australia. *Geomorphology*, **354**: 1-13. doi:10.1016/j.geomorph.2020.107044.

Dojack, L. 2012. Ground Penetrating Radar Theory, Data Collection, Processing, and Interpretation: A Guide for Archaeologist. University of British Columbia, Laboratory of Archaeology, University of British Columbia.

Ékes, C., and Friele, P. 2003. Sedimentary architecture and post-glacial evolution of Cheekye fan, southwestern British Columbia, Canada. Geological Society, London, Special Publications, **211**: 87-98. doi:10.1144/gsl.Sp.2001.211.01.08.

Falcon-Lang, H.J. 2009. Earliest history of coal mining and grindstone quarrying at Joggins, Nova Scotia, and its implications for the meaning of the place name “Joggins”. *Atlantic Geology*, **45**: 1-20. doi:10.4138/atlgeol.2009.001.

Gibling, M.R. 2006. Width and Thickness of Fluvial Channel Bodies and Valley Fills in the Geological Record: A Literature Compilation and Classification. *Journal of Sedimentary Research*, **76**: 731-770. doi:10.2110/jsr.2006.060.

Gibling, M.R., Calder, J.H., Ryan, R., Poll, H.W.v.d., and Yeo, G.M. 1992. Late Carboniferous and Early Permian drainage patterns in Atlantic Canada. *Canadian Journal of Earth Sciences*, **29**: 338-352. doi:10.1139/e92-030.

Google. 2013. Streetview. Google Inc.

Google Maps. 2020. Google basemap of Joggins Area. Google.

Grey, M., and Finkel, Z.V. 2011. The Joggins Fossil Cliffs UNESCO World Heritage site: a review of recent research. *Atlantic Geology*, **47**: 185-200. doi:10.4138/atlgeol.2011.009.

Heteren, S.V., Fitzgerald, D.M., Mckinlay, P.A., and Buynevich, I.V. 1998. Radar facies of paraglacial barrier systems: coastal New England, USA. *Sedimentology*, **45**: 181-200. doi:10.1046/j.1365-3091.1998.00150.x.

Jol, H.M. 2009. *Ground Penetrating Radar Theory and Applications*. Elsevier Science, Oxford.

Jol, H.M., and Smith, D.G. 1991. Ground penetrating radar of northern lacustrine deltas. *Canadian Journal of Earth Sciences*, **28**: 1939-1947. doi:10.1139/e91-175.

Kelly, T.B., and Wach, G.D. 2020. Analysis of factors influencing the interpretation of a digitally examined fluvial meanderbelt system: Joggins Formation, Nova Scotia. *Canadian Journal of Earth Sciences*, **57**: 524-541. doi:10.1139/cjes-2018-0263.

Keys, K., Neily, P., and Quigley, E. 2010. Forest Ecosystem Classification for Nova Scotia (Part II: Soil Types). *Edited by N.S.D.o.N. Resources*. Nova Scotia Department of Natural Resources, Halifax, Nova Scotia. p. 121.

Knight, R., Tercier, P., and Jol, H. 1997. The role of ground penetrating radar and geostatistics in reservoir description. *The Leading Edge*, **16**: 1576-1584. doi:10.1190/1.1437526.

Kostic, B., and Aigner, T. 2007. Sedimentary architecture and 3D ground-penetrating radar analysis of gravelly meandering river deposits (Neckar Valley, SW Germany). *Sedimentology*, **54**: 789-808. doi:10.1111/j.1365-3091.2007.00860.x.

Lanzarone, P., Garrison, E., Bobe, R., and Getahun, A. 2016. Examining Fluvial Stratigraphic Architecture Using Ground-Penetrating Radar at the Fanta Stream Fossil and Archaeological Site, Central Ethiopia. *Geoarchaeology*, **31**: 577-591. doi:10.1002/gea.21584.

Leandro, C.G., Barboza, E.G., Caron, F., and de Jesus, F.A. 2019. GPR trace analysis for coastal depositional environments of southern Brazil. *Journal of Applied Geophysics*, **162**: 1-12. doi:10.1016/j.jappgeo.2019.01.002.

Martel, T.A. 1987. Seismic Stratigraphy and Hydrocarbon Potential of the Strike-Slip Sackville Sub-Basin, New Brunswick. *In* Memoir 12 - Sedimentary basins and basin-forming mechanisms. *Edited by* C. Beaumont and A.J. Tankard. Atlantic Geoscience Society, Halifax. pp. 319-334.

McMechan, G.A., Gaynor, G.C., and Szerbiak, R.B. 1997. Use of ground-penetrating radar for 3-D sedimentological characterization of clastic reservoir analogs. *Geophysics*, **62**: 786-796. doi:10.1190/1.1444188.

Møller, I., and Anthony, D. 2003. A GPR study of sedimentary structures within a transgressive coastal barrier along the Danish North Sea coast. Geological Society, London, Special Publications, **211**: 55-65. doi:10.1144/gsl.Sp.2001.211.01.05.

Neal, A. 2004. Ground-penetrating radar and its use in sedimentology: principles, problems and progress. *Earth-Science Reviews*, **66**: 261-330. doi:10.1016/j.earscirev.2004.01.004.

Neal, A., and Roberts, C.L. 2000. Applications of ground-penetrating radar (GPR) to sedimentological, geomorphological and geoarchaeological studies in coastal environments. Geological Society, London, Special Publications, **175**: 139-171. doi:10.1144/gsl.Sp.2000.175.01.12.

Nowland, J.L., and MacDougall, J.I. 1973. Nova Scotia Soil Survey - Soils of Cumberland County Nova Scotia. *Edited by* Canada Department of Agriculture. D.W. Friesen and Sons Ltd., Ottawa. p. 154.

Prothero, D.R., and Schwab, F. 2003. *Sedimentary Geology : An Introduction to Sedimentary Rocks and Stratigraphy*. 2 ed. Freeman & Company, W&H.

Quann, S.L., Young, A.B., Laroque, C.P., Falcon-Lang, H.J., and Gibling, M.R. 2010. Dendrochronological dating of coal mine workings at the Joggins Fossil Cliffs, Nova Scotia, Canada.

Reisz, R.R., and Modesto, S.P. 1996. Archerpeton anthracos from the Joggins Formation of Nova Scotia: a microsauro, not a reptile. *Canadian Journal of Earth Sciences*, **33**: 703-709. doi:10.1139/e96-053.

Rey, J., Martínez, J., and Hidalgo, M.C. 2013. Investigating fluvial features with electrical resistivity imaging and ground-penetrating radar: The Guadalquivir River terrace (Jaen, Southern Spain). *Sedimentary Geology*, **295**: 27-37. doi:10.1016/j.sedgeo.2013.07.003.

RPS Energy. 2010. Screening of Potential CO₂ Storage Sites Onshore Nova Scotia. Carbon Capture and Storage Research Consortium of Nova Scotia

Rust, B.R., Gibling, M.R., and Legun, A.S. 1985. Coal deposition in an anastomosing-fluvial system: the Pennsylvanian Cumberland Group south of Joggins, Nova Scotia, Canada. *Sedimentology of Coal and Coal-Bearing Sequences*: 105-120.

Ryan, R.J., and Boehner, R.C. 1994. Geology of the Cumberland Basin, Cumberland, Colchester and Pictou Counties, Nova Scotia - Memoir 10. *Edited by* Mines and Energy Branch - Department of Natural Resources. Department of Natural Resources, Halifax.

Ryan, R.J., Calder, J.H., Donohoe Jr., H.V., and Naylor, R. 1987. Late Paleozoic Sedimentation and Basin Development Adjacent to the Cobequid Highlands Massif, Eastern Canada. *In* Memoir 12 - Sedimentary basins and basin-forming mechanisms. *Edited by* C. Beaumont and A.J. Tankard. Atlantic Geoscience Society, Halifax. pp. 311-317.

Rygel, M.C. 2005. Alluvial sedimentology and basin analysis of Carboniferous strata near Joggins, Nova Scotia, Atlantic Canada. Earth Sciences, Dalhousie University, Halifax, NS.

Rygel, M.C., and Gibling, M.R. 2006. Natural Geomorphic Variability Recorded in a High-Accommodation Setting: Fluvial Architecture of the Pennsylvanian Joggins Formation of Atlantic Canada. *Journal of Sedimentary Research*, **76**: 1230-1251. doi:10.2110/jsr.2006.100.

Rygel, M.C., Gibling, M.R., and Calder, J.H. 2004. Vegetation-induced sedimentary structures from fossil forests in the Pennsylvanian Joggins Formation, Nova Scotia. *Sedimentology*, **51**: 531-552. doi:10.1111/j.1365-3091.2004.00635.x.

Smith, D.G., and Jol, H.M. 1992. Ground-penetrating radar investigation of a Lake Bonneville delta, Provo level, Brigham City, Utah. *Geology*, **20**: 1-4. doi:10.1130/0091.

Stea, R.R., and Finck, P.W. 1986. Surficial Geology, Chigneto Peninsula, Nova Scotia (Sheet 9). Geological Survey of Canada. p. Map 1630A.

Szymczyk, M., and Szymczyk, P. 2013. Preprocessing of GPR data. *Image Processing and Communications*, **18**: 83-90. doi:10.2478/v10248-012-0082-3.

Tibert, N.E., and Dewey, C.P. 2006. Velatomorpha, a new healdioidean ostracode genus from the early Pennsylvanian Joggins Formation, Nova Scotia, Canada. *Micropaleontology*, **52**: 51-66. doi:10.2113/gsmicropal.52.1.51.

UNESCO. 2008. World Heritage List - Joggins Fossil Cliffs. Available from whc.unesco.org/en/list/1285/ [accessed September 6 2018].

Van Sickle, J. 2015. GPS for Land Surveyors. CRC Press.

Waldron, J.W.F., and Rygel, M.C. 2005. Role of evaporite withdrawal in the preservation of a unique coal-bearing succession: Pennsylvanian Joggins Formation, Nova Scotia. *Geology*, **33**: 337-340. doi:10.1130/g21302.1.

Chapter 6: Episodic Marine Incursions Support a Late Carboniferous Mid-Euramerican Seaway: An Example from the Joggins Formation

T.B. Kelly and G.D. Wach

This chapter is based on the paper “Episodic Marine Incursions Support a Late Carboniferous Mid-Euramerican Seaway”, by Trevor B. Kelly and Grant D. Wach and was submitted to the journal *Sedimentary Geology*.

6.1 Abstract

We present evidence for a mid-Euramerican seaway connecting to the Paleo-Tethys Ocean during the Late Carboniferous, supported by new research on a sedimentary succession in the Cumberland Basin, northern Nova Scotia, Canada. The Joggins Formation of the Cumberland Basin preserves an unmatched record of terrestrial life in their environmental context during the Late Carboniferous ‘Coal Age’. Despite the past two centuries of research, questions persist regarding the paleoenvironment, including the degree and type of marine impact. The study of tidal rhythmites allows for past marine conditions, including tidal regimes, to be interpreted. This rhythmicity can only be produced by tides from marine incursions. We apply quantitative and visual frequency analyses to interpret the laminae-scale cyclicity of tidal rhythmite intervals. Visual core analysis identified three intervals of tidal rhythmites with cycles. Fast Fourier transform and continuous wavelet transform analyses determined the primary cycles and corroborated the visual evidence of tidal sedimentation with results showing tidal deposition, determined geomathematically. Our results indicate tidal rhythmite deposition followed a semi-diurnal tidal model with a lunar monthly tidal cycle. We conclude there is strong evidence for the existence of a mid-

Euramerican seaway, which has implications for explaining the variability in paleoecological trends between the northern and southern Paleo-Tethys Ocean.

6.2 Introduction

The study of modern and ancient sedimentary rocks has always occupied a large and significant share of active research conducted in earth sciences. It provides practical, diagnostic information for reconstructing depositional environments, age relationships, sediment transport mechanisms, and provenance. These features offer helpful diagnostic information for reconstructing depositional environments, age relationships, sediment transport mechanisms, and origin. Despite the varied array of structures that can form in sedimentary environments, only a limited number (e.g., tidal rhythmites, repeatedly occurring mud drapes, flaser/lenticular bedding, and directional bimodality) support the suggestion of paleotidal influences and have added value for the creation of tidal deposit depositional models (Shukla and Shukla 2013). Boersma and Terwindt (1981) suggested tidal rhythmites best demonstrate paleotidal activity since they are never developed in continental or fluvial depositional environments. Boersma (1969) proposed the tidal rhythmite term, which was used to define the depositional unit corresponding to one tidal cycle. Visser (1980) linked stacked tidal rhythmites and neap-spring tidal cyclicity.

Astronomical tides are a consistent and reliable phenomenon produced by the gravitational pull of the sun and the moon, with a sedimentation pattern unequivocally unique to the episodic rise and fall of sea level. Their forces are principally exerted on oceans, and to a lesser extent, lakes. When tidal forces are channeled between islands or into bays and estuaries, they are known as tidal currents (Shukla and Shukla 2013). Astronomical tides are classified as diurnal (one episode of high water and low water

daily), semi-diurnal (two episodes of high water and low water daily), and mixed (similar to semi-diurnal, except they do not rise and fall at the same levels). In an individual neap/spring/neap cycle, 28 and 14 dominant current events can be recorded in the semi-diurnal tidal and diurnal tidal systems, respectively. Other systems are intermediate between them (De Boer et al. 1989; Friedman and Chakraborty 2006).

The uniqueness of the Cumberland Basin of Atlantic Canada (Figure 6.1) is that it documents a nearly complete and well-preserved stratigraphic succession of sedimentation through its entire period of basin development (Ryan and Boehner 1994). Despite this, the majority of studies in the basin have concentrated exclusively on the Late Carboniferous (Pennsylvanian) strata of the world-renowned Joggins Formation, with the bulk of the research occupying one of three major categories; a general geology category that incorporates sedimentology and stratigraphy publications (e.g., Davies and Gibling 2003; Davies et al. 2005; Waldron and Rygel 2005; Rygel and Gibling 2006); a paleobiology category that includes taxonomic discoveries and descriptions (e.g., Carroll 1967; Archer et al. 1995b; Reisz and Modesto 1996; Tibert and Dewey 2006; Carpenter et al. 2015); and a paleoecology category (e.g., Brand 1994; Calder et al. 2006). The research conducted has been focused and thorough but has not been extrapolated to other Carboniferous successions other than perhaps Charles Lyell in the 1850s, who studied coal measures across North America and Europe.

The study of tidal rhythmites is common in the literature, with studies spanning the Cenozoic Era (e.g., Visser 1980; Tessier and Gigot 1989; Choi and Park 2000; Geel and Donselaar 2007; Wang et al. 2010; Choi and Kim 2016; Donselaar and Geel 2016; Jaiswal and Bhattacharya 2018), Mesozoic Era (e.g., Kreisa and Moila 1986; Smith 1988; Uhlir et

al. 1988; Dreyer 1992; Richards 1994; Fabuel-Perez et al. 2009b; Klausen and Mørk 2014), Paleozoic Era (e.g., Kvale et al. 1989; Archer 1991; Feldman et al. 1993; Archer et al. 1995a; Tessier et al. 1995; Miller and Eriksson 1997; Tape et al. 2003; Teedumae et al. 2004; Wells et al. 2005a; Bhattacharya et al. 2012; Coughenour et al. 2013), and the Precambrian Era (e.g., Williams 1989; Chan et al. 1994; Eriksson and Simpson 2000; Williams 2000; Eriksson and Simpson 2004; Williams 2004; Shukla and Shukla 2013). This research complements the work conducted on Paleozoic Era sediments by analyzing and describing tidal rhythmites within the Joggins Formation. Based on the rhythmicities indicated by the rhythmites, valuable information can be inferred regarding the paleotidal regime of this area during the Late Carboniferous. The alluvial drainage patterns seen in the Cumberland Basin give glimpses into its paleotopography, suggesting shallow seas may have transgressed westward from the Tethys Ocean along a speculative mid-Euramerican seaway corridor (e.g., Gibling et al. 1992; Calder 1998).

Open-marine conditions are well-documented in the literature as occurring within the Cumberland Basin and the Joggins Formation. The two main lines of evidence for this have been through the study of fossils and sedimentary structures that are diagnostic for marine environments. Davies et al. (2005) identified marine limestones containing bivalves, spirorbids, arthropods, and disarticulated fish and have linked their deposition to the open-marine environment. Sandstone units containing unidirectional ripple cross-laminations, mud drapes, and lineated plane beds with wave ripples and hummocky cross-stratification hint further at marine conditions (Davies et al. 2005). Carpenter et al. (2015) reviewed all available fossil fish specimens from the Joggins area and determined that the assemblage was widespread around the tropical coastal regions of Pangaea. An analysis of these

specimens using strontium isotopes and a facies context study concluded that the fish assemblage occupied water salinities from the fresh-to-marine realm. The study provided further evidence for Joggins Formation deposition in a paralic environment. Dafoe et al. (2018) performed an ichnological analysis using primarily invertebrate trace fossils from the Joggins Formation outcrop, and the same borehole analyzed for the current study. They combined the trace fossil record with the sedimentological framework of the Joggins Formation to interpret the respective depositional environments. The presence of the *Cruziana* ichnofacies suggests marine-influenced strata such as bayhead deltas and brackish bays may have existed, while the *Chondrites* and *Phycosiphon* trace fossils suggest purely marine (Dafoe et al. 2018). Chipman et al. (2020) used 71 coprolite samples from the Joggins Formation limestones. The coprolites are assumed to be produced from fish species known to inhabit open-marine brackish environments. Juby (2009) summarizes the abundant body fossils contained in the Joggins Formation, including body part fossils and scales from the coelacanth. The presence of coelacanth fossils and scales provides additional evidence for the presence of marine conditions. Furthermore, body fossils of horseshoe crabs have been found, suggesting shallow marine or at least brackish environments existed (Juby 2009).

To reveal the tidal cyclicity and regime in the Late Carboniferous sediments (Figure 6.1c) of the Cumberland Basin, we have conducted a detailed geomathematical analysis on three drill core intervals (TR1, TR2, and TR3) containing tidal rhythmites from the Joggins Formation by applying visual, fast Fourier transform (FFT), and 1D continuous wavelet transform (CWT) analyses. Evidence for tidal rhythmite deposition in an open marine environment during the Late Carboniferous through qualitative and quantitative techniques

will be revealed. We determine if tidal modulation is preserved in these wavy interlaminated mudstone and sandstone lithologies and, in doing so, provide crucial evidence of some aspects of the Joggins Formation tidal processes. The results of this study have the potential to provide further insight into the local and regional paleoecological trends that existed during the Late Carboniferous. This may also have important implications for a more global scale interpretation of paleoecological trends from North America to Europe along the proposed mid-Euramerican seaway proposed by Calder (1998) and others.

6.3 Geological Setting

The Joggins Formation crops out along Chignecto Bay, Nova Scotia (Figure 6.1b), and Joggins reveals the most complete fossil record of the Late Carboniferous “Coal Age”; a period when extensive wooded marshlands allowed for the accretion of substantial amounts of organic matter that would undergo coalification and form vast and prolific coal deposits (Figure 6.1a and Figure 6.2). It is centrally located in paleoequatorial Euramerica in an expansive intermontane paleoequatorial setting (Figure 6.2) throughout Late Carboniferous time (Calder 1998). The Joggins Formation exposure (complete section) is separated into 14 cycles marked by a basal limestone, coal, or fossiliferous shale. The cycles correspond to upper deltaic plain, lower deltaic plain, and open-marine facies (Davies and Gibling 2003; Davies et al. 2005). The upper deltaic plain facies include reddish mudstone and sandstone with slight grey mudstone, rare coal, and ostracod-bearing limestone (Davies et al. 2005). The lower deltaic plain facies contain sandstone and frequently rooted greenish-grey mudstone, coal, carbonaceous shale, and minimal limestone, with siderite nodules (Davies et al. 2005). Ostracods and bivalves are also present. The open-marine facies include fossiliferous limestones that pass vertically or are interbedded with fossiliferous siltstones and cover thick coal beds (Davies and Gibling 2003). The Springhill Mines Formation shows upper and lower deltaic plain facies, while the Little River Formation suggests alluvial plain facies dissected by shallow rivers (Calder et al. 2005; Rygel et al. 2014). Numerous authors provide a thorough synopsis of Cumberland Basin development during the Paleozoic (Waldron and Rygel 2005; Gibling et al. 2008b; Waldron et al. 2013).

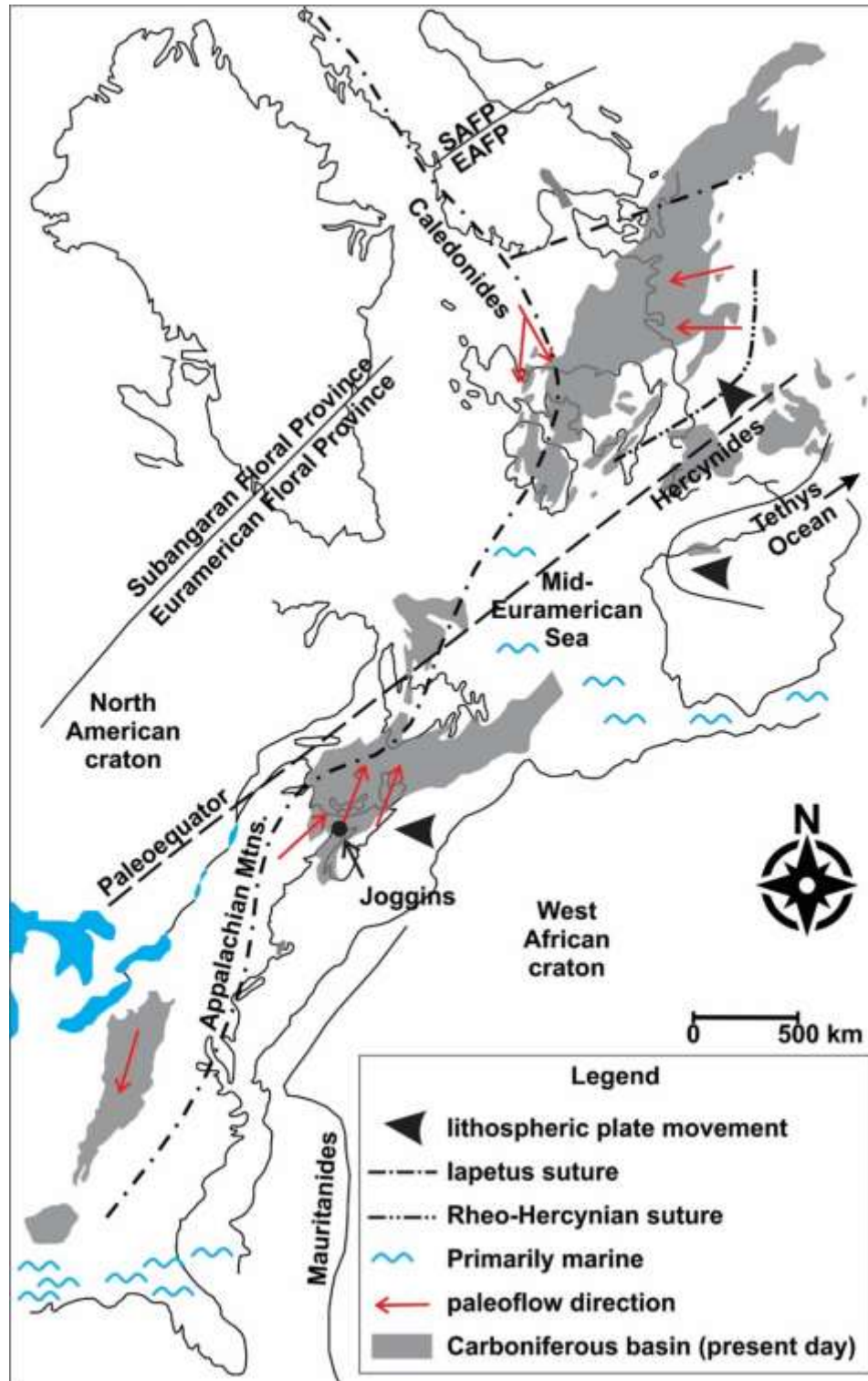


Figure 6.2: Carboniferous sketch of equatorial Euramerica indicates Joggins, Nova Scotia (Calder 1998). The base map was redrawn from Williams (1984) and Haszeldine (2009). Paleoflow directions were redrawn from Archer and Greb (1995) for the Appalachian Basin, Gibling et al. (1992) for the Maritimes Basin, and Leeder (1988); Leeder et al. (1992) for western Europe. The basin framework for western Europe was redrawn from Maynard et al. (1997).

6.4 Dataset

Paleotidal studies typically utilize data compiled from outcrop and subsurface boreholes and involves measuring the thickness of laminae in the outcrop or drill core. The Cumberland Basin contains more than 1,100 boreholes, with approximately half containing drill core stored at the Nova Scotia Department of Energy and Mines Geoscience and Mines Branch located in Stellarton, Nova Scotia. The examined borehole, REI-B2-1 or P-101, was drilled at 393,129 m east and 5,058,940 m northing (NAD 83/UTM Zone 20) (Figure 6.1). Continuous core retrieval occurred from 58 – 1,305.5 m (REI Nova Scotia 1995). Five downhole geophysical logs were continuously recorded for 855 m from 446 to 1,301 m. These include gamma ray (GR; gAPI), neutron porosity-sandstone (NPHI_SAN; %), density correction (DRHO; g/cm³), bulk density (RHOB; g/cm³), and density caliper (CALI; in.) logs (REI Nova Scotia 1995). A simplified lithology column was created based on the lithology descriptions from the borehole history report and visual analysis of the drill core (Figure 6.3). The borehole penetrated the Springhill Mines, Joggins, and Little River formations. For this study, only the Joggins Formation interval was utilized. Within the Joggins Formation interval, tidal rhythmite intervals were documented, and the three best intervals were chosen for data collection and analysis techniques (Figure 6.3).

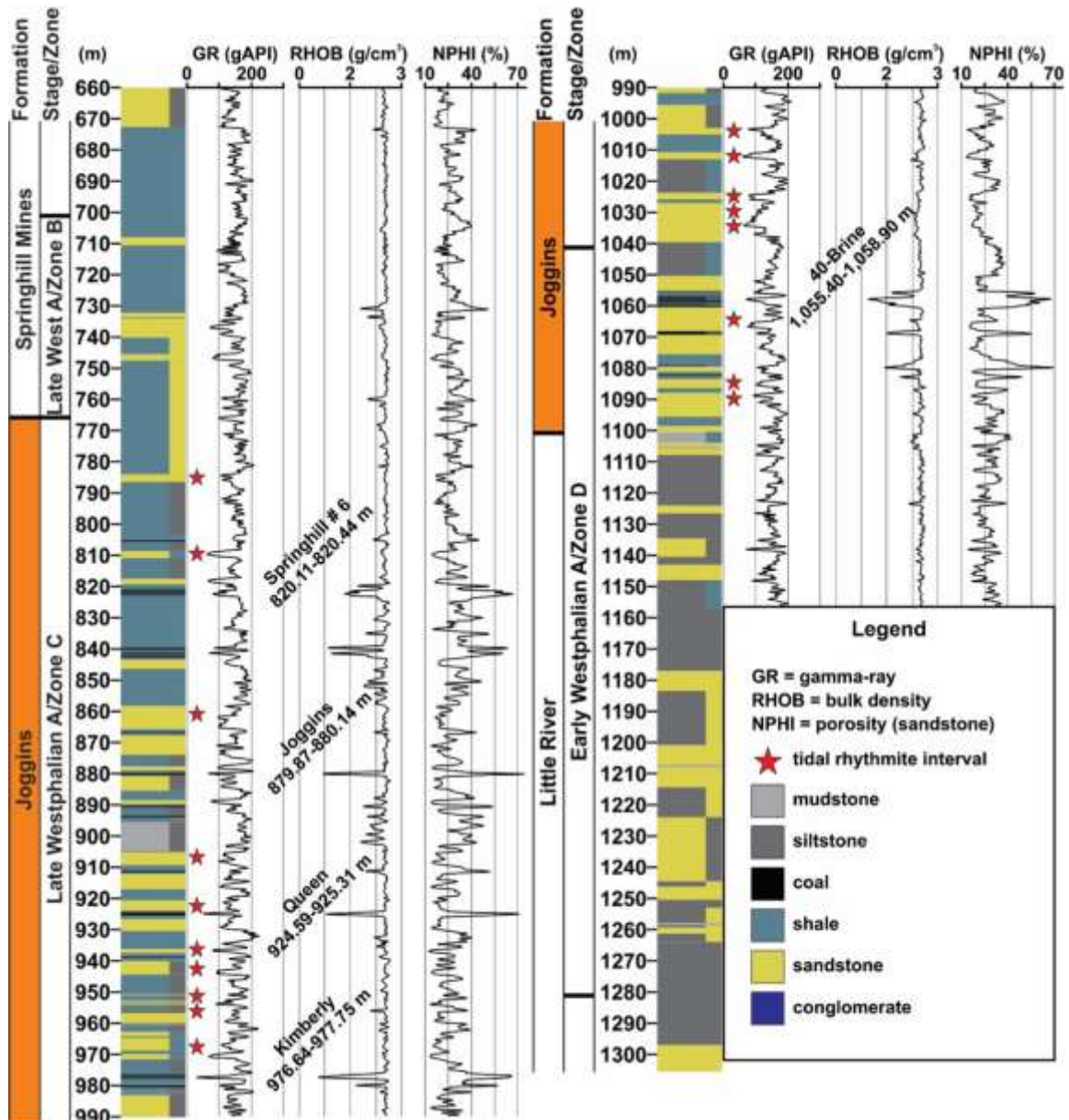


Figure 6.3: Simplified lithology, stratigraphy, and geophysical borehole log curves for the Joggins Formation interval of the examined borehole. The lithologies encountered are mudstone, siltstone, coal, shale, sandstone, conglomerate, or combination. The geophysical borehole log curves from left to right display gamma ray (gAPI), bulk density (g/cm³), and neutron porosity-sandstone (%). The significant, named coal seams are catalogued between the GR and RHOB curves. Tidal rhythmite intervals are shown with a red star. All represented data are adapted from the borehole history report by REI Nova Scotia (1995).

6.5 Methods

6.5.1 Data Collection

The identification of tidal rhythmite (tidal bundles) intervals was completed using the physical drill core of the Joggins Formation interval from borehole REI-B2-1. High-resolution digital drill core images were acquired using a standard 12-megapixel (4,290 pixels by 2,800 pixels) Samsung Galaxy S8+ paired with a custom-built drill core photography apparatus. The apparatus was built solely to acquire high-resolution, constant height (20 cm from the core) and width, panoramic photographs using the high-end camera present on modern smartphones. The digital photograph was imported into a vector graphics editor program (CorelDRAW®) and scaled to its true size. Measurements were completed using the dimension measuring tool directly within the graphics program. Each sandstone and mudstone lamina's thickness were measured, recorded, and tabulated. Thickness measurements were collected vertically (i.e., parallel to the core barrel). Lamina-thickness histograms for combined sandstone and mudstone laminae, sandstone-only laminae, and mudstone-only laminae were plotted for visual cyclicity analysis. The data collection and quantitative analysis workflow is summarized in Figure 6.4. The drill core images of the Joggins Formation are shown in Appendix D and the subsequent core description is shown in Appendix E. A specialized core photography apparatus was built to assist with capturing high-resolution photos. This apparatus is summarized in Appendix F. The tidal rhythmite thickness measurements are documented in Appendix G.

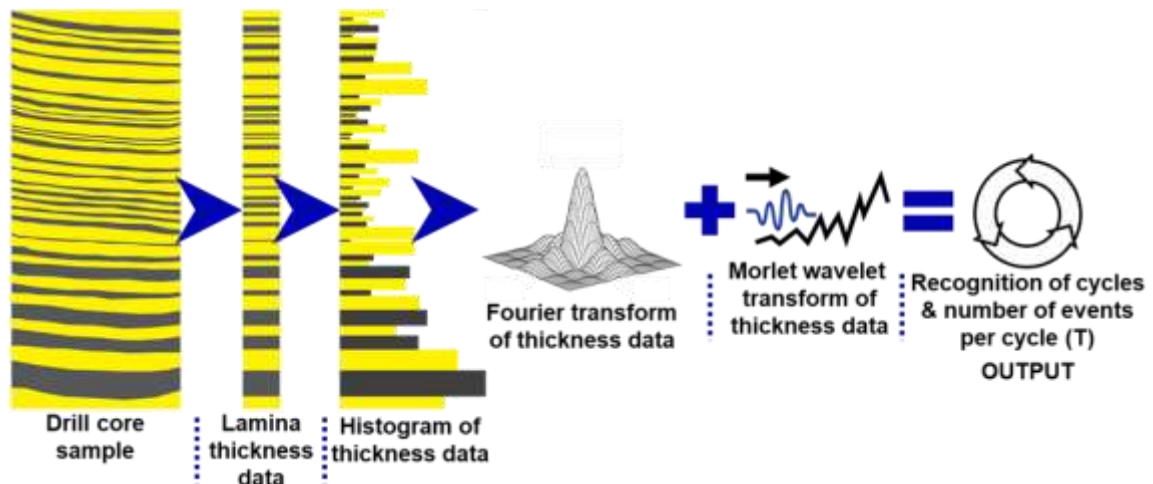


Figure 6.4: Representational flow diagram emphasizing the quantitative techniques used in this study. Drill core thickness data is measured and converted into a pseudo-time signal, where successive laminae measurements correspond to time steps. Thickness data correspond to the signal at each time step. The signal is then evaluated with an FFT and CWT, from which the primary periodicities (i.e., the number of events per cycle) are determined.

6.5.2 Fast Fourier Transform Analysis

The prevalent technique for determining signal cyclicity is the FFT method, which computes the intensity of each frequency from the initial time signal (e.g., Stage 1999; Labrecque et al. 2011; Timmer et al. 2016; Rampino et al. 2021). The FFT analysis of lamination thickness data is regularly applied to evaluate fundamental paleotidal periods, and is represented graphically with a periodogram (e.g., Horne and Baliunas 1986; Gent and Sonnenberg 2014). The FFT relates the variations in lamina-thickness cycles to the smooth, periodic oscillations presented by the sinusoidal (sine) function (Labrecque et al. 2011). The cyclical nature exhibited by lamina-thickness data are naturally imperfect when compared to the perfectly oscillating sinusoidal curve, and as a result both datasets will not share duplicate wavelengths (Labrecque et al. 2011). The FFT is unable to comprehensively evaluate a signal in which the frequency component fluctuates with time, unless the signal is filtered prior to analysis (Labrecque et al. 2011). The periodogram consists of the frequency from the FFT output on the x-axis and it varies from 0 to π

(3.145) (Archer 1996). The y-axis of the periodogram contains the amplitude values from the FFT with prominent amplitudes identified in bundles/cycle (Archer 1996). An FFT was applied to the lamina-thickness data from TR1, TR2, and TR3 to identify dominant frequencies and determine if an underlying tidal signature is present. The FFT algorithm was completed using MATLAB's 'Y = FFT(X)' function. The function computes the discrete FFT of X using an FFT algorithm. Periodograms were generated for each data set using all the lamination data. They provide an overall spectral peak characteristic for the data.

6.5.3 *Continuous Wavelet Transform (Morlet) Analysis*

The mechanism by which signals are separated into their various scaled spectral components is through the application of mathematical functions known as wavelets (Jafarpour 2010; Labrecque et al. 2011). For studies involving sediments, like this one, variations in sediment thicknesses can be used to establish cyclicity when the data is treated as a time series such that individual depositional episodes coincide with a consecutive time step (e.g., Prokoph and Agterberg 1999; Brauer et al. 2008; Timmer et al. 2016). It is through the conversion of time-series signals from the time domain and into the frequency domain that allows for the determination of signal periodicities in sedimentary-related studies (Timmer et al. 2016). The CWT is able to identify repetition in neighboring cycles and accentuate them for the calculation of more distant cycles (Labrecque et al. 2011).

While the FFT method has long been the standard for resolving signal cyclicity, it does suffer from not being able to preserve any temporal information from the initial signal (Timmer et al. 2016). This means the FFT method is capable of identifying intense, localized frequencies from a dataset, but is incapable of isolating where that frequency

component exists (Timmer et al. 2016). The benefit of applying the CWT over the FFT is that the CWT can individually evaluate specific segments of a signal in a way that preserves depth, and wavelength and magnitude components of cyclicity in the dataset (Labrecque et al. 2011). The result is the detection of geological cyclicity is more straightforward using the CWT method than the FFT method.

Like previous studies, this research uses the CWT integrated with a depth-domain signal, in this instance, lamina-thickness data, to compare it with a reference signal (i.e., the ‘mother’ wavelet) at each associated thickness and wavelength (Labrecque et al. 2011). The Morlet wavelet was employed as the mother wavelet for this study, which is often used to evaluate cyclicity (e.g., Goupillaud et al. 1984; Prokoph and Barthelmes 1996; Prokoph and Agterberg 1999; Labrecque et al. 2011; Timmer et al. 2016). The lamina number versus wavelength is plotted as a scalogram. This displays the agreeability of the data with the heavily cyclic portions showing as red colours (Labrecque et al. 2011). A prior study assessed the error levels in the amplitudes and wavelengths for wavelet analysis (Tanyel 2006). It was observed that amplitudes might be in error by up to 50%, and wavelengths were accurate to within 30% (Tanyel 2006). We assume comparable error quantities for this study since the measurement resolution and sample densities are similar.

6.6 Results

6.6.1 Tidal Rhythmite Intervals

The TR1 interval (Figure 6.5a) from 810.71 – 811.02 m is 313.83 mm long and consists of thin, rhythmically interlaminated sandstone and mudstone. The interval displays mainly planar parallel bedding with some wavy/lenticular bedding occurrences near the

top of the interval. Both upper and lower contacts are abrupt and sharp. The top of the interval is capped by a 10 cm thick dark grey/maroon mudstone bed. The base lies on a thick (+5 m) dark grey/maroon mudstone bed, like the top mudstone cap, and some short carbonaceous mudstone with fossilized shell fragments. Bioturbation is absent from this interval.

The TR2 interval (Figure 6.6a) from 1,003.40 – 1,003.60 m is 203.71 mm long and consists of varying thicknesses and rhythmically interlaminated sandstone and mudstone. The interval displays planar parallel bedding. Both upper and lower contacts are gradational. The top of the interval is capped by a 50 cm thick bed of massive fine- to medium-grained sandstone. The base lies on a thick (+1 m) bed of fine- to medium-grained sandstone and mudstone, displaying lenticular, flaser, and wavy bedding. Overall, bioturbation is absent to sparse, with possible burrowing occurrences (*Glossifungites* or *Skolithos*) in the middle and top of the interval as noted by the disturbance of the laminae.

The TR3 interval (Figure 6.7a) from 1,032.40 – 1,032.97 m is 574.90 mm long and consists of thin, rhythmically interlaminated sandstone and mudstone. The interval displays mainly planar parallel bedding with some wavy/lenticular bedding occurrences near the top of the interval. Both upper and lower contacts are gradational. The top of the interval is capped by a thick (+2 m) bed of mechanically fractured, medium-grained sandstone. The base lies on a thick (+1 m) bed of mainly massive medium-grained sandstone with mudstone and lenticular, flaser, and wavy bedding. This interval contains common fractures infilled with calcite. A summary of the three intervals is provided in Table 6.1.

Table 6.1: Summary of tidal rhythmite intervals.

Interval/ Parameter	TR1	TR2	TR3
Description	Thin, planar parallel, rhythmically interlaminated sandstone and mudstone	Variable thicknesses of rhythmically interlaminated sandstone and mudstone	Thin, planar parallel, rhythmically interlaminated sandstone and mudstone
Contacts	Upper: sharp Lower: sharp	Upper: gradational Lower: gradational	Upper: gradational Lower: gradational
Grain Size	Fine- to medium-grained sandstone; mudstone	Fine- to medium-grained sandstone; mudstone	Fine-grained sandstone; mudstone
Sedimentary Structures	Mainly planar parallel laminations with some lenticular to wavy laminations; rare climbing ripples	Mainly planar parallel laminations	Mainly planar parallel laminations; fractures infilled with calcite; rare mud rip-up clasts
Bioturbation	Absent	Virtually absent; rare <i>Glossifungites</i> or <i>Skolithos</i>	Absent
Interpretation	Deposition in a fluvial to estuarine transitional setting; meso to macrotidal conditions	Deposition in a fluvial to estuarine transitional setting; meso to macrotidal conditions	Deposition in a fluvial to estuarine transitional setting; meso to macrotidal conditions

6.6.2 Visual Cyclicity Analysis

The samples measured for visual cyclicity analysis are shown in Figure 6.5a, Figure 6.6a, and Figure 6.7a. The resulting thickness histograms for combined sandstone and mudstone laminae, sandstone-only laminae, and mudstone-only laminae are shown in Figure 6.5b-d, Figure 6.6b-d, and Figure 6.7b-d. Arrows are plotted where laminae thicknesses are thinnest (i.e., troughs). The number of laminae between each arrow is noted on these plots. A statistical analysis of the three intervals is provided in Table 6.2, and the visual cyclicity analysis summary is provided in the first three columns of Table 6.3.

For TR1, a total of 516 measurements (258 sandstone/258 mudstone) were recorded (Figure 6.5a). A thickness plot of the combined sandstone and mudstone laminae (Figure 6.5b) defines eight prominent cycles of 55 to 61 laminae across 474 laminae with an average of 58.6 laminae/cycle. A thickness plot of mudstone-only laminae (Figure 6.5c) defines 17 cycles ranging from 12 to 16 laminae across 238 laminae, with an average of 14 laminae/cycle. A thickness plot of sandstone-only laminae (Figure 6.5d) defines 17 cycles ranging from 13 to 16 laminae across 244 laminae, with an average of 14.4 laminae/cycle.

For TR2, a total of 79 measurements (40 sandstone/39 mudstone) were recorded (Figure 6.6a). A thickness plot of the combined sandstone and mudstone laminae (Figure 6.6b) defines one prominent cycle of 63 laminae across 63 laminae with an average of 63 laminae/cycle. A thickness plot of mudstone-only laminae (Figure 6.6c) depicts two cycles of 14 and 15 laminae each across 29 laminae, with an average of 14.5 laminae/cycle. A thickness plot of sandstone-only laminae (Figure 6.6d) defines two cycles of 14 laminae each across 29 laminae.

For TR3, a total of 289 measurements (145 sandstone/144 mudstone) were recorded (Figure 6.7a). A thickness plot of the combined sandstone and mudstone laminae (Figure 6.7b) defines four prominent cycles of 58 to 63 laminae across 242 laminae with an average of 60.8 laminae/cycle. A thickness plot of sandstone-only laminae (Figure 6.7c) defines ten cycles ranging from 12 to 17 laminae each across 122 laminae, with an average of 13.5 laminae/cycle. A thickness plot of mudstone-only laminae (Figure 6.7d) defines nine cycles ranging from 12 to 15 laminae each across 121 laminae, with an average of 13.4 laminae/cycle.

Table 6.2: Statistical analysis from the three tidal rhythmite sequences.

Statistical Measure	Interval TR1		Interval TR2		Interval TR3	
	SST	MST	SST	MST	SST	MST
Maximum (mm)	2.65	1.10	13.00	11.50	10.00	4.40
Minimum (mm)	0.21	0.14	0.50	0.50	0.60	0.40
Total Thick. (mm)	222.27	91.56	121.81	81.9	381.80	193.10
Percentage (%)	70.83	29.17	59.80	40.20	66.41	33.59
Mean (mm)	0.86	0.35	3.05	2.10	2.63	1.34
Median (mm)	0.77	0.31	2.10	1.40	2.20	1.20
Mode (mm)	0.73	0.26	1.80	1.40	1.60	1.00

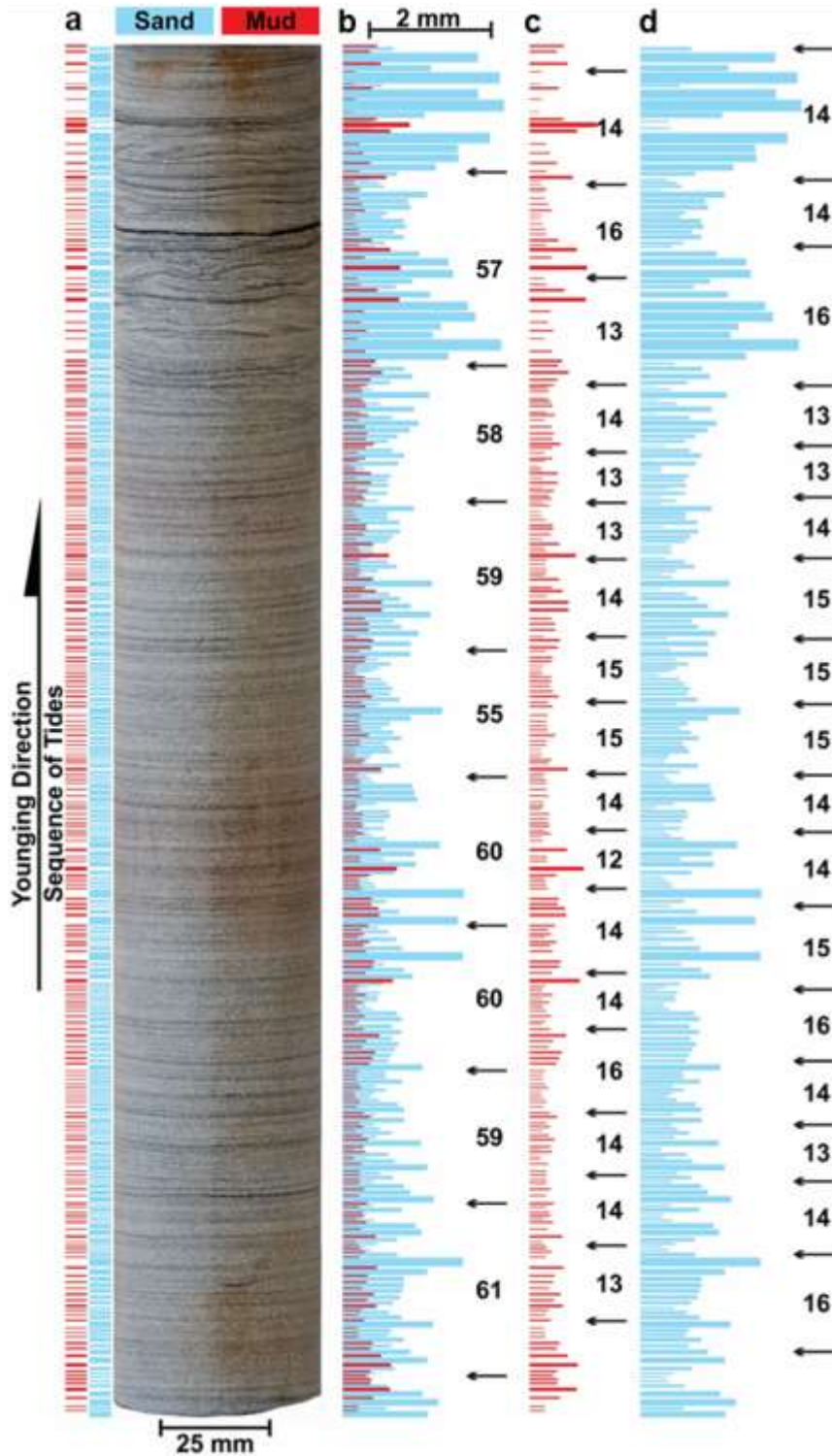


Figure 6.5: Visual cyclicality analysis results of core interval TR1. (a) Photograph of measured core interval TR1 from 810.71 – 811.02 m depth. Mudstone and sandstone laminae thicknesses are shown to the left of the photograph. (b) Histogram of combined mudstone and sandstone thickness measurements. (c) Histogram of mudstone thickness measurements. (d) Histogram of sandstone measurements. Numbers and arrows on histogram plots (b – d) indicate the number of laminae between each trough.

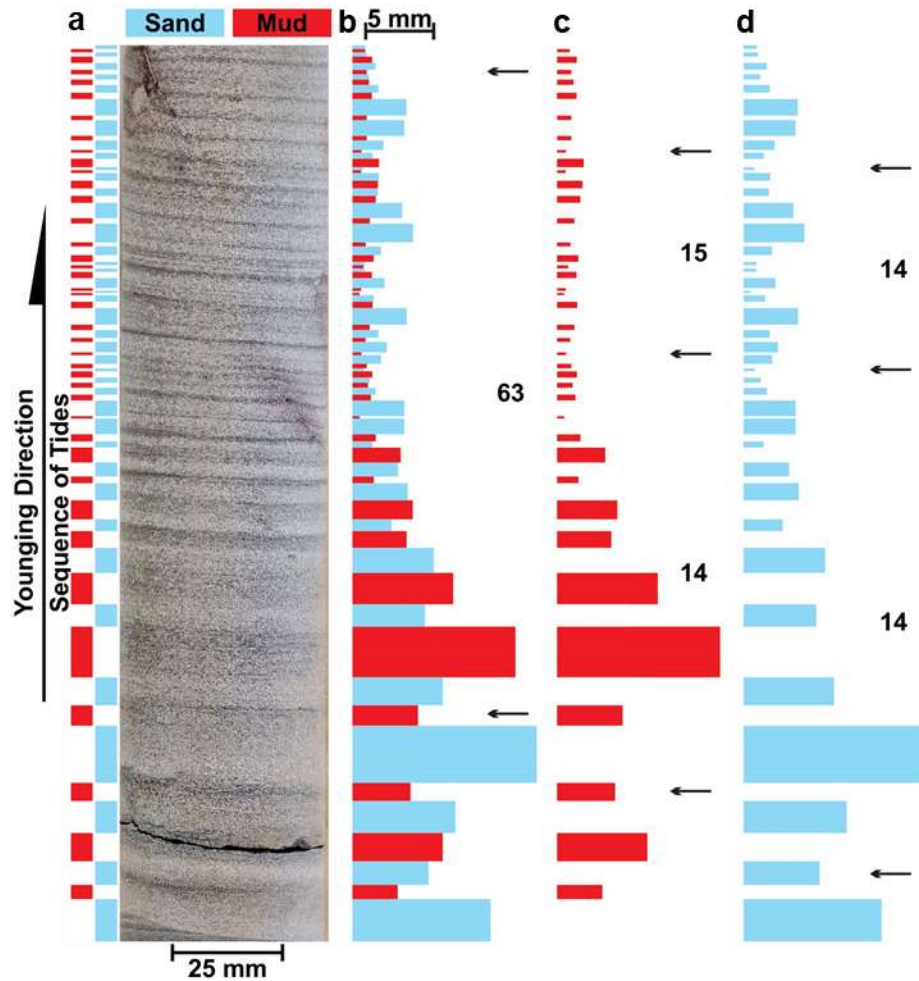


Figure 6.6: Visual cyclicity analysis results of core interval TR2. (a) Photograph of measured core interval TR2 from 1,003.40 – 1,003.60 m depth. Mudstone and sandstone laminae thicknesses are shown to the left of the photograph. (b) Histogram of combined mudstone and sandstone thickness measurements. (c) Histogram of mudstone thickness measurements. (d) Histogram of sandstone measurements. Numbers and arrows on histogram plots (b – d) indicate the number of laminae between each trough.

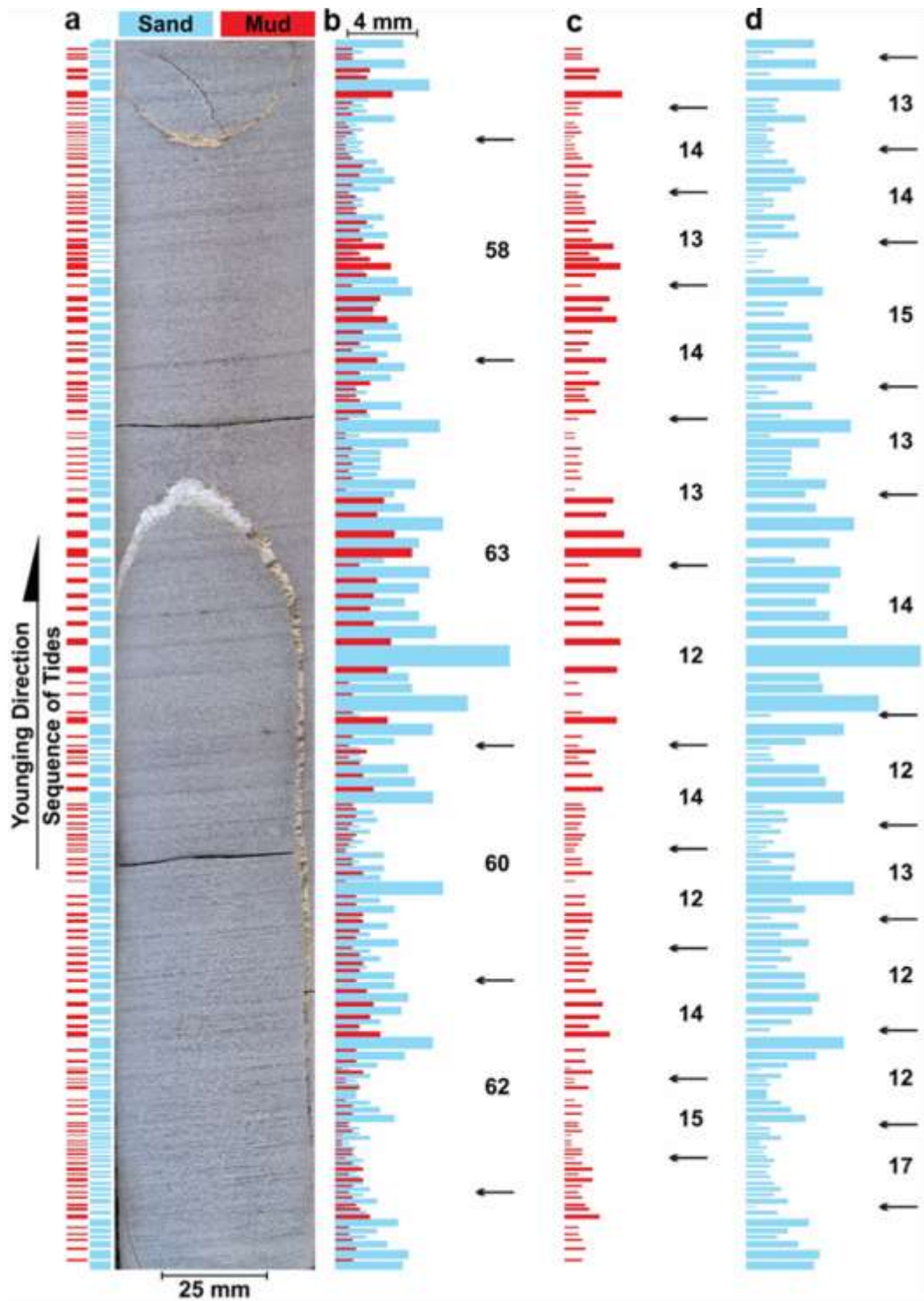


Figure 6.7: Visual cyclicity analysis results of core interval TR3. (a) Photograph of measured core interval TR3 from 1,032.40 – 1,032.97 m depth. Mudstone and sandstone laminae thicknesses are shown to the left of the photograph. Note the white calcite-filled fracture. (b) Histogram of combined mudstone and sandstone thickness measurements. (c) Histogram of mudstone thickness measurements. (d) Histogram of sandstone measurements. Numbers and arrows on histogram plots (b – d) indicate the number of laminae between each trough.

6.6.3 Fast Fourier Transform Cyclicity Analysis

Applying the FFT to the lamination thickness data (Figure 6.8a, c, and e) from the TR1, TR2, and TR3 core intervals resulted in a unique set of periodograms (Figure 6.8b, d, and f) for each interval showing the relationship between frequency (x-axis), from zero to pi, and magnitude (y-axis) of the FFT algorithm. Strong spectral peaks are noted in all three periodograms at a frequency of 3.14 (pi) or a period of 2.0 laminations per tidal cycle.

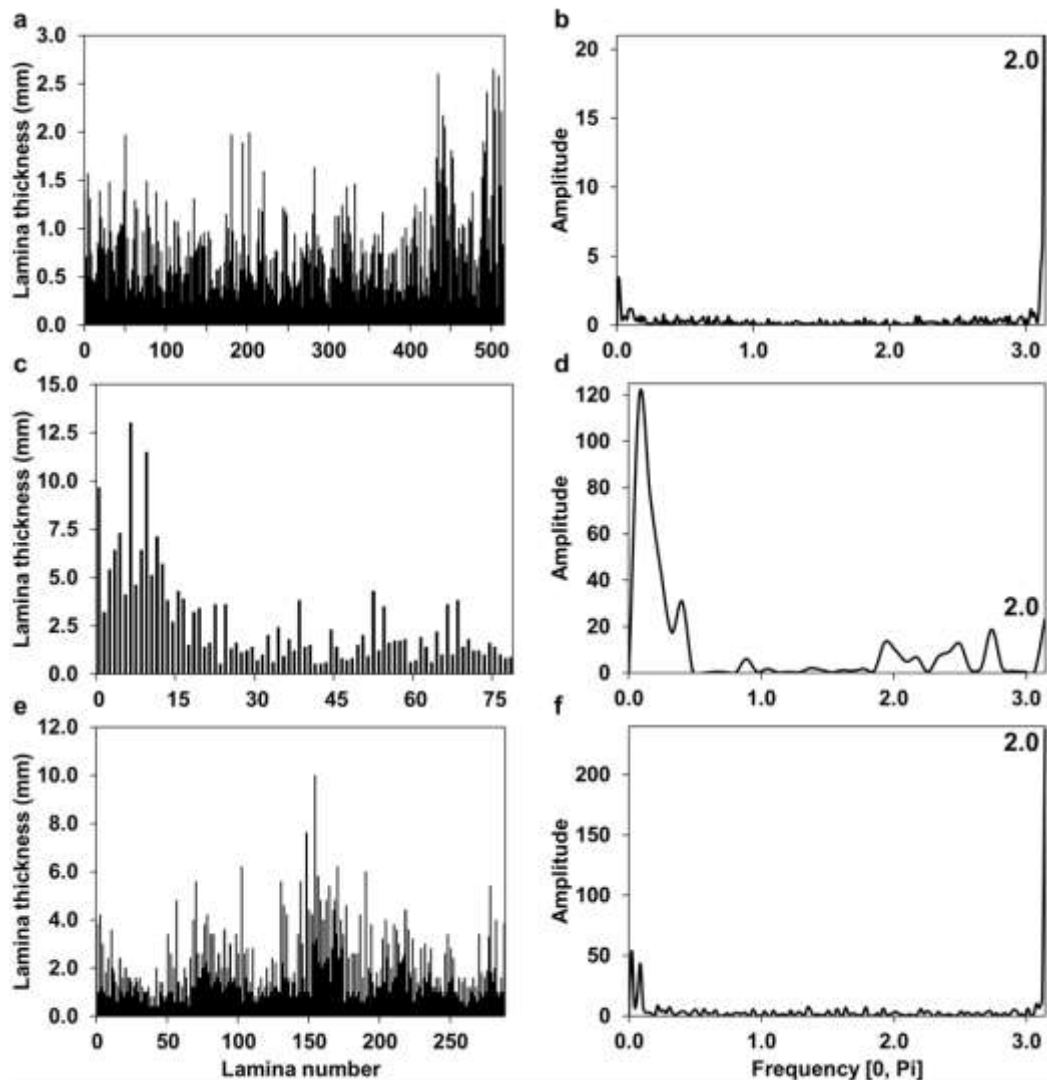


Figure 6.8: Lamina thickness histograms and accompanying periodograms for intervals TR1, TR2, and TR3. (a) The histogram of interval TR1. (b) The periodogram of interval TR1. (c) The histogram of interval TR2. (d) The periodogram of interval TR2. (e) The histogram of interval TR3. (f) The periodogram of interval TR3.

6.6.4 *Continuous Wavelet Transform Cyclicity Analysis*

The scalograms from the Morlet CWT analysis are displayed in Figure 6.9 for TR1, Figure 6.10 for TR2, and Figure 6.11 for TR3. The x-axis represents the consecutive laminae measured with decreasing depth of measurements from left to right. The x-axis denotes laminae count, not depth; thus the correlation to depth is distorted. The y-axis shows the calculated cycle periodicities. The colour spectrum of the scalogram shows the cycle magnitude. The warmer colours (i.e., red and orange) correspond to a larger cycle magnitude. The cooler colours (i.e., purple and blue) imply a lower cycle magnitude. The significant periodicities, that is, the periods that are least likely to be random noise have high frequencies (i.e., are red or orange) and occur at a certain period for a considerable number of thickness measurements (i.e., are relatively horizontally continuous on the plot). Lines are placed on the scalograms at the periods of the main cycles observed for each sample, with corresponding periods annotated. The cycle periods determined from the wavelet transform analysis are summarized in the last three columns of Table 6.3.

For TR1, the main periodicities correspond to 16 and 52 for combined sandstone and mudstone laminae (Figure 6.9a), 7 and 25 for sandstone laminae (Figure 6.9b), and 4, 26, and 61 for mudstone laminae (Figure 6.9c). For TR2, the main periodicities correspond to 4 and 28 for combined sandstone and mudstone laminae (Figure 6.10a), 3 and 14 for sandstone laminae (Figure 6.10b), and 3 and 14 for mudstone laminae (Figure 6.10c). For TR3, the main periodicities correspond to 6, 28, and 56 for combined sandstone and mudstone laminae (Figure 6.11a), 10 and 29 for sandstone laminae (Figure 6.11b), and 6 and 28 for mudstone laminae (Figure 6.11c).

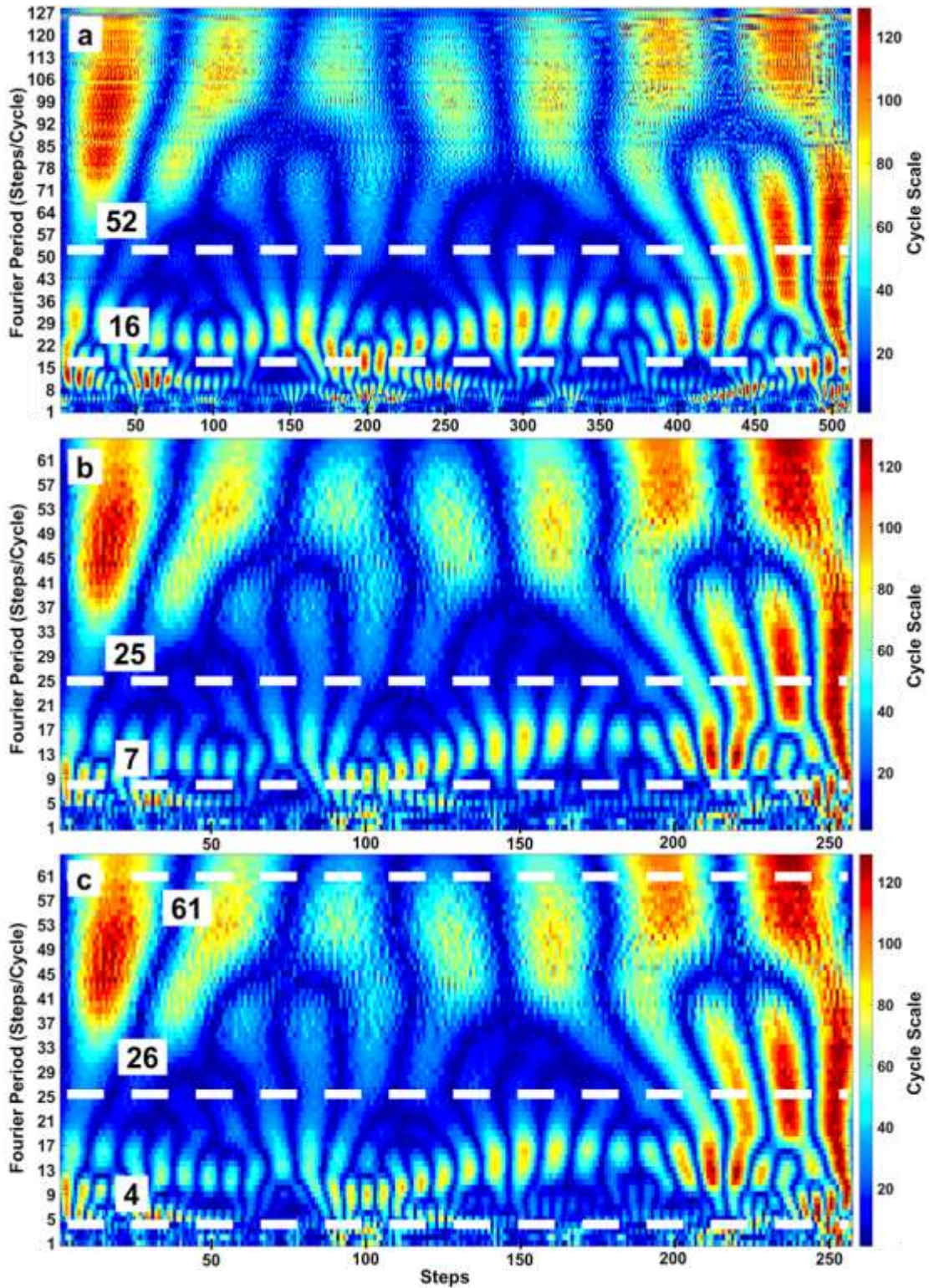


Figure 6.9: Scalograms of interval TR1. (a) Scalogram of the combined sandstone and mudstone laminae time series. The main periodicities are 52 and 16. (b) Scalogram of the sandstone laminae time series. The main periodicities are 25 and 7. (c) Scalogram of the mudstone laminae thickness time-series. The main periodicities are 61, 26, and 4.

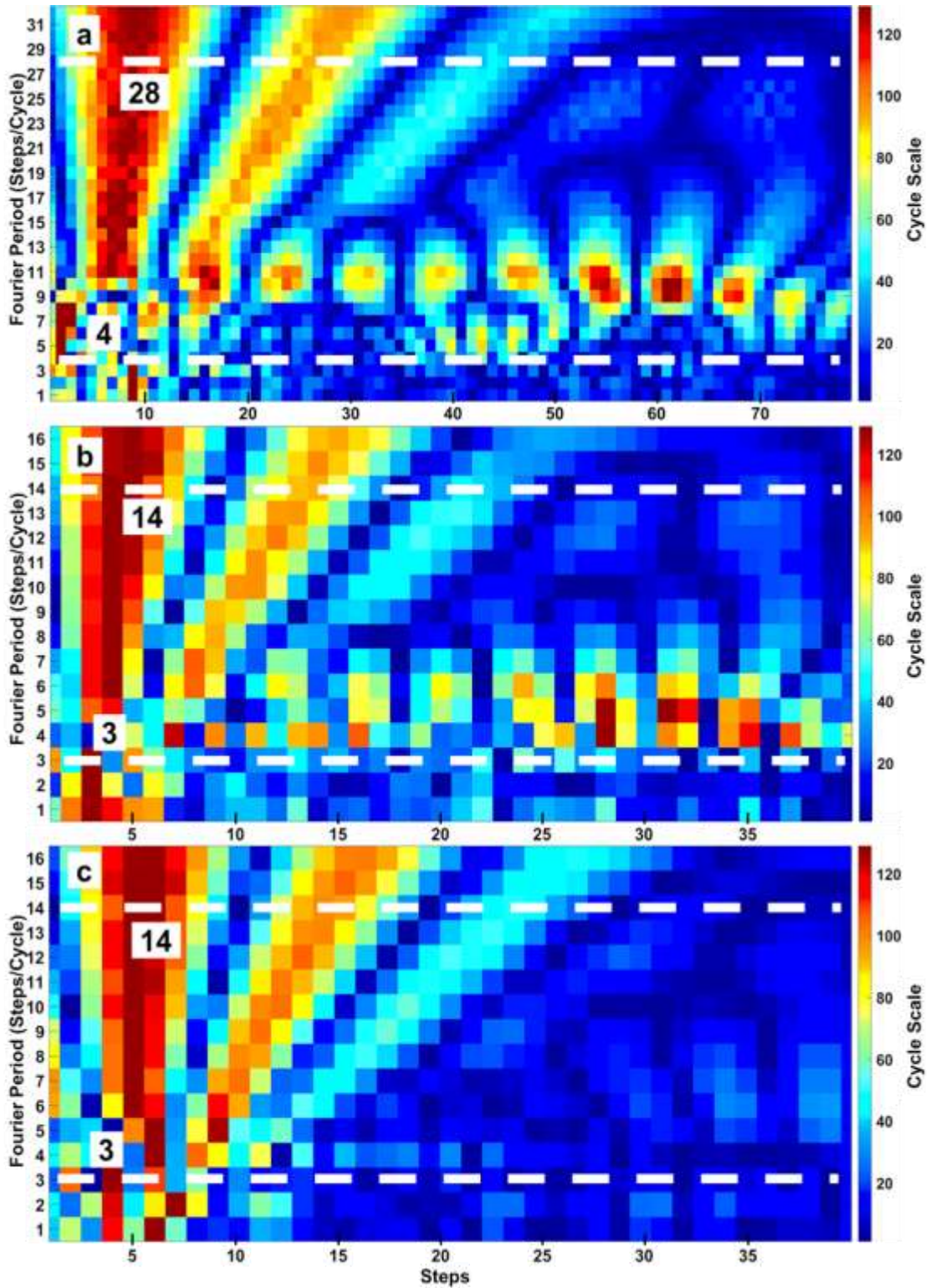


Figure 6.10: Scalograms of interval TR2. (a) Scalogram of the combined sandstone and mudstone laminae time series. The main periodicities are 28 and 4. (b) Scalogram of the sandstone laminae time series. The main periodicities are 14 and 3. (c) Scalogram of the mudstone laminae thickness time-series. The main periodicities are 14 and 3.

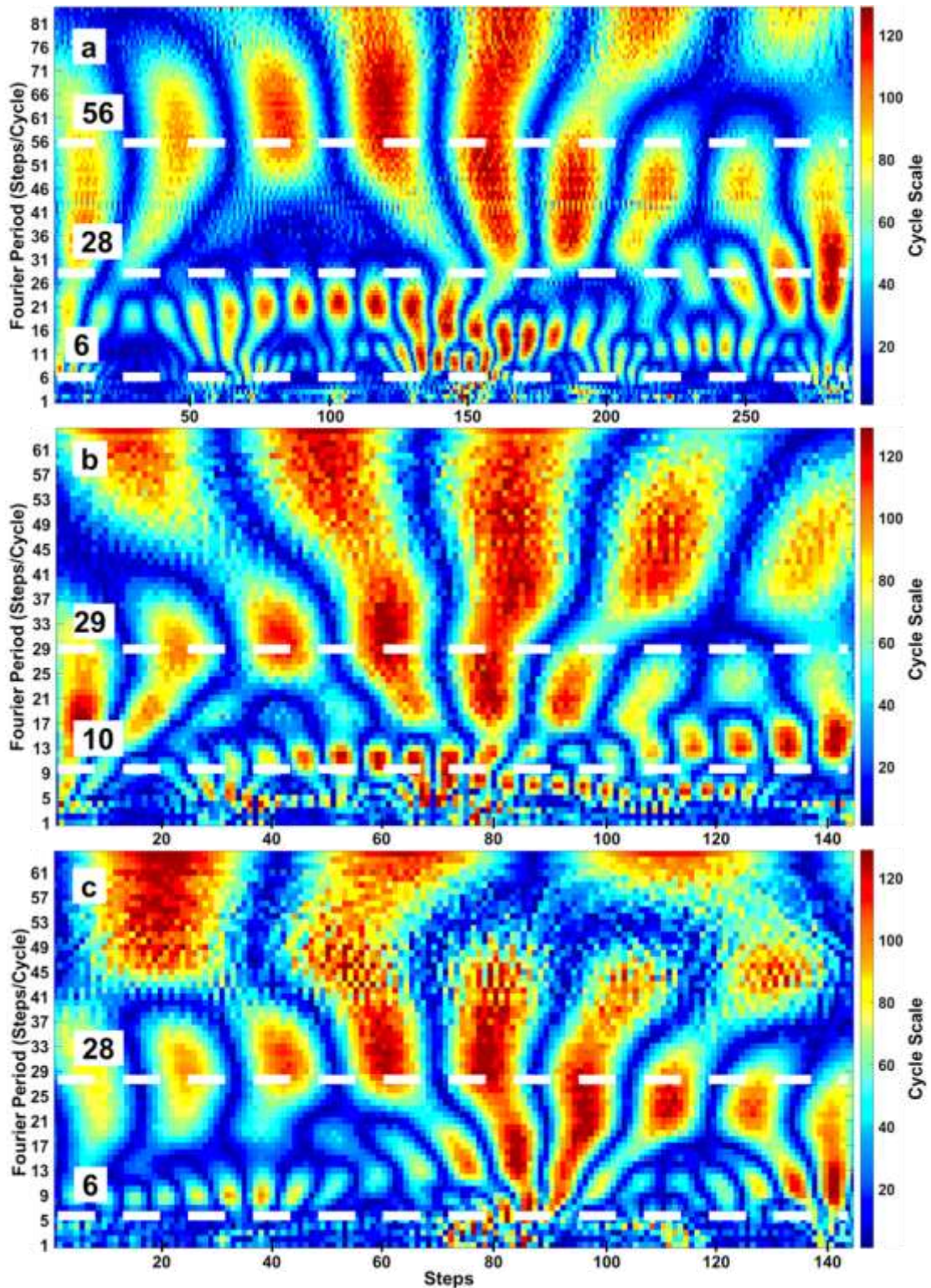


Figure 6.11: Scalograms of interval TR3. (a) Scalogram of the combined sandstone and mudstone laminae time series. The main periodicities are 6, 28, and 56. (b) Scalogram of the sandstone laminae time series. The main periodicities are 10 and 29. (c) Scalogram of the mudstone laminae thickness time series. The main periodicities are 6 and 28.

Table 6.3: Summary of tidal rhythmite interval cyclicity analysis results.

Interval	Cycles					
	SST	MST	SST + MST	CWT SST	CWT MST	CWT SST + MST
TR1	13 – 16	12 – 16	55 – 61	7, 25	4, 26, 61	16, 52
TR2	14	14 – 15	63	3, 14	3, 14	4, 28
TR3	12 – 17	12 – 15	58 – 63	10, 29	6, 28	6, 28, 56

6.7 Discussion

A lunar month is defined as the time duration for the moon to revolve around the earth, which is approximately 29.53 days (Kvale 2012). During each lunar month, there are two neap cycles (after the first or third quarters of the moon) and two spring cycles (after the new or full moon). The length of each neap or spring cycle is roughly 7.4 days (29.53 divided by 4). In a location that experiences two tides per day (semi-diurnal), each neap or spring event should ideally deposit 14 subordinate tidal laminae and 14 dominant tidal laminae (Kvale 2012). Therefore, each semi-diurnal neap-spring cycle should see the deposition of 56 laminae and each semi-diurnal lunar month should see the deposition of 112 laminae (Timmer et al. 2016). Events where greater than the ideal 56 laminae per cycle are deposited may correspond to subordinate tidal phase deposition, whereas the cycles that see less than the standard 56 laminae per cycle may correspond to non-deposition during either the receding or rising tidal phase.

Individual foresets represent the high and slack water phases of a single tidal oscillation (ebb current or flood current) (Ghosh et al. 2004). Most preserved tidal deposits tend to be subtidal because considerable reworking in the intertidal zone from wave activity and currents does occur, no matter how minor (Wach 1991). As a result, a complete tidal cycle is seldom preserved because non-deposition, erosion, or both can occur at various stages in the tidal cycle. When tidal deposits are preserved, the neap tide stage is typically characterized by the mud-dominated intervals associated with the pinstripe lamina-set and

the spring tide stage is typically characterized by the sand-dominated intervals related to the pinstripe lamina-set (Allen 1981).

6.7.1 Comparison with Carboniferous Examples

Tidal rhythmites have been documented within Carboniferous basins of North America (e.g., Kvale et al. 1989; Archer 1991; Kvale and Archer 1991; Feldman et al. 1993; Archer et al. 1995a; Miller and Eriksson 1997; Coughenour et al. 2013) and Europe (e.g., Read 1992; Wells et al. 2005a; Wells et al. 2005b; Allport et al. 2021). Examples of Carboniferous tidal rhythmites are found throughout the Western Interior Basin of the United States, such as those that occur in the Douglas Group of eastern Kansas. Lanier et al. (1993) recognized Douglas Group tidal evidence from the vertically accumulating, cyclic, and variable thickness bedsets, as well as biogenic and sedimentary structures. He measured lamina thicknesses that ranged from <1 mm to 125 mm. It was concluded that deposition occurred in an upper tidal flat setting where fluvial conditions transition to estuarine conditions because of macrotidal oscillations (Lanier et al. 1993).

In the Illinois Basin within the Mansfield Formation in southeast Indiana, Kvale et al. (1989) investigated a 10 m interval of tidal rhythmite-bearing sediments that were interpreted to have been deposited in an embayed tidal setting based on four observations: 1) the presence of upright standing lycopods which dismisses a deep-water setting, 2) drain features, such as wrinkle marks and flat-crested ripples suggest periodic, subaerial siltstone exposure, 3) the mixing of marine conodonts with terrestrial plant remains, and 4) alternating siltstone and sandstone laminations with lamina thicknesses that ranged from <1 mm to 4 mm. They concluded the periodicity suggested a semi-diurnal to mixed tidal cycle of a half lunar month.

Tidal rhythmites have been identified in the Marsdenian interval of the Pennine Basin in northern England where Brettle et al. (2002) demonstrated lamina thicknesses ranging from <1 mm to 60 mm. The lithofacies are interpreted to have been deposited in a tidally influenced delta-front mouth bar with a periodicity displaying as semi-diurnal to diurnal (Brettle et al. 2002). It is apparent from previous studies on Carboniferous basins from North America and Europe, including this work, that tidal rhythmite lamina thickness is highly variable, yet are all similar scale, magnitude, and cyclicity. The commonality is that they are well-preserved appear to have been deposited in a fluvial to estuarine setting with macrotidal conditions. The well-preserved cyclic nature and lack of sedimentary and biogenic structures of the sediments is likely due to rapid burial associated with a high tidal range. Of course, there can be corresponding erosion of sediments due to the high tidal range and tidal current velocity.

6.7.2 *Visual Cyclicity Analysis*

Periodicities of 14 are observed in histogram plot data for mudstone or sandstone laminae thicknesses. Troughs observed in the histogram plots reflect neap tide laminae and peaks represent spring tide laminae. Considering that laminae thicknesses observed in the histogram plots are not distributed in pairs of equal thicknesses, a certain degree of semi-diurnal inequality exists for both dominant and subordinate current deposition. That is, one flood/ebb event is stronger than the other daily flood/ebb event. Semi-diurnal inequality is most apparent in the TR2 sandstone histogram plot and the TR2 mudstone histogram plot (Figure 6.6b).

For the TR1 interval (Figure 6.5), the average periodicity of 58.6 laminae/cycle represents *c.* 14.65 days, denoting the semi-diurnal cycle. The tidal currents associated with

these bedforms were dominantly unidirectional, representing either ebb or flood. The estimated spring–neap–spring cycle (14.65 days) is slightly less than the ideal periodicity of 14.75 days. However, since the estimated spring–neap–spring cycle (14.65 days) nearly matches the ideal periodicity of 14.75 days, it is assumed that deposition commonly occurred during subordinate tidal phases, although in rare instances, there might have been no deposition during subordinate phases. There are at least eight complete lunar neap or spring cycles ranging from 55 – 61 laminae per cycle, representing at least four months of deposition. The results are summarized in row one of the first three columns of Table 6.3.

For the TR2 interval (Figure 6.6), the average periodicity of 63 laminae/cycle represents *c.* 15.75 days, denoting the semi-diurnal cycle. Again, the tidal currents associated with these bedforms were dominantly unidirectional, representing either ebb or flood. However, rarely there might have been deposition during subordinate phases, which might explain why the estimated spring–neap–spring cycle (15.75 days) is slightly higher than the ideal periodicity of 14.75 days. The visual evidence of this might be the thin, faint lamina that begin to appear near the middle (see Figure 6.6) of this interval and are regularly occurring to the top (youngest) of the interval. There is at least one complete lunar neap or spring cycle containing 63 laminae per cycle, representing at least a half-month deposition. The results are summarized in row two of the first three columns of Table 6.3.

For the TR3 interval (Figure 6.7), the average periodicity of 60.8 laminae/cycle represents *c.* 15.2 days, denoting the semi-diurnal cycle. Again, the tidal currents associated with these bedforms were dominantly unidirectional, representing either ebb or flood. However, rarely there might have been deposition during subordinate phases, which might

explain why the estimated spring–neap–spring cycle (15.2 days) is slightly higher than the ideal periodicity of 14.75 days. There are at least four complete lunar neap or spring cycles ranging from 58 – 63 laminae per cycle, representing at least two months of deposition. The results are summarized in row 3 of the first three columns of Table 6.3.

6.7.3 *Fast Fourier Transform Cyclicity Analysis*

The periodograms (Figure 6.8b, d, and f) of the TR1, TR2, and TR3 intervals, which are the graphical outputs from the FFT analysis all show a robust spectral peak at the frequency of 3.14 (pi) or a period of 2.0 laminations per tidal cycle, indicating a semi-diurnal tidal system (e.g., Gent and Sonnenberg 2014). The thick-thin laminations further corroborate the presence of a semi-diurnal tidal system from the thickness histograms (Figure 6.8a, c, and e) and the smooth oscillatory nature of the periodograms. This is particularly evident for intervals TR1 and TR3. The TR2 interval, which looks noticeably different from the other two intervals displays a periodogram (Figure 6.8d) with much more prominent peaks, particularly between the frequencies of two and three. These peaks could be the result of storms or another non-meteorological event, in addition to seasonal influences. It may also be the case that they are just simply anomalistic.

According to Torrence and Compo (1998), the calculated FFT periodicities of a shorter time series can be largely impacted by edge effects, resulting from padding the finite length with zeroes. Since the FFT analysis requires a times series (in this case, thickness measurements) to be of total length, 2^N , where N is a natural number (e.g., 1, 2, 3...etc.), it may be required to pad the time series with sufficient zeroes. As the wavelet increases in width, the magnitude of the edge effects will become more prominent (Timmer et al. 2016). For example, the TR2 interval contains 79 measurements. Since $2^6 = 64$ is not

long enough and $2^7 = 128$ is well over 79 measurements, zeroes must be added to the dataset; hence padding with zeroes. Similarly, edge effects become more pronounced when the time series duration is similar to the width of a wavelet corresponding to a periodicity of interest. This causes inaccurate, more prominent periodicities in short time series. Therefore, edge effects are probable in TR2 because it is a short interval with relatively few measurements. Since we are interested in periodicities of approximately 56 laminae deposited semidiurnally during a complete lunar neap-spring cycle, time-series containing less than two full cycles (approximately 112 laminae) are expected to generate incorrect CWT results. Shorter time series are also more prone to erroneous cycle lumping or splitting if less than two complete cycles are preserved.

6.7.4 *Continuous Wavelet Transform (Morlet) Analysis*

The majority of the scalograms and visual cyclicity analyses match rather well, although substantial variations exist between the two techniques, probably because of interference associated with the thickness data, which is explained further on in this section. The scalograms that match the visual cyclicity analysis the closest are TR1 for the combined sandstone and mudstone thickness dataset (Figure 6.9a), TR2 for the sandstone laminae thickness dataset (Figure 6.10b) and the mudstone laminae thickness dataset (Figure 6.10c), and TR3 for the sandstone laminae thickness dataset (Figure 6.11a) and the combined sandstone and mudstone thickness dataset (Figure 6.11c). The planar parallel nature of the interlaminated sediment is likely responsible for the overall decent matches in the two analysis techniques.

Thickness data may cause interference where the interlaminated sediments display an undulatory nature, such as in TR1 (Figure 6.5a) (Timmer et al. 2016). When calculating

periodicities using CWT analysis, the impacts of interference become apparent, as follows. Small amplitude troughs, with corresponding small laminae thicknesses can be obscured by large amplitude peaks, with corresponding large laminae thicknesses (Timmer et al. 2016). Since the lunar fortnightly inequality is generally not preserved and, therefore, not discernible, multiple cycles that are confined by prominent amplitude peaks are susceptible to being grouped collectively into an artificially protracted interval (Timmer et al. 2016). Conversely, if a large amplitude (thick laminae) neap-spring cycle or a single spring cycle is present in the time series, it can delineate smaller, false periodicities. Both depositional patterns are demonstrated in TR2, where visual cycles and CWT cycles differ significantly in the combined mudstone and sandstone series, an apparent common problem in other studies of tidal deposits (e.g., Timmer et al. 2016). When numerous cycles are grouped together because there is a deficiency in high amplitude laminae separating the cycles, it tends to generate unnaturally long periodicities for the mudstone and sandstone scalograms (Timmer et al. 2016).

6.7.5 *Comparison to Modern Analogues*

The Carboniferous provides perhaps the best examples of tidal rhythmites (e.g., Kvale et al. 1989; Archer 1991; Kvale and Archer 1991; Feldman et al. 1993; Archer et al. 1995a; Miller and Eriksson 1997; Wells et al. 2005a; Coughenour et al. 2013), whereas modern analogues are seemingly less common. If we consider tidal rhythmites in regard to their rapid vertical accumulation rates and biogenic and sedimentary structures, then examples of modern analogues could be the Bay of Fundy located between New Brunswick and Nova Scotia in Atlantic Canada, and Mont-Saint-Michel Bay in northern France (Tessier et al. 1995). These are depositional environments where fluvial to estuarine

sedimentation occurs within a recessed coastline and exhibit a significant tidal range (an average of 16 m in the Bay of Fundy and an average of 12 m in Mont-Saint-Michel Bay). The tidal range at the transition between fluvial and estuarine environments are magnified by the cone-shaped geometry of their respective bay, with accumulation rates that might locally surpass 1 m per year (Tessier 1990; Dalrymple et al. 1991). Individual lamina thicknesses in the Bay of Fundy were measured and ranged between <1 to 38 mm for sand laminae and <1 to 18 mm for mud laminae (Dalrymple et al. 1991). Individual lamina thicknesses in Mont-Saint-Michel Bay were measured and ranged from 1-2 mm to 1-2 cm (Tessier et al. 1995). These are comparable to <1 to 13 mm for sand laminae and < 1 to 11.5 mm for mud laminae in this study.

6.8 Conclusions

We provide strong evidence of a mid-Euramerican seaway possibly connecting to the Paleo-Tethys Ocean during the Late Carboniferous, which conforms with other tidal rhythmite-bearing intervals from North America to Europe based upon their characteristics. We suggest the Joggins Formation is affected by open-marine conditions, at least episodically, as indicated by the abundant tidal rhythmite intervals. Given the well-preserved nature of the tidal rhythmite intervals, it would suggest mesotidal to macrotidal conditions were prevalent in a fluvial to estuarine depositional setting.

Visual cyclicity analysis suggests the tidal regime represented by the studied intervals is a semi-diurnal tidal model with a lunar monthly tidal cycle. The FFT analysis of the intervals show strong spectral peaks at frequencies of 3.14 (pi) or a period of 2.0 laminations per tidal cycle on their respective periodograms. This indicates a semi-diurnal tidal system during the Late Carboniferous. The thick-thin laminations further substantiate

the evidence from the lamina thickness histograms and the smooth oscillatory trend of the curve in the periodograms. The CWT analysis results match the visual cyclicity analysis and further suggest a semi-diurnal tidal system.

While there is an abundance of quality research conducted on the Joggins Formation, it has been largely focused on the outcrop section. This study, based on drill core obtained further inland from the Joggins Formation outcrop has attempted to broaden the research conducted on this world-famous sedimentary succession. In doing so, it has confirmed the existence of marine conditions by way of tidal rhythmites, which has ramifications for clarifying the variability in paleoecological trends between the northern and southern Paleo-Tethys Ocean. An avenue for future work could be focused on comparing the paleoecology suggested by the outcrop with that suggested by the drill core interval. On a global scale, future work could compare the paleoecological trends from other North American and European Carboniferous basins to that of the Cumberland Basin.

6.9 Acknowledgements

This work was made possible by the Dalhousie University Basin and Reservoir Laboratory. I would like to thank Mick O'Neill (core supervisor) at the Nova Scotia Department of Natural Resources Core Library for retrieving the core from warehouse storage and accommodating me over several days. We are grateful to Bill Richards for overseeing the data collection, data processing, and data interpretation aspects and providing helpful suggestions and sound advice for improving this paper.

6.10 References Cited in Chapter 6

Allen, J.P., Fielding, C.R., Rygel, M.C., and Gibling, M.R. 2013. Deconvolving Signals of Tectonic and Climatic Controls From Continental Basins: An Example From the Late Paleozoic Cumberland Basin, Atlantic Canada. *Journal of Sedimentary Research*, **83**: 847-872. doi:10.2110/jsr.2013.58.

Allen, J.R.L. 1981. Lower Cretaceous tides revealed by cross-bedding with mud drapes. *Nature*, **289**: 579-581. doi:10.1038/289579a0.

Allport, H.A., Davies, N.S., Shillito, A.P., Mitchell, E.G., and Herron, S.T. 2021. Non-palimpsested crowded Skolithos ichnofabrics in a Carboniferous tidal rhythmite: Disentangling ecological signatures from the spatio-temporal bias of outcrop. *Sedimentology*, **69**: 1-23. doi:10.1111/sed.12947.

Archer, A.W. 1991. Modeling of tidal rhythmites using modern tidal periodicities and implications for short-term sedimentation rates. *In Sedimentary Modeling: Computer Simulations and Methods for Improved Parameter Definition (Bulletin 233)*. Edited by E.K. Franseen and W.L. Watney and C.G. Kendall and W. Ross. Kansas Geological Survey, Lawrence, Kansas. pp. 185-194.

Archer, A.W. 1996. Reliability of lunar orbital periods extracted from ancient cyclic tidal rhythmites. *Earth and Planetary Science Letters*, **141**: 1-10.

Archer, A.W., and Greb, S.F. 1995. An Amazon-Scale Drainage System in the Early Pennsylvanian of Central North America. *The Journal of Geology*, **103**: 611-627. doi:10.1086/629784.

Archer, A.W., Kuecher, G.J., and Kvale, E.P. 1995a. The Role of Tidal-Velocity Asymmetries in the Deposition of Silty Tidal Rhythmites (Carboniferous, Eastern Interior Coal Basin, U.S.A.). *Journal of Sedimentary Research*, **65**: 408-416. doi:10.1306/d42680d6-2b26-11d7-8648000102c1865d.

Archer, A.W., Calder, J.H., Gibling, M.R., Naylor, R.D., Reid, D.R., and Wightman, W.G. 1995b. Invertebrate trace fossils and agglutinated foraminifera as indicators of marine influence within the classic Carboniferous section at Joggins, Nova Scotia, Canada. *Canadian Journal of Earth Sciences*, **32**: 2027-2039. doi:10.1139/e95-156.

Bhattacharya, B., Bandyopadhyay, S., Mahapatra, S., and Banerjee, S. 2012. Record of tide-wave influence on the coal-bearing Permian Barakar Formation, Raniganj Basin, India. *Sedimentary Geology*, **267-268**: 25-35. doi:10.1016/j.sedgeo.2012.05.006.

Boersma, J.R. 1969. Internal structure of some tidal mega-ripples on a shoal in the Westerschelde Estuary, the Netherlands: report of a preliminary investigation. *Netherlands Journal of Geosciences/Geologie en Mijnbouw*, **48**: 409-414.

Boersma, J.R., and Terwindt, J.H.J. 1981. Neap-spring tide sequences of intertidal shoal deposits in a mesotidal estuary. *Sedimentology*, **28**: 151-170. doi:10.1111/j.1365-3091.1981.tb01674.x.

Brand, U. 1994. Continental hydrology and climatology of the Carboniferous Joggins Formation (lower Cumberland Group) at Joggins, Nova Scotia: evidence from the geochemistry of bivalves. *Palaeogeography, Palaeoclimatology, Palaeoecology*, **106**: 307-321. doi:10.1016/0031-0182(94)90016-7.

Brauer, A., Mangili, C., Moscariello, A., and Witt, A. 2008. Palaeoclimatic implications from micro-facies data of a 5900 varve time series from the Piànico interglacial sediment record, southern Alps. *Palaeogeography, Palaeoclimatology, Palaeoecology*, **259**: 121-135. doi:10.1016/j.palaeo.2007.10.003.

Brettell, M.J., McIlroy, D., Elliott, T., Davies, S.J., and Waters, C.N. 2002. Identifying cryptic tidal influences within deltaic successions: an example from the Marsdenian (Namurian) interval of the Pennine Basin, UK. *Journal of the Geological Society*, **159**: 379-391. doi:10.1144/0016-764901-070.

Calder, J.H. 1998. The Carboniferous evolution of Nova Scotia. Geological Society, London, Special Publications, **143**: 261-302. doi:10.1144/gsl.Sp.1998.143.01.19.

Calder, J.H., Rygel, M.C., Ryan, R.J., Falcon-Lang, H.J., and Herbert, B.L. 2005. Stratigraphy and sedimentology of early Pennsylvanian red beds at Lower Cove, Nova Scotia, Canada: the Little River Formation with redefinition of the Joggins Formation. *Atlantic Geology*, **41**: 87-102. doi:10.4138/183.

Calder, J.H., Gibling, M.R., Scott, A.C., Davies, S.J., Herbert, B.L., Greb, S.F., and DiMichele, W.A. 2006. A fossil lycopsid forest succession in the classic Joggins section of Nova Scotia: paleoecology of a disturbance-prone Pennsylvanian wetland. *Special Papers - Geological Society of America*, **399**: 169. doi:10.1130/2006.2399(09).

Carpenter, D.K., Falcon-Lang, H.J., Benton, M.J., and Grey, M. 2015. Early Pennsylvanian (Langsettian) fish assemblages from the Joggins Formation, Canada, and their implications for palaeoecology and palaeogeography. *Palaeontology*, **58**: 661-690. doi: 10.5061/dryad.b0551.

Carroll, R.L. 1967. Labyrinthodonts from the Joggins Formation. *Journal of Paleontology*, **41**: 111-142.

Chan, M.A., Kvale, E.P., Archer, A.W., and Sonett, C.P. 1994. Oldest direct evidence of lunar-solar tidal forcing encoded in sedimentary rhythmmites, Proterozoic Big Cottonwood Formation, central Utah. *Geology*, **22**: 791-794. doi:10.1130/0091-7613(1994)022<0791:Odeols>2.3.Co;2.

Chipman, M., Grey, M., and Pufahl, P.K. 2020. Coprolites from a brackish ecosystem in the Pennsylvanian Joggins Formation, Nova Scotia, Canada and their palaeoecological implications. *Palaeogeography, Palaeoclimatology, Palaeoecology*, **538**. doi:10.1016/j.palaeo.2019.109407.

Choi, K.S., and Park, Y.A. 2000. Late Pleistocene silty tidal rhythmmites in the macrotidal flat between Youngjong and Yongyou Islands, west coast of Korea. *Marine Geology*, **167**: 231-241. doi:10.1016/s0025-3227(00)00037-2.

Choi, K.S., and Kim, D.H. 2016. Morphologic and hydrodynamic controls on the occurrence of tidal bundles in an open-coast macrotidal environment, northern Gyeonggi Bay, west coast of Korea. *Sedimentary Geology*, **339**: 68-82. doi:10.1016/j.sedgeo.2016.04.008.

Coughenour, C.L., Archer, A.W., and Lacovara, K.J. 2013. Calculating Earth–Moon system parameters from sub-yearly tidal deposit records: An example from the carboniferous tradewater formation. *Sedimentary Geology*, **295**: 67-76. doi:10.1016/j.sedgeo.2013.08.001.

Dafoe, L.T., Stimson, M.R., and Gibling, M.R. Terrestrial to marine transitions recorded in invertebrate trace fossils of the Joggins Formation. *In* 1st Joggins Research Symposium. Joggins, Nova Scotia 2018. *Atlantic Geology*. Vol. 54.

Dalrymple, R.W., Makino, Y., and Zaitlin, B.A. 1991. Temporal and spatial patterns of rhythmite deposition on mud flats in the macrotidal Cobequid Bay-Salmon River Estuary, Bay of Fundy, Canada. *In* *Clastic Tidal Sedimentology - Memoir 16. Edited by D.G. Smith and G.E. Reinson and B.A. Zaitlin and R.A. Rahmani*. Canadian Society of Petroleum Geologists, Calgary, Alberta. pp. 137-160.

Davies, S.J., and Gibling, M.R. 2003. Architecture of coastal and alluvial deposits in an extensional basin: the Carboniferous Joggins Formation of eastern Canada. *Sedimentology*, **50**: 415-439. doi:10.1046/j.1365-3091.2003.00553.x

Davies, S.J., Gibling, M.R., Rygel, M.C., Calder, J.H., and Skilliter, D.M. 2005. The Pennsylvanian Joggins Formation of Nova Scotia: sedimentological log and stratigraphic framework of the historic fossil cliffs. *Atlantic Geology*, **41**: 87-102. doi:10.4138/182.

De Boer, P.L., Oost, A.P., and Visser, M.J. 1989. The Diurnal Inequality of the Tide as a Parameter for Recognizing Tidal Influences. *Journal of Sedimentary Research*, **59**: 912-921. doi:10.1306/212f90b1-2b24-11d7-8648000102c1865d.

Donselaar, M.E., and Geel, C.R. 2016. Facies architecture of heterolithic tidal deposits: the Holocene Holland Tidal Basin. *Netherlands Journal of Geosciences - Geologie en Mijnbouw*, **86**: 389-402. doi:10.1017/s001677460002360x.

Dreyer, T. 1992. Significance of tidal cyclicity for modelling of reservoir heterogeneities in the lower Jurassic Tilje Formation, mid-Norwegian shelf. *Norsk Geologisk Tidsskrift*, **72**: 159-170.

Eriksson, K.A., and Simpson, E.L. 2000. Quantifying the oldest tidal record: The 3.2 Ga Moodies Group, Barberton Greenstone Belt, South Africa. *Geology*, **28**: 831-834. doi:10.1130/0091-7613(2000)28<831:Qtotrt>2.0.Co;2.

Eriksson, K.A., and Simpson, E.L. 2004. Precambrian Tidalites: Recognition and Significance. *In* *The Precambrian Earth: Tempos and Events*. Edited by P.G. Eriksson and W. Altermann and D.R. Nelson and W.U. Mueller and O. Catuneanu. Elsevier Science, The Netherlands. pp. 631-642.

Fabuel-Perez, I., Redfern, J., and Hodgetts, D. 2009b. Sedimentology of an intra-montane rift-controlled fluvial dominated succession: The Upper Triassic Oukaimeden Sandstone Formation, Central High Atlas, Morocco. *Sedimentary Geology*, **218**: 103-140. doi:10.1016/j.sedgeo.2009.04.006.

Feldman, H.R., Archer, A.W., Kvale, E.P., Cunningham, C.R., Maples, C.G., and West, R.R. 1993. A Tidal Model of Carboniferous Konservat-Lagerstätten Formation. *Palaios*, **8**: 485-498. doi:10.2307/3515022.

Friedman, G.M., and Chakraborty, C. 2006. Interpretation of tidal bundles: Two reasons for a paradigm shift. *Carbonates and Evaporites*, **21**: 170-175. doi:10.1007/bf03175666.

Geel, C.R., and Donselaar, M.E. 2007. Reservoir modelling of heterolithic tidal deposits: sensitivity analysis of an object-based stochastic model. *Netherlands Journal of Geosciences*, **86**: 403-411.

Gent, V.A., and Sonnenberg, S.A. Fourier Analysis of the Laminated Facies of the Middle Bakken Member, Sanish-Parshall Field, Mountrail County, North Dakota. *In AAPG Rocky Mountain Section Meeting*. Denver, CO 2014. AAPG.

Ghosh, S.K., Chakraborty, C., and Chakraborty, T. 2004. Combined tide and wave influence on sedimentation of Lower Gondwana coal measures of central India: Barakar Formation (Permian), Satpura basin. *Journal of the Geological Society*, **161**: 117-131. doi:10.1144/0016-764902-077.

Gibling, M.R., Culshaw, N., Rygel, M.C., and Pascucci, V. 2008b. The Maritimes Basin of Atlantic Canada: Basin Creation and Destruction in the Collisional Zone of Pangea. *In Sedimentary basins of the world. Edited by A.D. Miall*. Elsevier, Amsterdam. pp. 211-244.

Gibling, M.R., Calder, J.H., Ryan, R., Poll, H.W.v.d., and Yeo, G.M. 1992. Late Carboniferous and Early Permian drainage patterns in Atlantic Canada. *Canadian Journal of Earth Sciences*, **29**: 338-352. doi:10.1139/e92-030.

Goupillaud, P., Grossmann, A., and Morlet, J. 1984. Cycle-octave and related transforms in seismic signal analysis. *Geoexploration*, **23**: 85-102. doi:10.1016/0016-7142(84)90025-5.

Haszeldine, R.S. 2009. Carboniferous North Atlantic palaeogeography: stratigraphic evidence for rifting, not megashear or subduction. *Geological Magazine*, **121**: 443-463. doi:10.1017/s0016756800029988.

Horne, J.H., and Baliunas, S.L. 1986. A prescription for period analysis of unevenly sampled time series. *The Astrophysical Journal*, **302**: 757-763. doi:10.1086/164037

Jafarpour, B. 2010. Wavelet reconstruction of geologic facies from nonlinear dynamic flow measurements. *IEEE Transactions on Geoscience and Remote Sensing*, **49**: 1520-1535.

Jaiswal, S., and Bhattacharya, B. 2018. Characterization of middle Eocene tide-influenced delta: A study from core samples of Hazad Member, Ankleshwar Formation, South Cambay Basin, India. *Journal of Earth System Science*, **127**: 65. doi:10.1007/s12040-018-0966-8.

Juby, I. 2009. The Joggins Polystrate Fossils. In *Rock Solid Answers*. Edited by M. Oard and J.K. Reed. Creation Research Society Books, Chino Valley, Arizona. pp. 217-225.

Klausen, T.G., and Mørk, A. 2014. The upper Triassic paralic deposits of the De Geerdalen Formation on Hopen: Outcrop analog to the subsurface Snadd Formation in the Barents Sea. *AAPG Bulletin*, **98**: 1911-1941. doi:10.1306/02191413064.

Kreisa, R.D., and Moila, R.J. 1986. Sigmoidal tidal bundles and other tide-generated sedimentary structures of the Curtis Formation, Utah. *Geological Society of America Bulletin*, **97**: 381-387. doi:10.1130/0016-7606(1986)97<381:Stbaot>2.0.Co;2.

Kvale, E.P. 2012. Tidal Constituents of Modern and Ancient Tidal Rhythmites: Criteria for Recognition and Analyses. In *Principles of Tidal Sedimentology*. Edited by R.A. Davis Jr and R.W. Dalrymple. Springer, New York. pp. 1-17.

Kvale, E.P., and Archer, A.W. 1991. Characteristics of two, Pennsylvanian-age, semidiurnal tidal deposits in the Illinois Basin, USA. In *Clastic Tidal Sedimentology - Memoir 16*. Edited by D.G. Smith and G.E. Reinson and B.A. Zaitlin and R.A. Rahmani. Canadian Society of Petroleum Geologists, Calgary, Alberta. pp. 179-188.

Kvale, E.P., Archer, A.W., and Johnson, H.R. 1989. Daily, monthly, and yearly tidal cycles within laminated siltstones of the Mansfield Formation (Pennsylvanian) of Indiana. *Geology*, **17**: 365-368. doi:10.1130/0091-7613(1989)017.

Labrecque, P.A., Jensen, J.L., and Hubbard, S.M. 2011. Cyclicity in Lower Cretaceous point bar deposits with implications for reservoir characterization, Athabasca Oil Sands, Alberta, Canada. *Sedimentary Geology*, **242**: 18-33. doi:10.1016/j.sedgeo.2011.06.011.

Lanier, W.P., Feldman, H.R., and Archer, A.W. 1993. Tidal sedimentation from a fluvial to estuarine transition, Douglas Group, Missourian-Virgilian, Kansas. *Journal of Sedimentary Research*, **63**: 860-873. doi:10.1306/D4267C2B-2B26-11D7-8648000102C1865D.

Leeder, M.R. 1988. Devonian-Carboniferous river systems and sediment dispersal from the orogenic belts and cratons of NW Europe. Geological Society, London, Special Publications, **38**: 549-558. doi:10.1144/gsl.Sp.1988.038.01.37.

Leeder, M.R., Duff, P.M.D., and Smith, A.J. 1992. Dinantian. *Geology of England and Wales*: 207-237.

Maynard, J.R., Hofmann, W., Dunay, R.E., Benthan, P.N., Dean, K.P., and Watson, I. 1997. The Carboniferous of Western Europe; the development of a petroleum system. *Petroleum Geoscience*, **3**: 97-115. doi:10.1144/petgeo.3.2.97.

Miller, D.J., and Eriksson, K.A. 1997. Late Mississippian Prodeltaic Rhythmites in the Appalachian Basin: A Hierarchical Record of Tidal and Climatic Periodicities. *Journal of Sedimentary Research*, **67**: 653-660. doi:10.1306/d4268608-2b26-11d7-8648000102c1865d.

Prokoph, A., and Barthelmes, F. 1996. Detection of nonstationarities in geological time series: wavelet transform of chaotic and cyclic sequences. *Computers & geosciences*, **22**: 1097-1108. doi:10.1016/S0098-3004(96)00054-4.

Prokoph, A., and Agterberg, F.P. 1999. Detection of sedimentary cyclicality and stratigraphic completeness by wavelet analysis; an application to late Albian cyclostratigraphy of the Western Canada Sedimentary Basin. *Journal of Sedimentary Research*, **69**: 862-875. doi:10.2110/jsr.69.862.

Rampino, M.R., Caldeira, K., and Zhu, Y. 2021. A pulse of the Earth: A 27.5-Myr underlying cycle in coordinated geological events over the last 260 Myr. *Geoscience Frontiers*, **12**: 1-7. doi:10.1016/j.gsf.2021.101245.

Read, W.A. 1992. Evidence of tidal influences in Arnsbergian rhythmites in the Kincardine Basin. *Scottish Journal of Geology*, **28**: 135-142. doi:10.1144/sjg28020135.

REI Nova Scotia. 1995. The Coring and Logging of REI-B2-1. Halifax, Nova Scotia.

Reisz, R.R., and Modesto, S.P. 1996. Archerpeton anthracos from the Joggins Formation of Nova Scotia: a microsauro, not a reptile. *Canadian Journal of Earth Sciences*, **33**: 703-709. doi:10.1139/e96-053.

Richards, M.T. 1994. Transgression of an estuarine channel and tidal flat complex: the Lower Triassic of Barles, Alpes de Haute Provence, France. *Sedimentology*, **41**: 55-82. doi:10.1111/j.1365-3091.1994.tb01392.x.

Ryan, R.J., and Boehner, R.C. 1994. Geology of the Cumberland Basin, Cumberland, Colchester and Pictou Counties, Nova Scotia - Memoir 10. *Edited by Mines and Energy Branch - Department of Natural Resources*. Department of Natural Resources, Halifax.

Rygel, M.C., and Gibling, M.R. 2006. Natural Geomorphic Variability Recorded in a High-Accommodation Setting: Fluvial Architecture of the Pennsylvanian Joggins Formation of Atlantic Canada. *Journal of Sedimentary Research*, **76**: 1230-1251. doi:10.2110/jsr.2006.100.

Rygel, M.C., Sheldon, E.P., Stimson, M.R., Calder, J.H., Ashley, K.T., and Salg, J.L. 2014. The Pennsylvanian Springhill Mines Formation: sedimentological framework for a portion of the Joggins Fossil Cliffs UNESCO World Heritage Site. *Atlantic Geology*, **50**: 249-289. doi:10.4138/atlgol.2014.013.

Shukla, T., and Shukla, U. 2013. Tidal bundles: An evidence of mixed tidal regime in scarp sandstone formation of the proterozoic Kaimur Group, Vindhyan Basin, Mirzapur District, (Uttar Pradesh), India. *Gondwana Geological Magazine*, **28**: 93-99.

Smith, D.G. 1988. Tidal bundles and mud couplets in the McMurray Formation, northeastern Alberta, Canada. *Bulletin of Canadian Petroleum Geology*, **36**: 216-219. doi:10.35767/gscpgbull.36.2.216.

Stage, M. 1999. Signal analysis of cyclicity in Maastrichtian pelagic chalks from the Danish North Sea. *Earth and Planetary Science Letters*, **173**: 75-90. doi:10.1016/S0012-821X(99)00213-7.

Tanyel, E.D. 2006. Formation evaluation using wavelet analysis on logs of the Chinji and Nagri Formations, northern Pakistan. Texas A&M University.

Tape, C.H., Cowan, C.A., and Runkel, A.C. 2003. Tidal-Bundle Sequences in the Jordan Sandstone (Upper Cambrian), Southeastern Minnesota, U.S.A.: Evidence for Tides Along Inboard Shorelines of the Sauk Epicontinental Sea. *Journal of Sedimentary Research*, **73**: 354-366. doi:10.1306/091602730354.

Teedumae, A., Heldur, N., and Kallaste, T. Sedimentary cyclicity and dolomitization of the Raikkiila Formation in the Nurme drill core (Silurian, Estonia). *In Proceedings of the Estonian Academy of Sciences, Geology*. 2004. *Edited by* H. Aben and V. Kurnitski. Estonian Academy Publishers. Vol. 53, pp. 42-62.

Tessier, B. 1990. Enregistrement des cycles Tidaux en accretion verticale dans un milieu actuel (la Baie du Mont Saint Michel) et dans une formation ancienne (la molasse marine miocène du bassin de Digne): mesure du temps et application à la reconstitution des paléoenvironnements. Université de Caen.

Tessier, B., and Gigot, P. 1989. A vertical record of different tidal cyclicities: an example from the Miocene Marine Molasse of Digne (Haute Provence, France). *Sedimentology*, **36**: 767-776. doi:10.1111/j.1365-3091.1989.tb01745.x.

Tessier, B., Archer, A.W., Lanier, W.P., and Feldman, H.R. 1995. Comparison of ancient tidal rhythmites (Carboniferous of Kansas and Indiana, USA) with modern analogues. *In* *Tidal Signatures in Modern and Ancient Sediments*. Edited by B.W. Flemming and A. Bartholoma. Wiley-Blackwell, Oxford, UK. pp. 259-271.

Tibert, N.E., and Dewey, C.P. 2006. Velatomorpha, a new healdioidean ostracode genus from the early Pennsylvanian Joggins Formation, Nova Scotia, Canada. *Micropaleontology*, **52**: 51-66. doi:10.2113/gsmicropal.52.1.51.

Timmer, E.R., Gingras, M.K., Morin, M.L., Ranger, M.J., and Zonneveld, J.P. 2016. Laminae-scale rhythmicity of inclined heterolithic stratification, Lower Cretaceous McMurray Formation, NE Alberta, Canada. *Bulletin of Canadian Petroleum Geology*, **64**: 199-217. doi:10.2113/gscpgbull.64.2.199.

Torrence, C., and Compo, G.P. 1998. A Practical Guide to Wavelet Analysis. *Bulletin of the American Meteorological Society*, **79**: 61-78. doi:10.1175/1520-0477(1998)079<0061:Apgtwa>2.0.Co;2.

Uhlir, D.M., Akers, A., and Vondra, C.F. 1988. Tidal inlet sequence, Sundance Formation (Upper Jurassic), north-central Wyoming. *Sedimentology*, **35**: 739-752. doi:10.1111/j.1365-3091.1988.tb01248.x.

Visser, M.J. 1980. Neap-spring cycles reflected in Holocene subtidal large-scale bedform deposits: A preliminary note. *Geology*, **8**: 543-546. doi:10.1130/0091-7613(1980)8<543:Ncrihs>2.0.Co;2.

Wach, G.D. 1991. *Sedimentology and Stratigraphy of the Lower Cretaceous of the Channel Basin*. Department of Earth Sciences, University of Oxford, Oxford, UK.

Waldron, J.W.F., and Rygel, M.C. 2005. Role of evaporite withdrawal in the preservation of a unique coal-bearing succession: Pennsylvanian Joggins Formation, Nova Scotia. *Geology*, **33**: 337-340. doi:10.1130/g21302.1.

Waldron, J.W.F., Rygel, M.C., Gibling, M.R., and Calder, J.H. 2013. Evaporite tectonics and the late Paleozoic stratigraphic development of the Cumberland basin, Appalachians of Atlantic Canada. *Geological Society of America Bulletin*, **125**: 945-960. doi:10.1130/b30718.1.

Wang, J., Bai, C., Xu, Y., and Bai, S. 2010. Tidal Couplet Formation and Preservation, and Criteria for Discriminating Storm-Surge Sedimentation on the Tidal Flats of Central Jiangsu Province, China. *Journal of Coastal Research*, **2010**: 976-981. doi:10.2112/jcoastres-d-09-00166.1.

Wells, M.R., Allison, P.A., Hampson, G.J., Piggott, M.D., and Pain, C.C. 2005a. Modelling ancient tides: the Upper Carboniferous epi-continental seaway of Northwest Europe. *Sedimentology*, **52**: 715-735. doi:10.1111/j.1365-3091.2005.00718.x.

Wells, M.R., Allison, P.A., Piggott, M.D., Pain, C.C., Hampson, G.J., and De Oliveira, C.R.E. 2005b. Large sea, small tides: the Late Carboniferous seaway of NW Europe. *Journal of the Geological Society*, **162**: 417-420.

Williams, G.E. 1989. Precambrian tidal sedimentary cycles and Earth's paleorotation. *Eos, Transactions American Geophysical Union*, **70**: 33-41. doi:10.1029/89eo00012.

Williams, G.E. 2000. Geological constraints on the Precambrian history of Earth's rotation and the Moon's orbit. *Reviews of Geophysics*, **38**: 37-59. doi:10.1029/1999rg900016.

Williams, G.E. 2004. Earth's Precambrian rotation and the evolving lunar orbit: Implications of tidal rhythmite data for palaeogeophysics. *In* *The Precambrian Earth: Tempos and Events*. Elsevier, Amsterdam. *Edited by* P.G. Eriksson and W. Altermann and D.R. Nelson and W.U. Mueller and O. Catuneanu. Elsevier Science, The Netherlands. pp. 473-482.

Williams, H. 1984. Miogeoclines and suspect terranes of the Caledonian–Appalachian Orogen: tectonic patterns in the North Atlantic region. *Canadian Journal of Earth Sciences*, **21**: 887-901. doi:10.1139/e84-095.

Chapter 7: Uncovering the Milankovitch Record from a Late Carboniferous Cyclothem Succession in Paleoequatorial Euramerica

T.B. Kelly, F.W. Richards, and G.D. Wach

This chapter is based on the paper “Uncovering the Milankovitch Record from a Late Carboniferous Cyclothem Succession in Paleoequatorial Euramerica”, by Trevor B. Kelly, Grant D. Wach, and Bill (F.W.) Richards and will be submitted to the *Atlantic Geology* journal.

7.1 Abstract

A cyclothem describes the climate-driven deposition of repetitive and vertically accreted successions of marine and non-marine sediments such as sandstone, thinly interbedded, heterolithic sandstone and mudrock, mudrock, limestone, and coal. The Late Carboniferous was characterized by the deposition of these repetitive successions in the Pangean interior near the equatorial boundary. This research tests the theory that orbital forcing signals will be recognizable due to sea level and climate change. We present quantitative evidence of preserved Milankovitch cycles within a prominent, conformable Late Carboniferous succession using a geomathematical approach. We can identify specific ratios corresponding to Milankovitch cycles by combining a fast Fourier transform and one-dimensional continuous wavelet transform analyses on a non-subjective natural gamma ray geophysical borehole log. We show that fast Fourier transform and continuous wavelet transform analyses reveal cycles for long and short eccentricity, obliquity, and precession. Our results indicate that Milankovitch cyclicity is preserved and is in keeping with other Euramerican Late Carboniferous-aged basins. Quantitative results from this study show evidence for Milankovitch cycles in these strata and suggest that cyclicity may be present basin-wide, despite the tectonic regime of a basin with a high subsidence rate. The fast

Fourier transform produced a noteworthy ratio of 18.99:5.15:2.02:1, similar to the ratio of 20:5:2:1, which defines the four main orbital periods of long (400 kyr) and short (100 kyr) eccentricity, obliquity (40 kyr), and precession (20 kyr). The continuous wavelet transform generated a ratio of 1:4, equal to the ratio of short (100 kyr) and long (400 kyr) eccentricity orbital periods.

7.2 Introduction

The late Paleozoic Era exhibited ice-house climatic conditions, with the southern poles covered by ice caps, yet the study area displayed a tropical environment (Figure 7.1a) (Atlantic Geoscience Society 2001; Calder 2017; Svensen et al. 2018). This timeframe hosted the prolific deposition of Late Carboniferous (Pennsylvanian) cyclothems within the paleoequatorial latitudes of Euramerica and are considered representative examples of glacio-eustatic sedimentation, with sea-level variations moderated by the increasing and decreasing ice volume in the Southern Hemisphere (Veevers and Powell 1987).

With publications by Udden (1912) and Weller (1930), relative sea-level control emerged as an important theory during the first half of the twentieth century (van den Belt et al. 2015). However, the earliest to connect widespread late Paleozoic glaciation with the cyclic nature of coal-bearing Late Carboniferous deposits was Wanless and Shepard (1936). The assumption that orbital cycles are responsible for regulating Earth's climate was initially suggested by Croll (1890) and Gilbert (1895) but was studied further and considerably enhanced by Milankovitch (1941) and is supported by thorough geological evidence (Fischer 1995; Gale 1998). Despite the Milankovitch theory dating back to the early 1940s, it was not applied in the stratigraphic context until well into the 1970s when deep-sea cores from sediments deposited within the last 500 kyr displayed regular cycles

of 100 kyr, 41 kyr, 23 kyr, and 19 kyr periods from oxygen isotope data (Hays et al. 1976). These periodicities complemented Milankovitch's previously discerned primary orbital cycle frequencies.

Cyclothem formation, sea-level control, and Milankovitch control have been further reinforced by various studies occurring in a variety of sedimentary depositional environments and spanning a wide array of time periods (e.g., Cooper 1995; Valdes et al. 1995; Olsen and Kent 1996; Olsen et al. 1999; Prokoph and Agterberg 1999; Andreas Prokoph 2000; Prokoph and Thurow 2000; Wonik 2001; Huaichun et al. 2007; Yu et al. 2008; Wu et al. 2013; Yuan et al. 2013; Wu et al. 2014; van den Belt et al. 2015). Identifying the controlling characteristics of Late Carboniferous climate change, not only has meaningful implications for reconstructing the Late Carboniferous climate record but may also provide indications of future icehouse climate change (Lear et al. 2021). The controlling aspects of glacial-interglacial cycles are logically explained from the global climate change model recommended by the Milankovitch theory (Milankovitch 1941; Berger 1988). Several studies indicated that Milankovitch climate forcing was substantial during the Carboniferous (e.g., van den Belt et al. 2015; Chesnel et al. 2016; Fang et al. 2018; Jirásek et al. 2018; del Strother et al. 2021). The examples illustrated a wide variety of different environments in which cycles have been observed (Schwarzacher 1993).

Periodic climate change caused by the periods of astronomical orbital parameters (Milankovitch climate forcing) results in sedimentary cycles expressed as periodicities (Berger et al. 1994; Schwarzacher 2000). The periodicities stand out in the sedimentary strata by means of sedimentary structures, lithology, lithofacies, and geophysical and geochemical properties. Continuous, high-resolution geophysical borehole logs are often

utilized to investigate Milankovitch cycles in sedimentary strata and to identify the duration of geological events (e.g., Rampino et al. 2000; Morten 2001; Prokoph et al. 2001).

The Cumberland Basin of Atlantic Canada is unique since it provides a complete and well-preserved stratigraphic sequence documenting sediment deposition during its period of basin evolution (Ryan and Boehner 1994). However, most studies in the basin have been focused solely on the Pennsylvanian strata of the fossiliferous Joggins Formation, with the majority of the research concerning one of three general groups; a broad geology group that includes sedimentology and stratigraphy publications (e.g., Davies and Gibling 2003; Davies et al. 2005; Waldron and Rygel 2005; Rygel and Gibling 2006; Kelly and Wach 2020; Kelly et al. 2021a); a paleobiology group that includes taxonomic discoveries and descriptions (e.g., Carroll 1967; Archer et al. 1995b; Reisz and Modesto 1996; Tibert and Dewey 2006; Carpenter et al. 2015); and a paleoecology group (e.g., Brand 1994; Calder et al. 2006).

Cyclicality in the Cumberland Basin is well-documented, with perhaps the most significant volume of work relating to the Cumberland Group strata that crop out along Chignecto Bay. Alluvial drainage patterns reveal the topography of the Cumberland Basin, suggesting the occurrence of westward transgressing shallow seas from the Tethys Ocean along a hypothetical mid-Euramerican seaway (Gibling et al. 1992; Calder 1998). The variations in sea level are attributed to glacioeustasy and are likely regulated by Milankovitch-scale orbital cycles (Waters and Davies 2006). Cyclicality studies focused on the Joggins Formation have identified 15 sedimentary cycles alternating between open-marine facies association deposits formed during widespread transgressions, lower deltaic plain facies association deposits formed as coastal wetlands or low-lying portions of the floodplain, and upper deltaic plain facies association deposits formed as aggradation of the

alluvial surface allowed for regular subaerial exposure of sediments (Rygel et al. 2014). Milankovitch-driven glacio-eustatic fluctuations probably facilitated these sedimentary cycles and, therefore, might be expected to have been of similar duration (Carpenter et al. 2015). Additional proof that the Joggins Formation was deposited in a paralic setting is provided by the interpretation of fish ecology (Carpenter et al. 2015). Moreover, a previously concealed brackish incursion reinforces the connection between sedimentary sequences at Joggins and Milankovitch-induced glacio-eustatic change (Grey et al. 2011; Carpenter et al. 2015). In the Springhill Mines Formation, vague and underdeveloped cyclicity appears compatible with astronomically forced cycles in the Milankovitch band (Calder 1994). Thus, the alternations between open-marine facies association deposits and upper deltaic plain facies association deposits in the Springhill Mines Formation may record the up-dip expression of glacioeustatically forced cyclicity in a rapidly subsiding basin, a situation approximately identical to that envisioned for the underlying Joggins Formation (Davies and Gibling 2003; Gibling et al. 2008a).

To establish whether Milankovitch climate forcing had influences on the Late Carboniferous sediments of the Cumberland Basin, we have conducted a detailed geomathematical analysis on a natural gamma ray geophysical log of the conformable Springhill Mines, Joggins, and Little River formations (Figure 7.1b-c) by applying fast Fourier transform (FFT), and 1D continuous wavelet transform (CWT) analyses. A previous palynological analysis published in the borehole history report constrains the age of sediments into stages and zones during the Westphalian. This study reveals compelling evidence for Milankovitch cycles in these strata and suggests that cyclicity may be present basin-wide, despite the tectonic regime of a high subsidence basin. The FFT analysis

produced a notable ratio of 18.99:5.15:2.02:1, similar to the ratio of 20:5:2:1, which defines the four main orbital periods of long (400 kyr) and short (100 kyr) eccentricity, obliquity (40 kyr), and precession (20 kyr). The CWT analysis yielded a ratio of 1:4, equal to the ratio of short (100 kyr) and long (400 kyr) eccentricity orbital periods.

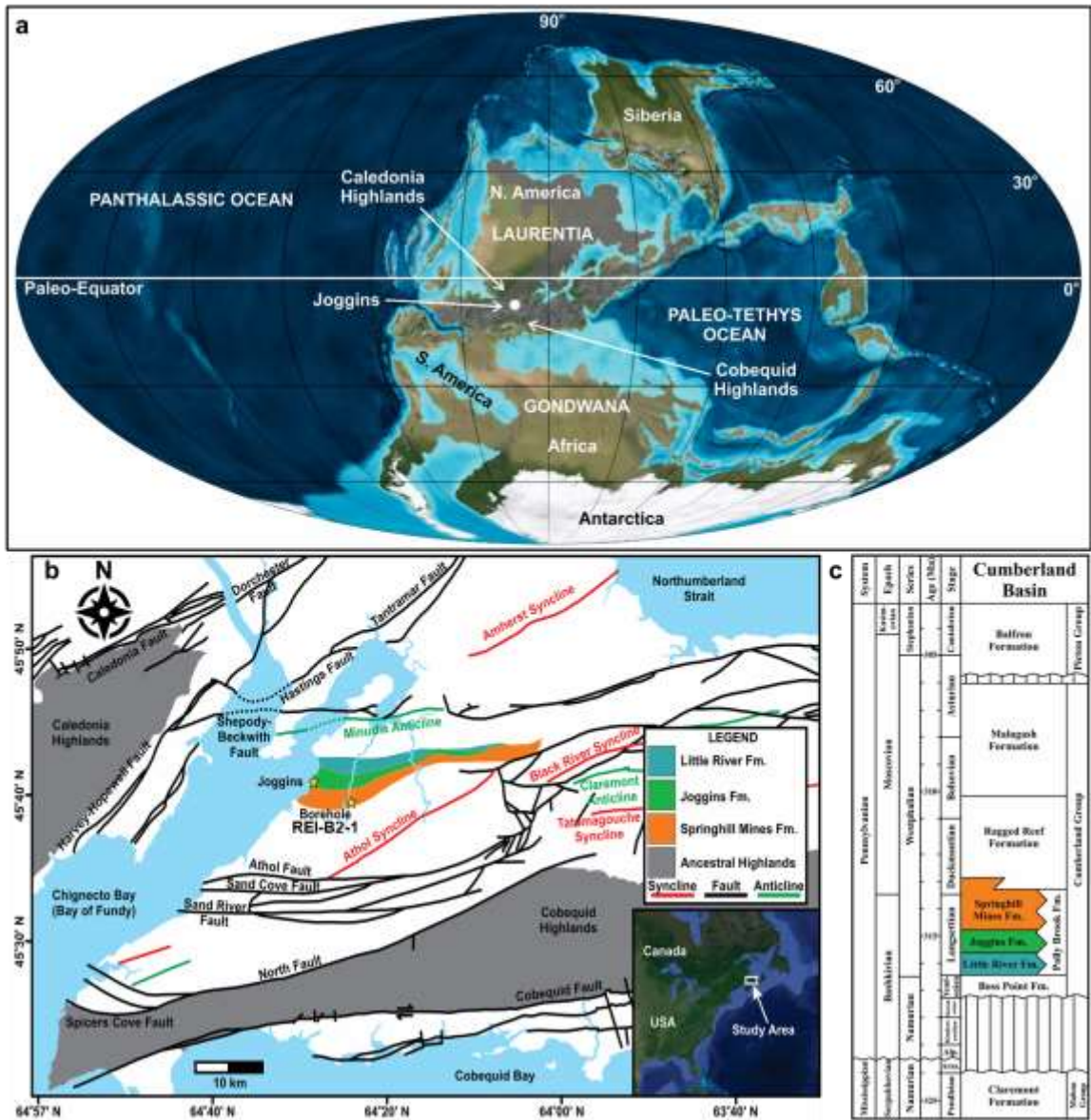


Figure 7.1: Present-day location map, stratigraphic position, and position of the study area during the Late Carboniferous. (a) Late Carboniferous continental reconstruction indicating the position of Joggins (Base map courtesy of Ron Blakey, Northern Arizona University). (b) Modern-day location of Joggins and the utilized borehole. The three formations penetrated by the borehole are shown, along with known anticlines, synclines, and faults (Davies et al. 2005; Allen et al. 2013). (c) The stratigraphic position of the Joggins and Springhill Mines formations in the Cumberland Group (Davies et al. 2005).

7.3 Geological Setting

The Springhill Mines, Joggins, and Little River formations crop out along Chignecto Bay, Nova Scotia, and reveal the most comprehensive fossil record of the Late Carboniferous “Coal Age”; a time when expansive forested wetlands allowed for the accumulation of large quantities of organic matter, forming vast coal deposits in prolific basins (Figure 7.2). It was centrally located in paleoequatorial Euramerica in a vast intermontane paleoequatorial setting (Figure 7.2) during the Late Carboniferous (Calder 1998). The Joggins Formation contains 14 cycles marked by a basal limestone, coal, or fossiliferous shale and represent upper deltaic plain, lower deltaic plain, and open-marine facies (Davies and Gibling 2003; Davies et al. 2005). The upper deltaic plain facies comprise reddish mudstone and sandstone with minor grey mudstone, rare coal, and ostracod-bearing limestone (Davies et al. 2005). The lower deltaic plain facies contain sandstone and rooted greenish-grey mudstone, coal, carbonaceous shale, and minor limestone, with siderite nodules (Davies et al. 2005). Ostracods and bivalves are also present. The open-marine facies of the lower delta plain comprise fossiliferous limestones that pass vertically or are interbedded with fossiliferous siltstones and overlie thick coal beds (Davies and Gibling 2003). The Springhill Mines Formation displays upper and lower deltaic plain facies, while the Little River Formation suggests alluvial plain facies dissected by shallow rivers (Calder et al. 2005; Rygel et al. 2014). Several authors provide a thorough overview of the Cumberland Basin evolution during the Paleozoic (e.g., Waldron and Rygel 2005; Gibling et al. 2008c; Waldron et al. 2013).

7.4 Dataset

Typical Milankovitch cycle studies utilize data from outcrop and subsurface boreholes and typically rely on the counting of laminae in the outcrop or drill core (Yu et al. 2008). The Cumberland Basin contains +1,100 boreholes, with nearly half containing drill core stored at the Nova Scotia Department of Energy and Mines Geoscience and Mines Branch located in Stellarton, Nova Scotia. The studied borehole (REI-B2-1 or P-101) was drilled at 393,129 m east and 5,058,940 m northing (NAD 83/UTM Zone 20). Core retrieval was continuous from 58 – 1,305.5 m (REI Nova Scotia 1995). Five downhole geophysical logs were recorded from 446 to 1,301 m (855 m continuous) and include gamma ray (GR; gAPI; Figure 7.3), neutron porosity-sandstone (NPHI_SAN; m³/m³; Figure 7.3), density correction (DRHO; g/cm³), bulk density (RHOB; g/cm³; Figure 7.3), and density caliper (CALI; in.) (REI Nova Scotia 1995).

This study used the gamma ray geophysical borehole log. A lithology column (Figure 7.3) was made based on the lithology descriptions from the borehole history report and visual analysis of the drill core. According to Yu et al. (2008), geophysical borehole log data provides geological information with a vertical resolution of 10 cm or even less, although the geological information must be interpreted carefully. While drill core is helpful for understanding geology, borehole logs provide an additional aid with their respective properties revealing features not detectable visually. For example, gamma ray geophysical borehole logs are susceptible to alternation in the sedimentary environment, which can be proxies for ancient climate changes in the geological record (Doyle and Bennett 1998).

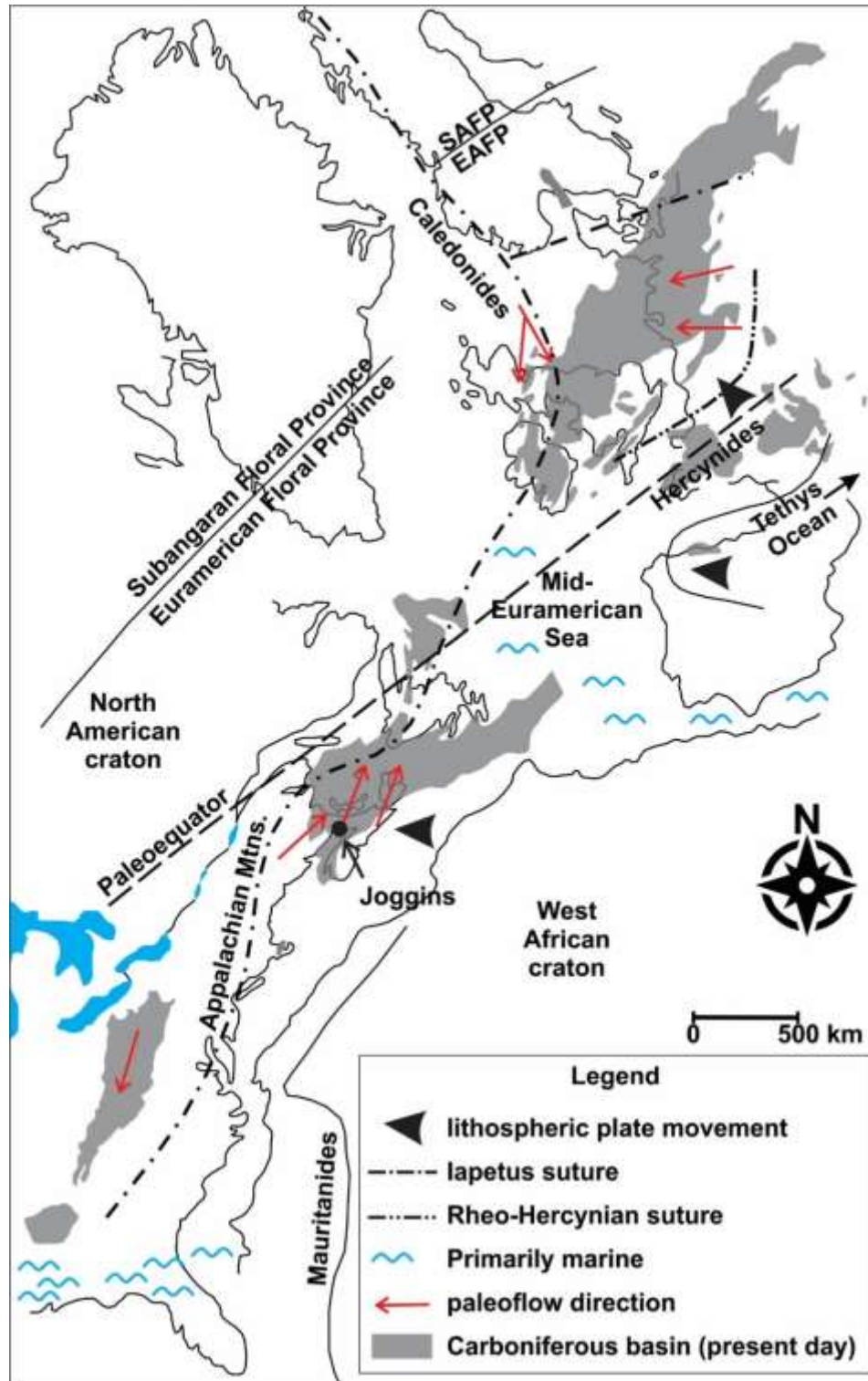


Figure 7.2: Carboniferous reconstruction of equatorial Euramerica showing the location of Joggins, Nova Scotia (Calder 1998). The base map was redrawn from Haszeldine (2009) and Williams (1984). Paleoflow directions were redrawn from Archer and Greb (1995) for the Appalachian Basin, Gibling et al. (1992) for the Maritimes Basin, and Leeder (1988); Leeder et al. (1992) for western Europe. The basin outline for western Europe was redrawn from Maynard et al. (1997).

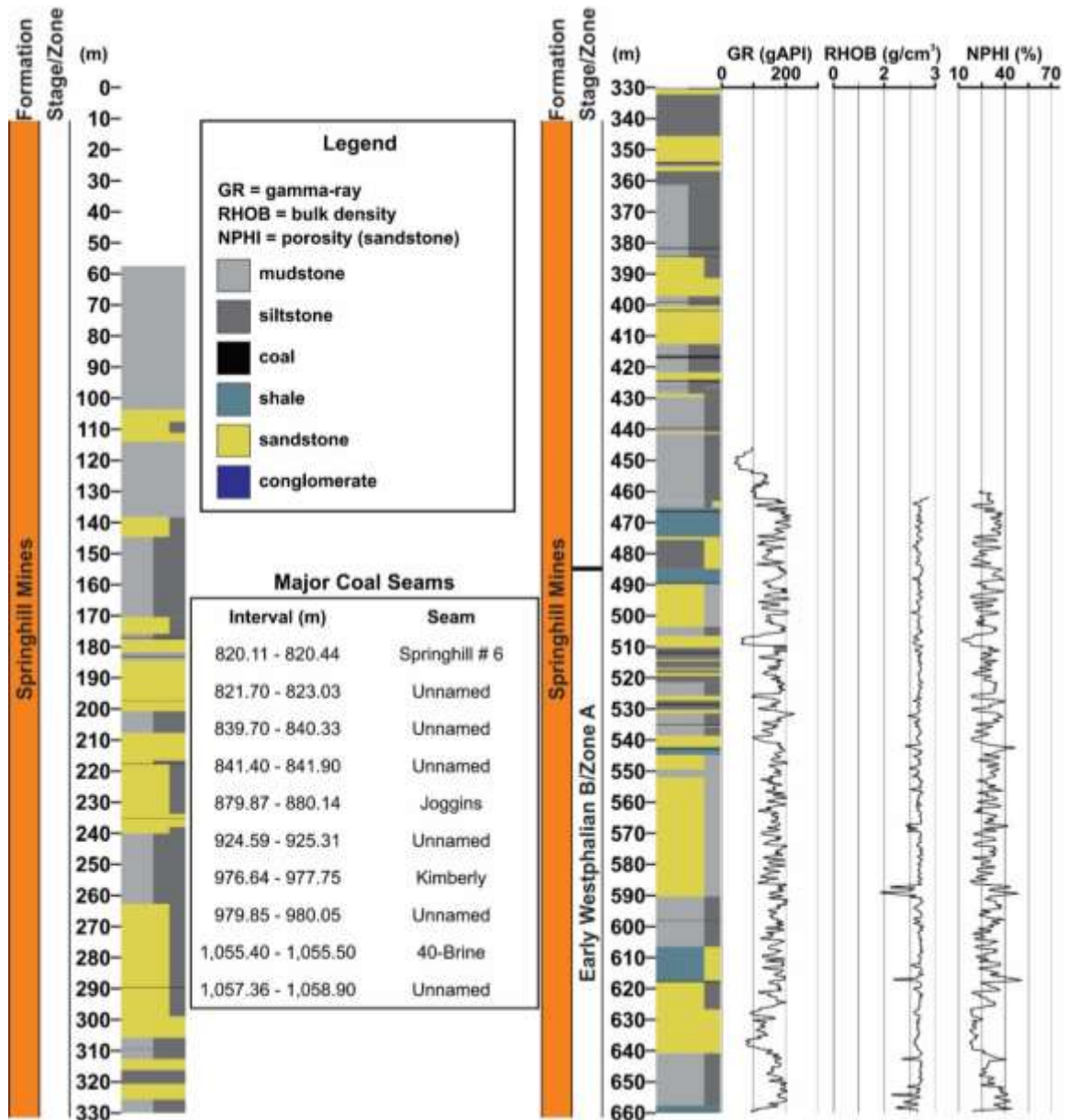


Figure 7.3: Stratigraphy, simplified lithology, and geophysical borehole log curves for the studied borehole. The lithologies represented in the drill core are either mudstone, siltstone, coal, shale, sandstone, or conglomerate, or some combination thereof. The geophysical borehole log curves from left to right display gamma ray (gAPI), bulk density (g/cm^3), and neutron porosity- sandstone (m^3/m^3). The significant coal seams (many unnamed) are also listed below the legend since they are not apparent in the lithology column. The borehole intersected portions of the Springhill Mines, Joggins, and Little River formations. All data are from the borehole history report by REI Nova Scotia (1995).

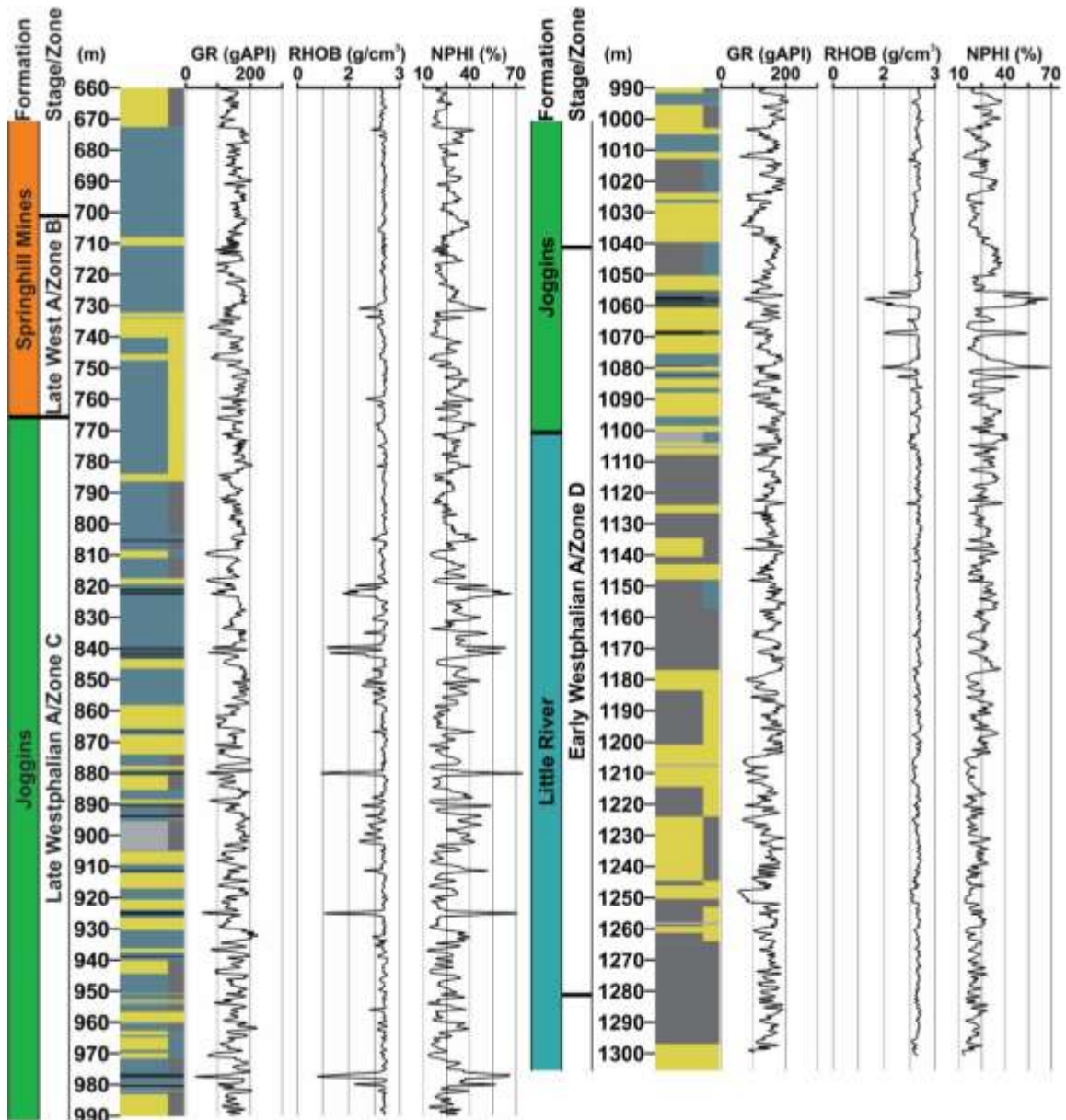


Figure 7.3: Continued.

7.5 Methods

7.5.1 Palynology

Twenty-seven core samples (Table 7.1) were collected post-drilling for palynological analysis between 486.5 to 1,281.5 m depth among three intersected formations; the Springhill Mines (9 samples), Joggins (12 samples), and Little River formations (6

samples) (REI Nova Scotia 1995). The samples were analyzed by Dolby and Associates in Calgary, Alberta. The samples allowed for correlating chronostratigraphic stages to each of the formations as described by the International Commission on Stratigraphy (ICS) (Table 7.2).

The age justification for the Early Westphalian B (Zone A) was the absence of *Crassispora kosankei* above 675.5 m and the presence of Late Westphalian A assemblages below 705.4 m (REI Nova Scotia 1995). The age justification for the Late Westphalian A (Zone B) stage was the occurrence of Spore Type A below 705.4 m, *Vestispora tortuosa* at 765.6 m, and a greater abundance of *Crassispora kosankei* below 705.4 m (REI Nova Scotia 1995). The presence of Spore Type A defined the top of the Westphalian A, and the zonal index species *Vestispora tortuosa* defined the base of the section at 765.6 m (REI Nova Scotia 1995). The age justification for the Late Westphalian A (Zone C) stage was the occurrence of *Cananoropollis mehtae* at and above 1,041.5 m and the occurrence of *Raistrickia fulva micra* at 975.5 m (REI Nova Scotia 1995). The base of the zone was identified by the stratigraphic presence of *Cananoropollis mehtae* at 1,041.5 m (REI Nova Scotia 1995). The age justification for the Early Westphalian A interval (Zone D) was the definition of the base of Zone C and the occurrence of *Spelaeotriletes arenaceus* at 1,101.5 m (REI Nova Scotia 1995).

A publication by van den Belt et al. (2015) assigns the top age of the Early Westphalian B stage at 314.4 Ma and the basal Early Westphalian A at 317.6 Ma. Combining these ages with the chronostratigraphic stages from the palynostratigraphic analysis, the theoretical age range for these sediments is 314.4 Ma to 317.6 Ma (3.2 Myr).

Table 7.1: Summary of core samples sent for palynological analysis (REI Nova Scotia 1995).

Sample #	Depth (m)	Sample #	Depth (m)	Sample #	Depth (m)
1 ^a	486.50	10	765.60 ^b	19	1,041.50 ^b
2 ^a	513.50	11	795.70 ^b	20	1,071.50 ^b
3 ^a	543.10	12	828.50 ^b	21	1,101.50 ^b
4 ^a	574.60	13	855.40 ^b	22	1,131.50 ^c
5 ^a	603.40	14	885.50 ^b	23	1,161.50 ^c
6 ^a	634.40	15	915.40 ^b	24	1,191.50 ^c
7 ^a	675.50	16	945.50 ^b	25	1,221.10 ^c
8 ^a	705.40	17	975.50 ^b	26	1,251.50 ^c
9 ^a	735.50	18	1,005.50 ^b	27	1,281.50 ^c

^a – Springhill Mines Formation; ^b – Joggins Formation; ^c – Little River Formation

Table 7.2: Summary of palynostratigraphic results (REI Nova Scotia 1995).

Interval (m)	Stage	Zone	Species
486.5 – 705.4	Early Westphalian B	A	<i>Punctatosporites spp.</i>
705.4 – 765.6	Late Westphalian A	B	<i>Vestispora tortuosa</i>
765.6 – 1,041.5	Late Westphalian A	C	<i>C. Mehtae</i> – <i>R. Fulva Micra</i>
1,041.5 – 1,281.5	Early Westphalian A	D	<i>S. Arenaceus</i> – <i>Florinites spp.</i>

7.5.2 Data Preprocessing

The quantitative analysis workflow is summarized in Figure 7.4. The original gamma ray geophysical log data (Figure 7.5a) first underwent the noise removal process (Figure 7.5b) from the signal. This was completed using the ‘XDEN = WDENOISE(X)’ function provided by MATLAB. The denoise function uses the empirical Bayesian method with a Cauchy prior distribution to achieve results. The removed noise (Figure 7.5c) was minor, leading to slightly sharpened gamma ray geophysical log data. This was followed by removing the trend from the data (Figure 7.5d). This was completed using the ‘Y = DETREND(X)’ function provided by MATLAB. The detrend function removes the best straight-fit line from the data by subtracting the trend from the data elements. The trend removal is shown by comparing the denoised and detrended gamma ray geophysical log data (Figure 7.5e). The gamma ray geophysical log helps identify lithology and respective depositional settings. As applied here, it also has the benefit of being non-subjective.

7.5.3 *Fast Fourier Transform Analysis*

When applied to a wireline log curve, the FFT analysis computes any cyclical components' frequency and amplitude variables (Labrecque et al. 2011). This is accomplished by comparing gamma ray geophysical log cyclic variations to the ideal cyclic variations occurring in the sinusoidal mathematical function (Labrecque et al. 2011). Therefore, they are unlikely to share similar wavelengths because the cyclicities in the rock record are usually imperfect when compared to the sinusoid (Labrecque et al. 2011). The FFT cannot wholly analyze a signal in which the frequency component varies with time unless signal filtering precedes the analysis (Labrecque et al. 2011). Resulting Fourier spectral curves plot as line graphs with the abscissa representing the periodicity wavelength and the ordinate representing the equivalent magnitude of the cyclicity (Labrecque et al. 2011). A FFT was applied to the detrended gamma ray geophysical log data (Fig. 3) to identify dominant frequencies and determine how much Milankovitch cycle information may be preserved in the strata (Figure 7.6). This process was achieved using MATLAB's 'Y = FFT(X)' function. The function calculates the discrete FFT of X by applying a FFT algorithm.

7.5.4 *Continuous Wavelet Transform Analysis*

A wavelet is a mathematical function that divides input signals into distinct scaled components (Labrecque et al. 2011). Variations in sediment thickness can be applied to determine cyclicity by considering the sediment thickness as a time series where each depositional event correlates with a consecutive time step (Timmer et al. 2016). To determine the signal periodicities or the inverse of frequencies, the time-series signals are

altered from the time domain to the frequency domain (Timmer et al. 2016). The CWT identifies repetition in cycles of close proximity and accentuates them in the calculation more than cycles of further proximity (Labrecque et al. 2011).

For determining signal cyclicity, the FFT method is most often applied. It computes the intensity of each frequency present in the primary time signal; however, it does not preserve any of the temporal information from the primary signal (Timmer et al. 2016). Consequently, if the signal shows a strong frequency component focused in a specific temporal region of the data, the FFT will respond to this information but cannot differentiate where the frequency component is occurring within the signal (Timmer et al. 2016). The main benefit to applying the CWT over the FFT is its ability to independently evaluate specific sections of a signal, which preserves depth, along with the wavelength and magnitude components of cyclicity in the dataset (Labrecque et al. 2011). Hence, the CWT analysis makes recognizing geological cyclicity within borehole log data simpler.

The wavelet is combined with a depth-domain signal, a gamma ray geophysical borehole log, to evaluate the log against a reference signal (i.e., the ‘mother’ wavelet) at all depths and wavelengths (Labrecque et al. 2011). The mother wavelet applied in this study is a Morlet wavelet, which is used regularly to evaluate cyclicity (Goupillaud et al. 1984). The degree of match is presented on a depth versus wavelength plot, known as a scalogram; strongly cyclic portions show up as red colours on the plot (Figure 7.7). A previous study evaluated the error levels in the amplitudes and wavelengths for wavelet analysis (Tanyel 2006). Results indicated that amplitudes might exhibit an error of up to 50% but that the associated wavelengths were accurate to within 30% (Tanyel 2006). We

anticipate comparable error levels for the analyses here since the dataset's measurement resolution, and sample densities are similar.

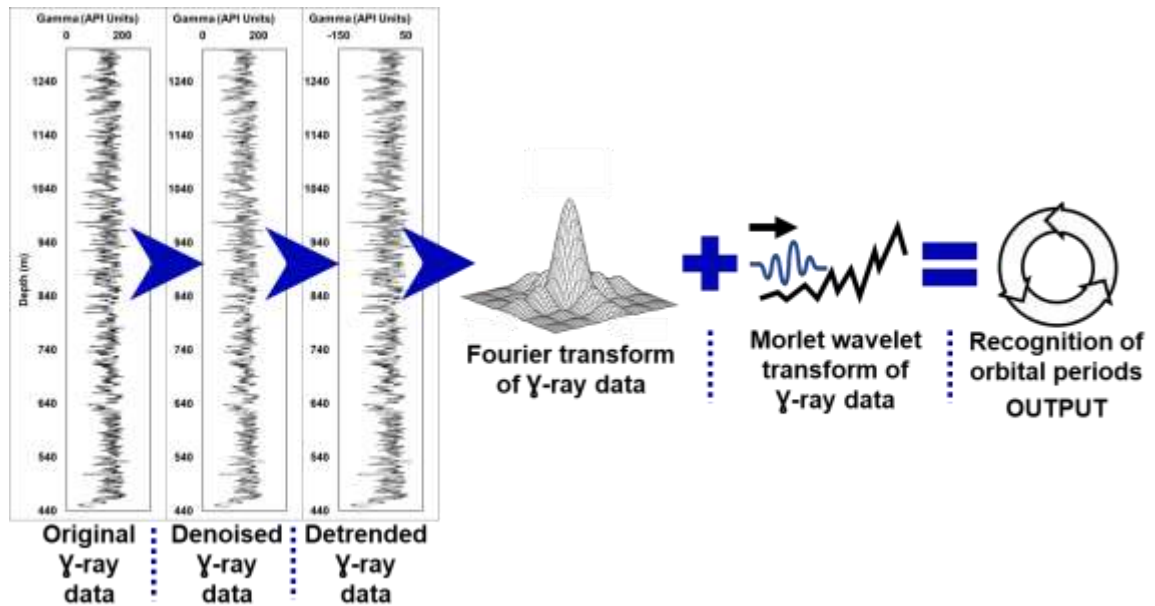


Figure 7.4: Schematic diagram emphasizing the quantitative methods used in this study. Gamma ray geophysical log data was first denoised and detrended. The detrended gamma ray geophysical log data underwent a FFT analysis and a CWT analysis using a Morlet wavelet for the 'mother' wavelet. The outputs of both analyses provided quantitative data that was evaluated for cyclicity matching those of the four major orbital periods.

7.6 Results

7.6.1 Data Preprocessing

Figure 7.5 displays a preliminary analysis of the natural gamma ray plot; in each case, the dashed line indicates the linear trendline fitted to the data with the corresponding equation and regression. The data preprocessing results of the natural gamma ray geophysical log plot are displayed in Figure 7.5a. The denoised gamma ray geophysical log is shown in Figure 7.5b. The difference between the natural and denoised gamma ray geophysical log is displayed in Figure 7.5c. The detrended gamma ray geophysical log is

displayed in Figure 7.5d. Finally, the denoised and detrended gamma ray geophysical logs are shown in Figure 7.5e for comparison purposes.

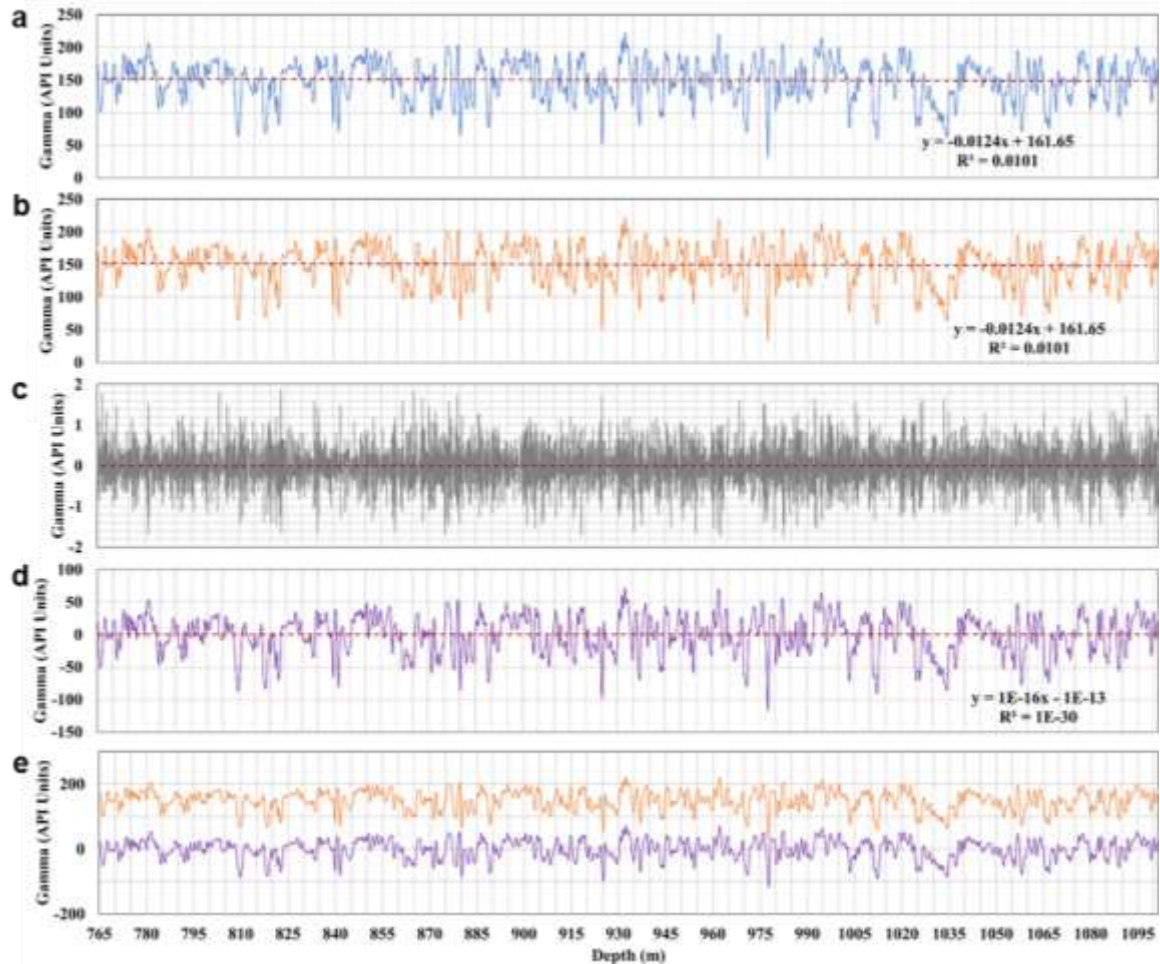


Figure 7.5: Plots relating to the preprocessing of REI-B2-1 borehole gamma ray geophysical log data. (a) The original, unprocessed gamma ray geophysical log data, (b) the denoised gamma ray geophysical log data, (c) the difference between the original gamma ray geophysical log data and the denoised gamma ray geophysical log data, (d) the detrended gamma ray geophysical log data, and (e) the denoised (upper) and detrended (lower) gamma ray geophysical log data. The red dashed lines in a-d are linear trendlines with the equations and regression values displayed.

7.6.2 Fast Fourier Transform Cyclicity Analysis

Applying the FFT resulted in a plot (Figure 7.6) of the relationship between frequency (abscissa) and magnitude (ordinate) of the FFT algorithm. The results (Table 7.3) show that statistically significant frequencies occur at $f = 0.01053$, $f = 0.03860$, $f = 0.09825$, and $f = 0.19883$, which translates to a ratio of 18.99:5.15:2.02:1. Hence, the ratio

is closely similar to the ratio of 20:5:2:1, which defines the four main orbital periods of long (400 kyr) and short (100 kyr) eccentricity, obliquity (40 kyr), and precession (20 kyr). The corresponding cyclic thicknesses of the four main orbital periods are ~ 31.67 m, ~ 8.64 m, ~ 3.39 m, and ~ 1.68 m, respectively (Table 7.3). The numbers of each Milankovitch cycle recorded in the strata can be determined based on the main cyclic thicknesses and the stratigraphic thicknesses of the study strata. The approximate time duration for sediment accumulation was ~ 3.277 Myr, calculated from an integration of cycle thickness and their individual durations, with an average sediment accumulation rate of 26.1 cm/kyr.

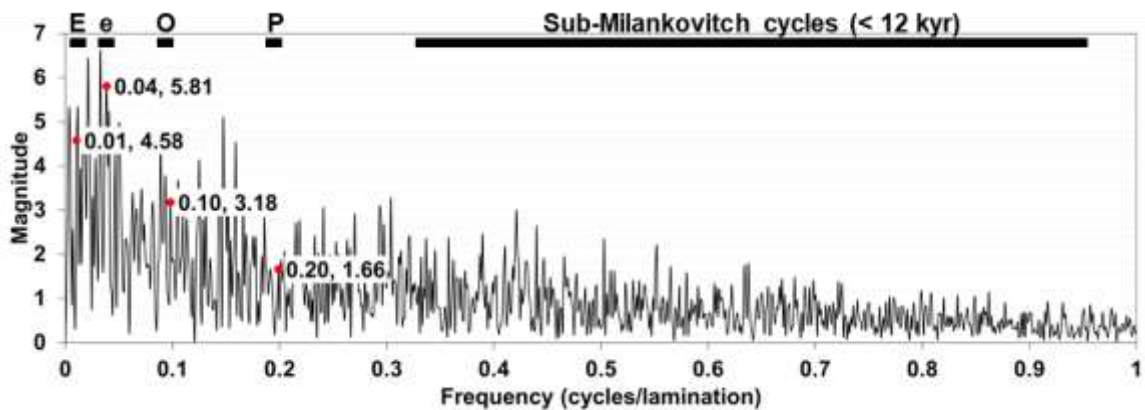


Figure 7.6: The FFT analysis of the borehole gamma ray geophysical log data. Statistically significant frequency peaks occur at $f = 0.01053$, $f = 0.03860$, $f = 0.09825$, and $f = 0.19883$. The cycle bands across the top represent long eccentricity (E), short eccentricity (e), obliquity (O), precession (P), and sub-Milankovitch cycle windows.

Table 7.3: Statistics for various frequencies, including the four major orbital periods.

Frequency (cycles/lamination)	Wavelength (m)	Cycle Thickness (m)	Thickness Ratio	Orbital Period (kyr)
0.007017544	142.50	47.50	28.48	----
0.010526316	95.00	31.67	18.99	400
0.014035088	71.25	23.75	14.24	----
:	:	:	:	:
0.035087719	28.50	9.50	5.66	----
0.038596491	25.91	8.64	5.15	100
0.042105263	23.75	7.92	4.72	----
:	:	:	:	:
0.094736842	10.56	3.52	2.10	----
0.098245614	10.18	3.39	2.02	40
0.101754386	9.83	3.28	1.95	----
:	:	:	:	:
0.195321637	5.12	1.71	1.02	----
0.198830409	5.03	1.68	1.00	20
0.202339181	4.94	1.65	0.98	----

7.6.3 Continuous Wavelet Transform Cyclicity Analysis

The CWT analysis of the natural gamma ray geophysical log data resulted in the plot shown in Figure 7.7. The wavelet coefficient contour map (Figure 7.7) was used to extract wavelet coefficients, analyze for the maximum values of the wavelet modules and identify the maximums of three wavelet modules, including those at scales of $a = 25$, $a = 50$, and $a = 100$ (Figure 7.8), with a ratio of low ($a = 25$) to high ($a = 100$) scale being 1:4. This ratio is identical to the short (100 kyr) and long (400 kyr) eccentricity orbital periods. Consequently, the wavelet coefficient curve at $a = 25$ corresponds with the eccentricity period of 100 kyr with 278 cycles (Figure 7.9a). The wavelet coefficient curve at $a = 100$ corresponds with the eccentricity period of 400 kyr with 75 cycles (Figure 7.9b). The approximate time duration for sediment accumulation was calculated to be ~ 2.922 Myr with an average sediment accumulation rate of 29.3 cm/kyr.

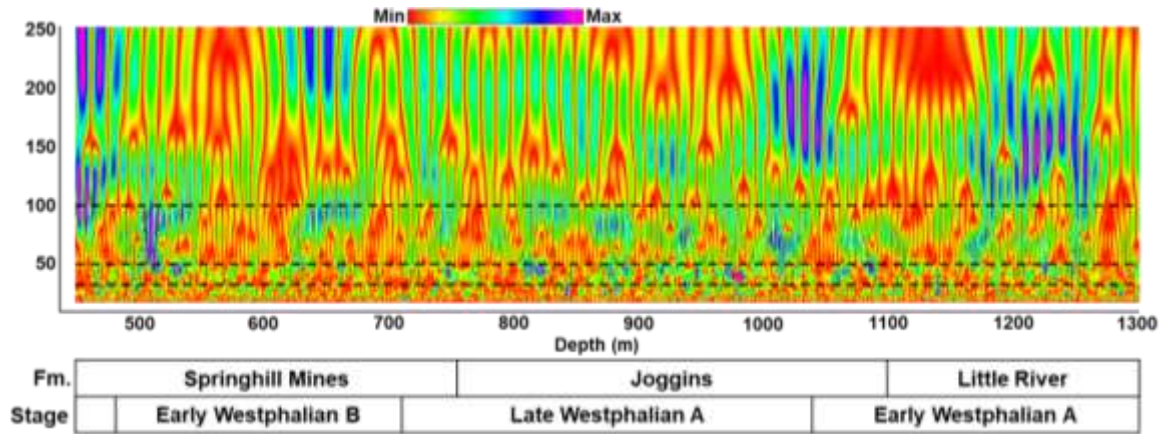


Figure 7.7: The scalogram of the gamma ray geophysical log data. The Morlet wavelet scalogram with a scale of $a = 256$ and a frequency of 0.003 . The black dashed lines at 25, 50, and 100 represent the maximums from Figure 7.8. The stages were determined from palynological analysis (Table 7.2).

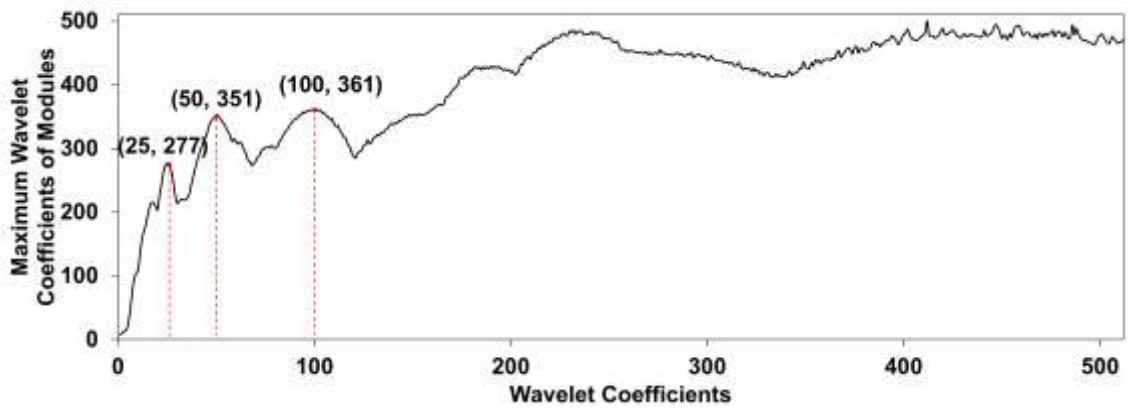


Figure 7.8: A plot of the maximum module values for the Morlet wavelet coefficients. The maximums of three Morlet wavelet modules are identified. The abscissa is the scale coefficients, which in this example are from 1 to 512. The ordinate is the maximum value at each of the scale coefficients.

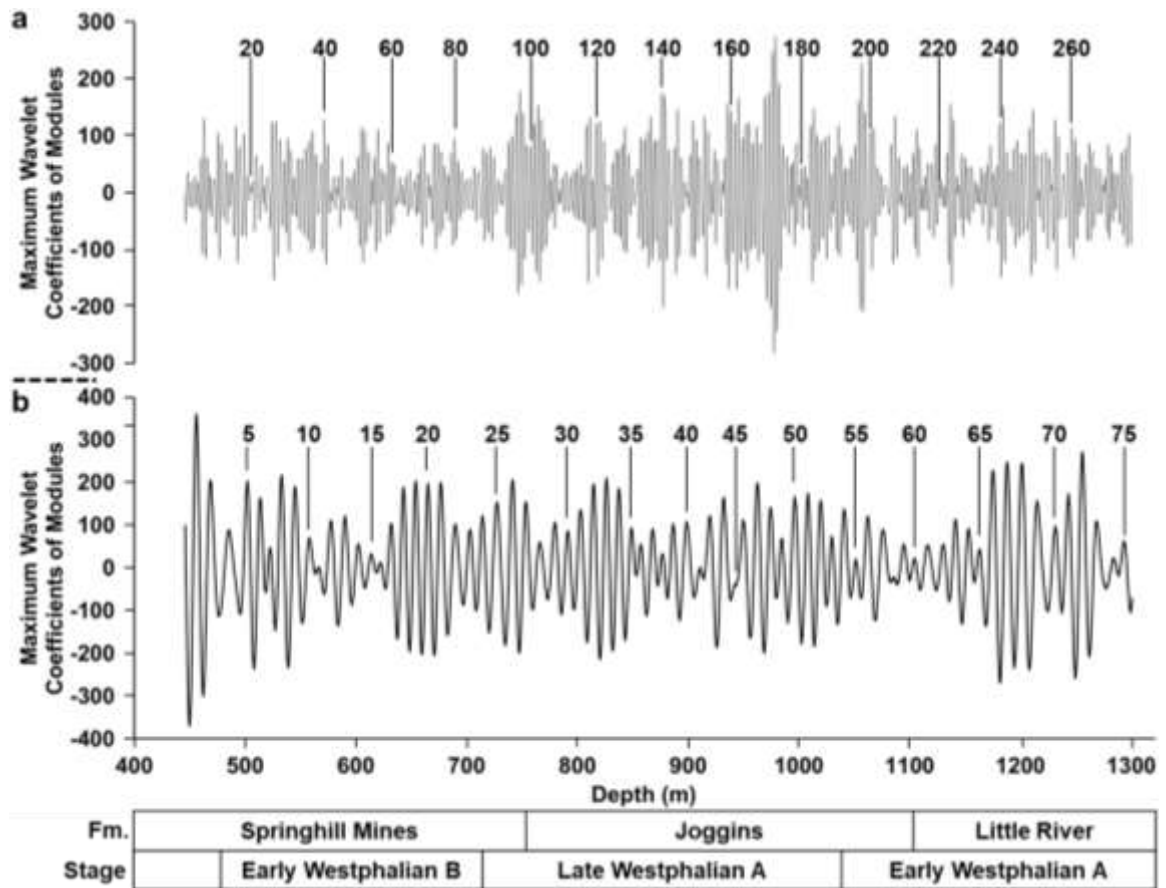


Figure 7.9: Plots of Morlet wavelet coefficients at the scales of $\alpha = 25$ and $\alpha = 100$. The stages were determined from palynological analysis (Table 7.2). (a) The plot of Morlet wavelet coefficients at the scale of $\alpha = 25$ displays 278 cycles corresponding to short eccentricity periods. The numbers above the plot indicate every 20th cycle. (b) A plot of Morlet wavelet coefficients at the scale of $\alpha = 100$ displaying 75 cycles corresponding to long eccentricity periods. The numbers above the plot indicate every 5th cycle.

7.7 Discussion

The Late Carboniferous of Euramerica is regarded as an important period for studying cyclic sedimentation, although direct evidence for Milankovitch cyclicity is lacking overall. The cause of this is the lack of chronometric dates for the individual stages in which cyclicity studies have been researched (Schwarzacher 1993). This is a common issue with older formations, which, unless several Milankovitch cycle orders can be discovered, results in uncertainty with the identification of the cycles (Schwarzacher 1993).

This study applied geomathematical analysis on natural gamma ray geophysical log data to detect hidden cycles. We identified cycles through a combination of FFT analysis and one-dimensional CWT analysis, some of which appear to be at the frequency of the major orbital periods. The FFT analysis generated four frequencies with a ratio of 18.99:5.15:2.02:1.00, which closely mimics the ratio of 20:5:2:1 for long (400 kyr) and short (100 kyr) eccentricity, obliquity (40 kyr), and precession (20 kyr). The cyclic thicknesses corresponding to the frequencies of long and short eccentricity, obliquity, and precession (20:5:2:1) were ~ 31.67 m, ~ 8.64 m, ~ 3.39 m, and ~ 1.68 m, respectively. The chronological period of the studied strata, in combination with the corresponding theoretical periods, is calculated to be approximately 3.277 Myr. Based on the cyclic thicknesses and the corresponding theoretical periods, the average sediment accumulation rate of the study strata is approximately 26.1 cm/kyr.

The one-dimensional CWT analysis identified three wavelet module extremes at scales of $\alpha = 25$, 50, and 100, with a ratio of low ($\alpha = 25$) to high ($\alpha = 100$) scale being 1:4, which is identical to the long and short eccentricity periods. The wavelet coefficient curve at $\alpha = 25$ corresponds with the eccentricity period of 100 kyr with 278 cycles. The wavelet coefficient curve at $\alpha = 100$ corresponds with the eccentricity period of 400 kyr with 75 cycles. The chronological period from this analysis is calculated at approximately 2.922 Myr with a sediment accumulation rate of 29.3 cm/kyr. This value strongly correlates with the FFT calculated sediment accumulation rate.

It is recognized that sedimentation rates were not constant and that erosion rates are difficult to account for (Wach 1991). According to Wach (1991), the preserved net sedimentation record for a cycle probably mimics an exponential rate where the lowest

sediment accumulation rates and maximum condensation occurring at the cycle bases. Sedimentation rates would have strengthened with a decreasing relative sea level and proximity to land (Wach 1991).

The stratigraphy of the Cumberland Basin is generally poorly constrained concerning age. The borehole history report suggests the sediments range from Early Westphalian B to Early Westphalian A, based on a comprehensive palynostratigraphic analysis. A publication by van den Belt et al. (2015) uses U/Pb radiometric age dating to assign ages to Late Carboniferous sediments from western Europe. These ages were applied to the sediments in this study. These results are not all that different from Late Carboniferous cycles studied in midcontinent North America, such as those in the west Texas, Kansas, Illinois, and Appalachian basins (Strasser and Heckel 2007).

An example from the Carboniferous Jiyang depression in China revealed Milankovitch cyclicity among nine intervals of a borehole using FFT and CWT analyses of borehole data (Yu et al. 2008). One 54 m thick interval uncovered 29 precession cycles, 15 obliquity cycles, and 7 short eccentricity cycles (Yu et al. 2008). The CWT analysis uncovered prominent signals at scales of $\alpha = 12, 24,$ and 60 , subsequently matching the theoretical values of Milankovitch's 23 kyr (precession), 40 kyr (obliquity), and 100 kyr (eccentricity) cycles (Yu et al. 2008). The FFT results show the wavelengths of the orbital forcing cycles are 2.7, 4.4 and 7.8 m for precession, obliquity and eccentricity, respectively (Yu et al. 2008).

A time-series analysis by Gebhardt and Hiete (2013) revealed 16 cycles with 100 m lengths from a drilled section of Late Carboniferous non-marine sediments from the Saale Basin, Germany. This indicated a time span of approximately 5 – 7 Myr for the complete

section, with individual cycles being 323 – 453 kyr long (Gebhardt and Hiete 2013). It was hypothesized that the cycles belong to the Milankovitch Band, possibly demonstrating variations in the eccentricity of Earth's orbit and lasting nearly 400 kyr. Prominent cycles at 26 and 110 m give a proportion of approximately 1:4 and are particularly apparent during the fine clastic section analysis above 1,050 m (Gebhardt and Hiete 2013). The results reinforce the suggestion that these cycles represent short and long eccentricity, with the short eccentricity cycle being well developed and the long eccentricity cycle being less developed but traceable throughout the profile (Gebhardt and Hiete 2013).

Previous and current studies demonstrate that cyclostratigraphy can enhance our knowledge of geologic time scales and restrict paleoclimatic processes that affect oceanic, biological, and sedimentary systems (Strasser and Heckel 2007). Nevertheless, the appropriate cyclostratigraphical interpretation of the sedimentary record may be impeded for numerous reasons, as described by Strasser and Heckel (2007). During periods of non-deposition or erosion, orbital cycles may not be recorded (Strasser and Heckel 2007). Furthermore, a depositional hiatus may well be associated with individual cycles, especially in shallow lake and platform environments (Strasser and Heckel 2007).

Stratigraphic uncertainties attributed to an incomplete rock record or a non-conformable sequence of sediments can also result in the failure of orbital cycles being recorded. However, the sediments in this study represent a conformable sequence, based on the well-studied conformable coeval succession that crops out along the coast (e.g., Grey and Finkel 2011).

There is also uncertainty in records extending beyond 60 Ma because astronomical models beyond that age are significantly impacted by the chaos and uncertainties of Solar

System motion (e.g., Olsen et al. 2019). Local or regional autocyclic processes that develop within a sedimentary environment and are separate from orbital forcing have the potential to replicate facies patterns with comparable time scales (e.g., Strasser et al. 1991; Westphal et al. 2000; Burgess 2001; Strasser and Heckel 2007). This is particularly important since they also influence the behavior of ice caps and oceans, not just adjacent sedimentary basins (Strasser and Heckel 2007). According to Zuhlke (2004), climate-related cycles with periods different from Milankovitch cycle periods can record comparable repetitions in the sedimentary environment, known as sub-Milankovitch cycles.

Evidence for sub-Milankovitch cycles (less than 12 kyr) is also suggested by this dataset (Figure 7.6). In lacustrine, deep basin, and carbonate platform depositional environments, sub-Milankovitch cycles are frequently revealed in the Quaternary and pre-Quaternary sediments (e.g., Anderson 1982; McIntyre and Molino 1996; Zuhlke et al. 2003; Elrick and Hinnov 2007; Tucker et al. 2009; Boulila et al. 2010). Despite their prominence in sediments of those ages and depositional environments, their origins lack a unified understanding. According to Wu et al. (2012), there are three central working theories as to their origins: (1) the response to orbital forcing is non-linear (e.g., McIntyre and Molino 1996; Willis et al. 1999); (2) hemi-precession caused by the twice-yearly passing of the sun over the intertropical region (e.g., Berger et al. 1997; Bond et al. 1997; Sun and Huang 2006); and (3) the harmonics of millennial solar oscillations, precession, or mixed tones of the primary orbital components (e.g., Yiou et al. 1991; Berger et al. 2006).

While cyclicity in the Cumberland Basin has been studied in the past, there has been a lack of quantitative evidence to support it. A recent publication by Letourmy et al. (2021)

used fine-scale fluvial aggradational cycles (474) to conclude that rhythmicity in the Cumberland Basin was generally attributed to salt-induced tectonics. A geomathematical approach consisting of threshold autoregressive models based on thickness, paleosol thickness, sandstone content, and the paleosol-to-sandstone ratio was used (Letourmy et al. 2021). The study found a lack of evidence for statistically significant cyclicity, which challenged prior studies implying sedimentation was motivated by glacio-eustatic cyclothem.

Despite the research for and against the idea of orbital forcing and whether this phenomenon can be recognized in sediments from the Cumberland Basin is one for debate, but our research implies that statistically significant cyclicity corresponds to the four main orbital periods does exist. There are likely several reasons why the study mentioned above disagrees with this study regarding the lack of statistically significant cyclicity. The 474 cycles identified are probably the result of autocyclic processes (internal basin processes), which would affect the ability to detect allocyclic processes (external basin processes), such as Milankovitch cycles. The geomathematical analyses in which Letourmy et al. (2021) used threshold autoregression and this study used FFT and CWT differ significantly in both the theory and application to the respective data used. The fluvial aggradational cycles analysis involved the recognition and data collection along the exposed Joggins Formation outcrop section. In contrast, this study used non-subjective geophysical borehole log data from a borehole further inland that partially penetrated three formations, including the Joggins Formation.

This evidence for Milankovitch cycles hidden in the natural gamma ray geophysical log may offer a new research method for identifying high-resolution stratigraphic intervals

and correlations of the Cumberland Basin strata. Furthermore, this geomathematical approach may lead to an enhanced reservoir characterization of sedimentary basins with limited drill core and seismic data. These results are an important first step towards constraining a Late Carboniferous astronomical solution and extending the astronomical time scale into the Late Carboniferous. The recognition and quantification of these cycles may help improve our understanding of the basin, especially regarding other prolific coal basins formed in Euramerica during the Late Carboniferous. Based on the results of this study, we suggest that additional boreholes in the Cumberland Basin be subjected to a similar geomathematical analysis to determine if the apparent cyclicality uncovered in this borehole occurs basin-wide or if this was an isolated instance.

7.8 Conclusion

Cyclostratigraphic analysis of the gamma ray geophysical borehole log of the lower Cumberland Group in the Cumberland Basin of Northern Nova Scotia uncovers distinctive depositional sequences. The FFT analysis indicates that the depositional cycles of 31.67 m, 8.64 m, 3.39 m, and 1.68 m were formed by Milankovitch forcing of ~ 400 kyr (long eccentricity), ~ 100 kyr (short eccentricity), ~ 40 kyr (obliquity), and ~ 20 kyr (precession), respectively. The approximate time duration for sediment accumulation was calculated to be ~ 3.277 Myr with an average sediment accumulation rate of 26.1 cm/kyr.

The CWT analysis yielded a ratio of 1:4, equal to the ratio of short (100 kyr) and long (400 kyr) eccentricity orbital periods. A total of 75 cycles were identified for the long eccentricity orbital period, and 278 were identified for the short eccentricity orbital period. The approximate time duration for sediment accumulation was calculated to be ~ 2.922 Myr with an average sediment accumulation rate of 29.3 cm/kyr.

The sub-Milankovitch cycles observed in this study might be common at the tropical and sub-tropical latitudes of the Paleotethys Ocean and associated water bodies. Their origins are not well-understood and could result from theories, including non-linear orbital forcing, hemi-precession, and irregular harmonics associated with precession, solar fluctuations, and blended orbital elements.

7.9 Acknowledgements

This work was made possible by the Dalhousie University Basin and Reservoir Laboratory. I want to thank Mick O'Neill (core supervisor) at the Nova Scotia Department of Natural Resources Core Library for retrieving the core from warehouse storage and accommodating me over several days. We are grateful to Martin Gibling, Bill Richards, Pamela Reynolds, David Reynolds, and Darragh O'Connor for providing helpful suggestions and sound advice for improving this paper. We also thank the anonymous reviewers for their comments and feedback.

7.10 References Cited in Chapter 7

Allen, J.P., Fielding, C.R., Rygel, M.C., and Gibling, M.R. 2013. Deconvolving Signals of Tectonic and Climatic Controls From Continental Basins: An Example From the Late Paleozoic Cumberland Basin, Atlantic Canada. *Journal of Sedimentary Research*, **83**: 847-872. doi:10.2110/jsr.2013.58.

Anderson, R.Y. 1982. A long geoclimatic record from the Permian. *Journal of Geophysical Research*, **87**: 7285-7294. doi:10.1029/JC087iC09p07285.

Andreas Prokoph, F.P.A. 2000. Wavelet analysis of well-logging data from oil source rock, Egret Member, offshore eastern Canada. *AAPG Bulletin*, **84**: 1617-1632. doi:10.1306/8626bf15-173b-11d7-8645000102c1865d.

Archer, A.W., and Greb, S.F. 1995. An Amazon-Scale Drainage System in the Early Pennsylvanian of Central North America. *The Journal of Geology*, **103**: 611-627. doi:10.1086/629784.

Archer, A.W., Calder, J.H., Gibling, M.R., Naylor, R.D., Reid, D.R., and Wightman, W.G. 1995b. Invertebrate trace fossils and agglutinated foraminifera as indicators of marine influence within the classic Carboniferous section at Joggins, Nova Scotia, Canada. *Canadian Journal of Earth Sciences*, **32**: 2027-2039. doi:10.1139/e95-156.

Atlantic Geoscience Society. 2001. The last billion years: a geological history of the Maritime Provinces of Canada. No. 15. Nimbus Publishing Limited.

Berger, A. 1988. Milankovitch Theory and climate. *Reviews of Geophysics*, **26**: 624-657. doi:10.1029/RG026i004p00624.

Berger, A., Loutre, M.-F., and McIntyre, A. 1997. Intertropical latitudes and precessional and half-precessional cycles. *Science*, **278**: 1476-1478.

Berger, A., Loutre, M.F., and Mélice, J.L. 2006. Equatorial insolation: from precession harmonics to eccentricity frequencies. *Climate of the Past*, **2**: 131-136. doi:10.5194/cp-2-131-2006.

Berger, A., Loutre, M., De Boer, P., and Smith, D. 1994. Astronomical forcing through geological time. *In* *Orbital forcing and cyclic sequences*. Blackwell Scientific Publications Oxford. pp. 15-24.

Bond, G., Showers, W., Cheseby, M., Lotti, R., Almasi, P., deMenocal, P., Priore, P., Cullen, H., Hajdas, I., and Bonani, G. 1997. A Pervasive Millennial-Scale Cycle in North Atlantic Holocene and Glacial Climates. *Science*, **278**: 1257-1266. doi:10.1126/science.278.5341.1257.

Boulila, S., Galbrun, B., Hinnov, L.A., Collin, P.Y., Ogg, J.G., Fortwengler, D., and Marchand, D. 2010. Milankovitch and sub-Milankovitch forcing of the Oxfordian (Late Jurassic) Terres Noires Formation (SE France) and global implications. *Basin Research*, **22**: 717-732. doi:10.1111/j.1365-2117.2009.00429.x.

Brand, U. 1994. Continental hydrology and climatology of the Carboniferous Joggins Formation (lower Cumberland Group) at Joggins, Nova Scotia: evidence from the geochemistry of bivalves. *Palaeogeography, Palaeoclimatology, Palaeoecology*, **106**: 307-321. doi:10.1016/0031-0182(94)90016-7.

Burgess, P.M. 2001. Modeling carbonate sequence development without relative sea-level oscillations. *Geology*, **29**: 1127-1130. doi:10.1130/0091-7613(2001)029<1127: Mcdswr>2.0.Co;2.

Calder, J.H. 1994. The impact of climate change, tectonism and hydrology on the formation of Carboniferous tropical intermontane mires: the Springhill coalfield, Cumberland Basin, Nova Scotia. *Palaeogeography, Palaeoclimatology, Palaeoecology*, **106**: 323-351. doi:10.1016/0031-0182(94)90017-5.

Calder, J.H. 1998. The Carboniferous evolution of Nova Scotia. Geological Society, London, Special Publications, **143**: 261-302. doi:10.1144/gsl.Sp.1998.143.01.19.

Calder, J.H. 2017. The Joggins fossil cliffs: coal age Galápagos. Formac Publishing Company.

Calder, J.H., Rygel, M.C., Ryan, R.J., Falcon-Lang, H.J., and Herbert, B.L. 2005. Stratigraphy and sedimentology of early Pennsylvanian red beds at Lower Cove, Nova Scotia, Canada: the Little River Formation with redefinition of the Joggins Formation. *Atlantic Geology*, **41**: 87-102. doi:10.4138/183.

Calder, J.H., Gibling, M.R., Scott, A.C., Davies, S.J., Herbert, B.L., Greb, S.F., and DiMichele, W.A. 2006. A fossil lycopsid forest succession in the classic Joggins section of Nova Scotia: paleoecology of a disturbance-prone Pennsylvanian wetland. *Special Papers - Geological Society of America*, **399**: 169. doi:10.1130/2006.2399(09).

Carpenter, D.K., Falcon-Lang, H.J., Benton, M.J., and Grey, M. 2015. Early Pennsylvanian (Langsettian) fish assemblages from the Joggins Formation, Canada, and their implications for palaeoecology and palaeogeography. *Palaeontology*, **58**: 661-690. doi:10.5061/dryad.b0551.

Carroll, R.L. 1967. Labyrinthodonts from the Joggins Formation. *Journal of Paleontology*, **41**: 111-142.

Chesnel, V., Merino-Tomé, Ó., Fernández, L.P., Villa, E., and Samankassou, E. 2016. Isotopic fingerprints of Milankovitch cycles in Pennsylvanian carbonate platform-top deposits: the Valdorria record, Northern Spain. *Terra Nova*, **28**: 364-373. doi:10.1111/ter.12229.

Cooper, P. Milankovitch cycles from Fourier analysis of logs from Sites 865 and 866: Northwest Pacific atolls and guyots. *In Proceedings of the Ocean Drilling Program. Scientific results.* 1995. Vol. 142, pp. 317-327.

Croll, J. 1890. *Climate and time in their geological relations: a theory of secular changes of the Earth's climate.* Appleton.

Davies, S.J., and Gibling, M.R. 2003. Architecture of coastal and alluvial deposits in an extensional basin: the Carboniferous Joggins Formation of eastern Canada. *Sedimentology*, **50**: 415-439. doi:10.1046/j.1365-3091.2003.00553.x

Davies, S.J., Gibling, M.R., Rygel, M.C., Calder, J.H., and Skilliter, D.M. 2005. The Pennsylvanian Joggins Formation of Nova Scotia: sedimentological log and stratigraphic framework of the historic fossil cliffs. *Atlantic Geology*, **41**: 87-102. doi:10.4138/182.

del Strother, P., Gize, A., Hollis, C., and McLean, D. 2021. Bituminous coals on emergent surfaces in an Asbian, lower Carboniferous (Mississippian) limestone succession on the North Wales carbonate platform, UK, and implications for palaeoclimate. *Proceedings of the Yorkshire Geological Society*, **63**: 22. doi:10.1144/pygs2020-006.

Doyle, P., and Bennett, M.R. 1998. *Unlocking the Stratigraphical Record: Advances in Modern Stratigraphy.* Wiley, University of California.

Elrick, M., and Hinnov, L.A. 2007. Millennial-scale paleoclimate cycles recorded in widespread Palaeozoic deeper water rhythmites of North America. *Palaeogeography, Palaeoclimatology, Palaeoecology*, **243**: 348-372. doi:10.1016/j.palaeo.2006.08.008.

Fang, Q., Wu, H., Wang, X., Yang, T., Li, H., and Zhang, S. 2018. Astronomical cycles in the Serpukhovian-Moscovian (Carboniferous) marine sequence, South China and their implications for geochronology and icehouse dynamics. *Journal of Asian Earth Sciences*, **156**: 302-315. doi:10.1016/j.jseaes.2018.02.001.

Fischer, A.G. 1995. Cyclostratigraphy, Quo Vadis? *In Orbital Forcing Timescales and Cyclostratigraphy. Edited by M.R. House and A.S. Gale.* The Geological Society, London, UK. pp. 199-204.

Gale, A.S. 1998. Cyclostratigraphy. *In Unlocking the stratigraphical record: advances in modern stratigraphy. Edited by P. Doyle and M.R. Bennett.* Wiley Chichester, UK.

Gebhardt, U., and Hiete, M. 2013. Continental Upper Carboniferous red beds in the Variscan intermontane Saale Basin, central Germany: orbital forcing detected by wavelet analysis. *Geological Society, London, Special Publications*, **376**: 177-199. doi:10.1144/sp376.12.

Gibling, M., Rygel, M., Fielding, C., Frank, T., and Isbell, J. 2008a. Late Paleozoic cyclic strata of Euramerica: Recognition of Gondwanan glacial signatures during periods of thermal subsidence. Resolving the Late Paleozoic Ice Age in Time and Space: Geological Society of America Special Publication, **441**: 219-233. doi:10.1130/2008.2441(15).

Gibling, M.R., Culshaw, N., Rygel, M.C., and Pascucci, V. 2008c. Chapter 6 The Maritimes Basin of Atlantic Canada: Basin Creation and Destruction in the Collisional Zone of Pangea. *In* The Sedimentary Basins of the United States and Canada. Elsevier. pp. 211-244.

Gibling, M.R., Calder, J.H., Ryan, R., Poll, H.W.v.d., and Yeo, G.M. 1992. Late Carboniferous and Early Permian drainage patterns in Atlantic Canada. *Canadian Journal of Earth Sciences*, **29**: 338-352. doi:10.1139/e92-030.

Gilbert, G.K. 1895. Sedimentary measurement of Cretaceous time. *The Journal of Geology*, **3**: 121-127. doi:10.1086/607150.

Goupillaud, P., Grossmann, A., and Morlet, J. 1984. Cycle-octave and related transforms in seismic signal analysis. *Geoexploration*, **23**: 85-102. doi:10.1016/0016-7142(84)90025-5.

Grey, M., and Finkel, Z.V. 2011. The Joggins Fossil Cliffs UNESCO World Heritage site: a review of recent research. *Atlantic Geology*, **47**: 185-200. doi:10.4138/atlgel.2011.009.

Grey, M., Pufahl, P.K., and Aziz, A.A. 2011. Using Multiple Environmental Proxies to Determine Degree of Marine Influence and Paleogeographical Position of the Joggins Fossil Cliffs, Unesco World Heritage Site. *Palaios*, **26**: 256-263. doi:10.2110/palo.2010.p10-118r.

Haszeldine, R.S. 2009. Carboniferous North Atlantic palaeogeography: stratigraphic evidence for rifting, not megashear or subduction. *Geological Magazine*, **121**: 443-463. doi:10.1017/s0016756800029988.

Hays, J.D., Imbrie, J., and Shackleton, N.J. 1976. Variations in the Earth's Orbit: Pacemaker of the Ice Ages. *Science*, **194**: 1121-1132. doi:10.1126/science.194.4270.1121.

Huaichun, W.U., Shihong, Z., Suwen, S.U.I., and Qinghua, H. 2007. Recognition of Milankovitch Cycles in the Natural Gamma-Ray Logging of Upper Cretaceous Terrestrial Strata in the Songliao Basin. *Acta Geologica Sinica - English Edition*, **81**: 996-1001. doi:10.1111/j.1755-6724.2007.tb01021.x.

Jirásek, J., Opluštil, S., Sivek, M., Schmitz, M.D., and Abels, H.A. 2018. Astronomical forcing of Carboniferous paralic sedimentary cycles in the Upper Silesian Basin, Czech Republic (Serpukhovian, latest Mississippian): New radiometric ages afford an astronomical age model for European biozonations and substages. *Earth-Science Reviews*, **177**: 715-741. doi:10.1016/j.earscirev.2017.12.005.

Kelly, T.B., and Wach, G.D. 2020. Analysis of factors influencing the interpretation of a digitally examined fluvial meanderbelt system: Joggins Formation, Nova Scotia. *Canadian Journal of Earth Sciences*, **57**: 524-541. doi:10.1139/cjes-2018-0263.

Kelly, T.B., Wach, G.D., and O'Connor, D.E. 2021a. The technical challenges and outcomes of ground-penetrating radar: A site-specific example from Joggins, Nova Scotia. *AIMS Geosciences*, **7**: 22-55. doi:10.3934/geosci.2021002.

Labrecque, P.A., Jensen, J.L., and Hubbard, S.M. 2011. Cyclicity in Lower Cretaceous point bar deposits with implications for reservoir characterization, Athabasca Oil Sands, Alberta, Canada. *Sedimentary Geology*, **242**: 18-33. doi:10.1016/j.sedgeo.2011.06.011.

Lear, C.H., Anand, P., Blenkinsop, T., Foster, G.L., Gagen, M., Hoogakker, B., Larter, R.D., Lunt, D.J., McCave, I.N., and McClymont, E. 2021. Geological Society of London Scientific Statement: what the geological record tells us about our present and future climate. Geological Society of London.

Leeder, M.R. 1988. Devonian-Carboniferous river systems and sediment dispersal from the orogenic belts and cratons of NW Europe. Geological Society, London, Special Publications, **38**: 549-558. doi:10.1144/gsl.Sp.1988.038.01.37.

Leeder, M.R., Duff, P.M.D., and Smith, A.J. 1992. Dinantian. *Geology of England and Wales*: 207-237.

Letourmy, Y., Driese, S.G., and Sims, J.R. 2021. Absence of evidence of climate-driven cycles in Carboniferous deposits of Joggins, Nova Scotia, Canada: influence of salt withdrawal tectonics on deposition and pedogenesis. *Journal of Sedimentary Research*, **91**: 167-185. doi:10.2110/jsr.2020.78.

Maynard, J.R., Hofmann, W., Dunay, R.E., Benthon, P.N., Dean, K.P., and Watson, I. 1997. The Carboniferous of Western Europe; the development of a petroleum system. *Petroleum Geoscience*, **3**: 97-115. doi:10.1144/petgeo.3.2.97.

McIntyre, A., and Molfino, B. 1996. Forcing of Atlantic Equatorial and Subpolar Millennial Cycles by Precession. *Science*, **274**: 1867-1870. doi:10.1126/science.274.5294.1867.

Milankovitch, M. 1941. Kanon der Erdbestrahlung und seine Anwendung auf das Eiszeitproblem. Acad. Roy. Serbe, Ed. spec, **133**.

Morten, S. 2001. Recognition of cyclicity in the petrophysical properties of a Maastrichtian pelagic chalk oil field reservoir from the Danish North Sea. *AAPG Bulletin*, **85**: 2003-2015. doi:10.1306/8626d0d1-173b-11d7-8645000102c1865d.

Olsen, P.E., and Kent, D.V. 1996. Milankovitch climate forcing in the tropics of Pangaea during the Late Triassic. *Palaeogeography, Palaeoclimatology, Palaeoecology*, **122**: 1-26. doi:10.1016/0031-0182(95)00171-9.

Olsen, P.E., Shackleton, N.J., McCave, I.N., Weedon, G.P., and Kent, D.V. 1999. Long-period Milankovitch cycles from the Late Triassic and Early Jurassic of eastern North America and their implications for the calibration of the Early Mesozoic time-scale and the long-term behaviour of the planets. *Philosophical Transactions of the Royal Society of London. Series A: Mathematical, Physical and Engineering Sciences*, **357**: 1761-1786. doi:10.1098/rsta.1999.0400.

Olsen, P.E., Laskar, J., Kent, D.V., Kinney, S.T., Reynolds, D.J., Sha, J., and Whiteside, J.H. 2019. Mapping Solar System chaos with the Geological Orrery. *Proc Natl Acad Sci U S A*, **116**: 10664-10673. doi:10.1073/pnas.1813901116.

Prokoph, A., and Agterberg, F.P. 1999. Detection of sedimentary cyclicity and stratigraphic completeness by wavelet analysis; an application to late Albian cyclostratigraphy of the Western Canada Sedimentary Basin. *Journal of Sedimentary Research*, **69**: 862-875. doi:10.2110/jsr.69.862.

Prokoph, A., and Thurow, J. 2000. Diachronous pattern of Milankovitch cyclicity in late Albian pelagic marlstones of the North German Basin. *Sedimentary Geology*, **134**: 287-303. doi:10.1016/s0037-0738(00)00050-6.

Prokoph, A., Villeneuve, M., Agterberg, F.P., and Rachold, V. 2001. Geochronology and calibration of global Milankovitch cyclicity at the Cenomanian-Turonian boundary. *Geology*, **29**: 523-526. doi:10.1130/0091-7613(2001)029<0523:Gacogm>2.0.Co;2.

Rampino, M.R., Prokoph, A., and Adler, A. 2000. Tempo of the end-Permian event: High-resolution cyclostratigraphy at the Permian-Triassic boundary. *Geology*, **28**: 643-646. doi:10.1130/0091-7613(2000)28<643:Toteeh>2.0.Co;2.

REI Nova Scotia. 1995. The Coring and Logging of REI-B2-1. Halifax, Nova Scotia.

Reisz, R.R., and Modesto, S.P. 1996. Archerpeton anthracos from the Joggins Formation of Nova Scotia: a microsauro, not a reptile. *Canadian Journal of Earth Sciences*, **33**: 703-709. doi:10.1139/e96-053.

Ryan, R.J., and Boehner, R.C. 1994. Geology of the Cumberland Basin, Cumberland, Colchester and Pictou Counties, Nova Scotia - Memoir 10. *Edited by* Mines and Energy Branch - Department of Natural Resources. Department of Natural Resources, Halifax.

Rygel, M.C., and Gibling, M.R. 2006. Natural Geomorphic Variability Recorded in a High-Accommodation Setting: Fluvial Architecture of the Pennsylvanian Joggins Formation of Atlantic Canada. *Journal of Sedimentary Research*, **76**: 1230-1251. doi:10.2110/jsr.2006.100.

Rygel, M.C., Sheldon, E.P., Stimson, M.R., Calder, J.H., Ashley, K.T., and Salg, J.L. 2014. The Pennsylvanian Springhill Mines Formation: sedimentological framework for a portion of the Joggins Fossil Cliffs UNESCO World Heritage Site. *Atlantic Geology*, **50**: 249-289. doi:10.4138/atlgol.2014.013.

Schwarzacher, W. 1993. *Developments in Sedimentology: Chapter 7 Examples from the Carboniferous*. Elsevier. pp. 107-124.

Schwarzacher, W. 2000. Repetitions and cycles in stratigraphy. *Earth-Science Reviews*, **50**: 51-75. doi:10.1016/s0012-8252(99)00070-7.

Strasser, A., Einsele, G., and Ricken, W. 1991. Lagoonal-peritidal sequences in carbonate environments: autocyclic and allocyclic processes. *Cycles and events in stratigraphy*: 709-721.

Strasser, A.H., and Heckel, P.H. 2007. Cyclostratigraphy concepts, definitions, and applications. *Newsletters on Stratigraphy*, **42**: 75-114. doi:10.1127/0078-0421/2006/0042-0075.

Sun, J., and Huang, X. 2006. Half-precessional cycles recorded in Chinese loess: response to low-latitude insolation forcing during the Last Interglaciation. *Quaternary Science Reviews*, **25**: 1065-1072. doi:10.1016/j.quascirev.2005.08.004.

Svensen, H.H., Torsvik, T.H., Callegaro, S., Augland, L., Heimdal, T.H., Jerram, D.A., Planke, S., and Pereira, E. 2018. Gondwana Large Igneous Provinces: plate reconstructions, volcanic basins and sill volumes. Geological Society, London, Special Publications, **463**: 17-40. doi:10.1144/sp463.7.

Tanyel, E.D. 2006. Formation evaluation using wavelet analysis on logs of the Chinji and Nagri Formations, northern Pakistan. Texas A&M University.

Tibert, N.E., and Dewey, C.P. 2006. *Velatomorpha*, a new healdioidean ostracode genus from the early Pennsylvanian Joggins Formation, Nova Scotia, Canada. *Micropaleontology*, **52**: 51-66. doi:10.2113/gsmicropal.52.1.51.

Timmer, E.R., Gingras, M.K., Morin, M.L., Ranger, M.J., and Zonneveld, J.P. 2016. Laminae-scale rhythmicity of inclined heterolithic stratification, Lower Cretaceous McMurray Formation, NE Alberta, Canada. *Bulletin of Canadian Petroleum Geology*, **64**: 199-217. doi:10.2113/gscpgbull.64.2.199.

Tucker, M.E., Gallagher, J., and Leng, M.J. 2009. Are beds in shelf carbonates millennial-scale cycles? An example from the mid-Carboniferous of northern England.... *Sedimentary Geology*, **214**: 19-34. doi:10.1016/j.sedgeo.2008.03.011.

Udden, J.A. 1912. Geology and mineral resources of the Peoria quadrangle, Illinois. U.S. Geological Survey Bulletin 506: 1-103.

Valdes, P.J., Sellwood, B.W., and Price, G.D. 1995. Modelling Late Jurassic Milankovitch climate variations. *In* *Orbital Forcing Timescales and Cyclostratigraphy*. Edited by M.R. House and A.S. Gale. The Geological Society, London, UK. pp. 115-132.

van den Belt, F.J.G., van Hoof, T.B., and Pagnier, H.J.M. 2015. Revealing the hidden Milankovitch record from Pennsylvanian cyclothem successions and implications regarding late Paleozoic chronology and terrestrial-carbon (coal) storage. *Geosphere*, **11**: 1062-1076. doi:10.1130/ges01177.1.

Veevers, J.J., and Powell, C.M. 1987. Late Paleozoic glacial episodes in Gondwanaland reflected in transgressive-regressive depositional sequences in Euramerica. *Geological Society of America Bulletin*, **98**: 475-487. doi:10.1130/0016-7606(1987)98<475:Lpgeig>2.0.Co;2.

Wach, G.D. 1991. *Sedimentology and Stratigraphy of the Lower Cretaceous of the Channel Basin*. Department of Earth Sciences, University of Oxford, Oxford, UK.

Waldron, J.W.F., and Rygel, M.C. 2005. Role of evaporite withdrawal in the preservation of a unique coal-bearing succession: Pennsylvanian Joggins Formation, Nova Scotia. *Geology*, **33**: 337-340. doi:10.1130/g21302.1.

Waldron, J.W.F., Rygel, M.C., Gibling, M.R., and Calder, J.H. 2013. Evaporite tectonics and the late Paleozoic stratigraphic development of the Cumberland basin, Appalachians of Atlantic Canada. *Geological Society of America Bulletin*, **125**: 945-960. doi:10.1130/b30718.1.

Wanless, H.R., and Shepard, F.P. 1936. Sea level and climatic changes related to late Paleozoic cycles. *Geological Society of America Bulletin*, **47**: 1177-1206. doi:10.1130/gsab-47-1177.

Waters, C., and Davies, S. 2006. Carboniferous: extensional basins, advancing deltas and coal swamps. In: *The geology of England and Wales*/edited by PJ Brenchley and PF Rawson. London: Geological Society of London, **2006**: 173-223. doi:10.1144/GOEWP.9.

Weller, J.M. 1930. Cyclical Sedimentation of the Pennsylvanian Period and Its Significance. *The Journal of Geology*, **38**: 97-135. doi:10.1086/623695.

Westphal, H., Head, M.J., and Munnecke, A. 2000. Differential Diagenesis of Rhythmic Limestone Alternations Supported by Palynological Evidence. *Journal of Sedimentary Research*, **70**: 715-725. doi:10.1306/2dc40932-0e47-11d7-8643000102c1865d.

Williams, H. 1984. Miogeoclines and suspect terranes of the Caledonian–Appalachian Orogen: tectonic patterns in the North Atlantic region. *Canadian Journal of Earth Sciences*, **21**: 887-901. doi:10.1139/e84-095.

Willis, K.J., Kleczkowski, A., Briggs, K.M., and Gilligan, C.A. 1999. The role of sub-milankovitch climatic forcing in the initiation of the northern hemisphere glaciation. *Science*, **285**: 568-571. doi:10.1126/science.285.5427.568.

Wonik, T. 2001. Gamma-ray measurements in the Kirchrode I and II boreholes. *Palaeogeography, Palaeoclimatology, Palaeoecology*, **174**: 97-105. doi:10.1016/s0031-0182(01)00288-7.

Wu, H., Zhang, S., Feng, Q., Jiang, G., Li, H., and Yang, T. 2012. Milankovitch and sub-Milankovitch cycles of the early Triassic Daye Formation, South China and their geochronological and paleoclimatic implications. *Gondwana Research*, **22**: 748-759. doi:10.1016/j.gr.2011.12.003.

Wu, H., Zhang, S., Hinnov, L.A., Jiang, G., Feng, Q., Li, H., and Yang, T. 2013. Time-calibrated Milankovitch cycles for the late Permian. *Nat Commun*, **4**: 2452. doi:10.1038/ncomms3452.

Wu, H., Zhang, S., Hinnov, L.A., Jiang, G., Yang, T., Li, H., Wan, X., and Wang, C. 2014. Cyclostratigraphy and orbital tuning of the terrestrial upper Santonian–Lower Danian in Songliao Basin, northeastern China. *Earth and Planetary Science Letters*, **407**: 82-95. doi:10.1016/j.epsl.2014.09.038.

Yiou, P., Genthon, C., Ghil, M., Jouzel, J., Le Treut, H., Barnola, J.M., Lorius, C., and Korotkevitch, Y.N. 1991. High-frequency paleovariability in climate and CO₂ levels from Vostok Ice Core Records. *Journal of Geophysical Research: Solid Earth*, **96**: 20365-20378. doi:10.1029/91jb00422.

Yu, J.-f., Sui, F.-g., Li, Z.-x., Liu, H., and Wang, Y.-l. 2008. Recognition of Milankovitch cycles in the stratigraphic record: application of the CWT and the FFT to well-log data. *Journal of China University of Mining and Technology*, **18**: 594-598. doi:10.1016/s1006-1266(08)60301-6.

Yuan, X., Guo, Y., Yu, J., Shen, Y., and Shao, Y. 2013. Correlation and analysis of well-log sequence with Milankovitch cycles as rulers: A case study of coal-bearing strata of late Permian in western Guizhou. *International Journal of Mining Science and Technology*, **23**: 563-568. doi:10.1016/j.ijmst.2013.07.015.

Zuhlke, R. 2004. Integrated cyclostratigraphy of a model Mesozoic carbonate platform—the Latemar (Middle Triassic, Italy). *In Cyclostratigraphy: Approaches and Case Histories - SEPM Special Publication No. 81. Edited by B. D'Argenio, Fischer, A.G., Premoli Silva, I., Weissert, H., Ferreri, V.* pp. 183-211.

Zuhlke, R., Bechstadt, T., and Mundil, R. 2003. Sub-Milankovitch and Milankovitch forcing on a model Mesozoic carbonate platform - the Latemar (Middle Triassic, Italy). *Terra Nova*, **15**: 69-80. doi:10.1046/j.1365-3121.2003.00366.x.

Chapter 8: Conclusions

This dissertation comprises six independent chapters (Table 8.1). The research presented in these chapters reflects investigations at outcrop and subsurface to provide high-resolution characterization of reservoirs for hydrocarbons, CCS, and geothermal projects. The study interval selected for this research is the Late Carboniferous Joggins Formation in the Cumberland Basin of northern Nova Scotia, Canada.

Five challenges were identified by the Society for Petroleum Engineers Research & Development Committee: (1) higher resolution subsurface imaging, (2) increasing hydrocarbon recovery factors, and (3) carbon capture, utilization, and storage (SPE Research & Development Committee 2012). Each of the separate studies, presented as dissertation chapters, makes a new contribution to our overall understanding of these challenges while also contributing to the knowledge of Joggins Formation sedimentology (Table 8.1). While the work presented here was focused on the Joggins Formation, it was done so at a wide range of scales, from the grain size scale to the much larger basin size scale (Figure 8.1). New methodologies were developed, or existing methodologies were modified for data collection for reservoir characterization and sedimentology, and their applicability to the three challenges (Table 8.1). Directions for future research are also mentioned.

Table 8.1: A summary of the equipment/methods, software, and resulting innovations/contributions for each chapter of this dissertation.

Chapter	Equipment & Method(s)	Software	Innovation(s)/Contribution(s)
2 (Georef. Workflow) Published	terrestrial laser scanner, RTK DGPS, georef. targets	Optech, Notepad, Excel, ArcGIS™, Petrel™	<ul style="list-style-type: none"> - high-resolution definition of stratigraphy, geobodies, architectural elements, & baffles/barriers. - novel integration of lidar with ArcGIS™ & Petrel™ software. - novel workflow achieving georeferenced data.
3 (Outcrop Study near Coal Mine Point) Published	terrestrial laser scanner, RTK DGPS, georef. targets, spectrometer, air permeameter, thin sections	Optech, Notepad, Excel, ArcGIS™, Petrel™, Image-Pro Plus, CorelDraw	<ul style="list-style-type: none"> - increase understanding of fluvial reservoirs, which provides lateral facies relationships for geobody analysis. - impact/limits of combined data collection approach. - show architectural element complexity. - provide awareness of reservoir heterogeneity, architectural elements, & baffles/barriers. - offer architectural element data.
4 (GPR Geoforensic study) Published	GPR pulseEKKO Pro SmartCart	EKKO Project, Petrel™, Excel, CorelDraw	<ul style="list-style-type: none"> - 3D renderings delineate shallow subsurface objects; transferrable to delineation of architectural elements within geobodies. - high-resolution mapping by subtracting low amplitude data. - map potential leachate plumes. - peer-review methodology corroborates the validity of geoforensics & GPR.
5 (Joggins GPR study) Published	GPR pulseEKKO Pro SmartCart, RTK DGPS	EKKO Project, Excel, CorelDraw	<ul style="list-style-type: none"> - first conventional GPR study with applicability to high-resolution subsurface imaging for reservoir characterization. - angular unconformity imaged, enabling mapping of 8 m of overlying glacial till. - pitfalls of GPR in this environment. - reveal correlatable links between surface & shallow surface objects.
6 (Tidal bundles study) In-review	FFT, CWT, visual cyclicity analysis	Excel, MATLAB, CorelDraw	<ul style="list-style-type: none"> - novel account of tidal rhythmites. - provide first quantitative data of tidal bundles from the Joggins Formation. - provide evidence for marine & brackish incursions & suggests presence of a mid-Euramerican seaway. - delineate fine-scale baffles/barriers for reservoir characterization studies.
7 (Cyclostrat. study) Submitted	palynology, FFT, CWT	Excel, MATLAB, CorelDraw	<ul style="list-style-type: none"> - identify Milankovitch cycles. - determine orbital factors. - learn about sedimentation rates. - aid stratigraphic correlation and high-resolution reservoir characterization.

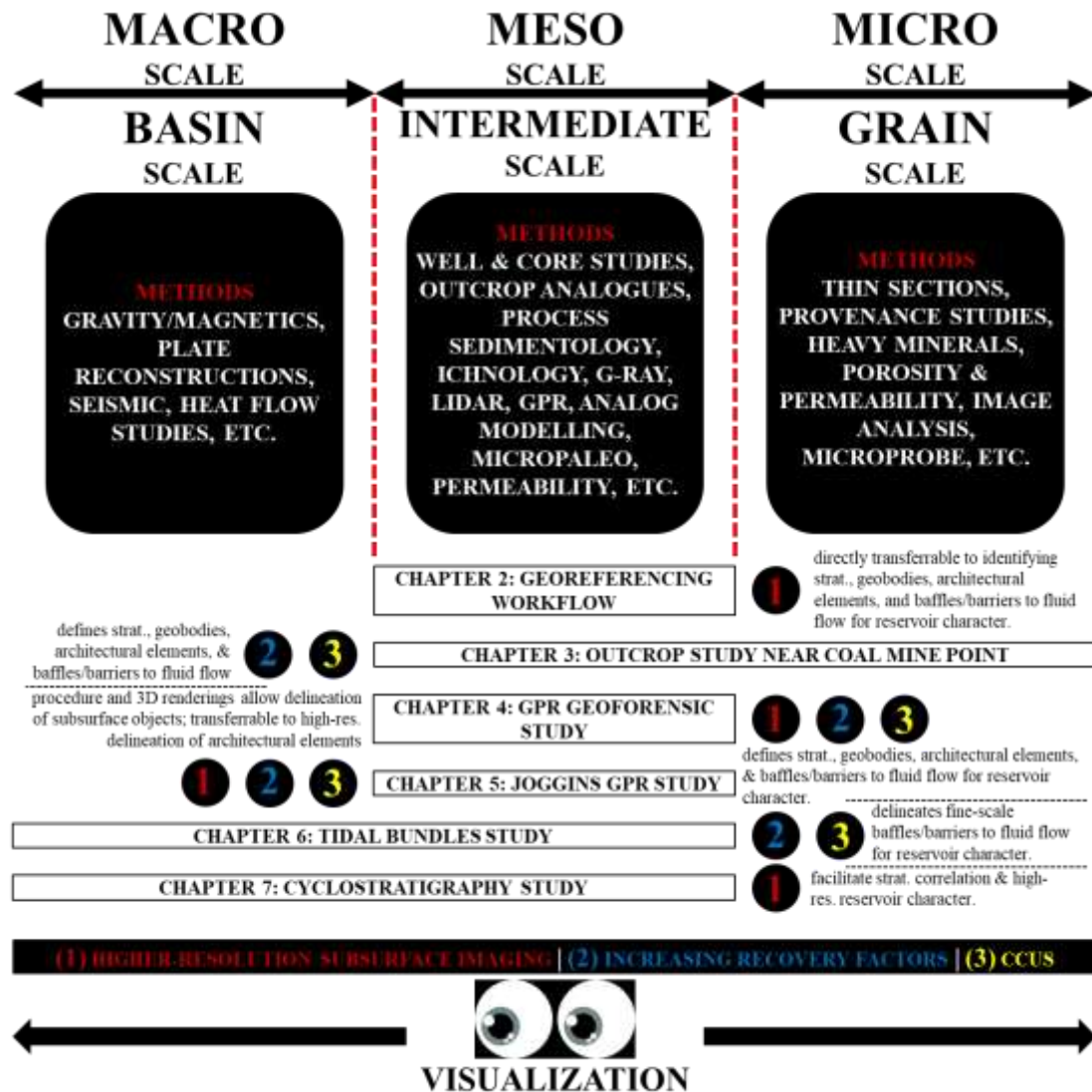


Figure 8.1: A summary of the basin to grain scale concept of visualization. Data collection methods occupy the basin (macro) scale, the grain (micro) scale, or the intermediate scale between the two. Within each of the three scales (basin, intermediate, and grain), it is possible to relate each of the six chapters to one or more of the visualization scales. The figure also shows the three grand challenges this dissertation addresses and assigns one or more challenge numbers (1, 2, or 3) to each of the six chapters they are represented by.

8.1 Manuscript 1: Chapter 2 – Georeferencing Workflow

This chapter relates to objective 1 discussed in the introduction. It develops and demonstrates methodologies for collecting data for high-resolution imaging from outcrops for reservoir characterization studies. A technique for implementing post-scan georeferencing on a large geological outcrop section scanned by a static terrestrial lidar scanner and paired with an RTK DGPS and control points. The application of commonly accessible software ensures that the technique can be employed regularly and effectively with replicatable results. The unique example offered by Chapter 2 emphasizes the demand for and importance of the integration of data with software such as ArcGIS™ and Schlumberger Petrel™. The georeferencing of a lidar point cloud post-scan has been shown to be a method for the accurate incorporation of data from lidar scans performed in environments where time must be considered (e.g., because of tides). Post-scan georeferencing is beneficial when the laser scanner lacks built-in GPS capabilities. Additionally, georeferencing targets can serve as a backup if potential errors in collecting GPS data directly during the scan should arise.

This research relates to the overall themes of sedimentology and reservoir characterization because it is a directly pertinent and transferrable method for identifying stratigraphy, geobodies, architectural elements, and baffles and barriers to fluid movement. Lidar scanning offers the ability of high-resolution imaging of outcrop analogues that can serve as case studies for their subsurface counterparts. The high-resolution imaging offered by lidar allows for the spatial determination of geobodies in a reservoir, which can facilitate studies on increasing recovery factors and the dynamics of fluid extraction or injection.

Future research investigations could include a revised workflow that streamlines and simplifies the process of georeferencing a point cloud collected by lidar, with the point cloud georeferenced in real-time as the points are collected.

8.2 Manuscript 2: Chapter 3 – Outcrop Study near Coal Mine Point

This chapter relates to objective 1 discussed in the introduction. This chapter also demonstrates methodologies for high-resolution outcrop characterization by integrating the high-resolution lidar imaging from Chapter 2 with a portable handheld gamma ray spectrometer, portable handheld air permeameter, and thin section data. These data define and characterize reservoir heterogeneity, architectural elements, and baffles and barriers to reservoir fluid flow. The application of these techniques on the outcrop supports the understanding of the controls of lateral facies on fluid flow and geobody analysis.

The gamma ray spectrometry data reveal a broad range of values, which are the result of the variable bed lithology of the interbedded strata. Gamma ray spectrometry is particularly useful for highlighting lithology contrasts in complex geological situations but is unable to selectively measure and identify reservoir heterogeneity such as clast variability (Kelly and Wach 2020). Permeability data vary extensively from a minimum of 7 md to a maximum of approximately 2,000 md. This variability is not solely the result of a change in lithology between beds but rather the result of subtle changes in lithology and composition within individual beds (Kelly and Wach 2020).

The use of high-resolution imaging, such as lidar, can facilitate the recognition of reservoir heterogeneity in an outcrop because of the detail in the resulting generated point cloud (Kelly and Wach 2020). The reflected light intensity from the rock outcrop being scanned by the lidar system has the additional advantage of being a proxy for lithology, at

least for an outcrop that demonstrates extensively variable and alternating geology, such as at Joggins.

Reservoir characterization studies are increasingly enhanced when lidar is combined with more traditional approaches to measurement, such as the use of gamma ray spectrometry or an air permeameter. Reservoir heterogeneity in the Joggins Formation is stratigraphically controlled, with variations in alternating lithology being the apparent reason (Kelly and Wach 2020). Individual beds exhibit vertical and horizontal heterogeneity because of lithological changes within or changes in grain size. Sedimentary structures probably also play a role in reservoir heterogeneity within single beds.

A continuation of the present study could include the collection gamma ray spectrometer measurements from the Joggins Formation interval of the REI-B2-1 borehole for direct comparison with those collected from the studied portion of the Joggins Formation outcrop to determine if there are changes occurring to the lithologies observed and why these changes are occurring. A similar exercise could include the collection of air permeameter measurements from the Joggins Formation sandstone sections of the REI-B2-1 borehole with a comparison to those values from the outcrop. Does the permeability of the sandstone sections in the outcrop vary greatly from the sandstone sections seen in the drill core? Additionally, thin sections could be made from the Joggins Formation sandstone sections of the REI-B2-1 borehole and compared with those from the outcrop. Are the porosity values varying greatly between them? Furthermore, a detailed 3D model could be created using the point cloud produced from the lidar scan and populated with known information (more measurements would be needed, such as additional air permeameter measurements for permeability, additional thin section data for porosity determination,

etc.) to simulate reservoir fluid flow. How much detail is required, and how does inputting a large quantity of data affect the output compared with a smaller quantity of data?

8.3 Manuscript 3: Chapter 4 – GPR Geoforensic Study

This chapter relates to objective 2 discussed in the introduction. It uses high-resolution shallow geophysical techniques (GPR) to demonstrate the significance and limitations of conducting a gridded GPR survey using a church cemetery to produce and assess 2D- and 3D-modelled reconstructions of the cemetery burial sites. Shallow geophysical renderings demonstrate the stratigraphic complexity that is not resolvable using conventional seismic acquisition, processing streams, and interpretation techniques. In the past, these reconstructions have primarily been performed and displayed as 2D horizontal and vertical planes, meaning the visualization of subsurface 3D objects and their spatial extents have been limited (e.g., Smith and Jol 1992; Vandenberghe and Van Overmeeren 1999; Clement et al. 2006; Fiedler et al. 2009; Schultz et al. 2012).

The peer-reviewed methodology substantiates the application of GPR for geoforensic use and the legitimacy of allowing GPR data, analysis, and interpretation to be presented as evidence in a court of law, especially for criminal investigations. Moreover, the methodology and resultant 3D renderings allow for the direct delineation of shallow objects (in the case of Chapter 4, the objects were burials) in the subsurface. This is directly transferable to the high-resolution definition of architectural components within geobodies for geology-related studies and can be related back to three of the five grand challenges (SPE Research & Development Committee 2012). The GPR study demonstrated that the results could be used to accurately map a cemetery, whereby burial sites are distinguished from one another by removing low amplitude data (Kelly et al. 2021b). The results also

provided accurate identification of otherwise unknown burial sites. An additional innovative outcome of this research was the suggestion that GPR can be used to detect potential leachate plumes from older decaying bodies (Kelly et al. 2021b). The detection of leachate plumes using GPR has significance for the potential mapping of subsurface contaminant plumes for environmental studies, as an example.

This research developed the acquisition methodology, processing streams, interpretation, and results, creating an overall more intuitive, easily manipulatable, 3D model to optimize visualization for accurate interpretation. This was feasible through site examination, optimal data acquisition equipment testing, and a unique 3D modelling method applying finite-element modelling in Petrel™ software from Schlumberger, which allows for viewing a GPR cube using cross-sections and depth slices (Kelly et al. 2021b).

Future research recommendations include investigation of the potential and reliability of GPR to detect leachate plumes emanating from burials and further testing of the methodology on outcrops for reservoir delineation, with preliminary investigations demonstrated in Chapter 4.

8.4 Manuscript 4: Chapter 5 – Joggins GPR Study

This chapter relates to objective 2 discussed in the introduction. It documents the first example of a conventional ground-penetrating radar survey at Joggins, Nova Scotia, with the intent of imaging near-surface, dipping strata of the Joggins Formation. This shallow subsurface imaging technique was utilized to enable the elucidation of shallow subsurface architectural components within the Joggins Formation. Specifically, the intent was imaging the larger channel bodies using GPR, such as the one imaged at Coal Mine Point using the lidar scanner (Chapter 2 and Chapter 3). Capturing these channel bodies using

the GPR would have allowed for their geometries to be extended inland, providing useful information for reservoir characterization.

Despite the absence of imaged geobodies and architectural elements from the Joggins Formation, substantial insight was achieved as to the limitations of the GPR (Kelly et al. 2021a). Some moderate geological success was achieved in imaging the angular unconformity between the Quaternary and Carboniferous strata, evident in the radargrams. The research results suggest imaging of the geobodies within the Carboniferous strata beneath the unconformity was constrained to a combination of the formation dip angle of ~ 21 degrees, variations in overburden thickness, clay content, and fractures and faulting throughout the outcrop, associated with both salt kinematics and subsequent basin inversion. All of these factors can serve to attenuate the GPR signal strength.

Although the primary objective of imaging the Joggins Formation geobodies by defining the fluvial channel bodies was unsuccessful, it nevertheless increased our knowledge concerning the true impact of clay-rich overburden sediments on bedrock imaging, in addition to the impacts that surface features can cause on GPR data collection. The knowledge gained from this study can be applied to future GPR surveys, particularly with respect to geoforensic and archaeological studies where the study areas contain similar surface infrastructure (e.g., utility poles, power lines, etc.). The study shows clearly correlatable links between surface/shallow surface objects and the ground-penetrating radar profiles.

This research investigation also demonstrates the usefulness of shallow subsurface GPR for geohazard assessments. This area was the site of extensive subsurface coal mining with well-developed surface and subsurface infrastructure. Surface infrastructure is often

obscured by surface vegetation, relying on delineation from historic maps and photographs that are in some cases georeferenced to the sites. Therefore, the area probably contains an abundance of erratic metal objects of abandoned machinery, large boulders with glacial sediments, etc., that could influence signal acquisition and resolution on the generated radargrams.

Recommendations for further research include a repeat of the GPR survey using a lower frequency antenna configuration (with potential for deeper penetration of the subsurface strata) to investigate if we can image the dipping strata below the unconformity at Joggins. The study presented in this dissertation utilized the 50 MHz antennae; however, the deeper penetrating 25 MHz and 12.5 MHz antennae could be applied to the study area. The additional depth provided by the lower frequency configuration might allow for the detection of strata and allow for the 2D cliff to be projected in the 3D sense. Of course, potential stratigraphic resolution may be compromised.

Application of a defined 2D grid survey, as developed in the methodology for Chapter 4, on a discrete area with known geobodies (e.g., Coal Mine Point) above the Joggins Formation could be used to create a 3D cube for the purposes of reservoir modelling. Initial results are promising. A preliminary 2D grid survey was undertaken at the site of a former baseball field (lines 45-50) at Coal Mine Point. The results from that set of GPR lines demonstrated the capability for administering a broader survey to identify and characterize the geobodies and architectural elements.

8.5 Manuscript 5: Chapter 6 – Tidal Bundles Study

This chapter relates to objective 4 discussed in the introduction. It identifies and documents for the first time tidal rhythmites in the Late Carboniferous and the first quantitative data of tidal bundles from drill core penetrating the Joggins Formation. The results support the existence of a mid-Euramerican seaway connecting to the Paleo-Tethys Ocean. The presence of tidal bundles provides convincing evidence of marine influence for the debate that has been ongoing for years. When paired with additional evidence, such as the presence of marine trace fossils, marine fish scales and body fossils, and horseshoe crab imprints, the evidence for brackish and marine environments appears certain. This research indicates sediment deposition was controlled by tides and followed a semi-diurnal model with a lunar monthly tidal cycle through a high-resolution geomathematical approach integrating Fourier transform and continuous wavelet transform analyses. Identification of tidal processes and associated depositional environments using this unique approach provides delineation of fine-scale baffles and barriers to fluid flow for reservoir characterization studies.

This evidence for Milankovitch cycles hidden in the natural gamma ray geophysical log may offer a new research method for identifying high-resolution stratigraphic intervals and correlations of the Cumberland Basin strata and other Carboniferous strata. Furthermore, this geomathematical approach may lead to predicting enhanced reservoir characterization of sedimentary basins with limited drill core and seismic data. These results are an important first step towards constraining a Late Carboniferous astronomical solution and extending the astronomical time scale into the Late Carboniferous. The recognition and quantification of these cycles may help improve our understanding of the

basin, especially regarding other prolific coal basins formed in Euramerica during the Late Carboniferous.

Further research should include the application of Fourier transform and continuous wavelet transform analyses to other tidal bundle intervals from the Joggins Formation interval of the REI-B2-1 borehole. There are additional tidal bundle intervals within the Joggins Formation interval of the REI-B2-1 borehole that provide further tidal regime data, although some of the remaining tidal bundle intervals have faint laminations. Results could be integrated and compared with results from other Carboniferous basins in Euramerica to establish a more assertive presence for the existence of a mid-Euramerican seaway during the Carboniferous. While this study was able to detect tidal modulation, future research could be focused on determining the scale of the tidal forces that existed during this time and in this area.

8.6 Manuscript 6: Chapter 7 – Cyclostratigraphy Study

This research relates to objective 3 discussed in the introduction. It tests the premise that orbital forcing signals will be recognizable due to sea level and climate change. Quantitative evidence is presented of preserved Milankovitch cycles within a prominent, conformable Late Carboniferous succession using a geomathematical approach. We can identify specific ratios corresponding to Milankovitch cycles by combining a fast Fourier transform and one-dimensional continuous wavelet transform analyses on a non-subjective natural gamma ray geophysical borehole log. We show that fast Fourier transform and continuous wavelet transform analyses reveal cycles for long and short eccentricity, obliquity, and precession. The detection of cyclic events affecting deposition can facilitate stratigraphic correlation and high-resolution reservoir characterization.

Our results indicate that Milankovitch cyclicity is preserved and is in keeping with other Euramerican Late Carboniferous-aged basins. Quantitative results from this study show evidence for Milankovitch cycles in these strata and suggest that cyclicity may be present basin-wide, despite the tectonic regime of a high subsidence basin. The fast Fourier transform produced a noteworthy ratio of 18.99:5.15:2.02:1, similar to the ratio of 20:5:2:1, which defines the four main orbital periods of long (400 kyr) and short (100 kyr) eccentricity, obliquity (40 kyr), and precession (20 kyr). The continuous wavelet transform generated a ratio of 1:4, equal to the ratio of short (100 kyr) and long (400 kyr) eccentricity orbital periods.

Future research includes the application of a similar method on additional borehole gamma ray logs from the Cumberland Basin to establish whether the Milankovitch cyclicity observed in the REI-B2-1 borehole is apparent in other sedimentary successions in the Cumberland Basin. For comparison purposes, this would involve the selection of boreholes containing gamma ray data from the Cumberland Basin. Ideally, the boreholes would be chosen from the list presented by the Nova Scotia Department of Energy Report 2017-08 entitled, “Schedule of Petroleum Wells, onshore Nova Scotia, Part 2: Cumberland Region”. Examples of boreholes that are potential suitors for this kind of research include, but are not limited to P-83, P-85, P-86, P-93, P-103, P-104, P-122, P-124, and P-135. These boreholes all possess gamma ray log data that is continuous for at least 300 m.

This study utilizes palynological analysis results from the borehole history report to define the geological time scale stage that is represented by the cored interval and a study by van den Belt et al. (2015) to apply ages based on radiometric dating from western European samples. An enhancement of the work from this chapter, which has been

suggested by Hinnov (2013) is to perform an inter-calibration of the cyclostratigraphy output using high-precision radiometric dating to further refine the ages of stratigraphic horizons. The application of the preserved cyclostratigraphic signal and related distortions could be used to help with the reconstruction of paleoclimate and paleodepositional systems.

Uncertainty with respect to Milankovitch cycles is well-discussed in the literature, with numerous researchers defining these uncertainties quantitatively. Waltham (2015) provides a thorough review of uncertainties relating to Milankovitch cyclicity and how they impact cyclostratigraphy. The research conducted in Chapter 7 could be improved upon further by incorporating climate constraints and depositional system responses. Overall, that would help with the reduction in uncertainty associated with the study.

Continuous wavelet transforms are commonly utilized to help deconvolve cycles in cyclostratigraphic studies. This chapter applied the Morlet wavelet as the ‘mother’ wavelet, which is typically the wavelet of choice used to evaluate cyclicity (e.g., Goupillaud et al. 1984; Labrecque et al. 2011). A task that is more of interest than anything else would be to apply a different type of ‘mother’ wavelet (e.g., Haar, Symlet, Daubechies, Morse, etc.).

8.7 Summary

The six chapters forming this dissertation relate to reservoir characterization, particularly reservoir compartmentalization and fluid flow. The Late Carboniferous Joggins Formation is ideal for studying reservoir characterization in fluvial and non-marine settings at the surface and in the subsurface while assisting with the knowledge gaps associated with higher resolution subsurface imaging, increasing recovery factors, and carbon capture, utilization, and storage.

The second chapter, while purely a methods-based study, is directly applicable to the high-resolution definition of stratigraphic boundaries, geobodies, architectural elements, and baffles and barriers to reservoir fluid flow utilizing lidar. These fundamental components must be established and understood, particularly with the ongoing challenges of increasing recovery factors and the carbon capture, utilization, and storage of greenhouse gases.

The third chapter builds upon the second chapter by introducing an interpreted high-resolution outcrop scan using lidar and integrates this data with a portable handheld gamma ray spectrometer, a portable handheld air permeameter, and hand samples that allow for porosity analysis. These combined data collection procedures emphasize the appreciation for reservoir heterogeneity, architectural elements, and baffles and barriers to reservoir fluid flow. The application of these techniques on the outcrop supports the understanding of lateral facies relationships for geobody analysis.

The fourth and fifth chapters relate to the shallow subsurface imaging technique, known as GPR, which has become increasingly popular for reservoir characterization studies. The approach developed from these two studies, especially the geoforensics study (Chapter 4) and ensuing 3D interpretations, facilitates the elucidation of shallow subsurface objects and is transferrable to the high-resolution definition of architectural components within geobodies.

The sixth chapter innovatively documents the quantitative analysis of Late Carboniferous tidal rhythmites within the Joggins Formation, offering support for a mid-Euramerican seaway linking to the Paleo-Tethys Ocean and indicating sediment deposition followed a semi-diurnal tidal model with a lunar monthly cycle. The identification of these

tidal processes and related depositional environments using a high-resolution geomathematical approach consisting of Fourier transform and continuous wavelet transform analyses is an example of the delineation of fine-scale baffles and barriers to fluid flow for reservoir characterization studies.

The seventh chapter utilizes borehole log data from an interval containing the Joggins Formation and identifies spectral peaks corresponding to the four main orbital periods (400 kyr, 100 kyr, 40 kyr, and 20 kyr) of Milankovitch cyclicity, yielding a ratio of 18.99:5.15:2.02:1. The detection of cyclic events affecting deposition can facilitate stratigraphic correlation and high-resolution reservoir characterization.

The results from the investigations in this dissertation demonstrate the ability for higher resolution reservoir analyses that can minimize the risks associated for reservoir development as outlined by the SPE Research & Development Committee (2012). Higher resolution imaging of reservoirs mitigates risk associated with enhanced secondary hydrocarbon recovery, CO₂ sequestration, development of geothermal resources from sedimentary basins; all key elements to further the energy transition and diversification to achieve carbon neutrality.

8.8 References cited in Chapter 8

Clement, W.P., Barrash, W., and Knoll, M.D. 2006. Reflectivity modeling of a ground-penetrating-radar profile of a saturated fluvial formation. *Geophysics*, **71**: 59-66. doi:10.1190/1.2194528.

Fiedler, S., Illich, B., Berger, J., and Graw, M. 2009. The effectiveness of ground-penetrating radar surveys in the location of unmarked burial sites in modern cemeteries. *Journal of Applied Geophysics*, **68**: 380-385. doi:10.1016/j.jappgeo.2009.03.003.

Goupillaud, P., Grossmann, A., and Morlet, J. 1984. Cycle-octave and related transforms in seismic signal analysis. *Geoexploration*, **23**: 85-102. doi:10.1016/0016-7142(84)90025-5.

Hinnov, L.A. 2013. Cyclostratigraphy and its revolutionizing applications in the earth and planetary sciences. *Geological Society of America Bulletin*, **125**: 1703-1734. doi:10.1130/B30934.1.

Kelly, T.B., and Wach, G.D. 2020. Analysis of factors influencing the interpretation of a digitally examined fluvial meanderbelt system: Joggins Formation, Nova Scotia. *Canadian Journal of Earth Sciences*, **57**: 524-541. doi:10.1139/cjes-2018-0263.

Kelly, T.B., Wach, G.D., and O'Connor, D.E. 2021a. The technical challenges and outcomes of ground-penetrating radar: A site-specific example from Joggins, Nova Scotia. *AIMS Geosciences*, **7**: 22-55. doi:10.3934/geosci.2021002.

Kelly, T.B., Angel, M.N., O'Connor, D.E., Huff, C.C., Morris, L.E., and Wach, G.D. 2021b. A novel approach to 3D modelling ground-penetrating radar (GPR) data—A case study of a cemetery and applications for criminal investigation. *Forensic science international*, **325**. doi:10.1016/j.forsciint.2021.110882.

Labrecque, P.A., Jensen, J.L., and Hubbard, S.M. 2011. Cyclicity in Lower Cretaceous point bar deposits with implications for reservoir characterization, Athabasca Oil Sands, Alberta, Canada. *Sedimentary Geology*, **242**: 18-33. doi:10.1016/j.sedgeo.2011.06.011.

Schultz, J.J., Grasmueck, M., Weger, R., Muztaza, N.M., Saidin, M.M., Azwin, I.N., Saad, R., Kofun, H., and Leucci, G. 2012. Detecting buried remains using ground penetrating radar. U.S. Department of Justice.

Smith, D.G., and Jol, H.M. 1992. Ground-penetrating radar investigation of a Lake Bonneville delta, Provo level, Brigham City, Utah. *Geology*, **20**: 1-4. doi:10.1130/0091.

SPE Research & Development Committee. 2012. Grand Challenges Facing the E&P Industry. Available from <https://www.spe.org/en/industry/globalchallenges/2022>].

van den Belt, F.J.G., van Hoof, T.B., and Pagnier, H.J.M. 2015. Revealing the hidden Milankovitch record from Pennsylvanian cyclothem successions and implications regarding late Paleozoic chronology and terrestrial-carbon (coal) storage. *Geosphere*, **11**: 1062-1076. doi:10.1130/ges01177.1.

Vandenberghe, J., and Van Overmeeren, R. 1999. Ground penetrating radar images of selected fluvial deposits in the Netherlands. *Sedimentary Geology*, **128**: 245-270. doi:10.1016/S0037-0738(99)00072-X.

Waltham, D. 2015. Milankovitch period uncertainties and their impact on cyclostratigraphy. *Journal of Sedimentary Research*, **85**: 990-998. doi:10.2110/jsr.2015.66.

References

- Alhumimidi, M.S., Alfarhan, M.S., Cline, J.R., and Aiken, C.L. 2017. Application of a 3D photorealistic model for the geological analysis of the Permian carbonates (Khuff Formation) in Saudi Arabia. *Arabian Journal of Geosciences*, **10**: 112. doi:10.1007/s12517-017-2874-7.
- Allen, J. 2016. Numerical Modeling of Salt Tectonics at Rifted Continental Margins. Department of Earth and Environmental Sciences, Dalhousie University, Halifax, Nova Scotia.
- Allen, J.P., Fielding, C.R., Rygel, M.C., and Gibling, M.R. 2013. Deconvolving Signals of Tectonic and Climatic Controls From Continental Basins: An Example From the Late Paleozoic Cumberland Basin, Atlantic Canada. *Journal of Sedimentary Research*, **83**: 847-872. doi:10.2110/jsr.2013.58.
- Allen, J.R.L. 1981. Lower Cretaceous tides revealed by cross-bedding with mud drapes. *Nature*, **289**: 579-581. doi:10.1038/289579a0.
- Allport, H.A., Davies, N.S., Shillito, A.P., Mitchell, E.G., and Herron, S.T. 2021. Non-palimpsested crowded Skolithos ichnofabrics in a Carboniferous tidal rhythmite: Disentangling ecological signatures from the spatio-temporal bias of outcrop. *Sedimentology*, **69**: 1-23. doi:10.1111/sed.12947.
- Anderson, R.Y. 1982. A long geoclimatic record from the Permian. *Journal of Geophysical Research*, **87**: 7285-7294. doi:10.1029/JC087iC09p07285.
- Andreas Prokoph, F.P.A. 2000. Wavelet analysis of well-logging data from oil source rock, Egret Member, offshore eastern Canada. *AAPG Bulletin*, **84**: 1617-1632. doi:10.1306/8626bf15-173b-11d7-8645000102c1865d.
- Annan, A.P. Practical Processing of GPR Data. *In* Second Government Workshop on Ground Penetrating Radar. 1999. Sensors and Software Inc., pp. 1-18.
- Annan, A.P. 2003. Ground Penetrating Radar Principles, Procedures & Applications. Sensors and Software Inc. pp. 1-286.

Annan, A.P. 2009. Electromagnetic Principles of Ground-Penetrating Radar Theory. *In* Ground Penetrating Radar Theory and Applications. *Edited by* H.M. Jol. Elsevier Science, Amsterdam, The Netherlands. pp. 3-40.

Antonellini, M., Cilona, A., Tondi, E., Zambrano, M., and Agosta, F. 2014. Fluid flow numerical experiments of faulted porous carbonates, Northwest Sicily (Italy). *Marine and Petroleum Geology*, **55**: 186-201. doi:10.1016/j.marpetgeo.2013.12.003.

Archer, A.W. 1991. Modeling of tidal rhythmites using modern tidal periodicities and implications for short-term sedimentation rates. *In* Sedimentary Modeling: Computer Simulations and Methods for Improved Parameter Definition (Bulletin 233). *Edited by* E.K. Franseen and W.L. Watney and C.G. Kendall and W. Ross. Kansas Geological Survey, Lawrence, Kansas. pp. 185-194.

Archer, A.W. 1996. Reliability of lunar orbital periods extracted from ancient cyclic tidal rhythmites. *Earth and Planetary Science Letters*, **141**: 1-10.

Archer, A.W., and Greb, S.F. 1995. An Amazon-Scale Drainage System in the Early Pennsylvanian of Central North America. *The Journal of Geology*, **103**: 611-627. doi:10.1086/629784.

Archer, A.W., Kuecher, G.J., and Kvale, E.P. 1995a. The Role of Tidal-Velocity Asymmetries in the Deposition of Silty Tidal Rhythmites (Carboniferous, Eastern Interior Coal Basin, U.S.A.). *Journal of Sedimentary Research*, **65**: 408-416. doi:10.1306/d42680d6-2b26-11d7-8648000102c1865d.

Archer, A.W., Calder, J.H., Gibling, M.R., Naylor, R.D., Reid, D.R., and Wightman, W.G. 1995b. Invertebrate trace fossils and agglutinated foraminifera as indicators of marine influence within the classic Carboniferous section at Joggins, Nova Scotia, Canada. *Canadian Journal of Earth Sciences*, **32**: 2027-2039. doi:10.1139/e95-156.

Arcone, S.A. 1996. High resolution of glacial ice stratigraphy: a ground-penetrating radar study of Pegasus Runway, McMurdo Station, Antarctica. *Geophysics*, **61**: 1653-1663. doi:10.1190/1.1444084.

Atekwana, E.A., Sauck, W.A., and Werkema Jr, D.D. 2000. Investigations of geoelectrical signatures at a hydrocarbon contaminated site. *Journal of Applied Geophysics*, **44**: 167-180. doi:10.1016/S0926-9851(98)00033-0.

Atlantic Geoscience Society. 2001. The last billion years: a geological history of the Maritime Provinces of Canada. No. 15. Nimbus Publishing Limited.

Atlas Obscura. 2020. Most Holy Trinity Cemetery, Brooklyn, New York: A burial ground of rusting metal grave markers. Available from <https://www.atlasobscura.com/places/most-holy-trinity-cemetery>.

Aziz, A.S., Stewart, R.R., Green, S.L., and Flores, J.B. 2016. Locating and characterizing burials using 3D ground-penetrating radar (GPR) and terrestrial laser scanning (TLS) at the historic Mueschke Cemetery, Houston, Texas. *Journal of Archaeological Science: Reports*, **8**: 392-405. doi:10.1016/j.jasrep.2016.06.035.

Baker, P.L. Fluid, lithology, geometry, and permeability information from ground-penetrating radar for some petroleum industry applications. *In* SPE Asia-Pacific Conference. Perth, Australia 1991. OnePetro.

Baldrige, A.M., Hook, S.J., Grove, C.I., and Rivera, G. 2009. The ASTER spectral library version 2.0. *Remote Sensing of Environment*, **113**: 711-715. doi:10.1016/j.rse.2008.11.007.

Barboza, E.G., Rosa, M.L.C.C., Dillenburg, S.R., da Silva, A.B., and Tomazelli, L.J. 2014. Stratigraphic analysis applied on the recognition of the interface between marine and fluvial depositional systems. *Journal of Coastal Research*, **70**: 687-692. doi:10.2112/SI70-116.1.

Barone, P.M., Di Maggio, R.M., and Ferrara, C. 2015. Not necessarily buried bodies: forensic GPR investigations from criminal to civil justice. *In* 8th International Workshop on Advanced Ground Penetrating Radar (IWAGPR). 2015. IEEE, pp. 1-4.

Bell, W.A. 1912. Joggins Carboniferous section of Nova Scotia. *In* Summary Report for 1911. Geological Survey of Canada. pp. 328-333.

Bellian, J.A., Kerans, C., and Jennette, D.C. 2005. Digital outcrop models: applications of terrestrial scanning lidar technology in stratigraphic modeling. *Journal of Sedimentary Research*, **75**: 166-176. doi:10.2110/jsr.2005.013.

Bellian, J.A., Beck, R., and Kerans, C. 2007. Analysis of hyperspectral and lidar data: Remote optical mineralogy and fracture identification. *Geosphere*, **3**: 491-500. doi:10.1130/GES00097.1.

Benedetto, A., Benedetto, F., and Tosti, F. 2012. GPR applications for geotechnical stability of transportation infrastructures. *Nondestructive Testing and Evaluation*, **27**: 253-262. doi:10.1080/10589759.2012.694884.

Beres Jr., M., and Haeni, F.P. 1991. Application of ground-penetrating-radar Methods in Hydrogeologic Studies. *Groundwater*, **29**: 375-386. doi:10.1111/j.1745-6584.1991.tb00528.x.

Berger, A. 1988. Milankovitch Theory and climate. *Reviews of Geophysics*, **26**: 624-657. doi:10.1029/RG026i004p00624.

Berger, A., Loutre, M.-F., and McIntyre, A. 1997. Intertropical latitudes and precessional and half-precessional cycles. *Science*, **278**: 1476-1478.

Berger, A., Loutre, M.F., and Mélice, J.L. 2006. Equatorial insolation: from precession harmonics to eccentricity frequencies. *Climate of the Past*, **2**: 131-136. doi:10.5194/cp-2-131-2006.

Berger, A., Loutre, M., De Boer, P., and Smith, D. 1994. Astronomical forcing through geological time. *In* *Orbital forcing and cyclic sequences*. Blackwell Scientific Publications Oxford. pp. 15-24.

Beumier, C. Vehicle Speed Estimation from Two Images for LIDAR Second Assessment. *In* *Proceedings of the International Conference on Computer Vision Theory and Applications (VISAPP-2012)*. Rome, Italy 2012. Vol. 1, pp. 381-386.

Bhattacharya, B., Bandyopadhyay, S., Mahapatra, S., and Banerjee, S. 2012. Record of tide-wave influence on the coal-bearing Permian Barakar Formation, Raniganj Basin, India. *Sedimentary Geology*, **267-268**: 25-35. doi:10.1016/j.sedgeo.2012.05.006.

Bier, J. 2018. Bodily circulation and the measure of a life: Forensic identification and valuation after the Titanic disaster. *Social Studies of Science*, **48**: 635-662. doi:10.1177/0306312718801173.

Billinger, M.S. 2009. Utilizing ground penetrating radar for the location of a potential human burial under concrete. *Canadian Society of Forensic Science Journal*, **42**: 200-209. doi:10.1080/00085030.2009.10757607.

Bingham-Koslowski, N., Grey, M., Pufahl, P., and Ehrman, J.M. 2018. Breaking down Late Carboniferous fish coprolites from the Joggins Formation. *In* 1st Joggins Research Symposium. Atlantic Geoscience Society, Joggins, Nova Scotia.

Blott, J.E., Davis, T.L., and Benson, R.D. 1999. Morrow sandstone reservoir characterization: A 3-D multicomponent seismic success. *The Leading Edge*, **18**: 394-397. doi:10.1190/1.1438305.

Boersma, J.R. 1969. Internal structure of some tidal mega-ripples on a shoal in the Westerschelde Estuary, the Netherlands: report of a preliminary investigation. *Netherlands Journal of Geosciences/Geologie en Mijnbouw*, **48**: 409-414.

Boersma, J.R., and Terwindt, J.H.J. 1981. Neap-spring tide sequences of intertidal shoal deposits in a mesotidal estuary. *Sedimentology*, **28**: 151-170. doi:10.1111/j.1365-3091.1981.tb01674.x.

Bond, G., Showers, W., Cheseby, M., Lotti, R., Almasi, P., deMenocal, P., Priore, P., Cullen, H., Hajdas, I., and Bonani, G. 1997. A Pervasive Millennial-Scale Cycle in North Atlantic Holocene and Glacial Climates. *Science*, **278**: 1257-1266. doi:10.1126/science.278.5341.1257.

Boro, H., Rosero, E., and Bertotti, G. 2014. Fracture-network analysis of the Latemar Platform (northern Italy): integrating outcrop studies to constrain the hydraulic properties of fractures in reservoir models. *Petroleum Geoscience*, **20**: 79-92. doi:10.1144/petgeo2013-007.

Botelho, M.A., and Mufti, I.R. 1998. Exploitation of limestone quarries in Brazil with depth migrated ground-penetrating radar data. *In* SEG Technical Program Expanded Abstracts 1998. Society of Exploration Geophysicists pp. 836-839.

Boulila, S., Galbrun, B., Hinnov, L.A., Collin, P.Y., Ogg, J.G., Fortwengler, D., and Marchand, D. 2010. Milankovitch and sub-Milankovitch forcing of the Oxfordian (Late Jurassic) Terres Noires Formation (SE France) and global implications. *Basin Research*, **22**: 717-732. doi:10.1111/j.1365-2117.2009.00429.x.

Brand, U. 1994. Continental hydrology and climatology of the Carboniferous Joggins Formation (lower Cumberland Group) at Joggins, Nova Scotia: evidence from the geochemistry of bivalves. *Palaeogeography, Palaeoclimatology, Palaeoecology*, **106**: 307-321. doi:10.1016/0031-0182(94)90016-7.

Brauer, A., Mangili, C., Moscariello, A., and Witt, A. 2008. Palaeoclimatic implications from micro-facies data of a 5900 varve time series from the Piànico interglacial sediment record, southern Alps. *Palaeogeography, Palaeoclimatology, Palaeoecology*, **259**: 121-135. doi:10.1016/j.palaeo.2007.10.003.

Brettell, M.J., McIlroy, D., Elliott, T., Davies, S.J., and Waters, C.N. 2002. Identifying cryptic tidal influences within deltaic successions: an example from the Marsdenian (Namurian) interval of the Pennine Basin, UK. *Journal of the Geological Society*, **159**: 379-391. doi:10.1144/0016-764901-070.

Breuning-Madsen, H., Holst, M.K., and Rasmussen, M. 2001. The chemical environment in a burial mound shortly after construction—an archaeological–pedological experiment. *Journal of Archaeological Science*, **28**: 691-697. doi:10.1006/jasc.1999.0570.

Bridge, J.S., Alexander, J., Collier, R.E.L., Gawthorpe, R.L., and Jarvis, J. 1995. Ground-penetrating radar and coring used to study the large-scale structure of point-bar deposits in three dimensions. *Sedimentology*, **42**: 839-852. doi:10.1111/j.1365-3091.1995.tb00413.x.

Brown, S., and Smith, M. 2013. A transient-flow syringe air permeameter. *Geophysics*, **78**: 307-313.

Browne, G.H., and Plint, G.A. 1994. Alternating braidplain and lacustrine deposition in a strike-slip setting: The Pennsylvanian Boss Point Formation of the Cumberland Basin, Maritime Canada. *Journal of Sedimentary Research*, **64**: 40-59. doi:10.1318/94/0B64-40/\$03.0.

Bryant, I.D., and Flint, S.S. 1993. The geological modelling of hydrocarbon reservoirs and outcrop analogues. *In* The geological modelling of hydrocarbon reservoirs and outcrop analogues. *Edited by* S.S. Flint and I.D. Bryant. Blackwell Scientific Publications, Oxford, UK. pp. 3-20.

Buckley, S.J., Howell, J.A., Enge, H.D., and Kurz, T.H. 2008. Terrestrial laser scanning in geology: data acquisition, processing and accuracy considerations. *Journal of the Geological Society*, **165**: 625-638. doi:10.1144/0016-76492007-100.

Buckley, S.J., Enge, H.D., Carlsson, C., and Howell, J.A. 2010. Terrestrial laser scanning for use in virtual outcrop geology. *The Photogrammetric Record*, **25**: 225-239. doi:10.1111/j.1477-9730.2010.00585.x.

Buhler, P.B., and Grey, M. 2017. Xiphosuran digging traces at the Late Carboniferous Joggins Fossil Cliffs UNESCO World Heritage Site, Nova Scotia, Canada. *Ichnos*, **24**: 179-190. doi:10.1080/10420940.2016.1244055.

Burgess, P.M. 2001. Modeling carbonate sequence development without relative sea-level oscillations. *Geology*, **29**: 1127-1130. doi:10.1130/0091-7613(2001)029<1127: Mcdwr>2.0.Co;2.

Burton, D., Dunlap, D.B., Wood, L.J., and Flaig, P.P. 2011. Lidar Intensity as a Remote Sensor of Rock Properties. *Journal of Sedimentary Research*, **81**: 339-347. doi:10.2110/jsr.2011.31.

Butnor, J.R., Doolittle, J., Johnsen, K.H., Samuelson, L., Stokes, T., and Kress, L. 2003. Utility of ground-penetrating radar as a root biomass survey tool in forest systems. *Soil Science Society of America Journal*, **67**: 1607-1615. doi:10.2136/sssaj2003.1607.

Calder, J.H. 1994. The impact of climate change, tectonism and hydrology on the formation of Carboniferous tropical intermontane mires: the Springhill coalfield, Cumberland Basin, Nova Scotia. *Palaeogeography, Palaeoclimatology, Palaeoecology*, **106**: 323-351. doi:10.1016/0031-0182(94)90017-5.

Calder, J.H. 1998. The Carboniferous evolution of Nova Scotia. Geological Society, London, Special Publications, **143**: 261-302. doi:10.1144/gsl.Sp.1998.143.01.19.

Calder, J.H. 2017. The Joggins fossil cliffs: coal age Galápagos. Formac Publishing Company.

Calder, J.H., and Boon, J. 2007. Joggins Fossil Cliffs: Property Nominated for Inscription on the World Heritage List. Nova Scotia Department of Natural Resources, Mineral Resources Branch, Halifax, NS. pp. Open File Map ME 2007-2001.

Calder, J.H., Rygel, M.C., Ryan, R.J., Falcon-Lang, H.J., and Herbert, B.L. 2005. Stratigraphy and sedimentology of early Pennsylvanian red beds at Lower Cove, Nova Scotia, Canada: the Little River Formation with redefinition of the Joggins Formation. *Atlantic Geology*, **41**: 87-102. doi:10.4138/183.

Calder, J.H., Gibling, M.R., Scott, A.C., Davies, S.J., Herbert, B.L., Greb, S.F., and DiMichele, W.A. 2006. A fossil lycopsid forest succession in the classic Joggins section of Nova Scotia: paleoecology of a disturbance-prone Pennsylvanian wetland. *Special Papers - Geological Society of America*, **399**: 169. doi:10.1130/2006.2399(09).

Campbell, D.C. 2011. The Late Cretaceous and Cenozoic Geological History of the Outer Continental Margin off Nova Scotia, Canada: Insights into Margin Evolution from a Mature Passive Margin. Earth and Environmental Sciences, Dalhousie University, Halifax, Nova Scotia.

Cann, D.B., Hilchey, J.D., and Smith, G.R. 1954. Nova Scotia Soil Survey: Soil Survey of Hants County, Nova Scotia. Nova Scotia Department of Agriculture, Truro, Nova Scotia.

Carpenter, D.K., Falcon-Lang, H.J., Benton, M.J., and Grey, M. 2015. Early Pennsylvanian (Langsettian) fish assemblages from the Joggins Formation, Canada, and their implications for palaeoecology and palaeogeography. *Palaeontology*, **58**: 661-690. doi:10.5061/dryad.b0551.

Carroll, R.L. 1967. Labyrinthodonts from the Joggins Formation. *Journal of Paleontology*, **41**: 111-142.

Casini, G., Hunt, D.W., Monsen, E., and Bounaim, A. 2016. Fracture characterization and modeling from virtual outcrops. *AAPG Bulletin*, **100**: 41-61. doi:10.1306/09141514228.

Chan, M.A., Kvale, E.P., Archer, A.W., and Sonett, C.P. 1994. Oldest direct evidence of lunar-solar tidal forcing encoded in sedimentary rhythmites, Proterozoic Big Cottonwood Formation, central Utah. *Geology*, **22**: 791-794. doi:10.1130/0091-7613(1994)022<0791:Odeols>2.3.Co;2.

Chesnel, V., Merino-Tomé, Ó., Fernández, L.P., Villa, E., and Samankassou, E. 2016. Isotopic fingerprints of Milankovitch cycles in Pennsylvanian carbonate platform-top deposits: the Valdorria record, Northern Spain. *Terra Nova*, **28**: 364-373. doi:10.1111/ter.12229.

Chipman, M., Grey, M., and Pufahl, P.K. 2020. Coprolites from a brackish ecosystem in the Pennsylvanian Joggins Formation, Nova Scotia, Canada and their palaeoecological implications. *Palaeogeography, Palaeoclimatology, Palaeoecology*, **538**. doi:10.1016/j.palaeo.2019.109407.

Choi, K.S., and Park, Y.A. 2000. Late Pleistocene silty tidal rhythmites in the macrotidal flat between Youngjong and Yongyou Islands, west coast of Korea. *Marine Geology*, **167**: 231-241. doi:10.1016/s0025-3227(00)00037-2.

Choi, K.S., and Kim, D.H. 2016. Morphologic and hydrodynamic controls on the occurrence of tidal bundles in an open-coast macrotidal environment, northern Gyeonggi Bay, west coast of Korea. *Sedimentary Geology*, **339**: 68-82. doi:10.1016/j.sedgeo.2016.04.008.

Clement, W.P., Barrash, W., and Knoll, M.D. 2006. Reflectivity modeling of a ground-penetrating-radar profile of a saturated fluvial formation. *Geophysics*, **71**: 59-66. doi:10.1190/1.2194528.

Cooper, P. Milankovitch cycles from Fourier analysis of logs from Sites 865 and 866: Northwest Pacific atolls and guyots. *In Proceedings of the Ocean Drilling Program. Scientific results*. 1995. Vol. 142, pp. 317-327.

Copeland, M.J. 1959. Coalfields west half Cumberland County, Nova Scotia. Geological Survey of Canada Memoir 298. p. 89.

Costandi, M. 2015. Life after death: The science of human decomposition. Available from <https://www.theguardian.com/science/neurophilosophy/2015/may/05/life-after-death>.

Coughenour, C.L., Archer, A.W., and Lacovara, K.J. 2013. Calculating Earth–Moon system parameters from sub-yearly tidal deposit records: An example from the carboniferous tradewater formation. *Sedimentary Geology*, **295**: 67-76. doi:10.1016/j.sedgeo.2013.08.001.

Croll, J. 1890. *Climate and time in their geological relations: a theory of secular changes of the Earth's climate*. Appleton.

Dafoe, L.T., Stimson, M.R., and Gibling, M.R. Terrestrial to marine transitions recorded in invertebrate trace fossils of the Joggins Formation. *In 1st Joggins Research Symposium*. Joggins, Nova Scotia 2018. *Atlantic Geology*. Vol. 54.

Dalrymple, R.W., Makino, Y., and Zaitlin, B.A. 1991. Temporal and spatial patterns of rhythmite deposition on mud flats in the macrotidal Cobequid Bay-Salmon River Estuary, Bay of Fundy, Canada. *In Clastic Tidal Sedimentology - Memoir 16. Edited by D.G. Smith and G.E. Reinson and B.A. Zaitlin and R.A. Rahmani*. Canadian Society of Petroleum Geologists, Calgary, Alberta. pp. 137-160.

Daniels, J.J., Roberts, R., and Vendl, M. 1992. Site studies of ground penetrating radar for monitoring petroleum product contaminants. *In* Symposium on the Application of Geophysics to Engineering and Environmental Problems. 1992. Society of Exploration Geophysicists, pp. 597-609.

Davies, D., Williams, B., and Vessell, R. 1992. Models for meandering and braided fluvial reservoirs with examples from the Travis Peak Formation, East Texas. *In* SPE Annual Technical Conference and Exhibition. Society of Petroleum Engineers.

Davies, S.J., and Gibling, M.R. 2003. Architecture of coastal and alluvial deposits in an extensional basin: the Carboniferous Joggins Formation of eastern Canada. *Sedimentology*, **50**: 415-439. doi:10.1046/j.1365-3091.2003.00553.x

Davies, S.J., Gibling, M.R., Rygel, M.C., Calder, J.H., and Skilliter, D.M. 2005. The Pennsylvanian Joggins Formation of Nova Scotia: sedimentological log and stratigraphic framework of the historic fossil cliffs. *Atlantic Geology*, **41**: 87-102. doi:10.4138/182.

Dawson, J.W. 1854. On the coal-measures of the South Joggins, Nova Scotia. *Quarterly Journal of the Geological Society*, **10**: 1-42.

De Boer, P.L., Oost, A.P., and Visser, M.J. 1989. The Diurnal Inequality of the Tide as a Parameter for Recognizing Tidal Influences. *Journal of Sedimentary Research*, **59**: 912-921. doi:10.1306/212f90b1-2b24-11d7-8648000102c1865d.

De Boever, W., Bultreys, T., Derluyn, H., Van Hoorebeke, L., and Cnudde, V. 2016. Comparison between traditional laboratory tests, permeability measurements and CT-based fluid flow modelling for cultural heritage applications. *Sci Total Environ*, **554-555**: 102-112. doi:10.1016/j.scitotenv.2016.02.195.

De Pascale, G.P., Pollard, W.H., and Williams, K.K. 2008. Geophysical mapping of ground ice using a combination of capacitive coupled resistivity and ground-penetrating radar, Northwest Territories, Canada. *Journal of Geophysical Research: Earth Surface*, **113**. doi:10.1029/2006JF000585.

Del Sole, L., Antonellini, M., and Calafato, A. 2020. Characterization of sub-seismic resolution structural diagenetic heterogeneities in porous sandstones: Combining ground-penetrating radar profiles with geomechanical and petrophysical in situ measurements (Northern Apennines, Italy). *Marine and Petroleum Geology*, **117**: 1-22. doi:10.1016/j.marpetgeo.2020.104375.

del Strother, P., Gize, A., Hollis, C., and McLean, D. 2021. Bituminous coals on emergent surfaces in an Asbian, lower Carboniferous (Mississippian) limestone succession on the North Wales carbonate platform, UK, and implications for palaeoclimate. *Proceedings of the Yorkshire Geological Society*, **63**: 22. doi:10.1144/pygs2020-006.

Di Prima, S., Winiarski, T., Angulo-Jaramillo, R., Stewart, R.D., Castellini, M., Abou Najm, M.R., Ventrella, D., Pirastru, M., Giadrossich, F., and Capello, G. 2020. Detecting infiltrated water and preferential flow pathways through time-lapse ground-penetrating radar surveys. *Science of The Total Environment*: 138511. doi:10.1016/j.scitotenv.2020.138511.

Dillenburg, S.R., Barboza, E.G., Rosa, M.L.C., Caron, F., and Sawakuchi, A.O. 2017. The complex prograded Cassino barrier in southern Brazil: Geological and morphological evolution and records of climatic, oceanographic and sea-level changes in the last 7–6 ka. *Marine Geology*, **390**: 106-119. doi:10.1016/j.margeo.2017.06.007.

Dillenburg, S.R., Hesp, P.A., Keane, R., da Silva, G.M., Sawakuchi, A.O., Moffat, I., Barboza, E.G., and Bitencourt, V.J. 2020. Geochronology and evolution of a complex barrier, Younghusband Peninsula, South Australia. *Geomorphology*, **354**: 1-13. doi: 10.1016/j.geomorph.2020.107044.

DiMichele, W.A., and Falcon-Lang, H.J. 2011. Pennsylvanian 'fossil forests' in growth position (T0 assemblages): origin, taphonomic bias and palaeoecological insights. *Journal of the Geological Society*, **168**: 585-605. doi:10.1144/0016-76492010-103.

Dojack, L. 2012. *Ground Penetrating Radar Theory, Data Collection, Processing, and Interpretation: A Guide for Archaeologist*. University of British Columbia, Laboratory of Archaeology, University of British Columbia.

Donnelly, L.J. 2002. How forensic geology helps solve crime. Record of presentation on Forensic Geology and the Moors Murders to the House of commons, Westminster Palace, on 12th March.

Donnelly, L.J. 2012. Use of geology in forensic science: Search to locate burials. *Encyclopaedia of Quaternary Science*. Elsevier.

Donnelly, L.J. 2013. The Applications of Forensic Geology & Geophysics for Police and Law Enforcement Ground Searches. *In* Second EAGE International Conference on Engineering Geophysics. 2013. European Association of Geoscientists & Engineers, pp. cp-368-00049.

Donnelly, L.J., and Harrison, M. 2010. Development of geoforensic strategy & methodology to search the ground for an unmarked burial or concealed object. Emergency Global Barclay media Limited: 30-35.

Donnelly, L.J., and Harrison, M. 2015. A collaborative methodology for ground searches by a forensic geologist and law enforcement (police) officer: detecting evidence related to homicide, terrorism and organized crime. *In* International Conference on Engineering Geophysics, Al Ain, United Arab Emirates. 2015. Society of Exploration Geophysicists, pp. 88-95.

Donnelly, L.J., and Harrison, M. 2017. Ground searches for graves and buried targets related to homicide, terrorism and organised crime. *Journal of International Geoscience*, **40**: 106-117. doi:10.18814/epiiugs/2017/v40i2/017012.

Donselaar, M.E., and Geel, C.R. 2016. Facies architecture of heterolithic tidal deposits: the Holocene Holland Tidal Basin. *Netherlands Journal of Geosciences - Geologie en Mijnbouw*, **86**: 389-402. doi:10.1017/s001677460002360x.

Doolittle, J.A., and Bellantoni, N.F. 2010. The search for graves with ground-penetrating radar in Connecticut. *Journal of Archaeological Science*, **37**: 941-949. doi:10.1016/j.jas.2009.11.027.

Doughty, C. 2015. Morbid minute: Coffins vs. caskets. Available from <https://www.youtube.com/watch?v=nUaqKZnClGQ>.

Doughty, C. 2018. Adipocere aka grave wax. Available from <https://www.youtube.com/watch?v=gi0Gi0sqXwg>.

Doughty, C. 2019. We recreated a Victorian funeral. Available from <https://www.youtube.com/watch?v=0OIF-EtoGBo>.

Doyle, P., and Bennett, M.R. 1998. *Unlocking the Stratigraphical Record: Advances in Modern Stratigraphy*. Wiley, University of California.

Dreyer, T. 1992. Significance of tidal cyclicity for modelling of reservoir heterogeneities in the lower Jurassic Tilje Formation, mid-Norwegian shelf. *Norsk Geologisk Tidsskrift*, **72**: 159-170.

Ékes, C., and Friele, P. 2003. Sedimentary architecture and post-glacial evolution of Cheekye fan, southwestern British Columbia, Canada. Geological Society, London, Special Publications, **211**: 87-98. doi:10.1144/gsl.Sp.2001.211.01.08.

Elrick, M., and Hinnov, L.A. 2007. Millennial-scale paleoclimate cycles recorded in widespread Palaeozoic deeper water rhythmites of North America. Palaeogeography, Palaeoclimatology, Palaeoecology, **243**: 348-372. doi:10.1016/j.palaeo.2006.08.008.

Enge, H.v.D., Buckley, S.J., Rotevatn, A., and Howell, J.A. 2007. From outcrop to reservoir simulation model: Workflow and procedures. Geosphere, **3**: 469-490. doi: 10.1130/GES00099.1.

Environment Canada. 2020. Daily Data Report for July 2019: Halifax Stanfield International Airport. Available from https://climate.weather.gc.ca/climate_data/daily_data_e.html?StationID=50620&timeframe=2&StartYear=1840&EndYear=2020&Day=5&Year=2019&Month=7.

Eriksson, K.A., and Simpson, E.L. 2000. Quantifying the oldest tidal record: The 3.2 Ga Moodies Group, Barberton Greenstone Belt, South Africa. Geology, **28**: 831-834. doi:10.1130/0091-7613(2000)28<831:Qtotr>2.0.Co;2.

Eriksson, K.A., and Simpson, E.L. 2004. Precambrian Tidalites: Recognition and Significance. *In* The Precambrian Earth: Tempos and Events. *Edited by* P.G. Eriksson and W. Altermann and D.R. Nelson and W.U. Mueller and O. Catuneanu. Elsevier Science, The Netherlands. pp. 631-642.

Exploranium - Radiation Detection Systems. 2001. GR-130 MiniSPEC User Manual (Revision 15.1).

Fabuel-Perez, I., Hodgetts, D., and Redfern, J. 2009a. A new approach for outcrop characterization and geostatistical analysis of a low-sinuosity fluvial-dominated succession using digital outcrop models: Upper Triassic Oukaimeden Sandstone Formation, central High Atlas, Morocco. AAPG Bulletin, **93**: 795-827. doi:10.1306/02230908102.

Fabuel-Perez, I., Redfern, J., and Hodgetts, D. 2009b. Sedimentology of an intra-montane rift-controlled fluvial dominated succession: The Upper Triassic Oukaimeden Sandstone Formation, Central High Atlas, Morocco. Sedimentary Geology, **218**: 103-140. doi: 10.1016/j.sedgeo.2009.04.006.

Fabuel-Perez, I., Hodgetts, D., and Redfern, J. 2010. Integration of digital outcrop models (DOMs) and high resolution sedimentology-workflow and implications for geological modelling: Oukaimeden Sandstone Formation, High Atlas (Morocco). *Petroleum Geoscience*, **16**: 133-154. doi:10.1144/1354-079309-820.

Falcon-Lang, H.J. 2005. Small cordaitalean trees in a marine-influenced coastal habitat in the Pennsylvanian Joggins Formation, Nova Scotia. *Journal of the Geological Society*, **162**: 485-500. doi:10.1144/0016-764904-080.

Falcon-Lang, H.J. 2006. A history of research at the Joggins Fossil Cliffs of Nova Scotia, Canada, the world's finest Pennsylvanian section. *Proceedings of the Geologists' Association*, **117**: 377-392. doi:10.1016/S0016-7878(06)80044-1.

Falcon-Lang, H.J. 2009. Earliest history of coal mining and grindstone quarrying at Joggins, Nova Scotia, and its implications for the meaning of the place name "Joggins". *Atlantic Geology*, **45**: 1-20. doi:10.4138/atlgeol.2009.001.

Falcon-Lang, H.J., Rygel, M.C., Calder, J.H., and Gibling, M.R. 2004. An early Pennsylvanian waterhole deposit and its fossil biota in a dryland alluvial plain setting, Joggins, Nova Scotia. *Journal of the Geological Society*, **161**: 209-222. doi:10.1144/0016-764903-109.

Falcon-Lang, H.J., Benton, M.J., Braddy, S.J., and Davies, S.J. 2006. The Pennsylvanian tropical biome reconstructed from the Joggins Formation of Nova Scotia, Canada. *Journal of the Geological Society*, **163**: 561-576. doi:10.1144/0016-764905-063.

Fang, Q., Wu, H., Wang, X., Yang, T., Li, H., and Zhang, S. 2018. Astronomical cycles in the Serpukhovian-Moscovian (Carboniferous) marine sequence, South China and their implications for geochronology and icehouse dynamics. *Journal of Asian Earth Sciences*, **156**: 302-315. doi:10.1016/j.jseaes.2018.02.001.

Faulkner, S.J., Stimson, M.R., Calder, J.H., and Lucas, S.G. 2017. The first unambiguous pterygote ichnofossil from the Joggins Fossil Cliffs, UNESCO World Heritage Site, Joggins, Nova Scotia, Canada.

Feldman, H.R., Archer, A.W., Kvale, E.P., Cunningham, C.R., Maples, C.G., and West, R.R. 1993. A Tidal Model of Carboniferous Konservat-Lagerstätten Formation. *Palaios*, **8**: 485-498. doi:10.2307/3515022.

Fernández-Álvarez, J.-P., Rubio-Melendi, D., Martínez-Velasco, A., Pringle, J.K., and Aguilera, H.-D. 2016. Discovery of a mass grave from the Spanish Civil War using Ground Penetrating Radar and forensic archaeology. *Forensic science international*, **267**: 10-17. doi:10.1016/j.forsciint.2016.05.040.

Fernández-Álvarez, J.-P., Rubio-Melendi, D., Castillo, J.A.Q., González-Quirós, A., and Cimadevilla-Fuente, D. 2017. Combined GPR and ERT exploratory geophysical survey of the Medieval Village of Pancorbo Castle (Burgos, Spain). *Journal of Applied Geophysics*, **144**: 86-93. doi:10.1016/j.jappgeo.2017.07.002.

Fiedler, S., Schneckenberger, K., and Graw, M. 2004. Characterization of soils containing adipocere. *Archives of environmental contamination and toxicology*, **47**: 561-568. doi:10.1007/s00244-004-3237-4.

Fiedler, S., Illich, B., Berger, J., and Graw, M. 2009. The effectiveness of ground-penetrating radar surveys in the location of unmarked burial sites in modern cemeteries. *Journal of Applied Geophysics*, **68**: 380-385. doi:10.1016/j.jappgeo.2009.03.003.

Filomena, C.M., Hornung, J., and Stollhofen, H. 2014. Assessing accuracy of gas-driven permeability measurements: a comparative study of diverse Hassler-cell and probe permeameter devices. *Solid Earth*, **5**: 1-11. doi:10.5194/se-5-1-2014.

Fischer, A.G. 1995. Cyclostratigraphy, Quo Vadis? *In* *Orbital Forcing Timescales and Cyclostratigraphy*. Edited by M.R. House and A.S. Gale. The Geological Society, London, UK. pp. 199-204.

Fossen, H. 2010. Deformation bands formed during soft-sediment deformation: Observations from SE Utah. *Marine and Petroleum Geology*, **27**: 215-222. doi:10.1016/j.marpetgeo.2009.06.005.

Fossen, H., Schultz, R.A., and Torabi, A. 2011. Conditions and implications for compaction band formation in the Navajo Sandstone, Utah. *Journal of Structural Geology*, **33**: 1477-1490. doi:10.1016/j.jsg.2011.08.001.

Friedman, G.M., and Chakraborty, C. 2006. Interpretation of tidal bundles: Two reasons for a paradigm shift. *Carbonates and Evaporites*, **21**: 170-175. doi:10.1007/bf03175666.

Funeral Guide. 2016. What is embalming? A guide to the embalming process. Available from <https://www.funeralguide.co.uk/help-resources/arranging-a-funeral/funeral-guides/what-is-embalming>.

Gale, A.S. 1998. Cyclostratigraphy. *In* Unlocking the stratigraphical record: advances in modern stratigraphy. *Edited by* P. Doyle and M.R. Bennett. Wiley Chichester, UK.

Gawthorpe, R.L., Li Collier, R.E., Alexander, J., Bridge, J.S., and Leeder, M.R. 1993. Ground penetrating radar: application to sandbody geometry and heterogeneity studies. Geological Society, London, Special Publications, **73**: 421-432. doi:10.1144/GSL.SP.1993.073.01.24.

Gebhardt, U., and Hiete, M. 2013. Continental Upper Carboniferous red beds in the Variscan intermontane Saale Basin, central Germany: orbital forcing detected by wavelet analysis. Geological Society, London, Special Publications, **376**: 177-199. doi: 10.1144/sp376.12.

Geel, C.R., and Donselaar, M.E. 2007. Reservoir modelling of heterolithic tidal deposits: sensitivity analysis of an object-based stochastic model. Netherlands Journal of Geosciences, **86**: 403-411.

Gent, V.A., and Sonnenberg, S.A. Fourier Analysis of the Laminated Facies of the Middle Bakken Member, Sanish-Parshall Field, Mountrail County, North Dakota. *In* AAPG Rocky Mountain Section Meeting. Denver, CO 2014. AAPG.

Ghosh, R. 1987. The variation in thickness and composition of coal seams and its use in interpretation of palaeocurrents—A case study from the Raniganj Coalfield, West Bengal, India. International Journal of Coal Geology, **9**: 209-220. doi:10.1016/0166-5162(87)90046-2.

Ghosh, S.K., Chakraborty, C., and Chakraborty, T. 2004. Combined tide and wave influence on sedimentation of Lower Gondwana coal measures of central India: Barakar Formation (Permian), Satpura basin. Journal of the Geological Society, **161**: 117-131. doi: 10.1144/0016-764902-077.

Giannopoulos, A. 2005. Modelling ground penetrating radar by GprMax. Construction and Building Materials, **19**: 755-762. doi:10.1016/j.conbuildmat.2005.06.007.

Gibling, M., Rygel, M., Fielding, C., Frank, T., and Isbell, J. 2008a. Late Paleozoic cyclic strata of Euramerica: Recognition of Gondwanan glacial signatures during periods of thermal subsidence. Resolving the Late Paleozoic Ice Age in Time and Space: Geological Society of America Special Publication, **441**: 219-233. doi:10.1130/2008.2441(15).

Gibling, M.R. 2006. Width and Thickness of Fluvial Channel Bodies and Valley Fills in the Geological Record: A Literature Compilation and Classification. *Journal of Sedimentary Research*, **76**: 731-770. doi:10.2110/jsr.2006.060.

Gibling, M.R., and Kalkreuth, W.D. 1991. Petrology of selected carbonaceous limestones and shales in Late Carboniferous coal basins of Atlantic Canada. *International Journal of Coal Geology*, **17**: 239-271. doi:10.1016/0166-5162(91)90034-G.

Gibling, M.R., Culshaw, N., Rygel, M.C., and Pascucci, V. 2008b. The Maritimes Basin of Atlantic Canada: Basin Creation and Destruction in the Collisional Zone of Pangea. *In Sedimentary basins of the world. Edited by A.D. Miall. Elsevier, Amsterdam.* pp. 211-244.

Gibling, M.R., Culshaw, N., Rygel, M.C., and Pascucci, V. 2008c. Chapter 6 The Maritimes Basin of Atlantic Canada: Basin Creation and Destruction in the Collisional Zone of Pangea. *In The Sedimentary Basins of the United States and Canada. Elsevier.* pp. 211-244.

Gibling, M.R., Calder, J.H., Ryan, R., Poll, H.W.v.d., and Yeo, G.M. 1992. Late Carboniferous and Early Permian drainage patterns in Atlantic Canada. *Canadian Journal of Earth Sciences*, **29**: 338-352. doi:10.1139/e92-030.

Gilbert, G.K. 1895. Sedimentary measurement of Cretaceous time. *The Journal of Geology*, **3**: 121-127. doi:10.1086/607150.

Godfrey, S., Holmes, R.B., and Laurin, M. 1991. Articulated remains of a Pennsylvanian Embolomere (Amphibia: Anthracosauria) from Joggins, Nova Scotia. *Journal of Vertebrate Paleontology*, **11**: 213-219.

Google. 2013. Streetview. Google Inc.

Google. 2020. Google Earth Satellite Image. Google.

Google Maps. 2020. Google basemap of Joggins Area. Google.

Goupillaud, P., Grossmann, A., and Morlet, J. 1984. Cycle-octave and related transforms in seismic signal analysis. *Geoexploration*, **23**: 85-102. doi:10.1016/0016-7142(84)90025-5.

Grammer, G.M., Harris, P.M.M., and Eberli, G.P. 2004. Integration of outcrop and modern analogs in reservoir modeling: overview with examples from the Bahamas. *In* Integration of Outcrop and Modern Analogs in Reservoir Modeling - AAPG Memoir 80. The American Association of Petroleum Geologists, Houston, Texas. pp. 1-22.

Grasshoff, K. 1975. The hydrochemistry of landlocked basins and fjords. *Chemical oceanography*, **2**: 455-597.

Grechishnikova, A. 2016. Integrated application of a high-resolution LIDAR outcrop survey of an unconventional Niobrara Reservoir, Denver Basin, Colorado. *First Break*, **34**: 65-71. doi:10.3997/1365-2397.34.5.84449.

Grey, M., and Finkel, Z.V. 2011. The Joggins Fossil Cliffs UNESCO World Heritage site: a review of recent research. *Atlantic Geology*, **47**: 185-200. doi:10.4138/atlgeol.2011.009.

Grey, M., Pufahl, P.K., and Aziz, A.A. 2011. Using Multiple Environmental Proxies to Determine Degree of Marine Influence and Paleogeographical Position of the Joggins Fossil Cliffs, Unesco World Heritage Site. *Palaios*, **26**: 256-263. doi:10.2110/palo.2010.p10-118r.

Griggs, M., and Ludwig, C.B. 1978. Legal aspects of remote sensing and air enforcement. *Journal of the Air Pollution Control Association*, **28**: 119-122. doi:10.1080/00022470.1978.10470578.

Habib, A., Jarvis, A., Kersting, A., and Alghamdi, Y. Comparative analysis of georeferencing procedures using various sources of control data. *In* 21st ISPRS Proceedings. Beijing, China 2008. *Edited by* J. Chen and J. Jiang and S. Nayak. International Society for Photogrammetry and Remote Sensing. Vol. XXXVII, pp. 1147-1152.

Haffen, S., Geraud, Y., Diraison, M., and Dezayes, C. 2013. Determination of fluid-flow zones in a geothermal sandstone reservoir using thermal conductivity and temperature logs. *Geothermics*, **46**: 32-41. doi:10.1016/j.geothermics.2012.11.001.

Hamzah, U., Samsudin, A.R., and Ismail, M.A. 2009. Geoelectrical resistivity and ground penetrating radar techniques in the study of hydrocarbon-contaminated soil. *Sains Malaysiana*, **38**: 305-311.

Hartzell, P., Glennie, C., Biber, K., and Khan, S. 2014. Application of multispectral LiDAR to automated virtual outcrop geology. *ISPRS Journal of Photogrammetry and Remote Sensing*, **88**: 147-155. doi:10.1016/j.isprsjprs.2013.12.004.

Hastings, J.O. 1990. Coarse-grained meander-belt reservoirs, Rocky Ridge field, North Dakota. *In Sandstone Petroleum Reservoirs*. Springer. pp. 57-84.

Haszeldine, R.S. 2009. Carboniferous North Atlantic palaeogeography: stratigraphic evidence for rifting, not megashear or subduction. *Geological Magazine*, **121**: 443-463. doi:10.1017/s0016756800029988.

Hays, J.D., Imbrie, J., and Shackleton, N.J. 1976. Variations in the Earth's Orbit: Pacemaker of the Ice Ages. *Science*, **194**: 1121-1132. doi:10.1126/science.194.4270.1121.

Hebert, B.L., and Calder, J.H. 2004. On the discovery of a unique terrestrial faunal assemblage in the classic Pennsylvanian section at Joggins, Nova Scotia. *Canadian Journal of Earth Sciences*, **41**: 247-254. doi:10.1139/e03-096.

Heteren, S.V., Fitzgerald, D.M., Mckinlay, P.A., and Buynevich, I.V. 1998. Radar facies of paraglacial barrier systems: coastal New England, USA. *Sedimentology*, **45**: 181-200. doi:10.1046/j.1365-3091.1998.00150.x.

Hinnov, L.A. 2013. Cyclostratigraphy and its revolutionizing applications in the earth and planetary sciences. *Geological Society of America Bulletin*, **125**: 1703-1734. doi:10.1130/B30934.1.

Ho, K., and Gader, P.D. 2002. A linear prediction land mine detection algorithm for hand held ground penetrating radar. *IEEE Transactions on Geoscience and Remote Sensing*, **40**: 1374-1384. doi:10.1109/TGRS.2002.800276.

Hodgetts, D. 2013. Laser scanning and digital outcrop geology in the petroleum industry: a review. *Marine and Petroleum Geology*, **46**: 335-354. doi:10.1016/j.marpetgeo.2013.02.014.

Holmes, R.B., and Carroll, R.L. 2010. An articulated embolomere skeleton (Amphibia: Anthracosauria) from the Lower Pennsylvanian (Bashkirian) of Nova Scotia. *Canadian Journal of Earth Sciences*, **47**: 209-219. doi:10.1139/E10-008.

Holmes, R.B., Carroll, R.L., and Reisz, R.R. 1998. The first articulated skeleton of *Dendrerpeton acadianum* (Temnospondyli, Dendrerpetontidae) from the Lower Pennsylvanian locality of Joggins, Nova Scotia, and a review of its relationships. *Journal of Vertebrate Paleontology*, **18**: 64-79. doi:10.1080/02724634.1998.10011034.

Horne, J.H., and Baliunas, S.L. 1986. A prescription for period analysis of unevenly sampled time series. *The Astrophysical Journal*, **302**: 757-763. doi:10.1086/164037

Howell, J.A., Martinius, A.W., and Good, T.R. 2014. The application of outcrop analogues in geological modelling: a review, present status and future outlook. Geological Society, London, Special Publications, **387**: 1-25. doi:10.1144/SP387.12.

Hower, J.C., Calder, J.H., Eble, C.F., Scott, A.C., Robertson, J.D., and Blanchard, L.J. 2000. Metalliferous coals of the Westphalian A Joggins Formation, Cumberland Basin, Nova Scotia, Canada: petrology, geochemistry, and palynology. *International Journal of Coal Geology*, **42**: 185-206. doi:10.1016/S0166-5162(99)00039-7.

Huaichun, W.U., Shihong, Z., Suwen, S.U.I., and Qinghua, H. 2007. Recognition of Milankovitch Cycles in the Natural Gamma-Ray Logging of Upper Cretaceous Terrestrial Strata in the Songliao Basin. *Acta Geologica Sinica - English Edition*, **81**: 996-1001. doi:10.1111/j.1755-6724.2007.tb01021.x.

Huisman, J.A., Hubbard, S.S., Redman, J.D., and Annan, A.P. 2003. Measuring soil water content with ground penetrating radar: A review. *Vadose zone journal*, **2**: 476-491. doi:10.2136/vzj2003.4760.

Huysmans, M., Peeters, L., Moermans, G., and Dassargues, A. 2008. Relating small-scale sedimentary structures and permeability in a cross-bedded aquifer. *Journal of Hydrology*, **361**: 41-51. doi:10.1016/j.jhydrol.2008.07.047.

Ielpi, A., Gibling, M.R., Bashforth, A.R., and Dennar, C.I. 2015. Impact of vegetation on Early Pennsylvanian fluvial channels: insight from the Joggins Formation of Atlantic Canada. *Journal of Sedimentary Research*, **85**: 999-1018. doi:10.2110/jsr.2015.50.

Imposa, S., Grassi, S., Patti, G., and Boso, D. 2018. New data on buried archaeological ruins in Messina area (Sicily-Italy) from a ground penetrating radar survey. *Journal of Archaeological Science: Reports*, **17**: 358-365. doi:10.1016/j.jasrep.2017.11.031.

Jafarpour, B. 2010. Wavelet reconstruction of geologic facies from nonlinear dynamic flow measurements. *IEEE Transactions on Geoscience and Remote Sensing*, **49**: 1520-1535.

Jaiswal, S., and Bhattacharya, B. 2018. Characterization of middle Eocene tide-influenced delta: A study from core samples of Hazad Member, Ankleshwar Formation, South Cambay Basin, India. *Journal of Earth System Science*, **127**: 65. doi:10.1007/s12040-018-0966-8.

Jangara, H., and Ozturk, C.A. 2021. Longwall top coal caving design for thick coal seam in very poor strength surrounding strata. *International Journal of Coal Science & Technology*, **8**: 641-658.

Jirásek, J., Opluštil, S., Sivek, M., Schmitz, M.D., and Abels, H.A. 2018. Astronomical forcing of Carboniferous paralic sedimentary cycles in the Upper Silesian Basin, Czech Republic (Serpukhovian, latest Mississippian): New radiometric ages afford an astronomical age model for European biozonations and substages. *Earth-Science Reviews*, **177**: 715-741. doi:10.1016/j.earscirev.2017.12.005.

Jol, H.M. 2009. *Ground Penetrating Radar Theory and Applications*. Elsevier Science, Oxford.

Jol, H.M., and Smith, D.G. 1991. Ground penetrating radar of northern lacustrine deltas. *Canadian Journal of Earth Sciences*, **28**: 1939-1947. doi:10.1139/e91-175.

Jones, R.R., Mccaffrey, K.J., Imber, J., Wightman, R., Smith, S.A., Holdsworth, R.E., Clegg, P., De Paola, N., Healy, D., and Wilson, R.W. 2008. Calibration and validation of reservoir models: the importance of high resolution, quantitative outcrop analogues. *Geological Society, London, Special Publications*, **309**: 87-98. doi:10.1144/SP309.7.

Juby, I. 2009. The Joggins Polystrate Fossils. In *Rock Solid Answers*. Edited by M. Oard and J.K. Reed. Creation Research Society Books, Chino Valley, Arizona. pp. 217-225.

Kadioglu, S. 2008. Photographing layer thicknesses and discontinuities in a marble quarry with 3D GPR visualisation. *Journal of Applied Geophysics*, **64**: 109-114. doi:10.1016/j.jappgeo.2008.01.001.

Kadioglu, S. 2013. Transparent 2D/3D Half Bird's-Eye View of Ground Penetrating Radar Data Set in Archaeology and Cultural Heritage. *In Imaging and Radioanalytical Techniques in Interdisciplinary Research - Fundamentals and Cutting Edge Applications*. Edited by F. Kharfi. Intechopen, Rijeka, Croatia. p. 204.

Kadioglu, S., and Daniels, J.J. 2008. 3D visualization of integrated ground penetrating radar data and EM-61 data to determine buried objects and their characteristics. *Journal of Geophysics and Engineering*, **5**: 448-456. doi:10.1088/1742-2132/5/4/008.

Kadioglu, S., and Ulugergerli, E.U. 2012. Imaging karstic cavities in transparent 3D volume of the GPR data set in Akkopru dam, Mugla, Turkey. *Nondestructive Testing and Evaluation*, **27**: 263-271. doi:10.1080/10589759.2012.694885.

Keighley, D.G., Calder, J.H., Park, A.F., Pickerill, R.K., Waldron, J.W., Falcon-Lang, H.J., and Benton, M.J. 2008. Discussion on ecology of earliest reptiles inferred from basal Pennsylvanian trackways. *Journal of the Geological Society*, **165**: 983-987. doi:10.1144/0016-76492008-045.

Kelly, T.B., and Wach, G.D. 2020. Analysis of factors influencing the interpretation of a digitally examined fluvial meanderbelt system: Joggins Formation, Nova Scotia. *Canadian Journal of Earth Sciences*, **57**: 524-541. doi:10.1139/cjes-2018-0263.

Kelly, T.B., and Wach, G.D. 2021. Post-Scan Georeferencing of Optech ILRIS-3D Lidar Data from the Joggins Formation Geologic Exposure using ArcGIS for Adjustment.

Kelly, T.B., Wach, G.D., and O'Connor, D.E. 2021a. The technical challenges and outcomes of ground-penetrating radar: A site-specific example from Joggins, Nova Scotia. *AIMS Geosciences*, **7**: 22-55. doi:10.3934/geosci.2021002.

Kelly, T.B., Angel, M.N., O'Connor, D.E., Huff, C.C., Morris, L.E., and Wach, G.D. 2021b. A novel approach to 3D modelling ground-penetrating radar (GPR) data—A case study of a cemetery and applications for criminal investigation. *Forensic science international*, **325**. doi:10.1016/j.forsciint.2021.110882.

Keogh, K.J., Leary, S., Martinius, A.W., Scott, A.S., Riordan, S., Viste, I., Gowland, S., Taylor, A.M., and Howell, J. 2014. Data capture for multiscale modelling of the Lourinha Formation, Lusitanian Basin, Portugal: an outcrop analogue for the Statfjord Group, Norwegian North Sea. *Geological Society, London, Special Publications*, **387**: 27-56. doi:10.1144/SP387.11.

Keppie, J.D. 2000. *Geological Map of the Province of Nova Scotia*. Nova Scotia Department of Natural Resources: Minerals and Energy Branch, Halifax, Nova Scotia.

Kerans, C., Lucia, F.J., and Senger, R. 1994. Integrated characterization of carbonate ramp reservoirs using Permian San Andres Formation outcrop analogs. *AAPG Bulletin*, **78**: 181-216. doi:10.1306/BDF905A-1718-11D7-8645000102C1865D.

Keys, K., Neily, P., and Quigley, E. 2010. Forest Ecosystem Classification for Nova Scotia (Part II: Soil Types). *Edited by N.S.D.o.N. Resources*. Nova Scotia Department of Natural Resources, Halifax, Nova Scotia. p. 121.

King, O.A., and Stimson, M. 2018. Kouphichnium aspodon, a new occurrence of invertebrate traces from the Joggins Fossil Cliffs UNESCO World Heritage Site, Nova Scotia, Canada. *In 1st Joggins Research Symposium*. Atlantic Geoscience Society, Joggins, Nova Scotia.

King, O.A., Stimson, M.R., MacRae, R.A., Calder, J., Hebert, B., and Reid, L. 2019. An ichnotaxonomic and paleoenvironmental study of the xiphosuran ichnogenus Kouphichnium from the UNESCO World Heritage Site Joggins Fossil Cliffs, Nova Scotia, Canada.

Klausen, T.G., and Mørk, A. 2014. The upper Triassic paralic deposits of the De Geerdalen Formation on Hopen: Outcrop analog to the subsurface Snadd Formation in the Barents Sea. *AAPG Bulletin*, **98**: 1911-1941. doi:10.1306/02191413064.

Knight, R., Tercier, P., and Jol, H. 1997. The role of ground penetrating radar and geostatistics in reservoir description. *The Leading Edge*, **16**: 1576-1584. doi:10.1190/1.1437526.

Kostic, B., and Aigner, T. 2007. Sedimentary architecture and 3D ground-penetrating radar analysis of gravelly meandering river deposits (Neckar Valley, SW Germany). *Sedimentology*, **54**: 789-808. doi:10.1111/j.1365-3091.2007.00860.x.

Kreisa, R.D., and Moila, R.J. 1986. Sigmoidal tidal bundles and other tide-generated sedimentary structures of the Curtis Formation, Utah. *Geological Society of America Bulletin*, **97**: 381-387. doi:10.1130/0016-7606(1986)97<381:Stbaot>2.0.Co;2.

Kumlu, D., and Erer, I. 2019. Clutter removal techniques in ground penetrating radar for landmine detection: A Survey. *In Operations Research for Military Organizations*. IGI Global. pp. 375-399.

Kvale, E.P. 2012. Tidal Constituents of Modern and Ancient Tidal Rhythmites: Criteria for Recognition and Analyses. *In Principles of Tidal Sedimentology. Edited by R.A. Davis Jr and R.W. Dalrymple.* Springer, New York. pp. 1-17.

Kvale, E.P., and Archer, A.W. 1991. Characteristics of two, Pennsylvanian-age, semidiurnal tidal deposits in the Illinois Basin, USA. *In Clastic Tidal Sedimentology - Memoir 16. Edited by D.G. Smith and G.E. Reinson and B.A. Zaitlin and R.A. Rahmani.* Canadian Society of Petroleum Geologists, Calgary, Alberta. pp. 179-188.

Kvale, E.P., Archer, A.W., and Johnson, H.R. 1989. Daily, monthly, and yearly tidal cycles within laminated siltstones of the Mansfield Formation (Pennsylvanian) of Indiana. *Geology*, **17**: 365-368. doi:10.1130/0091-7613(1989)017.

Kwon, S., Park, J.-W., Moon, D., Jung, S., and Park, H. 2017. Smart merging method for hybrid point cloud data using UAV and LIDAR in earthwork construction. *Procedia engineering*, **196**: 21-28. doi:10.1016/j.proeng.2017.07.168.

Labourdette, R., and Jones, R.R. 2007. Characterization of fluvial architectural elements using a three-dimensional outcrop data set: Escanilla braided system, South-Central Pyrenees, Spain. *Geosphere*, **3**: 422-434. doi:10.1130/GES00087.1.

Labrecque, P.A., Jensen, J.L., and Hubbard, S.M. 2011. Cyclicity in Lower Cretaceous point bar deposits with implications for reservoir characterization, Athabasca Oil Sands, Alberta, Canada. *Sedimentary Geology*, **242**: 18-33. doi:10.1016/j.sedgeo.2011.06.011.

Lalagüe, A. 2015. Use of ground penetrating radar for transportation infrastructure maintenance.

Lanier, W.P., Feldman, H.R., and Archer, A.W. 1993. Tidal sedimentation from a fluvial to estuarine transition, Douglas Group, Missourian-Virgilian, Kansas. *Journal of Sedimentary Research*, **63**: 860-873. doi:10.1306/D4267C2B-2B26-11D7-8648000102C1865D.

Lanzarone, P., Garrison, E., Bobe, R., and Getahun, A. 2016. Examining Fluvial Stratigraphic Architecture Using Ground-Penetrating Radar at the Fanta Stream Fossil and Archaeological Site, Central Ethiopia. *Geoarchaeology*, **31**: 577-591. doi:10.1002/gea.21584.

Leandro, C.G., Barboza, E.G., Caron, F., and de Jesus, F.A. 2019. GPR trace analysis for coastal depositional environments of southern Brazil. *Journal of Applied Geophysics*, **162**: 1-12. doi:10.1016/j.jappgeo.2019.01.002.

Lear, C.H., Anand, P., Blenkinsop, T., Foster, G.L., Gagen, M., Hoogakker, B., Larter, R.D., Lunt, D.J., McCave, I.N., and McClymont, E. 2021. Geological Society of London Scientific Statement: what the geological record tells us about our present and future climate. Geological Society of London.

Leeder, M.R. 1988. Devonian-Carboniferous river systems and sediment dispersal from the orogenic belts and cratons of NW Europe. Geological Society, London, Special Publications, **38**: 549-558. doi:10.1144/gsl.Sp.1988.038.01.37.

Leeder, M.R., Duff, P.M.D., and Smith, A.J. 1992. Dinantian. *Geology of England and Wales*: 207-237.

Lester, J., and Bernold, L.E. 2007. Innovative process to characterize buried utilities using ground penetrating radar. *Automation in Construction*, **16**: 546-555. doi:10.1016/j.autcon.2006.09.004.

Letourmy, Y., Driese, S.G., and Sims, J.R. 2021. Absence of evidence of climate-driven cycles in Carboniferous deposits of Joggins, Nova Scotia, Canada: influence of salt withdrawal tectonics on deposition and pedogenesis. *Journal of Sedimentary Research*, **91**: 167-185. doi:10.2110/jsr.2020.78.

Leucci, G., and Negri, S. 2006. Use of ground penetrating radar to map subsurface archaeological features in an urban area. *Journal of Archaeological Science*, **33**: 502-512. doi:10.1016/j.jas.2005.09.006.

Levorsen, A.I. 1954. *Geology of Petroleum*. W.H. Freeman Company, San Francisco, California.

Lichti, D.D., and Harvey, B.R. 2002. The Effects of Reflecting Surface Material Properties on Time-of-Flight Laser Scanner Measurements. *In* Symposium on Geospatial Theory, Processing and Applications, Ottawa, ON. p. 9.

Lim, S., Thatcher, C.A., Brock, J.C., Kimbrow, D.R., Danielson, J.J., and Reynolds, B.J. 2013. Accuracy assessment of a mobile terrestrial lidar survey at Padre Island National Seashore. *International Journal of Remote Sensing*, **34**: 6355-6366. doi:10.1080/01431161.2013.800658.

Liu, X., Dong, X., Xue, Q., Leskovar, D.I., Jifon, J., Butnor, J.R., and Marek, T. 2018. Ground penetrating radar (GPR) detects fine roots of agricultural crops in the field. *Plant and soil*, **423**: 517-531. doi:10.1007/s11104-017-3531-3.

Llorens, J., Gil, E., Llop, J., and Queralto, M. 2011. Georeferenced LiDAR 3D vine plantation map generation. *Sensors (Basel)*, **11**: 6237-6256. doi:10.3390/s110606237.

Logan, W.E. 1845. A section of the Nova Scotia coal measures as developed at Joggins on the Bay of Fundy, in descending order, from the neighbourhood of the west Ragged Reef to Minudie, reduced to vertical thickness. *Journals of the Legislative Assembly of the Province of Canada*, **4**: 28-45.

Lorenzo, H., Pérez-Gracia, V., Novo, A., and Armesto, J. 2010. Forestry applications of ground-penetrating radar. *Forest Systems*, **19**: 5-17.

Lundberg, A., Richardson-Näslund, C., and Andersson, C. 2006. Snow density variations: consequences for ground-penetrating radar. *Hydrological Processes: An International Journal*, **20**: 1483-1495. doi:10.1002/hyp.5944.

MacDonald, S.Y. 2020. With Respect to the Dead: Reconstructing a Historic View of Death in Gaelic Nova Scotia. *Genealogy*, **4**: 66. doi:10.3390/genealogy4020066.

Maddin, H.C., Mann, A., and Hebert, B. 2020. Varanopid from the Carboniferous of Nova Scotia reveals evidence of parental care in amniotes. *Nat Ecol Evol*, **4**: 50-56. doi:10.1038/s41559-019-1030-z.

Magnabosco, C., Braathen, A., and Ogata, K. 2014. Permeability model of tight reservoir sandstones combining core-plug and Miniperm analysis of drillcore; Longyearbyen CO2 Lab, Svalbard. *Norwegian Journal of Geology*, **94**: 189-200.

Maierhofer, C. 2003. Nondestructive evaluation of concrete infrastructure with ground penetrating radar. *Journal of Materials in Civil Engineering*, **15**: 287-297.

Mann, A., Gee, B.M., Pardo, J.D., Marjanović, D., Adams, G.R., Calthorpe, A.S., Maddin, H.C., and Anderson, J.S. 2020. Reassessment of historic ‘microsaurs’ from Joggins, Nova Scotia, reveals hidden diversity in the earliest amniote ecosystem. *Papers in Palaeontology*, **6**: 605-625. doi:10.1002/spp2.1316.

Martel, T.A. 1987. Seismic Stratigraphy and Hydrocarbon Potential of the Strike-Slip Sackville Sub-Basin, New Brunswick. *In* Memoir 12 - Sedimentary basins and basin-forming mechanisms. *Edited by* C. Beaumont and A.J. Tankard. Atlantic Geoscience Society, Halifax. pp. 319-334.

Maser, K.R. 1996. Condition assessment of transportation infrastructure using ground-penetrating radar. *Journal of infrastructure systems*, **2**: 94-101. doi:10.1061/(ASCE)1076-0342(1996)2:2(94).

Maynard, J.R., Hofmann, W., Dunay, R.E., Benthan, P.N., Dean, K.P., and Watson, I. 1997. The Carboniferous of Western Europe; the development of a petroleum system. *Petroleum Geoscience*, **3**: 97-115. doi:10.1144/petgeo.3.2.97.

McIntyre, A., and Molfino, B. 1996. Forcing of Atlantic Equatorial and Subpolar Millennial Cycles by Precession. *Science*, **274**: 1867-1870. doi:10.1126/science.274.5294.1867.

McMechan, G.A., and Soegaard, K. 1998. Sedimentological and geophysical studies of clastic reservoir analogs: Methods, applications and developments of ground-penetrating radar for determination of reservoir geometries in near-surface settings. Final report. Texas Univ., Dallas, TX (United States).

McMechan, G.A., Gaynor, G.C., and Szerbiak, R.B. 1997. Use of ground-penetrating radar for 3-D sedimentological characterization of clastic reservoir analogs. *Geophysics*, **62**: 786-796. doi:10.1190/1.1444188.

Meyer, R., and Krause, F.F. 2006. Permeability anisotropy and heterogeneity of a sandstone reservoir analogue: An estuarine to shoreface depositional system in the Virgelle Member, Milk River Formation, Writing-on-Stone Provincial Park, southern Alberta. *Bulletin of Canadian Petroleum Geology*, **54**: 301-318. doi:10.2113/gscpgbull.54.4.301.

Milankovitch, M. 1941. Kanon der Erdbestrahlung und seine Anwendung anf das Eiszeitproblem. *Acad. Roy. Serbe, Ed. spec*, **133**.

Miller, D.J., and Eriksson, K.A. 1997. Late Mississippian Prodeltaic Rhythmites in the Appalachian Basin: A Hierarchical Record of Tidal and Climatic Periodicities. *Journal of Sedimentary Research*, **67**: 653-660. doi:10.1306/d4268608-2b26-11d7-8648000102c1865d.

Minisini, D., Wang, M., Bergman, S.C., and Aiken, C. 2014. Geological data extraction from lidar 3-D photorealistic models: A case study in an organic-rich mudstone, Eagle Ford Formation, Texas. *Geosphere*, **10**: 610-626. doi:10.1130/GES00937.1.

Mitterer, C., Heilig, A., Schweizer, J., and Eisen, O. 2011. Upward-looking ground-penetrating radar for measuring wet-snow properties. *Cold regions science and technology*, **69**: 129-138. doi:10.1016/j.coldregions.2011.06.003.

Mohamed, A., and Wilkinson, B. 2009. Direct georeferencing of stationary LiDAR. *Remote sensing*, **1**: 1321-1337. doi:10.3390/rs1041321.

Møller, I., and Anthony, D. 2003. A GPR study of sedimentary structures within a transgressive coastal barrier along the Danish North Sea coast. *Geological Society, London, Special Publications*, **211**: 55-65. doi:10.1144/gsl.Sp.2001.211.01.05.

Moore, J., Taylor, A., Johnson, C., Ritts, B.D., and Archer, R. 2012. Facies analysis, reservoir characterization, and LIDAR modeling of an Eocene lacustrine delta, Green River Formation, southwest Uinta Basin, Utah. *In* *Lacustrine sandstone reservoirs and hydrocarbon systems: AAPG Memoir 95. Edited by O.W. Baganz and Y. Bartov and K. Bohacs and D. Nummedal. The American Association of Petroleum Geologists, Houston, Texas. pp. 183-208.*

Morgan, B.C., and Murray, K.E. 2015. *Characterizing Small-Scale Permeability of the Arbuckle Group, Oklahoma. Oklahoma Geological Survey, Norman, Ok.*

Morten, S. 2001. Recognition of cyclicity in the petrophysical properties of a Maastrichtian pelagic chalk oil field reservoir from the Danish North Sea. *AAPG Bulletin*, **85**: 2003-2015. doi:10.1306/8626d0d1-173b-11d7-8645000102c1865d.

Mukhopadhyay, P.K., Hatcher, P., and Calder, J.H. 1991. Hydrocarbon generation of coal and coaly shale from fluvio-deltaic and deltaic environments of Nova Scotia and Texas. *Organic Geochemistry*: 17,765-783.

Musial, G., Reynaud, J.-Y., Gingras, M.K., Féliès, H., Labourdette, R., and Parize, O. 2012. Subsurface and outcrop characterization of large tidally influenced point bars of the Cretaceous McMurray Formation (Alberta, Canada). *Sedimentary Geology*, **279**: 156-172. doi:10.1016/j.sedgeo.2011.04.020.

Nabawy, B.S., Rochette, P., and Géraud, Y. 2009. Petrophysical and magnetic pore network anisotropy of some cretaceous sandstone from Tushka Basin, Egypt. *Geophysical Journal International*, **177**: 43-61. doi:10.1111/j.1365-246X.2008.04061.x.

Nalendra, S., Kuncoro, B., and Burhanudin, A. Thickness variation of Coal Seams in Loa Janan Anticline: Implication for Exploration and Mining Activities. *In* Natural Resources and Infrastructure Development for National Sovereignty. Malang, Indonesia 2017. *Edited by* D. Ralanarko. Indonesian Association of Geophysicist.

Neal, A. 2004. Ground-penetrating radar and its use in sedimentology: principles, problems and progress. *Earth-Science Reviews*, **66**: 261-330. doi:10.1016/j.earscirev.2004.01.004.

Neal, A., and Roberts, C.L. 2000. Applications of ground-penetrating radar (GPR) to sedimentological, geomorphological and geoarchaeological studies in coastal environments. Geological Society, London, Special Publications, **175**: 139-171. doi:10.1144/gsl.Sp.2000.175.01.12.

New England Research. 2013. TinyPerm II: Portable Air Permeameter User's Manual. San Ramon, California.

Ni, S.-H., Huang, Y.-H., Lo, K.-F., and Lin, D.-C. 2010. Buried pipe detection by ground penetrating radar using the discrete wavelet transform. *Computers and Geotechnics*, **37**: 440-448. doi:10.1016/j.compgeo.2010.01.003.

Nickerson, J.D. 2010. Architecture and Geometry of Braided Channel Complex in the Triassic Wolfville Formation. *Earth Sciences*, Dalhousie University, Halifax, NS.

North, C.P., and Prosser, D.J. 1993. Characterization of fluvial and aeolian reservoirs: problems and approaches. Geological Society, London, Special Publications, **73**: 1-6. doi:10.1144/gsl.Sp.1993.073.01.01.

Nova Scotia Department of Natural Resources. 2005. Aerial Photography - 2005 Colour Photographs.

Nowland, J.L., and MacDougall, J.I. 1973. Nova Scotia Soil Survey - Soils of Cumberland County Nova Scotia. *Edited by* Canada Department of Agriculture. D.W. Friesen and Sons Ltd., Ottawa. p. 154.

O'Connor, D. 2016. Facies Distribution, Fluvial Architecture, Provenance, Diagenesis, and Reservoir Quality of Synrift Successions from the Breakup of Pangea: Examples from the Fundy Basin and Orpheus Graben. Earth Sciences, Dalhousie University, Halifax, NS.

Olsen, M.J. 2011. Putting the pieces together: laser scan geo-referencing. LiDAR Magazine, **1**.

Olsen, M.J., Johnstone, E., Driscoll, N., Ashford, S.A., and Kuester, F. 2009. Terrestrial laser scanning of extended cliff sections in dynamic environments: Parameter analysis. *Journal of Surveying Engineering*, **135**: 161-169. doi:10.1061/(ASCE)0733-9453(2009)135:4(161).

Olsen, M.J., Johnstone, E., Kuester, F., Driscoll, N., and Ashford, S.A. 2011. New automated point-cloud alignment for ground-based light detection and ranging data of long coastal sections. *Journal of Surveying Engineering*, **137**: 14-25. doi:10.1061/(ASCE)SU.1943-5428.0000030.

Olsen, P.E., and Kent, D.V. 1996. Milankovitch climate forcing in the tropics of Pangaea during the Late Triassic. *Palaeogeography, Palaeoclimatology, Palaeoecology*, **122**: 1-26. doi:10.1016/0031-0182(95)00171-9.

Olsen, P.E., Shackleton, N.J., McCave, I.N., Weedon, G.P., and Kent, D.V. 1999. Long-period Milankovitch cycles from the Late Triassic and Early Jurassic of eastern North America and their implications for the calibration of the Early Mesozoic time-scale and the long-term behaviour of the planets. *Philosophical Transactions of the Royal Society of London. Series A: Mathematical, Physical and Engineering Sciences*, **357**: 1761-1786. doi:10.1098/rsta.1999.0400.

Olsen, P.E., Laskar, J., Kent, D.V., Kinney, S.T., Reynolds, D.J., Sha, J., and Whiteside, J.H. 2019. Mapping Solar System chaos with the Geological Orrery. *Proc Natl Acad Sci U S A*, **116**: 10664-10673. doi:10.1073/pnas.1813901116.

Optech Incorporated. 2006a. Optech ILRIS-3D, Vaughan, ON.

Optech Incorporated. 2006b. ILRIS-3D Operation Manual.

Pälli, A., Kohler, J.C., Isaksson, E., Moore, J.C., Pinglot, J.F., Pohjola, V.A., and Samuelsson, H. 2002. Spatial and temporal variability of snow accumulation using ground-penetrating radar and ice cores on a Svalbard glacier. *Journal of Glaciology*, **48**: 417-424. doi:10.3189/172756502781831205.

Pardo, J.D., and Mann, A. 2018. A basal aistopod from the earliest Pennsylvanian of Canada, and the antiquity of the first limbless tetrapod lineage. *R Soc Open Sci*, **5**: 181056. doi:10.1098/rsos.181056.

Pessemiers, M., Huysmans, M., Peeters, L., Batelaan, O., and Dassargues, A. 2012. Relationship between sedimentary features and permeability at different scales in the Brussels Sands. *Geologica Belgica*, **15**: 156-164.

Pettersson, J.K., and Nobes, D.C. 2003. Environmental geophysics at Scott Base: ground penetrating radar and electromagnetic induction as tools for mapping contaminated ground at Antarctic research bases. *Cold regions science and technology*, **37**: 187-195. doi:10.1016/S0165-232X(03)00037-5.

Porsani, J.L., Sauck, W.A., and Júnior, A.O. 2006. GPR for mapping fractures and as a guide for the extraction of ornamental granite from a quarry: A case study from southern Brazil. *Journal of Applied Geophysics*, **58**: 177-187. doi:10.1016/j.jappgeo.2005.05.010.

Poulter, G. 2011. What's traditional about "the traditional funeral"? Funeral rituals and the evolution of the funeral industry in Nova Scotia. *Journal of the Canadian Historical Association/Revue de la Société historique du Canada*, **22**: 133-159. doi: 10.7202/1008960ar.

Pranter, M.J., Ellison, A.I., Cole, R.D., and Patterson, P.E. 2007. Analysis and modeling of intermediate-scale reservoir heterogeneity based on a fluvial point-bar outcrop analog, Williams Fork Formation, Piceance Basin, Colorado. *AAPG Bulletin*, **91**: 1025-1051. doi:10.1306/02010706102.

Pranter, M.J., Hewlett, A.C., Cole, R.D., Wang, H., and Gilman, J. 2014. Fluvial architecture and connectivity of the Williams Fork Formation: use of outcrop analogues for stratigraphic characterization and reservoir modelling. *Geological Society, London, Special Publications*, **387**: 57-83. doi:10.1144/SP387.1.

Prescott, Z.M., Stimson, M.R., Dafoe, L.T., Gibling, M.R., MacRae, R.A., Calder, J.H., and Hebert, B.L. 2014. Microbial mats and ichnofauna of a fluvial-tidal channel in the Lower Pennsylvanian Joggins Formation, Canada. *Palaios*, **29**: 624-645. doi:10.2110/palo.2013.073.

Pringle, J., Howell, J., Hodgetts, D., Westerman, A., and Hodgson, D. 2006. Virtual outcrop models of petroleum reservoir analogues: a review of the current state-of-the-art. *First Break*, **24**: 33-42. doi:10.3997/1365-2397.2006005.

Pringle, J.K., Jervis, J.R., Hansen, J.D., Jones, G.M., Cassidy, N.J., and Cassella, J.P. 2012a. Geophysical monitoring of simulated clandestine graves using electrical and ground-penetrating radar methods: 0–3 years after burial. *Journal of Forensic Sciences*, **57**: 1467-1486. doi:10.1111/j.1556-4029.2012.02151.x.

Pringle, J.K., Ruffell, A., Jervis, J.R., Donnelly, L., McKinley, J., Hansen, J., Morgan, R., Pirrie, D., and Harrison, M. 2012b. The use of geoscience methods for terrestrial forensic searches. *Earth-Science Reviews*, **114**: 108-123. doi:10.1016/j.earscirev.2012.05.006.

Prokop, J., Pecharová, M., Nel, A., Grey, M., and Hörschemeyer, T. 2017. A remarkable insect from the Pennsylvanian of the Joggins Formation in Nova Scotia, Canada: insights into unusual venation of Brodiidae and nymphs of Megasecoptera. *Journal of Systematic Palaeontology*, **15**: 1051-1065. doi:10.1080/14772019.2017.1283364.

Prokoph, A., and Barthelmes, F. 1996. Detection of nonstationarities in geological time series: wavelet transform of chaotic and cyclic sequences. *Computers & geosciences*, **22**: 1097-1108. doi:10.1016/S0098-3004(96)00054-4.

Prokoph, A., and Agterberg, F.P. 1999. Detection of sedimentary cyclicity and stratigraphic completeness by wavelet analysis; an application to late Albian cyclostratigraphy of the Western Canada Sedimentary Basin. *Journal of Sedimentary Research*, **69**: 862-875. doi:10.2110/jsr.69.862.

Prokoph, A., and Thurow, J. 2000. Diachronous pattern of Milankovitch cyclicity in late Albian pelagic marlstones of the North German Basin. *Sedimentary Geology*, **134**: 287-303. doi:10.1016/s0037-0738(00)00050-6.

Prokoph, A., Villeneuve, M., Agterberg, F.P., and Rachold, V. 2001. Geochronology and calibration of global Milankovitch cyclicity at the Cenomanian-Turonian boundary. *Geology*, **29**: 523-526. doi:10.1130/0091-7613(2001)029<0523:Gacogm>2.0.Co;2.

Prothero, D.R., and Schwab, F. 2003. *Sedimentary Geology : An Introduction to Sedimentary Rocks and Stratigraphy*. 2 ed. Freeman & Company, W&H.

Puri, N., and Turkan, Y. 2020. Bridge construction progress monitoring using lidar and 4D design models. *Automation in Construction*, **109**: 1-15. doi:10.1016/j.autcon.2019.102961.

Qin, T., Zhao, Y., Lin, G., Hu, S., An, C., Geng, D., and Rao, C. 2018. Underwater archaeological investigation using ground penetrating radar: A case analysis of Shanglinhu Yue Kiln sites (China). *Journal of Applied Geophysics*, **154**: 11-19. doi:10.1016/j.jappgeo.2018.04.018.

Quann, S.L., Young, A.B., Laroque, C.P., Falcon-Lang, H.J., and Gibling, M.R. 2010. Dendrochronological dating of coal mine workings at the Joggins Fossil Cliffs, Nova Scotia, Canada.

Raduha, S., Butler, D., Mozley, P.S., Person, M., Evans, J., Heath, J.E., Dewers, T.A., Stauffer, P.H., Gable, C.W., and Kelkar, S. 2016. Potential seal bypass and caprock storage produced by deformation-band-to-opening-mode-fracture transition at the reservoir/caprock interface. *Geofluids*, **16**: 752-768. doi:10.1111/gfl.12177.

Rafezi, H., Novo, A., and Hassani, F.P. 2015. An investigation into application of Ground Penetrating Radar (GPR) in surface mining. *In* Symposium on the Application of Geophysics to Engineering and Environmental Problems 2015. 2015. Society of Exploration Geophysicists and Environment and Engineering Geophysical Society, pp. 54-60.

Rafuse, C., and Wach, G. 2011. Reservoir architecture of meanderbelt systems and vegetation density in the Carboniferous using LiDAR imagery. *Earth Sciences*, Dalhousie University, Halifax, NS.

Ralston, J.C., and Hainsworth, D.W. Application of ground penetrating radar for coal depth measurement. *In* 1999 IEEE International Conference on Acoustics, Speech, and Signal Processing. Proceedings. ICASSP99 (Cat. No. 99CH36258). 1999. IEEE. Vol. 4, pp. 2275-2278.

Rampino, M.R., Prokoph, A., and Adler, A. 2000. Tempo of the end-Permian event: High-resolution cyclostratigraphy at the Permian-Triassic boundary. *Geology*, **28**: 643-646. doi:10.1130/0091-7613(2000)28<643:Toteeh>2.0.Co;2.

Rampino, M.R., Caldeira, K., and Zhu, Y. 2021. A pulse of the Earth: A 27.5-Myr underlying cycle in coordinated geological events over the last 260 Myr. *Geoscience Frontiers*, **12**: 1-7. doi:10.1016/j.gsf.2021.101245.

Rarity, F., Van Lanen, X., Hodgetts, D., Gawthorpe, R., Wilson, P., Fabuel-Perez, I., and Redfern, J. 2014. LiDAR-based digital outcrops for sedimentological analysis: workflows and techniques. Geological Society, London, Special Publications, **387**: 153-183. doi: 10.1144/SP387.5.

Read, W.A. 1992. Evidence of tidal influences in Arnsbergian rhythmites in the Kincardine Basin. *Scottish Journal of Geology*, **28**: 135-142. doi:10.1144/sjg28020135.

REI Nova Scotia. 1995. The Coring and Logging of REI-B2-1. Halifax, Nova Scotia.

Reisz, R.R., and Modesto, S.P. 1996. Archerpeton anthracos from the Joggins Formation of Nova Scotia: a microsauro, not a reptile. *Canadian Journal of Earth Sciences*, **33**: 703-709. doi:10.1139/e96-053.

Rey, J., Martínez, J., and Hidalgo, M.C. 2013. Investigating fluvial features with electrical resistivity imaging and ground-penetrating radar: The Guadalquivir River terrace (Jaen, Southern Spain). *Sedimentary Geology*, **295**: 27-37. doi:10.1016/j.sedgeo.2013.07.003.

Reyes-López, J.A., Ramírez-Hernández, J., Lázaro-Mancilla, O., Carreón-Díazconti, C., and Garrido, M.M.-L. 2008. Assessment of groundwater contamination by landfill leachate: A case in México. *Waste Management*, **28**: S33-S39. doi:10.1016/j.wasman.2008.03.024.

Richards, M.T. 1994. Transgression of an estuarine channel and tidal flat complex: the Lower Triassic of Barles, Alpes de Haute Provence, France. *Sedimentology*, **41**: 55-82. doi:10.1111/j.1365-3091.1994.tb01392.x.

Risk, J. 2020. Church of the Holy Spirit Information. *Edited by G. Wach*, Halifax, Nova Scotia.

Roark, M.S., Strohmeyer, J., Anderson, N., Shoemaker, M., and Oppert, S. 1998. Applications of the ground-penetrating radar technique in the detection and delineation of homicide victims and crime scene paraphernalia. *In 11th EEGS Symposium on the Application of Geophysics to Engineering and Environmental Problems*. 1998. European Association of Geoscientists & Engineers, pp. cp-203-00112.

Rogiers, B., Beerten, K., Smeekens, T., and Mallants, D. 2011. Air permeability measurements on Neogene and Quaternary sediments from the Campine area: using outcrop analogues for determining hydrodynamic aquifer properties. *Belgian Nuclear Research Centre*: 23.

Rogiers, B., Beerten, K., Smeekens, T., Mallants, D., Gedeon, M., Huysmans, M., Batelaan, O., and Dassargues, A. 2013. The usefulness of outcrop-analogue air-permeameter measurements for analysing aquifer heterogeneity: testing outcrop hydrogeological parameters with independent borehole data. *Hydrology and Earth System Sciences*, **17**: 5155-5166. doi:10.5194/hess-17-5155-2013.

Rogiers, B., Winters, P., Huysmans, M., Beerten, K., Mallants, D., Gedeon, M., Batelaan, O., and Dassargues, A. 2014. High-resolution saturated hydraulic conductivity logging of borehole cores using air permeability measurements. *Hydrogeology Journal*, **22**: 1345-1358. doi:10.1007/s10040-014-1144-y.

Rotevatn, A., Torabi, A., Fossen, H., and Braathen, A. 2008. Slipped deformation bands: A new type of cataclastic deformation bands in Western Sinai, Suez rift, Egypt. *Journal of Structural Geology*, **30**: 1317-1331. doi:10.1016/j.jsg.2008.06.010.

Rotevatn, A., Buckley, S.J., Howell, J.A., and Fossen, H. 2009. Overlapping faults and their effect on fluid flow in different reservoir types: A LIDAR-based outcrop modeling and flow simulation study. *AAPG Bulletin*, **93**: 407-427. doi:10.1306/09300807092.

RPS Energy. 2010. Screening of Potential CO₂ Storage Sites Onshore Nova Scotia. Carbon Capture and Storage Research Consortium of Nova Scotia

Rubio-Melendi, D., Gonzalez-Quirós, A., Roberts, D., García, M.d.C.G., Domínguez, A.C., Pringle, J.K., and Fernández-Álvarez, J.-P. 2018. GPR and ERT detection and characterization of a mass burial, Spanish Civil War, Northern Spain. *Forensic science international*, **287**: e1-e9.

Ruffell, A., McCabe, A., Donnelly, C., and Sloan, B. 2009. Location and assessment of an historic (150–160 years old) mass grave using geographic and ground penetrating radar investigation, NW Ireland. *Journal of Forensic Sciences*, **54**: 382-394.

Rust, B.R., Gibling, M.R., and Legun, A.S. 1985. Coal deposition in an anastomosing-fluvial system: the Pennsylvanian Cumberland Group south of Joggins, Nova Scotia, Canada. *Sedimentology of Coal and Coal-Bearing Sequences*: 105-120.

Ryan, R.J., and Boehner, R.C. 1994. Geology of the Cumberland Basin, Cumberland, Colchester and Pictou Counties, Nova Scotia - Memoir 10. *Edited by Mines and Energy Branch - Department of Natural Resources*. Department of Natural Resources, Halifax.

Ryan, R.J., Calder, J.H., Donohoe Jr., H.V., and Naylor, R. 1987. Late Paleozoic Sedimentation and Basin Development Adjacent to the Cobequid Highlands Massif, Eastern Canada. *In* Memoir 12 - Sedimentary basins and basin-forming mechanisms. *Edited by* C. Beaumont and A.J. Tankard. Atlantic Geoscience Society, Halifax. pp. 311-317.

Ryer, T.A., and Langer, A.W. 1980. Thickness change involved in the peat-to-coal transformation for a bituminous coal of Cretaceous age in central Utah. *Journal of Sedimentary Research*, **50**.

Rygel, M.C. 2005. Alluvial sedimentology and basin analysis of Carboniferous strata near Joggins, Nova Scotia, Atlantic Canada. Earth Sciences, Dalhousie University, Halifax, NS.

Rygel, M.C., and Shipley, B.C. 2005. "Such a section as never was put together before": Logan, Dawson, Lyell, and mid-Nineteenth-Century measurements of the Pennsylvanian Joggins section of Nova Scotia. *Atlantic Geology*, **41**: 87-102.

Rygel, M.C., and Gibling, M.R. 2006. Natural Geomorphic Variability Recorded in a High-Accommodation Setting: Fluvial Architecture of the Pennsylvanian Joggins Formation of Atlantic Canada. *Journal of Sedimentary Research*, **76**: 1230-1251. doi:10.2110/jsr.2006.100.

Rygel, M.C., Gibling, M.R., and Calder, J.H. 2004. Vegetation-induced sedimentary structures from fossil forests in the Pennsylvanian Joggins Formation, Nova Scotia. *Sedimentology*, **51**: 531-552. doi:10.1111/j.1365-3091.2004.00635.x.

Rygel, M.C., Sheldon, E.P., Stimson, M.R., Calder, J.H., Ashley, K.T., and Salg, J.L. 2014. The Pennsylvanian Springhill Mines Formation: sedimentological framework for a portion of the Joggins Fossil Cliffs UNESCO World Heritage Site. *Atlantic Geology*, **50**: 249-289. doi:10.4138/atlgeol.2014.013.

Sahoo, H., and Gani, N.D. 2015. Creating three-dimensional channel bodies in LiDAR-integrated outcrop characterization: A new approach for improved stratigraphic analysis. *Geosphere*, **11**: 777-785. doi:10.1130/GES01075.1.

Schlumberger. 2014. 2014 Petrel Fundamentals: Training and Exercise Guide. Schlumberger, Houston, Texas.

Schuhmacher, S., and Böhm, J. Georeferencing of terrestrial laserscanner data for applications in architectural modeling. *In* Proceedings of the ISPRS Working Group V/4 Workshop 3DARCH “Virtual Reconstruction and Visualization of Complex Architectures”. Mestre-Venice, Italy, August 22-24 2005, pp. 1-7.

Schultz, J.J. 2007. Using ground-penetrating radar to locate clandestine graves of homicide victims: forming forensic archaeology partnerships with law enforcement. *Homicide Studies*, **11**: 15-29. doi:10.1177/1088767906296234.

Schultz, J.J., Grasmueck, M., Weger, R., Muztaza, N.M., Saidin, M.M., Azwin, I.N., Saad, R., Kofun, H., and Leucci, G. 2012. Detecting buried remains using ground penetrating radar. U.S. Department of Justice.

Schwarzacher, W. 1993. Developments in Sedimentology: Chapter 7 Examples from the Carboniferous. Elsevier. pp. 107-124.

Schwarzacher, W. 2000. Repetitions and cycles in stratigraphy. *Earth-Science Reviews*, **50**: 51-75. doi:10.1016/s0012-8252(99)00070-7.

Scott, A.C. 1998. The legacy of Charles Lyell: advances in our knowledge of coal and coal-bearing strata. Geological Society, London, Special Publications, **143**: 243-260. doi:10.1144/GSL.SP.1998.143.01.18.

Selim, S.S., Wafdy, R., and Khadrah, A.M.A. 2021. Sedimentological analysis and reservoir quality of the early Cenomanian transgressive sandstones, northern Western desert, Egypt. *Journal of Petroleum Science and Engineering*, **197**: 107948. doi:10.1016/j.petrol.2020.107948.

Sensors and Software Inc. 2018a. EKKO_Project: User's Manual, Mississauga, Ontario.

Sensors and Software Inc. 2018b. EKKO_Project: Processing Module Users Guide.

Shukla, T., and Shukla, U. 2013. Tidal bundles: An evidence of mixed tidal regime in scarp sandstone formation of the proterozoic Kaimur Group, Vindhyan Basin, Mirzapur District, (Uttar Pradesh), India. *Gondwana Geological Magazine*, **28**: 93-99.

Siddiqui, N.A., Ramkumar, M., Rahman, A.H.A., Mathew, M.J., Santosh, M., Sum, C.W., and Menier, D. 2018. High resolution facies architecture and digital outcrop modeling of the Sandakan formation sandstone reservoir, Borneo: Implications for reservoir characterization and flow simulation. *Geoscience Frontiers*. doi:10.1016/j.gsf.2018.04.008.

Slatt, R.M., Jordan, D.W., D'Agostino, A.E., and Gillespie, R.H. 1992. Outcrop gamma-ray logging to improve understanding of subsurface well log correlations. Geological Society, London, Special Publications, **65**: 3-19. doi:10.1144/GSL.SP.1992.065.01.02.

Smith, D.G. 1988. Tidal bundles and mud couplets in the McMurray Formation, northeastern Alberta, Canada. *Bulletin of Canadian Petroleum Geology*, **36**: 216-219. doi:10.35767/gscpgbull.36.2.216.

Smith, D.G., and Jol, H.M. 1992. Ground-penetrating radar investigation of a Lake Bonneville delta, Provo level, Brigham City, Utah. *Geology*, **20**: 1-4. doi:10.1130/0091.

Sonnenberg, S.A., McKenna, D.J., and McKenna, P.J. 1991. Sorrento Field--USA Denver Basin, Colorado.

SPE Research & Development Committee. 2012. Grand Challenges Facing the E&P Industry. Available from <https://www.spe.org/en/industry/globalchallenges/2022>].

Stage, M. 1999. Signal analysis of cyclicity in Maastrichtian pelagic chalks from the Danish North Sea. *Earth and Planetary Science Letters*, **173**: 75-90. doi:10.1016/S0012-821X(99)00213-7.

Stea, R.R., and Finck, P.W. 1986. Surficial Geology, Chigneto Peninsula, Nova Scotia (Sheet 9). Geological Survey of Canada. p. Map 1630A.

Stimson, M., Lucas, S.G., and Melanson, G. 2012. The smallest known tetrapod footprints: *Batrachichnus salamandroides* from the Carboniferous of Joggins, Nova Scotia, Canada. *Ichnos*, **19**: 127-140. doi:10.1080/10420940.2012.685206.

Strange, A.D., Ralston, J.C., and Chandran, V. Application of ground penetrating radar technology for near-surface interface determination in coal mining. *In Proceedings.(ICASSP'05)*. IEEE International Conference on Acoustics, Speech, and Signal Processing, 2005. 2005. IEEE. Vol. 5, pp. v/701-v/704 Vol. 705.

Strasser, A., Einsele, G., and Ricken, W. 1991. Lagoonal-peritidal sequences in carbonate environments: autocyclic and allocyclic processes. *Cycles and events in stratigraphy*: 709-721.

Strasser, A.H., and Heckel, P.H. 2007. Cyclostratigraphy concepts, definitions, and applications. *Newsletters on Stratigraphy*, **42**: 75-114. doi:10.1127/0078-0421/2006/0042-0075.

Sturzenegger, M., Yan, M., Stead, D., and Elmo, D. Application and limitations of ground-based laser scanning in rock slope characterization. *In* 1st Canada-US Rock Mechanics Symposium. Vancouver, BC 2007, pp. 29-36.

Sun, J., and Huang, X. 2006. Half-precessional cycles recorded in Chinese loess: response to low-latitude insolation forcing during the Last Interglaciation. *Quaternary Science Reviews*, **25**: 1065-1072. doi:10.1016/j.quascirev.2005.08.004.

Svensen, H.H., Torsvik, T.H., Callegaro, S., Augland, L., Heimdal, T.H., Jerram, D.A., Planke, S., and Pereira, E. 2018. Gondwana Large Igneous Provinces: plate reconstructions, volcanic basins and sill volumes. Geological Society, London, Special Publications, **463**: 17-40. doi:10.1144/sp463.7.

Szymczyk, M., and Szymczyk, P. 2013. Preprocessing of GPR data. *Image Processing and Communications*, **18**: 83-90. doi:10.2478/v10248-012-0082-3.

Tanner, L.H. 2013. A Pennsylvanian Tetrapod Trackway from Joggins, Nova Scotia: The Size Continuum of *Batrachichnus Salamandroides*. *In* The Carboniferous-Permian Transition: Bulletin 60. Edited by S.G. Lucas and W.A. DiMichele and J.E. Barrick and J.W. Schneider and J.A. Spielmann. New Mexico Museum of Natural History and Science, Albuquerque, New Mexico. pp. 427-433.

Tanyel, E.D. 2006. Formation evaluation using wavelet analysis on logs of the Chinji and Nagri Formations, northern Pakistan. Texas A&M University.

Tape, C.H., Cowan, C.A., and Runkel, A.C. 2003. Tidal-Bundle Sequences in the Jordan Sandstone (Upper Cambrian), Southeastern Minnesota, U.S.A.: Evidence for Tides Along Inboard Shorelines of the Sauk Epicontinental Sea. *Journal of Sedimentary Research*, **73**: 354-366. doi:10.1306/091602730354.

Tatum, D.I., and Francke, J. 2012. Constructing hydrocarbon reservoir analogues of aeolian systems using ground penetrating radar. *Journal of Applied Geophysics*, **81**: 21-28. doi:10.1016/j.jappgeo.2011.09.014.

Teedumae, A., Heldur, N., and Kallaste, T. Sedimentary cyclicality and dolomitization of the Raikkiila Formation in the Nurme drill core (Silurian, Estonia). *In Proceedings of the Estonian Academy of Sciences, Geology*. 2004. *Edited by* H. Aben and V. Kurnitski. Estonian Academy Publishers. Vol. 53, pp. 42-62.

Tessier, B. 1990. Enregistrement des cycles Tidaux en accretion verticale dans un milieu actuel (la Baie du Mont Saint Michel) et dans une formation ancienne (la molasse marine miocène du bassin de Digne): mesure du temps et application à la reconstitution des paléoenvironnements. Université de Caen.

Tessier, B., and Gigot, P. 1989. A vertical record of different tidal cyclicities: an example from the Miocene Marine Molasse of Digne (Haute Provence, France). *Sedimentology*, **36**: 767-776. doi:10.1111/j.1365-3091.1989.tb01745.x.

Tessier, B., Archer, A.W., Lanier, W.P., and Feldman, H.R. 1995. Comparison of ancient tidal rhythmites (Carboniferous of Kansas and Indiana, USA) with modern analogues. *In Tidal Signatures in Modern and Ancient Sediments*. *Edited by* B.W. Flemming and A. Bartholoma. Wiley-Blackwell, Oxford, UK. pp. 259-271.

The Australian Museum. 2020. Decomposition - Body Changes. Available from <https://australian.museum/about/history/exhibitions/death-the-last-taboo/decomposition-body-changes/2020>].

Thomas, A.M., Rogers, C.D.F., Chapman, D.N., Metje, N., and Castle, J. 2009. Stakeholder needs for ground penetrating radar utility location. *Journal of Applied Geophysics*, **67**: 345-351. doi:10.1016/j.jappgeo.2008.07.006.

Tibert, N.E., and Dewey, C.P. 2006. Velatomorpha, a new healdioidean ostracode genus from the early Pennsylvanian Joggins Formation, Nova Scotia, Canada. *Micropaleontology*, **52**: 51-66. doi:10.2113/gsmicropal.52.1.51.

Tibert, N.E., Rygel, M.C., Sanders, S.C., Elrick, S.D., and Nelson, J. 2013. Temporal and spatial distribution of ostracodes across the Pennsylvanian–Permian boundary interval in eastern North America. *International Journal of Coal Geology*, **119**: 93-105. doi:10.1016/j.coal.2013.08.002.

- Timmer, E.R., Gingras, M.K., Morin, M.L., Ranger, M.J., and Zonneveld, J.P. 2016. Laminae-scale rhythmicity of inclined heterolithic stratification, Lower Cretaceous McMurray Formation, NE Alberta, Canada. *Bulletin of Canadian Petroleum Geology*, **64**: 199-217. doi:10.2113/gscpgbull.64.2.199.
- Torabi, A. 2012. Heterogeneity within deformation bands in sandstone reservoirs. *In* 46th US Rock Mechanics / Geomechanics Symposium, Chicago, Il.
- Torrence, C., and Compo, G.P. 1998. A Practical Guide to Wavelet Analysis. *Bulletin of the American Meteorological society*, **79**: 61-78. doi:10.1175/1520-0477(1998)079<0061:Apgtwa>2.0.Co;2.
- Tucker, M.E., Gallagher, J., and Leng, M.J. 2009. Are beds in shelf carbonates millennial-scale cycles? An example from the mid-Carboniferous of northern England.... *Sedimentary Geology*, **214**: 19-34. doi:10.1016/j.sedgeo.2008.03.011.
- Udden, J.A. 1912. Geology and mineral resources of the Peoria quadrangle, Illinois. U.S. Geological Survey Bulletin 506: 1-103.
- Uhlir, D.M., Akers, A., and Vondra, C.F. 1988. Tidal inlet sequence, Sundance Formation (Upper Jurassic), north-central Wyoming. *Sedimentology*, **35**: 739-752. doi:10.1111/j.1365-3091.1988.tb01248.x.
- UNESCO. 2008. World Heritage List - Joggins Fossil Cliffs. Available from whc.unesco.org/en/list/1285/ [accessed September 6 2018].
- Utting, J., Giles, P.S., and Dolby, G. 2010. Palynostratigraphy of Mississippian and Pennsylvanian rocks, Joggins area, Nova Scotia and New Brunswick, Canada. *Palynology*, **34**: 43-89. doi:10.1080/01916121003620569.
- Valdes, P.J., Sellwood, B.W., and Price, G.D. 1995. Modelling Late Jurassic Milankovitch climate variations. *In* *Orbital Forcing Timescales and Cyclostratigraphy*. Edited by M.R. House and A.S. Gale. The Geological Society, London, UK. pp. 115-132.
- van den Belt, F.J.G., van Hoof, T.B., and Pagnier, H.J.M. 2015. Revealing the hidden Milankovitch record from Pennsylvanian cyclothem successions and implications regarding late Paleozoic chronology and terrestrial-carbon (coal) storage. *Geosphere*, **11**: 1062-1076. doi:10.1130/ges01177.1.

van Lanen, X.M., Hodgetts, D., Redfern, J., and Fabuel-Perez, I. 2009. Applications of digital outcrop models: two fluvial case studies from the Triassic Wolfville Fm., Canada and Oukaimeden Sandstone Fm., Morocco. *Geological Journal*, **44**: 742-760. doi: 10.1002/gj.1196.

Van Sickle, J. 2015. *GPS for Land Surveyors*. CRC Press.

Vandenbergh, J., and Van Overmeeren, R. 1999. Ground penetrating radar images of selected fluvial deposits in the Netherlands. *Sedimentary Geology*, **128**: 245-270. doi:10.1016/S0037-0738(99)00072-X.

Varela-Ortiz, W., Cintrón, C.Y.L., Velázquez, G.I., and Stanton, T.R. 2013. Load testing and GPR assessment for concrete bridges on military installations. *Construction and Building Materials*, **38**: 1255-1269. doi:10.1016/j.conbuildmat.2010.09.044.

Vaughan, D.G., Corr, H.F.J., Doake, C.S.M., and Waddington, E.D. 1999. Distortion of isochronous layers in ice revealed by ground-penetrating radar. *Nature*, **398**: 323-326. doi:10.1038/18653.

Veevers, J.J., and Powell, C.M. 1987. Late Paleozoic glacial episodes in Gondwanaland reflected in transgressive-regressive depositional sequences in Euramerica. *Geological Society of America Bulletin*, **98**: 475-487. doi:10.1130/0016-7606(1987)98<475:Lpgeig>2.0.Co;2.

Venkateswarlu, B., and Tewari, V.C. 2014. Geotechnical applications of ground penetrating radar (gpr). *Jour. Ind. Geol. Cong*, **6**: 35-46.

Visser, M.J. 1980. Neap-spring cycles reflected in Holocene subtidal large-scale bedform deposits: A preliminary note. *Geology*, **8**: 543-546. doi:10.1130/0091-7613(1980)8<543:Ncrihs>2.0.Co;2.

Wach, G.D. 1991. *Sedimentology and Stratigraphy of the Lower Cretaceous of the Channel Basin*. Department of Earth Sciences, University of Oxford, Oxford, UK.

Waldron, J.W.F., and Rygel, M.C. 2005. Role of evaporite withdrawal in the preservation of a unique coal-bearing succession: Pennsylvanian Joggins Formation, Nova Scotia. *Geology*, **33**: 337-340. doi:10.1130/g21302.1.

Waldron, J.W.F., Rygel, M.C., Gibling, M.R., and Calder, J.H. 2013. Evaporite tectonics and the late Paleozoic stratigraphic development of the Cumberland basin, Appalachians of Atlantic Canada. *Geological Society of America Bulletin*, **125**: 945-960. doi:10.1130/b30718.1.

Waltham, D. 2015. Milankovitch period uncertainties and their impact on cyclostratigraphy. *Journal of Sedimentary Research*, **85**: 990-998. doi:10.2110/jsr.2015.66.

Wang, J., Bai, C., Xu, Y., and Bai, S. 2010. Tidal Couplet Formation and Preservation, and Criteria for Discriminating Storm-Surge Sedimentation on the Tidal Flats of Central Jiangsu Province, China. *Journal of Coastal Research*, **2010**: 976-981. doi:10.2112/jcoastres-d-09-00166.1.

Wanless, H.R., and Shepard, F.P. 1936. Sea level and climatic changes related to late Paleozoic cycles. *Geological Society of America Bulletin*, **47**: 1177-1206. doi:10.1130/gsab-47-1177.

Waters, C., and Davies, S. 2006. Carboniferous: extensional basins, advancing deltas and coal swamps. In: *The geology of England and Wales*/edited by PJ Brenchley and PF Rawson. London: Geological Society of London, **2006**: 173-223. doi:10.1144/GOEWP.9.

Weimer, R.J., and Tillman, R.W. 1980. Tectonic influence on deltaic shoreline facies, Fox Hills Sandstone, West-central Denver Basin. *Professional Contributions of the Colorado School of Mines*. Colorado School of Mines, Golden, CO.

Weller, J.M. 1930. Cyclical Sedimentation of the Pennsylvanian Period and Its Significance. *The Journal of Geology*, **38**: 97-135. doi:10.1086/623695.

Wells, M.R., Allison, P.A., Hampson, G.J., Piggott, M.D., and Pain, C.C. 2005a. Modelling ancient tides: the Upper Carboniferous epi-continental seaway of Northwest Europe. *Sedimentology*, **52**: 715-735. doi:10.1111/j.1365-3091.2005.00718.x.

Wells, M.R., Allison, P.A., Piggott, M.D., Pain, C.C., Hampson, G.J., and De Oliveira, C.R.E. 2005b. Large sea, small tides: the Late Carboniferous seaway of NW Europe. *Journal of the Geological Society*, **162**: 417-420.

Westphal, H., Head, M.J., and Munnecke, A. 2000. Differential Diagenesis of Rhythmic Limestone Alternations Supported by Palynological Evidence. *Journal of Sedimentary Research*, **70**: 715-725. doi:10.1306/2dc40932-0e47-11d7-8643000102c1865d.

Wilkinson, B.E., Mohamed, A.H., Dewitt, B.A., and Seedahmed, G.H. 2010. A novel approach to terrestrial LiDAR georeferencing. *Photogrammetric Engineering & Remote Sensing*, **76**: 683-690. doi:10.14358/PERS.76.6.683.

Williams, G.E. 1989. Precambrian tidal sedimentary cycles and Earth's paleorotation. *Eos, Transactions American Geophysical Union*, **70**: 33-41. doi:10.1029/89eo00012.

Williams, G.E. 2000. Geological constraints on the Precambrian history of Earth's rotation and the Moon's orbit. *Reviews of Geophysics*, **38**: 37-59. doi:10.1029/1999rg900016.

Williams, G.E. 2004. Earth's Precambrian rotation and the evolving lunar orbit: Implications of tidal rhythmite data for palaeogeophysics. *In The Precambrian Earth: Tempos and Events*. Elsevier, Amsterdam. *Edited by* P.G. Eriksson and W. Altermann and D.R. Nelson and W.U. Mueller and O. Catuneanu. Elsevier Science, The Netherlands. pp. 473-482.

Williams, H. 1984. Miogeoclines and suspect terranes of the Caledonian–Appalachian Orogen: tectonic patterns in the North Atlantic region. *Canadian Journal of Earth Sciences*, **21**: 887-901. doi:10.1139/e84-095.

Willis, K.J., Kleczkowski, A., Briggs, K.M., and Gilligan, C.A. 1999. The role of sub-milankovitch climatic forcing in the initiation of the northern hemisphere glaciation. *Science*, **285**: 568-571. doi:10.1126/science.285.5427.568.

Wong, C. 2014. Lidar survey of the Joggins Formation in the Coal Mine Point section, Cumberland Basin (Nova Scotia, Canada). BSc Thesis, Department of Earth Sciences, Dalhousie University, Halifax, Nova Scotia.

Wonik, T. 2001. Gamma-ray measurements in the Kirchrode I and II boreholes. *Palaeogeography, Palaeoclimatology, Palaeoecology*, **174**: 97-105. doi:10.1016/s0031-0182(01)00288-7.

Wu, B.-T., Li, P.-C., Chen, J.-H., Li, Y.-J., and Fan, Y.-C. 3D Environment Detection Using Multi-View Color Images and LiDAR Point Clouds. *In 2018 IEEE International Conference on Consumer Electronics-Taiwan (ICCE-TW)*. 2018. IEEE, pp. 1-2.

Wu, H., Zhang, S., Feng, Q., Jiang, G., Li, H., and Yang, T. 2012. Milankovitch and sub-Milankovitch cycles of the early Triassic Daye Formation, South China and their geochronological and paleoclimatic implications. *Gondwana Research*, **22**: 748-759. doi:10.1016/j.gr.2011.12.003.

Wu, H., Zhang, S., Hinnov, L.A., Jiang, G., Feng, Q., Li, H., and Yang, T. 2013. Time-calibrated Milankovitch cycles for the late Permian. *Nat Commun*, **4**: 2452. doi:10.1038/ncomms3452.

Wu, H., Zhang, S., Hinnov, L.A., Jiang, G., Yang, T., Li, H., Wan, X., and Wang, C. 2014. Cyclostratigraphy and orbital tuning of the terrestrial upper Santonian–Lower Danian in Songliao Basin, northeastern China. *Earth and Planetary Science Letters*, **407**: 82-95. doi:10.1016/j.epsl.2014.09.038.

Xharde, R., Long, B.F., and Forbes, D.L. 2006. Accuracy and limitations of airborne LiDAR surveys in coastal environments. *In International Geoscience and Remote Sensing Symposium*, Denver, CO. pp. 2412-2415.

Yelf, R.J. 2007. Application of ground penetrating radar to civil and geotechnical engineering. *Electromagnetic Phenomena*, **7**: 18.

Yeste, L.M., Henares, S., McDougall, N., García-García, F., and Viseras, C. 2019. Towards the multi-scale characterization of braided fluvial geobodies from outcrop, core, ground-penetrating radar and well log data. *In River to Reservoir: Geoscience to Engineering*. Edited by P.W.M. Corbett and A. Owen and A.J. Hartley and S. Pla-Pueyo and D. Barreto and C. Hackney and S.J. Kape. The Geological Society of London, London, UK. pp. 73-95.

Yiou, P., Genthon, C., Ghil, M., Jouzel, J., Le Treut, H., Barnola, J.M., Lorius, C., and Korotkevitch, Y.N. 1991. High-frequency paleovariability in climate and CO₂ levels from Vostok Ice Core Records. *Journal of Geophysical Research: Solid Earth*, **96**: 20365-20378. doi:10.1029/91jb00422.

Yoder, R.E., Freeland, R.S., Ammons, J.T., and Leonard, L.L. 2001. Mapping agricultural fields with GPR and EMI to identify offsite movement of agrochemicals. *Journal of Applied Geophysics*, **47**: 251-259.

Yoon, S., Wang, Q., and Sohn, H. Optimal Placement of Precast Bridge Deck Slabs with respect to Precast Girders using LiDAR. *In 34th International Symposium on Automation and Robotics in Construction (ISARC 2017)*. 2017. Vilnius Gediminas Technical University, Department of Construction Economics. Vol. 34, pp. 879-886.

Yu, J.-f., Sui, F.-g., Li, Z.-x., Liu, H., and Wang, Y.-l. 2008. Recognition of Milankovitch cycles in the stratigraphic record: application of the CWT and the FFT to well-log data. *Journal of China University of Mining and Technology*, **18**: 594-598. doi:10.1016/s1006-1266(08)60301-6.

Yuan, X., Guo, Y., Yu, J., Shen, Y., and Shao, Y. 2013. Correlation and analysis of well-log sequence with Milankovitch cycles as rulers: A case study of coal-bearing strata of late Permian in western Guizhou. *International Journal of Mining Science and Technology*, **23**: 563-568. doi:10.1016/j.ijmst.2013.07.015.

Zatoń, M., Grey, M., and Vinn, O. 2014. Microconchid tubeworms (Class Tentaculita) from the Joggins Formation (Pennsylvanian), Nova Scotia, Canada. *Canadian Journal of Earth Sciences*, **51**: 669-676. doi:10.1139/cjes-2014-0061.

Zeng, Q., Lu, W., Zhang, R., Zhao, J., Ren, P., and Wang, B. 2018. LIDAR-based fracture characterization and controlling factors analysis: An outcrop case from Kuqa Depression, NW China. *Journal of Petroleum Science and Engineering*, **161**: 445-457. doi:10.1016/j.petrol.2017.12.002.

Zenone, T., Morelli, G., Teobaldelli, M., Fischanger, F., Matteucci, M., Sordini, M., Armani, A., Ferrè, C., Chiti, T., and Seufert, G. 2008. Preliminary use of ground-penetrating radar and electrical resistivity tomography to study tree roots in pine forests and poplar plantations. *Functional Plant Biology*, **35**: 1047-1058. doi:10.1071/FP08062.

Zhang, Y., and Shen, X. 2013. Direct georeferencing of airborne LiDAR data in national coordinates. *ISPRS Journal of Photogrammetry and Remote Sensing*, **84**: 43-51. doi:10.1016/j.isprsjprs.2013.07.003.

Zuhlke, R. 2004. Integrated cyclostratigraphy of a model Mesozoic carbonate platform—the Latemar (Middle Triassic, Italy). *In Cyclostratigraphy: Approaches and Case Histories - SEPM Special Publication No. 81. Edited by B. D'Argenio, Fischer, A.G., Premoli Silva, I., Weissert, H., Ferreri, V.* pp. 183-211.

Zuhlke, R., Bechstadt, T., and Mundil, R. 2003. Sub-Milankovitch and Milankovitch forcing on a model Mesozoic carbonate platform - the Latemar (Middle Triassic, Italy). *Terra Nova*, **15**: 69-80. doi:10.1046/j.1365-3121.2003.00366.x.

Appendix A: Copyright Release Letters and Responses

Letter to the Canadian Journal of Earth Sciences

May 24, 2022

**Canadian Journal of Earth Sciences
1840 Woodward Drive, Suite 1
Ottawa, Ontario, Canada K2C 0P7**

I am preparing my Ph.D. dissertation for submission to the Faculty of Graduate Studies at Dalhousie University, Halifax, Nova Scotia, Canada. I am seeking your permission to include a manuscript version of the following paper as a chapter in the dissertation:

Kelly, T.B. and Wach, G.D. 2020. Analysis of factors influencing the interpretation of a digitally examined fluvial meanderbelt system: Joggins Formation, Nova Scotia. *Canadian Journal of Earth Sciences* 57(4), 524-541. doi:10.1139/cjes-2018-0263.

Canadian graduate theses are collected and stored online by the Library and Archives of Canada. I am also seeking your permission for the material described above to be stored online with the LAC. Further details about the LAC dissertation program are available on the LAC website (www.bac-lac.gc.ca).

Full publication details and a copy of this permission letter will be included in the dissertation.

Yours sincerely,

A solid black rectangular box redacting the signature of Trevor Kelly.

Trevor Kelly

Response from the Canadian Journal of Earth Sciences



This is a License Agreement between Trevor Kelly/Dalhousie University ("User") and Copyright Clearance Center, Inc. ("CCC") on behalf of the Rightsholder identified in the order details below. The license consists of the order details, the Marketplace Order General Terms and Conditions below, and any Rightsholder Terms and Conditions which are included below.

All payments must be made in full to CCC in accordance with the Marketplace Order General Terms and Conditions below.

Order Date	22-Jun-2022	Type of Use	Republish in a thesis/dissertation
Order License ID	1239584-1	Publisher	Canadian Science Publishing
ISSN	1480-3313	Portion	Chapter/article

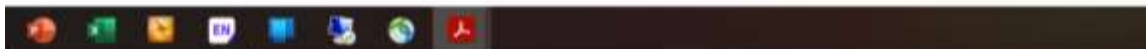
LICENSED CONTENT

Publication Title	Canadian journal of earth sciences : Revue canadienne des sciences de terre	Publication Type	e-journal
Article Title	Analysis of Factors Influencing the Interpretation of a Digitally Examined Fluvial Meanderbelt System: Joggins Formation, Nova Scotia	Start Page	524
Date	01/01/1998	End Page	541
Language	English, English, French	Issue	4
Country	Canada	Volume	57
Rightsholder	Canadian Science Publishing	URL	http://pubs.nrc-cnrc.gc.ca/cgi-bin/rp/rp2%5Fdesc%5Fe?cjes

REQUEST DETAILS

Portion Type	Chapter/article	Rights Requested	Main product
Page range(s)	524-541	Distribution	Canada
Total number of pages	18	Translation	Original language of publication
Format (select all that apply)	Print, Electronic	Copies for the disabled?	No
Who will republish the content?	Academic institution	Minor editing privileges?	Yes
Duration of Use	Life of current and all future editions	Incidental promotional use?	No
Lifetime Unit Quantity	Up to 499	Currency	CAD

NEW WORK DETAILS



Title	Subsurface and outcrop analysis of the Carboniferous Joggins Formation, Nova Scotia, Atlantic Canada: New insights into sedimentology and reservoir characteristics	Institution name	Dalhousie University
Instructor name	Dr. Grant Wach	Expected presentation date	2022-08-17

ADDITIONAL DETAILS

Order reference number	N/A	The requesting person / organization to appear on the license	Trevor Kelly/Dalhousie University
-------------------------------	-----	--	-----------------------------------

REUSE CONTENT DETAILS

Title, description or numeric reference of the portion(s)	Analysis of Factors Influencing the Interpretation of a Digitally Examined Fluvial Meanderbelt System: Joggins Formation, Nova Scotia	Title of the article/chapter the portion is from	Analysis of Factors Influencing the Interpretation of a Digitally Examined Fluvial Meanderbelt System: Joggins Formation, Nova Scotia
Editor of portion(s)	Wach, Grant; Kelly, Trevor Brian	Author of portion(s)	Wach, Grant; Kelly, Trevor Brian
Volume of serial or monograph	57	Issue, if republishing an article from a serial	4
Page or page range of portion	524-541	Publication date of portion	2019-08-13

Letter to the American Institute of Mathematical Sciences (AIMS) – Geosciences Journal

May 24, 2022

**American Institute of Mathematical Sciences (AIMS) – Geosciences
AIMS Press
P.O. Box 2604
Springfield, MO 65801-2604, USA**

I am preparing my Ph.D. dissertation for submission to the Faculty of Graduate Studies at Dalhousie University, Halifax, Nova Scotia, Canada. I am seeking your permission to include a manuscript version of the following paper as a chapter in the dissertation:

Kelly, T.B., Wach, G.D., and O'Connor, D.E. 2021. The technical challenges and outcomes of ground-penetrating radar: A site-specific example from Joggins, Nova Scotia. AIMS Geosciences 7(1), 22-55. doi: 10.3934/geosci.2021002.

Canadian graduate theses are collected and stored online by the Library and Archives of Canada. I am also seeking your permission for the material described above to be stored online with the LAC. Further details about the LAC dissertation program are available on the LAC website (www.bac-lac.gc.ca).

Full publication details and a copy of this permission letter will be included in the dissertation.

Yours sincerely,



Trevor Kelly

Response from the American Institute of Mathematical Sciences (AIMS) – Geosciences Journal

Re: Permission to include article in a Ph.D. thesis

geosciences@aimspress.org <geosciences@aimspress.org>

Wed 2022-05-25 3:04 AM

To: Trevor Kelly <tbkelly@dal.ca>

CAUTION: The Sender of this email is not from within Dalhousie.

Dear Dr. Kelly,

Thanks for your kind email.

Yes, the articles are Open Access under the Creative Commons Attribution License.

Under this license, authors retain ownership of the copyright for their content, and anyone can copy, distribute, or reuse these articles, as long as the author and original source are properly cited.

Please consider our journal as your publishing venue once you have feature work to be published.

We are willing to waive the publishing fee for you.

I wish you and your family all the best.

Kind regards,



AIMS Geosciences

E-mail: geosciences@aimspress.org

Website: <https://www.aimspress.com/>

Letter to the Forensic Science International journal

May 24, 2022

**Forensic Science International
Elsevier Canada Ltd (Corporate Office)
111 Gordon Baker Road, Suite 900
North York, ON M2H 3R1**

I am preparing my Ph.D. dissertation for submission to the Faculty of Graduate Studies at Dalhousie University, Halifax, Nova Scotia, Canada. I am seeking your permission to include a manuscript version of the following paper as a chapter in the dissertation:

Kelly, T.B., Angel, M.N., O'Connor, D.E., Huff, C.C., Morris, L.E., and Wach, G.D. 2021. A novel approach to 3D modelling ground-penetrating radar (GPR) data—A case study of a cemetery and applications for criminal investigation. *Forensic science international*, 325. doi:10.1016/j.forsciint.2021.110882.

Canadian graduate theses are collected and stored online by the Library and Archives of Canada. I am also seeking your permission for the material described above to be stored online with the LAC. Further details about the LAC dissertation program are available on the LAC website (www.bac-lac.gc.ca).

Full publication details and a copy of this permission letter will be included in the dissertation.

Yours sincerely,

A black rectangular redaction box covering the signature of Trevor Kelly.

Trevor Kelly

Response from the Forensic Science International journal

Re: Copyright permission for article inclusion in thesis [220524-016967]

Permissions Helpdesk <permissionshelpdesk@elsevier.com>

Wed 2022-05-25 10:30 AM

To: Trevor Kelly <tbkelly@dal.ca>

CAUTION: The Sender of this email is not from within Dalhousie.


Dear Trevor Kelly,

Thank you for your query.

This article is available under the terms of the [Creative Commons Attribution License \(CC BY\)](#). You may copy and distribute the article, create extracts, abstracts and new works from the article, alter and revise the article, text or data mine the article and otherwise reuse the article commercially (including reuse and/or resale of the article) without permission from Elsevier. You must give appropriate credit to the original work, together with a link to the formal publication through the relevant DOI and a link to the Creative Commons user license above. You must indicate if any changes are made but not in any way that suggests the licensor endorses you or your use of the work.

Permission is not required for this type of reuse.

Kind regards,


Copyrights Coordinator
ELSEVIER | HCM - Health Content Management

Visit [Elsevier Permissions](#)

Letter to the Modern Environmental Science and Engineering journal

May 24, 2022

**Modern Environmental Science and Engineering
Academic Star Publishing Company
228 East 45th Street, Ground Floor #CN00000267
New York, NY 10017, USA**

I am preparing my Ph.D. dissertation for submission to the Faculty of Graduate Studies at Dalhousie University, Halifax, Nova Scotia, Canada. I am seeking your permission to include a manuscript version of the following paper as a chapter in the dissertation:

Kelly, T.B., Wach, G.D., and O'Connor, D.E. 2020. Post-Scan Georeferencing of LiDAR Data from a Geological Exposure using ArcGIS™ for Adjustment. *Modern Environmental Science and Engineering* 6(6). doi: 10.15341/mese(2333-2581)/06.06.2020/001.

Canadian graduate theses are collected and stored online by the Library and Archives of Canada. I am also seeking your permission for the material described above to be stored online with the LAC. Further details about the LAC dissertation program are available on the LAC website (www.bac-lac.gc.ca).

Full publication details and a copy of this permission letter will be included in the dissertation.

Yours sincerely,

A solid black rectangular box redacting the signature of Trevor Kelly.

Trevor Kelly

Response from the Modern Environmental Science and Engineering journal



service@academicstar.us

To: Trevor Kelly



Fri 2022-06-10 8:19 PM

CAUTION: The Sender of this email is not from within Dalhousie.

Dear Trevor Kelly,

Glad to hear from you. You can include it in your thesis.

Best regards,



service@academicstar.us



Appendix B: Processed Radargrams Supporting Chapter 4 – GPR Geoforensic Study

The following images are the processed radargrams of the individual lines collected from the GPR survey documented in Chapter 4.

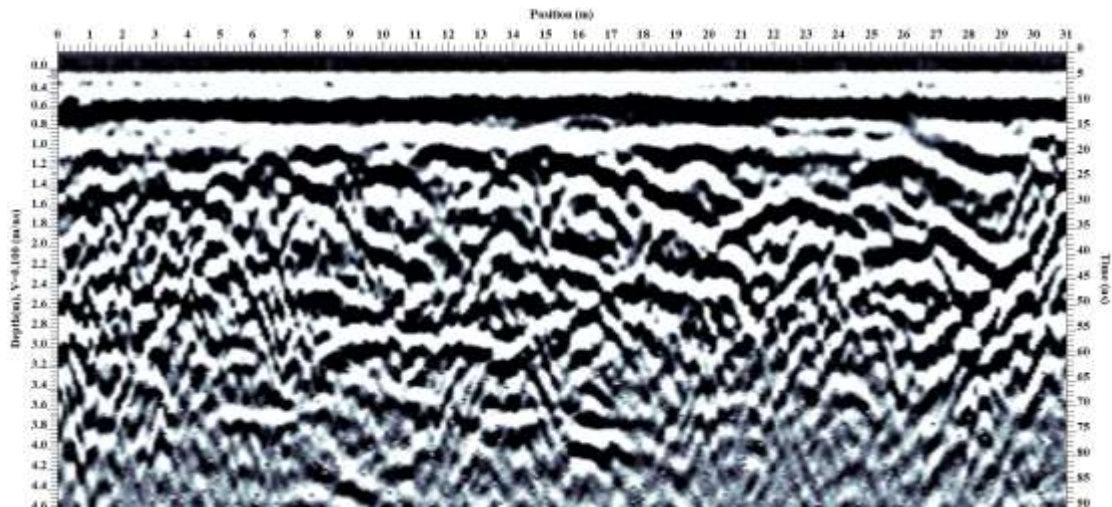


Figure B1: Processed radargram of Line 06.

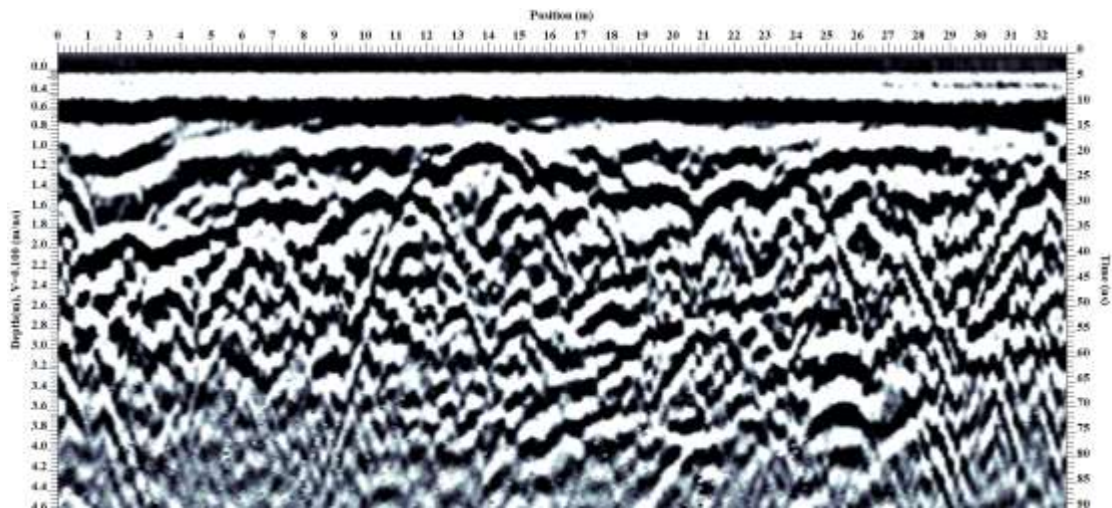


Figure B2: Processed radargram of Line 07.

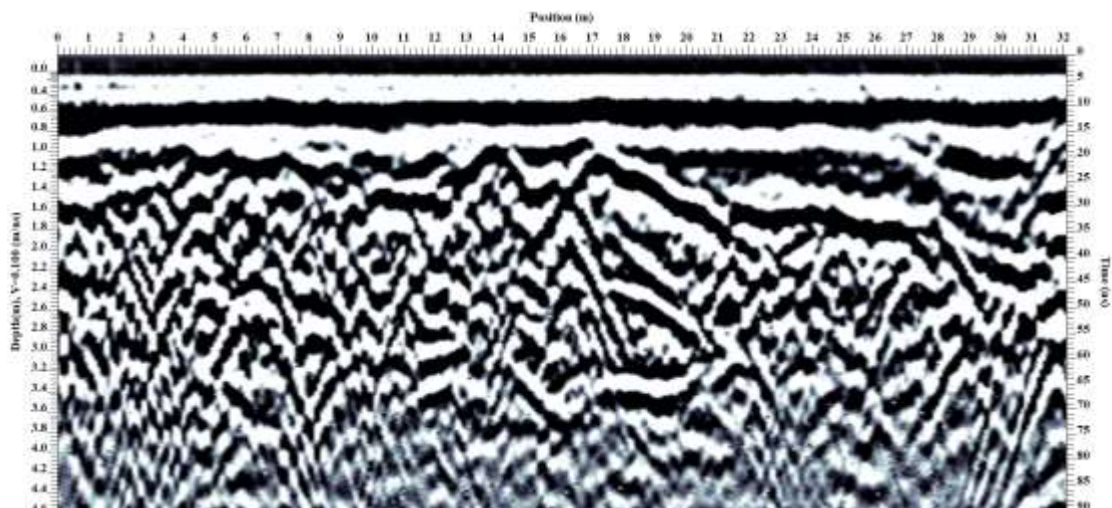


Figure B3: Processed radargram of Line 08.

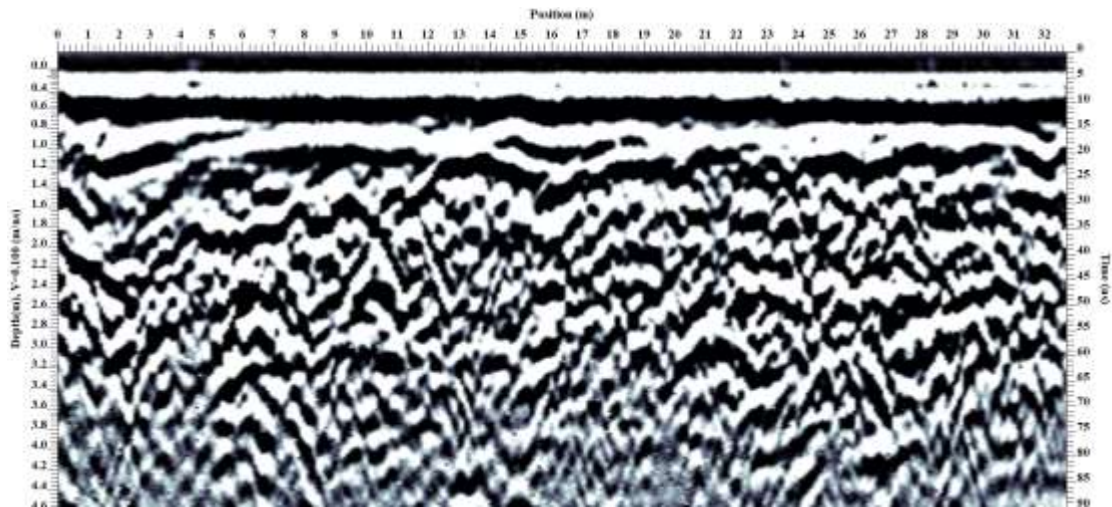


Figure B4: Processed radargram of Line 09.

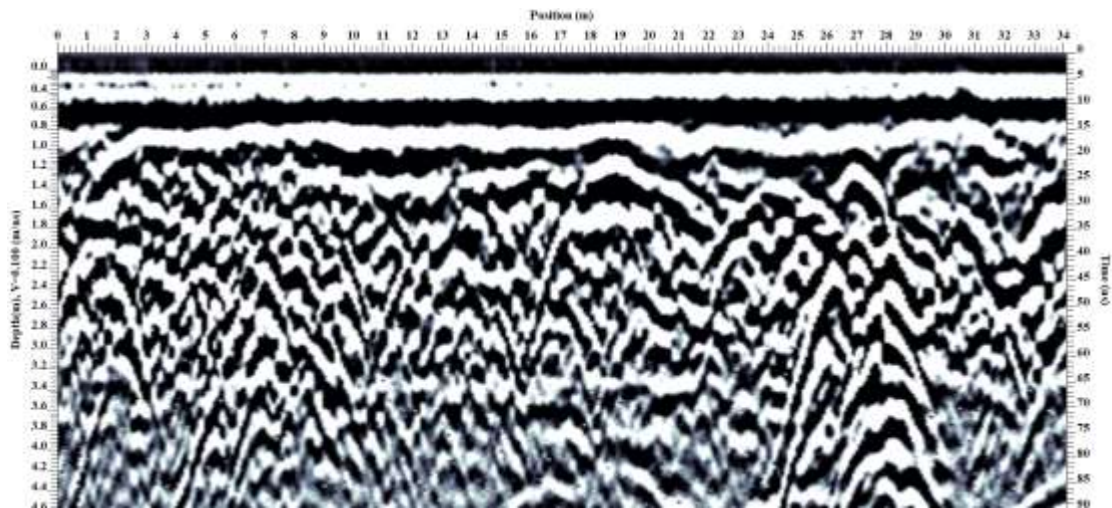


Figure B5: Processed radargram of Line 10.

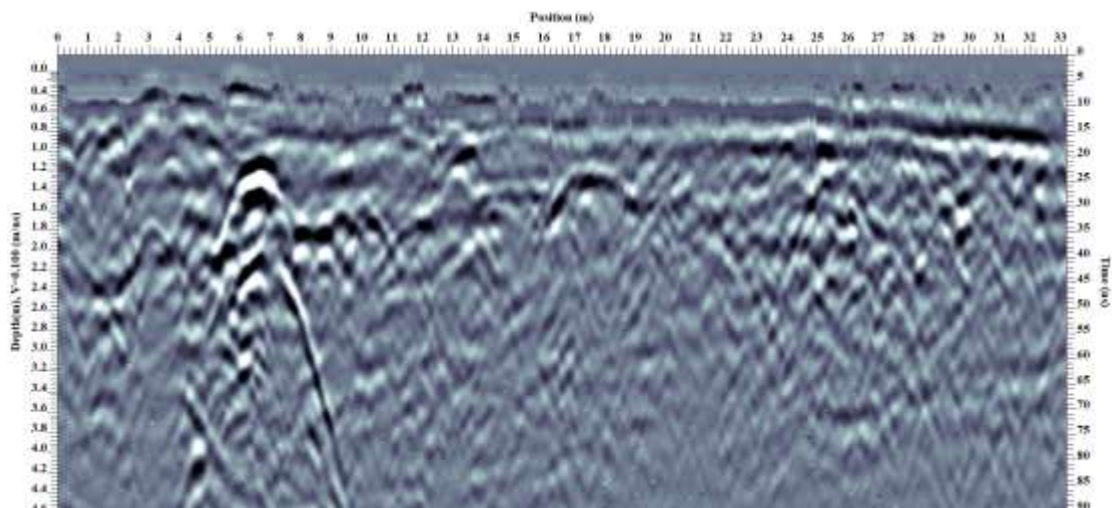


Figure B6: Processed radargram of Line 11.

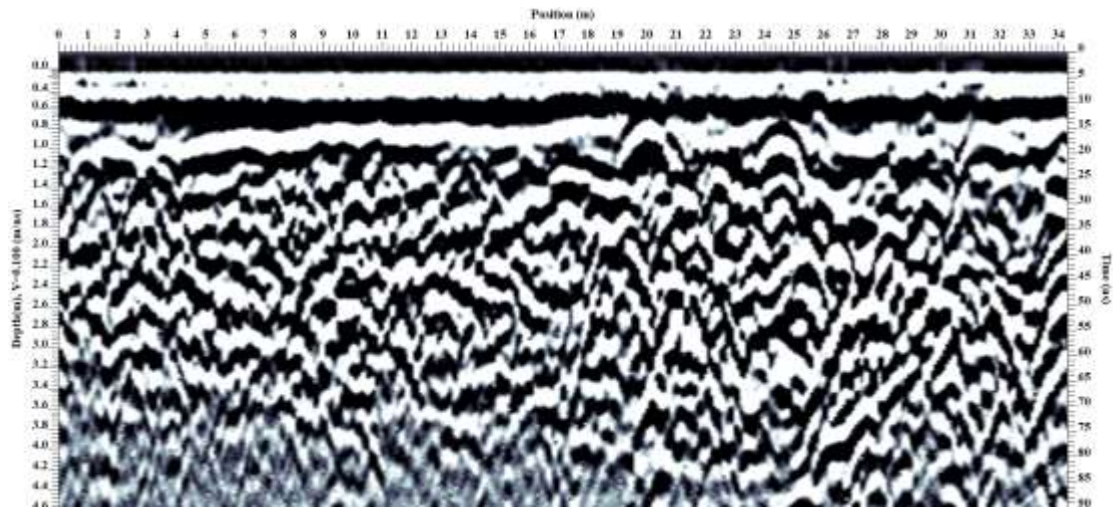


Figure B7: Processed radargram of Line 12.

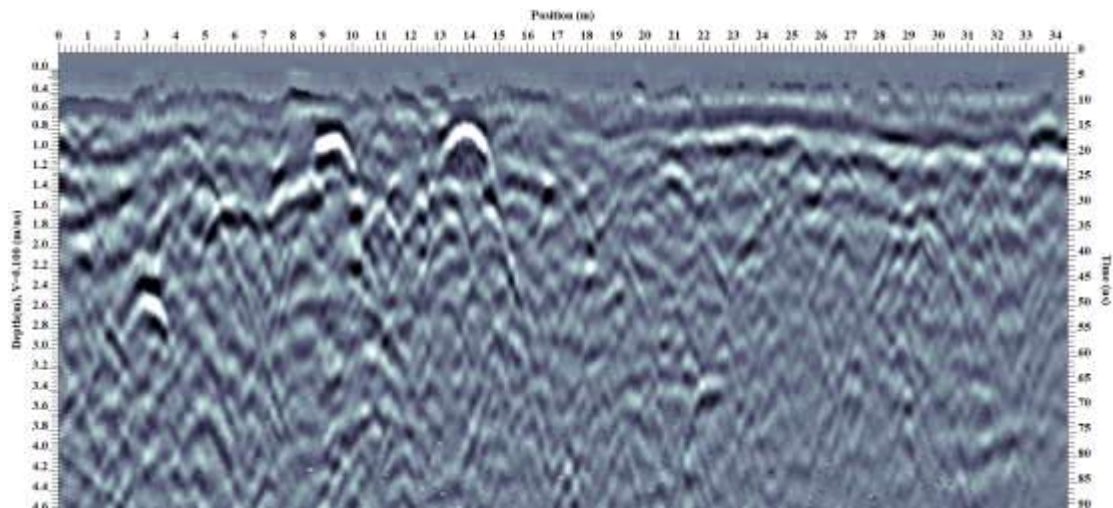


Figure B8: Processed radargram of Line 13.

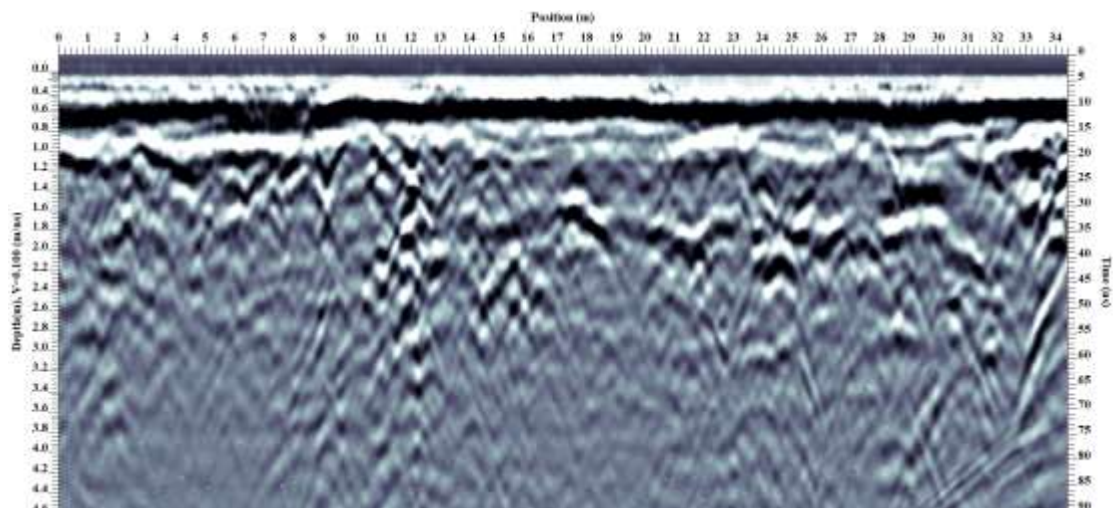


Figure B9: Processed radargram of Line 14.

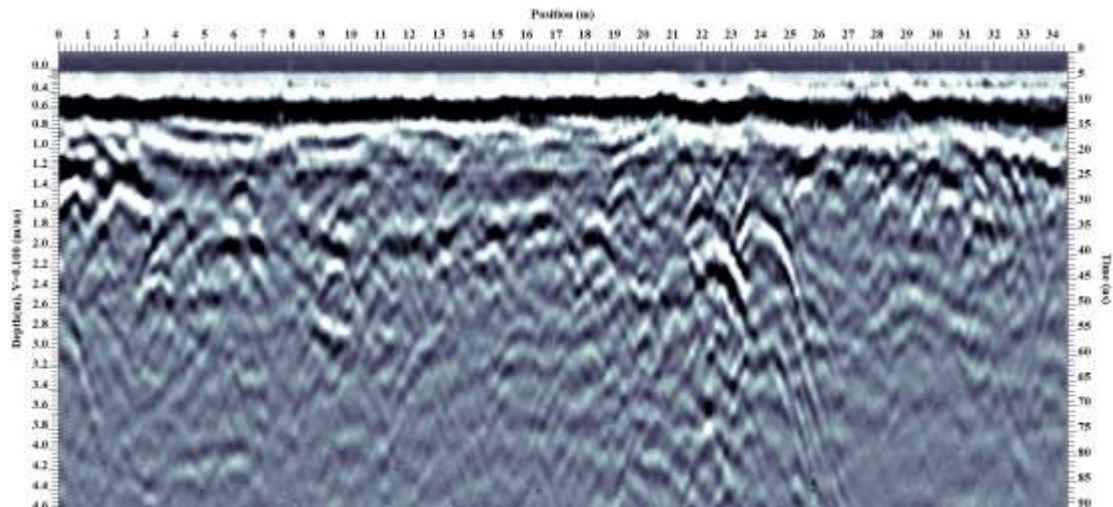


Figure B10: Processed radargram of Line 15.

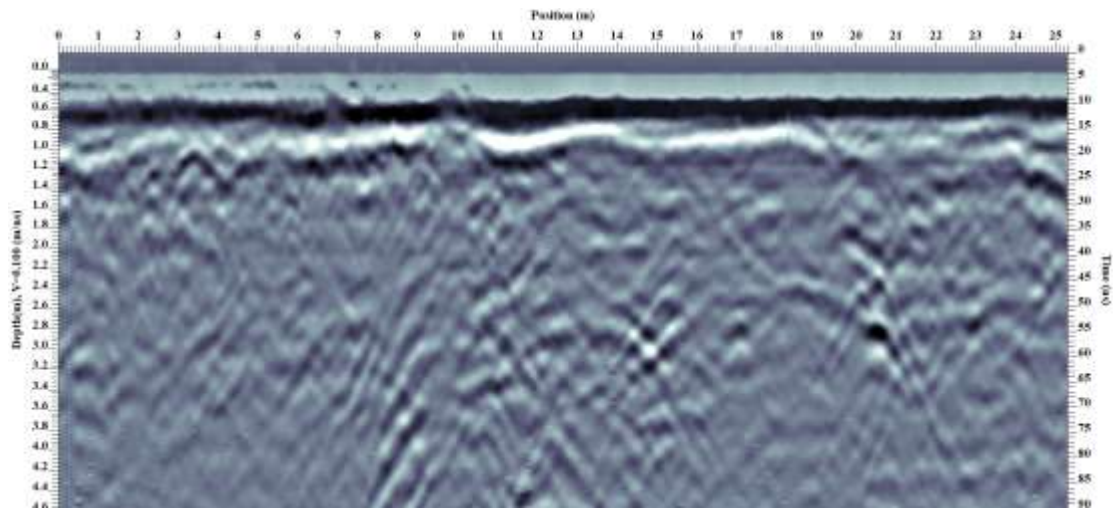


Figure B11: Processed radargram of Line 16.

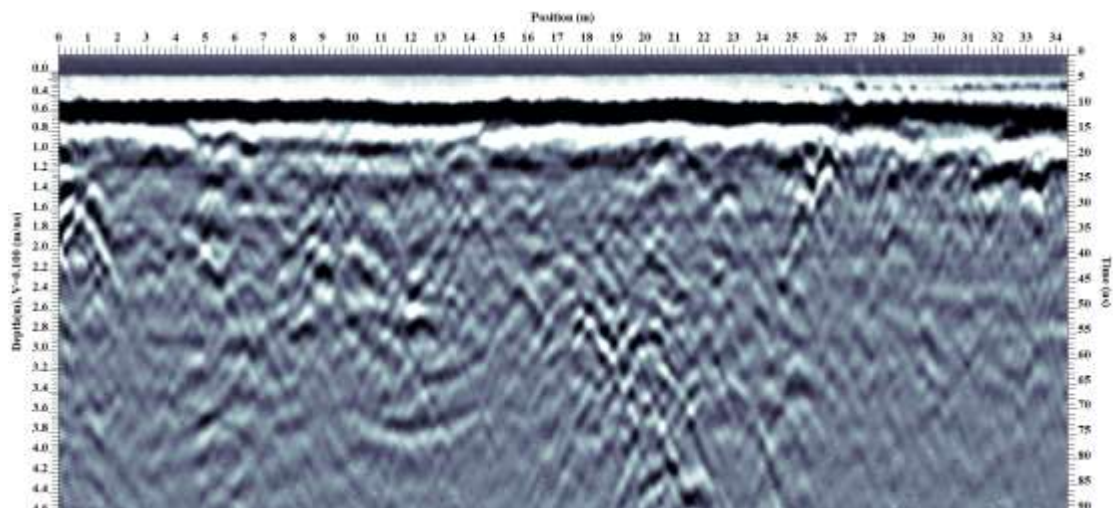


Figure B12: Processed radargram of Line 17.

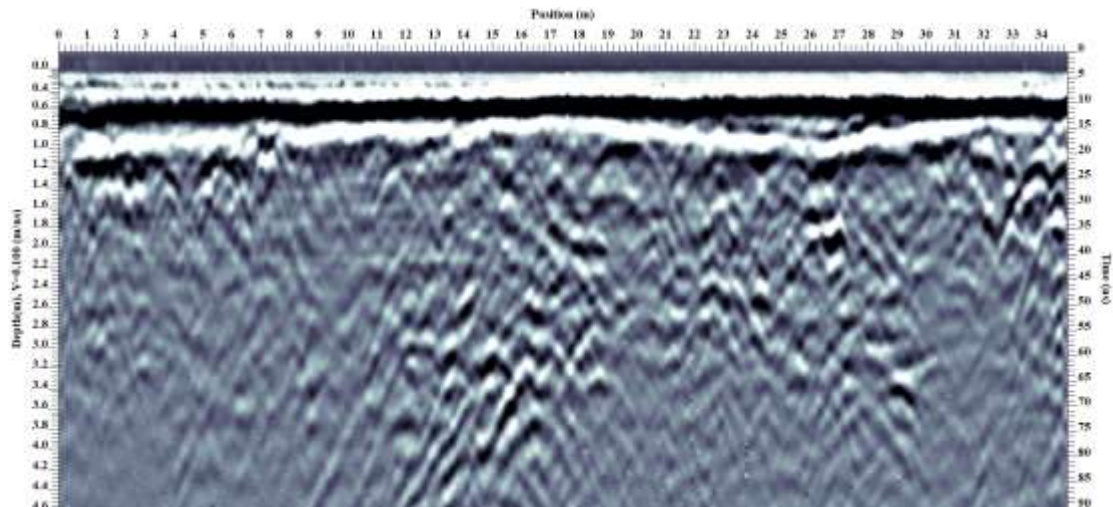


Figure B13: Processed radargram of Line 18.

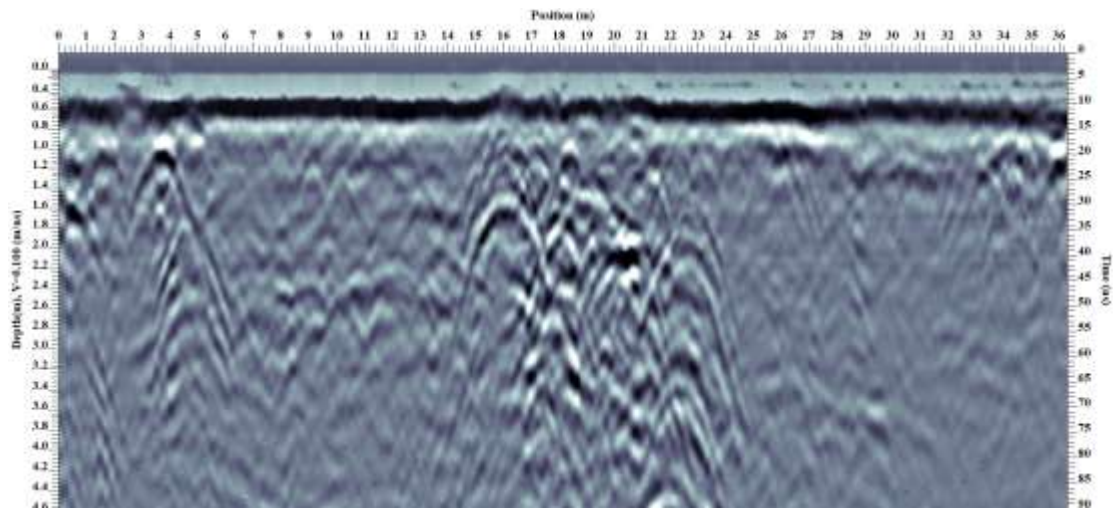


Figure B14: Processed radargram of Line 19.

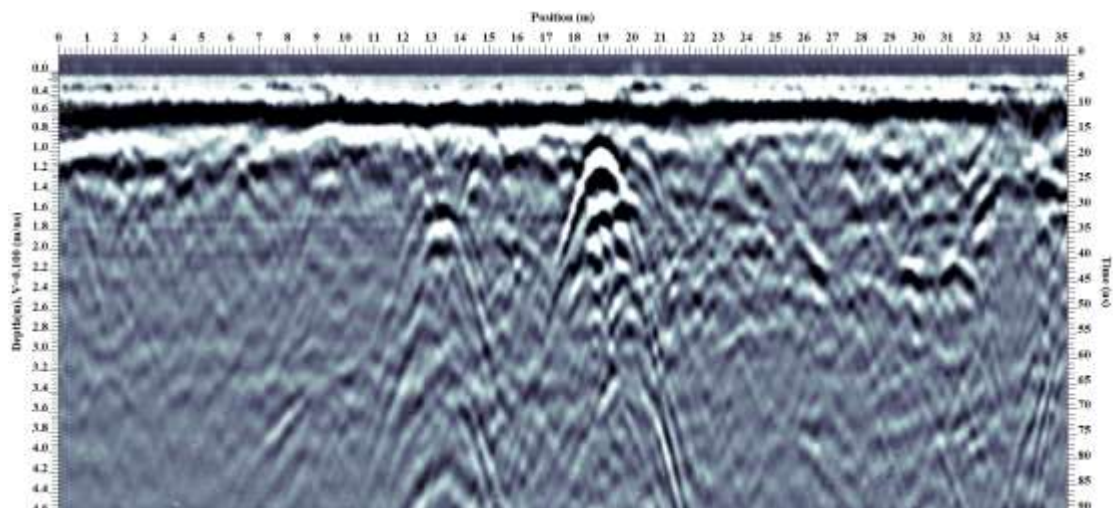


Figure B15: Processed radargram of Line 20.

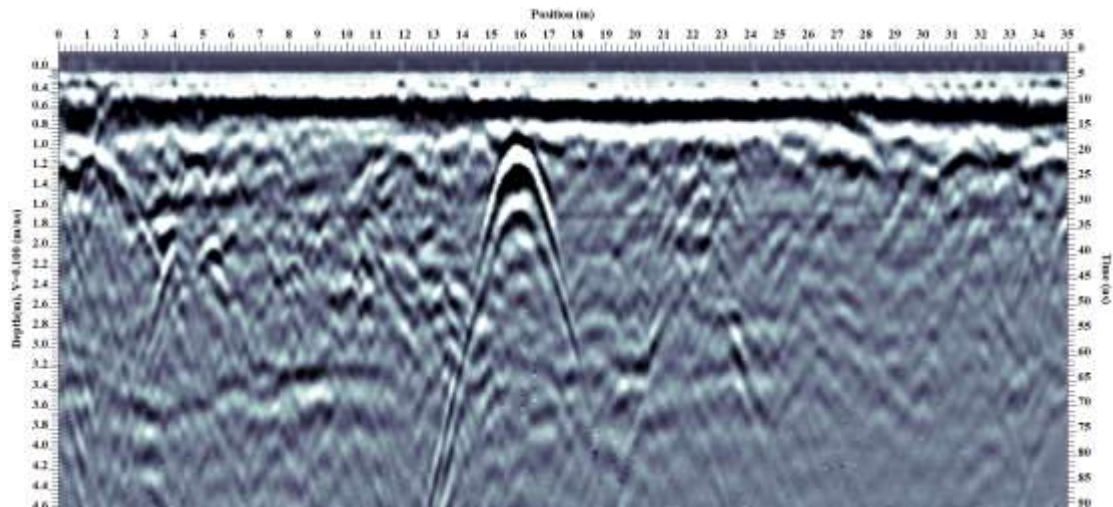


Figure B16: Processed radargram of Line 21.

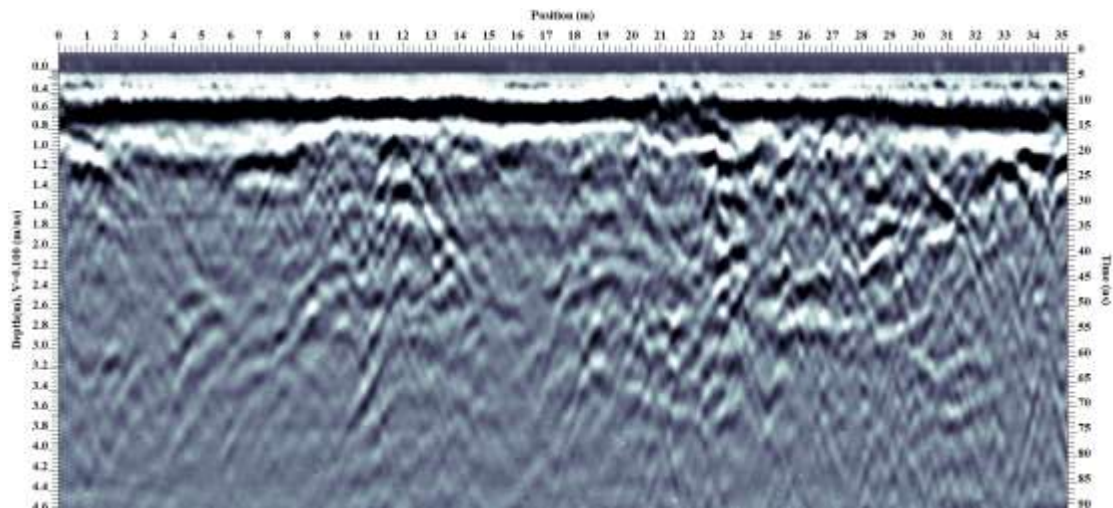


Figure B17: Processed radargram of Line 22.

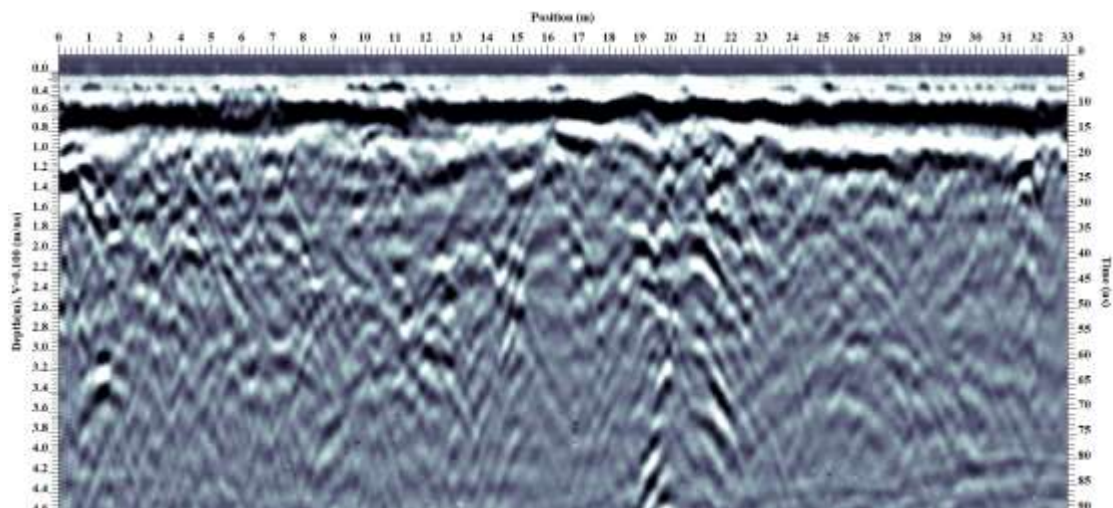


Figure B18: Processed radargram of Line 23.

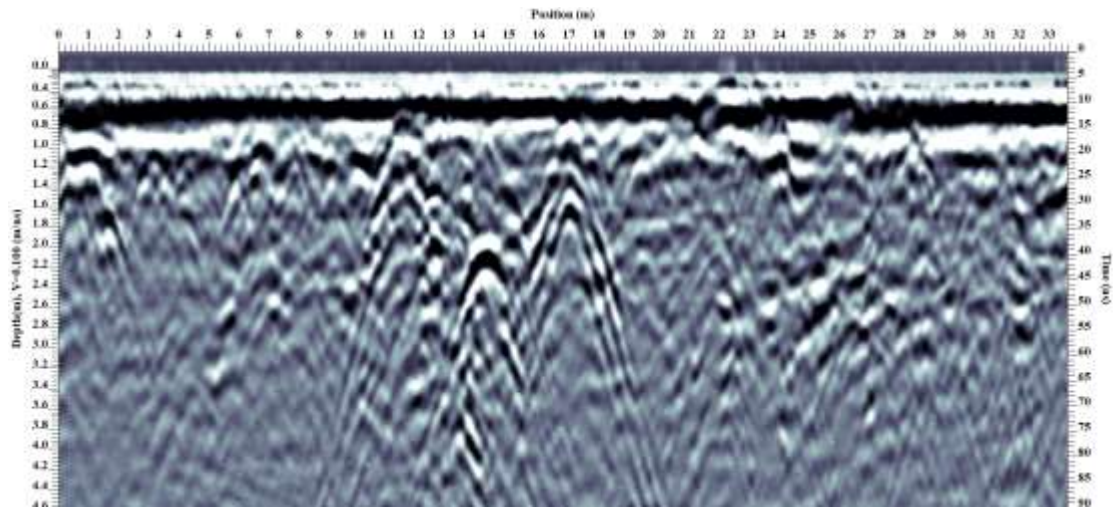


Figure B19: Processed radargram of Line 24.

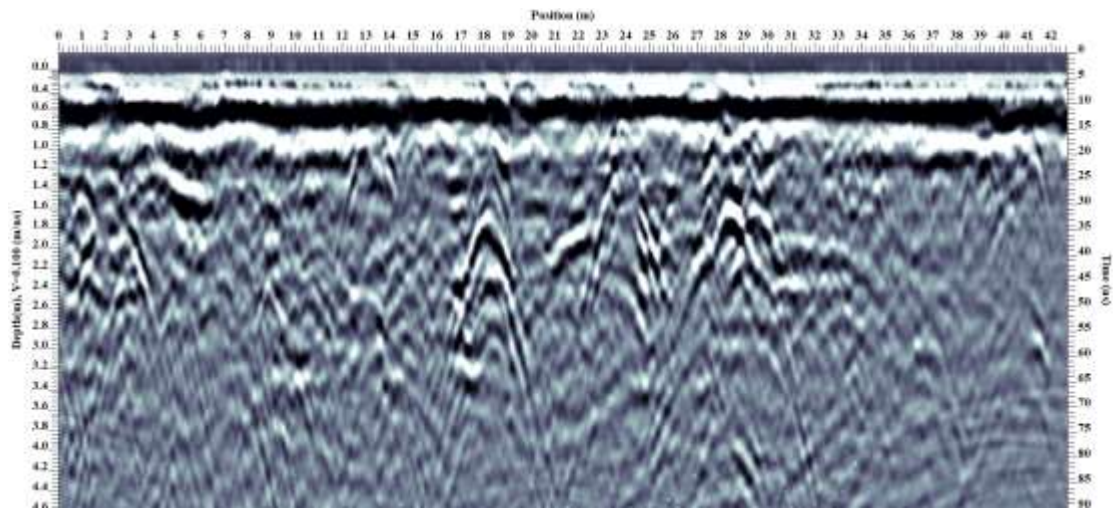


Figure B20: Processed radargram of Line 25.

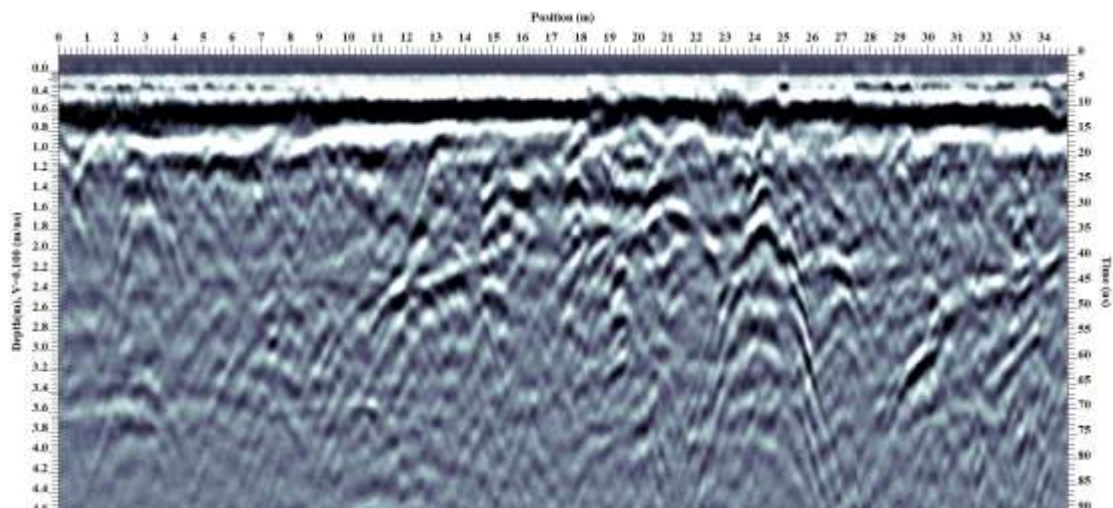


Figure B21: Processed radargram of Line 26.

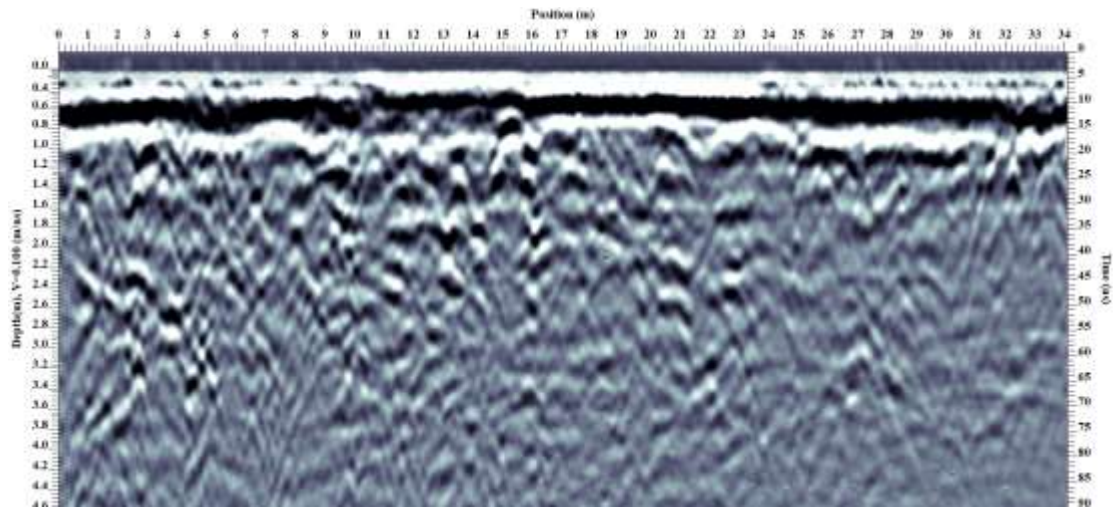


Figure B22: Processed radargram of Line 27.

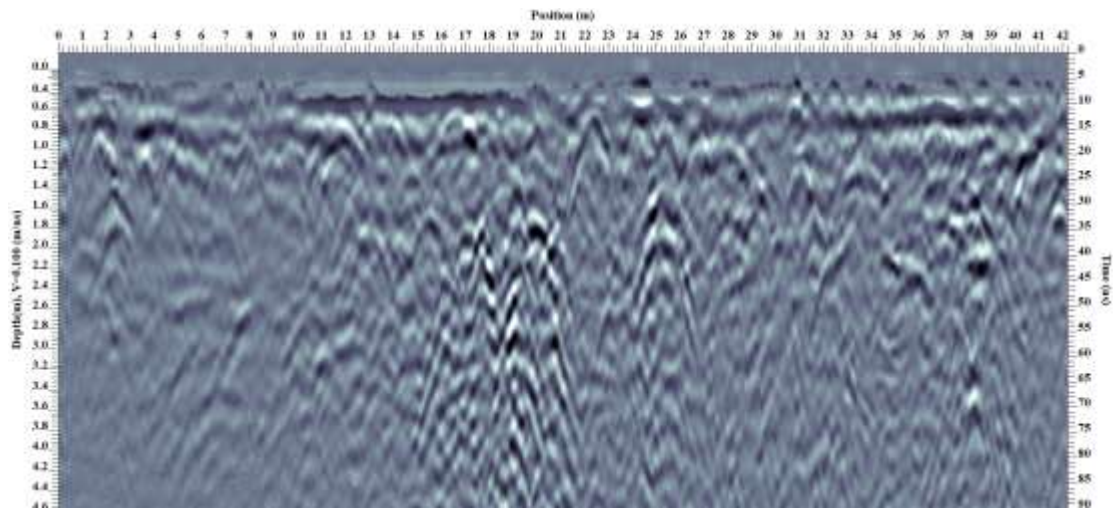


Figure B23: Processed radargram of Line 28.

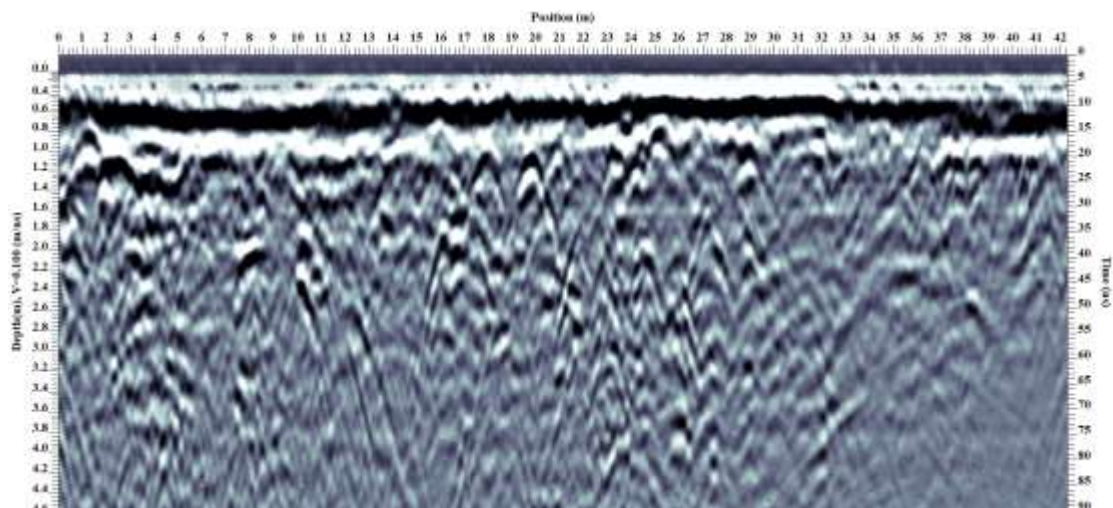


Figure B24: Processed radargram of Line 29.

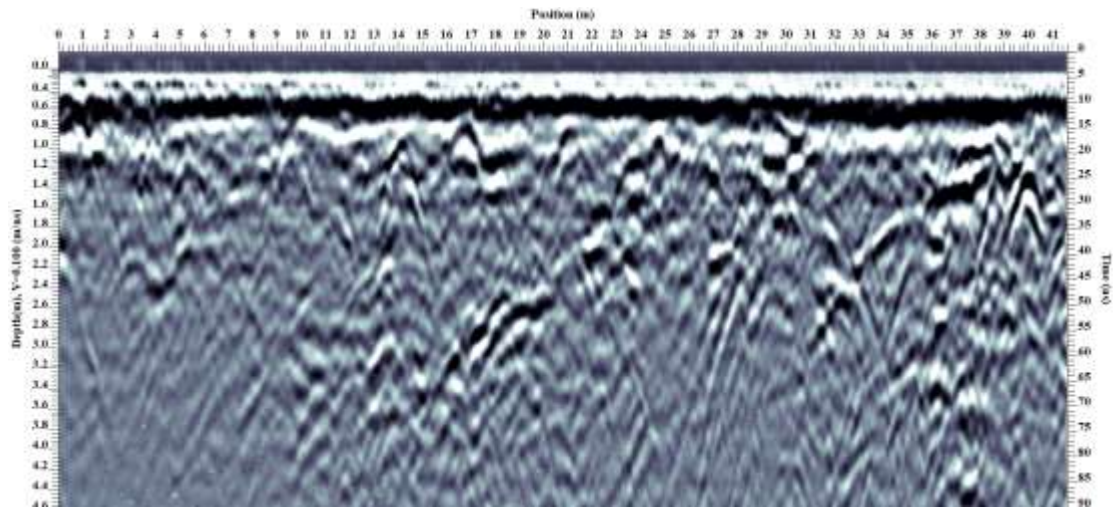


Figure B25: Processed radargram of Line 30.

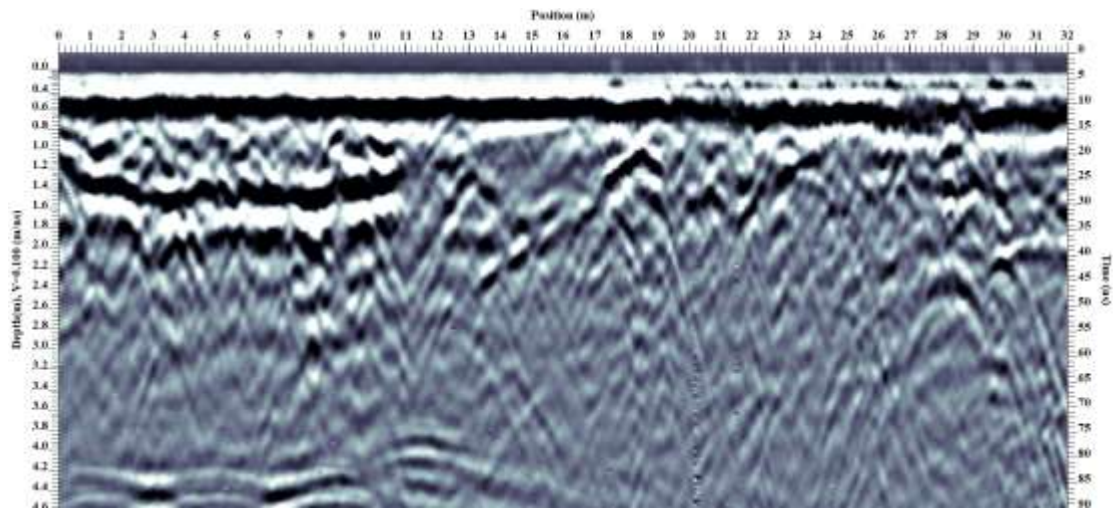


Figure B26: Processed radargram of Line 31.

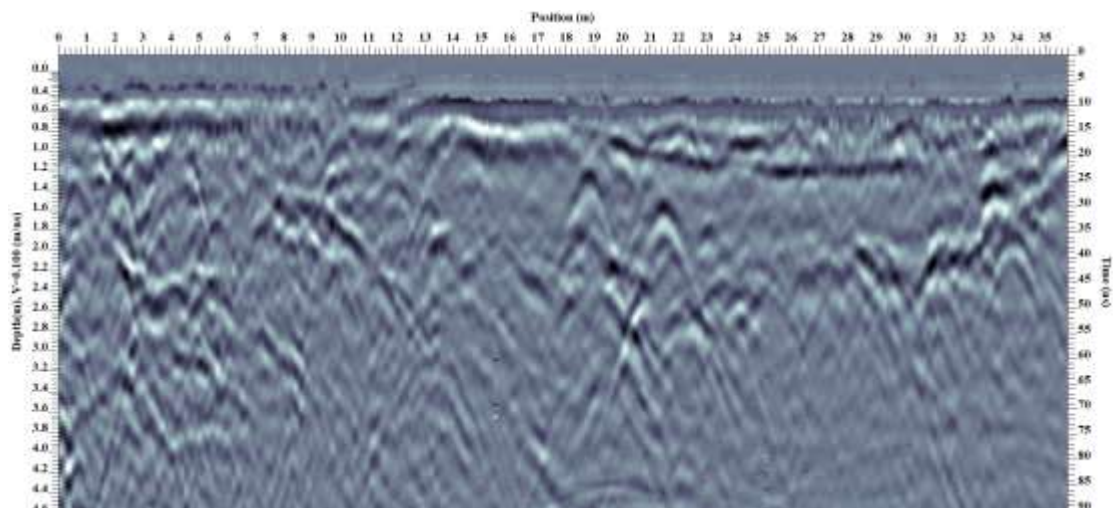


Figure B27: Processed radargram of Line 32.

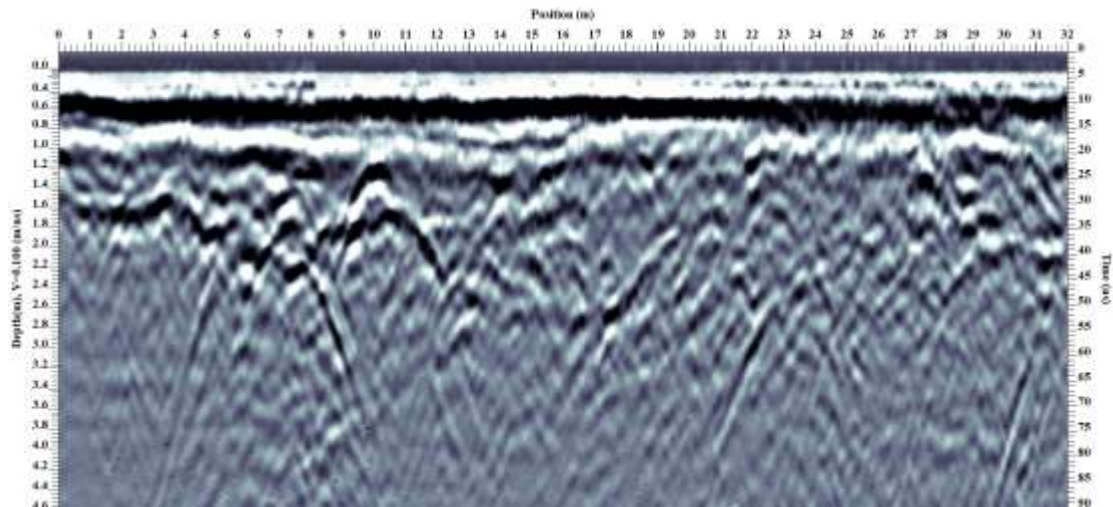


Figure B28: Processed radargram of Line 33.

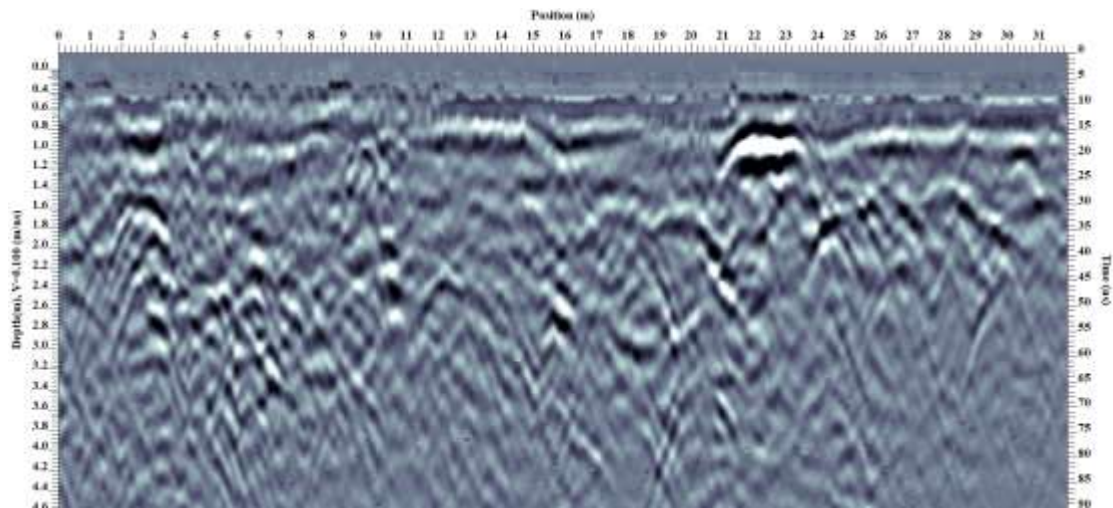


Figure B29: Processed radargram of Line 34.

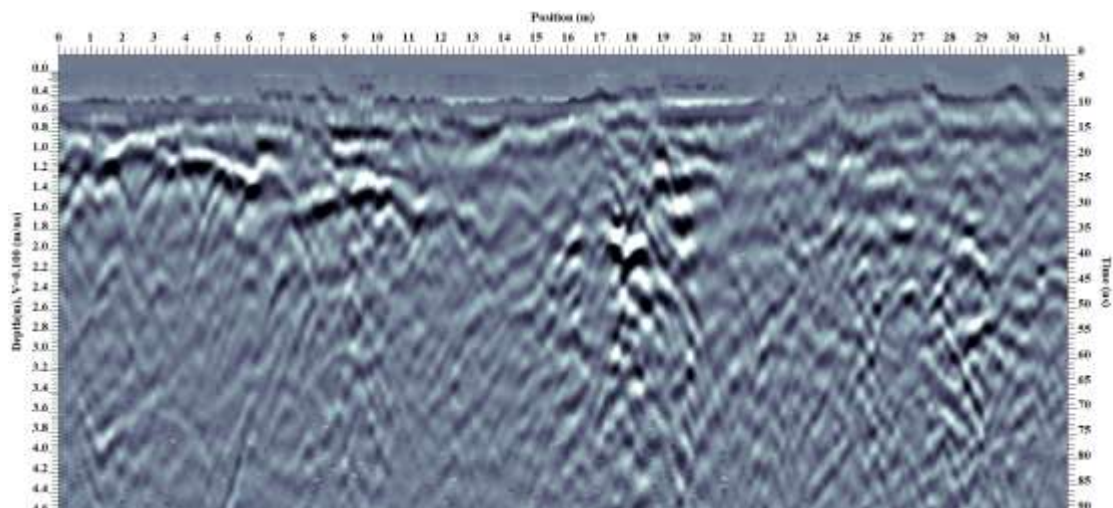


Figure B30: Processed radargram of Line 35.

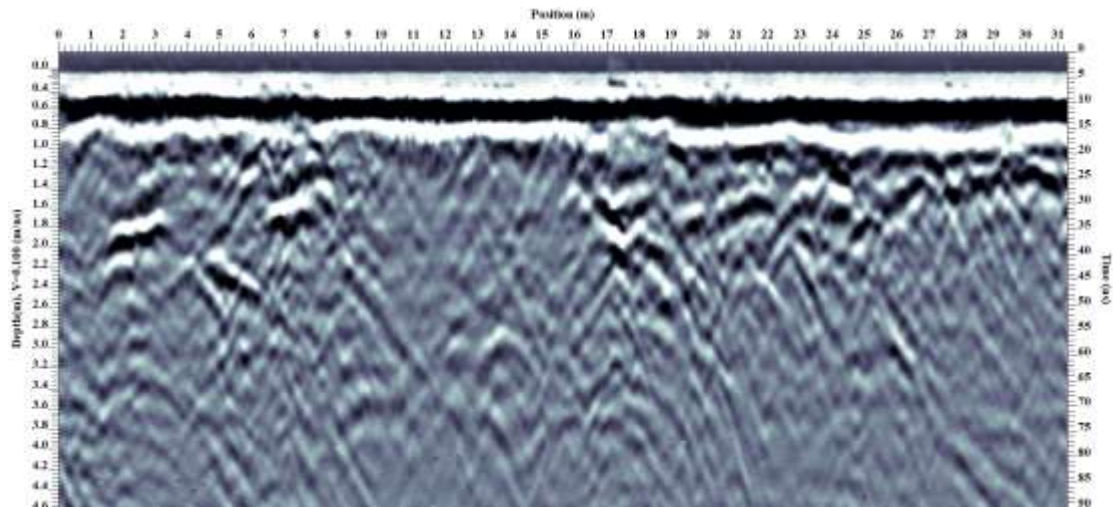


Figure B31: Processed radargram of Line 36.

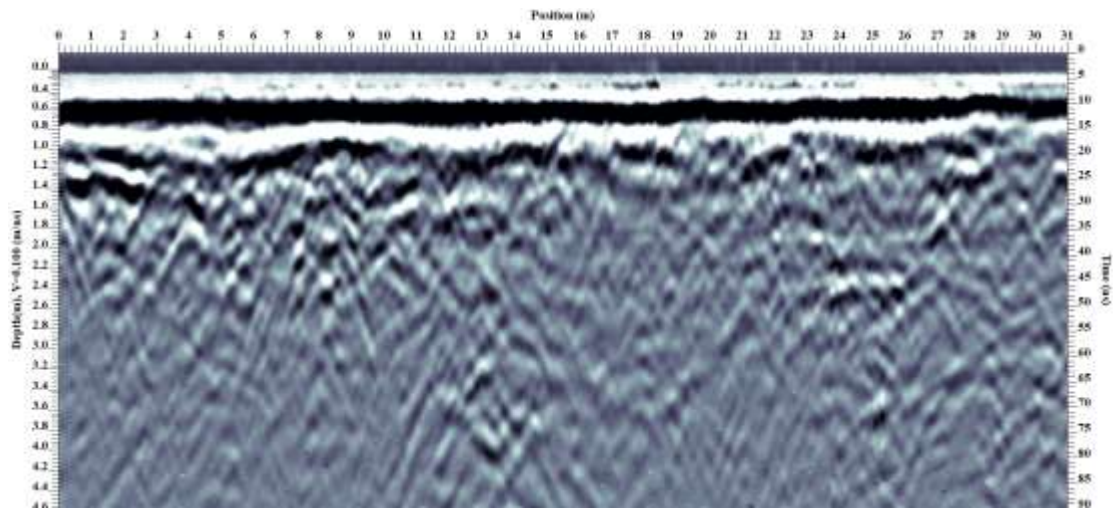


Figure B32: Processed radargram of Line 37.

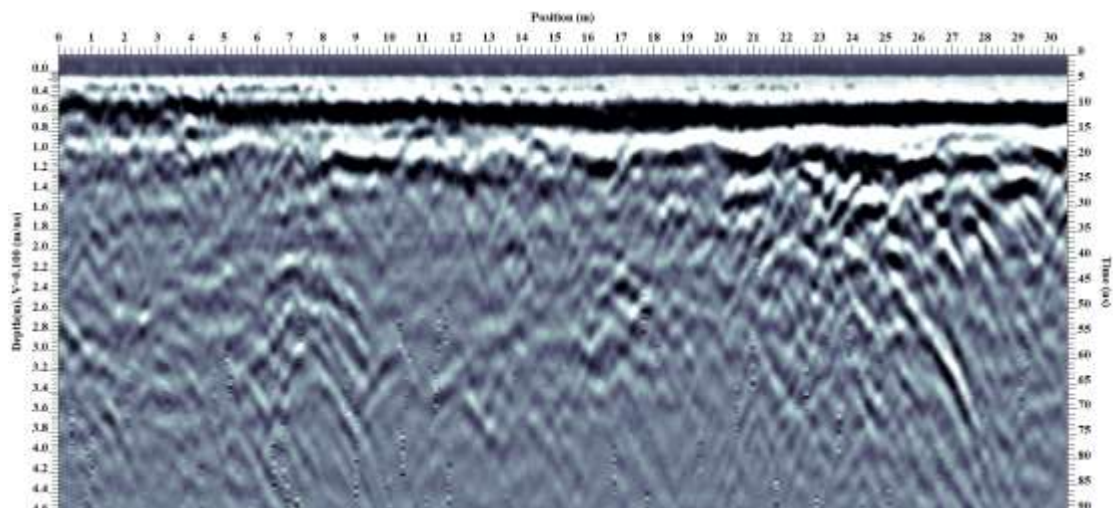


Figure B33: Processed radargram of Line 38.

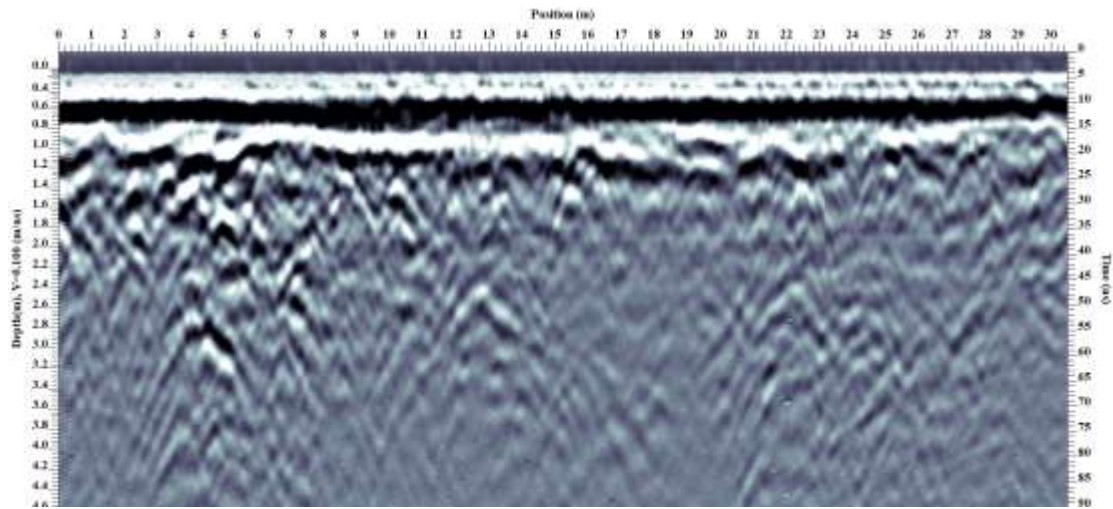


Figure B34: Processed radargram of Line 39.

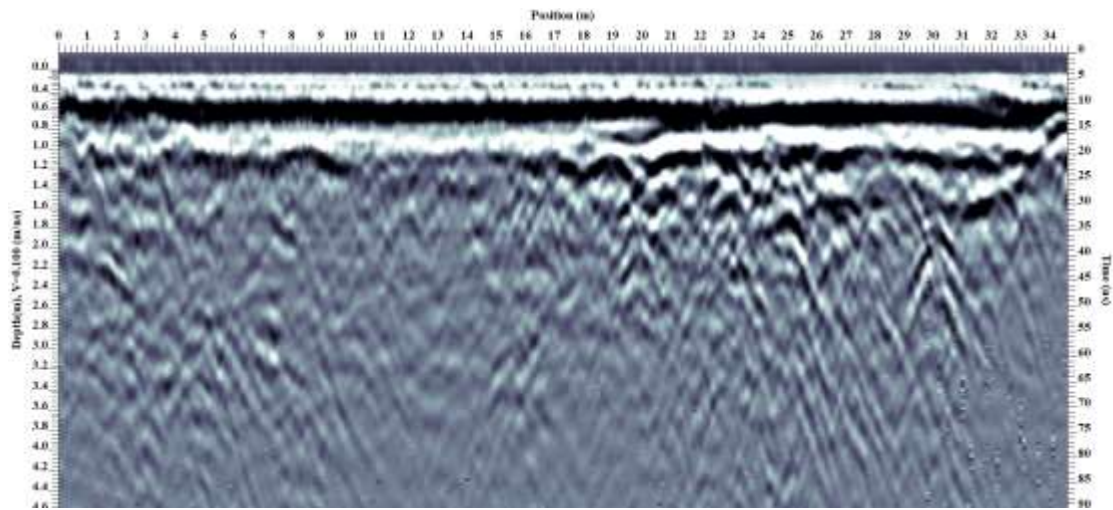


Figure B35: Processed radargram of Line 40.

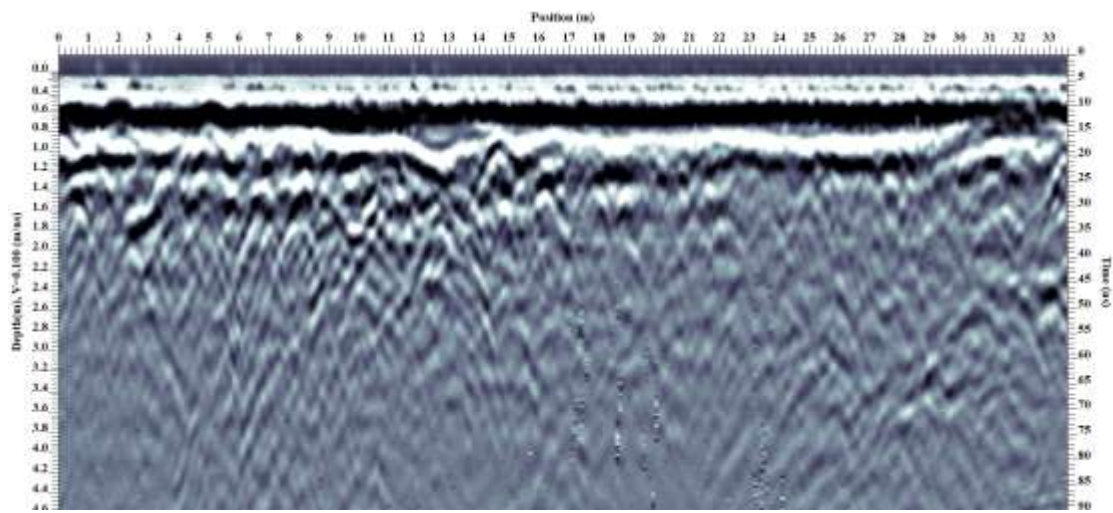


Figure B36: Processed radargram of Line 41.

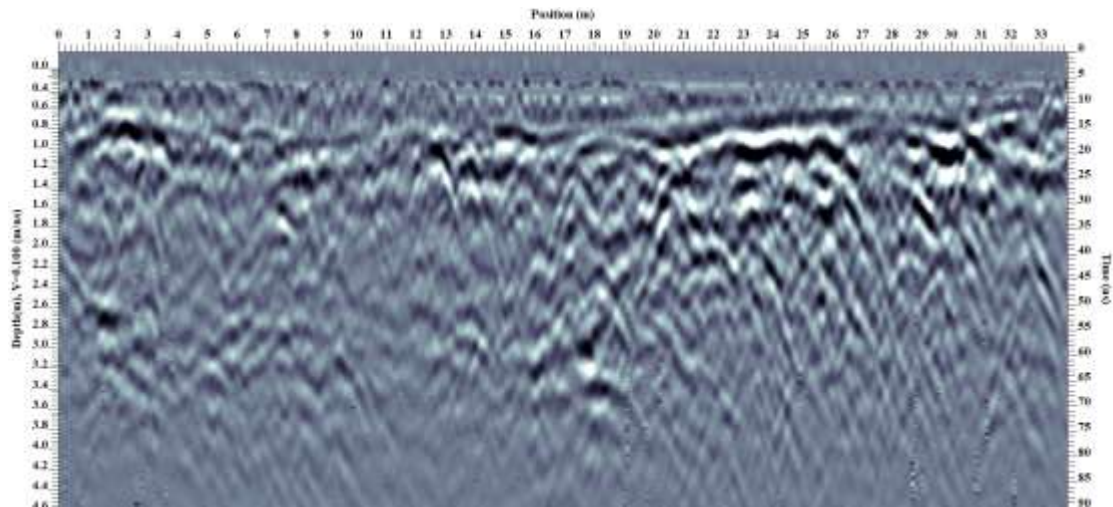


Figure B37: Processed radargram of Line 42.

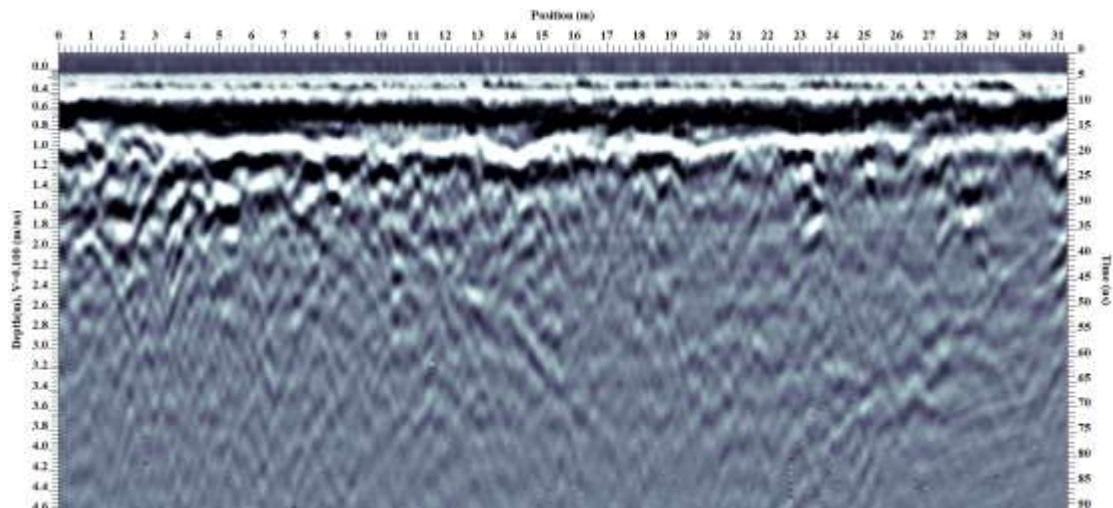


Figure B38: Processed radargram of Line 43.

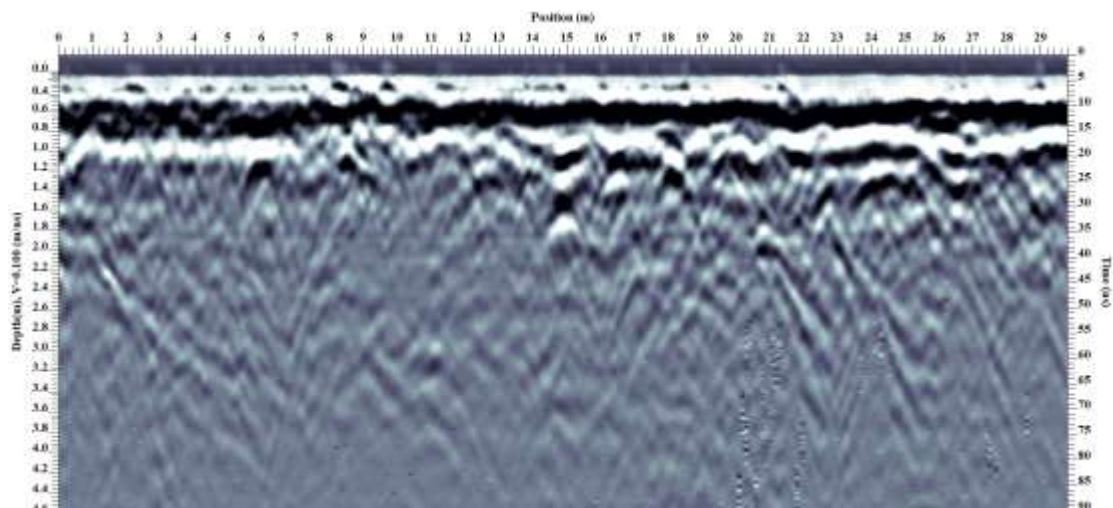


Figure B39: Processed radargram of Line 44.

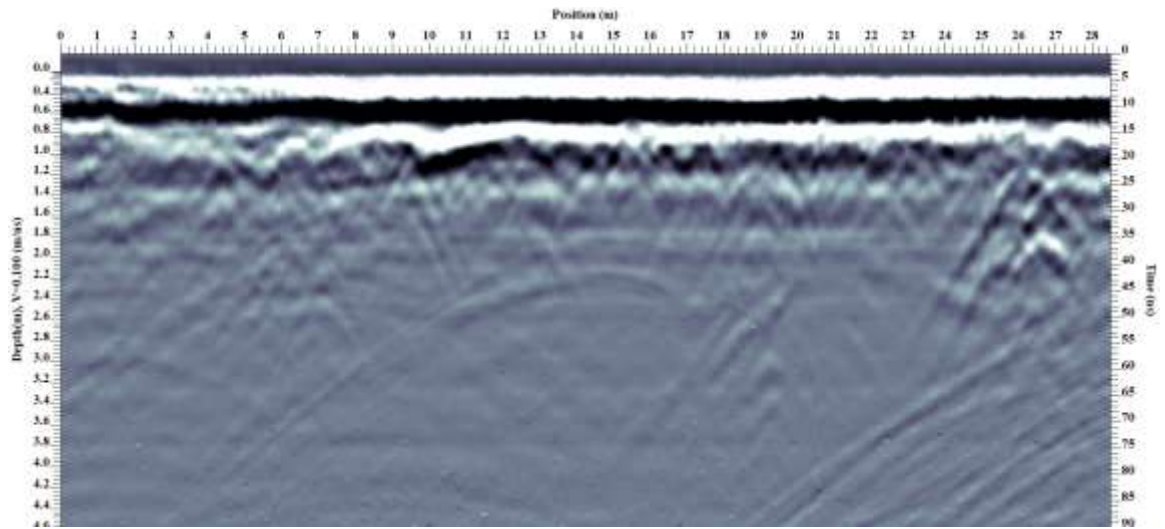


Figure B40: Processed radargram of Line 45.

Appendix C: Processed Radargrams Supporting Chapter 5 – Joggins GPR Study

The following images are the processed radargrams of the individual lines collected from the GPR survey documented in Chapter 5.

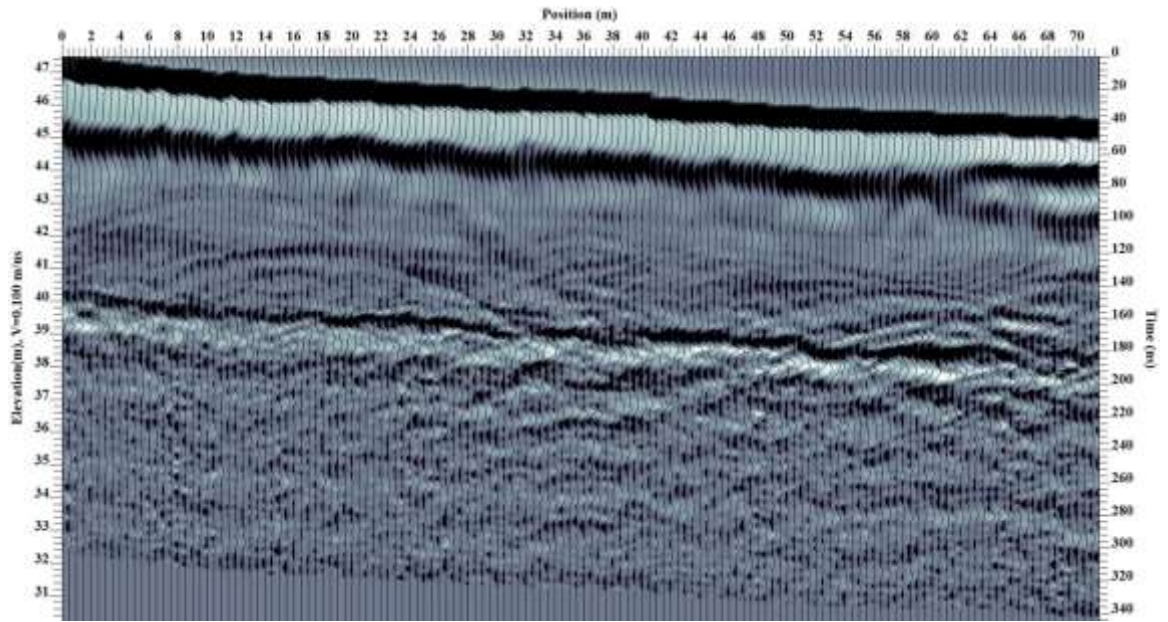


Figure C1: Processed radargram of Line 09

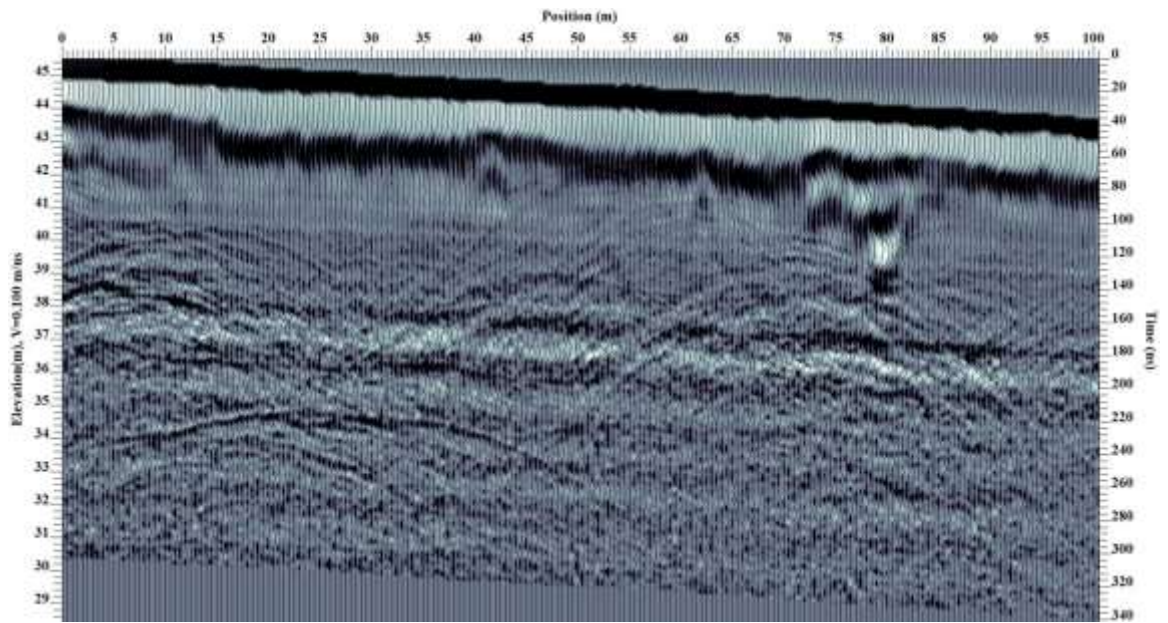


Figure C2: Processed radargram of Line 10

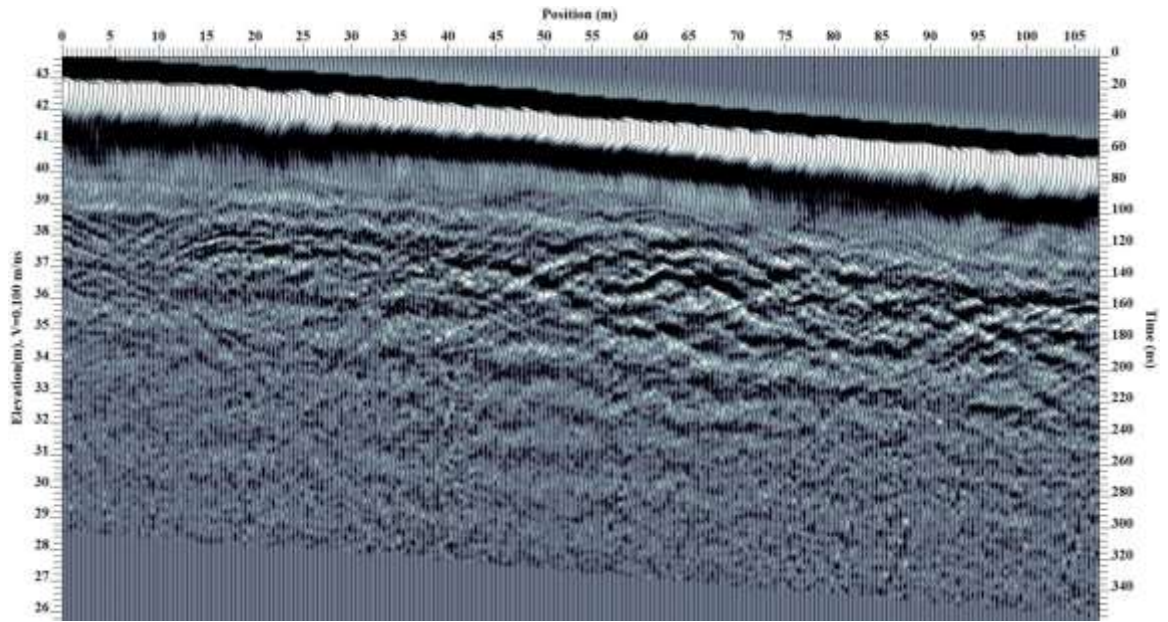


Figure C3: Processed radargram of Line 11

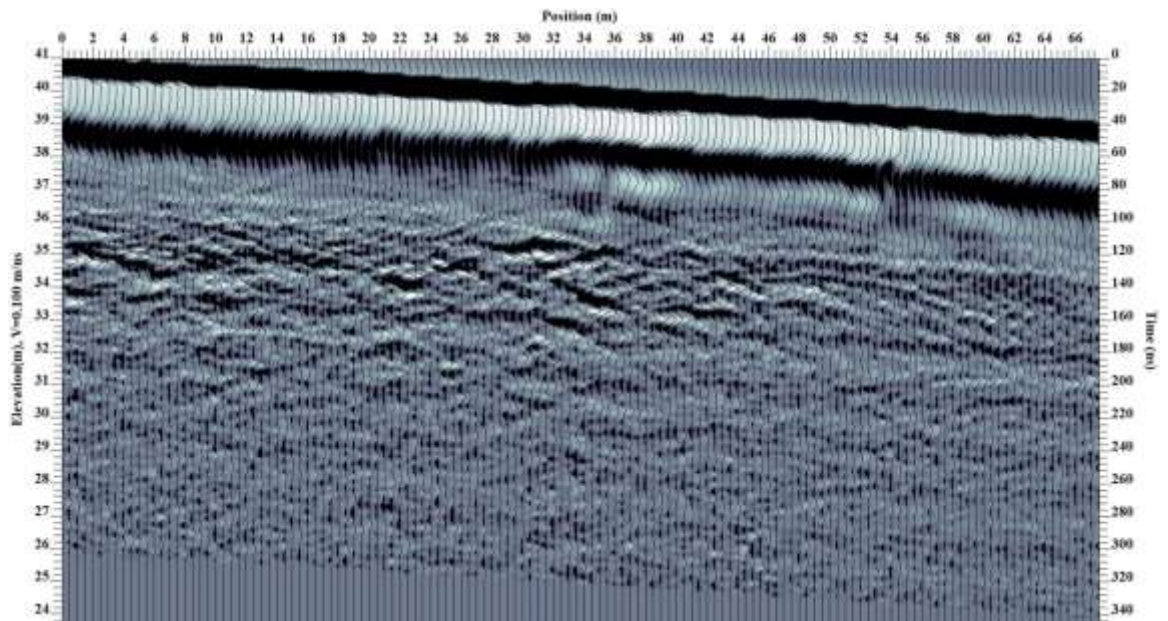


Figure C4: Processed radargram of Line 12

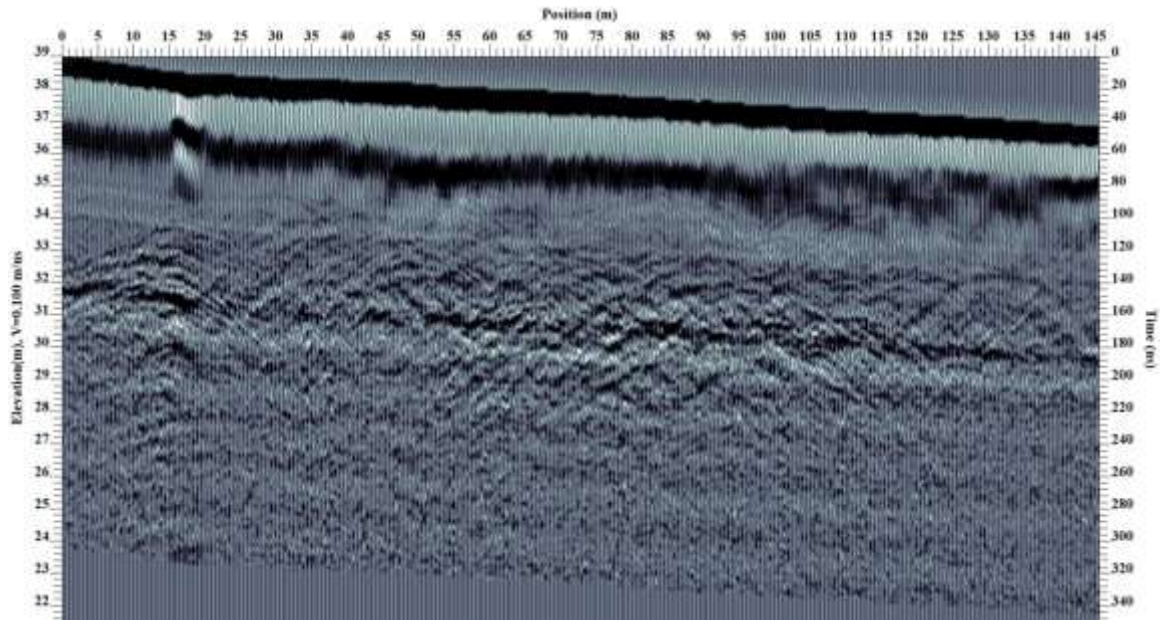


Figure C5: Processed radargram of Line 13

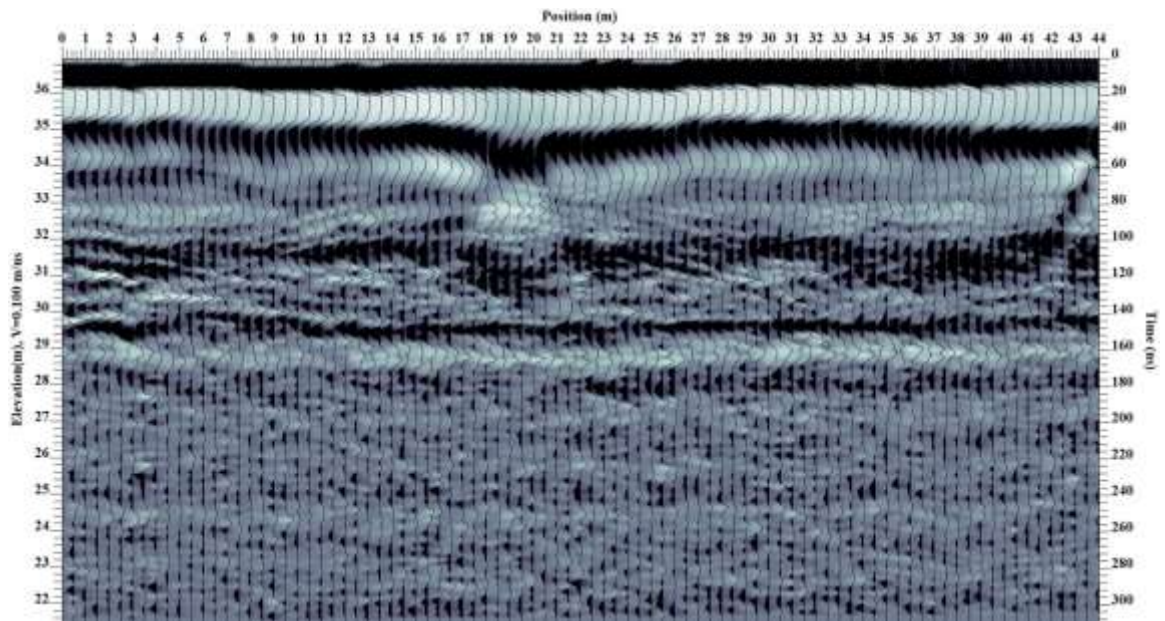


Figure C6: Processed radargram of Line 14

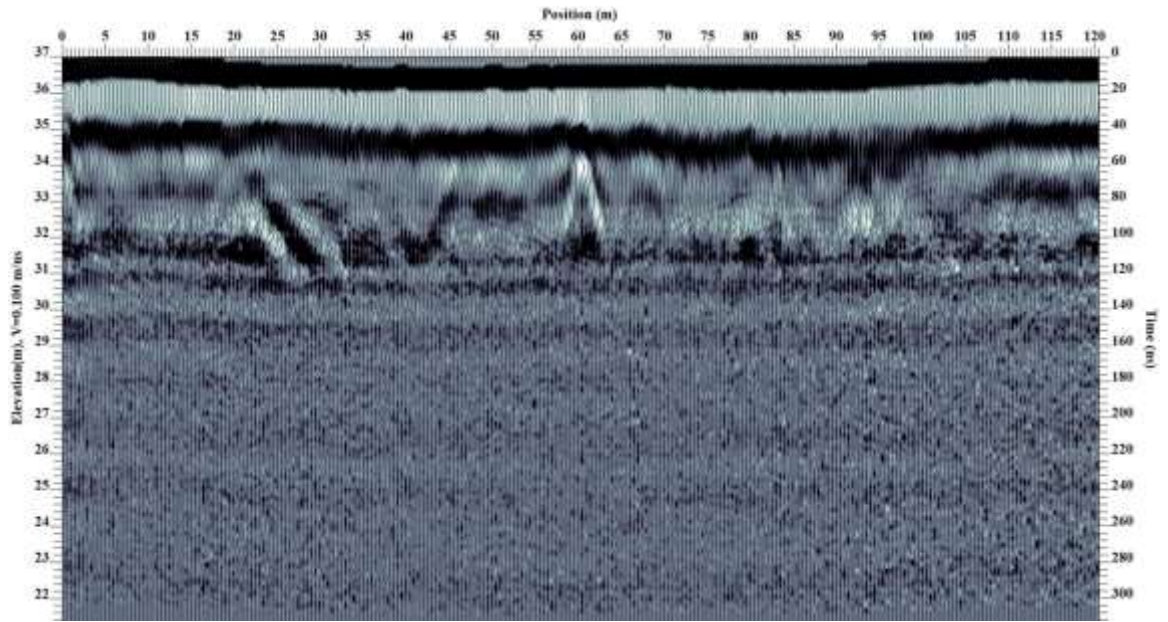


Figure C7: Processed radargram of Line 15

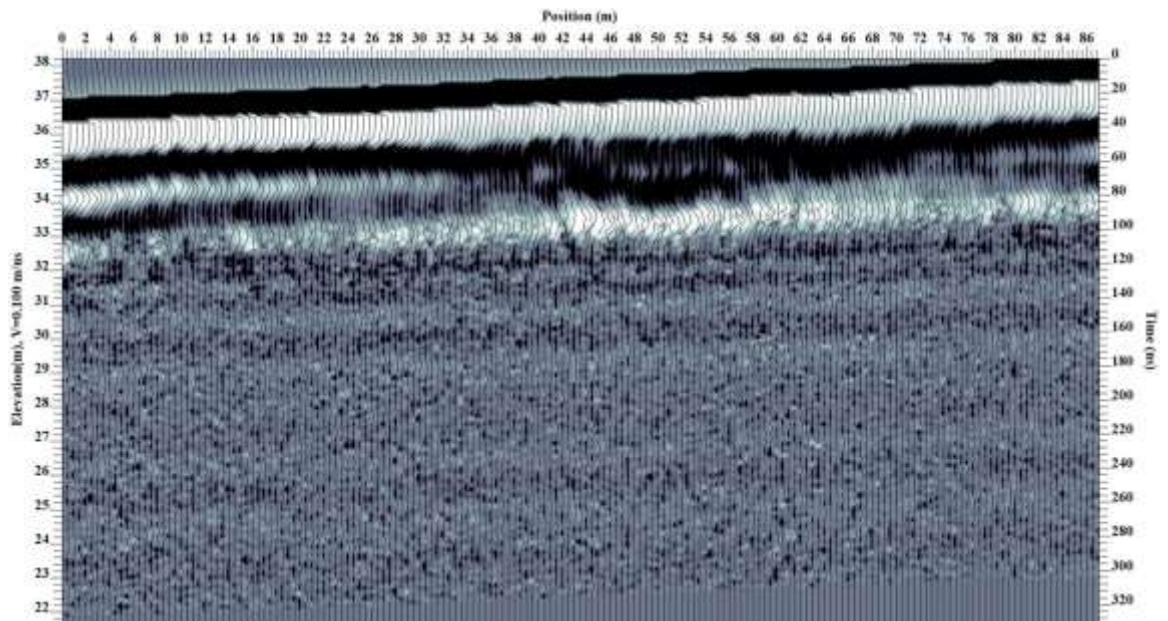


Figure C8: Processed radargram of Line 16

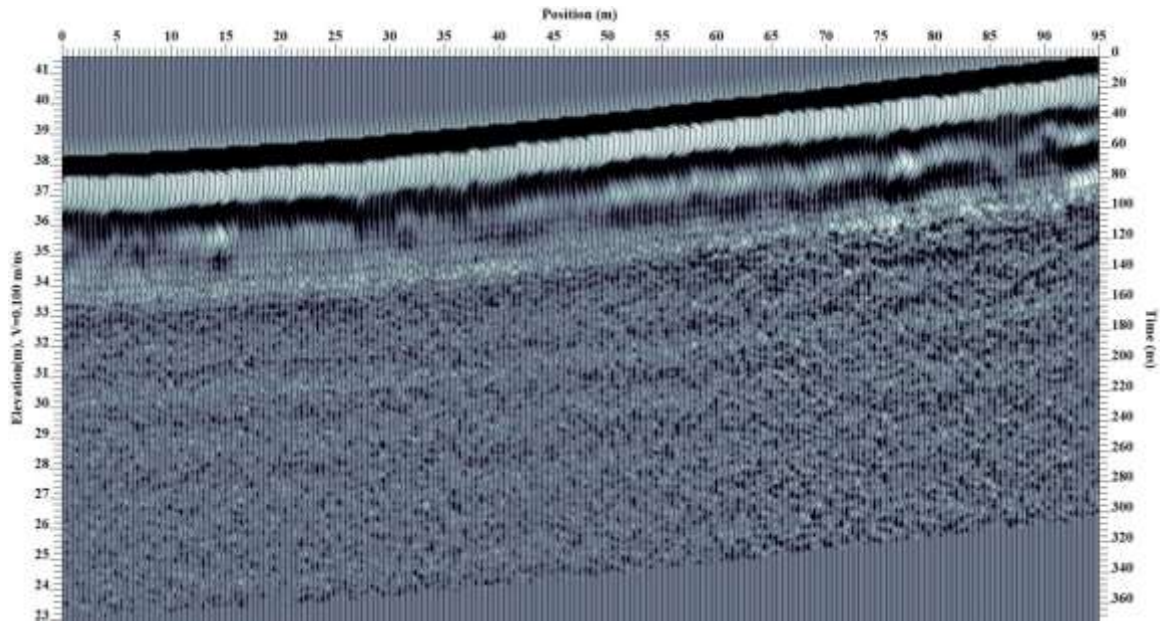


Figure C9: Processed radargram of Line 17

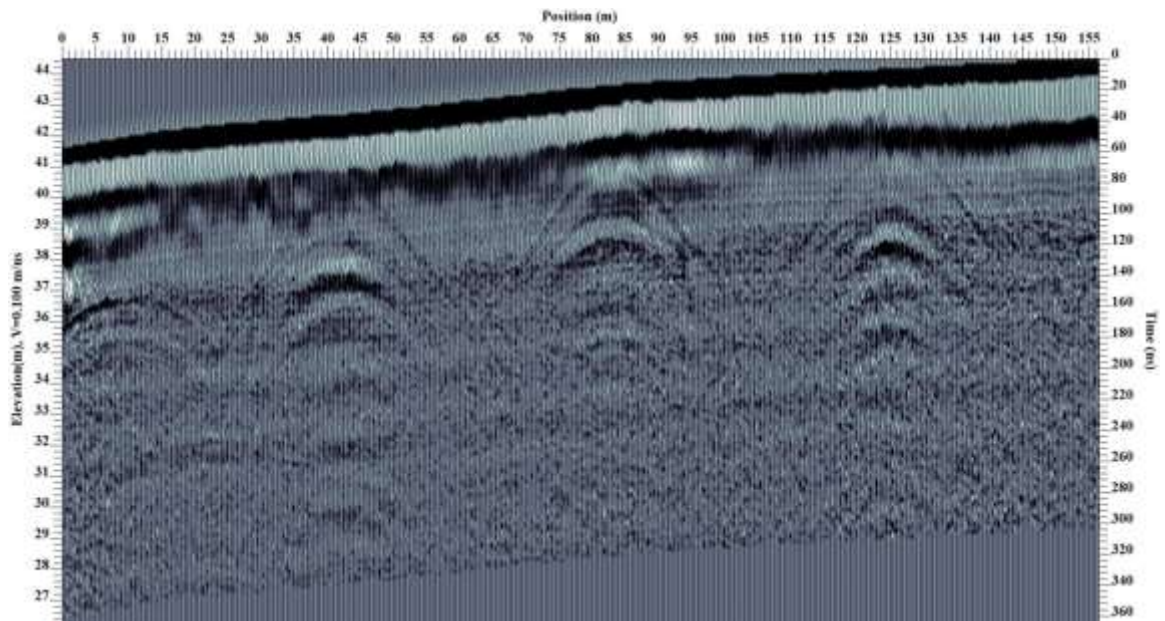


Figure C10: Processed radargram of Line 18

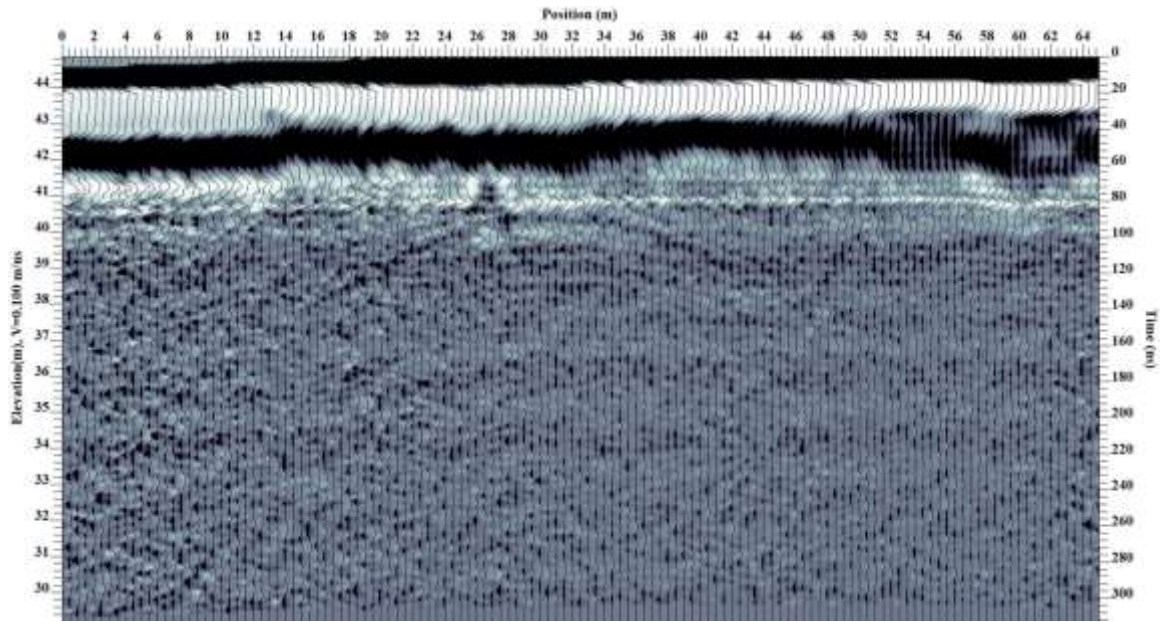


Figure C11: Processed radargram of Line 19

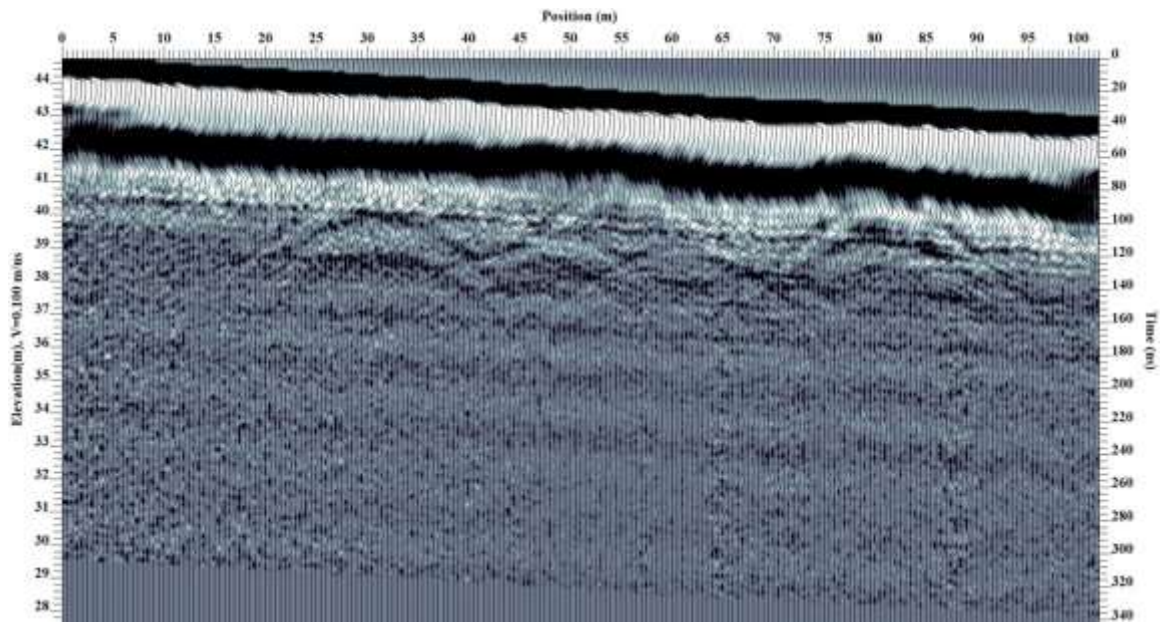


Figure C12: Processed radargram of Line 20

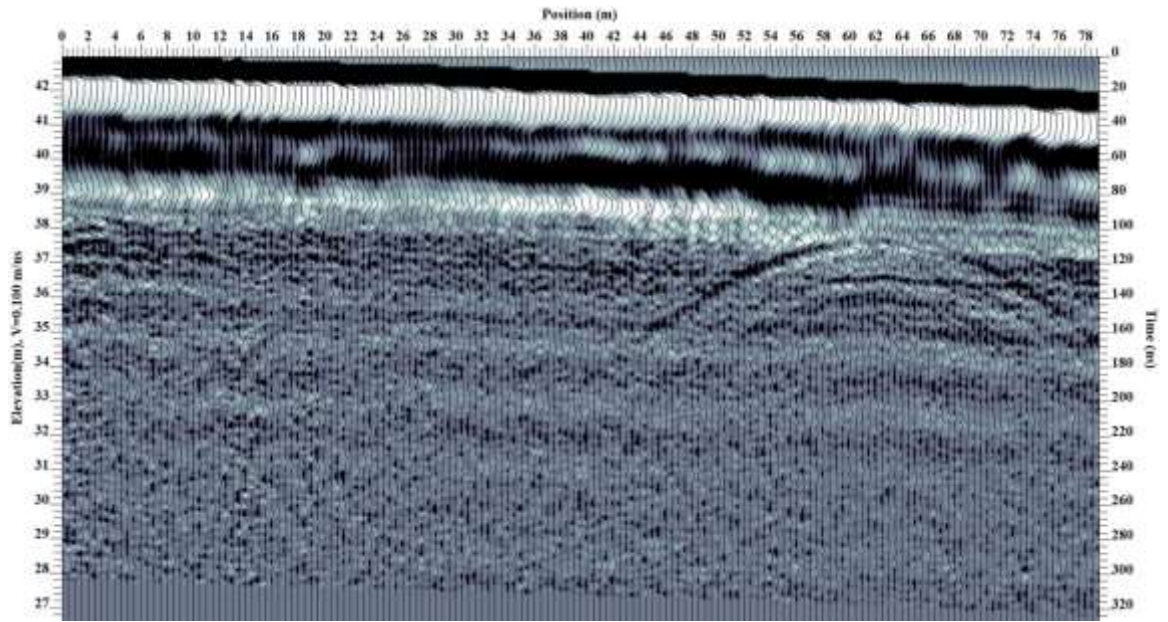


Figure C13: Processed radargram of Line 21

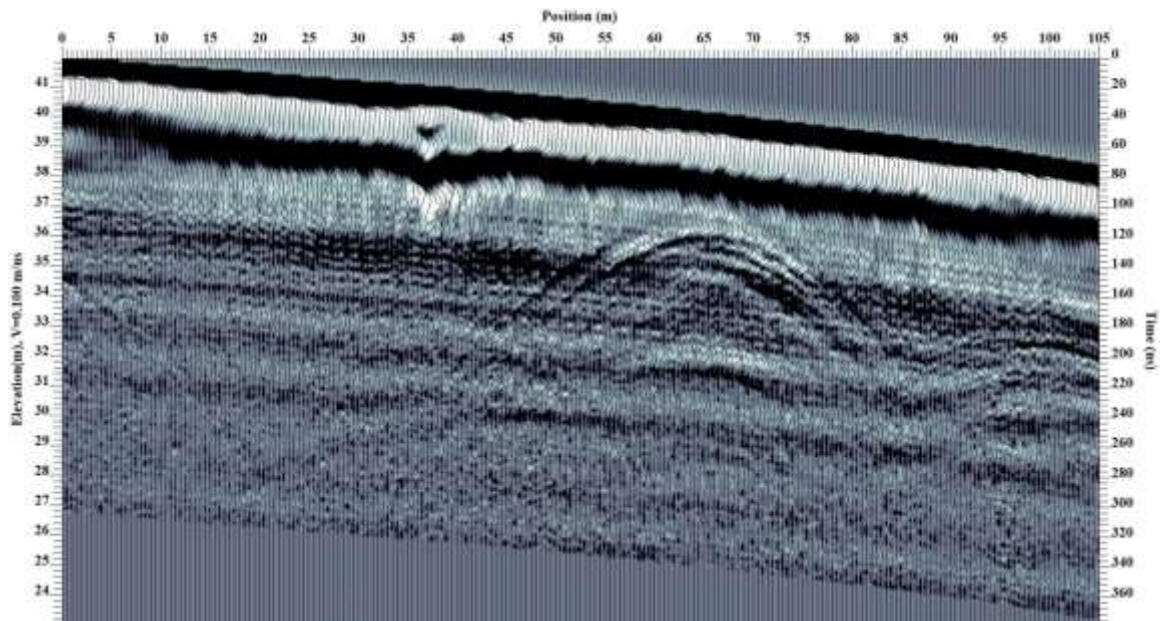


Figure C14: Processed radargram of Line 22

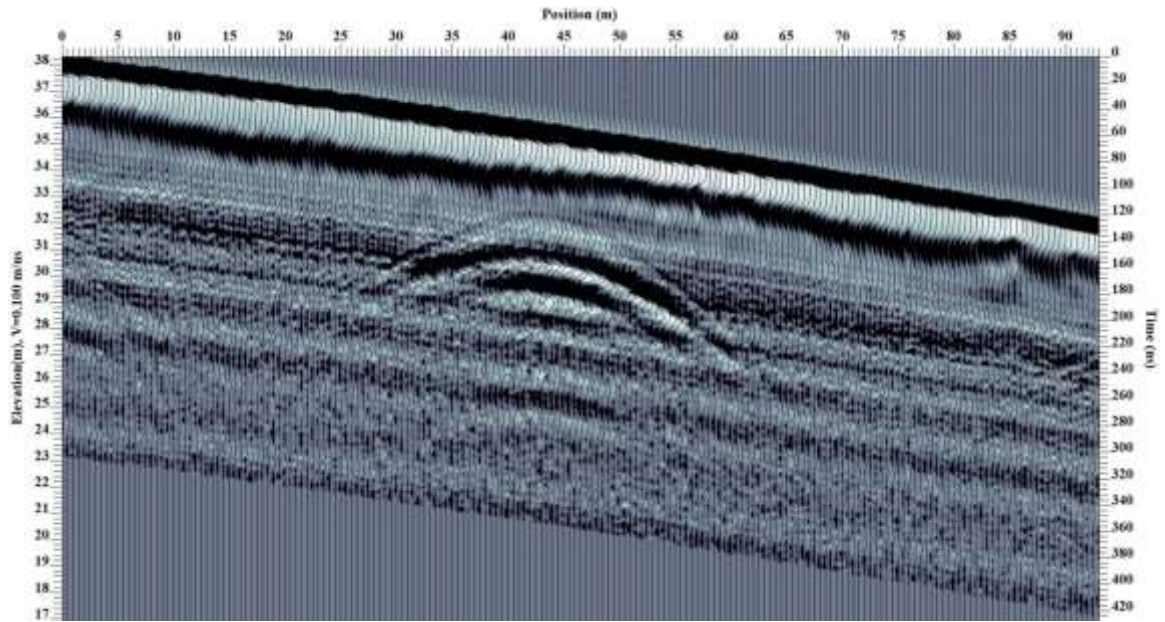


Figure C15: Processed radargram of Line 23

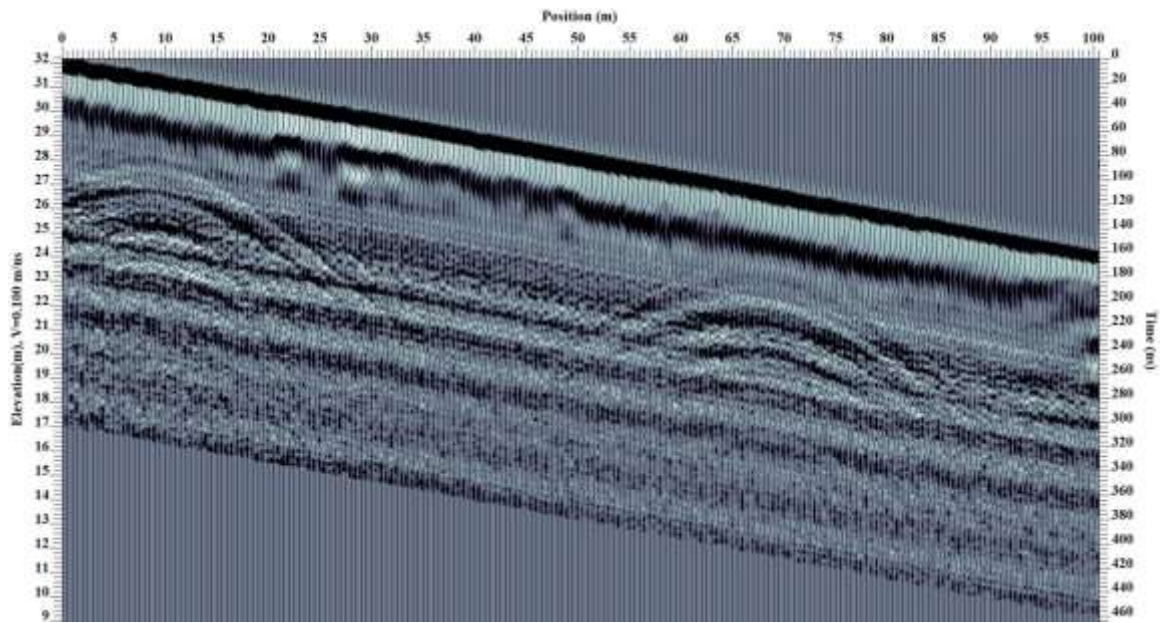


Figure C16: Processed radargram of Line 24

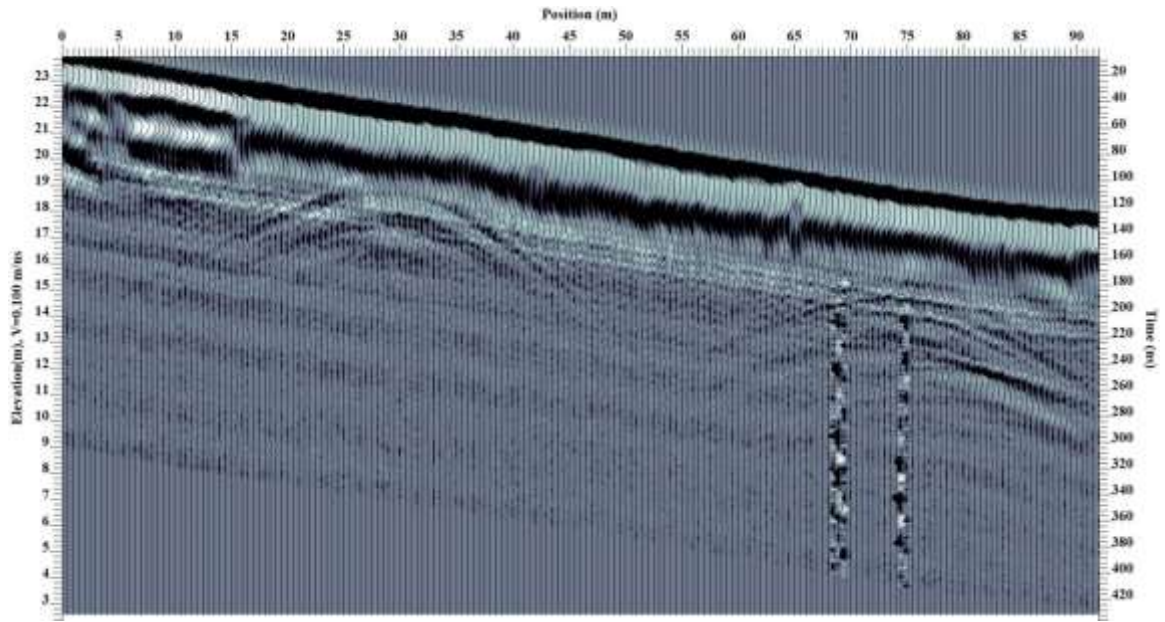


Figure C17: Processed radargram of Line 25

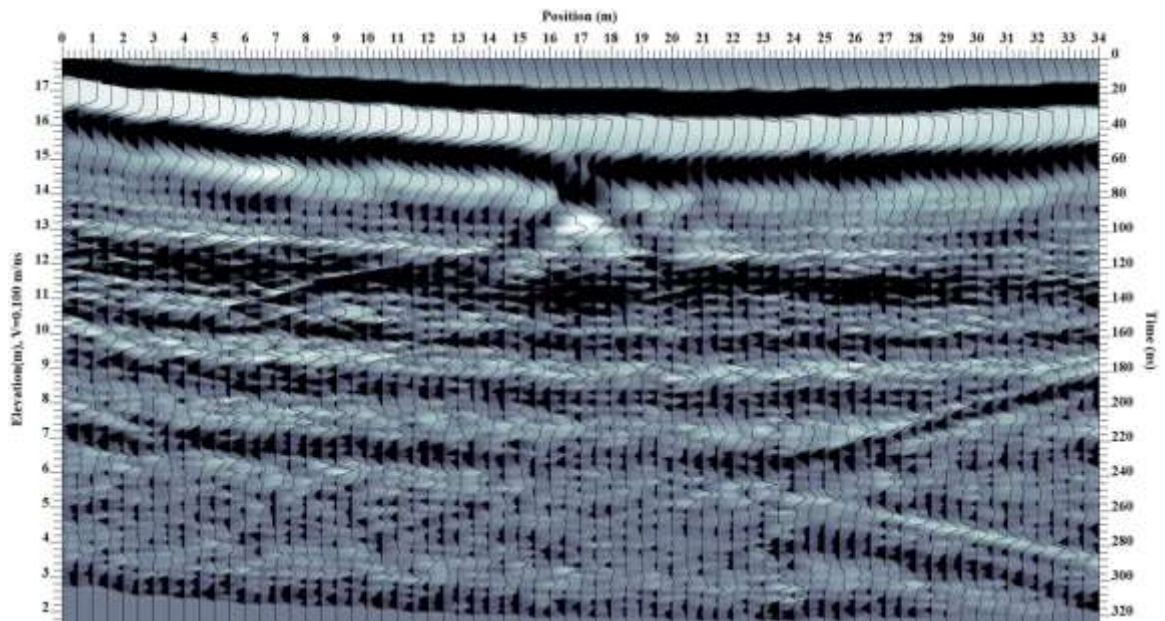


Figure C18: Processed radargram of Line 26

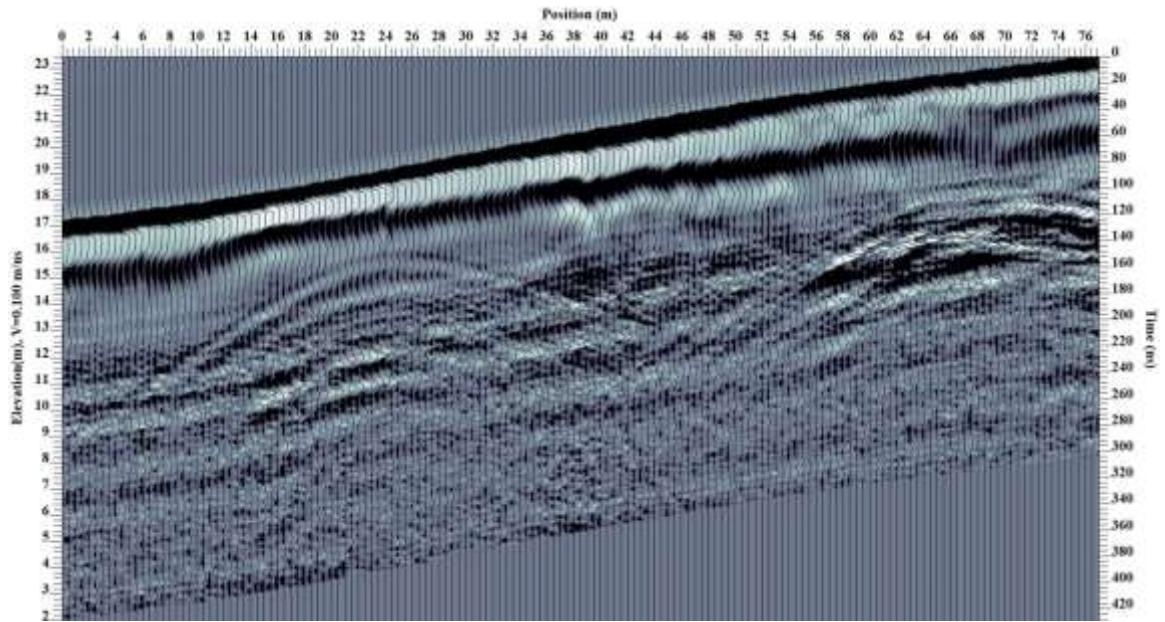


Figure C19: Processed radargram of Line 27

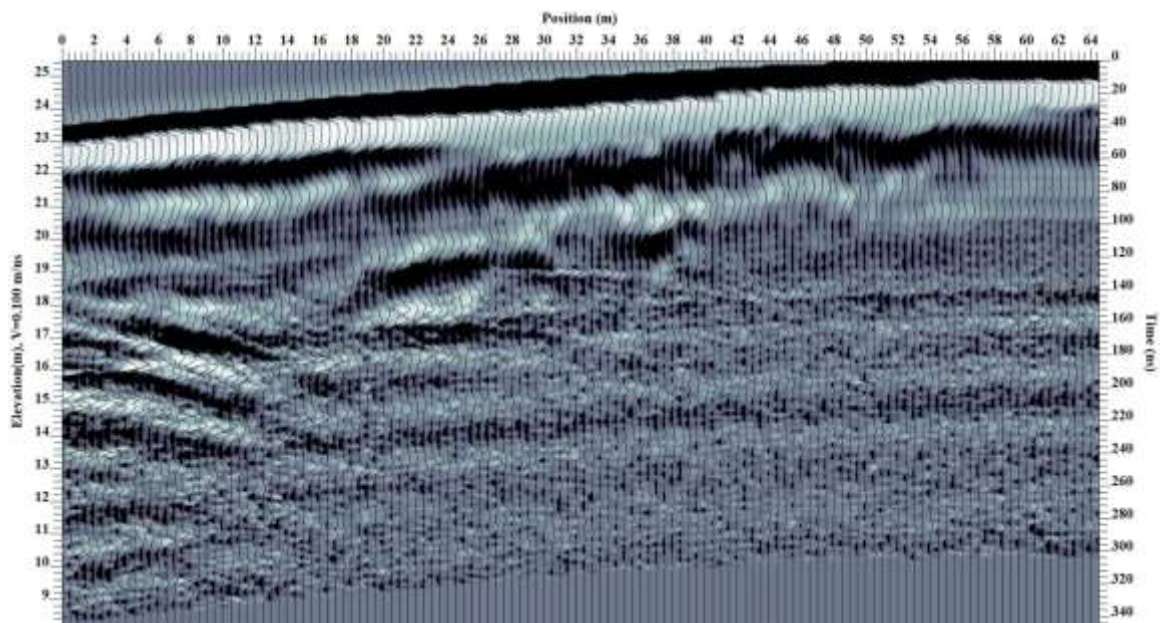


Figure C20: Processed radargram of Line 28

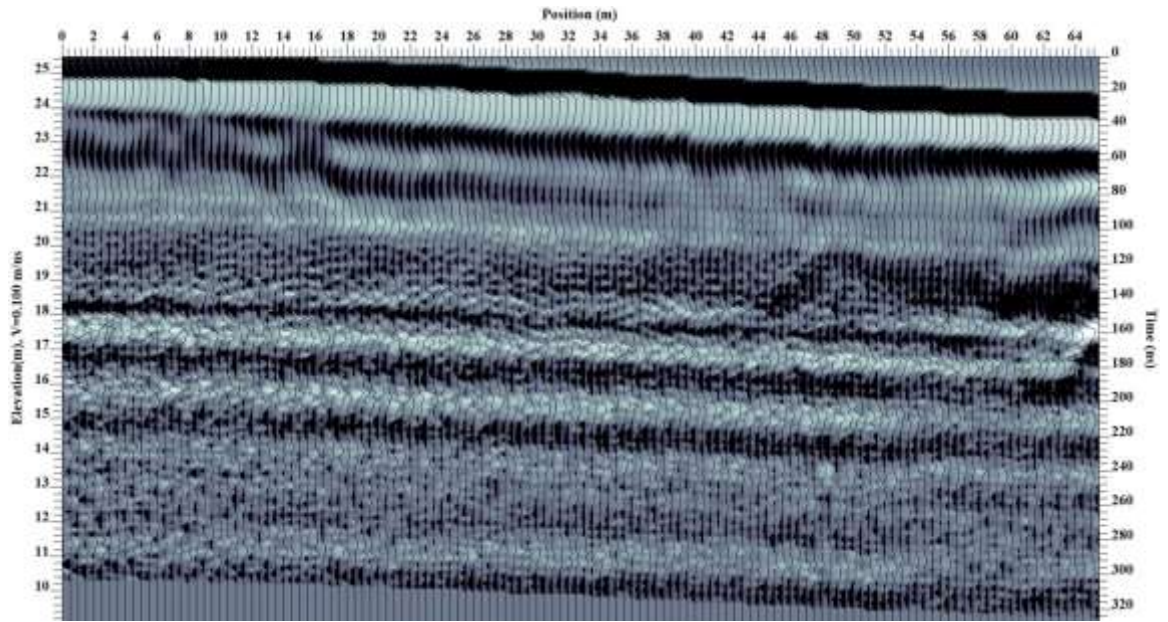


Figure C21: Processed radargram of Line 29

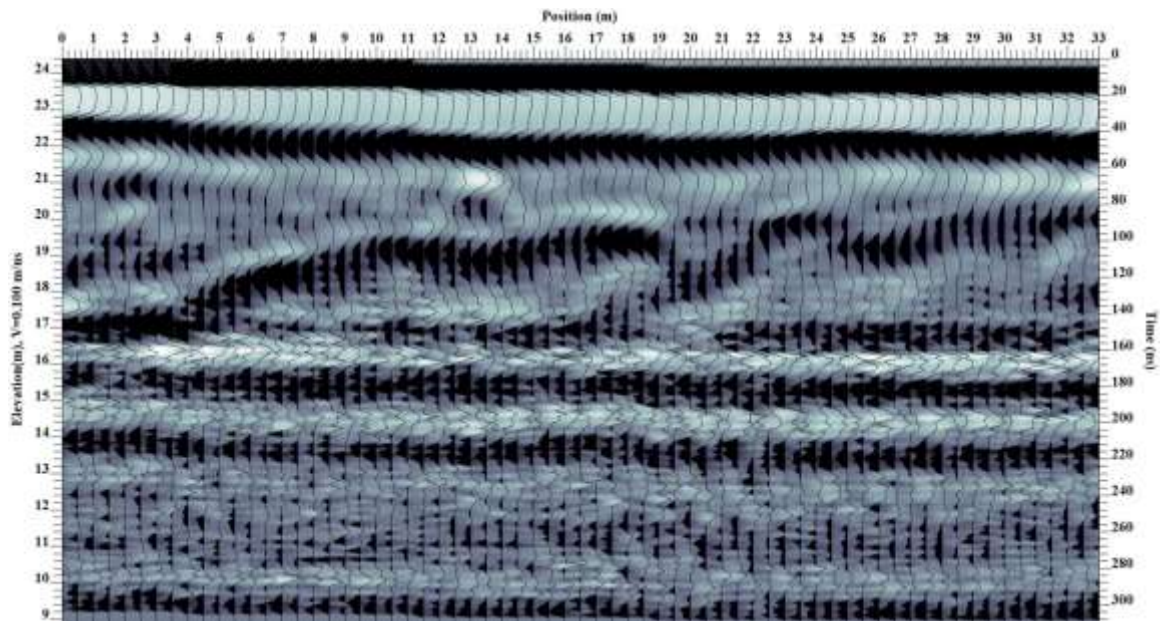


Figure C22: Processed radargram of Line 30

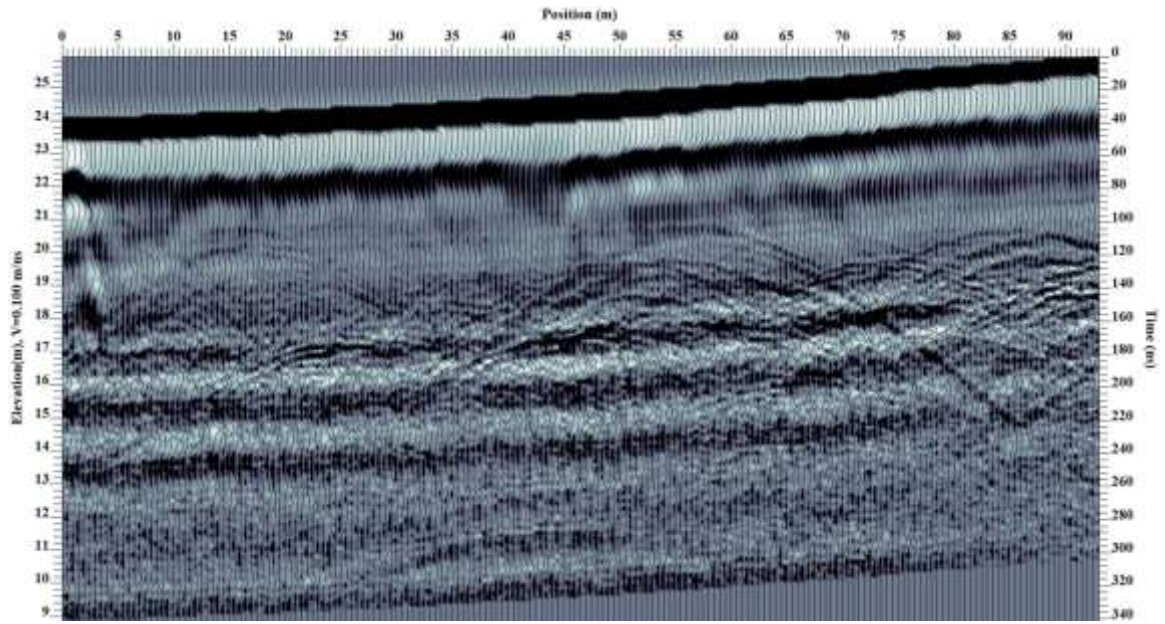


Figure C23: Processed radargram of Line 31

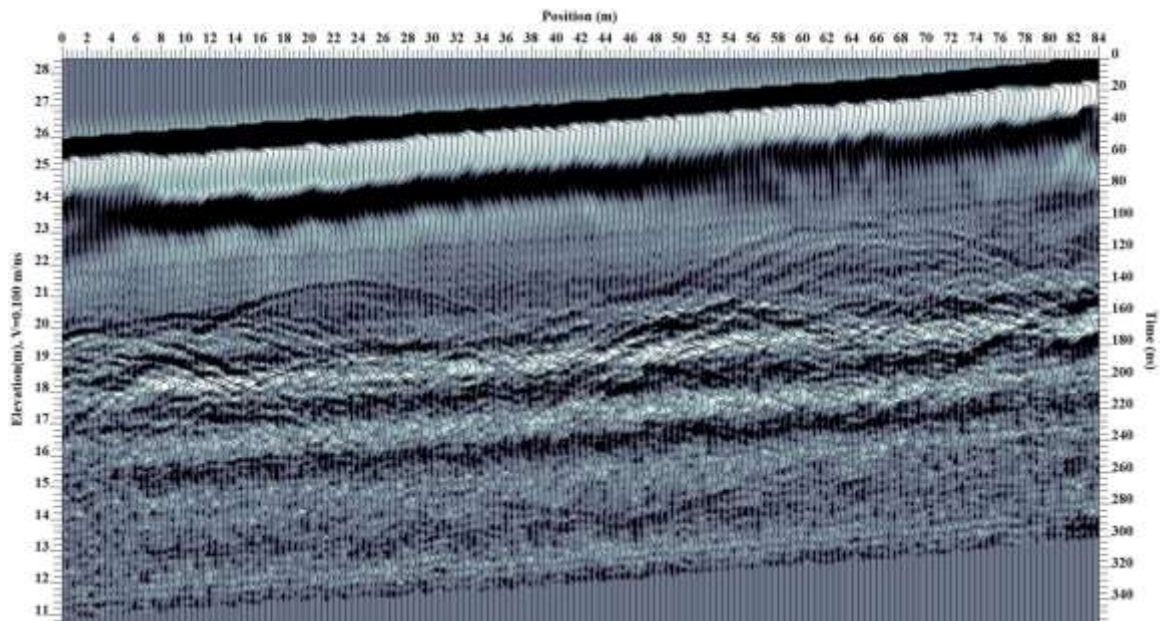


Figure C24: Processed radargram of Line 32

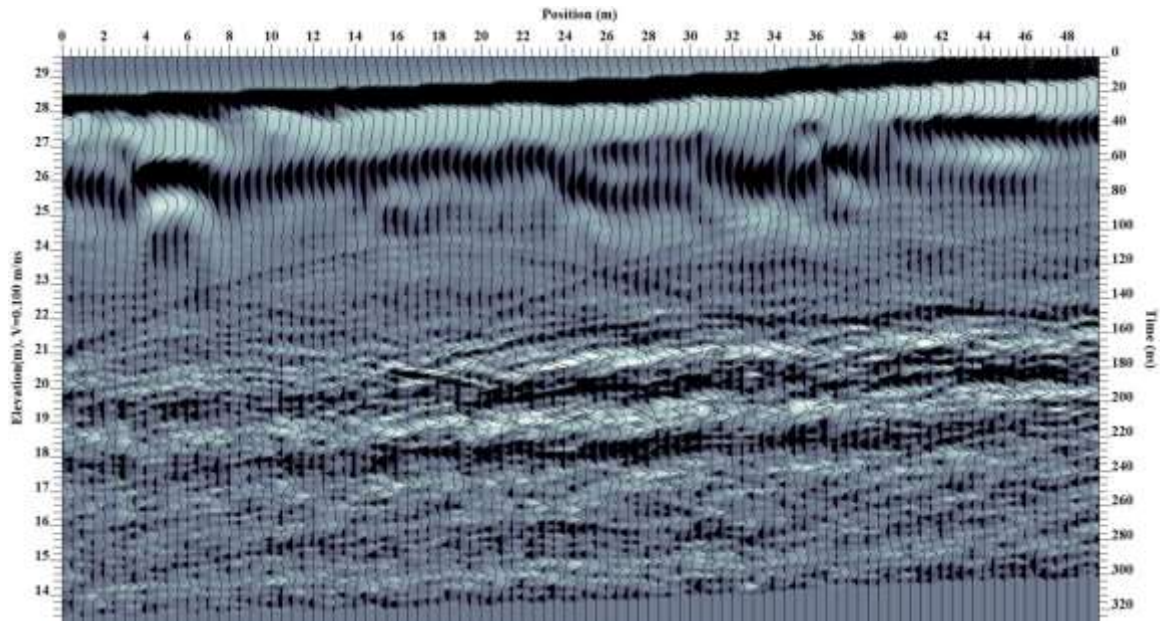


Figure C25: Processed radargram of Line 33

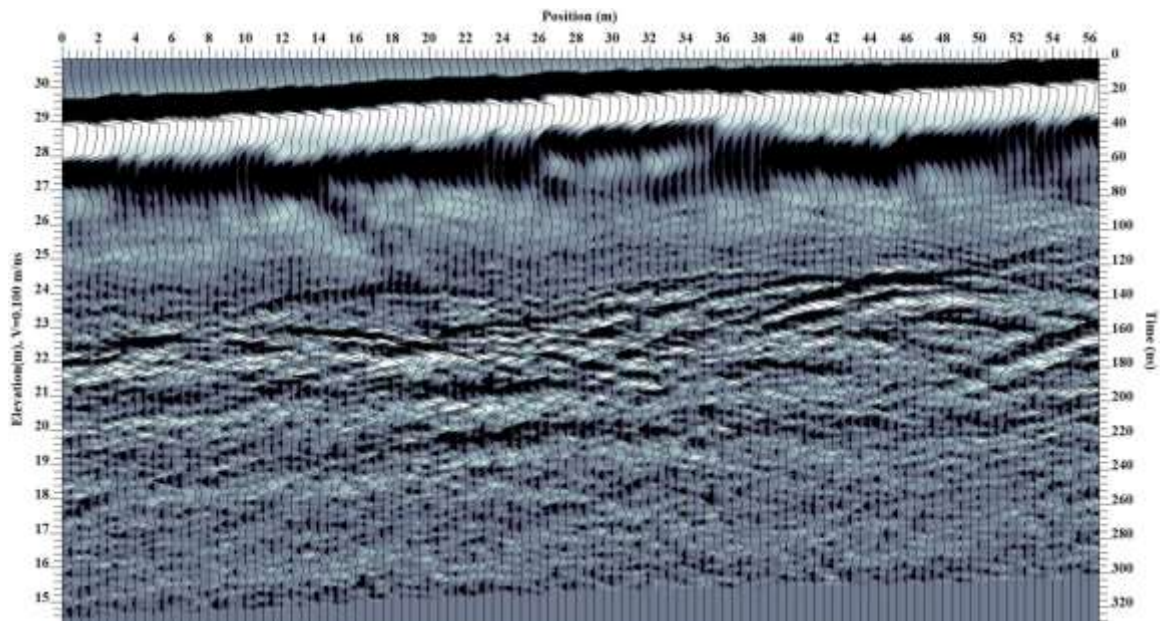


Figure C26: Processed radargram of Line 34

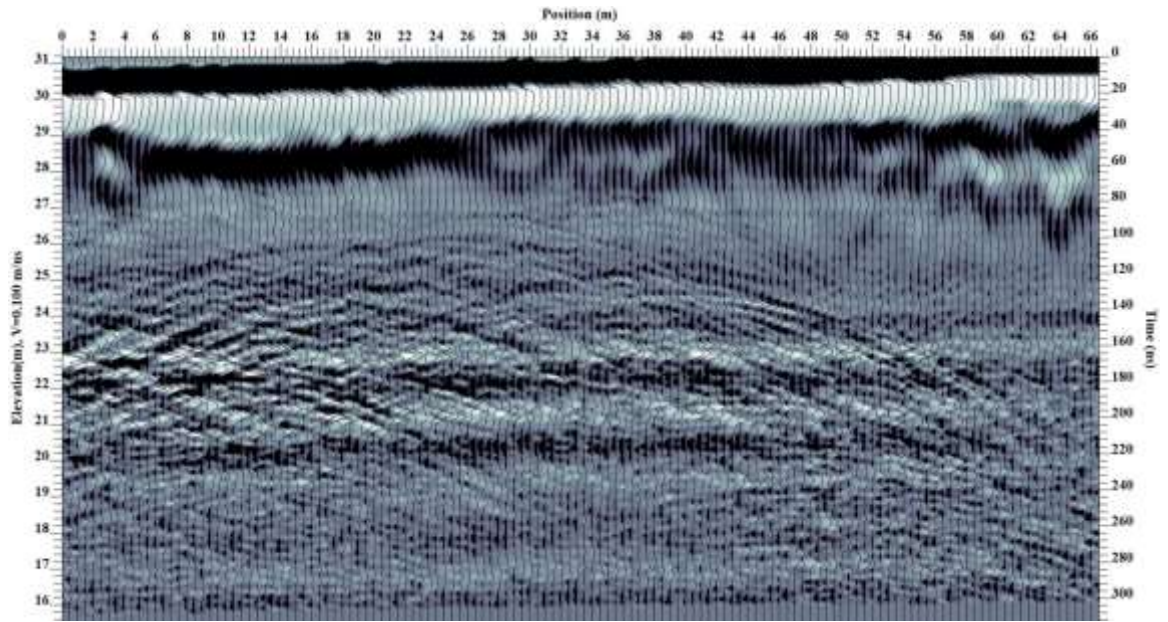


Figure C27: Processed radargram of Line 35

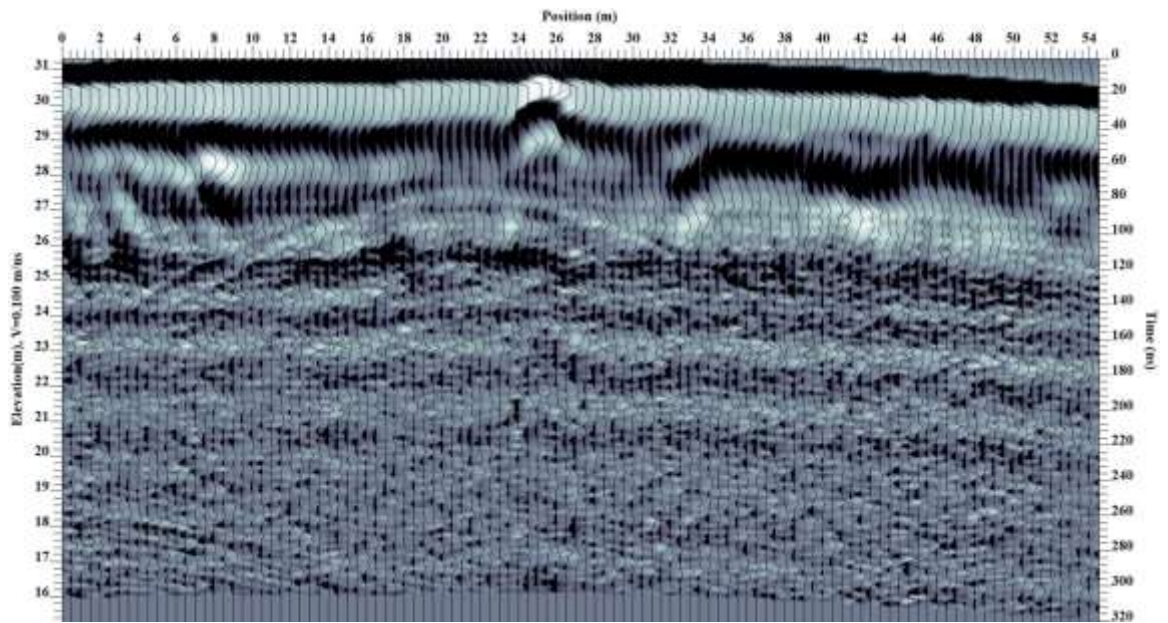


Figure C28: Processed radargram of Line 36

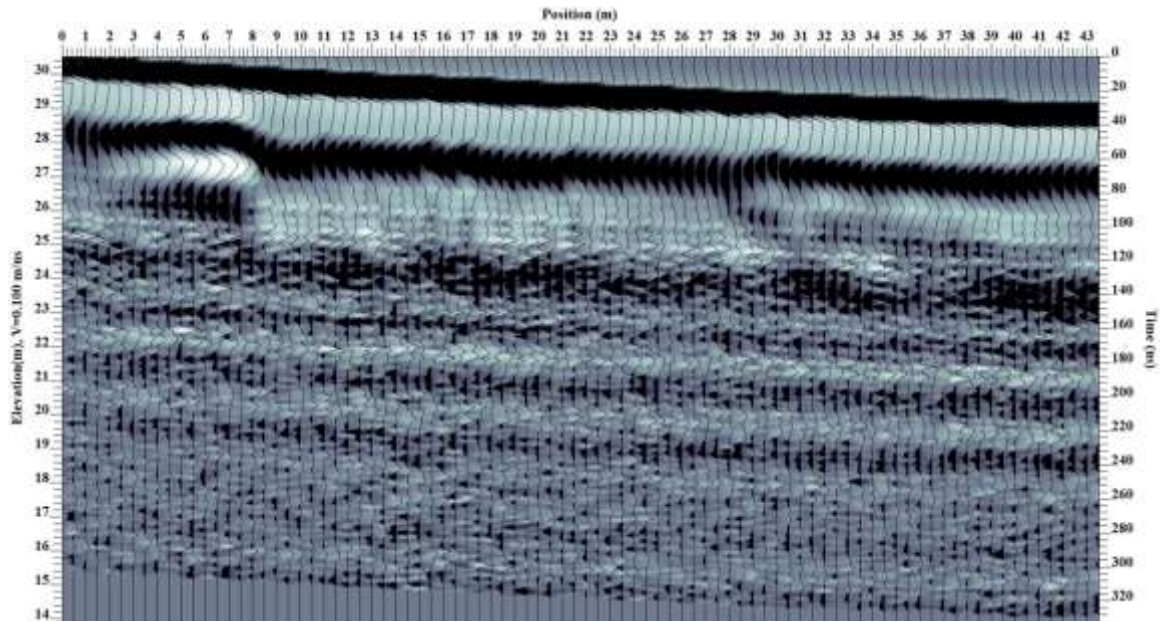


Figure C29: Processed radargram of Line 37

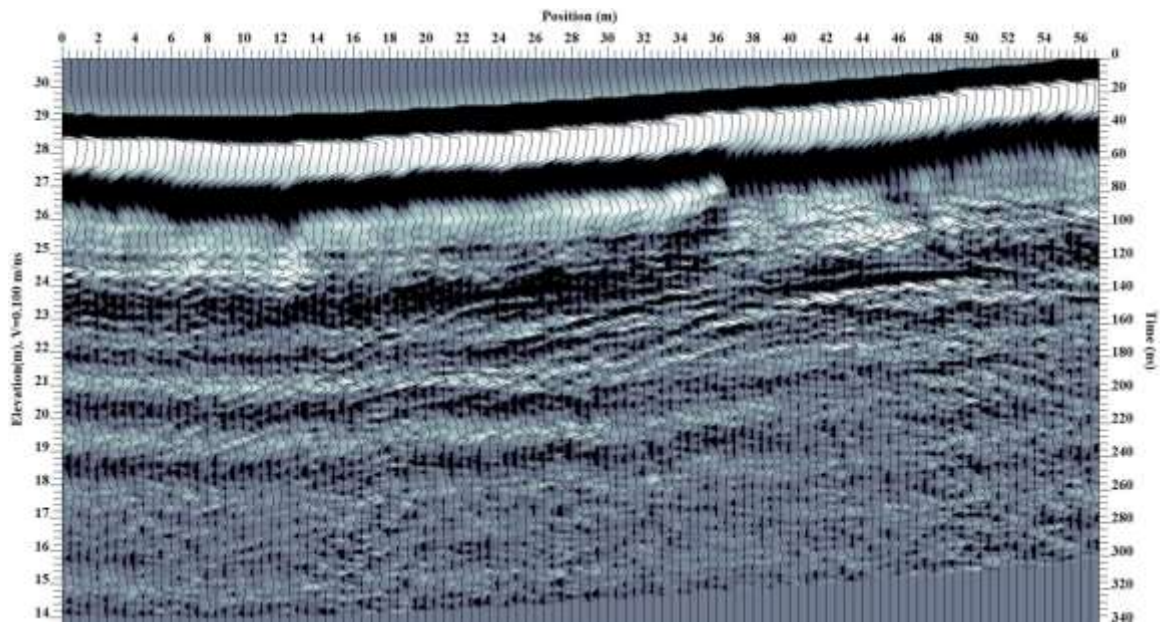


Figure C30: Processed radargram of Line 38

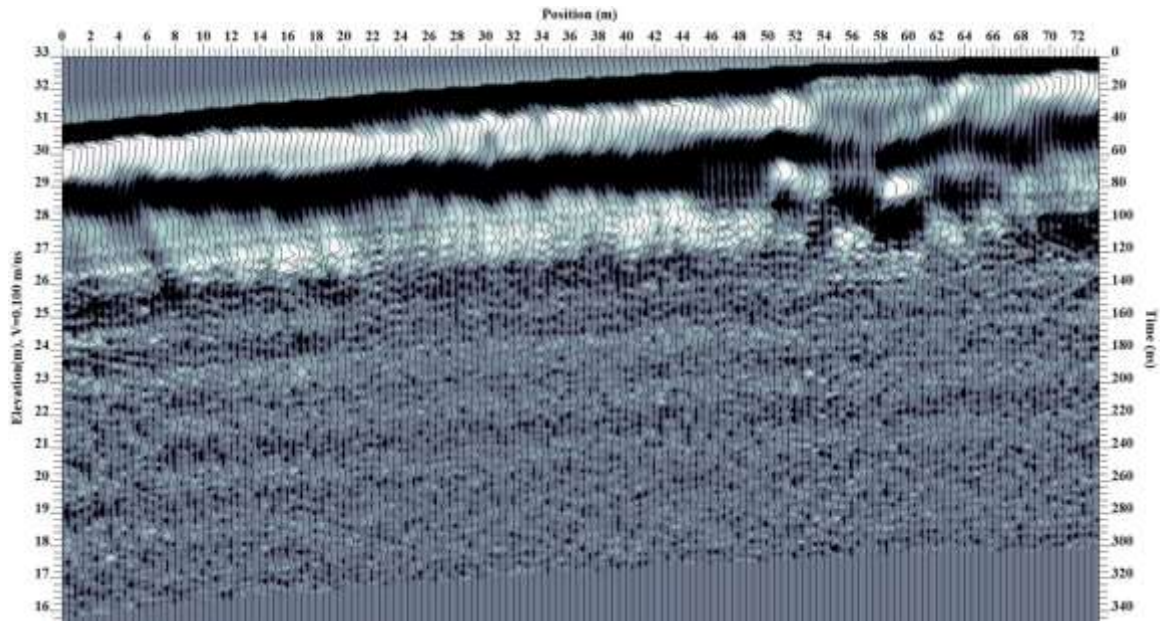


Figure C31: Processed radargram of Line 39

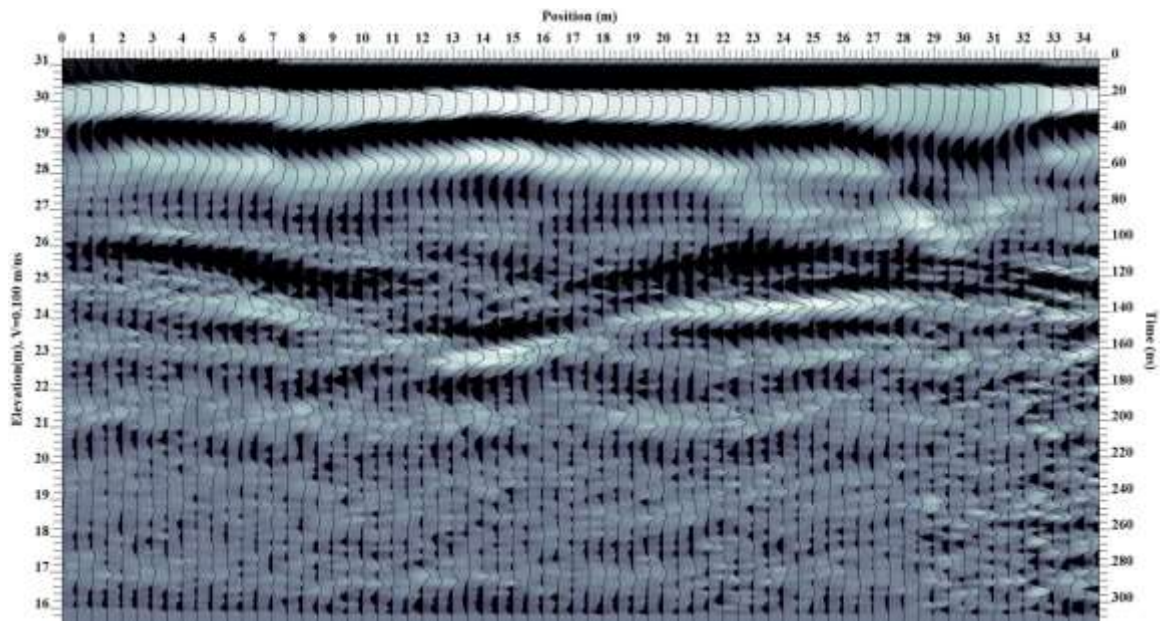


Figure C32: Processed radargram of Line 40

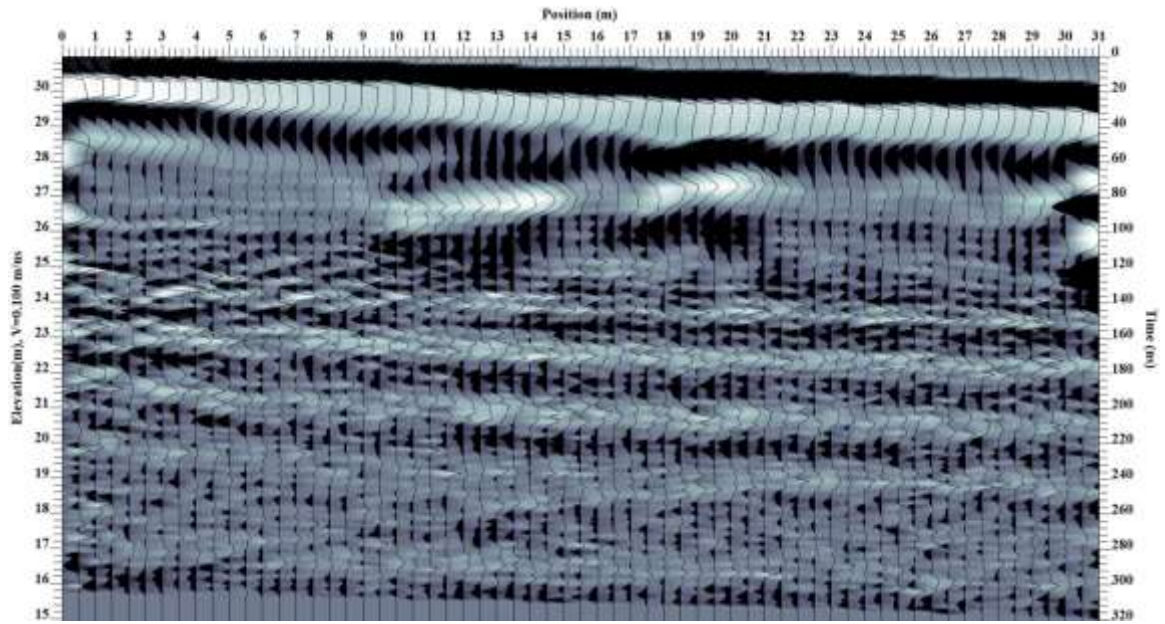


Figure C33: Processed radargram of Line 41

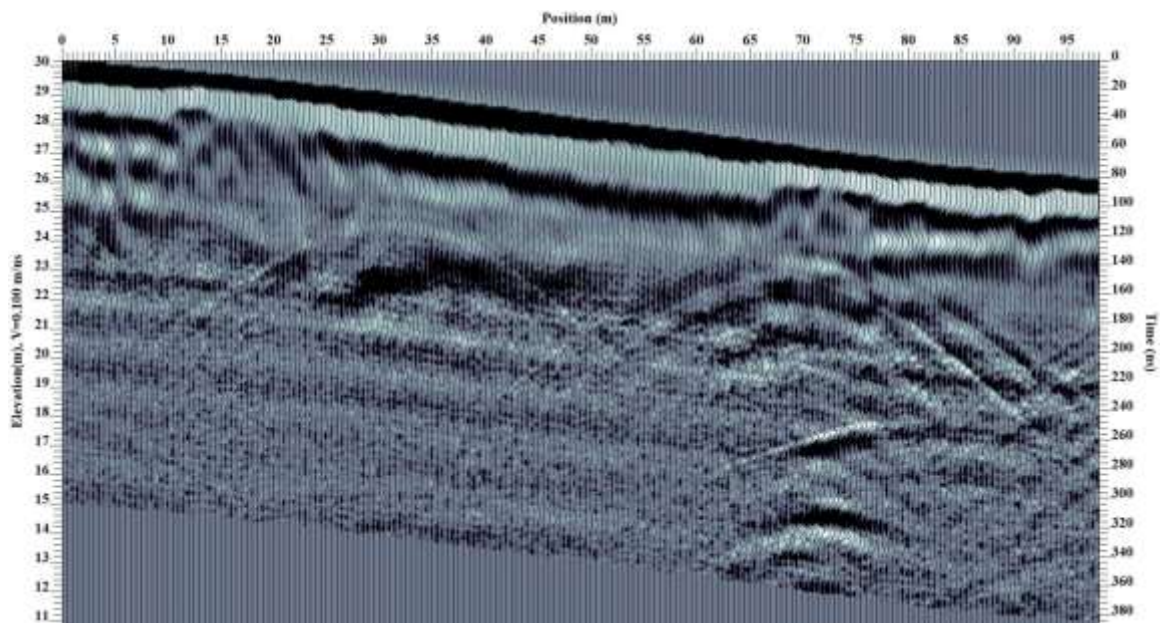


Figure C34: Processed radargram of Line 42

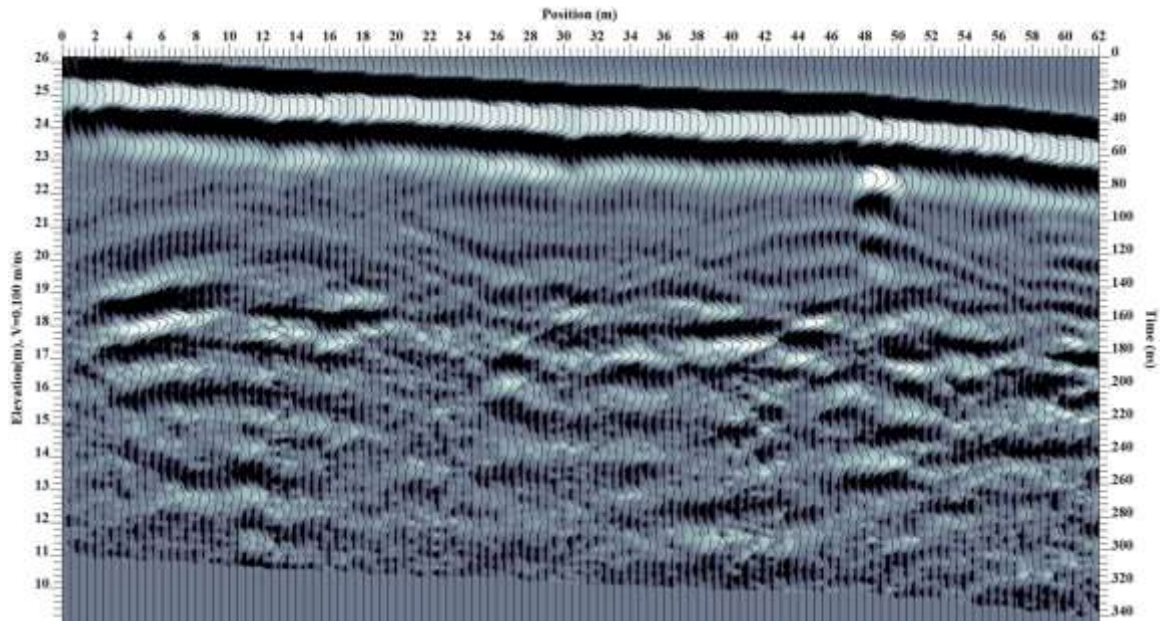


Figure C35: Processed radargram of Line 43

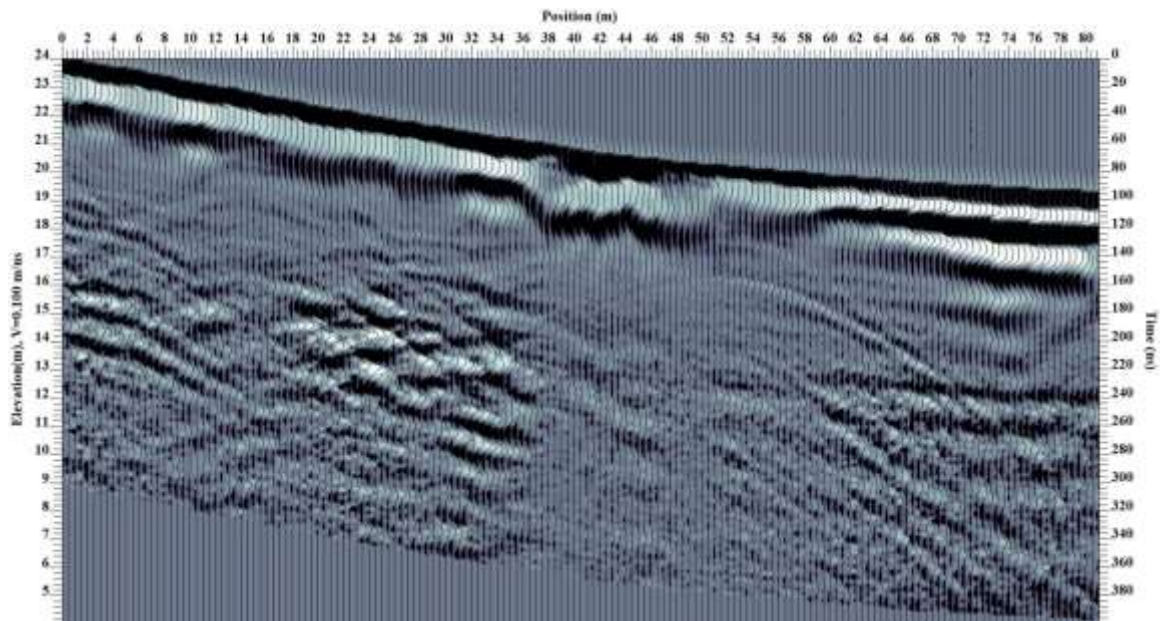


Figure C36: Processed radargram of Line 44

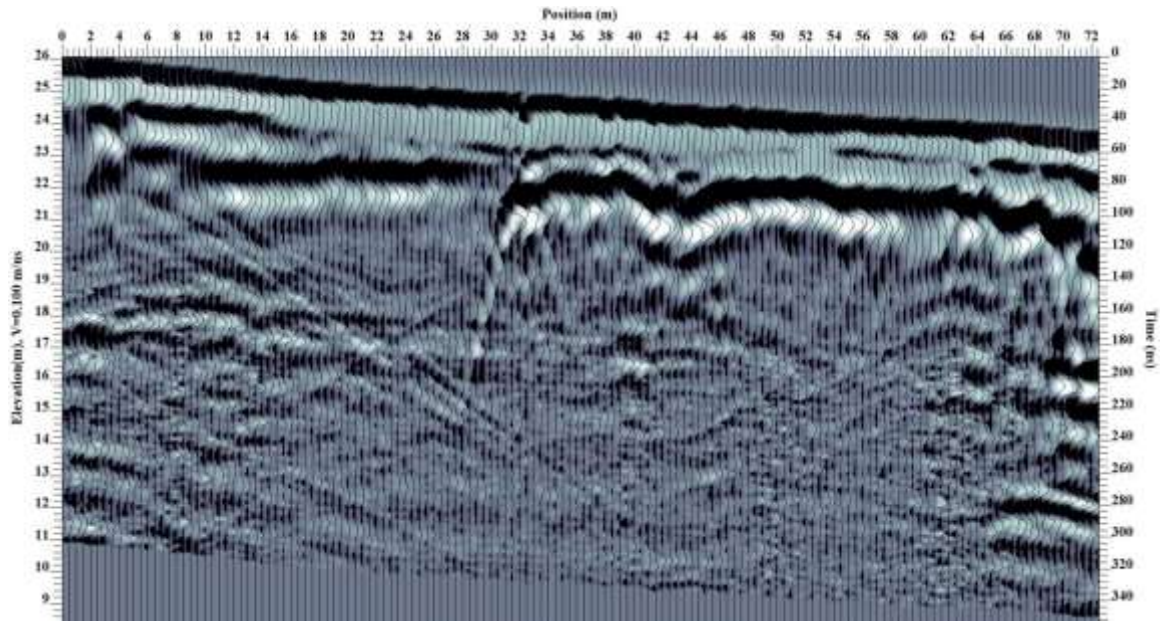


Figure C37: Processed radargram of Line 45

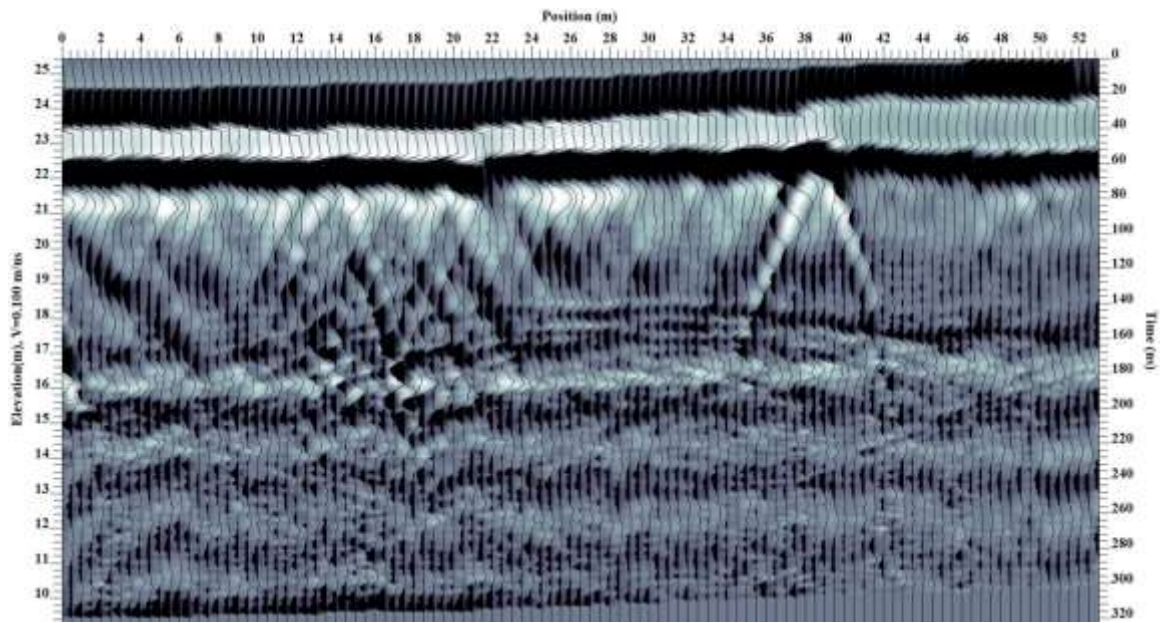


Figure C38: Processed radargram of Line 46

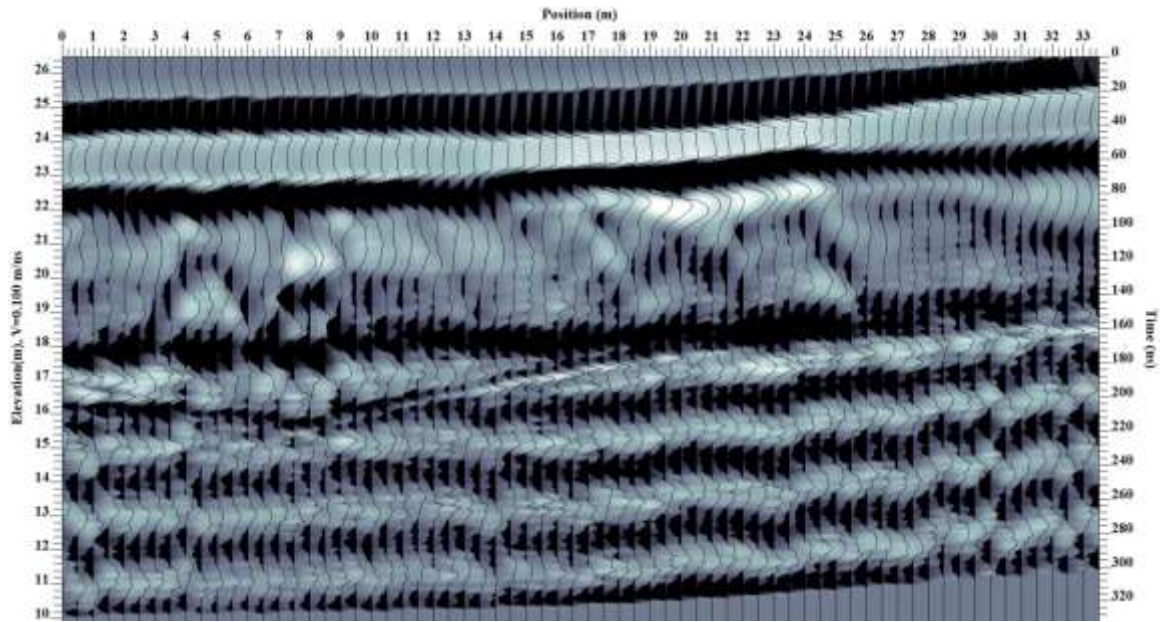


Figure C39: Processed radargram of Line 47

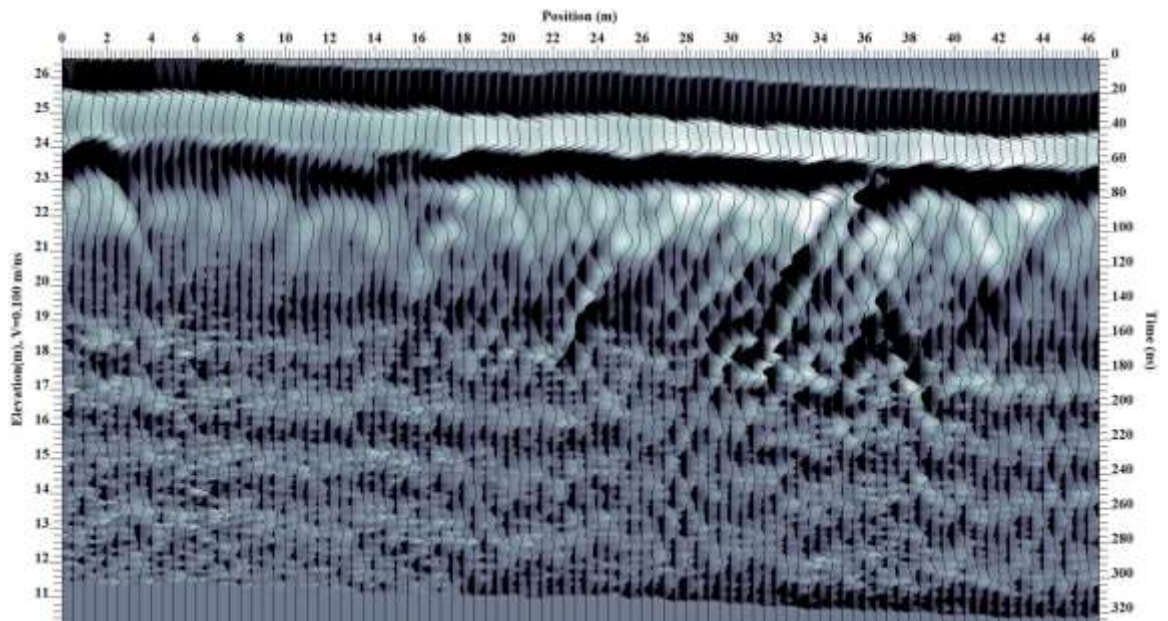


Figure C40: Processed radargram of Line 49

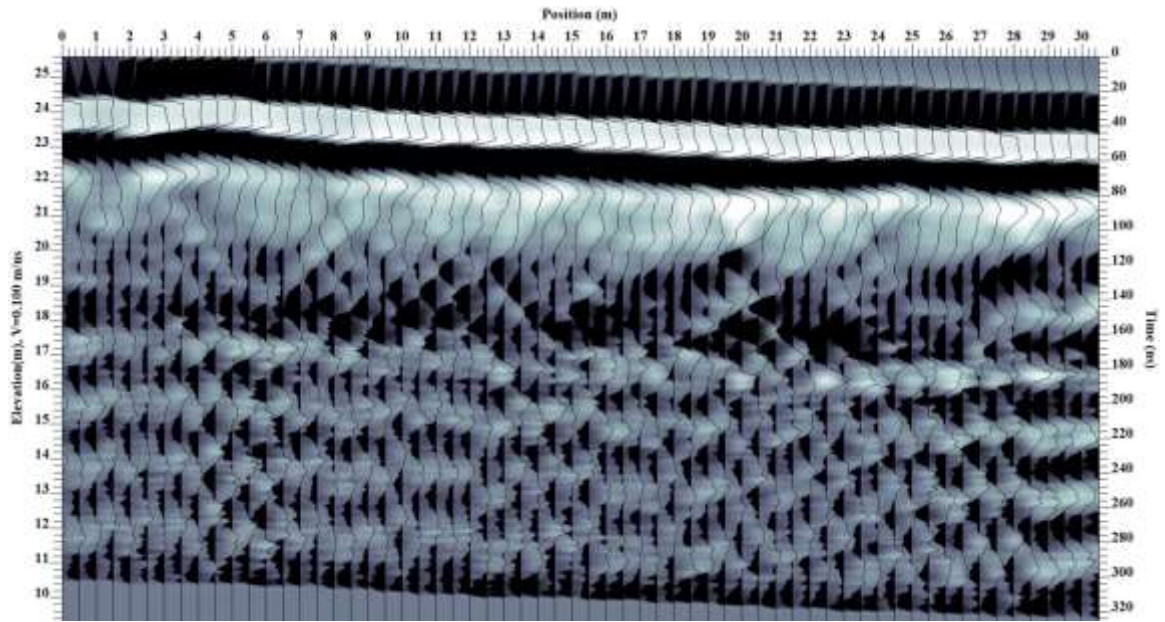


Figure C41: Processed radargram of Line 50

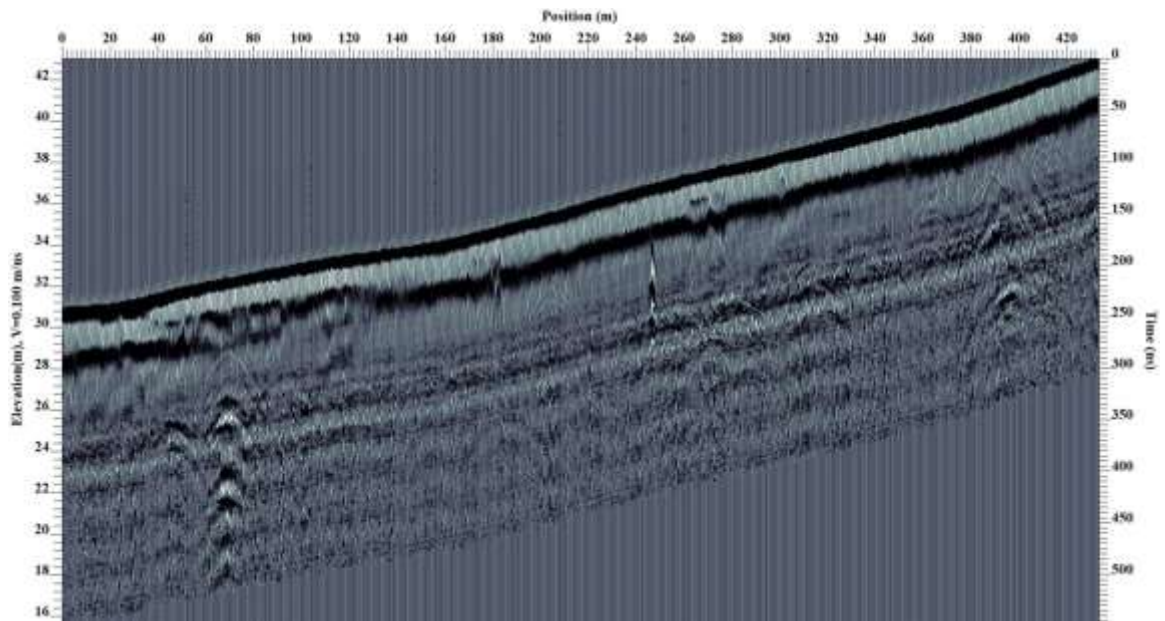


Figure C42: Processed radargram of Line 51

Appendix D: Drill Core Images of Borehole REI-B2-1

The following images are a documentation of the Joggins Formation core interval. They were collected using the apparatus discussed in Appendix F. The related core description of these photographed cores is documented in Appendix E.

Box 216	Box 217	Box 218	Box 219	Box 220	Box 221
765.00	763.50				
766.40	765.00				
767.90	766.40				
769.40	767.90				
770.90	769.40				
772.40	770.90				
773.85	772.40				
775.25	773.85				
776.70	775.25				
778.20	776.70				
779.80	778.20				
781.30	779.80				
782.80	781.30				
784.20	782.80				
785.60	784.20				
787.10	785.60				
788.60	787.10				
790.10	788.60				

Box 222	Box 223	Box 224	Box 225	Box 226	Box 227
791.60					790.10
793.04					791.60
794.50					793.04
795.65					794.50
797.21					795.65
798.50					797.21
800.00					798.50
801.50					800.00
803.00					801.50
804.50					803.00
806.00					804.50
807.50					806.00
808.92					807.50
810.35					808.92
811.80					810.35
813.40					811.80
814.90					813.40
816.40					814.90

	Box 228	Box 229	Box 230	Box 231	Box 232	Box 233
817.90						
819.40						
820.90						
822.20						
823.50						
824.80						
826.30						
827.80						
829.30						
830.80						
832.30						
833.80						
835.10						
836.50						
838.00						
839.45						
840.87						
842.00						

Box 234	Box 235	Box 236	Box 237	Box 238	Box 239
843.40					842.00
844.85					843.40
846.30					844.85
847.75					846.30
849.20					847.75
850.60					849.20
852.00					850.60
853.40					852.00
854.70					853.40
856.10					854.70
857.60					856.10
859.10					857.60
860.60					859.10
862.00					860.60
863.50					862.00
864.95					863.50
866.45					864.95
867.50					866.45

	Box 240	Box 241	Box 242	Box 243	Box 244	Box 245
869.05						867.50
870.60						869.05
872.10						870.60
873.45						872.10
874.80						873.45
876.30						874.80
877.80						876.30
879.30						877.80
880.80						879.30
882.35						880.80
883.90						882.35
885.40						883.90
886.70						885.40
888.15						886.70
889.60						888.15
891.15						889.60
892.65						891.15
894.20						892.65

	Box 246	Box 247	Box 248	Box 249	Box 250	Box 251
895.65						
897.10						
898.50						
899.95						
901.40						
902.80						
904.20						
905.70						
907.10						
908.55						
909.95						
911.30						
912.70						
914.15						
915.50						
916.90						
918.40						
919.90						

Box 252	Box 253	Box 254	Box 255	Box 256	Box 257
921.40					919.90
922.83					921.40
924.33					922.83
925.50					924.33
926.90 ...					925.50
928.30					926.90
929.80					928.30
931.30					929.80
932.80					931.30
934.20					932.80
935.60 ...					934.20
937.10					935.60
938.55					937.10
939.85					938.55
941.30					939.85
942.80					941.30
944.30					942.80
945.70					944.30

Box 258	Box 259	Box 260	Box 261	Box 262	Box 263
947.20	948.65	949.90	951.40	952.80	954.30
948.65	949.90	951.40	952.80	954.30	955.80
949.90	951.40	952.80	954.30	955.80	957.30
951.40	952.80	954.30	955.80	957.30	958.80
952.80	954.30	955.80	957.30	958.80	960.25
954.30	955.80	957.30	958.80	960.25	961.75
955.80	957.30	958.80	960.25	961.75	963.20
957.30	958.80	960.25	961.75	963.20	964.60
958.80	960.25	961.75	963.20	964.60	966.10
960.25	961.75	963.20	964.60	966.10	967.60
961.75	963.20	964.60	966.10	967.60	969.00
963.20	964.60	966.10	967.60	969.00	970.40
964.60	966.10	967.60	969.00	970.40	971.90
966.10	967.60	969.00	970.40	971.90	
967.60	969.00	970.40			
969.00	970.40				
970.40					
971.90					

Box 264	Box 265	Box 266	Box 267	Box 268	Box 269
---------	---------	---------	---------	---------	---------

973.40	971.90				
974.90	973.40				
976.40	974.90				
977.70	976.40				
979.00	977.70				
980.30	797.00				
981.50	980.30				
983.00	981.50				
984.50	983.00				
986.00	984.50				
987.50	986.00				
989.00	987.50				
990.50	989.00				
991.90	990.50				
993.40	991.90				
994.70	993.40				
996.10	994.70				
997.60	996.10				

	Box 270	Box 271	Box 272	Box 273	Box 274	Box 275
999.10						997.60
1,000.50						999.10
1,002.00						1,000.50
1,003.40						1,002.00
1,004.90						1,003.40
1,006.20						1,004.90
1,007.70						1,006.20
1,009.20						1,007.70
1,010.70						1,009.20
1,012.10						1,010.70
1,013.60						1,012.10
1,015.10						1,013.60
1,016.50						1,015.10
1,017.90						1,016.50
1,019.30						1,017.90
1,020.80						1,019.30
1,022.30						1,020.80
1,023.70						1,022.30

	Box 276	Box 277	Box 278	Box 279	Box 280	Box 281
1,025.20						1,023.70
1,026.70						1,025.20
1,028.20						1,026.70
1,029.60						1,028.20
1,031.00						1,029.60
1,032.40						1,031.00
1,033.70						1,032.40
1,035.00						1,033.70
1,036.30						1,035.00
1,037.80						1,036.30
1,039.20						1,037.80
1,040.70						1,039.20
1,042.00						1,040.70
1,043.30						1,042.00
1,044.60						1,043.30
1,045.10						1,044.60
1,047.40						1,046.10
1,048.90						1,047.40

	Box 282	Box 283	Box 284	Box 285	Box 286	Box 287
1,050.40						1,048.90
1,051.90						1,050.40
1,053.40						1,051.90
1,054.80						1,053.40
1,056.10						1,054.80
1,057.40						1,056.10
1,058.70						1,057.40
1,060.10						1,058.70
1,061.60						1,060.10
1,063.10						1,061.60
1,064.40						1,063.10
1,065.80						1,064.40
1,067.30						1,065.80
1,068.80						1,067.30
1,070.30						1,068.80
1,071.70						1,070.30
1,073.20						1,071.70
1,074.50						1,073.20

	Box 288	Box 289	Box 290	Box 291	Box 292	Box 293
1,076.00						1,074.50
1,077.50						1,076.00
1,079.70						1,077.50
1,080.40						1,079.70
1,081.40						1,080.40
1,082.40						1,081.40
1,084.00						1,082.40
1,085.60						1,084.00
1,087.10						1,085.60
1,088.50						1,087.10
1,089.90						1,088.50
1,091.30						1,089.90
1,092.70						1,091.30
1,094.20						1,092.70
1,095.60						1,094.20
1,097.10						1,095.60
1,098.50						1,097.10
1,100.00						1,098.50

Box 294

1,100.00
1,101.40
1,102.80



1,101.40
1,102.80
1,104.30

Appendix E: Drill Core Description of Borehole REI-B2-1

The following is a documentation of the core description for the Joggins Formation interval photographed in Appendix D.

The following core description incorporates my own visualization with those observations from the borehole history report. Depths are in metres.

765.00 to 765.70	[shale (90%), siltstone (10%)] grain size = clay contact = sharp dark grey; minor carbonaceous material; bands of reddish/brownish (siderite)
765.70 to 766.99	[sandstone (60%), shale (40%)] grain size = fine sand contact = gradational light grey, interlaminated sandstone and shale; flaser bedding; wavy bedding; horizontal planar lamination; minor bands of siderite
766.99 to 771.34	[shale (90%), sandstone (10%)] grain size = clay contact = sharp light to dark grey sandy shale; minor interlaminated shale and sandstone; minor carbonaceous material; minor coal; coalified plant roots; undulous laminations
771.34 to 771.74	[sandstone (90%), shale (10%)] grain size = fine to medium sand contact = sharp light grey; fine shale laminations; flaser bedding; rare bioturbation
771.74 to 775.70	[shale (85%), sandstone (15%)] grain size = clay contact = sharp light to medium grey; beds of interlaminated shale and sandstone; common bands of siderite; microfaulting
775.70 to 776.39	[shale (100%)] grain size = clay contact = gradational dark grey; frequent carbonaceous material; abundant shell frags.; minor bands of reddish/brownish (siderite)
776.39 to 784.00	[shale (80%), sandstone (20%)] grain size = clay contact = gradational medium grey; interlaminated shale and sandstone; minor bands of reddish/brownish (siderite); lenticular and wavy bedding; minor beds of carbonaceous shale; rare shell frags.; calcite veining
784.00 to 786.50	[sandstone (95%), shale (5%)] grain size = fine to medium sand contact = erosional light to medium grey; bedding at 80 degrees to core axis soft sediment deformation; syneresis (dewatering) cracks; rare bioturbation

786.50 to 803.27	[shale (50%), siltstone (50%)] grain size = clay contact = gradational dark grey; competent rock; bedding at 90 degrees to core axis; minor fine- to medium-grained sandstone sections; plant fossils/imprints common along fractures; three minor (~1 mm) calcite veins between
803.27 to 805.27	[shale (100%)] grain size = clay contact = sharp dark grey; carbonaceous; undifferentiated shell fragments
805.27 to 805.30	[coal (100%)] grain size = clay contact = sharp bituminous; fractured
805.30 to 805.73	[shale (80%), siltstone (20%)] grain size = clay contact = sharp medium grey, thinly laminated silty shale; minor bands of siderite
805.73 to 805.79	[shale (80%), coal (20%)] grain size = clay contact = sharp dark grey; carbonaceous shale; thin coal lamination rare shell fragments
805.79 to 808.68	[shale (95%), sandstone (5%)] grain size = clay contact = sharp light to dark grey; interlaminated fine sandstone; minor bands of siderite
808.68 to 808.92	[sandstone (70%), shale (30%)] grain size = medium sand contact = gradational light tan; shaley towards the base; thinly lam. with shale; bioturbation; syneresis cracks
808.92 to 809.2	[shale (80%), sandstone (20%)] grain size = clay contact = sharp light to dark grey; minor intervals of fs; becoming sandier at base; interlaminated; minor bands of siderite
809.20 to 810.63	[sandstone (95%), shale (5%)] grain size = medium sand contact = sharp light tan; interlaminated with thin shale; horizontal planar laminations; flaser laminations; rare siderite clasts

810.63 to 810.71	[shale (100%)] grain size = clay contact = sharp light to dark grey; minor intervals of interlaminated fine sandstone; minor bands of siderite
810.71 to 811.02	[sandstone (70%), shale (30%)] grain size = medium sand contact = sharp light tan; interbedded medium sandstone with thin shale laminations; horizontal planar laminations; lenticular laminations; trough cross laminations
811.02 to 813.45	[shale (90%), siltstone (10%)] grain size = clay contact = sharp light to medium grey; beds of interlaminated shale and sandstone; common bands of siderite
813.45 to 814.69	[shale (80%), sandstone (20%)] grain size = clay contact = sharp dark grey to black; carbonaceous shale; abundant undifferentiated shell frags; intervals of interlaminated fine sandstone; rare bands of siderite?
814.69 to 817.71	[shale (90%), siltstone (10%)] grain size = clay contact = sharp light to medium grey; beds of interlaminated shale and sandstone; common bands of siderite; abundant undifferentiated shell frags towards base
817.71 to 819.34	[sandstone (90%), shale (10%)] grain size = medium sand contact = sharp light tan; interlaminated with common shale laminations; microfaulting; siderite nodules and mudclasts; flaser bedding; syneresis cracks
819.34 to 819.84	[shale (80%), sandstone (20%)] grain size = clay contact = sharp medium grey shale with interlaminated fine-grained sandstone; rare shell fragments; common bands of siderite?
819.84 to 820.11	[shale (95%), sandstone (5%)] grain size = clay contact = sharp dark grey carbonaceous shale with short intervals of fine-grained sandstone; rare shell fragments

820.11 to 820.44	[coal (100%)] grain size = clay contact = sharp bituminous; fractured well-developed cleat
820.44 to 821.70	[shale (100%)] grain size = clay contact = sharp medium grey, thinly laminated shale
821.70 to 821.86	[coal (100%)] grain size = clay contact = sharp bituminous; fractured well-developed cleat
821.86 to 821.96	[shale (100%)] grain size = clay contact = sharp dark grey, thinly laminated carbonaceous shale; thin coal laminations
821.96 to 822.23	[coal (100%)] grain size = clay contact = sharp bituminous; fractured well-developed cleat
822.23 to 822.4	[shale (100%)] grain size = clay contact = sharp medium grey, thinly laminated shale
822.4 to 822.58	[coal (100%)] grain size = clay contact = sharp bituminous; fractured well-developed cleat
822.58 to 822.78	[shale (100%)] grain size = clay contact = sharp dark grey carbonaceous shale; rare shell fragments
822.78 to 823.03	[coal (100%)] grain size = clay contact = sharp bituminous; fractured well-developed cleat
823.03 to 833.26	[shale (100%)] grain size = clay contact = sharp medium to dark grey thinly laminated shale; intervals of interlaminated fine-grained sandstone; intervals of carbonaceous shale and coal; rare shell fragments
833.26 to 834.26	[sandstone (80%), shale (20%)] grain size = fine sand contact = sharp light tan, fine-grained sandstone interlaminated with shale

834.26 to 839.70	[shale (90%), coal (10%)] grain size = clay contact = sharp medium to dark grey shale; carbonaceous intervals; rare thin coal laminations; common bands of reddish/brownish (siderite); rare shell fragments
839.70 to 839.74	[coal (100%)] grain size = clay contact = sharp bituminous; fractured well-developed cleat
839.74 to 839.78	[shale (90%), coal (10%)] grain size = clay contact = sharp medium to dark grey shale carbonaceous intervals; rare thin coal laminations; common bands of reddish/brownish (siderite?); rare shell fragments
839.78 to 840.33	[coal (100%)] grain size = clay contact = sharp bituminous; fractured well-developed cleat
840.33 to 841.40	[shale (100%)] grain size = clay contact = sharp medium to dark grey shale; carbonaceous intervals; rare clasts of siderite; rare shell fragments
841.40 to 841.90	[coal (100%)] grain size = clay contact = sharp bituminous; fractured well-developed cleat
841.90 to 842.12	[shale (100%)] grain size = clay contact = sharp medium to dark grey shale; carbonaceous intervals
842.12 to 842.15	[coal (100%)] grain size = clay contact = sharp bituminous; fractured well-developed cleat
842.15 to 842.20	[shale (100)] grain size = clay contact = sharp grey shale
842.20 to 842.22	[coal (100%)] grain size = clay contact = sharp bituminous; fractured well-developed cleat

842.22 to 842.50	[shale (100%)] grain size = clay contact = sharp grey thinly laminated
842.50 to 842.59	[shale (100%)] grain size = clay contact = sharp shaley mud seam
842.59 to 842.85	[shale (100%)] grain size = clay contact = sharp shaley mudstone; calcareous
842.85 to 842.90	[mudstone (100%)] grain size = clay contact = sharp muddy
842.90 to 843.30	[shale (100%)] grain size = clay contact = sharp calcareous
843.30 to 845.77	[sandstone (90%), shale (10%)] grain size = fine to medium sand contact = sharp light to medium grey; grades into sandy silt in the last 50 cm; weakly calcareous along fractures; rare bands of siderite?
845.77 to 851.18	[shale (100%)] grain size = fine sand contact = sharp medium to dark grey; laminated; slickensides along fractures; slightly carbonaceous in intervals; thin coal laminations; rare bands of siderite?
851.18 to 851.65	[sandstone (90%), shale (10%)] grain size = fine to medium sand contact = gradational light tan; interlaminated with shale; rare bands and clasts of siderite; becoming shaley towards base; offset of laminations (microfaulting)
851.65 to 858.36	[shale (80%), sandstone (20%)] grain size = clay contact = sharp medium to dark grey; interlaminated with fine-grained sandstone; slickensides along fractures; silty carbonaceous in intervals; thin coal laminations; rare bands and clasts of reddish/brownish (siderite)
858.36 to 865.68	[sandstone (90%), silt (10%)] grain size = medium sand contact = sharp minor sandy silt

865.68 to 866.80	[shale (50%), silt (50%)] grain size = clay contact = sharp grey shale and silt; fractures at 80 degrees to core axis and parallel to bedding
866.80 to 866.88	[coal (100%)] grain size = clay contact = sharp bituminous; fractured poorly develop. cleat; pyritic
866.88 to 867.70	[shale (50%), silt (50%)] grain size = clay contact = sharp grey shale and silt; fractures at 80 degrees to core axis and parallel to bedding
867.70 to 874.00	[sandstone (100%)] grain size = medium sand contact = sharp light grey with occasional thin beds of sandy silt
874.00 to 877.20	[shale (50%), silt (50%)] grain size = clay contact = sharp medium to dark grey; coaly laminae
877.2 to 878.6	[sandstone (100%)] grain size = medium sand contact = sharp grey sandstone; competent
878.6 to 879.87	[shale (50%), silt (50%)] grain size = clay contact = sharp medium to dark grey shale and silt; coaly laminae
879.87 to 880.14	[coal (100%)] grain size = clay contact = sharp bituminous; fractured; poorly developed. cleat; pyritic
880.14 to 880.22	[shale (50%), silt (50%)] grain size = clay contact = sharp medium to dark grey shale and silt; coaly laminae
880.22 to 880.23	[coal (100%)] grain size = clay contact = sharp bituminous; fractured poorly develop. cleat; pyritic
880.23 to 880.8	[shale (50%), silt (50%)] grain size = clay contact = sharp medium to dark grey shale and silt; coaly laminae

880.80 to 885.40	[sandstone (50%), silt (50%)] grain size = fine to medium sand contact = sharp light to medium grey sandstone and silt; minor laminated shale; plant fossils/imprints along fractures
885.40 to 888.5	[shale (100%)] grain size = clay contact = sharp dark grey; laminated; plant fossils/imprints along fractures
888.50 to 889.80	[sandstone (100%)] grain size = medium to coarse sand contact = sharp light to medium grey
889.80 to 890.36	[shale (70%), silt (30%)] grain size = clay contact = sharp medium dark grey laminations; plant fossils along fractures
890.36 to 890.40	[coal (100%)] grain size = clay contact = sharp bituminous; fractured poorly developed cleat; pyritic
890.40 to 890.58	[shale (70%), silt (30%)] grain size = clay contact = sharp medium dark grey laminations; plant fossils along fractures
890.58 to 890.59	[coal (100%)] grain size = clay contact = sharp bituminous; fractured poorly developed cleat; pyritic
890.59 to 890.80	[shale (70%), silt (30%)] grain size = clay contact = sharp medium dark grey laminations; plant fossils along fractures
890.8 to 890.83	[coal (100%)] grain size = clay contact = sharp bituminous; fractured poorly developed cleat; pyritic
890.83 to 893.65	[shale (70%), silt (30%)] grain size = clay contact = sharp medium dark grey laminations; plant fossils along fractures
893.65 to 893.68	[coal (100%)] grain size = clay contact = sharp bituminous; fractured poorly developed cleat; pyritic

893.68 to 893.80	[shale (70%), silt (30%)] grain size = clay contact = sharp medium dark grey laminations; plant fossils along fractures
893.80 to 893.92	[coal (100%)] grain size = clay contact = sharp bituminous; fractured poorly developed cleat; pyritic
893.92 to 894.40	[shale (70%), silt (30%)] grain size = clay contact = sharp medium dark grey laminations; plant fossils along fractures
894.40 to 894.43	[shale (70%), mudstone (30%)] grain size = clay contact = sharp medium dark grey laminations; plant fossils along fractures
894.43 to 894.91	[shale (70%), silt (30%)] grain size = clay contact = sharp medium dark grey laminations; plant fossils along fractures
894.91 to 894.95	[coal (100%)] grain size = clay contact = sharp bituminous; fractured poorly developed cleat; pyritic
894.95 to 896.09	[mudstone (100%)] grain size = clay contact = sharp dark grey mudstone; minor silt/shale; pitted texture; soft minor carbonaceous material
896.09 to 896.13	[coal (100%)] grain size = clay contact = sharp bituminous; fractured poorly developed cleat; pyritic
896.13 to 896.71	[mudstone (100%)] grain size = clay contact = sharp dark grey mudstone; minor silt/shale; pitted texture; soft minor carbonaceous material
896.71 to 896.82	[coal (100%)] grain size = clay contact = sharp bituminous; fractured poorly developed cleat; pyritic
896.82 to 896.91	[mudstone (100%)] grain size = clay contact = sharp dark grey mudstone; minor silt/shale; pitted texture; soft minor carbonaceous material

896.91 to 896.97	[coal (100%)] grain size = clay contact = sharp bituminous; fractured poorly developed cleat; pyritic
896.97 to 897.07	[mudstone (100%)] grain size = clay contact = sharp dark grey; minor silt/shale; pitted texture; soft minor carbonaceous material
897.07 to 897.17	[coal (100%)] grain size = clay contact = sharp bituminous; fractured poorly developed cleat; pyritic
897.17 to 905.24	[shale (100%)] grain size = clay contact = sharp dark grey; carbonaceous
905.24 to 909.30	[sandstone (100%)] grain size = fine sand contact = sharp light grey; minor thin beds of sandy silt
909.3 to 911.24	[shale (100%)] grain size = clay contact = sharp dark grey
911.24 to 911.3	[coal (100%)] grain size = clay contact = sharp bituminous; fractured well-developed cleat
911.30 to 911.33	[shale (100%)] grain size = clay contact = sharp dark grey
911.33 to 911.37	[coal (100%)] grain size = clay contact = sharp bituminous; fractured well-developed cleat
911.37 to 912.00	[shale (100%)] grain size = clay contact = sharp dark grey; carbonaceous
912.00 to 914.05	[sandstone (100%)] grain size = medium sand contact = sharp light grey; thin silt beds

914.05 to 915.58	[shale (100%)] grain size = clay contact = sharp grey; occasional sandy silt beds
915.58 to 916.92	[sandstone (100%)] grain size = fine sand contact = sharp light grey; thin silt beds; competent
916.92 to 919.44	[shale (100%)] grain size = clay contact = sharp dark grey; occasional sandy silt beds
919.44 to 920.73	[sandstone (100%)] grain size = medium sand contact = sharp light grey; thin silt beds
920.73 to 921.31	[shale (100%)] grain size = clay contact = sharp light grey; occasional sandy silt beds
921.31 to 923.63	[sandstone (100%)] grain size = fine sand contact = gradational light to medium grey; thinly laminated
923.9 to 924.59	[shale (100%)] grain size = clay contact = sharp light grey; carbonaceous
924.59 to 925.31	[coal (100%)] grain size = clay contact = sharp bituminous; fractured well-developed cleat
925.31 to 926.63	[shale (100%)] grain size = clay contact = sharp dark grey; carbonaceous
926.63 to 930.28	[sandstone (100%)] grain size = fine sand contact = sharp light grey; finely laminated
930.28 to 934.57	[shale (100%)] grain size = clay contact = sharp dark grey; carbonaceous; plant fossils/imprints along fractures

934.57 to 935.2	[sandstone (100%)] grain size = fine sand contact = gradational light grey; finely laminated
935.2 to 936.51	[shale (100%)] grain size = clay contact = sharp dark grey; plant fossils/imprints along fractures
936.51 to 937.5	[sandstone (100%)] grain size = fine to medium sand contact = sharp light grey
937.50 to 938.90	[shale (100%)] grain size = clay contact = sharp dark grey; plant fossils/imprints along fractures
938.9 to 938.92	[coal (100%)] grain size = clay contact = sharp bituminous; fractured well-developed cleat
938.92 to 939.01	[shale (100%)] grain size = clay contact = sharp dark grey; plant fossils/imprints along fractures
939.01 to 939.77	[sandstone (100%)] grain size = fine sand contact = gradational light grey; finely laminated
939.77 to 940.83	[shale (100%)] grain size = clay contact = gradational dark grey; plant fossils/imprints along fractures
940.83 to 944.61	[sandstone (100%)] grain size = fine sand contact = sharp light grey; occasional thin sandy silt bed
944.61 to 946.74	[shale (100%)] grain size = clay contact = sharp dark grey; plant fossils/imprints along fractures
946.74 to 948.65	[sandstone (100%)] grain size = fine sand contact = sharp light grey

948.65 to 950.72	[shale (100%)] grain size = clay contact = sharp dark grey; plant fossils/imprints along fractures
950.72 to 951.01	[sandstone (100%)] grain size = medium sand contact = sharp light grey
951.01 to 952.62	[shale (100%)] grain size = clay contact = sharp dark grey; plant fossils/imprints along fractures
952.62 to 953.1	[sandstone (100%)] grain size = medium sand contact = sharp light grey
953.1 to 953.37	[shale (100%)] grain size = clay contact = sharp dark grey; plant fossils/imprints along fractures
953.37 to 953.51	[sandstone (100%)] grain size = medium sand contact = sharp light grey
953.51 to 953.68	[shale (100%)] grain size = clay contact = sharp dark grey; plant fossils/imprints along fractures
953.68 to 954.25	[sandstone (100%)] grain size = medium sand contact = sharp light grey
954.25 to 955.95	[shale (100%)] grain size = clay contact = gradational dark grey; plant fossils/imprints along fractures
955.95 to 956.20	[coal (100%)] grain size = clay contact = sharp bituminous; fractured well-developed cleat
956.20 to 960.10	[sandstone (100%)] grain size = medium sand contact = sharp medium grey; minor shale sections

960.1 to 960.45	[silt (100%)] grain size = silt contact = sharp dark grey; plant fossils along fractures
960.45 to 960.5	[mudstone (100%)] grain size = clay contact = sharp shaley mud seam
960.50 to 962.80	[shale (50%), silt (50%)] grain size = clay to silt contact = sharp dark grey; plant fossils along fractures
962.80 to 964.20	[sandstone (90%), shale (10%)] grain size = medium sand contact = sharp medium grey; minor shale sections
964.20 to 964.80	[shale (100%)] grain size = clay contact = sharp dark grey; plant fossils/imprints along fractures
964.80 to 968.80	[sandstone (90%), shale (10%)] grain size = fine to medium sand contact = sharp medium grey; minor shale sections
968.80 to 969.90	[shale (100%)] grain size = clay contact = sharp dark grey; plant fossils/imprints along fractures
969.90 to 971.50	[sandstone (90%), shale (10%)] grain size = fine to medium sand contact = sharp medium grey; minor shale sections
971.50 to 976.40	[shale (90%), silt (10%)] grain size = clay contact = sharp dark grey; interbedded with silt and minor sandstone; plant fossils along fracture surfaces; carbonaceous shale
976.40 to 976.64	[shale (100%)] grain size = clay contact = sharp dark grey; interbedded with silt and minor sandstone; plant fossils along fracture surfaces; carbonaceous shale
976.64 to 976.95	[coal (100%)] grain size = clay contact = sharp bituminous; fractured well-developed cleat

976.95 to 977.14	[shale (100%)] grain size = clay contact = sharp dark grey; interbedded with silt and minor sandstone; plant fossils along fracture surfaces; carbonaceous shale
977.14 to 977.75	[coal (100%)] grain size = clay contact = sharp bituminous; fractured well-developed cleat
977.75 to 979.77	[shale (100%)] grain size = clay contact = sharp dark grey; interbedded with silt and minor sandstone; plant fossils along fracture surfaces; carbonaceous
979.77 to 979.85	[mudstone (100%)] grain size = clay contact = sharp
979.85 to 980.05	[coal (100%)] grain size = clay contact = sharp bituminous; fractured well-developed cleat
980.05 to 980.30	[shale (100%)] grain size = clay contact = sharp dark grey; interbedded with silt and minor sandstone; plant fossils along fracture surfaces; carbonaceous shale
980.3 to 982.08	[shale (70%), silt (30%)] grain size = clay contact = sharp interbedded grey shale and sandy silt
982.08 to 982.13	[mudstone (100%)] grain size = clay contact = sharp
982.13 to 983.15	[shale (70%), silt (30%)] grain size = clay contact = sharp interbedded grey shale and sandy silt
983.15 to 991.86	[sandstone (50%), silt (50%)] grain size = clay contact = sharp interbedded; light grey
991.86 to 995.59	[shale (100%)] grain size = clay contact = sharp dark grey; carbonaceous

995.59 to 1003.00	[sandstone (50%), silt (50%)] grain size = clay contact = sharp light grey
1003.00 to 1005.30	[sandstone (100%)] grain size = clay contact = sharp medium grey
1005.30 to 1010.70	[shale (100%)] grain size = clay contact = sharp dark grey; laminated; plant fossils along fractures
1010.70 to 1013.00	[sandstone (100%)] grain size = medium to coarse sand contact = sharp medium grey; lenses of carbonaceous material
1013.00 to 1023.80	[silt (50%), shale (50%)] grain size = clay to silt contact = sharp medium to dark grey; minor sandy silt sections; laminated
1023.80 to 1026.00	[sandstone (100%)] grain size = medium sand contact = sharp medium grey
1026.00 to 1027.00	[shale (100%)] grain size = clay contact = sharp
1027.00 to 1030.00	[sandstone (100%)] grain size = medium sand contact = sharp medium grey
1030.02 to 1030.20	[conglomerate (100%)] grain size = pebble contact = sharp polymictic, matrix-supported with pebble-sized clasts and moderately to poorly rounded and sorted
1030.22 to 1039.60	[sandstone (100%)] grain size = medium sand contact = sharp medium grey
1039.60 to 1050.30	[silt (50%), shale (50%)] grain size = clay to silt contact = sharp light grey; calcite along fracture surfaces

1050.28 to 1055.40	[sandstone (50%), silt (50%)] grain size = fine sand to silt contact = sharp interbedded
1055.44 to 1055.60	[coal (100%)] grain size = clay contact = sharp bituminous; fractured well-developed cleat
1055.57 to 1055.70	[shale (100%)] grain size = clay contact = sharp dark grey; carbonaceous
1055.68 to 1055.70	[mudstone (100%)] grain size = clay contact = sharp
1055.70 to 1055.90	[shale (100%)] grain size = clay contact = sharp dark grey; carbonaceous
1055.86 to 1055.90	[coal (100%)] grain size = clay contact = sharp bituminous; fractured well-developed cleat
1055.87 to 1056.30	[shale (100%)] grain size = clay contact = sharp dark grey; carbonaceous
1056.30 to 1056.30	[mudstone (100%)] grain size = clay contact = sharp
1056.31 to 1057.40	[shale (100%)] grain size = clay contact = sharp dark grey; carbonaceous
1057.36 to 1057.60	[coal (70%), shale (30%)] grain size = clay contact = sharp bituminous; fractured well-developed cleat
1057.63 to 1058.00	[coal (100%)] grain size = clay contact = sharp bituminous; fractured well-developed cleat
1058.04 to 1058.10	[shale (100%)] grain size = clay contact = sharp dark grey; carbonaceous

1058.10 to 1058.20	[coal (70%), shale (30%)] grain size = clay contact = sharp bituminous; fractured well-developed cleat
1058.18 to 1058.30	[shale (100%)] grain size = clay contact = sharp dark grey; carbonaceous
1058.31 to 1058.60	[coal (100%)] grain size = clay contact = sharp bituminous; fractured well-developed cleat
1058.59 to 1058.70	[shale (100%)] grain size = clay contact = sharp dark grey; carbonaceous
1058.72 to 1058.90	[coal (100%)] grain size = clay contact = sharp bituminous; fractured well-developed cleat
1058.90 to 1059.00	[shale (100%)] grain size = clay contact = sharp
1059.03 to 1059.10	[coal (100%)] grain size = clay contact = sharp bituminous; fractured well-developed cleat
1059.09 to 1059.50	[shale (100%)] grain size = clay contact = sharp
1059.50 to 1059.50	[coal (100%)] grain size = clay contact = sharp bituminous; fractured well-developed cleat
1059.53 to 1059.60	[shale (100%)] grain size = clay contact = sharp
1059.60 to 1059.70	[coal (100%)] grain size = clay contact = sharp bituminous; fractured well-developed cleat
1059.66 to 1060.20	[shale (100%)] grain size = clay contact = sharp

1060.15 to 1060.20	[coal (100%)] grain size = clay contact = sharp bituminous; fractured well-developed cleat
1060.17 to 1068.40	[sandstone (100%)] grain size = fine to medium sand contact = sharp
1068.35 to 1068.40	[coal (100%)] grain size = clay contact = sharp bituminous; fractured well-developed cleat
1068.42 to 1068.50	[coal (100%)] grain size = clay contact = sharp bituminous; fractured well-developed cleat
1068.50 to 1068.53	[coal (100%)] grain size = clay contact = sharp bituminous; fractured well-developed cleat
1068.53 to 1068.60	[coal (100%)] grain size = clay contact = sharp bituminous; fractured well-developed cleat
1068.60 to 1068.62	shale (100) grain size = clay contact = sharp
1068.62 to 1068.80	[coal (100%)] grain size = clay contact = sharp bituminous; fractured well-developed cleat
1068.80 to 1068.90	[coal (100%)] grain size = clay contact = sharp bituminous; fractured well-developed cleat
1068.85 to 1075.70	[sandstone (100%)] grain size = medium sand contact = sharp medium grey; minor carbonaceous material
1075.66 to 1079.30	[shale (100%)] grain size = clay contact = sharp
1079.29 to 1079.60	[coal (100%)] grain size = clay contact = sharp bituminous; fractured well-developed cleat

1079.60 to 1081.20	[sandstone (100%)] grain size = fine sand contact = sharp light grey
1081.17 to 1082.30	[shale (100%)] grain size = clay contact = sharp dark grey
1082.26 to 1082.40	[coal (100%)] grain size = clay contact = sharp bituminous; fractured well-developed cleat
1082.40 to 1083.50	[shale (100%)] grain size = clay contact = sharp dark grey; fractured
1083.48 to 1086.30	[sandstone (100%)] grain size = fine sand contact = gradational light grey
1086.30 to 1087.90	[shale (100%)] grain size = clay contact = sharp dark grey to brown; soft clay sections
1087.90 to 1095.60	[sandstone (100%)] grain size = fine to medium sand contact = sharp light grey; rare calcite-filled fracture
1095.60 to 1098.50	[shale (100%)] grain size = clay contact = sharp dark grey; sandy silt sections; common siderite nodules and banding
1098.50 to 1099.20	[sandstone (100%)] grain size = medium sand contact = sharp medium grey; minor siltstone; rare siderite nodules
1099.17 to 1099.90	[mudstone (100%)] grain size = clay contact = gradational sandy mudstone; sandier towards base; load structures, rare siderite nodules
1099.93 to 1100.60	[sandstone (100%)] grain size = fine sand contact = sharp

- 1100.60 to 1101.10 [mudstone (100%)]
grain size = clay | contact = sharp
dark grey shaley mudstone; featureless
- 1101.13 to 1101.20 [coal (100%)]
grain size = clay | contact = sharp
bituminous; fractured well-developed cleat
- 1101.15 to 1101.30 [mudstone (100%)]
grain size = clay | contact = sharp
dark grey shaley mudstone; featureless
- 1101.31 to 1101.40 [coal (100%)]
grain size = clay | contact = sharp
bituminous; fractured well-developed cleat
- 1101.35 to 1101.50 [mudstone (100%)]
grain size = clay | contact = gradational
dark grey shaley mudstone; featureless

Appendix F: Drill Core Photography Gantry/Apparatus

The following is a documentation of the drill core photography apparatus I developed and helped build to aid with capturing undistorted, high-resolution photographs.

Title:

Automated Drill Core Photography Gantry/Apparatus

Inventor:

Trevor Kelly

Invention Date:

March 9th, 2020

Builders:

Trevor Kelly, Brian Kelly, and Paul Boudreau

Significance/Advantages:

1. Allows the user to take high-resolution drill core photographs at a constant elevation using the panoramic mode on smartphones.
2. Makes use of a person's smartphone, which most of the population has, so it is high tech but with low technology investment
3. It saves the user time.
4. It captures an image from a constant height
5. It does not require expensive digital cameras, tripods, or overhead camera mounts.
6. It removes the distortions associated with taking a single overhead photograph.
7. It removes the need for photo-stitching, which is typically difficult to get right.
8. It helps to avoid image distortions
9. It does not require image merging software
10. It is portable
11. It is inexpensive
12. It can be used on a bench top, so it eliminates bending over, etc.

13. The sliding speed of the device from one to another is controlled by the user

Brief Background:

This apparatus was developed for the purpose of capturing drill core photographs using the panoramic camera mode available on smartphones. As part of my PhD in Earth Sciences, I am performing a detailed description of a certain drill core available at the Nova Scotia Core Library in Stellarton. Initially, I was using a Canon digital camera mounted to an overhead stand to take the photographs, however, I was getting distortions towards the ends of the photographs. I then attempted to take multiple close-up photographs along of the drill core and merge them using software. This too was unsuccessful and resulted in numerous distortions and incomplete merges. I decided to build a simple device that would be height adjustable and allow me to utilize the panoramic function on my smartphone to capture the photographs from a constant height; thereby avoiding the distortions and inabilities of software to merge separate photographs. I was able to use this device for one day only, prior to the facility closing due to the ongoing pandemic.

Target Consumers (Examples):

1. Government (provincial and federal) drill core storage libraries (over 30 in Canada), so a worldwide application
2. Universities and colleges
3. Consulting companies
4. Petroleum companies
5. Mining companies, especially those operating in remote locations

Similar Inventions:

None - I have done some background research into this and to date have yet to find a similar invention.

Description:

It consists of a plywood base with two metal tracks fastened to it. I placed 4 pieces of steel flat stock on either side of the track to ensure it stayed straight and to protect it. I used 2 simple rail cars, each with 2 pieces of stainless-steel tubing mounted vertically from the railcar base. I then bent 2 pieces of smaller diameter stainless steel tubing to link both rail cars together. These slide into the upright pieces of tube on the rail cars. I used 4 threaded nuts at the interface between the uprights and the bent tube to ensure the system was height adjustable. I decided to add in a couple of cross-braces (taped them on with green tape) as an afterthought. I place my smartphone on the piece of wood (outlined in black) with the camera hanging over the edge and slide the cart from one end to the other with the panoramic mode engaged on the camera. It seems to work very well and was simple/cheap to construct. I did manage to photograph an entire pallet (42 boxes) on that single day. Each box contains approximately 4.5 m (14.8 ft) of core. Therefore, I was able to photograph ~ 189 m (622 ft) easily in one normal working day. I have included a photograph showing the apparatus I built for utilizing the panoramic mode on my smartphone to take constant height core photographs.



Figure F1: Core photography gantry apparatus.

**Appendix G: Tidal Rhythmite (Bundles) Thickness Measurements used
in Chapter 6**

The following is a documentation of the tidal rhythmite thickness measurements that support the work carried out in Chapter 6.

Table G1: Thickness measurement data for tidal rhythmite interval # 1 (TR1)

Lamina #	Lithology	Thickness (mm)	Total Thickness (mm)
1	sandstone	1.390	1.390
2	mudstone	0.260	1.650
3	sandstone	0.710	2.360
4	mudstone	0.260	2.620
5	sandstone	1.570	4.190
6	mudstone	0.500	4.690
7	sandstone	1.310	6.000
8	mudstone	0.770	6.770
9	sandstone	0.730	7.500
10	mudstone	0.460	7.960
11	sandstone	0.470	8.430
12	mudstone	0.470	8.900
13	sandstone	0.430	9.330
14	mudstone	0.390	9.720
15	sandstone	0.530	10.250
16	mudstone	0.460	10.710
17	sandstone	0.850	11.560
18	mudstone	0.790	12.350
19	sandstone	1.390	13.740
20	mudstone	0.620	14.360
21	sandstone	1.110	15.470
22	mudstone	0.450	15.920
23	sandstone	0.800	16.720
24	mudstone	0.490	17.210
25	sandstone	1.000	18.210
26	mudstone	0.260	18.470
27	sandstone	0.740	19.210
28	mudstone	0.260	19.470
29	sandstone	0.790	20.260
30	mudstone	0.240	20.500
31	sandstone	1.480	21.980
32	mudstone	0.350	22.330
33	sandstone	0.970	23.300
34	mudstone	0.260	23.560
35	sandstone	0.760	24.320
36	mudstone	0.310	24.630
37	sandstone	0.560	25.190
38	mudstone	0.550	25.740
39	sandstone	0.820	26.560
40	mudstone	0.400	26.960
41	sandstone	0.930	27.890
42	mudstone	0.510	28.400

Lamina #	Lithology	Thickness (mm)	Total Thickness (mm)
43	sandstone	0.970	29.370
44	mudstone	0.320	29.690
45	sandstone	1.040	30.730
46	mudstone	0.390	31.120
47	sandstone	1.030	32.150
48	mudstone	0.410	32.560
49	sandstone	1.390	33.950
50	mudstone	0.560	34.510
51	sandstone	1.970	36.480
52	mudstone	0.270	36.750
53	sandstone	0.900	37.650
54	mudstone	0.360	38.010
55	sandstone	0.470	38.480
56	mudstone	0.290	38.770
57	sandstone	0.370	39.140
58	mudstone	0.260	39.400
59	sandstone	0.570	39.970
60	mudstone	0.220	40.190
61	sandstone	0.890	41.080
62	mudstone	0.540	41.620
63	sandstone	1.290	42.910
64	mudstone	0.300	43.210
65	sandstone	1.200	44.410
66	mudstone	0.390	44.800
67	sandstone	0.510	45.310
68	mudstone	0.230	45.540
69	sandstone	0.340	45.880
70	mudstone	0.340	46.220
71	sandstone	0.390	46.610
72	mudstone	0.330	46.940
73	sandstone	0.970	47.910
74	mudstone	0.280	48.190
75	sandstone	0.500	48.690
76	mudstone	0.400	49.090
77	sandstone	1.490	50.580
78	mudstone	0.270	50.850
79	sandstone	1.140	51.990
80	mudstone	0.350	52.340
81	sandstone	1.010	53.350
82	mudstone	0.280	53.630
83	sandstone	0.520	54.150
84	mudstone	0.280	54.430
85	sandstone	0.830	55.260

Lamina #	Lithology	Thickness (mm)	Total Thickness (mm)
86	mudstone	0.280	55.540
87	sandstone	0.610	56.150
88	mudstone	0.280	56.430
89	sandstone	1.380	57.810
90	mudstone	0.310	58.120
91	sandstone	0.860	58.980
92	mudstone	0.180	59.160
93	sandstone	0.400	59.560
94	mudstone	0.180	59.740
95	sandstone	0.760	60.500
96	mudstone	0.370	60.870
97	sandstone	0.350	61.220
98	mudstone	0.170	61.390
99	sandstone	0.330	61.720
100	mudstone	0.350	62.070
101	sandstone	1.280	63.350
102	mudstone	0.410	63.760
103	sandstone	0.560	64.320
104	mudstone	0.310	64.630
105	sandstone	0.810	65.440
106	mudstone	0.210	65.650
107	sandstone	0.610	66.260
108	mudstone	0.340	66.600
109	sandstone	0.520	67.120
110	mudstone	0.280	67.400
111	sandstone	1.080	68.480
112	mudstone	0.450	68.930
113	sandstone	0.540	69.470
114	mudstone	0.340	69.810
115	sandstone	1.070	70.880
116	mudstone	0.230	71.110
117	sandstone	0.910	72.020
118	mudstone	0.280	72.300
119	sandstone	0.600	72.900
120	mudstone	0.230	73.130
121	sandstone	0.440	73.570
122	mudstone	0.190	73.760
123	sandstone	0.520	74.280
124	mudstone	0.200	74.480
125	sandstone	0.710	75.190
126	mudstone	0.310	75.500
127	sandstone	0.530	76.030
128	mudstone	0.260	76.290

Lamina #	Lithology	Thickness (mm)	Total Thickness (mm)
129	sandstone	0.970	77.260
130	mudstone	0.230	77.490
131	sandstone	0.710	78.200
132	mudstone	0.230	78.430
133	sandstone	0.700	79.130
134	mudstone	0.260	79.390
135	sandstone	1.310	80.700
136	mudstone	0.440	81.140
137	sandstone	0.760	81.900
138	mudstone	0.490	82.390
139	sandstone	0.800	83.190
140	mudstone	0.530	83.720
141	sandstone	0.850	84.570
142	mudstone	0.320	84.890
143	sandstone	0.920	85.810
144	mudstone	0.390	86.200
145	sandstone	0.820	87.020
146	mudstone	0.600	87.620
147	sandstone	0.960	88.580
148	mudstone	0.340	88.920
149	sandstone	0.810	89.730
150	mudstone	0.200	89.930
151	sandstone	0.250	90.180
152	mudstone	0.260	90.440
153	sandstone	0.970	91.410
154	mudstone	0.350	91.760
155	sandstone	0.890	92.650
156	mudstone	0.270	92.920
157	sandstone	0.470	93.390
158	mudstone	0.230	93.620
159	sandstone	0.380	94.000
160	mudstone	0.210	94.210
161	sandstone	0.380	94.590
162	mudstone	0.320	94.910
163	sandstone	0.570	95.480
164	mudstone	0.220	95.700
165	sandstone	0.570	96.270
166	mudstone	0.380	96.650
167	sandstone	0.610	97.260
168	mudstone	0.220	97.480
169	sandstone	0.280	97.760
170	mudstone	0.200	97.960
171	sandstone	0.410	98.370

Lamina #	Lithology	Thickness (mm)	Total Thickness (mm)
172	mudstone	0.260	98.630
173	sandstone	0.650	99.280
174	mudstone	0.820	100.100
175	sandstone	1.150	101.250
176	mudstone	0.370	101.620
177	sandstone	1.000	102.620
178	mudstone	0.490	103.110
179	sandstone	0.660	103.770
180	mudstone	0.510	104.280
181	sandstone	1.970	106.250
182	mudstone	0.380	106.630
183	sandstone	0.970	107.600
184	mudstone	0.340	107.940
185	sandstone	0.360	108.300
186	mudstone	0.440	108.740
187	sandstone	0.870	109.610
188	mudstone	0.250	109.860
189	sandstone	0.270	110.130
190	mudstone	0.350	110.480
191	sandstone	0.740	111.220
192	mudstone	0.310	111.530
193	sandstone	0.570	112.100
194	mudstone	0.410	112.510
195	sandstone	1.890	114.400
196	mudstone	0.600	115.000
197	sandstone	0.930	115.930
198	mudstone	0.580	116.510
199	sandstone	0.490	117.000
200	mudstone	0.460	117.460
201	sandstone	0.720	118.180
202	mudstone	0.470	118.650
203	sandstone	1.990	120.640
204	mudstone	0.300	120.940
205	sandstone	0.540	121.480
206	mudstone	0.270	121.750
207	sandstone	0.500	122.250
208	mudstone	0.270	122.520
209	sandstone	0.430	122.950
210	mudstone	0.250	123.200
211	sandstone	0.360	123.560
212	mudstone	0.440	124.000
213	sandstone	0.840	124.840
214	mudstone	0.890	125.730

Lamina #	Lithology	Thickness (mm)	Total Thickness (mm)
215	sandstone	1.200	126.930
216	mudstone	0.290	127.220
217	sandstone	0.660	127.880
218	mudstone	0.290	128.170
219	sandstone	1.170	129.340
220	mudstone	0.620	129.960
221	sandstone	1.590	131.550
222	mudstone	0.220	131.770
223	sandstone	0.720	132.490
224	mudstone	0.200	132.690
225	sandstone	0.490	133.180
226	mudstone	0.340	133.520
227	sandstone	0.420	133.940
228	mudstone	0.260	134.200
229	sandstone	0.670	134.870
230	mudstone	0.330	135.200
231	sandstone	0.370	135.570
232	mudstone	0.310	135.880
233	sandstone	0.690	136.570
234	mudstone	0.300	136.870
235	sandstone	0.770	137.640
236	mudstone	0.330	137.970
237	sandstone	0.760	138.730
238	mudstone	0.170	138.900
239	sandstone	0.220	139.120
240	mudstone	0.210	139.330
241	sandstone	0.260	139.590
242	mudstone	0.230	139.820
243	sandstone	0.550	140.370
244	mudstone	0.230	140.600
245	sandstone	1.220	141.820
246	mudstone	0.310	142.130
247	sandstone	1.180	143.310
248	mudstone	0.280	143.590
249	sandstone	1.140	144.730
250	mudstone	0.280	145.010
251	sandstone	0.510	145.520
252	mudstone	0.270	145.790
253	sandstone	0.450	146.240
254	mudstone	0.210	146.450
255	sandstone	0.390	146.840
256	mudstone	0.260	147.100
257	sandstone	0.650	147.750

Lamina #	Lithology	Thickness (mm)	Total Thickness (mm)
258	mudstone	0.630	148.380
259	sandstone	0.940	149.320
260	mudstone	0.320	149.640
261	sandstone	0.400	150.040
262	mudstone	0.360	150.400
263	sandstone	0.430	150.830
264	mudstone	0.170	151.000
265	sandstone	0.470	151.470
266	mudstone	0.210	151.680
267	sandstone	0.800	152.480
268	mudstone	0.180	152.660
269	sandstone	0.750	153.410
270	mudstone	0.280	153.690
271	sandstone	0.690	154.380
272	mudstone	0.280	154.660
273	sandstone	0.960	155.620
274	mudstone	0.420	156.040
275	sandstone	0.830	156.870
276	mudstone	0.300	157.170
277	sandstone	0.640	157.810
278	mudstone	0.290	158.100
279	sandstone	0.780	158.880
280	mudstone	0.270	159.150
281	sandstone	1.150	160.300
282	mudstone	0.300	160.600
283	sandstone	1.630	162.230
284	mudstone	0.380	162.610
285	sandstone	0.600	163.210
286	mudstone	0.310	163.520
287	sandstone	0.930	164.450
288	mudstone	0.470	164.920
289	sandstone	0.780	165.700
290	mudstone	0.390	166.090
291	sandstone	0.810	166.900
292	mudstone	0.330	167.230
293	sandstone	0.730	167.960
294	mudstone	0.360	168.320
295	sandstone	0.640	168.960
296	mudstone	0.360	169.320
297	sandstone	0.320	169.640
298	mudstone	0.160	169.800
299	sandstone	0.230	170.030
300	mudstone	0.230	170.260

Lamina #	Lithology	Thickness (mm)	Total Thickness (mm)
301	sandstone	0.480	170.740
302	mudstone	0.180	170.920
303	sandstone	0.590	171.510
304	mudstone	0.230	171.740
305	sandstone	0.790	172.530
306	mudstone	0.360	172.890
307	sandstone	0.580	173.470
308	mudstone	0.380	173.850
309	sandstone	1.130	174.980
310	mudstone	0.270	175.250
311	sandstone	0.490	175.740
312	mudstone	0.460	176.200
313	sandstone	1.130	177.330
314	mudstone	0.500	177.830
315	sandstone	0.440	178.270
316	mudstone	0.230	178.500
317	sandstone	1.240	179.740
318	mudstone	0.420	180.160
319	sandstone	0.960	181.120
320	mudstone	0.420	181.540
321	sandstone	0.840	182.380
322	mudstone	0.360	182.740
323	sandstone	1.430	184.170
324	mudstone	0.640	184.810
325	sandstone	1.120	185.930
326	mudstone	0.640	186.570
327	sandstone	0.940	187.510
328	mudstone	0.290	187.800
329	sandstone	0.760	188.560
330	mudstone	0.540	189.100
331	sandstone	0.330	189.430
332	mudstone	0.360	189.790
333	sandstone	1.460	191.250
334	mudstone	0.490	191.740
335	sandstone	0.520	192.260
336	mudstone	0.240	192.500
337	sandstone	0.360	192.860
338	mudstone	0.280	193.140
339	sandstone	0.570	193.710
340	mudstone	0.280	193.990
341	sandstone	0.890	194.880
342	mudstone	0.260	195.140
343	sandstone	0.730	195.870

Lamina #	Lithology	Thickness (mm)	Total Thickness (mm)
344	mudstone	0.280	196.150
345	sandstone	0.420	196.570
346	mudstone	0.760	197.330
347	sandstone	0.510	197.840
348	mudstone	0.270	198.110
349	sandstone	0.470	198.580
350	mudstone	0.250	198.830
351	sandstone	0.520	199.350
352	mudstone	0.490	199.840
353	sandstone	0.740	200.580
354	mudstone	0.220	200.800
355	sandstone	0.820	201.620
356	mudstone	0.340	201.960
357	sandstone	0.940	202.900
358	mudstone	0.390	203.290
359	sandstone	0.370	203.660
360	mudstone	0.390	204.050
361	sandstone	0.930	204.980
362	mudstone	0.270	205.250
363	sandstone	0.740	205.990
364	mudstone	0.200	206.190
365	sandstone	0.740	206.930
366	mudstone	0.180	207.110
367	sandstone	1.160	208.270
368	mudstone	0.320	208.590
369	sandstone	0.360	208.950
370	mudstone	0.220	209.170
371	sandstone	0.580	209.750
372	mudstone	0.360	210.110
373	sandstone	0.360	210.470
374	mudstone	0.320	210.790
375	sandstone	0.730	211.520
376	mudstone	0.400	211.920
377	sandstone	0.430	212.350
378	mudstone	0.220	212.570
379	sandstone	0.750	213.320
380	mudstone	0.460	213.780
381	sandstone	0.730	214.510
382	mudstone	0.230	214.740
383	sandstone	0.790	215.530
384	mudstone	0.460	215.990
385	sandstone	0.340	216.330
386	mudstone	0.200	216.530

Lamina #	Lithology	Thickness (mm)	Total Thickness (mm)
387	sandstone	0.360	216.890
388	mudstone	0.200	217.090
389	sandstone	0.340	217.430
390	mudstone	0.140	217.570
391	sandstone	0.910	218.480
392	mudstone	0.260	218.740
393	sandstone	0.210	218.950
394	mudstone	0.370	219.320
395	sandstone	1.010	220.330
396	mudstone	0.250	220.580
397	sandstone	0.820	221.400
398	mudstone	0.370	221.770
399	sandstone	0.410	222.180
400	mudstone	0.510	222.690
401	sandstone	0.740	223.430
402	mudstone	0.380	223.810
403	sandstone	0.900	224.710
404	mudstone	0.400	225.110
405	sandstone	1.100	226.210
406	mudstone	0.360	226.570
407	sandstone	1.240	227.810
408	mudstone	0.260	228.070
409	sandstone	0.810	228.880
410	mudstone	0.410	229.290
411	sandstone	0.270	229.560
412	mudstone	0.270	229.830
413	sandstone	1.170	231.000
414	mudstone	0.380	231.380
415	sandstone	0.600	231.980
416	mudstone	0.350	232.330
417	sandstone	0.300	232.630
418	mudstone	0.300	232.930
419	sandstone	1.420	234.350
420	mudstone	0.320	234.670
421	sandstone	0.490	235.160
422	mudstone	0.300	235.460
423	sandstone	0.250	235.710
424	mudstone	0.400	236.110
425	sandstone	0.780	236.890
426	mudstone	0.460	237.350
427	sandstone	1.140	238.490
428	mudstone	0.640	239.130
429	sandstone	1.020	240.150

Lamina #	Lithology	Thickness (mm)	Total Thickness (mm)
430	mudstone	0.470	240.620
431	sandstone	0.560	241.180
432	mudstone	0.540	241.720
433	sandstone	1.730	243.450
434	mudstone	0.370	243.820
435	sandstone	2.600	246.420
436	mudstone	0.250	246.670
437	sandstone	1.480	248.150
438	mudstone	0.390	248.540
439	sandstone	1.610	250.150
440	mudstone	0.300	250.450
441	sandstone	2.170	252.620
442	mudstone	0.340	252.960
443	sandstone	2.050	255.010
444	mudstone	0.920	255.930
445	sandstone	1.430	257.360
446	mudstone	0.570	257.930
447	sandstone	0.870	258.800
448	mudstone	0.280	259.080
449	sandstone	1.140	260.220
450	mudstone	0.240	260.460
451	sandstone	1.810	262.270
452	mudstone	0.940	263.210
453	sandstone	1.730	264.940
454	mudstone	0.360	265.300
455	sandstone	1.250	266.550
456	mudstone	0.780	267.330
457	sandstone	0.520	267.850
458	mudstone	0.270	268.120
459	sandstone	0.700	268.820
460	mudstone	0.480	269.300
461	sandstone	1.000	270.300
462	mudstone	0.270	270.570
463	sandstone	0.840	271.410
464	mudstone	0.260	271.670
465	sandstone	1.040	272.710
466	mudstone	0.220	272.930
467	sandstone	1.010	273.940
468	mudstone	0.170	274.110
469	sandstone	0.650	274.760
470	mudstone	0.200	274.960
471	sandstone	0.730	275.690
472	mudstone	0.370	276.060

Lamina #	Lithology	Thickness (mm)	Total Thickness (mm)
473	sandstone	1.110	277.170
474	mudstone	0.310	277.480
475	sandstone	1.070	278.550
476	mudstone	0.260	278.810
477	sandstone	1.380	280.190
478	mudstone	0.250	280.440
479	sandstone	0.310	280.750
480	mudstone	0.280	281.030
481	sandstone	0.670	281.700
482	mudstone	0.190	281.890
483	sandstone	0.600	282.490
484	mudstone	0.170	282.660
485	sandstone	0.440	283.100
486	mudstone	0.710	283.810
487	sandstone	0.900	284.710
488	mudstone	0.270	284.980
489	sandstone	1.530	286.510
490	mudstone	0.450	286.960
491	sandstone	1.900	288.860
492	mudstone	0.330	289.190
493	sandstone	1.790	290.980
494	mudstone	0.270	291.250
495	sandstone	2.410	293.660
496	mudstone	0.780	294.440
497	sandstone	0.490	294.930
498	mudstone	1.100	296.030
499	sandstone	0.460	296.490
500	mudstone	0.550	297.040
501	sandstone	1.340	298.380
502	mudstone	0.160	298.540
503	sandstone	2.650	301.190
504	mudstone	0.210	301.400
505	sandstone	2.220	303.620
506	mudstone	0.480	304.100
507	sandstone	0.640	304.740
508	mudstone	0.190	304.930
509	sandstone	2.580	307.510
510	mudstone	0.210	307.720
511	sandstone	1.440	309.160
512	mudstone	0.620	309.780
513	sandstone	2.210	311.990
514	mudstone	0.450	312.440
515	sandstone	0.830	313.270

Lamina #	Lithology	Thickness (mm)	Total Thickness (mm)
516	mudstone	0.560	313.830

Table G2: Thickness measurement data for tidal rhythmite interval # 2 (TR2)

Lamina #	Lithology	Thickness (mm)	Total Thickness (mm)
1	sandstone	9.660	9.660
2	mudstone	3.200	12.860
3	sandstone	5.400	18.260
4	mudstone	6.400	24.660
5	sandstone	7.300	31.960
6	mudstone	4.100	36.060
7	sandstone	13.000	49.060
8	mudstone	4.600	53.660
9	sandstone	6.400	60.060
10	mudstone	11.500	71.560
11	sandstone	5.100	76.660
12	mudstone	7.100	83.760
13	sandstone	5.700	89.460
14	mudstone	3.800	93.260
15	sandstone	2.700	95.960
16	mudstone	4.300	100.260
17	sandstone	3.900	104.160
18	mudstone	1.500	105.660
19	sandstone	3.200	108.860
20	mudstone	3.400	112.260
21	sandstone	1.400	113.660
22	mudstone	1.600	115.260
23	sandstone	3.600	118.860
24	mudstone	0.500	119.360
25	sandstone	3.600	122.960
26	mudstone	1.300	124.260
27	sandstone	1.600	125.860
28	mudstone	1.100	126.960
29	sandstone	1.200	128.160
30	mudstone	1.400	129.560
31	sandstone	0.700	130.260
32	mudstone	1.000	131.260
33	sandstone	2.000	133.260
34	mudstone	0.600	133.860
35	sandstone	2.400	136.260
36	mudstone	0.900	137.160
37	sandstone	1.800	138.960
38	mudstone	1.200	140.160
39	sandstone	3.800	143.960
40	mudstone	1.400	145.360
41	sandstone	1.500	146.860
42	mudstone	0.500	147.360

Lamina #	Lithology	Thickness (mm)	Total Thickness (mm)
43	sandstone	0.500	147.860
44	mudstone	0.600	148.460
45	sandstone	2.300	150.760
46	mudstone	1.400	152.160
47	sandstone	0.800	152.960
48	mudstone	0.700	153.660
49	sandstone	0.800	154.460
50	mudstone	1.500	155.960
51	sandstone	2.000	157.960
52	mudstone	0.900	158.860
53	sandstone	4.300	163.160
54	mudstone	1.200	164.360
55	sandstone	3.500	167.860
56	mudstone	1.600	169.460
57	sandstone	1.700	171.160
58	mudstone	1.700	172.860
59	sandstone	1.800	174.660
60	mudstone	0.600	175.260
61	sandstone	0.700	175.960
62	mudstone	1.900	177.860
63	sandstone	1.400	179.260
64	mudstone	0.600	179.860
65	sandstone	2.200	182.060
66	mudstone	1.000	183.060
67	sandstone	3.600	186.660
68	mudstone	1.000	187.660
69	sandstone	3.800	191.460
70	mudstone	1.400	192.860
71	sandstone	1.800	194.660
72	mudstone	1.200	195.860
73	sandstone	1.200	197.060
74	mudstone	1.000	198.060
75	sandstone	1.600	199.660
76	mudstone	1.400	201.060
77	sandstone	1.000	202.060
78	mudstone	0.800	202.860
79	sandstone	0.850	203.710

Table G3: Thickness measurement data for tidal rhythmite interval # 3 (TR3)

Lamina #	Lithology	Thickness (mm)	Total Thickness (mm)
1	sandstone	3.85	3.85
2	mudstone	1.00	4.85
3	sandstone	4.20	9.05
4	mudstone	1.20	10.25
5	sandstone	3.00	13.25
6	mudstone	1.00	14.25
7	sandstone	1.80	16.05
8	mudstone	0.80	16.85
9	sandstone	2.40	19.25
10	mudstone	0.80	20.05
11	sandstone	3.60	23.65
12	mudstone	2.00	25.65
13	sandstone	1.80	27.45
14	mudstone	1.40	28.85
15	sandstone	0.60	29.45
16	mudstone	1.20	30.65
17	sandstone	2.40	33.05
18	mudstone	1.00	34.05
19	sandstone	1.60	35.65
20	mudstone	0.80	36.45
21	sandstone	2.00	38.45
22	mudstone	1.00	39.45
23	sandstone	1.60	41.05
24	mudstone	1.60	42.65
25	sandstone	1.40	44.05
26	mudstone	0.80	44.85
27	sandstone	1.20	46.05
28	mudstone	1.60	47.65
29	sandstone	1.40	49.05
30	mudstone	1.00	50.05
31	sandstone	1.60	51.65
32	mudstone	0.60	52.25
33	sandstone	1.20	53.45
34	mudstone	1.00	54.45
35	sandstone	1.00	55.45
36	mudstone	1.00	56.45
37	sandstone	1.20	57.65
38	mudstone	0.40	58.05

Lamina #	Lithology	Thickness (mm)	Total Thickness (mm)
39	sandstone	0.80	58.85
40	mudstone	0.40	59.25
41	sandstone	0.80	60.05
42	mudstone	0.40	60.45
43	sandstone	2.00	62.45
44	mudstone	0.40	62.85
45	sandstone	1.40	64.25
46	mudstone	1.00	65.25
47	sandstone	1.40	66.65
48	mudstone	0.80	67.45
49	sandstone	0.60	68.05
50	mudstone	0.80	68.85
51	sandstone	3.40	72.25
52	mudstone	1.00	73.25
53	sandstone	2.60	75.85
54	mudstone	1.00	76.85
55	sandstone	2.00	78.85
56	mudstone	0.60	79.45
57	sandstone	4.80	84.25
58	mudstone	1.40	85.65
59	sandstone	1.40	87.05
60	mudstone	0.60	87.65
61	sandstone	1.20	88.85
62	mudstone	0.60	89.45
63	sandstone	2.00	91.45
64	mudstone	1.60	93.05
65	sandstone	0.80	93.85
66	mudstone	0.40	94.25
67	sandstone	2.40	96.65
68	mudstone	1.20	97.85
69	sandstone	4.00	101.85
70	mudstone	1.20	103.05
71	sandstone	5.60	108.65
72	mudstone	2.60	111.25
73	sandstone	1.60	112.85
74	mudstone	1.60	114.45
75	sandstone	2.60	117.05
76	mudstone	2.00	119.05
77	sandstone	3.80	122.85

Lamina #	Lithology	Thickness (mm)	Total Thickness (mm)
78	mudstone	2.20	125.05
79	sandstone	4.20	129.25
80	mudstone	1.80	131.05
81	sandstone	3.40	134.45
82	mudstone	1.20	135.65
83	sandstone	3.40	139.05
84	mudstone	1.40	140.45
85	sandstone	1.80	142.25
86	mudstone	1.60	143.85
87	sandstone	2.60	146.45
88	mudstone	1.40	147.85
89	sandstone	2.00	149.85
90	mudstone	1.00	150.85
91	sandstone	3.60	154.45
92	mudstone	1.20	155.65
93	sandstone	2.00	157.65
94	mudstone	1.40	159.05
95	sandstone	3.00	162.05
96	mudstone	1.60	163.65
97	sandstone	1.40	165.05
98	mudstone	1.60	166.65
99	sandstone	3.40	170.05
100	mudstone	1.20	171.25
101	sandstone	2.60	173.85
102	mudstone	1.20	175.05
103	sandstone	6.20	181.25
104	mudstone	0.60	181.85
105	sandstone	2.60	184.45
106	mudstone	1.60	186.05
107	sandstone	2.80	188.85
108	mudstone	1.00	189.85
109	sandstone	1.40	191.25
110	mudstone	1.00	192.25
111	sandstone	2.80	195.05
112	mudstone	0.60	195.65
113	sandstone	0.80	196.45
114	mudstone	0.60	197.05
115	sandstone	1.20	198.25
116	mudstone	0.80	199.05

Lamina #	Lithology	Thickness (mm)	Total Thickness (mm)
117	sandstone	1.60	200.65
118	mudstone	1.00	201.65
119	sandstone	0.80	202.45
120	mudstone	1.20	203.65
121	sandstone	2.00	205.65
122	mudstone	0.80	206.45
123	sandstone	1.40	207.85
124	mudstone	1.00	208.85
125	sandstone	2.40	211.25
126	mudstone	1.20	212.45
127	sandstone	2.20	214.65
128	mudstone	1.20	215.85
129	sandstone	1.00	216.85
130	mudstone	1.00	217.85
131	sandstone	5.60	223.45
132	mudstone	2.20	225.65
133	sandstone	4.60	230.25
134	mudstone	1.60	231.85
135	sandstone	4.20	236.05
136	mudstone	1.40	237.45
137	sandstone	1.60	239.05
138	mudstone	0.80	239.85
139	sandstone	1.40	241.25
140	mudstone	1.80	243.05
141	sandstone	1.40	244.45
142	mudstone	0.80	245.25
143	sandstone	3.40	248.65
144	mudstone	1.00	249.65
145	sandstone	5.60	255.25
146	mudstone	3.00	258.25
147	sandstone	1.60	259.85
148	mudstone	1.00	260.85
149	sandstone	7.60	268.45
150	mudstone	1.00	269.45
151	sandstone	4.40	273.85
152	mudstone	0.80	274.65
153	sandstone	4.20	278.85
154	mudstone	3.00	281.85
155	sandstone	10.00	291.85

Lamina #	Lithology	Thickness (mm)	Total Thickness (mm)
156	mudstone	3.20	295.05
157	sandstone	5.80	300.85
158	mudstone	2.20	303.05
159	sandstone	4.80	307.85
160	mudstone	2.00	309.85
161	sandstone	4.00	313.85
162	mudstone	2.20	316.05
163	sandstone	4.80	320.85
164	mudstone	2.40	323.25
165	sandstone	5.40	328.65
166	mudstone	1.40	330.05
167	sandstone	2.80	332.85
168	mudstone	4.40	337.25
169	sandstone	4.80	342.05
170	mudstone	3.40	345.45
171	sandstone	6.20	351.65
172	mudstone	2.40	354.05
173	sandstone	4.00	358.05
174	mudstone	2.80	360.85
175	sandstone	3.40	364.25
176	mudstone	0.60	364.85
177	sandstone	4.60	369.45
178	mudstone	1.00	370.45
179	sandstone	2.40	372.85
180	mudstone	0.80	373.65
181	sandstone	2.60	376.25
182	mudstone	1.00	377.25
183	sandstone	2.60	379.85
184	mudstone	0.80	380.65
185	sandstone	2.60	383.25
186	mudstone	1.00	384.25
187	sandstone	4.20	388.45
188	mudstone	0.60	389.05
189	sandstone	1.60	390.65
190	mudstone	0.60	391.25
191	sandstone	6.00	397.25
192	mudstone	0.80	398.05
193	sandstone	2.00	400.05
194	mudstone	1.80	401.85

Lamina #	Lithology	Thickness (mm)	Total Thickness (mm)
195	sandstone	3.80	405.65
196	mudstone	1.40	407.05
197	sandstone	0.80	407.85
198	mudstone	1.20	409.05
199	sandstone	1.80	410.85
200	mudstone	1.20	412.05
201	sandstone	1.20	413.25
202	mudstone	2.00	415.25
203	sandstone	3.20	418.45
204	mudstone	1.40	419.85
205	sandstone	4.00	423.85
206	mudstone	2.40	426.25
207	sandstone	3.00	429.25
208	mudstone	1.00	430.25
209	sandstone	2.00	432.25
210	mudstone	1.40	433.65
211	sandstone	3.80	437.45
212	mudstone	1.60	439.05
213	sandstone	3.60	442.65
214	mudstone	3.00	445.65
215	sandstone	2.20	447.85
216	mudstone	2.20	450.05
217	sandstone	2.40	452.45
218	mudstone	2.60	455.05
219	sandstone	4.40	459.45
220	mudstone	1.00	460.45
221	sandstone	3.60	464.05
222	mudstone	1.80	465.85
223	sandstone	1.60	467.45
224	mudstone	3.20	470.65
225	sandstone	0.60	471.25
226	mudstone	2.00	473.25
227	sandstone	1.00	474.25
228	mudstone	1.40	475.65
229	sandstone	1.20	476.85
230	mudstone	2.80	479.65
231	sandstone	0.80	480.45
232	mudstone	1.60	482.05
233	sandstone	3.00	485.05

Lamina #	Lithology	Thickness (mm)	Total Thickness (mm)
234	mudstone	1.40	486.45
235	sandstone	2.20	488.65
236	mudstone	1.80	490.45
237	sandstone	2.80	493.25
238	mudstone	1.20	494.45
239	sandstone	1.00	495.45
240	mudstone	1.20	496.65
241	sandstone	1.60	498.25
242	mudstone	1.00	499.25
243	sandstone	1.60	500.85
244	mudstone	1.20	502.05
245	sandstone	1.00	503.05
246	mudstone	0.80	503.85
247	sandstone	2.60	506.45
248	mudstone	1.00	507.45
249	sandstone	3.40	510.85
250	mudstone	1.40	512.25
251	sandstone	2.80	515.05
252	mudstone	1.60	516.65
253	sandstone	2.40	519.05
254	mudstone	1.00	520.05
255	sandstone	1.00	521.05
256	mudstone	0.80	521.85
257	sandstone	1.60	523.45
258	mudstone	0.60	524.05
259	sandstone	1.40	525.45
260	mudstone	0.60	526.05
261	sandstone	1.60	527.65
262	mudstone	0.40	528.05
263	sandstone	1.20	529.25
264	mudstone	0.60	529.85
265	sandstone	1.20	531.05
266	mudstone	1.00	532.05
267	sandstone	1.60	533.65
268	mudstone	0.80	534.45
269	sandstone	1.20	535.65
270	mudstone	0.60	536.25
271	sandstone	3.40	539.65
272	mudstone	1.00	540.65

Lamina #	Lithology	Thickness (mm)	Total Thickness (mm)
273	sandstone	1.80	542.45
274	mudstone	0.80	543.25
275	sandstone	1.60	544.85
276	mudstone	1.00	545.85
277	sandstone	1.90	547.75
278	mudstone	3.30	551.05
279	sandstone	5.40	556.45
280	mudstone	1.80	558.25
281	sandstone	1.40	559.65
282	mudstone	2.00	561.65
283	sandstone	4.00	565.65
284	mudstone	1.00	566.65
285	sandstone	0.80	567.45
286	mudstone	1.00	568.45
287	sandstone	1.60	570.05
288	mudstone	1.00	571.05
289	sandstone	3.85	574.9

**Appendix H: Correlation between the REI-B2-1 Borehole and the
Outcrop using Major Coal Seams**

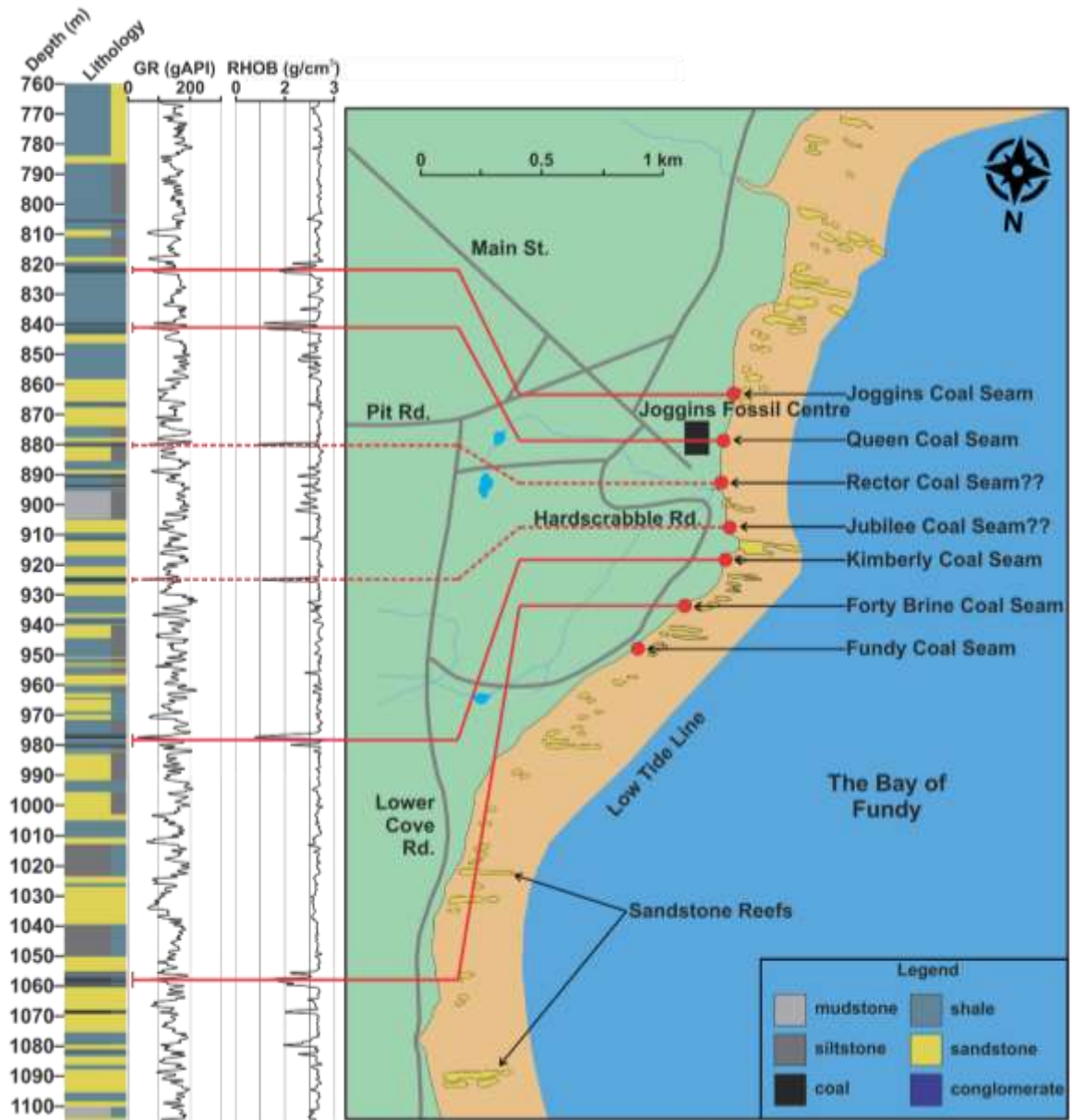


Figure H1: A correlation of significant coal seams between the P-101 borehole and the outcrop. Summary lithology log of the Joggins Formation interval from the P-101 borehole. The gamma-ray and density curves have also been plotted. The four major coal seams (Joggins, Queen, Kimberly, and Forty Brine) occur in the borehole and the outcrop. They are correlated using a solid red line. Two additional major coal seams (Rector and Jubilee) are visible in the borehole and were previously not identified as visible in the outcrop. They are correlated using a dashed red line and may not be present in the outcrop. The Fundy Coal Seam is present in the outcrop and is not identified in the borehole.

Appendix I: Maps Showing the Major Coal Mines in the Joggins Area

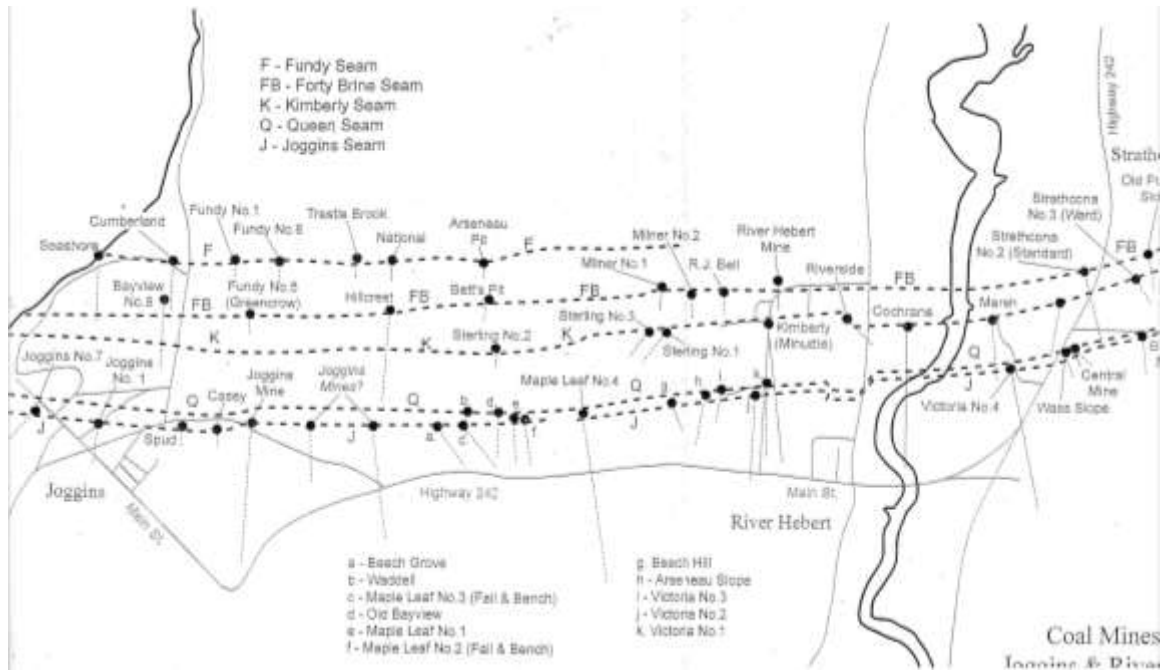


Figure 11: A map highlighting the major coal seams in the Joggins area and the locations of major coal mines (from Dana Brown of the Joggins Fossil Institute).

Reference:

Brown, D. ?. Coal Mines of the Joggins and River Hebert Areas.

Appendix J: Hand Sample Descriptions

This material originally appeared in my MEng thesis document:

Kelly, T.B. 2013. Reservoir Performance and Architecture of a Fluvial Meanderbelt System, Joggins Formation, Nova Scotia. MEng Thesis, Department of Engineering, Dalhousie University, Halifax, Nova Scotia.

Sample: GW101-2013TK

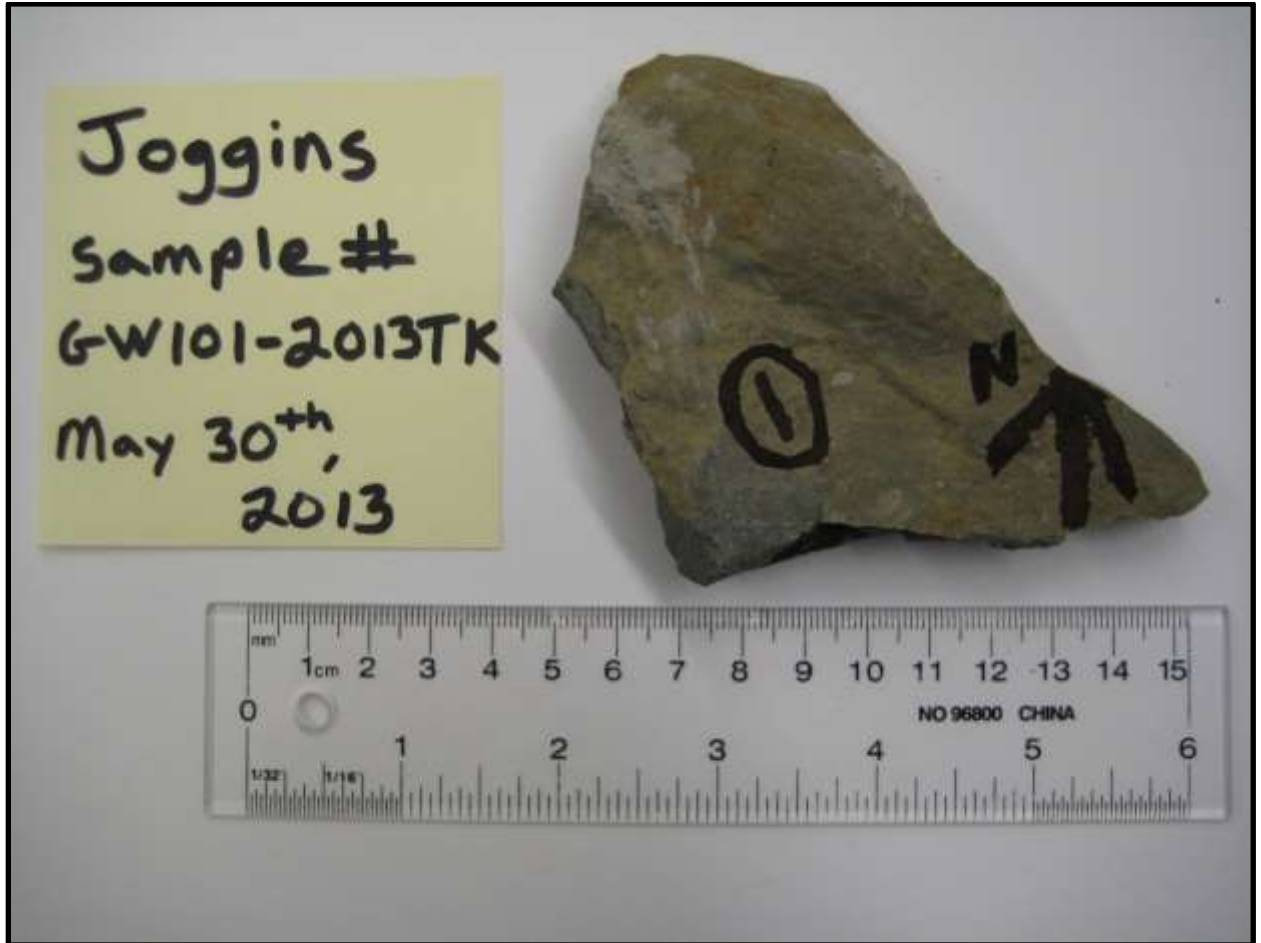


Figure J1: High-resolution photograph of hand sample GW101-2013TK.

Sample GW101-2013TK is a light grey to medium grey sandstone, most likely a quartzite variety. It appears to be medium-grained, clastic and equigranular. The sample reacts vigorously with 9 % HCl, suggesting cementation by a carbonate mineral; most likely calcite. The sample is hard and has gritty feel. The sample displays brittle, conchoidal-looking fractures. There are dark grey to black mineral occurrences in the sample that have random sizes and orientations that are ellipsoidal to thin, needle-like shapes. They may be fragments of rock or perhaps a mineral.

Sample: GW102-2013TK

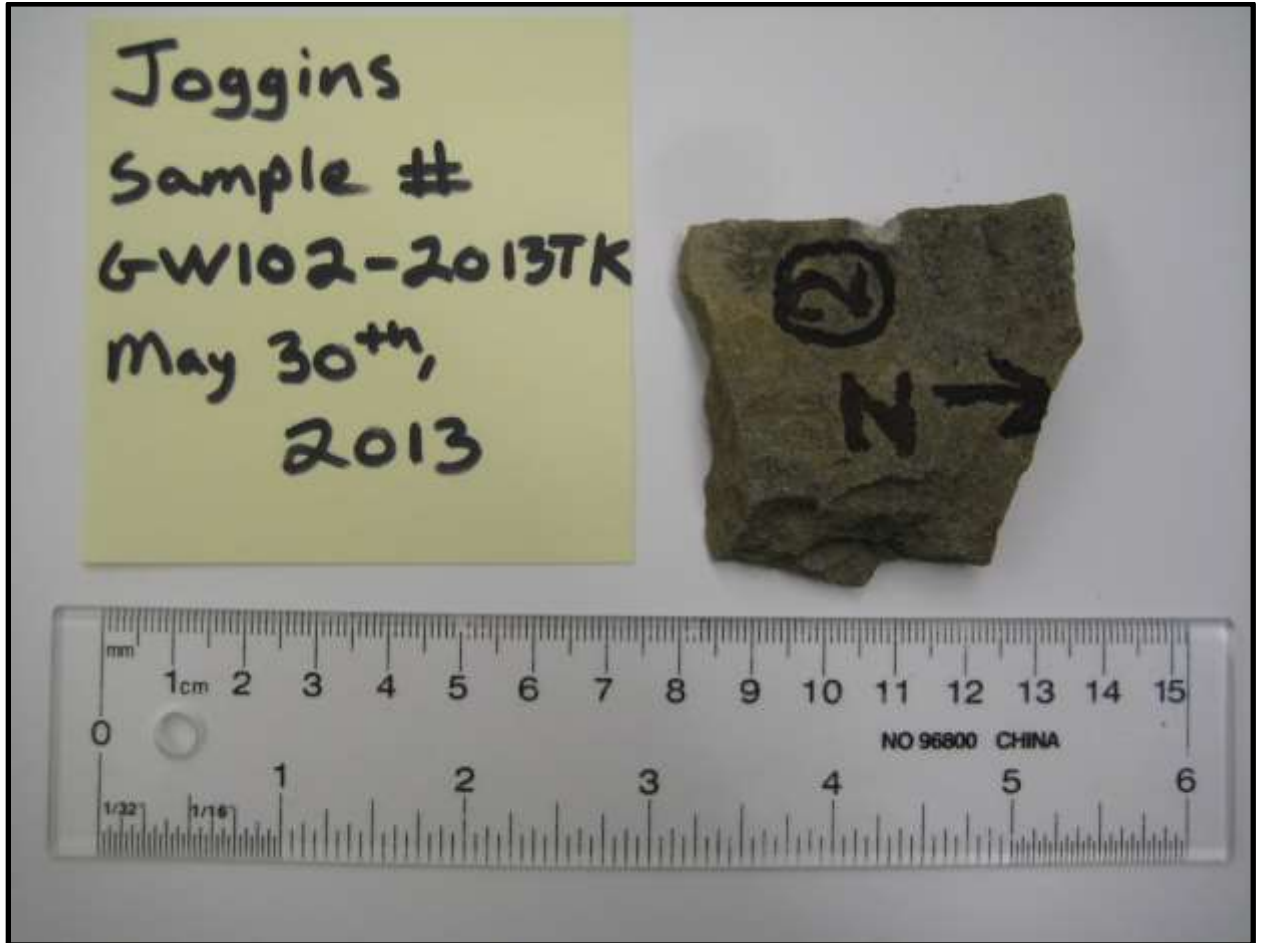


Figure J2: High-resolution photograph of hand sample GW102-2013TK.

Sample GW102-2013TK is a light grey sandstone that does not resemble the quartzite-looking appearance of GW010-2013TK. Viewing a fresh cut surface through a hand lens reveals the equigranular, clastic and medium-grained texture. The sample reacts weakly with 9 % HCl, suggesting the presence of calcite cement, but perhaps only as a minor constituent of the matrix cement. The sample lacks the hardness of sample GW101-2013TK. GW102-2013TK has a gritty feel along with brittle, conchoidal-looking fractures. The sample is most likely a quartz arenite.

Sample: GW103-2013TK

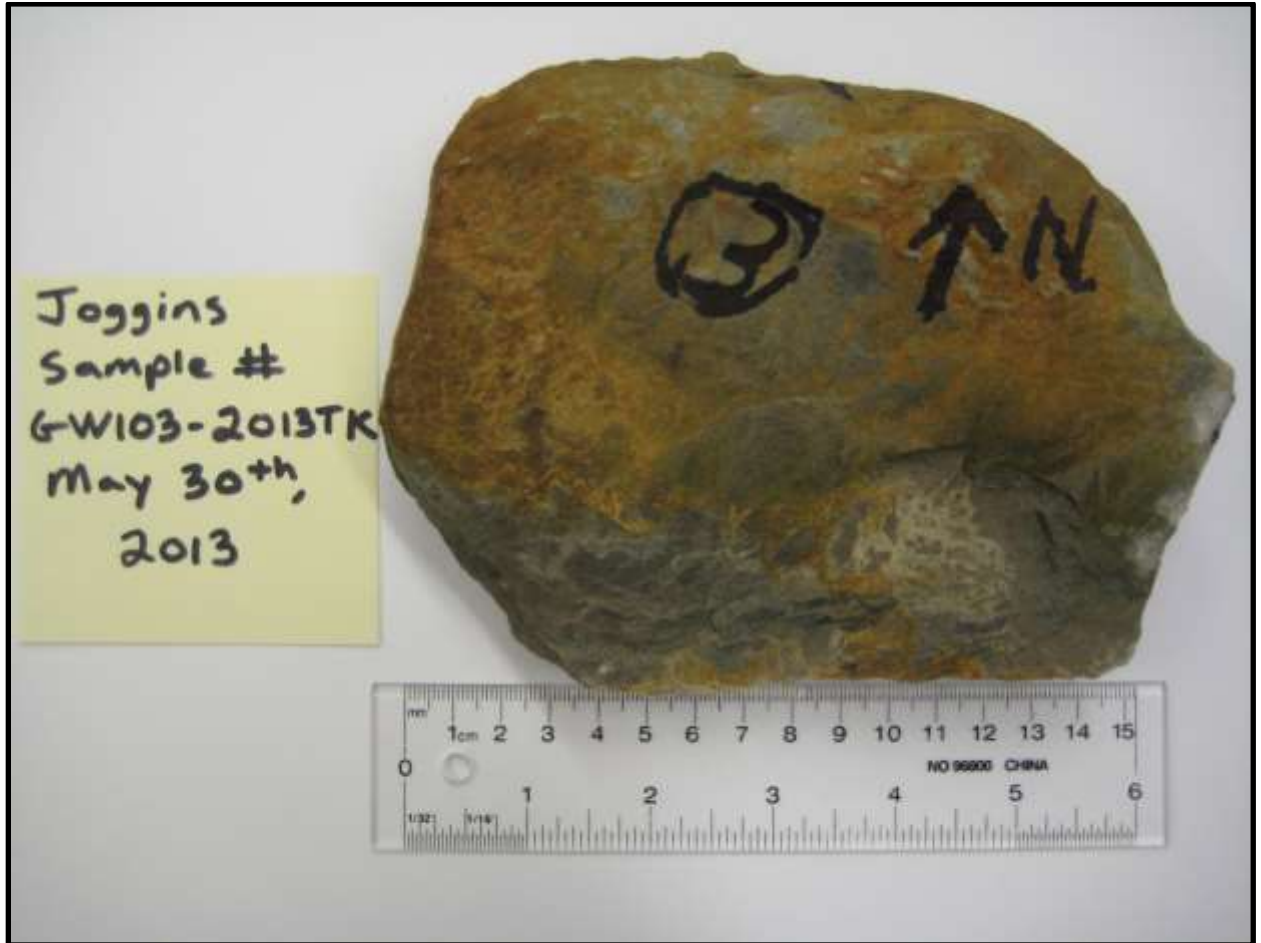


Figure J3: High-resolution photograph of hand sample GW103-2013TK.

Sample GW103-2013TK is a light grey, fine to medium grained, clastic and equigranular sandstone that is both massive and homogenous. The sample reacts weakly with 9 % HCl, suggesting that calcite cement is present, but perhaps only as a minor constituent of the cement. The hardness resembles that of Sample GW101-2013TK. The sample has a much smoother feel to it and is not as gritty as the previous samples had been. The sample is most likely a quartzite.

Sample: GW104-2013TK



Figure J4: High-resolution photograph of hand sample GW104-2013TK.

Sample GW104-2013TK is a very light, sub-vitreous, non-clastic, massive and homogenous carbonaceous shale or coal. The variety of the coal is probably that of anthracite due to its shiny appearance, massive and homogenous structure and the fact that it breaks conchoidally. The sample has a low hardness and is composed primarily of carbon. The sample displays an oily, rainbow sheen look with blues, purples and yellows visible at many locations within the hand sample. Calcite occurs as thin veinlets throughout and would have formed during secondary mineralization sometime after the coal fractured. It is likely that hydrothermal fluids are responsible for the calcite precipitation seen within the coal sample.

Sample: GW105-2013TK



Figure J5: High-resolution photograph of hand sample GW105-2013TK.

Sample GW105-2013TK is a medium to dark grey, dense, equigranular and fine-grained clastic limestone. It has a hardness of between 3 – 4. The sample breaks conchoidally. There are abundant ellipsoidally shaped features, possibly representing fossils or fossil fragments occurring throughout the sample. The hand sample reacts vigorously with acid. According to Folks classification, this rock would likely be classified as a biomicrite. According to the Dunham classification of carbonate rocks, this sample would most likely represent a wackestone.

Sample: GW106-2013TK



Figure J6: High-resolution photograph of hand sample GW106-2013TK.

Sample GW106-2013TK is a light grey, equigranular, medium-grained, clastic sandstone with some calcite cement as evidenced by a weak effervescence in the presence of 9 % HCl. The sample is homogenous, massive and hard, similar to that of GW101-2013TK. The sample has a gritty feel and displays conchoidal-looking fractures. The rock is most likely a quartz arenite or quartzite.

Sample: GW107-2013TK

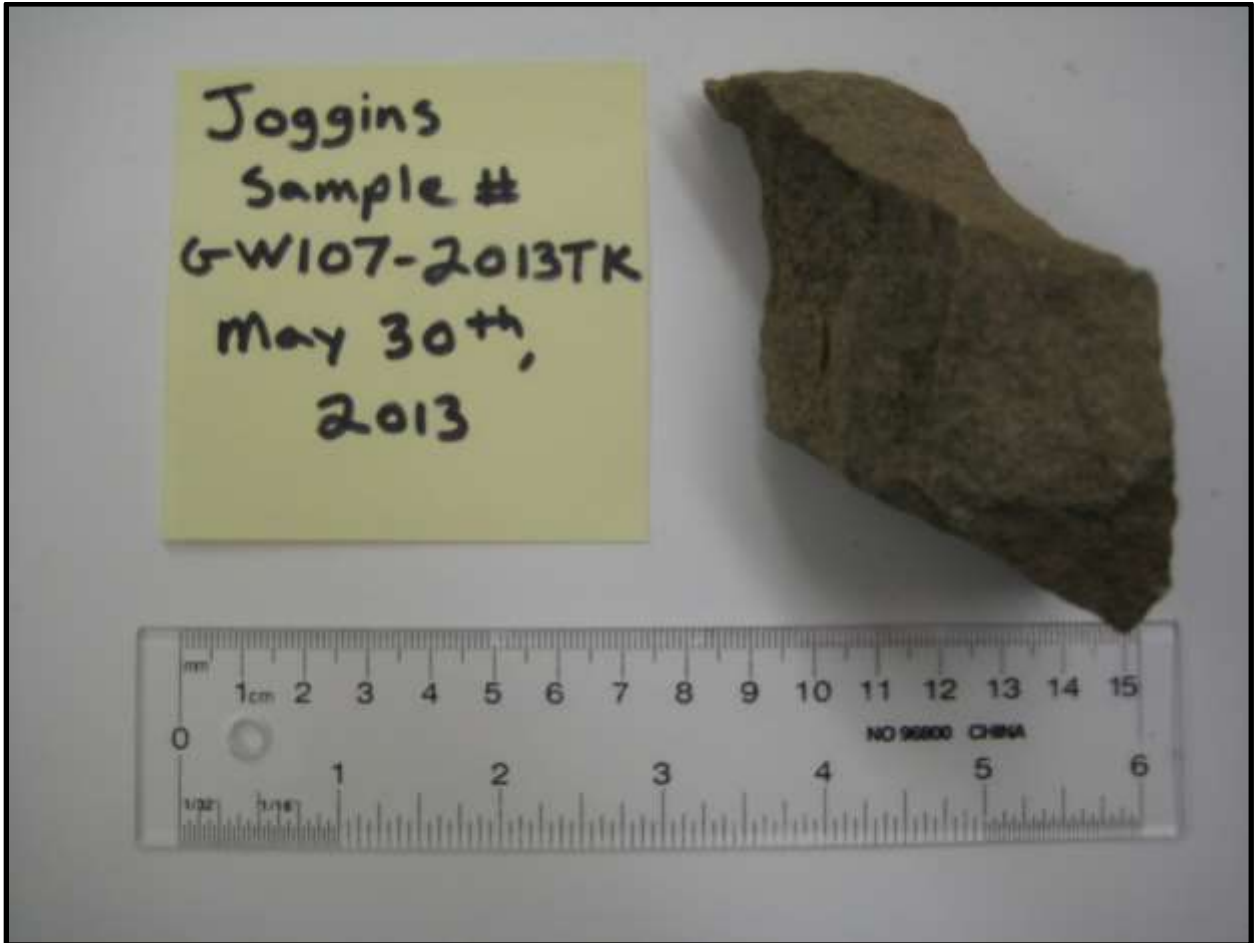


Figure J7: High-resolution photograph of hand sample GW107-2013TK.

Sample GW107-2013TK is a light grey, equigranular, medium-grained, clastic sandstone. It is highly reactive with 9 % HCl, indicating an abundance of calcite is present. Through a hand lens, the sample has a mottled-looking colour with white, black, brown and grey coloured grains. The sample is hard and has conchoidal fracture.

Sample: GW108-2013TK



Figure J8: High-resolution photograph of hand sample GW108-2013TK.

Sample GW108-2013TK is a light grey, medium grained, equigranular sandstone that displays conchoidal fractures. The sample is also hard and brittle with a gritty feel. The hand sample reacts moderately with acid, indicating the presence of calcite. There is an alignment of minerals or grains that appear as dark brown in colour. There is also a lithic fragment that occurs in the sample. It appears to be chert and is 10 mm long by 5 mm high and has a dark brown rim, yellow center and is ellipsoidal in shape.

Appendix K: Thin Section Descriptions (Mineralogy)

This material originally appeared in my MEng thesis document:

Kelly, T.B. 2013. Reservoir Performance and Architecture of a Fluvial Meanderbelt System, Joggins Formation, Nova Scotia. MEng Thesis, Department of Engineering, Dalhousie University, Halifax, Nova Scotia.

Sample: GW101-2013TK

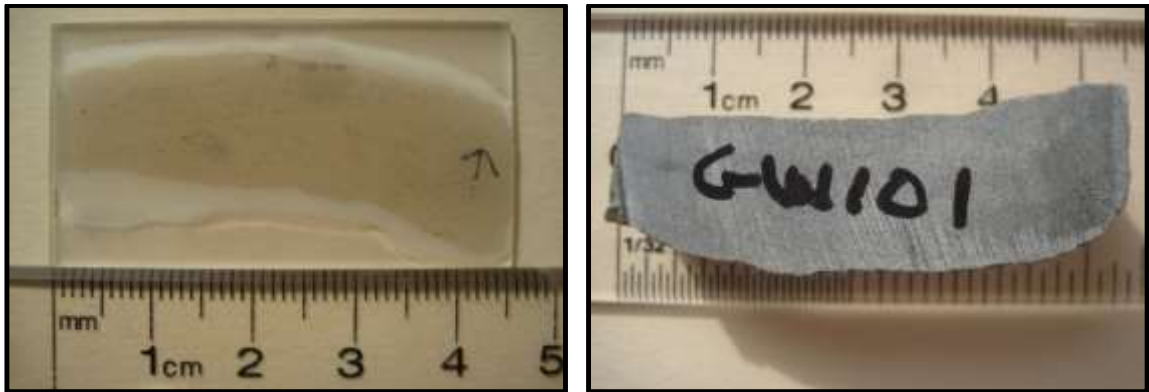


Figure K1: (Left) photograph of thin section from hand sample GW101-2013TK. (Right) corresponding photograph of rock sample that thin section was made from.

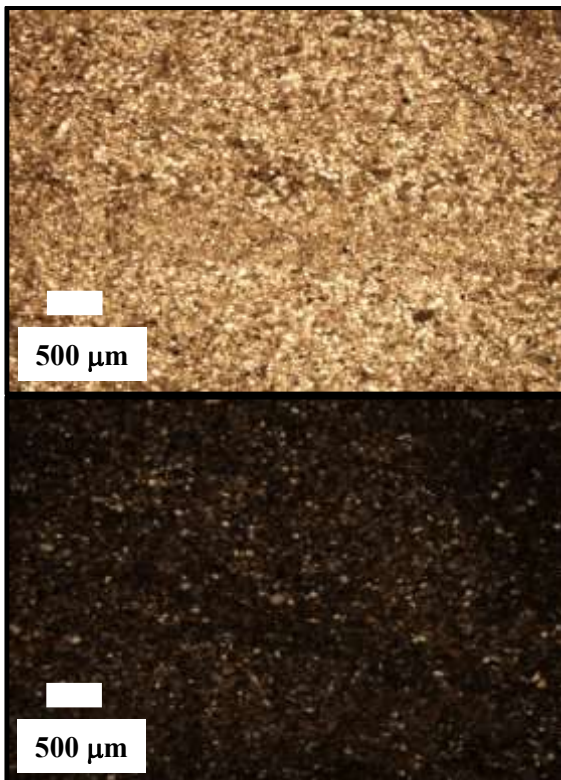


Figure K2: (Top) sample GW101-2013TK in ordinary light at 2X magnification. (Bottom) sample in plane polarized light at 2X magnification.

Sample: GW101-2013TK Continued...

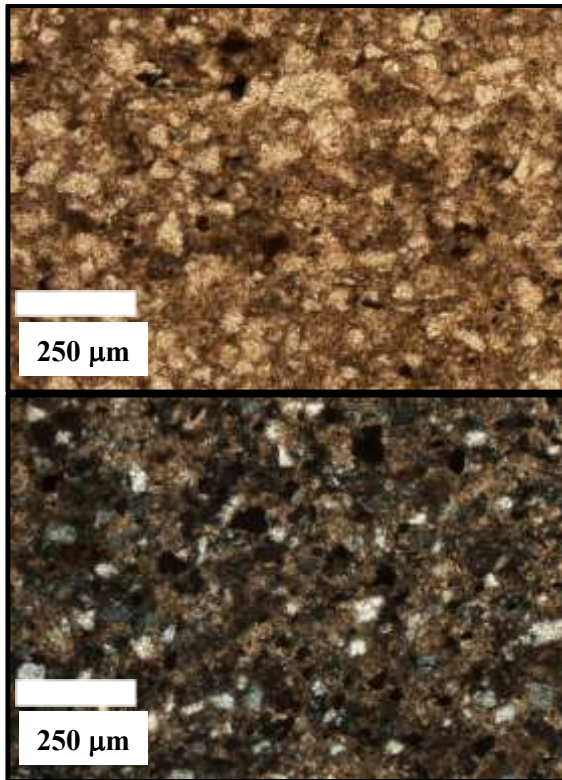


Figure K3: (Top) sample GW101-2013TK in ordinary light at 10X magnification. (Bottom) sample in plane polarized light at 10X magnification.

Description:

In thin section, the sample appears fine-grained and mainly equigranular. The dominant minerals are quartz and calcite. The quartz crystals are rounded to angular and randomly shaped with no preferred orientation. Less than 1% accessory hornblende is present. There is an opaque mineral, probably siderite, that occurs in the sample and makes up approximately 2 % of the sample. Calcite/ankerite occurs as a fine-grained greyish-brown coloured mineral, probably as a result of secondary mineralization. In plane polarized, there does appear to be a discrete layering texture which is exhibited by what appears to be a greater concentration of calcite occurring as bands as well as the apparent concentration of the black/dark brown opaque mineral along these bands.

Sample: GW102-2013TK

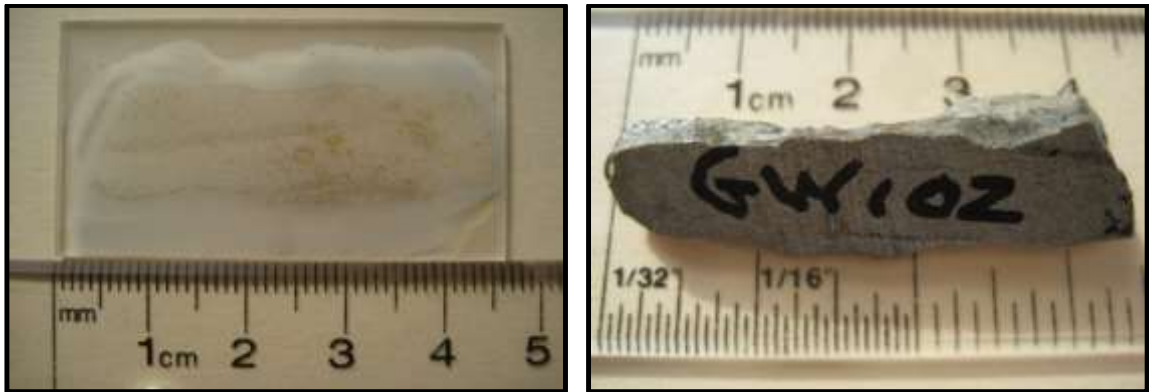


Figure K4: (Left) photograph of thin section from hand sample GW101-2013TK. (Right) corresponding photograph of rock sample that thin section was made from.

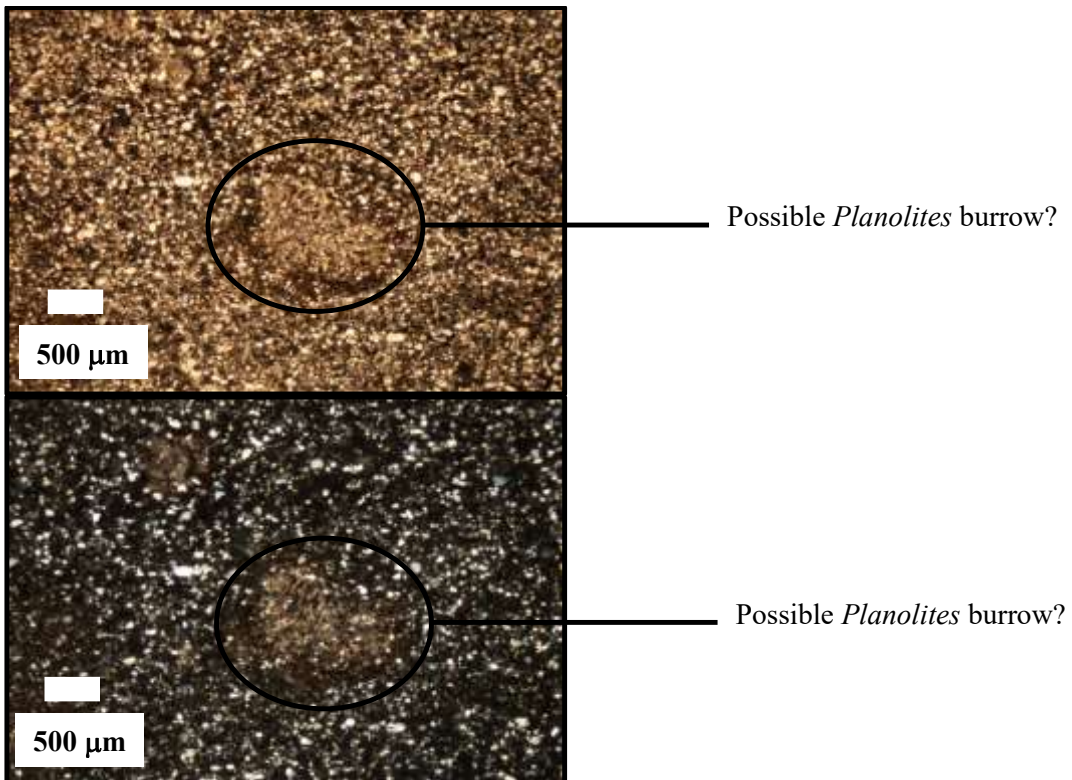


Figure K5: (Top) sample GW102-2013TK in ordinary light at 2X magnification. (Bottom) sample in plane polarized light at 2X magnification.

Sample: GW102-2013TK Continued...

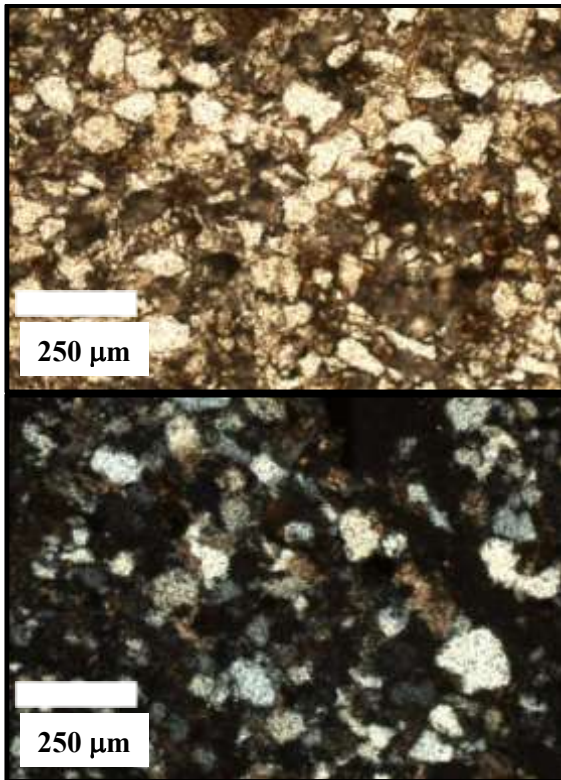


Figure K6: (Top) sample GW102-2013TK in ordinary light at 10X magnification. (Bottom) sample in plane polarized light at 10X magnification.

Description:

In thin section, the sample is mainly equigranular and fine-grained. Quartz and calcite are the dominant minerals with the quartz crystals being rounded to angular in shape and randomly oriented. The grain size is similar to that of sample GW101-2013TK. Calcite/ankerite occurs in the sample as a matrix material. There are zones that are round in shape and contain abundant calcite as infill and are rimmed by a yellowish/brown mineral, possibly siderite. These features could be *Planolites* burrows. There is also the occurrence of some accessory hornblende ($\ll 1\%$). The thin section can be divided into two approximately equal halves, with the halves separated by a gap/crack in the thin section; one side dark (more calcite/ankerite cement), one side light (less cement). The sample is composed of approximately 75 % quartz, 20 % calcite/ankerite and 5 % siderite.

Sample: GW103-2013TK

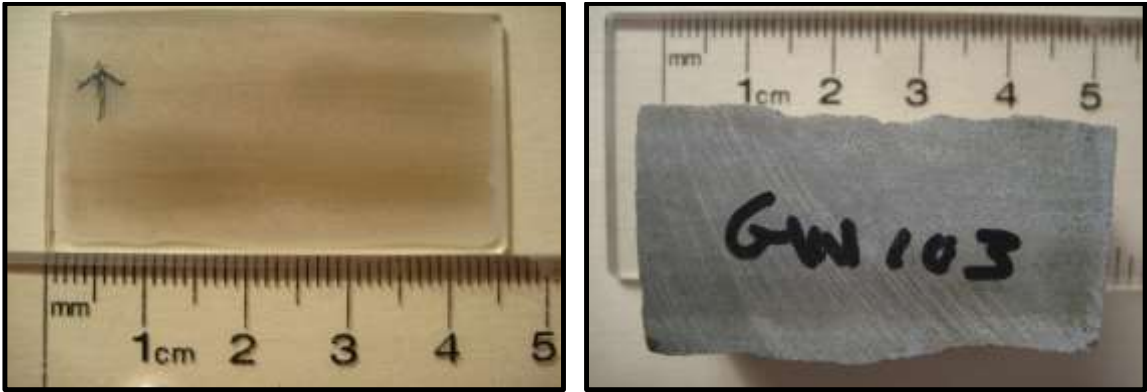


Figure K7: (Left) photograph of thin section from hand sample GW103-2013TK. (Right) corresponding photograph of rock sample that thin section was made from.

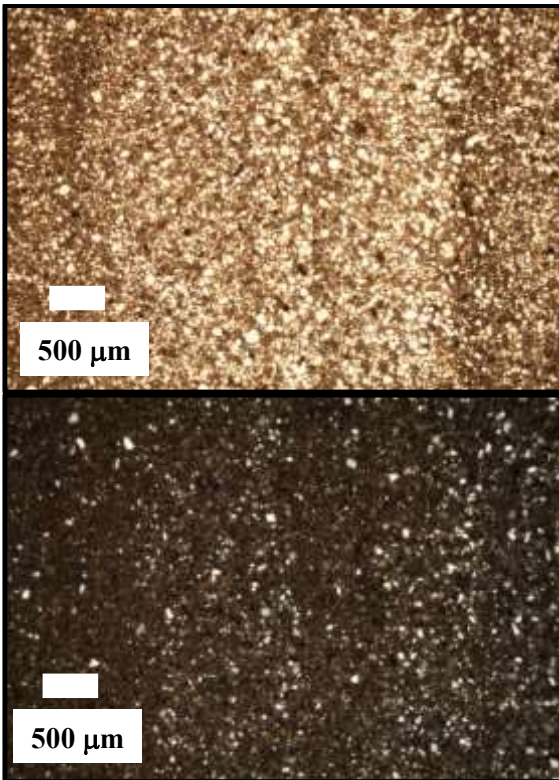


Figure K8: (Top) sample GW103-2013TK in ordinary light at 2X magnification. (Bottom) sample in plane polarized light at 2X magnification.

Sample: GW103-2013TK Continued...

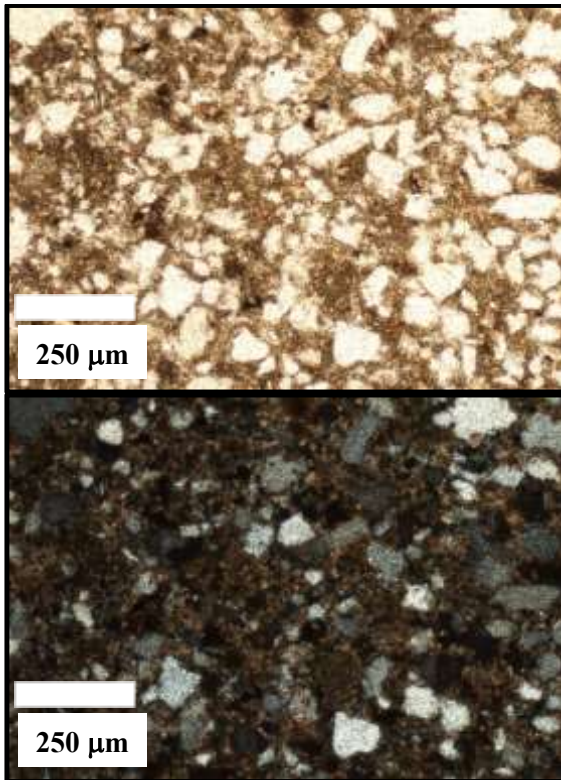


Figure K9: (Top) sample GW103-2013TK in ordinary light at 10X magnification. (Bottom) sample in plane polarized light at 10X magnification.

Description:

This thin section can be described as equigranular, fine-grained and angular crystals. The sample is layered with calcite-rich and quartz-rich layers occurring. The calcite-rich layers are brownish/grey in colour. The quartz-rich areas have much less calcite/ankerite cement and the quartz crystals are in greater contact with one another. The calcite/ankerite-rich areas contain minor quartz crystals that are surrounded with calcite/ankerite. Siderite occurs as a yellowish/brownish colour. Quartz is approximately 60 % of the sample, with calcite/ankerite the remaining 40 %.

Sample: GW104-2013TK

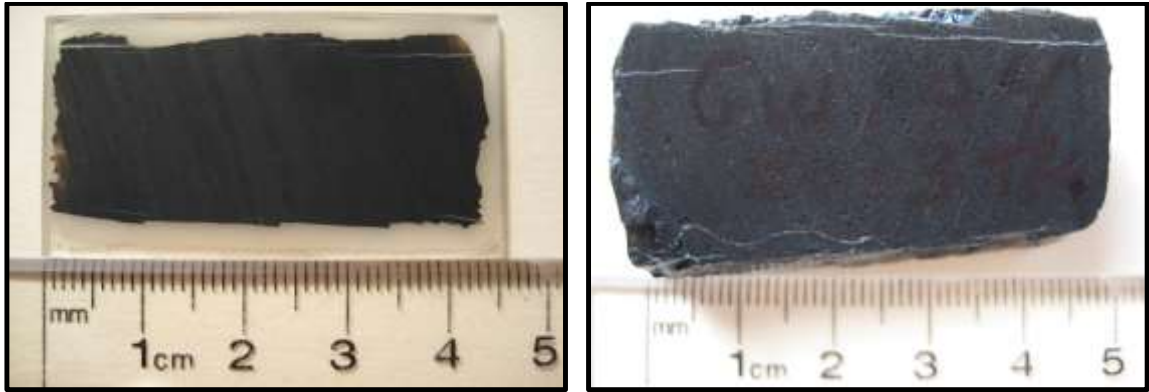


Figure K10: (Left) photograph of thin section from hand sample GW104-2013TK. (Right) corresponding photograph of rock sample that thin section was made from.

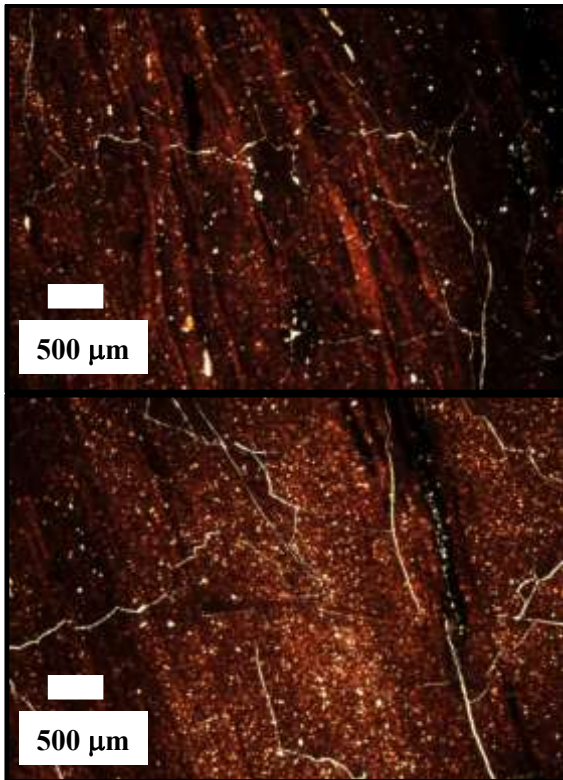


Figure K11: (Top) sample GW104-2013TK in ordinary light at 2X magnification. (Bottom) another image of the sample in ordinary light at 2X magnification.

Sample: GW104-2013TK Continued...

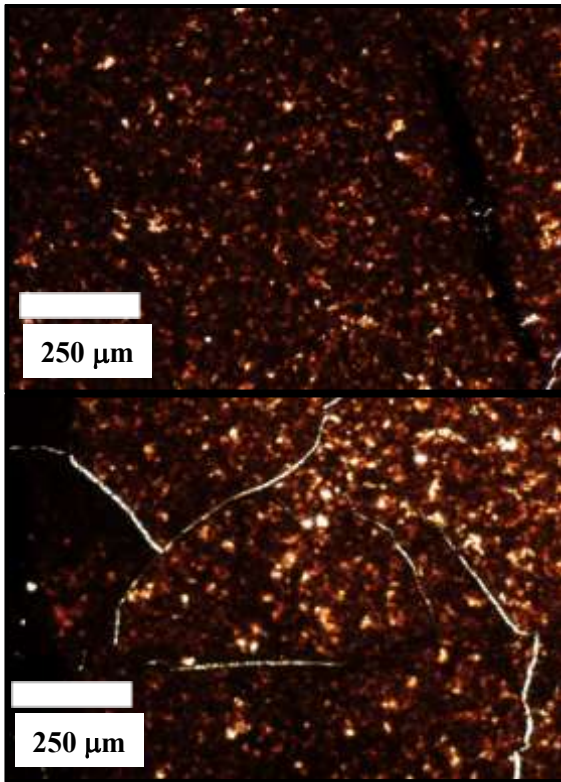


Figure K12: (Top) sample GW104-2013TK in ordinary light at 10X magnification. (Bottom) another image of the sample in ordinary light at 10X magnification.

Description:

This thin section represents coal. It is composed mainly of graphite/opaque mineral matter. The sample contains thin red shreds that are red in colour. They probably represent woody material that has been well preserved. The smaller yellow/orange coloured particles are likely spores or algal material.

Sample: GW105-2013TK



Figure K13: (Left) photograph of thin section from hand sample GW105-2013TK. (Right) corresponding photograph of rock sample that thin section was made from.

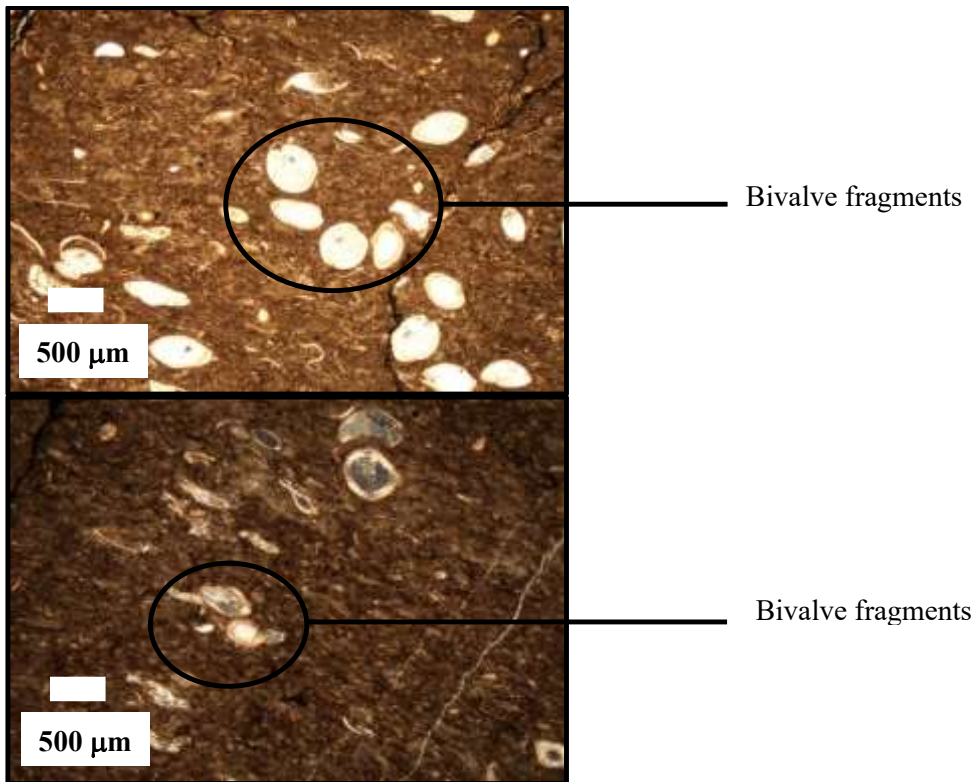


Figure K14: (Top) sample GW105-2013TK in ordinary light at 2X magnification. (Bottom) sample in plane polarized light at 2X magnification.

Sample: GW105-2013TK Continued...

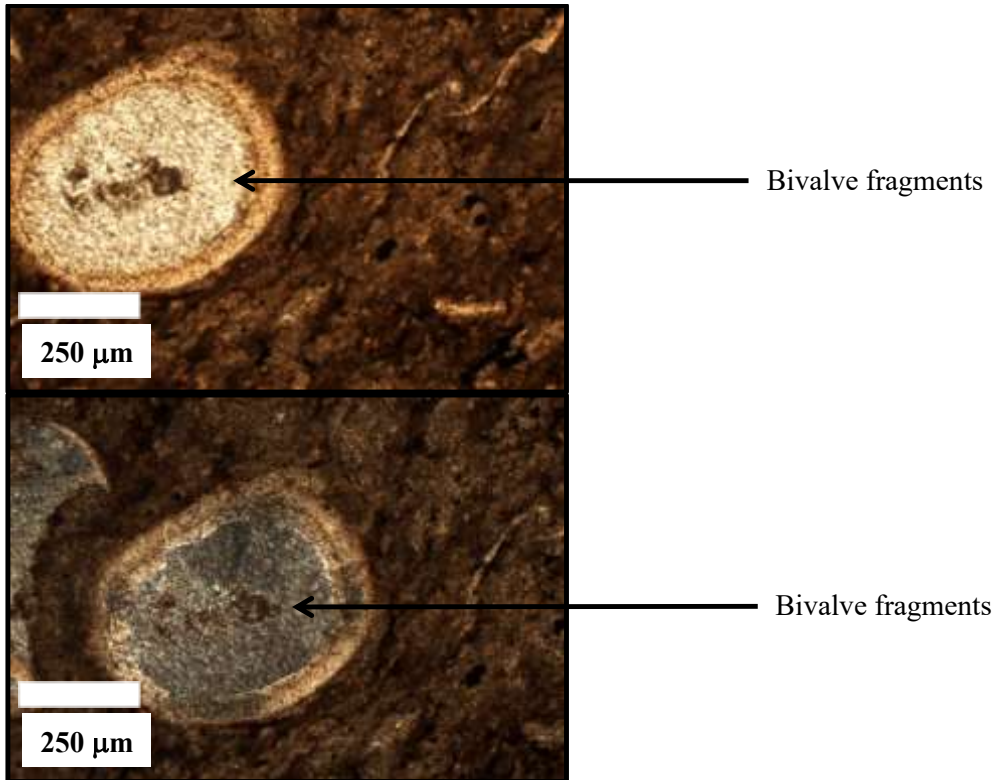


Figure K15: (Top) sample GW105-2013TK in ordinary light at 10X magnification. (Bottom) sample in plane polarized light at 10X magnification.

Description:

This thin section represents a fossiliferous limestone that is composed primarily of calcite with some residual siderite and opaque minerals. The sample contains abundant shell fragments that appear to represent bivalves. Calcite/ankerite combine to make up 95 % of the sample, while the black/opaque minerals combine for approximately 5 %. The black/opaque mineralization occurs as single crystals, groupings of crystals or as veinlets.

Sample: GW106-2013TK

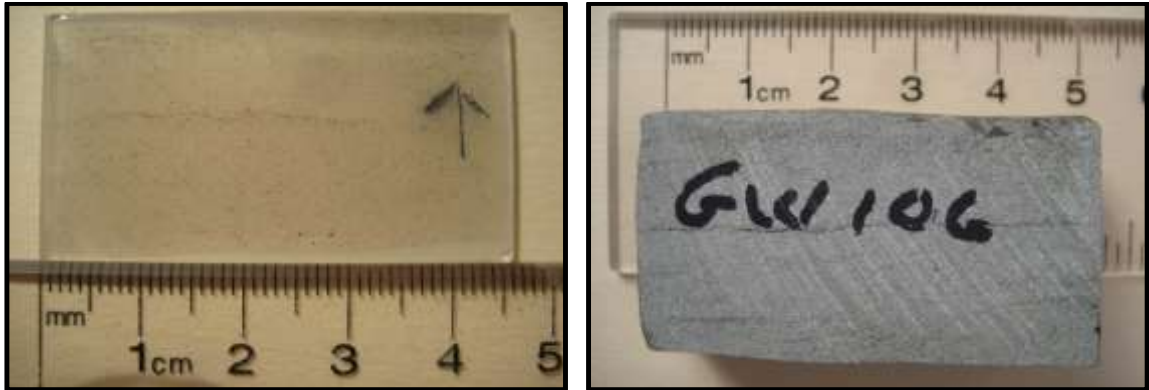


Figure K16: (Left) photograph of thin section from hand sample GW106-2013TK. (Right) corresponding photograph of rock sample that thin section was made from.

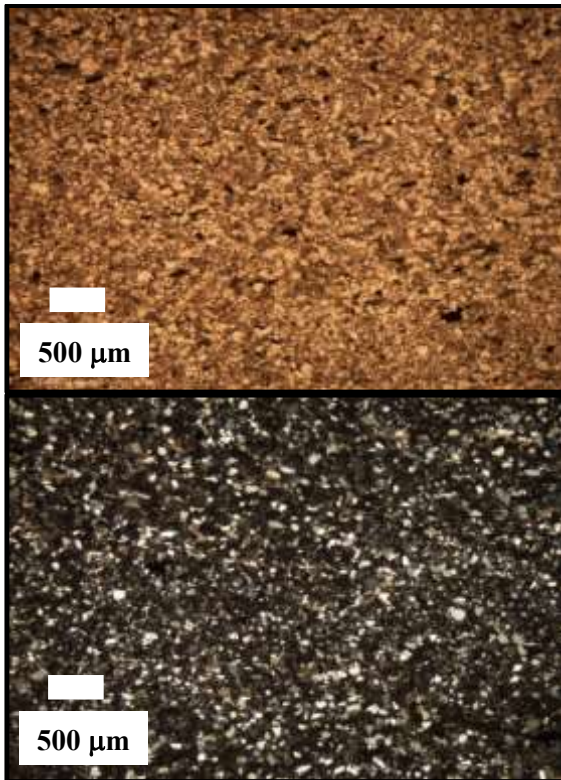


Figure K17: (Top) sample GW106-2013TK in ordinary light at 2X magnification. (Bottom) sample in plane polarized light at 2X magnification.

Sample: GW106-2013TK Continued...

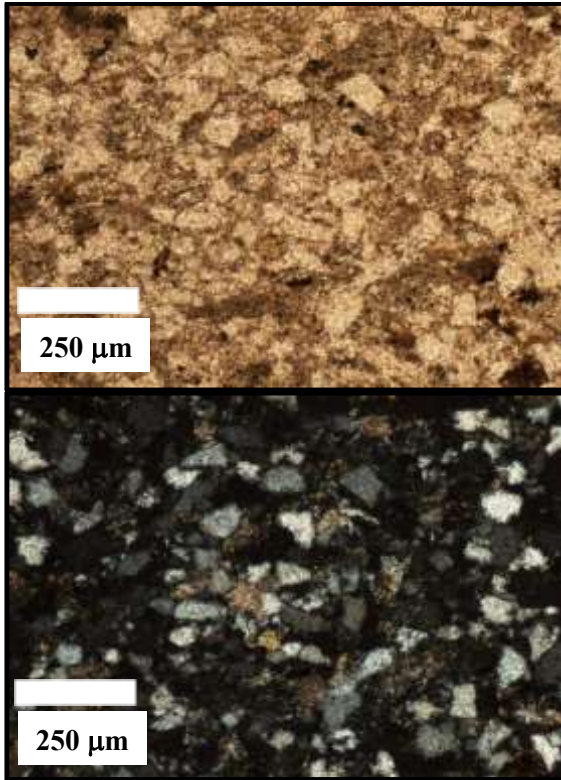


Figure K18: (Top) sample GW106-2013TK in ordinary light at 10X magnification. (Bottom) sample in plane polarized light at 10X magnification.

Description:

This thin section represents a sandstone that is equigranular, angular and fine-grained. The sample contains mainly quartz and calcite/ankerite with an accessory opaque mineral. Quartz composes of approximately 75 % of the sample, with calcite/ankerite being the remaining 25 %.

Sample: GW107-2013TK

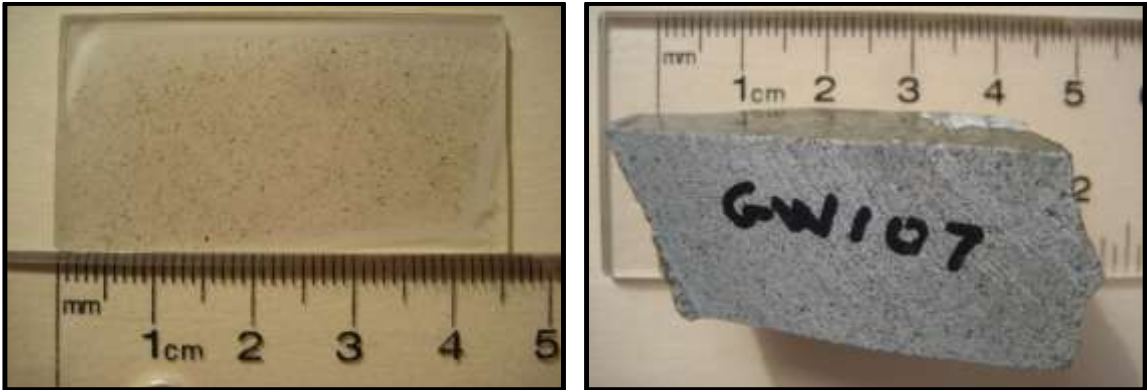


Figure K19: (Left) photograph of thin section from hand sample GW107-2013TK. (Right) corresponding photograph of rock sample that thin section was made from.

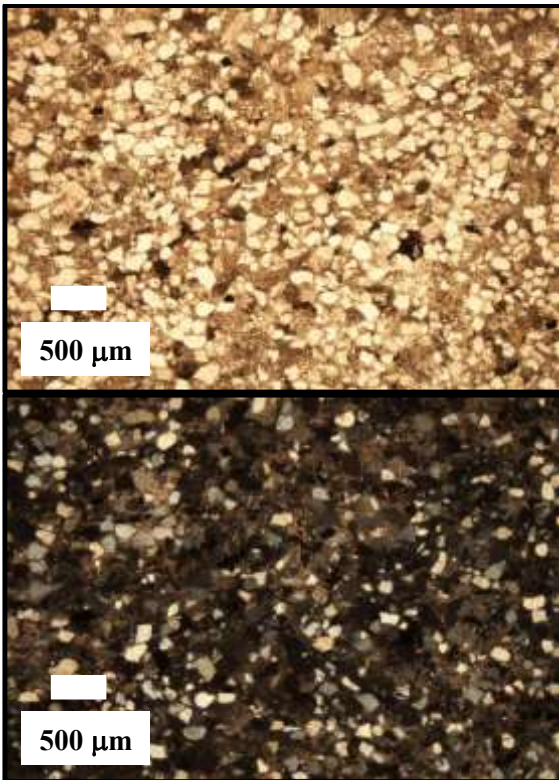


Figure K20: (Top) sample GW107-2013TK in ordinary light at 2X magnification. (Bottom) sample in plane polarized light at 2X magnification.

Sample: GW107-2013TK Continued...

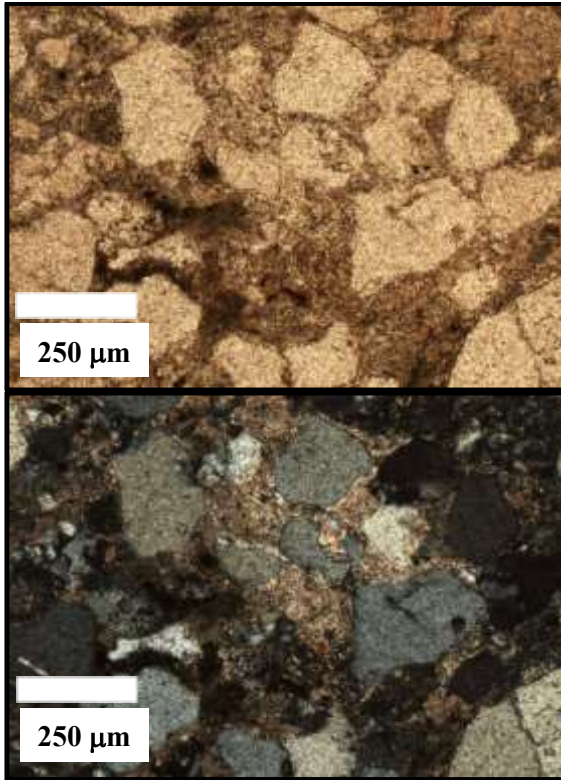


Figure K21: (Top) sample GW107-2013TK in ordinary light at 10X magnification. (Bottom) sample in plane polarized light at 10X magnification.

Description:

This thin section represents a sandstone that is equigranular, angular and fine-grained. The sample contains mainly quartz and calcite with an accessory opaque mineral. Quartz composes of approximately 65 % of the sample, with calcite/ankerite being the remaining 35 %.

Sample: GW108-2013TK

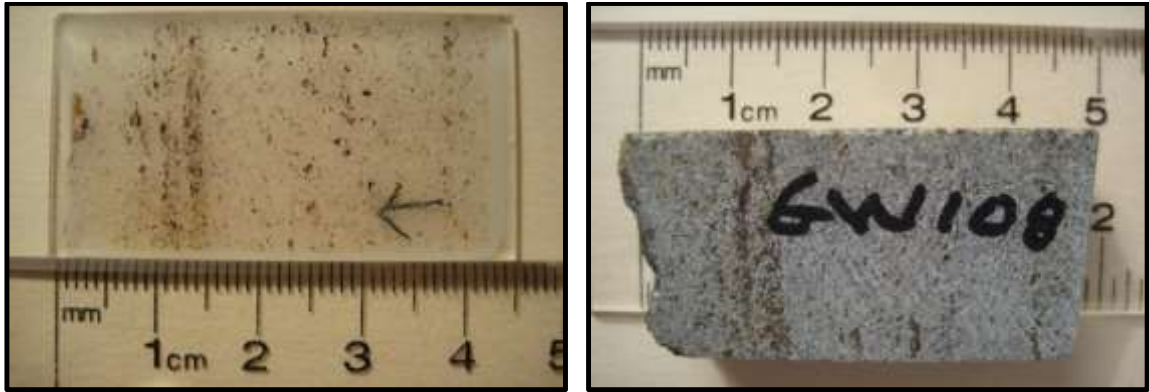


Figure K22: (Left) photograph of thin section from hand sample GW108-2013TK. (Right) corresponding photograph of rock sample that thin section was made from.

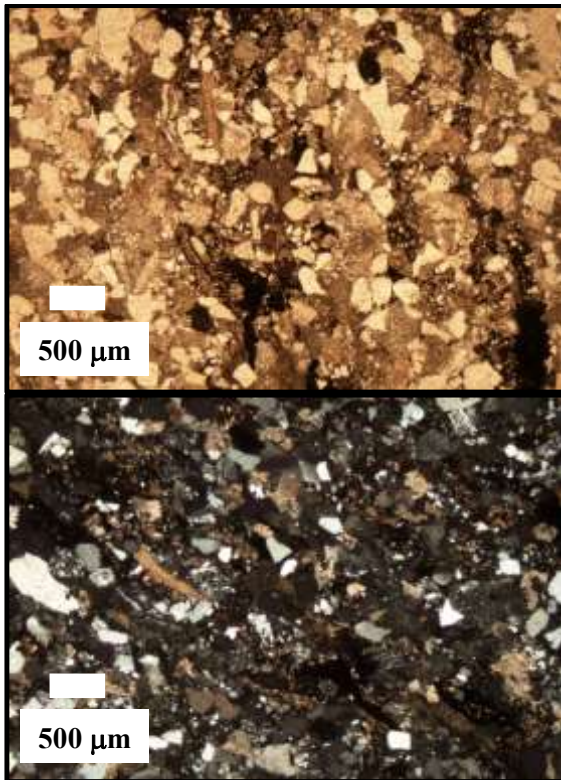


Figure K23: (Top) sample GW108-2013TK in ordinary light at 2X magnification. (Bottom) sample in plane polarized light at 2X magnification.

Sample: GW108-2013TK Continued...

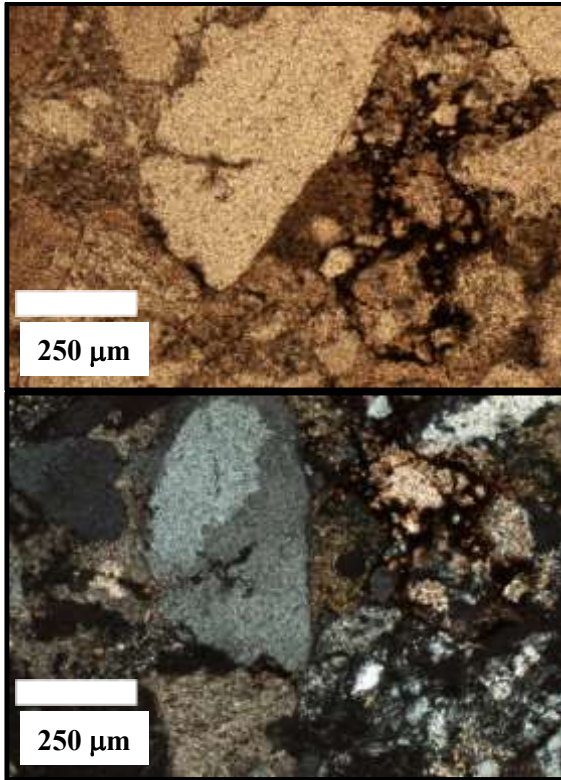


Figure K24: (Top) sample GW108-2013TK in ordinary light at 10X magnification. (Bottom) sample in plane polarized light at 10X magnification.

Description:

This thin section is an in-equigranular, angular, coarse-grained sandstone. Approximately 80 % of the sample is quartz and calcite/ankerite represents the remaining 20 %. Siderite occurs but at a low percentage. There is some banding/layering as a result of the siderite occurring in concentrated form as bands.

Appendix L: Thin Section Descriptions (Porosity)

This material originally appeared in my MEng thesis document:

Kelly, T.B. 2013. Reservoir Performance and Architecture of a Fluvial Meanderbelt System, Joggins Formation, Nova Scotia. MEng Thesis, Department of Engineering, Dalhousie University, Halifax, Nova Scotia.

Sample: GW101-2013TK

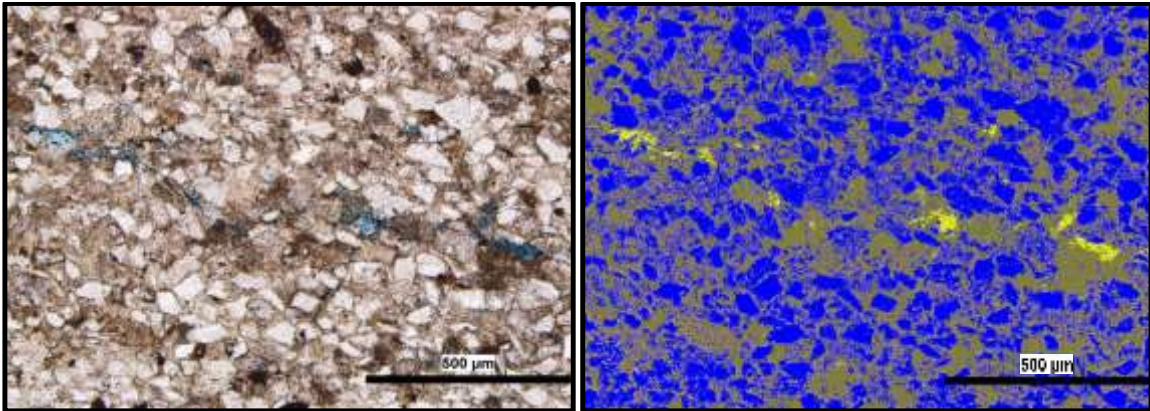


Figure L1: (Left) thin section image GW101-2013TK-1 (@ 10X) in normal light with porosity shown in blue (dye). (Right) same image, but with porosity shown in yellow, grains as blue and cement as brown.

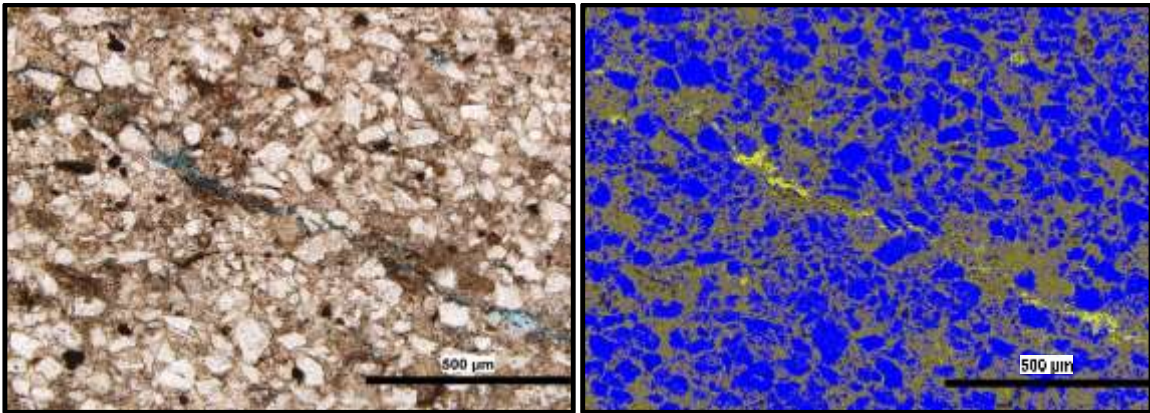


Figure L2: (Left) thin section image GW101-2013TK-2 (@ 10X) in normal light with porosity shown in blue (dye). (Right) same image, but with porosity shown in yellow, grains as blue and cement as brown.

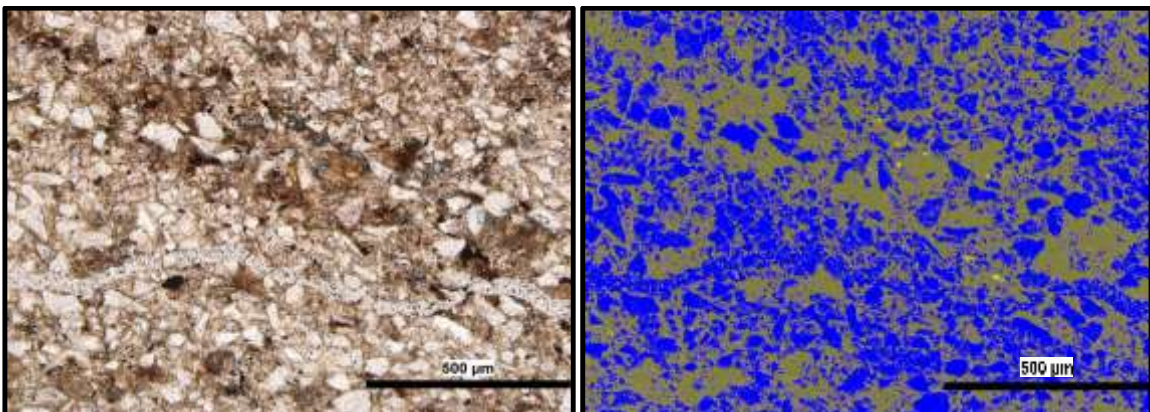


Figure L3: (Left) thin section image GW101-2013TK-3 (@ 10X) in normal light with porosity shown in blue (dye). (Right) same image, but with porosity shown in yellow, grains as blue and cement as brown.

Sample: GW101-2013TK Continued...

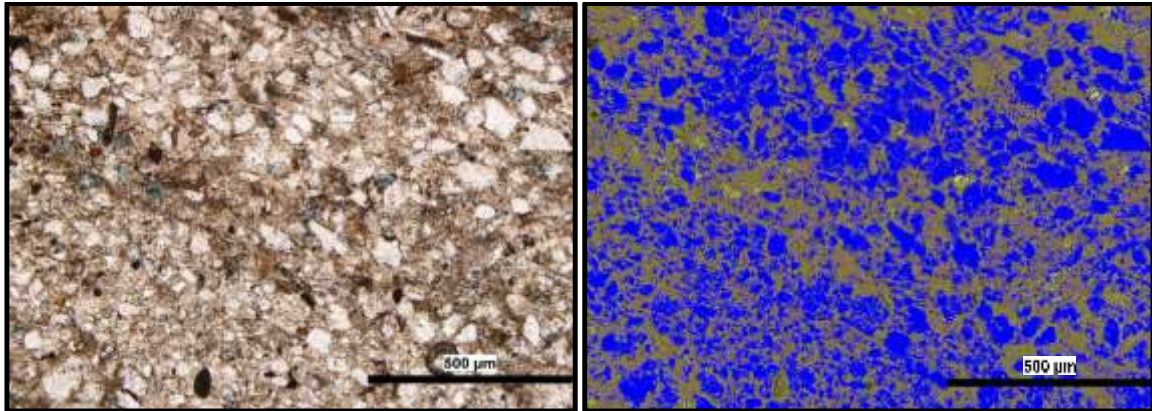


Figure L4: (Left) thin section image GW101-2013TK-4 (@ 10X) in normal light with porosity shown in blue (dye). (Right) same image, but with porosity shown in yellow, grains as blue and cement as brown.

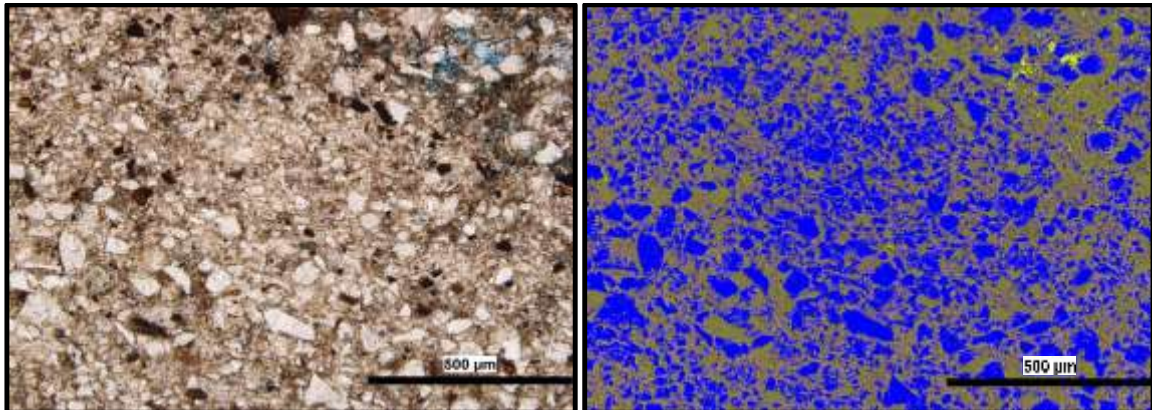


Figure L5: (Left) thin section image GW101-2013TK-5 (@ 10X) in normal light with porosity shown in blue (dye). (Right) same image, but with porosity shown in yellow, grains as blue and cement as brown.

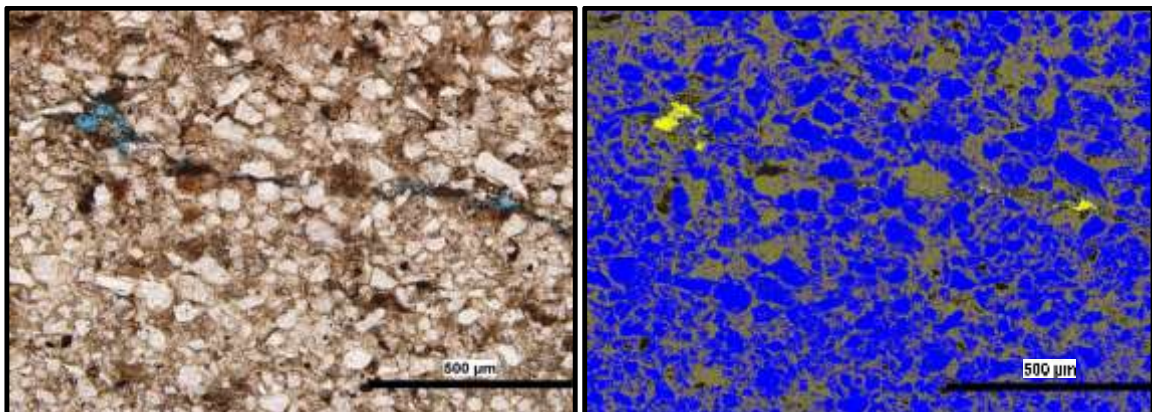


Figure L6: (Left) thin section image GW101-2013TK-6 (@ 10X) in normal light with porosity shown in blue (dye). (Right) same image, but with porosity shown in yellow, grains as blue and cement as brown.

Sample: GW101-2013TK Continued...

Table L1: Summary table for sample GW101-2013TK listing the area percentage for voids, grains and cement in each image captured of the thin section. The average area for each of the three parameters is also calculated.

Image Number	Area Type	Area %
GW101-2013TK-1	Voids	2.6
	Grains	72.8
	Cement	24.6
GW101-2013TK-2	Voids	2.5
	Grains	65.5
	Cement	32.0
GW101-2013TK-3	Voids	0.6
	Grains	58.8
	Cement	40.7
GW101-2013TK-4	Voids	2.0
	Grains	75.8
	Cement	22.2
GW101-2013TK-5	Voids	2.0
	Grains	72.2
	Cement	25.8
GW101-2013TK-6	Voids	0.7
	Grains	69.6
	Cement	29.7
Average	Voids	1.7
	Grains	69.1
	Cement	29.2

Sample: GW102-2013TK

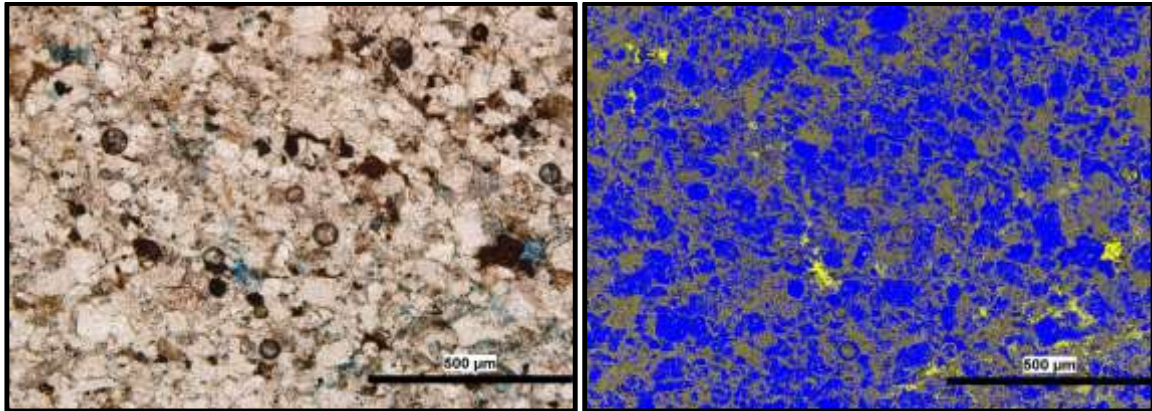


Figure L7: (Left) thin section image GW102-2013TK-1 (@ 10X) in normal light with porosity shown in blue (dye). (Right) same image, but with porosity shown in yellow, grains as blue and cement as brown.

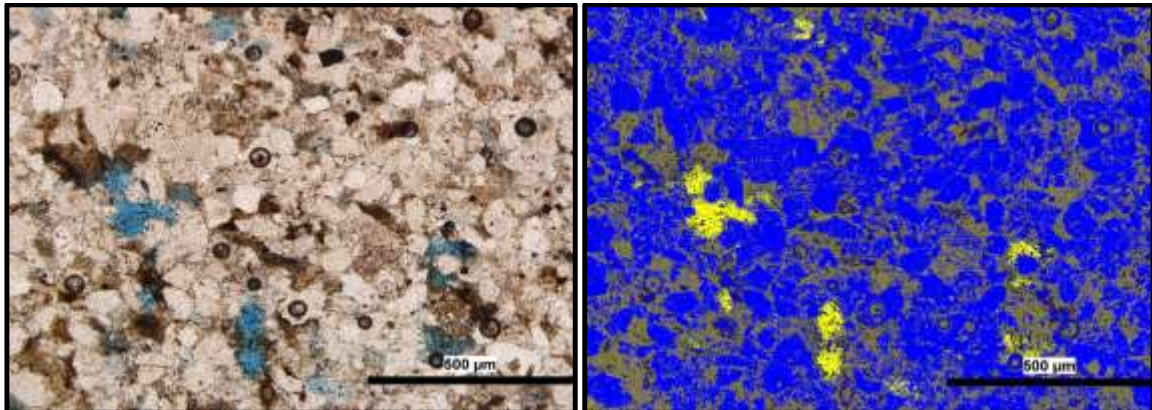


Figure L8: (Left) thin section image GW102-2013TK-2 (@ 10X) in normal light with porosity shown in blue (dye). (Right) same image, but with porosity shown in yellow, grains as blue and cement as brown.

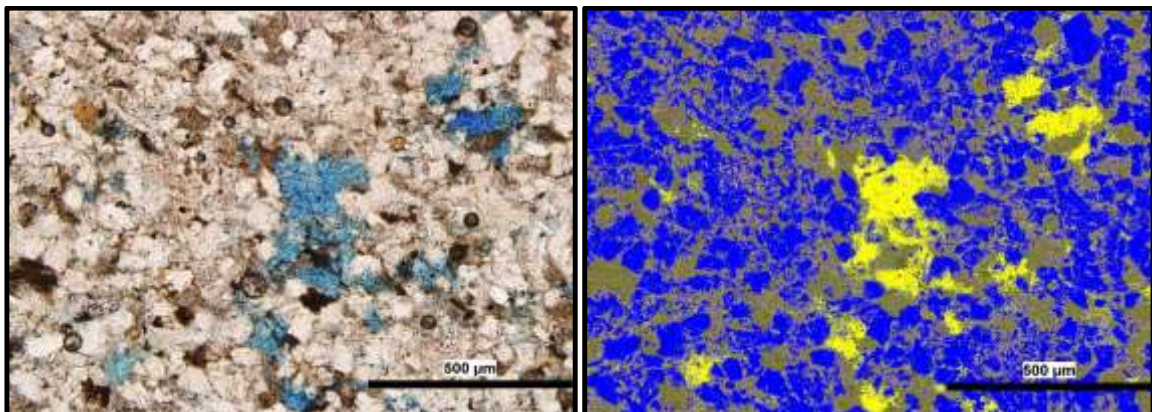


Figure L9: (Left) thin section image GW102-2013TK-3 (@ 10X) in normal light with porosity shown in blue (dye). (Right) same image, but with porosity shown in yellow, grains as blue and cement as brown.

Sample: GW102-2013TK Continued...

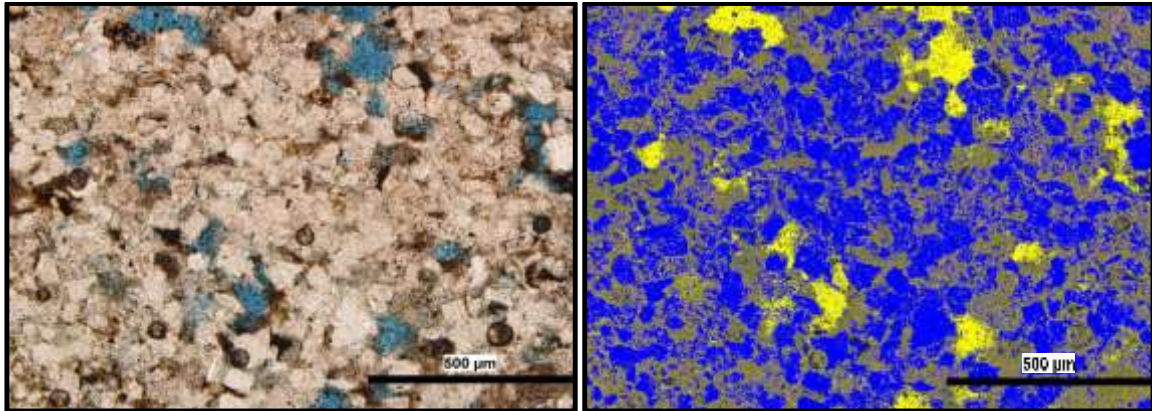


Figure L10: (Left) thin section image GW102-2013TK-4 (@ 10X) in normal light with porosity shown in blue (dye). (Right) same image, but with porosity shown in yellow, grains as blue and cement as brown.

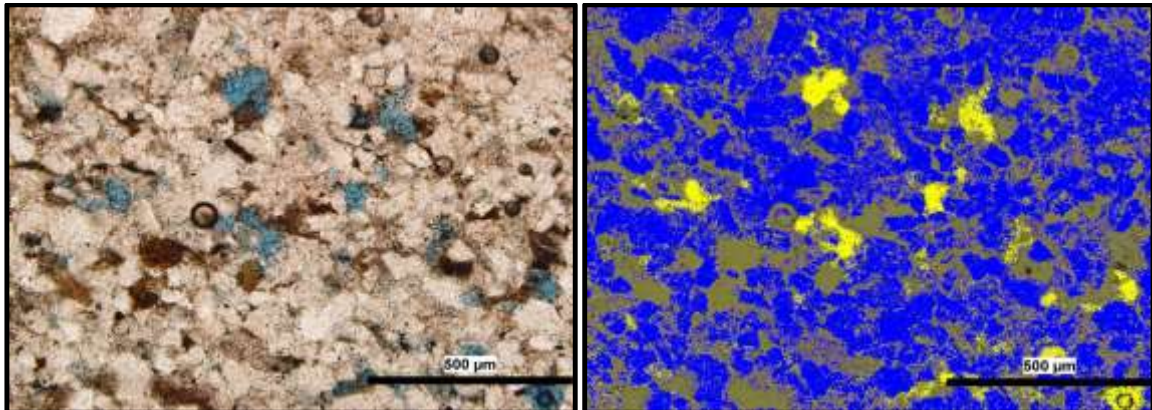


Figure L11: (Left) thin section image GW102-2013TK-5 (@ 10X) in normal light with porosity shown in blue (dye). (Right) same image, but with porosity shown in yellow, grains as blue and cement as brown.

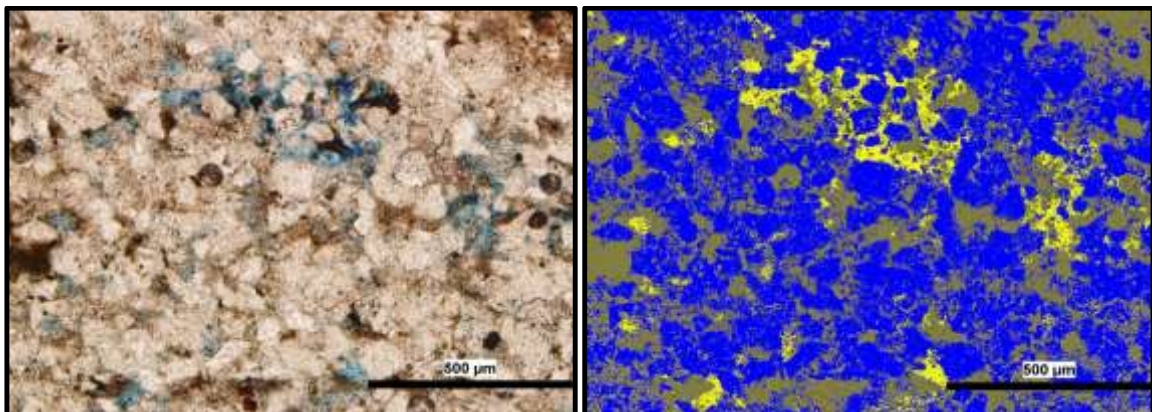


Figure L12: (Left) thin section image GW102-2013TK-6 (@ 10X) in normal light with porosity shown in blue (dye). (Right) same image, but with porosity shown in yellow, grains as blue and cement as brown.

Sample: GW102-2013TK Continued...

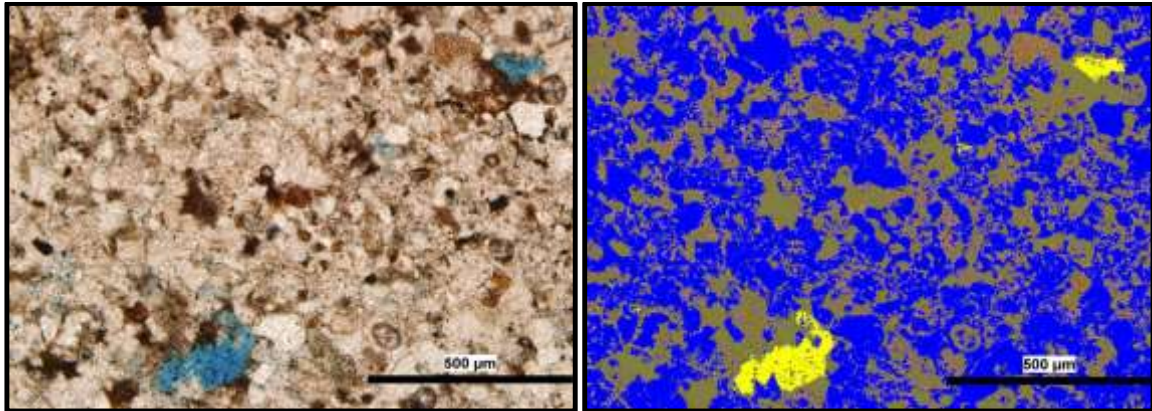


Figure L13: (Left) thin section image GW102-2013TK-7 (@ 10X) in normal light with porosity shown in blue (dye). (Right) same image, but with porosity shown in yellow, grains as blue and cement as brown.

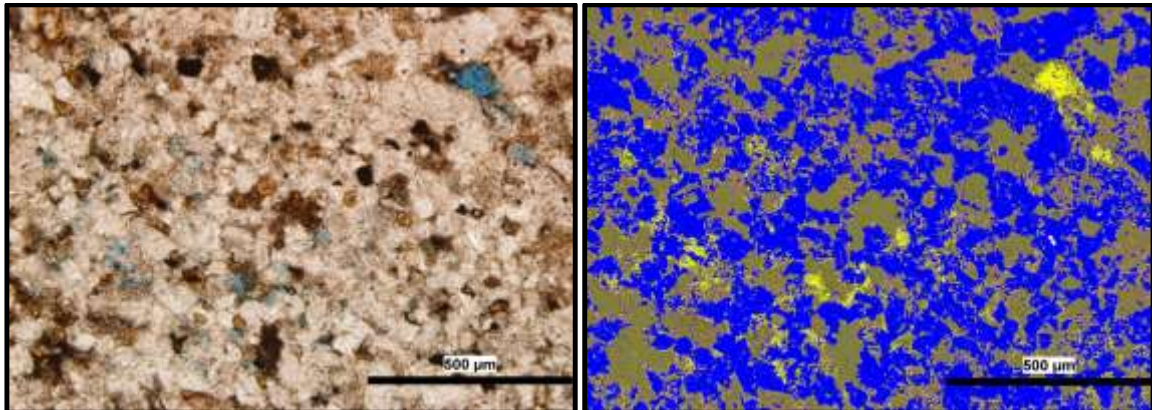


Figure L14: (Left) thin section image GW102-2013TK-8 (@ 10X) in normal light with porosity shown in blue (dye). (Right) same image, but with porosity shown in yellow, grains as blue and cement as brown.

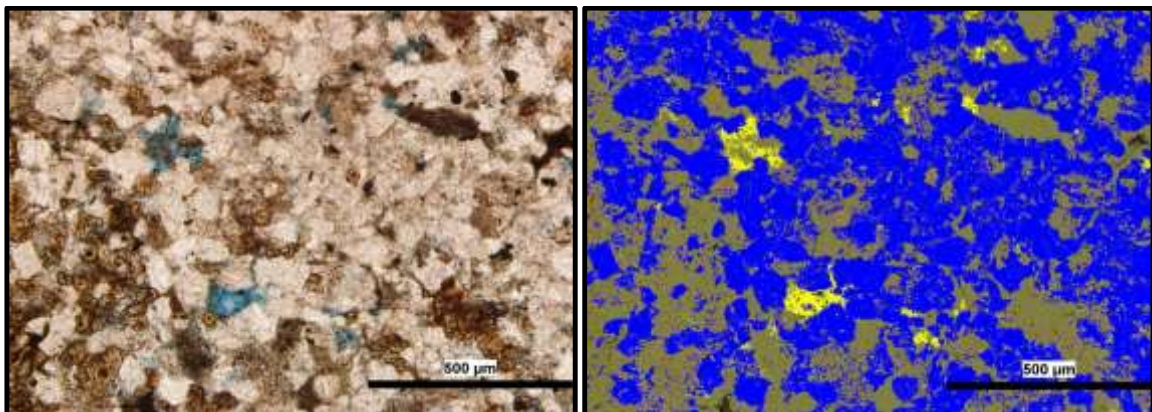


Figure L15: (Left) thin section image GW102-2013TK-9 (@ 10X) in normal light with porosity shown in blue (dye). (Right) same image, but with porosity shown in yellow, grains as blue and cement as brown.

Sample: GW102-2013TK Continued...

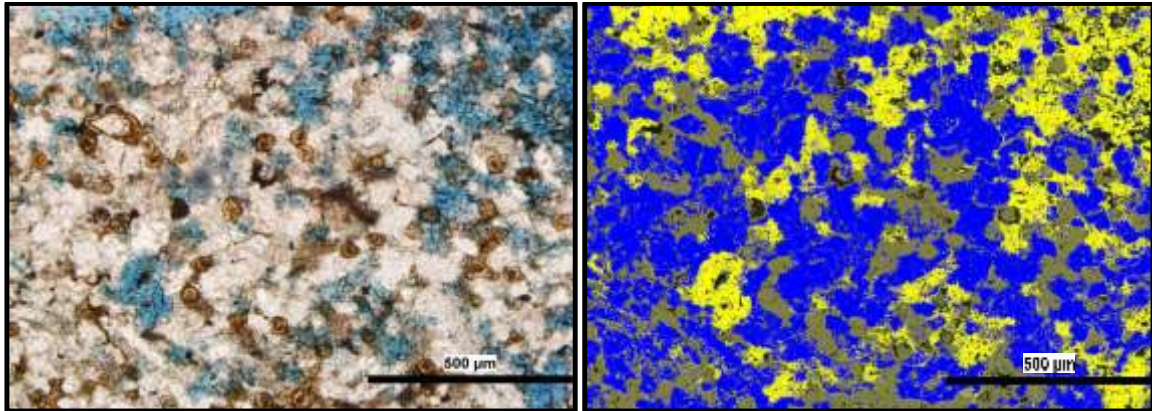


Figure L16: (Left) thin section image GW102-2013TK-10 (@ 10X) in normal light with porosity shown in blue (dye). (Right) same image, but with porosity shown in yellow, grains as blue and cement as brown.

Sample: GW102-2013TK Continued...

Table L2: Summary table for sample GW102-2013TK listing the area percentage for voids, grains and cement in each image captured of the thin section. The average area for each of the three parameters is also calculated.

Image Number	Area Type	Area %
GW102-2013TK-1	Voids	3.0
	Grains	60.2
	Cement	36.9
GW102-2013TK-2	Voids	7.6
	Grains	79.9
	Cement	12.5
GW102-2013TK-3	Voids	9.4
	Grains	64.2
	Cement	26.4
GW102-2013TK-4	Voids	8.5
	Grains	66.3
	Cement	25.2
GW102-2013TK-5	Voids	6.2
	Grains	76.1
	Cement	17.7
GW102-2013TK-6	Voids	7.0
	Grains	69.4
	Cement	23.7
GW102-2013TK-7	Voids	2.3
	Grains	80.3
	Cement	17.4
GW102-2013TK-8	Voids	5.7
	Grains	75.0
	Cement	19.3
GW102-2013TK-9	Voids	2.4
	Grains	68.3
	Cement	29.3
GW102-2013TK-10	Voids	22.3
	Grains	55.2
	Cement	22.5
Average	Voids	7.4
	Grains	69.5
	Cement	23.1

Sample: GW103-2013TK

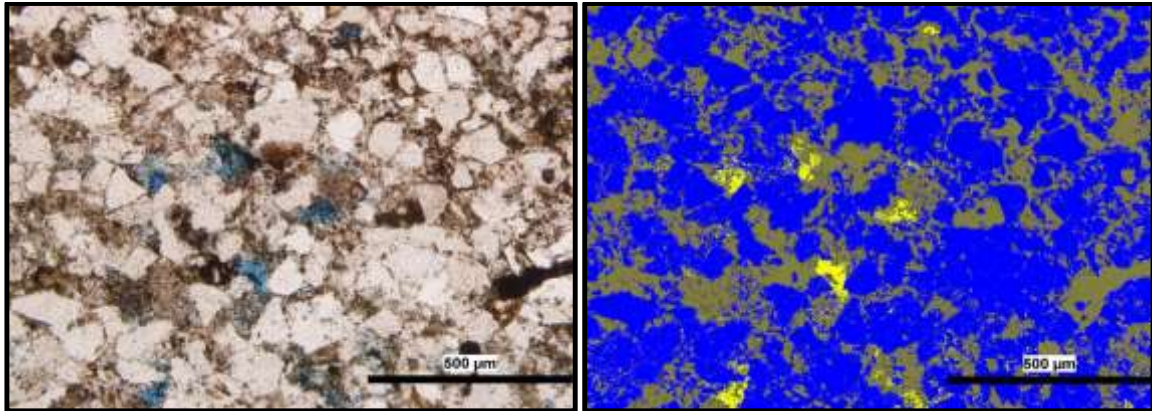


Figure L17: (Left) thin section image GW103-2013TK-1 (@ 10X) in normal light with porosity shown in blue (dye). (Right) same image, but with porosity shown in yellow, grains as blue and cement as brown.

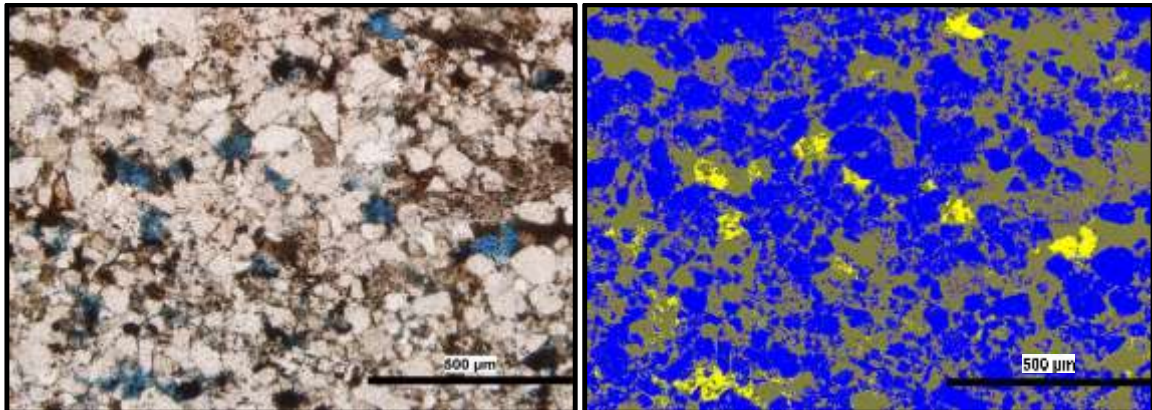


Figure L18: (Left) thin section image GW103-2013TK-2 (@ 10X) in normal light with porosity shown in blue (dye). (Right) same image, but with porosity shown in yellow, grains as blue and cement as brown.

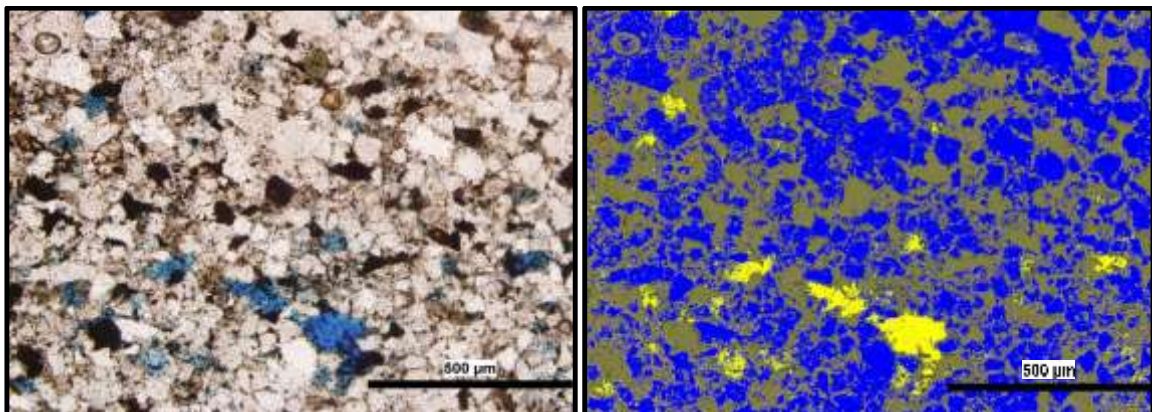


Figure L19: (Left) thin section image GW103-2013TK-3 (@ 10X) in normal light with porosity shown in blue (dye). (Right) same image, but with porosity shown in yellow, grains as blue and cement as brown.

Sample: GW103-2013TK Continued...

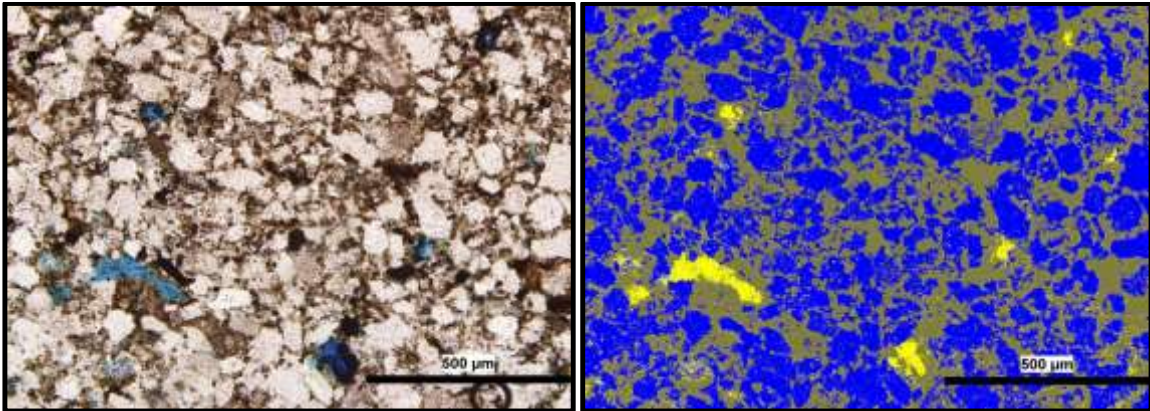


Figure L20: (Left) thin section image GW103-2013TK-4 (@ 10X) in normal light with porosity shown in blue (dye). (Right) same image, but with porosity shown in yellow, grains as blue and cement as brown.

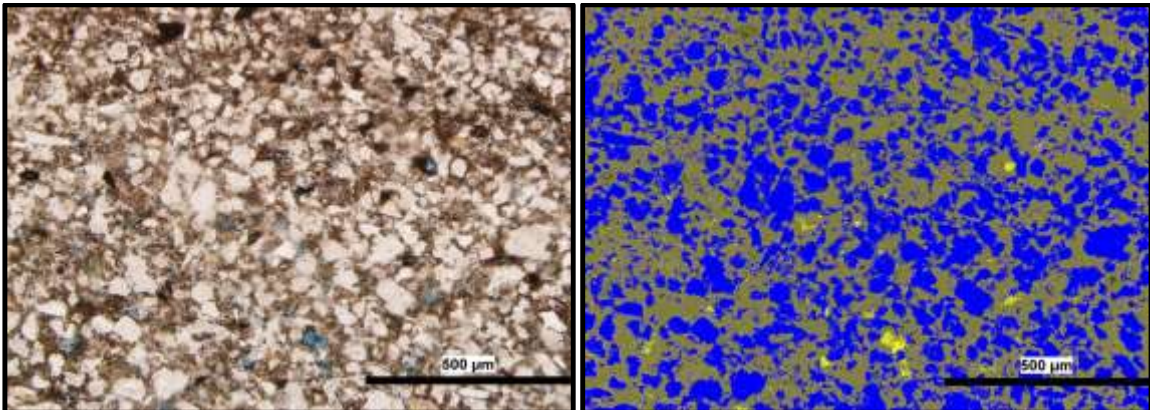


Figure L21: (Left) thin section image GW103-2013TK-5 (@ 10X) in normal light with porosity shown in blue (dye). (Right) same image, but with porosity shown in yellow, grains as blue and cement as brown.

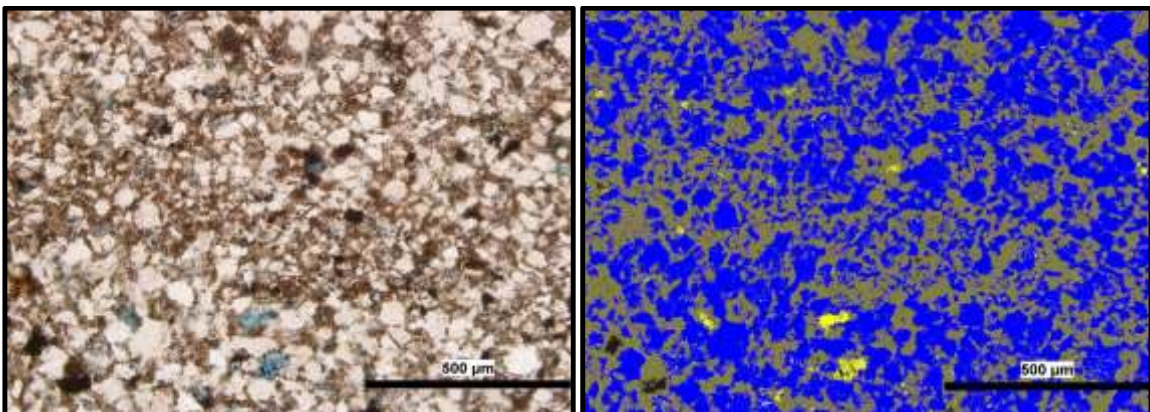


Figure L22: (Left) thin section image GW103-2013TK-6 (@ 10X) in normal light with porosity shown in blue (dye). (Right) same image, but with porosity shown in yellow, grains as blue and cement as brown.

Sample: GW103-2013TK Continued...

Table L3: Summary table for sample GW103-2013TK listing the area percentage for voids, grains and cement in each image captured of the thin section. The average area for each of the three parameters is also calculated.

Image Number	Area Type	Area %
GW103-2013TK-1	Voids	2.2
	Grains	73.4
	Cement	24.4
GW103-2013TK-2	Voids	4.0
	Grains	67.5
	Cement	28.6
GW103-2013TK-3	Voids	4.6
	Grains	51.7
	Cement	43.6
GW103-2013TK-4	Voids	3.6
	Grains	56.3
	Cement	40.1
GW103-2013TK-5	Voids	1.0
	Grains	39.5
	Cement	59.5
GW103-2013TK-6	Voids	1.3
	Grains	68.3
	Cement	30.4
Average	Voids	2.8
	Grains	59.5
	Cement	37.8

Sample: GW106-2013TK

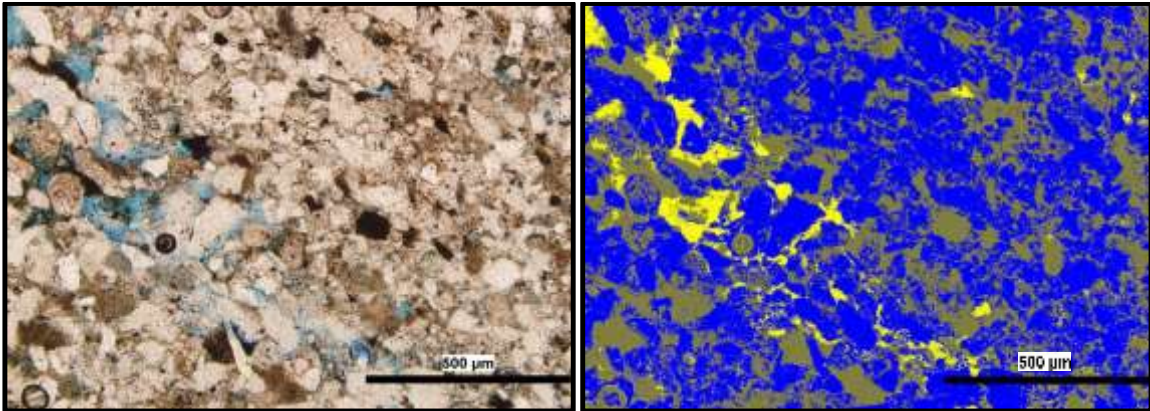


Figure L23: (Left) thin section image GW106-2013TK-1 (@ 10X) in normal light with porosity shown in blue (dye). (Right) same image, but with porosity shown in yellow, grains as blue and cement as brown.

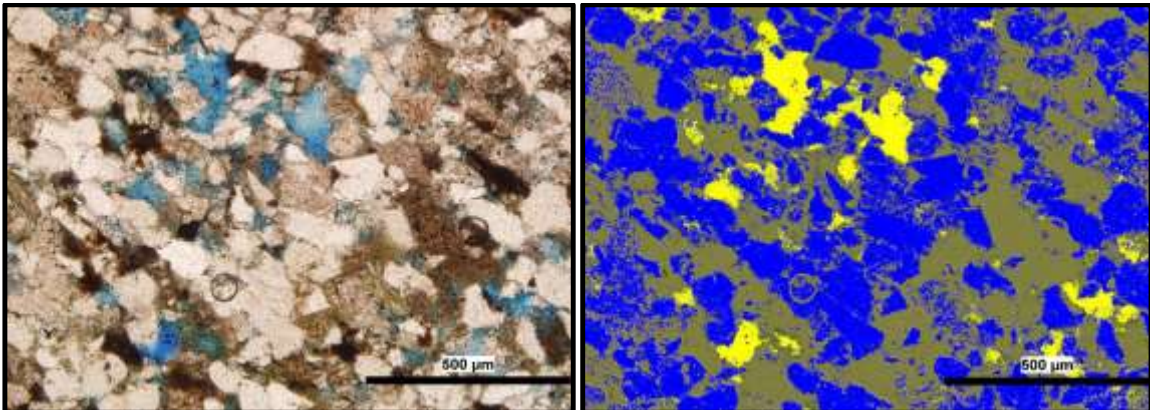


Figure L24: (Left) thin section image GW106-2013TK-2 (@ 10X) in normal light with porosity shown in blue (dye). (Right) same image, but with porosity shown in yellow, grains as blue and cement as brown.

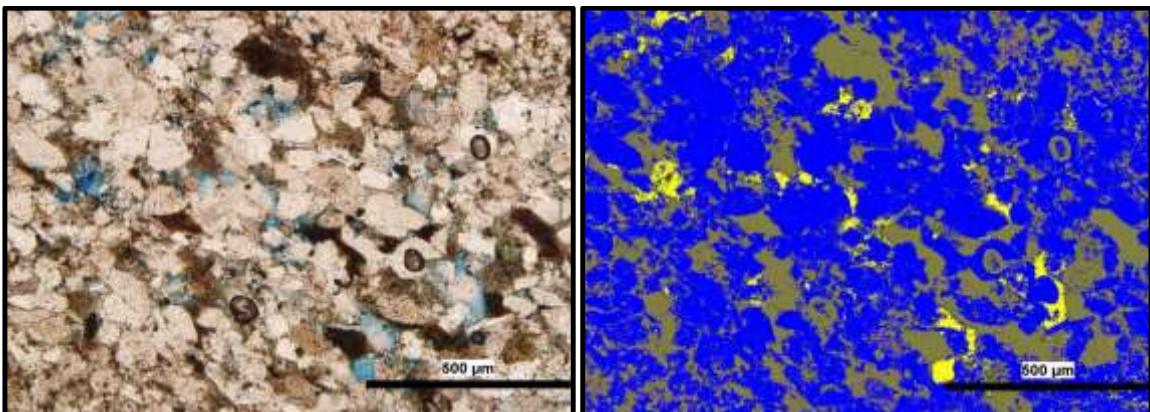


Figure L25: (Left) thin section image GW106-2013TK-3 (@ 10X) in normal light with porosity shown in blue (dye). (Right) same image, but with porosity shown in yellow, grains as blue and cement as brown.

Sample: GW106-2013TK Continued...

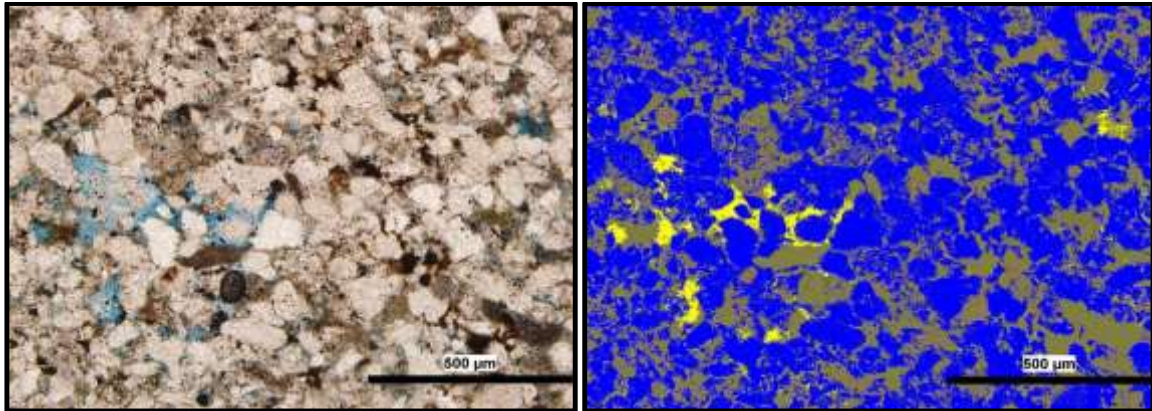


Figure L26: (Left) thin section image GW106-2013TK-4 (@ 10X) in normal light with porosity shown in blue (dye). (Right) same image, but with porosity shown in yellow, grains as blue and cement as brown.

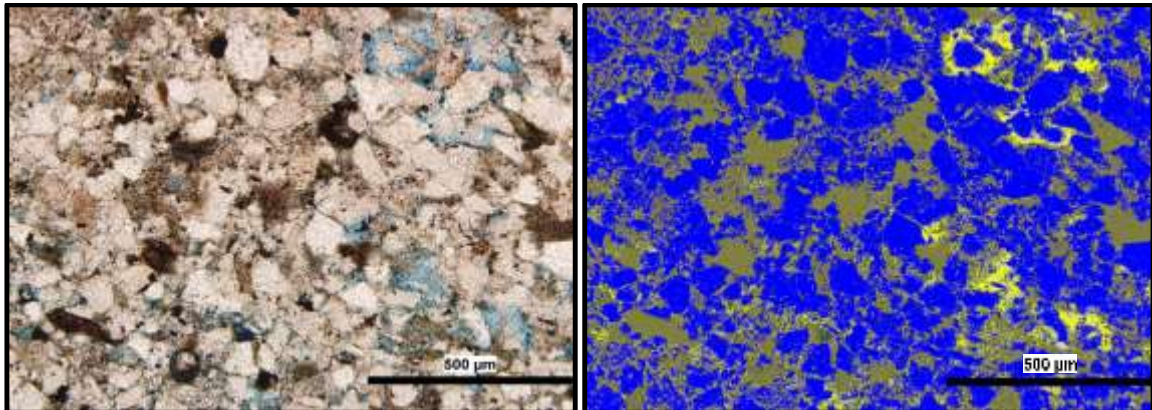


Figure L27: (Left) thin section image GW106-2013TK-5 (@ 10X) in normal light with porosity shown in blue (dye). (Right) same image, but with porosity shown in yellow, grains as blue and cement as brown.

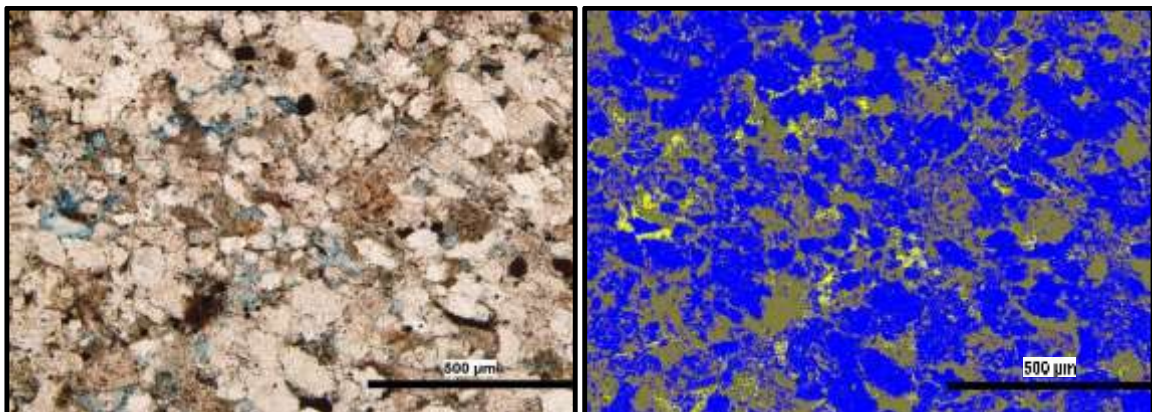


Figure L28: (Left) thin section image GW106-2013TK-6 (@ 10X) in normal light with porosity shown in blue (dye). (Right) same image, but with porosity shown in yellow, grains as blue and cement as brown.

Sample: GW106-2013TK Continued...

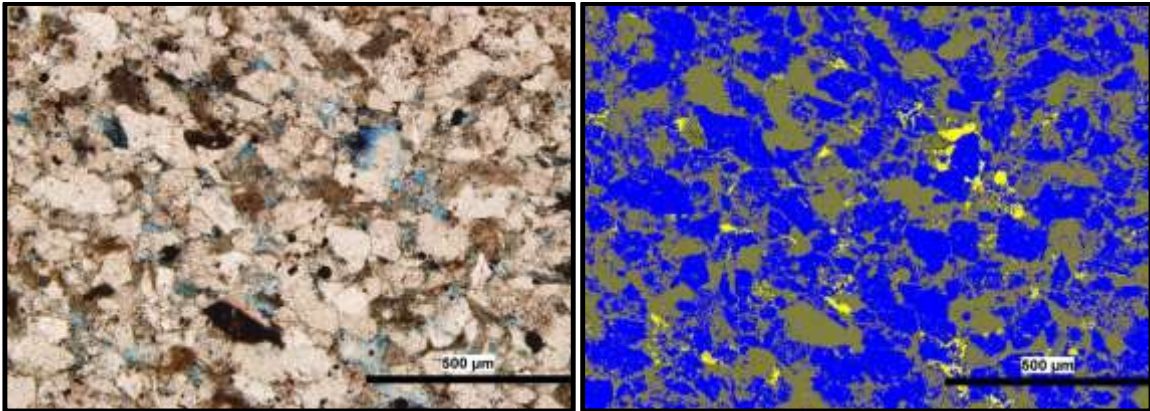


Figure L29: (Left) thin section image GW106-2013TK-7 (@ 10X) in normal light with porosity shown in blue (dye). (Right) same image, but with porosity shown in yellow, grains as blue and cement as brown.

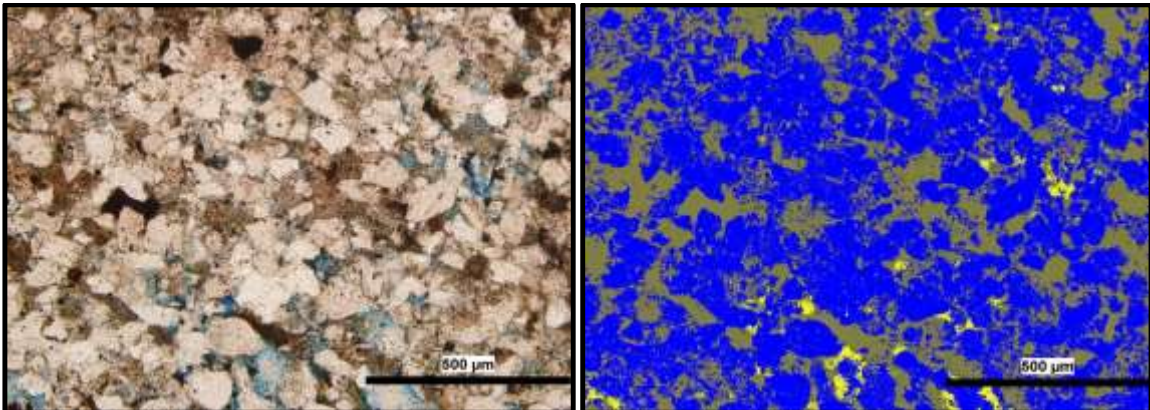


Figure L30: (Left) thin section image GW106-2013TK-8 (@ 10X) in normal light with porosity shown in blue (dye). (Right) same image, but with porosity shown in yellow, grains as blue and cement as brown.

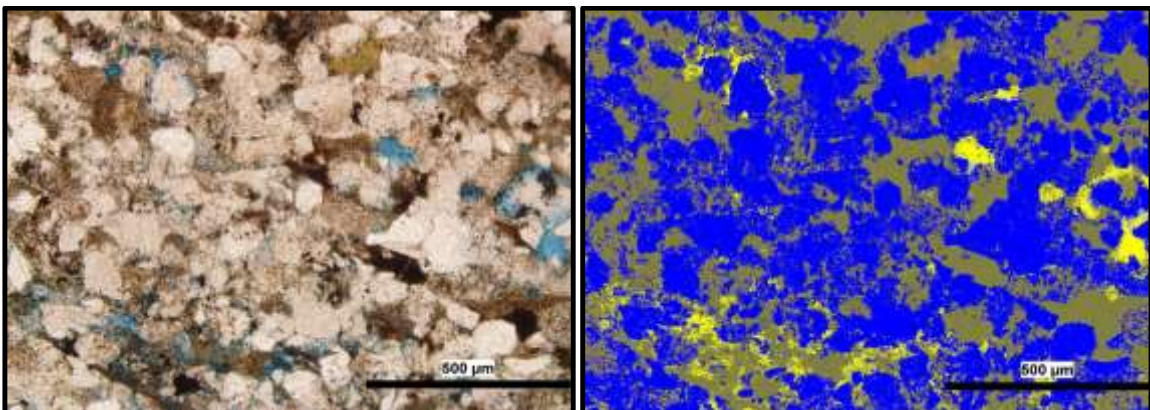


Figure L31: (Left) thin section image GW106-2013TK-9 (@ 10X) in normal light with porosity shown in blue (dye). (Right) same image, but with porosity shown in yellow, grains as blue and cement as brown.

Sample: GW106-2013TK Continued...

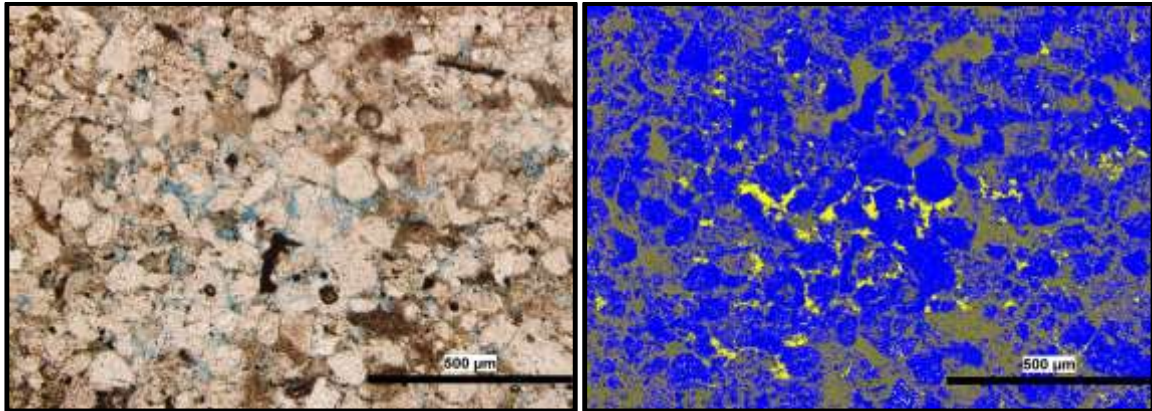


Figure L32: (Left) thin section image GW106-2013TK-10 (@ 10X) in normal light with porosity shown in blue (dye). (Right) same image, but with porosity shown in yellow, grains as blue and cement as brown.

Sample: GW106-2013TK Continued...

Table L4: Summary table for sample GW106-2013TK listing the area percentage for voids, grains and cement in each image captured of the thin section. The average area for each of the three parameters is also calculated.

Image Number	Area Type	Area %
GW106-2013TK-1	Voids	5.3
	Grains	67.6
	Cement	27.1
GW106-2013TK-2	Voids	7.2
	Grains	51.0
	Cement	41.8
GW106-2013TK-3	Voids	3.8
	Grains	77.5
	Cement	18.7
GW106-2013TK-4	Voids	2.8
	Grains	78.7
	Cement	18.5
GW106-2013TK-5	Voids	5.7
	Grains	72.8
	Cement	21.6
GW106-2013TK-6	Voids	3.4
	Grains	80.3
	Cement	16.3
GW106-2013TK-7	Voids	3.0
	Grains	65.1
	Cement	31.8
GW106-2013TK-8	Voids	1.5
	Grains	72.4
	Cement	26.2
GW106-2013TK-9	Voids	5.1
	Grains	64.0
	Cement	30.8
GW106-2013TK-10	Voids	3.6
	Grains	74.2
	Cement	22.3
Average	Voids	4.1
	Grains	70.4
	Cement	25.5

Sample: GW107-2013TK

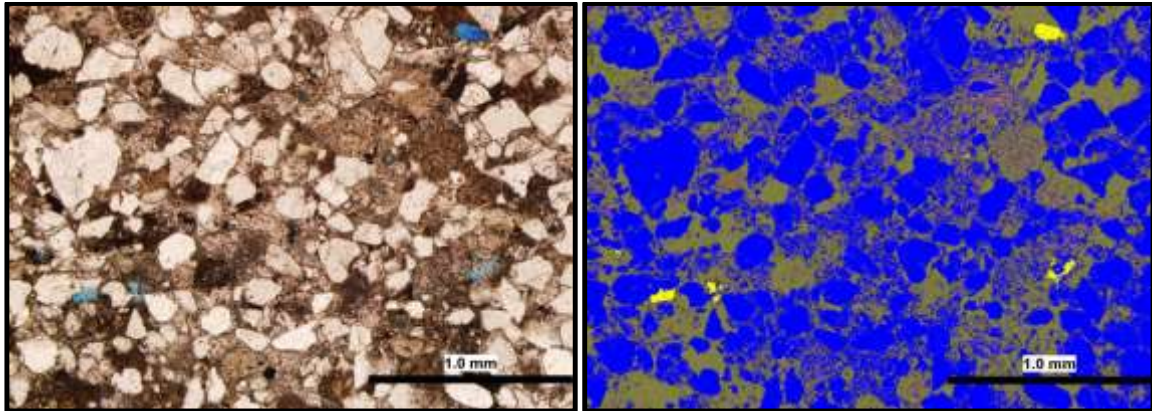


Figure L33: (Left) thin section image GW107-2013TK-1 (@ 5X) in normal light with porosity shown in blue (dye). (Right) same image, but with porosity shown in yellow, grains as blue and cement as brown.

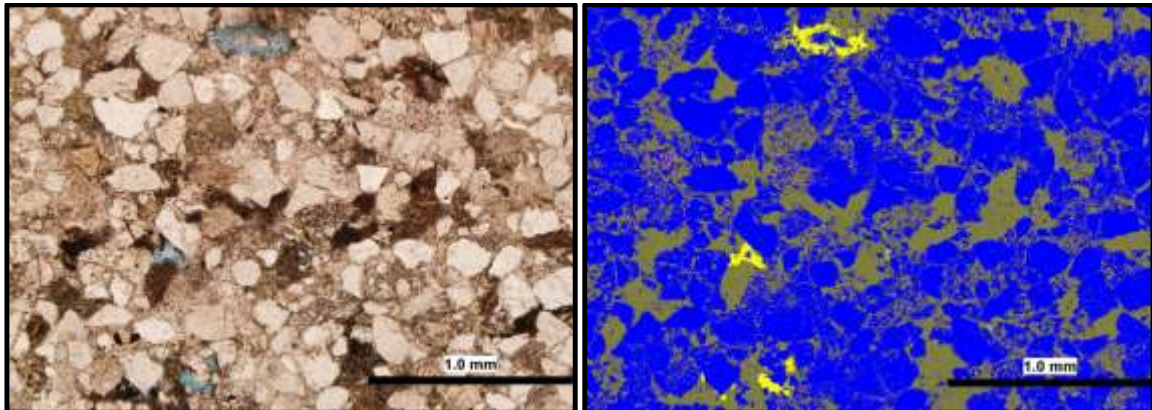


Figure L34: (Left) thin section image GW107-2013TK-2 (@ 5X) in normal light with porosity shown in blue (dye). (Right) same image, but with porosity shown in yellow, grains as blue and cement as brown.

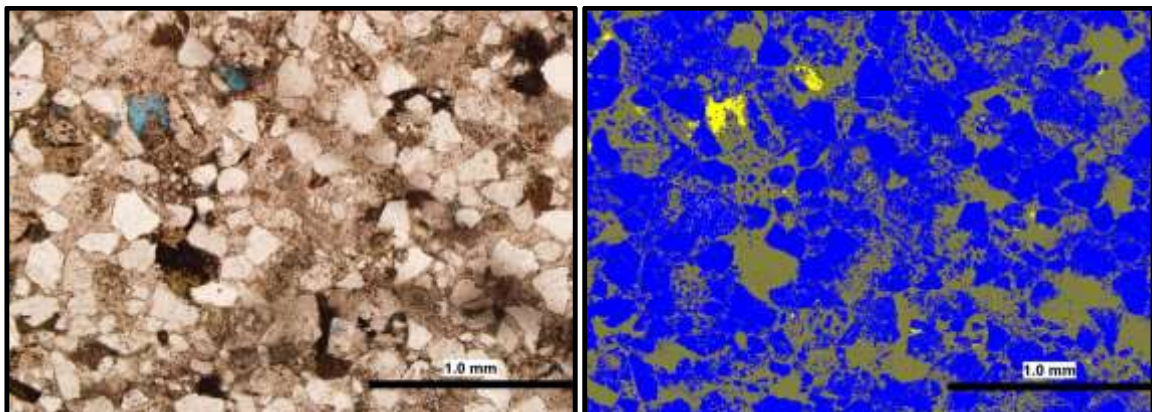


Figure L35: (Left) thin section image GW107-2013TK-3 (@ 5X) in normal light with porosity shown in blue (dye). (Right) same image, but with porosity shown in yellow, grains as blue and cement as brown.

Sample: GW107-2013TK Continued...

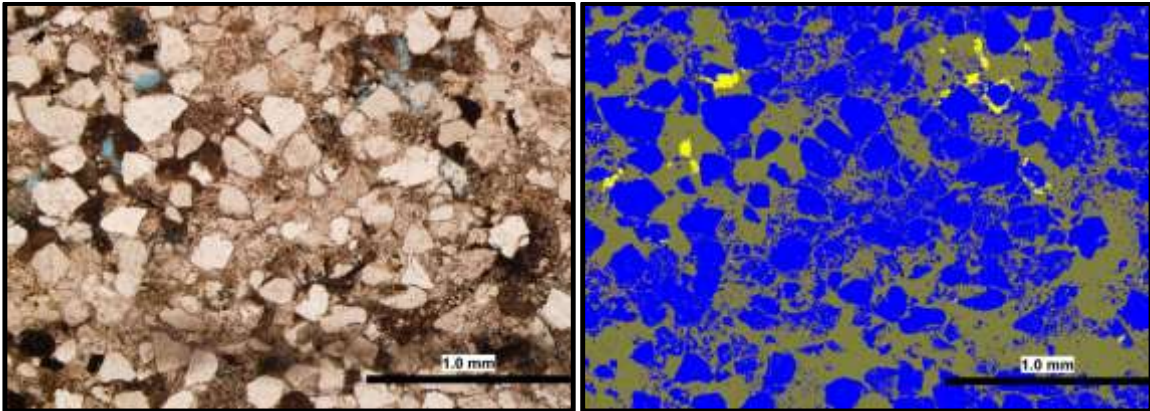


Figure L36: (Left) thin section image GW107-2013TK-4 (@ 5X) in normal light with porosity shown in blue (dye). (Right) same image, but with porosity shown in yellow, grains as blue and cement as brown.

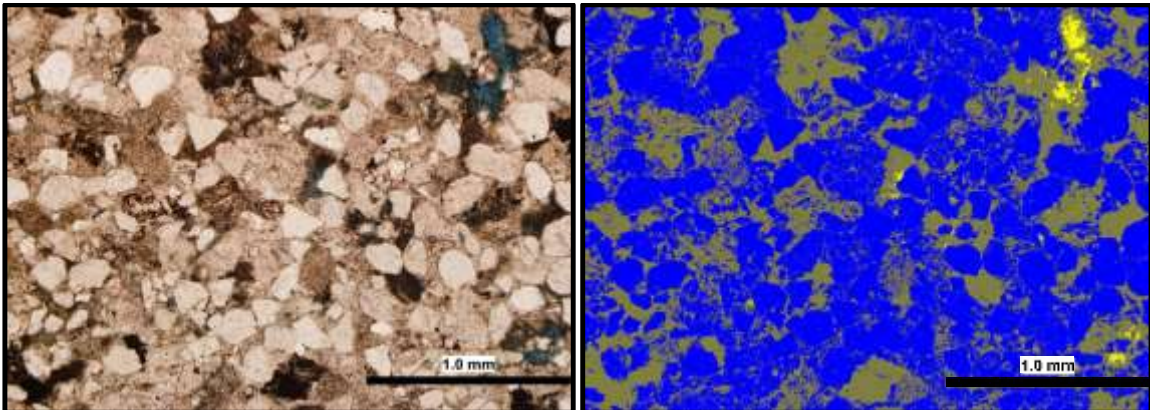


Figure L37: (Left) thin section image GW107-2013TK-5 (@ 5X) in normal light with porosity shown in blue (dye). (Right) same image, but with porosity shown in yellow, grains as blue and cement as brown.

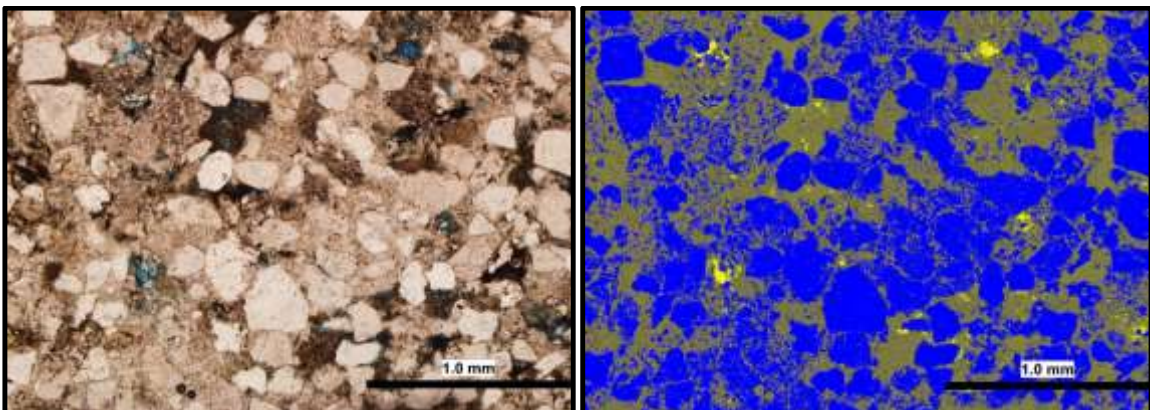


Figure L38: (Left) thin section image GW107-2013TK-6 (@ 5X) in normal light with porosity shown in blue (dye). (Right) same image, but with porosity shown in yellow, grains as blue and cement as brown.

Sample: GW107-2013TK Continued...

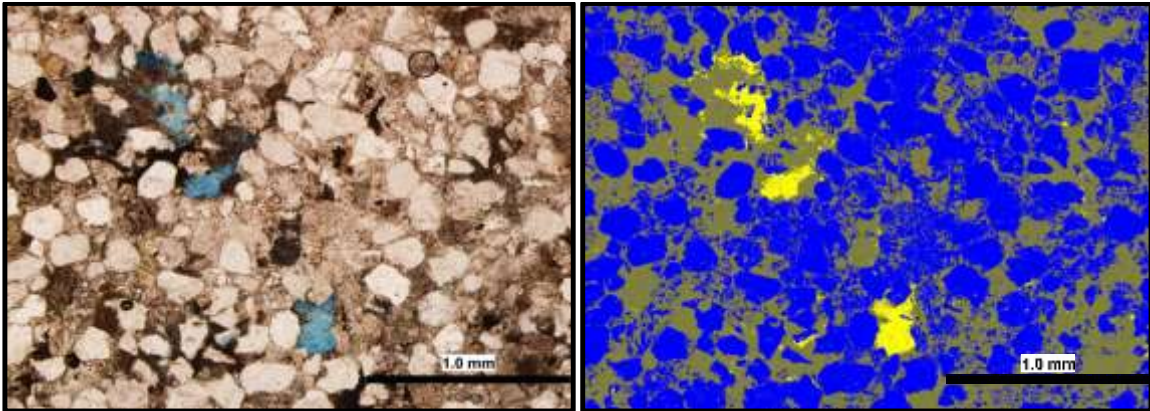


Figure L39: (Left) thin section image GW107-2013TK-7 (@ 5X) in normal light with porosity shown in blue (dye). (Right) same image, but with porosity shown in yellow, grains as blue and cement as brown.

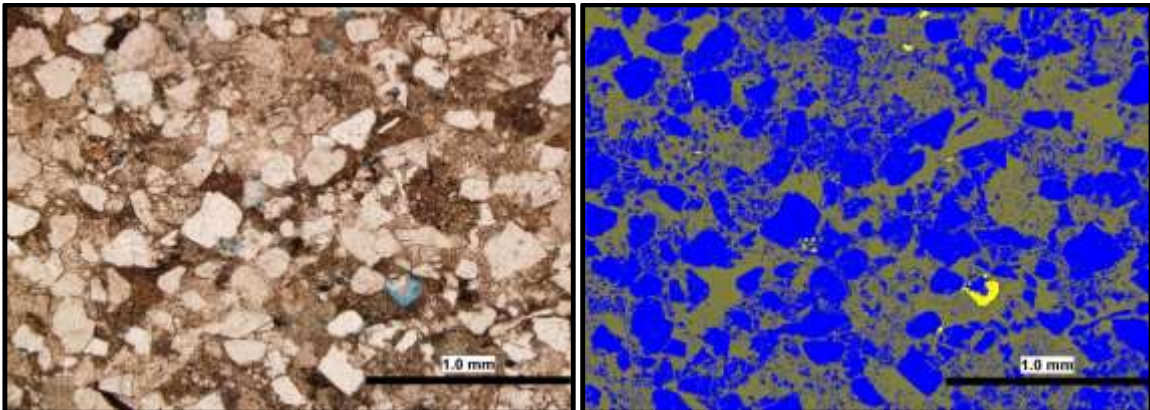


Figure L40: (Left) thin section image GW107-2013TK-8 (@ 5X) in normal light with porosity shown in blue (dye). (Right) same image, but with porosity shown in yellow, grains as blue and cement as brown.

Sample: GW107-2013TK Continued...

Table L5: Summary table for sample GW107-2013TK listing the area percentage for voids, grains and cement in each image captured of the thin section. The average area for each of the three parameters is also calculated.

Image Number	Area Type	Area %
GW107-2013TK-1	Voids	0.5
	Grains	69.4
	Cement	30.1
GW107-2013TK-2	Voids	1.0
	Grains	70.9
	Cement	28.1
GW107-2013TK-3	Voids	0.9
	Grains	66.4
	Cement	32.6
GW107-2013TK-4	Voids	0.7
	Grains	55.4
	Cement	43.9
GW107-2013TK-5	Voids	0.6
	Grains	67.4
	Cement	31.9
GW107-2013TK-6	Voids	0.7
	Grains	52.9
	Cement	46.3
GW107-2013TK-7	Voids	2.1
	Grains	53.6
	Cement	44.3
GW107-2013TK-8	Voids	0.3
	Grains	40.5
	Cement	59.2
Average	Voids	0.9
	Grains	59.6
	Cement	39.6

Sample: GW108-2013TK

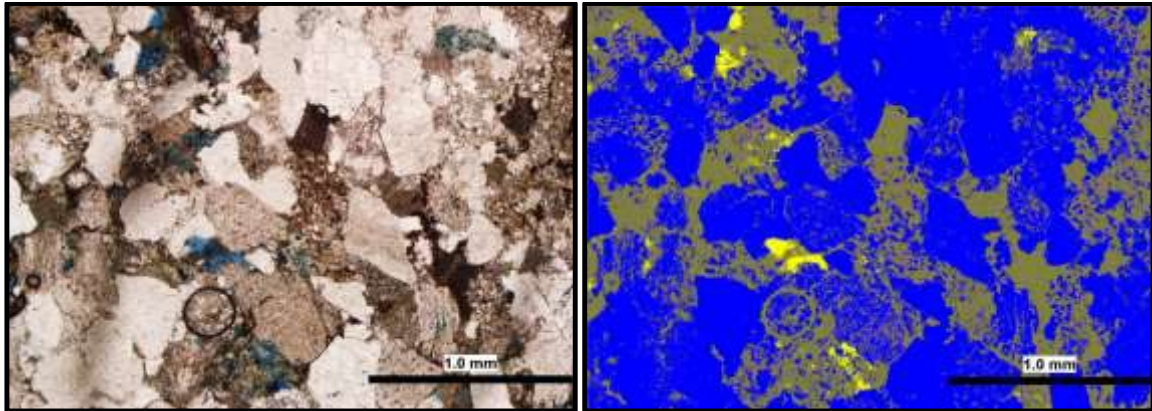


Figure L41: (Left) thin section image GW108-2013TK-1 (@ 5X) in normal light with porosity shown in blue (dye). (Right) same image, but with porosity shown in yellow, grains as blue and cement as brown.

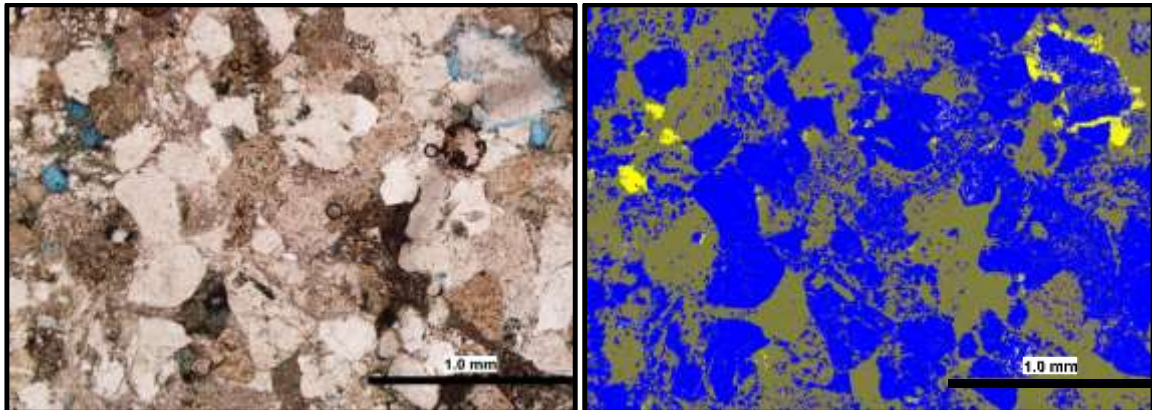


Figure L42: (Left) thin section image GW108-2013TK-2 (@ 5X) in normal light with porosity shown in blue (dye). (Right) same image, but with porosity shown in yellow, grains as blue and cement as brown.

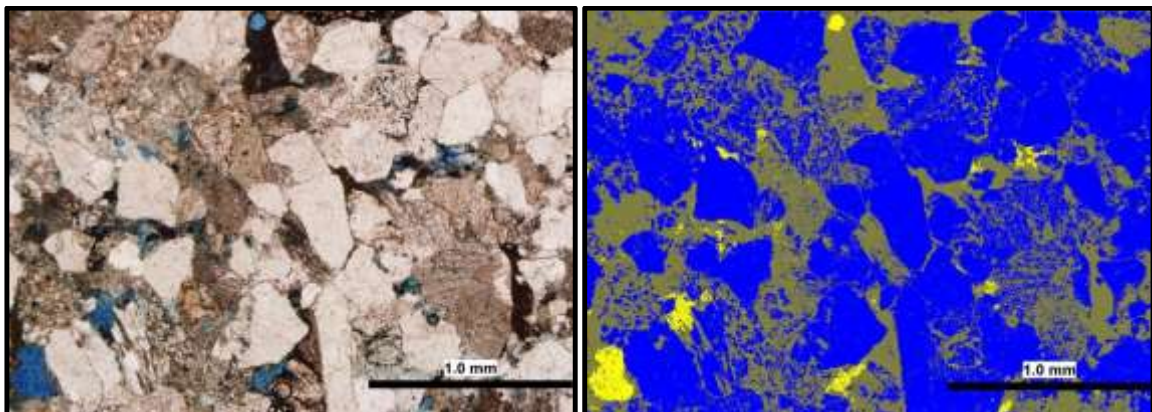


Figure L43: (Left) thin section image GW108-2013TK-3 (@ 5X) in normal light with porosity shown in blue (dye). (Right) same image, but with porosity shown in yellow, grains as blue and cement as brown.

Sample: GW108-2013TK Continued...

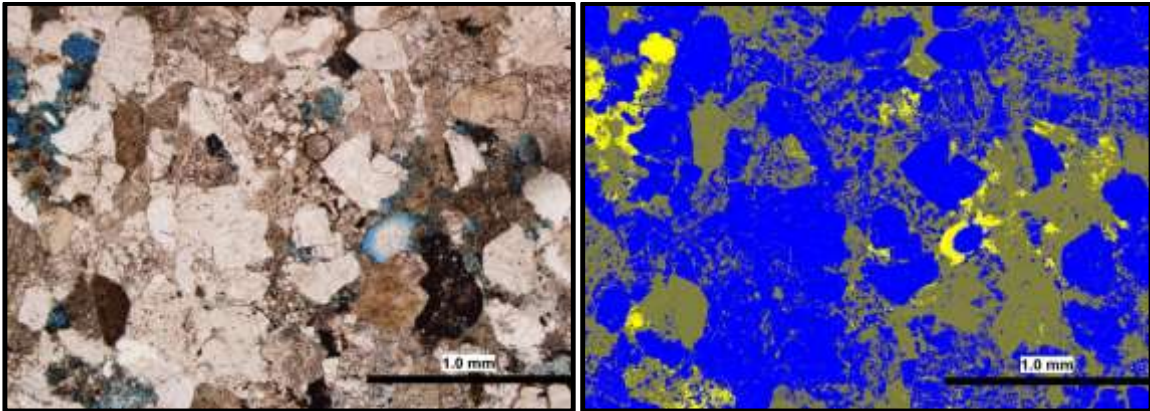


Figure L44: (Left) thin section image GW108-2013TK-4 (@ 5X) in normal light with porosity shown in blue (dye). (Right) same image, but with porosity shown in yellow, grains as blue and cement as brown.

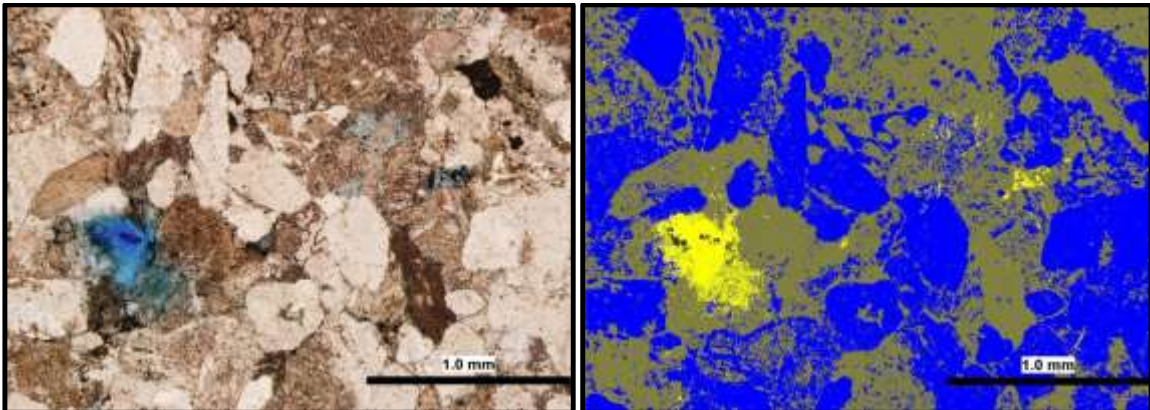


Figure L45: (Left) thin section image GW108-2013TK-5 (@ 5X) in normal light with porosity shown in blue (dye). (Right) same image, but with porosity shown in yellow, grains as blue and cement as brown.

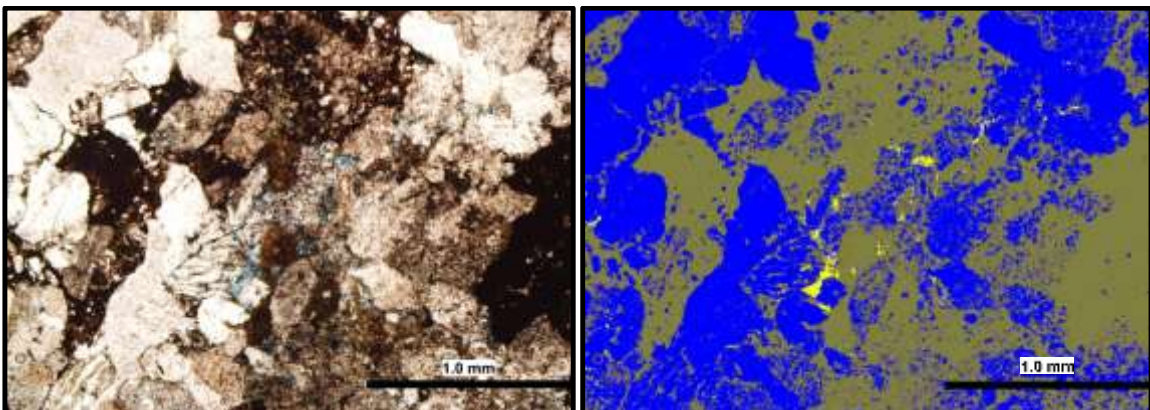


Figure L46: (Left) thin section image GW108-2013TK-6 (@ 5X) in normal light with porosity shown in blue (dye). (Right) same image, but with porosity shown in yellow, grains as blue and cement as brown.

Sample: GW108-2013TK Continued...

Table L6: Summary table for sample GW108-2013TK listing the area percentage for voids, grains and cement in each image captured of the thin section. The average area for each of the three parameters is also calculated.

Image Number	Area Type	Area %
GW108-2013TK-1	Voids	1.3
	Grains	69.9
	Cement	28.8
GW108-2013TK-2	Voids	1.3
	Grains	54.7
	Cement	44.0
GW108-2013TK-3	Voids	1.9
	Grains	59.0
	Cement	39.2
GW108-2013TK-4	Voids	3.5
	Grains	58.0
	Cement	38.5
GW108-2013TK-5	Voids	3.1
	Grains	47.5
	Cement	49.4
GW108-2013TK-6	Voids	0.9
	Grains	49.4
	Cement	49.7
Average	Voids	2.0
	Grains	56.4
	Cement	41.6

Appendix M: Measured Sections near Coal Mine Point

This material originally appeared in my MEng thesis document:

Kelly, T.B. 2013. Reservoir Performance and Architecture of a Fluvial Meanderbelt System, Joggins Formation, Nova Scotia. MEng Thesis, Department of Engineering, Dalhousie University, Halifax, Nova Scotia.

The measured sections are useful for providing hand sample locations

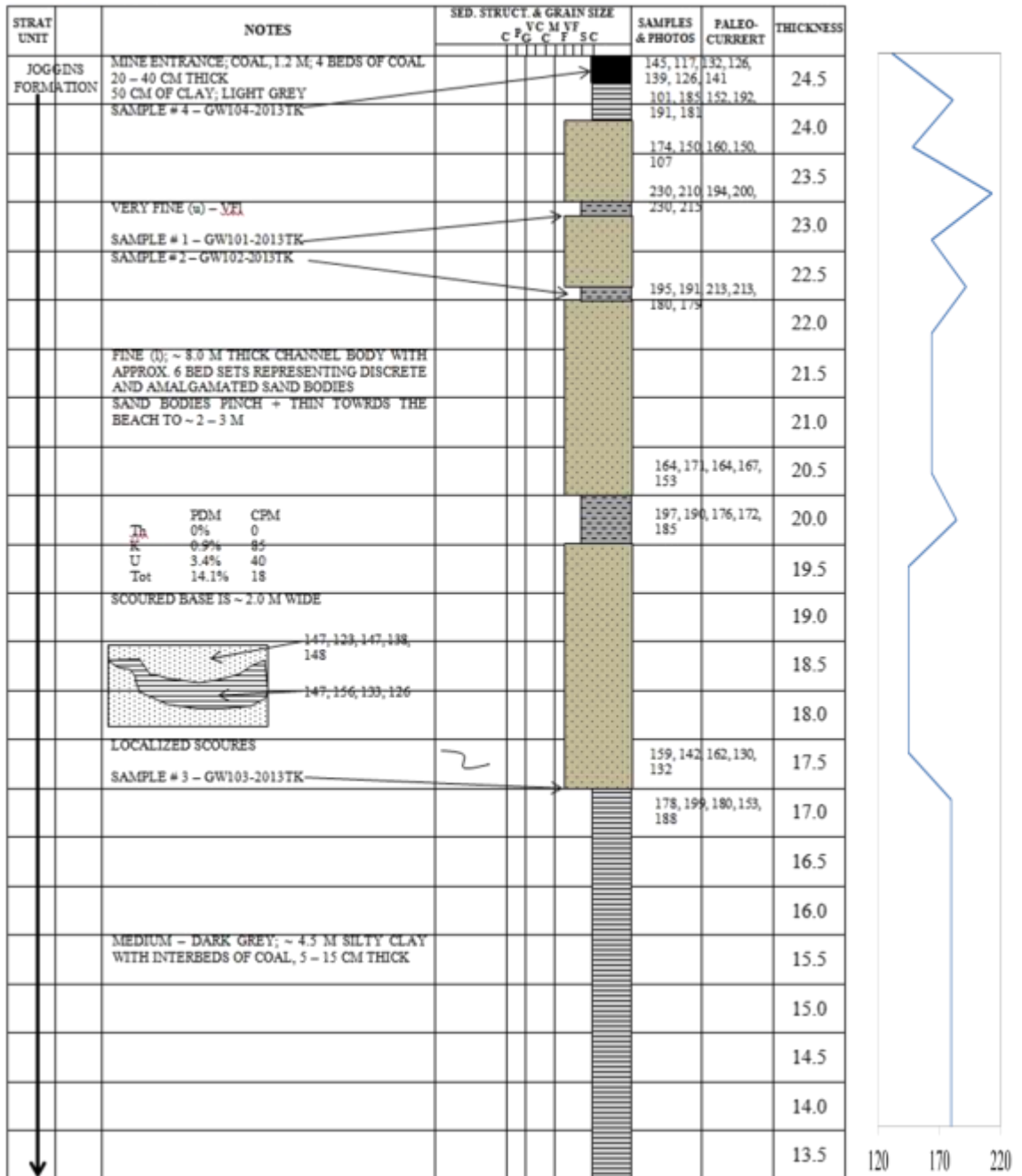


Figure M1: Measured section along the Fundy Coal Seam and Fundy Forest at Joggins. Gamma-ray readings were recorded at various points along this portion of the section and the corresponding plot is to the right of the section.

STRAT UNIT	NOTES	SED. STRUCT. & GRAIN SIZE						SAMPLES & PHOTOS	PALEO-CURRENT	THICKNESS
		C	P	V	M	F	SC			
										13.0
										12.5
										12.0
										11.5
	INTERBEDDED, 3.0 M F _A SANDSTONE WITH SMALL (3.0 CM) BLOCKY SILTSTONE VF (I); SOME SMALL 4.0 CM SILTSTONE NODULES									11.0
										10.5
										10.0
										9.5
	1.5 M FINE (a) – MED (a) SST; MASSIVE									9.0
										8.5
										8.0
	1.3 – 1.5 BROWNISH DARK GREY FISSILE ORGANIC-RICH									7.5
										7.0
	50 CM DIAM LYCOPSID TREE; 30 CM HIGH; ROOTED IN FISSILE ORGANIC-RICH SILTSTONE									6.5
										6.0
	2.0 M OF FINE (I) SANDSTONE WITH BEDS THAT ARE 20 – 30 CM THICK									5.5
										5.0
										4.5
										4.0
										3.5
										3.0
										2.5
										2.0

Figure M1: Continued....

LOCATION: Joggins – Fundy Coal Seam + Fundy Forest
 DATE: Thursday May 30th, 2013

PAGE: 3 of 3
 GEOLOGIST: Grant Wach + Trevor Kelly

STRAT UNIT	NOTES	SED. STRUCT. & GRAIN SIZE						SAMPLES & PHOTOS	PALEO- CURRERT	THICKNESS
		C	P	VC	M	VF	SC			
↓	MEDIUM TO DARK GREY FISSILE CLAY + SILT WITH SILTSTONE NODULES (UP TO 10 CM SIZE) WITH ORGANIC DETRITUS	○					○			1.5
							○			1.0
							○			0.5
							○			0.0

Figure M1: Continued....

STRAT UNIT	NOTES	SED. STRUCT. & GRAIN SIZE							SAMPLES & PHOTOS	PALEO-CURRENT	THICKNESS
		C	P	G	C	F	S	C			
JOGGINS FORMATION											12.0
											11.5
											11.0
											10.5
	4 – 6 M THICK MASSIVE + BLOCKY										10.0
	Mi – Fu SANDSTONE; MULTI-STORY CHANNEL BODY – VAGUE BED BOUNDARIES; 1 – 2.5 M AT BASE; BECOMING 50 CM TO 30 CM AT UNIT TOP										9.5
											9.0
											8.5
	SAMPLE # 6 – GW106-2013TK								116, 120, 121, 118, 122, 113, 121, 112		8.0
									176, 180, 182, 176, 166, 183		7.5
									144, 162, 137, 158, 153, 139, 155		7.0
	SAMPLE # 5 – GW105-2013TK								160, 153, 143, 148, 155, 153, 166		6.5
									149, 162, 155, 153, 166, 144, 163		6.0
	FLASSY INTERBEDDED SANDSTONE WITH THIN SAND/SILT; F-M-FI+VFu-VFI;										5.5
	SCoured CHANNELS DOWNCUTTING 1.5 M X 10 M WIDE – ABANDONED;										5.0
	INFILLED WITH THIN SILTSTONE AND V. FINE SANDSTONE + CLAYSTONE										4.5
											4.0
											3.5
	3.5 M OF DARK GREY FISSILE TO SMALL BLOCKY SILT + CLAY WITH THIN 10 – 15 CM VERY FINE SANDSTONE;										3.0
	LIGHT GREY WITH SOME IRON STAINING; SOME YELLOW STAINING										2.5
											2.0
											1.5
											1.0

Figure M2: Measured section at Hardscrabble Point/Coal Mine Point at Joggins.

LOCATION: Joggins – Hardscrabble Point/Coal Mine Point
 DATE: Friday May 31st, 2013

PAGE: 2 of 2
 GEOLOGIST: Grant Wach + Jillian Haynes

STRAT UNIT	NOTES	SED. STRUCT. & GRAIN SIZE							SAMPLES & PHOTOS	PALEO- CURRENT	THICKNESS
		C	P	G	C	F	S	C			
↓											0.5
	BASE/TOP OF SANDSTONE										0.0

Figure M2: Continued....